2023 DOE BES Synthesis and Processing Science Principal Investigators' Meeting

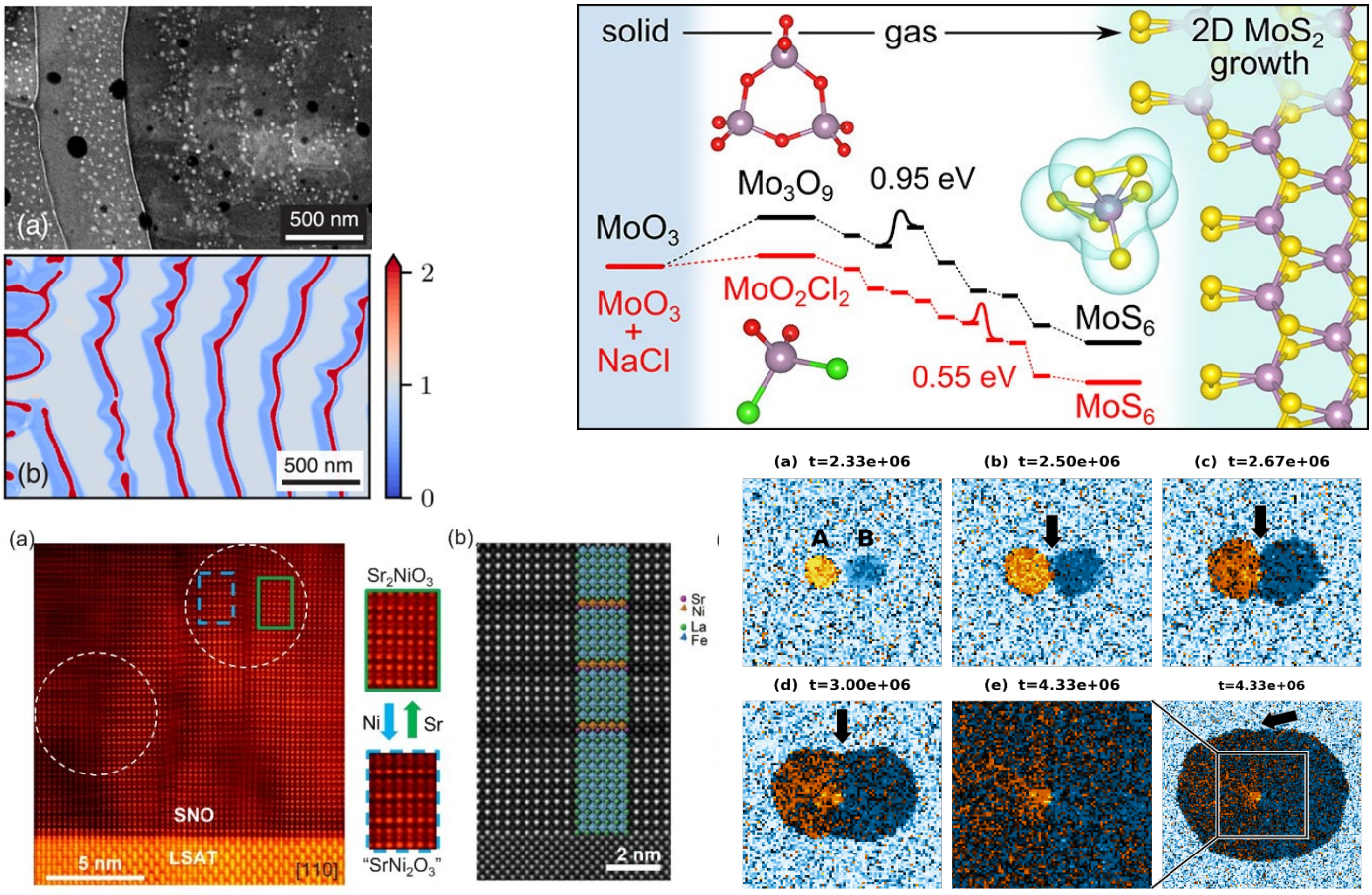

Meeting July 11-13, 2023

U.S. DEPARTMENT OF ENERGY | Office of Science

Office of Basic Energy Sciences Synthesis and Processing Science Division

On the Cover

Top Left: Dynamic transmission electron microscopy image (left) and phase-field simulation (right) of a banded microstructure formed during rapid solidification of an Al-9wt.%Cu alloy thin film. These results help to explain how far-from-equilibrium growth conditions characteristic of 3D metal printing (i.e., additive manufacturing) produce novel microstructures. *Phys. Rev. Lett.*, 2023, 130:026203 (Courtesy of Amy Clarke, Colorado School of Mines, and Alain Karma, Northeastern University)

Top Right: Schematic comparison of the gas phase reactions for salt-assisted and saltless growth of MoS_2 emphasizing the reduction of the critical barrier with the inclusion of salt. The sulfurization of molybdenum *oxyhalides* MoO_2X_2 (X = F, Cl, Br, and I), was found to display much lower activation barriers than that of molybdenum *oxide* in conventional "saltless" growth of MoS_2. *ACS Nano* **15**, 10525-10531 (2021) and *JACS* **144**, 7497-7503 (2022). (Courtesy of Boris Yakobson, Rice University).

Bottom Left: Metastable forms of complex nickelates revealed by scanning transmission electron microscopy: a) Spontaneous phase segregation occurs during the deposition of pure $SrNiO_3$ (SNO) thin films on perovskite oxide substrates by molecular beam epitaxy (left). Two co-existing oxygen-deficient phases, Sr_2NiO_3 and $SrNi_2O_3$, form to balance the material's stoichiometry and stabilize the energetically preferred Ni^{2+}. b) By using interface engineering, $SrNiO_3$ can be stabilized in the $(SrNiO_3)_m/(LaFeO_3)_n$ superlattices, but only at the thickness of a single SNO unit cell (m = 1) level (right). *Sci. Adv.* 7, eabe2866 (**2021**) (Courtesy of Yingge Du, Pacific Northwest National Laboratory)

Bottom Right: Simulation results of the growth of a single *d*-QC from two seeds, labelled A and B in (a), with 6° initial misorientation. Images of aperiodic {10000} plane show LGOs of *d*-QC grains at various time-steps. Data are coarse-grained such that one pixel represents ~20 particles. Contiguous regions of white are the liquid. Arrows point to GB groove. (Courtesy of Ashwin Shahani and Sharon Glover, University of Michigan, Ann Arbor)

FOREWORD

This abstract book comprises the scientific content of the 2023 Synthesis and Processing Science Principal Investigators' Meeting sponsored by the U.S. Department of Energy, Office of Science, Office of Basic Energy Sciences, Materials Sciences and Engineering (MSE) Division. The meeting, held on July 11–13, 2023, at the Hilton Rockville, Rockville, Maryland, is the eighth principal investigators' meeting on this topic and is one among a series of research theme-based principal investigators' meetings being held by the MSE division. This meeting is the first for the program since 2019 due to the COVID-19 pandemic, during which time the field, and the program, has undergone several changes.

The purpose of this principal investigators' meeting is to bring together all the principal investigators funded in the Synthesis and Processing Science core research area (CRA) so they can get a firsthand look at the broad range of materials science research being supported. The meeting will serve as a forum for the discussion of new results and research highlights, thus fostering a greater awareness of significant new advances in the field and the research of others in the program. Additionally, there will be two focused discussions to address the state of experimental and computational approaches in advancing synthesis science. The confidential and collegial meeting environment is intended to provide unique opportunities to develop new collaborations among PIs, and new ideas. In addition, the meeting affords BES program managers an opportunity to assess the state of the entire program at one time on a periodic basis, identifying programmatic needs and new research directions.

This year's meeting focuses on four topics within the Synthesis and Processing Science portfolio that align with the Basic Research Needs (BRNs) workshops and roundtables: The role of local and long-range forces to direct synthesis, AI/ML driven materials discovery, metastable intermediate states for synthesis of complex materials, and the synthesis science underlaying advanced manufacturing. These four complementary topics relying on a foundational understanding of the competition of kinetics, thermodynamics, and atomic diffusion made available through theory, computation, and in situ characterization. The meeting will also highlight the importance of synthesis science regarding recently funded projects responsive to topical Funding Opportunity Announcements (FOAs)

Let me take this opportunity to express my thanks to all the meeting attendees for their active participation and sharing their ideas and new research results. Special thanks are given to the Meeting Chairs, Julia Chan and Gerbrand Ceder, for their service to the program, understanding of the current state of the field, and assistance in organizing the meeting. Finally, this meeting would not be possible without the logistical support from Teresa Crockett at DOE-BES-MSE as well as Tia Moua and staff at Oak Ridge Institute for Science and Education (ORISE).

James Dorman

Program Manager, Synthesis and Processing Science
Materials Sciences and Engineering Division
Office of Basic Energy Sciences
Office of Science
U.S. Department of Energy

Table of Contents

Agendas

2023 DOE BES Synthesis and Processing Science Principal Investigators' Meeting

Meeting Chairs: Julia Chan (Baylor University) and Gerbrand Ceder (Lawrence Berkeley National Laboratory)

All times are Eastern Time

Day 1 – Tuesday July 11th, 2023

8:00-9:00	Breakfast
9:00-9:15	Welcome and Materials Science and Engineering Division Update **Andrew Schwartz,** Division Director, MSED, DOE/BES
9:15-9:30	Introductory Remarks from **James Dorman** Program Manager, BES Synthesis and Processing Sciences

Session 1 – Targeted FOAs and New Programs (Chair: Peter Sushko – Pacific Northwest National Laboratory)

9:30-9:50	**Mariana Bertoni** – Arizonia State University Acoustic Modification of Crystallization and Dislocation Dynamics in Energy Materials
9:50-10:10	**Michael Whitaker** – Lawrence Berkeley National Laboratory MINES – Minerals for Energy Storage Synthesis
10:10-10:30	**Shuolong Yang** – University of Chicago Electric field driven precision material synthesis
10:30-11:00	Break
11:00-11:20	**Ryan Comes** – Auburn University In Situ Studies of Charge Transfer Phenomena in Complex Oxide Heterostructures
11:20-11:40	**Nicholas Gaillard** – University of Hawaii Two-Dimensional Materials for Thin Film and Interface Manipulation in Solar Energy Conversion Devices
11:40-12:00	**Rebecca Lindsey** – University of Michigan ChIMES: Enabling an Agile Atomistic Simulation Capability for Complex, Inherently Multiscaled Systems

Working Lunch

12:10-12:40	**Julia Mundy** – Harvard University Synthesis of layered square planar nickelates
12:40-1:30	**Julia Chan** – Experimental Challenges in Synthesis Science Discussion

Session 2 – Local and Long-Range Forces in Synthesis Science (Chair: Kai Xiao – Oak Ridge National Laboratory)

1:30-2:00	**Bharat Jalan** – University of Minnesota Navigating Atomically-Precise Synthesis of Functional Oxides using Source Chemistry
2:00-2:30	**Alex Martinson** – Argonne National Laboratory Selective Interface Synthesis: Directing Atomic Structure at Defective Interfaces
2:30-3:00	**Rachel Goldman** – University of Michigan A Unified Model for Epitaxy of Metastable Crystal Polytypes at the Nanoscale
3:00-3:30	Break
3:30-4:00	**Paulette Clancy** – Johns Hopkins University Formulation Engineering of Energy Materials via Multiscale Learning Spirals
4:00-4:30	**Chang-Beom Eom** – University of Wisconsin, Madison Synthesis of Electronic-Grade Quantum Heterostructures by Hybrid PLD
4:30-5:00	**Haiyan Wang** – Purdue University Achieving Long Range Ordering in Oxide-Metal Hybrid Materials —A Combined Experimental and Modeling Approach

Working Dinner

6:00-8:00	**Poster Session 1**

Day 2 – Wednesday July 12th, 2023

8:00-9:00	**Breakfast**

Session 3 – Computational Synthesis Science (Chair: Anter El-Azab – Purdue University)

9:00-9:30	**Jun Liu** – Pacific Northwest National Laboratory Molecularly Organized Nanostructured Materials
9:30-10:00	**Liping Yu** – University of Maine Descriptor-enabled high-entropy materials design and discovery
10:00-10:30	**Bin Lin** and **Jeffrey Comer –** Kansas State University Boron-Rich Compounds for Applications in High-Density Energy Conversion Devices
10:30-11:00	Break
11:00-11:30	**Qiang (David) Wang** – Colorado State University PSCF+ and What We Have Done with It
11:30-12:00	**Jianwei Sun** – Tulane University Synergistical computational and experimental study of synthesis mechanism and discovery of complex layered magnetic quantum materials

Working Lunch

12:10-12:40	**Wenhao Sun** – University of Michigan The role of temperature in solid-state ceramic synthesis
12:40-1:30	**Gerbrand Ceder** – Discussion

Session 4 – Synthesis Pathways and Intermediates (Chair: Zhiqiang Mao – Penn State University)

1:30-2:00	**Mark Ediger** – University of Wisconsin, Madison Structure and stability of multicomponent vapor-deposited organic glasses
2:00-2:30	**Michael Tringides** – Ames National Laboratory Band structure tuning of 2-d intercalated quantum materials and nanographenes
2:30-3:00	**David Johnson** – University of Oregon A Mechanistic Approach to Solid State Synthesis by Controlling Interfacial Reactions in Designed Precursors
3:00-3:30	Break
3:30-4:00	**James DeYoreo** – Pacific Northwest National Laboratory Nucleation and Self-Assembly of Hierarchical Materials: Predicting Pathways, Dynamics, and Outcomes
4:00-4:30	**Chris Palmstrøm** – University of California, Santa Barbara Integrated Materials Platform for Topological Quantum Computing Devices
4:30-5:00	**Lynden Archer** – Cornell University Electrodeposition of metals in viscoelastic liquid electrolytes

Working Dinner

6:00-8:00	**Poster Session 2**

Day 3 – Thursday July 13th, 2023

8:00-9:00	**Breakfast**

Session 5 – Advanced Manufacturing (Chair: Andrei Fedorov – Georgia Tech)

9:00-9:30	**Atieh Moridi** – Cornell University Leveraging metastability in high entropy alloy design for grain refinement in additive manufacturing
9:30-10:00	**Andrei Fedorov** – Georgia Tech Radiolytic Redox Interplay Defines E-Beam Direct-Writing of Nanomaterials in Liquids
10:00-10:30	**Amy Clarke** – Colorado School of Mines and **Alain Karma** – Northeastern University In-situ Visualization of Microstructure Evolution in Metallic Alloys under Additive Manufacturing Conditions
10:30-11:00	**James Engstrom** – Cornell University Extending the reach and breadth of nanofabrication to atomic-scale precision in three dimensions

11:00-11:30	**Amit Naskar** – Oak Ridge National Laboratory Exploration and Design of Architected Polymers and Properties for Additive Manufacturing
11:30-12:00	Closing remarks – **James Dorman**

Poster Session Schedule

Tuesday July 11th, 6-8 pm

First Name	Last Name	Institution
Lynden	Archer	Cornell University
Michael	Arnold	University of Wisconsin-Madison
Scott	Auerbach	University of Massachusetts, Amherst
Stacey	Bent	Stanford University
Mariana	Bertoni	Arizona State University
Ksenia	Bets	Rice University
Ivan	Bozovic	Brookhaven National Laboratory
Gerbrand	Ceder	Lawrence Berkeley National Laboratory
Julia	Chan	Baylor University
Zhe	Cheng	Florida International University
Paulette	Clancy	Johns Hopkins University
Amy	Clarke	Colorado School of Mines
Jeffrey	Comer	Kansas State University
Ryan	Comes	Auburn University
Paul	Crowell	University of Minnesota
James	De Yoreo	Pacific Northwest National Laboratory
Volkmar	Dierolf	Lehigh University
Yingge	Du	Pacific Northwest National Laboratory
Mark	Ediger	University of Wisconsin-Madison
Anter	El-Azab	Purdue University
James	Engstrom	Cornell University
Chang-Beom	Eom	University of Wisconsin-Madison
Wei	Fan	University of Massachusetts Amherst

Andrei	Fedorov	Georgia Institute of Technology
Kristen	Fichthorn	Pennsylvania State University
Sergey	Frolov	University of Pittsburgh
Nicolas	Gaillard	University of Hawaii
Rachel	Goldman	University of Michigan
Sumner	Harris	Oak Ridge National Laboratory
Ryan	Hartman	New York University
Rigoberto	Hernandez	Johns Hopkins University
Jennifer	Hoffman	Harvard University
Jinwoo	Hwang	Ohio State University
Himanshu	Jain	Lehigh University
Bharat	Jalan	University of Minnesota
David	Johnson	University of Oregon
Alain	Karma	Northeastern University
Tiffany	Kaspar	Pacific Northwest National Laborabory
Carolyn	Koh	Colorado School of Mines
Benjamin	Legg	Pacific Northwest National Laboratory
Dongsheng	Li	Pacific Northwest National Laboratory
Rebecca	Lindsey	University of Michigan, Ann Arbor

Wednesday July 12th, 6-8 pm

Xi	Ling	Boston University
Jun	Liu	Pacific Northwest National Laboratory-University of Washington
Bin	Liu	Kansas State University
Zhiqiang	Mao	Pennsylvania State University
John	Marohn	Cornell University
Alex	Martinson	Argonne National Laboratory
Julia	Mundy	Harvard University
Badri	Narayanan	University of Louisville
Amit	Naskar	Oak Ridge National Laboratory
Eugene	Olevsky	San Diego State University
Jeremy	Palmer	University of Houston
Chris	Palmstrom	University of California, Santa Barbara
Michelle	Personick	Wesleyan University
Vlad	Pribiag	University of Minnesota
Jeffrey	Rimer	University of Houston
Brian	Rodgers	Colorado School of Mines
Alec	Saville	Colorado School of Mines
Linda	Schadler Feist	University of Vermont
Gurjyot	Sethi	University of Utah
Ashwin	Shahani	University of Michigan
Lior	Shani	University of Minnesota
Elizabeth	Sooby	University of Texas at San Antonio
Wenhao	Sun	University of Michigan Ann Arbor
Jianwei	Sun	Tulane University
Peter	Sushko	Pacific Northwest National Laboratory
Maria	Sushko	Pacific Northwest National Laboratory
Jinhui	Tao	Pacific Northwest National Laboratory

Lauren	Walters	Lawrence Berkeley National Laboratory
Qiang	Wang	Colorado State University
Xudong	Wang	University of Wisconsin-Madison
Haiyan	Wang	Purdue University
Le	Wang	Pacific Northwest National Laboratory
Hui	Wang	University of Louisville
Michael	Whittaker	Lawrence Berkeley National Laboratory
Kai	Xiao	Oak Ridge National Laboratory
Boris	Yakobson	Rice University
Shuolong	Yang	The University of Chicago
Judith	Yang	University of Pittsburgh
Liping	Yu	University of Maine
Francisco	Zaera	University of California
Guangwen	Zhou	Binghamton University

Laboratory
Abstracts

Atomic-layer-by-layer synthesis of oxide superconductors

Ivan Božović, Anthony T. Bollinger, and Xi He

Condensed Matter Physics and Materials Science Division, Brookhaven National Laboratory

Keywords: Molecular beam epitaxy, high-T_c superconductors

Research Scope

This program advances Synthesis and Processing Science by inventing and perfecting experimental techniques for (i) synthesis (e.g., atomic-layer-by-layer molecular beam epitaxy, combinatorial-spread epitaxy), (ii) processing (e.g., ozone annealing, electrolyte gating, and protonation), (iii) *in-situ* characterization (e.g., time-of-flight ion scattering and recoil spectroscopy; the analysis of dynamics of electron diffraction patterns; integrating MBE synthesis with *in-situ* angle-resolved photoelectron spectroscopy, scanning tunneling microscopy, low-energy electron microscopy, transport, and magnetic measurements), and (iv) patterning into micro- and nano-meter-scale devices (e.g., nanowires, nanorings, and tunnel junctions).

These exceptional experimental capabilities enable the synthesis of single-crystal thin films of various cuprates and other complex oxides, as well as heterostructures and superlattices with atomically smooth surfaces and interfaces. We engineer them down to a single atomic layer and beyond, customizing and optimizing the samples for the needs of a particular experiment.

Our unique samples make possible incisive and high-impact experiments that were not previously possible, in-house[1,2] or in collaboration with leading experimental groups elsewhere[3,4]. We are probing some of the most important open questions in Condensed Matter Physics, such as the microscopic origins of high-temperature superconductivity, electronic nematicity, and "strange metal" behavior. Guided by these new insights, we use atomic-layer engineering to create novel quantum materials and artificial superconductors[5]. This notably impacts research on strongly-correlated quantum materials with energy-relevant functional properties.

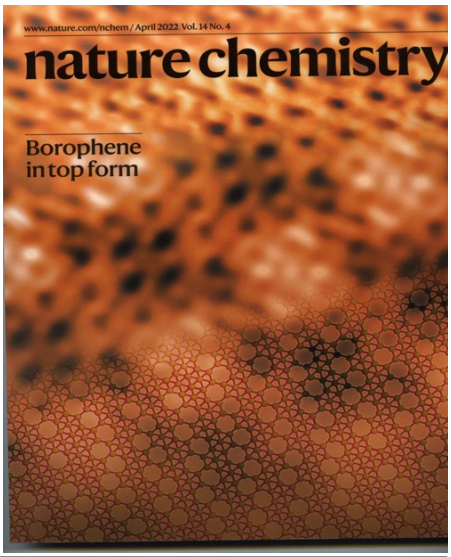

Figure 1. The atomic structure of borophene on Cu(100), based on LEED, STM, and ab initio

Recent Progress

1. Synthesis of a new quantum material: borophene on Cu(100) [*Nature Chemistry 2022*]

The discovery of graphene triggered research efforts worldwide and the quest for other quantum 2D materials that could host exotic quasiparticle excitations. By replacing carbon with other elements, several analogs of graphene, including silicene, germanene, stanene, etc., were synthesized. Boron does not form layered structures naturally, but theorists predicted that various 2D boron sheets, collectively called borophenes, may be epitaxially stabilized on metallic substrates. Since boron has one less electron than carbon, it is energetically more favorable

to add some extra boron atoms at the centers of hexagons. Different filling patterns are possible, and some of these structures are predicted to have similar energies, giving rise to polymorphism. Thus, by choosing the substrate and the synthesis conditions we engineer various borophene atomic structures and tailor their electronic properties. High- T_c superconductivity is anticipated, given the low atomic mass, the strong electron-phonon coupling, and the fact that MgB_2 is superconducting with $T_c \approx 40$ K.

A successful synthesis of borophene was first achieved on Ag(111) surfaces in the form of nanoflakes, way too small for transport measurements. Using the more adhesive Cu(111) substrate, we synthesized single-crystal borophene islands up to 100 μm^2 in size[5]. The (111) substrates were originally chosen because of their hexagonal symmetry. More recently, we chose a square-lattice Cu(100) surface, hoping to incommensurately modulate the adsorbed hexagonal boron lattice and alter the vacancy patterns. We synthesized large-scale, single-crystal borophene sheets using MBE. Combining LEED, high-resolution STM measurements, and *ab initio* density functional theory (DFT) calculations, we have deciphered the atomic structure of borophene on the Cu(100) surface (Figure 1**)**. DFT calculations showed four Dirac cones in the electron band structure. Some of these cones are anisotropic and tilted, possibly hosting type II Dirac and Weyl fermions.

2. ALL-MBE synthesis for quantum sensors. [*Nature Nanotechnology 2023*]

Superconducting nanowire single-photon detectors are critical for quantum computation, metrology, secure communication, single-molecule detection, remote sensing, and single-photon imaging. So far, they were all based on conventional superconductors with a low T_c, requiring bulky and costly cryocoolers. We used ALL-MBE to synthesize heterostructures comprised of a five unit-cells (UC) thick layer of La_2CuO_4 (LCO) grown on top of a 5 UC thick layer of $La_{1.55}Sr_{0.45}CuO_4$ (LSCO), grown on single-crystal $LaSrAlO_4$ substrates (Figure 2a). By electron-beam lithography, we define meandering nanowire structures (Figures 2b and 2c). In our LSCO-LCO heterostructures superconductivity is confined to a single CuO_2 monolayer, so the cross-section of our high-T_c nanowires is two orders of magnitude smaller than in prior art., enabling single-photon detection at the technologically-important telecom wavelength $l = 1.5$ μm.

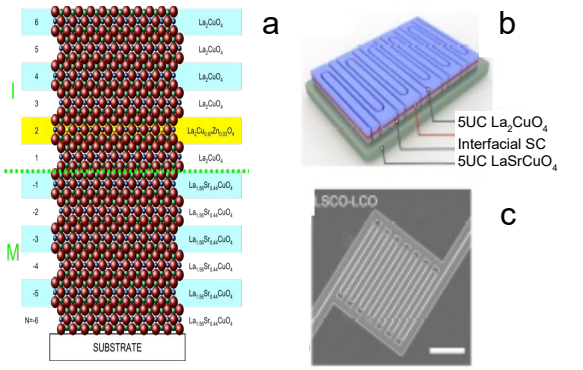

Figure 2. **a**, Schematic of the LSCO-LCO hetero-structure **b**, Schematic of a HTS nanowire. **c**, An SEM image of the fabricated device. The scale bar is 2 μm.

Future Plans

1. Probing the mystery of the demise of superconductivity in overdoped cuprates.

In cuprates, with increased doping, T_c first increases, reaches its maximum, then decreases to zero. This has been usually ascribed to the progressive weakening of the effective pairing interaction. In this case, one would expect the superfluid density $N_{s0} \equiv N_s(T \rightarrow 0)$ to be equal to the total carrier density n. However, in a study that took over a decade, we used ALL-MBE to synthesize over 2,000 LSCO films and showed that overdoped cuprates radically depart from this expectation: while n increases with doping, N_{s0} tracks T_c, decreases, and vanishes[1]. So far, this experimental fact has been a matter of much debate, and no consensus. To shed light on this puzzle, we plan

new experiments, including a study of resistivity, magnetoresistance, and the Hall effect in overdoped LSCO, as a function of the doping level tuned in minute increments. This is challenging since it requires meticulous MBE synthesis and suppression of oxygen vacancy formation; we will accomplish that by post-growth film processing (ozone annealing and electrochemical interdiffusion). Extending this study to other high-T_c cuprates, using the OASIS MBE module, we will synthesize thin films of various cuprate compounds, including LSCO, DBCO, different BSCCO phases (such as Bi2201, Bi2212, and Bi2223), $La_{2-x}Ba_xCuO_4$, and $(Sr,Ca,La)CuO_2$ (the so-called "infinite-layer cuprates"). We will study their electronic spectra resolved in inverse space by ARPES and in real space by SI-STM.

2. Probing the origins of electronic nematicity.

Electronic anisotropy (or 'nematicity') not expected from the crystal symmetry has been detected by various experimental techniques, in several families of cuprate superconductors. We observed it also in $La_{2-x}Sr_xCuO_4$ (LSCO) for $0.02 \leq x \leq 0.25$, using angle-resolved transverse resistance (ARTR) measurements, a sensitive and background-free characterization technique that can detect 0.5% anisotropy in transport[2]. Several important questions are still open, however. One is how big are domains with a single orientation of the nematic director. So far, no domain structure was detected, while the electronic anisotropy was observed on the mm scale. To address this puzzle, we will use ALL-MBE to synthesize single-crystal LSCO films doped to various levels and epitaxially constrained to be tetragonal. Using photolithography, we will pattern these films into many Hall bars of different widths (200 nm, 400 nm, …, 410 mm) spanning over three orders of magnitude. We will measure the longitudinal and transverse resistivity and study their dependence on the strip width, to reveal the existence of the domain structure (if any).

Next, in collaboration with J. Cerne (SUNY Buffalo) and N. P. Armitage (Johns Hopkins University), we will study second-harmonic generation (SHG) in LSCO films. SHG can detect electronic nematicity, which manifests via the rotation of the polarization of transmitted light (the Faraday rotation). This is a contactless technique, eliminating any artifacts that may originate from lithographic steps necessary for transport measurements. A preliminary result shown in Figure 3 reveals electronic nematicity in a tetragonal single-crystal LSCO film. Importantly, the effect persists at up to room temperature and high energies (in the mid-infrared region). We plan to extend such SHG measurements to a series of LSCO films synthesized by ALL-MBE, with the doping levels scanned across the phase diagram.

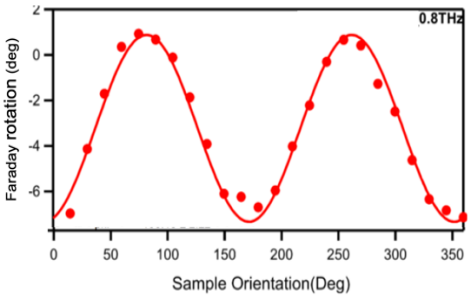

Figure 3. The Faraday rotation in an underdoped LSCO film.

3. Synthesis of HTS heterostructures and processing them on the nanoscale.

We will synthesize atomically precise S-I and S-I-S heterostructures, where S is an HTS cuprate and I is an insulator. Here, the main challenges to synthesis are that interfaces must be atomically sharp and perfect, the ultrathin (1-2 unit-cells thick) barrier layer must remain insulating and have no pinholes, and superconductivity should stay undiminished in the cuprate layers next to the interface. ALL-MBE is the only technique proven to meet these requirements. We will process such HTS heterostructures, patterning them down to the nanoscale. For this task, we have developed a new and unique *in situ* monitoring and diagnostic capability: Secondary ion mass spectrometry (SIMS) combined with ALL-MBE-enabled d-doping with an appropriate atomic

marker. Using this as an etch-stop indicator dramatically improves the accuracy of patterning. We will use HTS SIS sandwich junctions prepared in this way to perform the tunneling spectroscopy and reveal the spectroscopic signatures of the bosons that couple to the charge-carrying quasiparticles and mediate their pairing. In collaboration with D. Natelson (Rice University), we will study the shot noise[4] in such tunnel junctions to determine whether preformed pairs exist on the overdoped side. In collaboration with K. Berggren (MIT) and D. Bandurin (Singapore Technical University), we will fabricate LSCO and BSCCO nanowires for single-photon detection, extending their operation range further up in temperature and frequency.

4. Discovery of novel HTS quantum materials.

Discoveries of new superconductors trigger much excitement. For this quest, we are armed with unique technical capabilities, including the assembly of precise heterostructures and superlattices engineered down to the atomic-layer level. We can also leverage epitaxial strain and stabilization of meta-materials, interface-induced superconductivity, combinatorial (COMBE) search, as well as post-synthesis processing such as ozone annealing, electrolyte gating, and hydrogenation.

Recently, superconductivity was observed in $(Ba,K)SbO_3$. We will investigate various layered-perovskite antimonates, hoping to raise T_c further. In any case, high-quality films of these compounds would be of great interest for studying their physical properties by a range of techniques and groups. We plan to investigate also $Ba_3LaBi_2O_9$, an artificially layered material we synthesized earlier. BiO_2 layers should be hole-doped by electron transfer to the LaO layers. The latter should isolate pairs of coupled, conductive BiO_2 layers from one another, making this metastable compound a quasi-2D metal and superconductor, potentially with nontrivial topology. We demonstrated that $Ba_3LaBi_2O_9$ could be made metallic, but it showed no superconductivity because a competing CDW instability develops below 60 K. We will try to suppress this CDW, hoping for superconductivity to emerge. Next, we started experimenting with layered perovskites based on Zn and Co, such as $(La,Sr)_2ZnO_4$ and $(La, Sr)_2CoO_4$ with the "214" structure. We will use the undoped parent compounds, La_2ZnO_4 and La_2CoO_4, for the insulating barrier layers in SIS heterostructures, with S = LSCO, DBCO, or BSCCO. We will also try doping $(La,Sr)_2ZnO_4$ and $(La,Sr)_2CoO_4$, or their higher-*n* relatives (Ruddledsen-Popper phases), and check whether they may become superconducting. Finally, we will continue the synthesis and exploration of novel quasi-2D quantum materials, such as borophene, borophane (hydrogenated borophene), and other light-metal hydrides.

References

1. I. Božović, J. Wu, X. He, and A. T. Bollinger, *Dependence of critical temperature in overdoped copper oxides on superfluid density,* Nature **536**, 309 (2016).
2. J. Wu, A. T. Bollinger, X. He, and I. Božović, *Spontaneous breaking of rotational symmetry in copper oxide superconductors*, Nature **547**, 432 (2017).
3. P. Giraldo-Gallo, J. A. Galvis, Z. Stegen, K. A. Modic, F. F Balakirev, J. B. Betts, X.-J. Lian, C. Moir, S. C. Riggs, J. Wu, A. T. Bollinger, X. He, I. Bozovic, B. J. Ramshaw, R. D. McDonald, G. S. Boebinger and A. Shekhter, Scale-invariant *magnetoresistance in the strange metal phase of a cuprate superconductor*, Science **361**, 479 (2018).
4. P. Zhou, L. Chen, Y. Liu, I. Sochnikov, A. T. Bollinger, M.-G. Han, Y. Zhu, X. He, I. Božović, and D. Natelson, *Electron pairing in the pseudogap state revealed by shot noise in copper-oxide junctions,* Nature **572**, 493 (2019).
5. R. Wu, I. K. Drozdov, S. Eltinge, P. Zahl, S. Ismail-Beigi, I. Božović, and A. Gozar, *Large-area single-crystal sheets of borophene on Cu(111) surfaces*, Nature Nanotechnology **14**, 44 (2019).

Publications

1. I. Charaev, D. A. Bandurin, A. T. Bollinger, I. Y. Phinney, I. Drozdov, M. Colangelo, B. Butters, T. Taniguchi, K. Watanabe, X. He, I. Božović, P. Jarillo-Herrero, and K. K. Berggren, *Single-photon detection using high-temperature cuprate superconductors*, Nature Nanotechnology **18**, 343 (2023).
2. J. Wu and I. Božović, *Superconductivity in a strange metal*, Science Bulletin **68**, 851 (2023).
3. J. Wardh, M. Granath, J. Wu, A. T. Bollinger, X. He and I. Božović, *Nematic superconducting phase fluctuations in copper oxide*, under revision in Proc. Natl. Acad. Sci. USA Nexus (2023). https://doi.org/10.48550/arXiv.2203.06769
4. A. Gozar, R. Wu, and I. Božović, *Quo Vadis, Borophene,* Nano Today **50**, 101856 (2023).
5. X. He, X. Xu, X. Shi, and I. Božović, *Optimization of $La_{2-x}S_{rx}CuO_4$ Single Crystal Film Growth via Molecular Beam Epitaxy*, *Condens. Matter **8**,* 13 (2023).
6. R. Wu, S. Eltinge, I. K. Drozdov, A. Gozar, P. Zahl, J. T. Sadowski, S. Ismail-Beigi, and I. Božović, *Borophene on Cu(100) surface*, Nature Chemistry **14**, 377 (2022).
7. I. Božović, *Doubling-down on borophene electronics*, Nature Materials **21**, 11 (2022).
8. R. Wu, Z. Wu and I. Božović, *Two-dimensional Mg-Cu Intermetallic Compounds with Nontrivial Band Topology and Nodal Dirac Lines*, Advanced Electronic Materials 2100927 (2021).
9. I. Božović, *An unstable pathway to room temperature superconductivity?,* Proc. Natl. Acad. Sci. USA (PNAS) 118, e2111471118 (2021).
10. Y. Shen, J. Sears, G. Fabbris, J. Li, J. Pelliciari, I. Jarrige, X. He, I. Božović, M. Mitrano, J. Zhang, J. F. Mitchell, A. S. Botana, V. Bisogni, M. R. Norman, S. Johnston, and M. P. M. Dean, *Role of Oxygen States in the Low Valence Nickelate $La_4Ni_3O_8$*, Phys. Rev. X **12**, 011055 (2022).

Rationalizing Inorganic Synthesis through Synergistic Text-Mining, Simulation, and Experiment

Gerbrand Ceder, Anubhav Jain, Carolin M. Sutter-Fella, Kristin A. Persson, Haimei Zheng

Keywords: Inorganic synthesis, text mining, machine learning, DFT, nanoparticles

Research Scope

Understanding complex synthesis processes through data-driven methods requires a wealth and diversity of data sources. Direct experiment, atomistic modeling and simulation, and large-scale text mining of the scientific literature each lend unique advantages to this investigation, but each have individual disadvantages that limit their utility when used alone (e.g. experimental cost, computational intractability,[1] inconsistent writing styles or missing synthesis information from the literature, etc.). In tandem, these methods together can offer important insights into various synthesis reaction mechanisms. For this work, we focus on our methods to build comprehensive datasets from literature and simulation to study the syntheses of gold nanoparticles and $BiFeO_3$ thin films. These combined data-driven methods offer unique insights for a variety of synthesis environments and our works highlight their successes in this new synthesis science paradigm.

Recent Progress

As it is a relatively new subfield in the materials and chemical sciences, we summarize our current text-mining capabilities and existing datasets mined from the literature. Several datasets for this effort are shown in Figure 1. In this multi-faceted approach, we highlight the synergy of text mining, experiment, and modeling through two material case studies: gold nanoparticle (AuNP) and sol-gel $BiFeO_3$ thin film syntheses. To better understand the control of AuNP morphology, we used machine learning of text mined syntheses to train a decision tree that reflects existing knowledge in the field for morphology control based on the choice and amount of seed capping agent for seed-mediated growth.

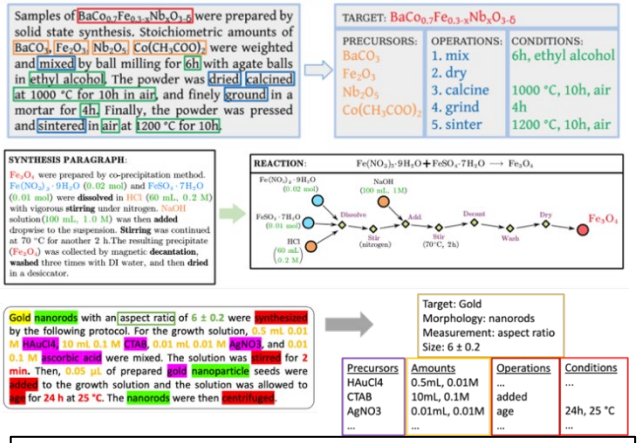

Figure 1. Large-scale text-mined datasets have been curated manually and through automated methods: 40k solid-state recipes, 22k hydrothermal recipes, 19k precipitation recipes, 11k sol-gel recipes, 8k AuNP recipes.

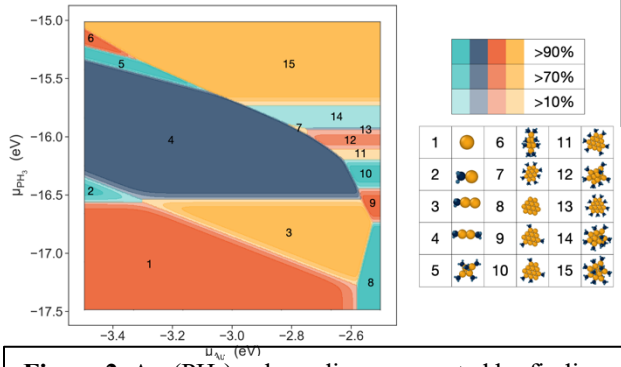

Figure 2. $Au_n(PH_3)_m$ phase diagram created by finding the most stable structure in the data set for a range of chemical potentials. The stable species are shown on the right. The fraction of the solution product that they would expect to represent is calculated at 300 K via Boltzmann population statistics.

Additionally, we developed a dataset of >10,000 DFT-calculated phosphine-ligated Au cluster structures, which helped to learn the effect of ligand-stabilization on morphology, bonding, and accessibility of new synthesis products, and also revealed that ligands are a necessary component of accurate nanocluster modeling. A phase diagram

representing the stable structures for this system is shown in Figure 2. For the $BiFeO_3$ system, we investigated the effects of precursor preparation conditions on the formation of impurity phases, using a text mined dataset and subsequent decision tree modeling to inform 21 insightful experiments that reveal the importance of incorporating excess bismuth, accurately reporting the precursor concentration, and the influence of chelating agents such as citric acid in mitigating impurity phase formation.

Future Plans

To improve on our existing text mining methods, we describe our developing methods for improved structured information extraction using GPT-based large language models[2], an example templated extraction for which is shown in Figure 3. This effort has been applied with success to the extraction of seed-mediated gold nanorod synthesis procedures and morphological outcomes. Additionally, we summarize developing work on a chemical reaction network for complex sol-gel synthesis mechanisms, which are difficult processes to model. These chemical reaction networks will eventually supply features to our text-mined datasets by reflecting the predicted reaction pathway followed in sol-gel environments based on the chemical reagents used in published procedures.

Figure 3. Structured information extraction using GPT-based LLMs addresses extraction issues encountered with existing methods (e.g. complex synthesis procedure extraction, linking procedure and outcome).

References

1. G. Barcaro, S. Monti, L. Sementa, and V. Carravetta, *Atomistic Modelling of Si Nanoparticles Synthesis,* Crystals, **7**, 54 (2017)

2. T. B. Brown, B. Mann, N. Ryder, M. Subbiah, J. Kaplan, P. Dhariwal, A. Neelakantan, P. Shyam, G. Sastry, A. Askell, S. Agarwal, A. Herbert-Voss, G. Krueger, T. Henighan, R. Child, A. Ramesh, D. M. Ziegler, J. Wu, C. Winter, C. Hesse, M. Chen, E. Sigler, M. Litwin, S. Gray, B. Chess, J. Clark, C. Berner, S. McCandlish, A. Radford, I. Sutskever, and D. Amodei, *Language Models Are Few- Shot Learners*, arXiv (2020)

Publications

1. K. Cruse, A. Trewartha, S. Lee, Z. Wang, H. Huo, T. He, O. Kononova, A. Jain, and G. Ceder, *Text-mined dataset of gold nanoparticle synthesis procedures, morphologies, and size entities*, Sci. Data, 9, 234 (2022)
2. T. J. He, W. H. Sun, H. Y. Huo, O. Kononova, Z. Q. Rong, V. Tshitoyan, T. Botari and G. Ceder. *"Similarity of precursors in solid-state synthesis as text-mined from scientific literature,"* Chemistry of Materials 32 (18), 7861-7873 (2020).
3. O. Kononova, T. J. He, H. Y. Huo, A. Trewartha, E. A. Olivetti and G. Ceder. *"Opportunities and challenges of text mining in materials research,"* Iscience 24 (3) (2021).
4. A. Trewartha, N. Walker, H. Huo, S. Lee, K. Cruse, J. Dagdelen, A. Dunn, K. Persson, G. Ceder and A. Jain. *"Quantifying the advantage of domain-specific pre-training on named entity recognition tasks in materials science,"* Patterns 3 (4) (2022)
5. C. A. McCandler, J. C. Dahl, K. A. Persson,*"Phosphine-Stabilized Hidden Ground States in Gold Clusters Investigated via a $Au_n(PH_3)_m$ Database"*, ACS Nano 17 (2), 1012-1021 (2022). 10.1021/acsnano.2c07223

6. R. X. Yang, C. A. McCandler, O. Andriuc, M. Siron, R. Woods-Robinson, M. K. Horton, K. A. Persson, *"Big Data in a Nano World: A Review on Computational, Data-Driven Design of Nanomaterials Structures, Properties, and Synthesis",* ACS Nano 16 (12), (2022).

Developing Synthesis Theories, Automating Synthesis, and Advanced Characterization Techniques

Gerbrand Ceder, Carolin Sutter-Fella, Anubhav Jain, Haimei Zheng, Kristin Persson

Keywords: Autonomous synthesis, solid state synthesis, thin film synthesis, in situ characterization

Research Scope

Developing more targeted synthesis guidelines for inorganic materials has been a longstanding problem and is an ideal setting for multi-faceted data-driven methods that combine theory, machine learning, automated labs, and advanced characterization. Inorganic synthesis lacks a unifying theory: there is no "Schrödinger equation equivalent" that can be solved to predict the synthesizability or necessary conditions to realize a material. Nonetheless, models for inorganic synthesis do exist, for example our developing theories on thermodynamic driving forces as a useful predictor for inorganic synthesis pathways. In this collaborative work, we highlight two developing synthesis hypotheses and their implications on synthesis pathway prediction: (1) the first phase to form is determined by the reaction with the largest thermodynamic driving force ("ΔG_{max} hypothesis")[1,2] and (2) the first polymorph to form contains the lowest surface energy ("Preferred polymorph selection"). To support these theories, we have constructed autonomous lab set ups for both solid state ceramic and thin film synthesis. As illustrated in Figure 1, we aim to use these laboratory setups in combination with *ab initio* simulation, *in situ* characterization during synthesis, and systematic text mining of the scientific literature to evaluate the validity of these hypotheses and gain better mechanistic insights for inorganic synthesis.

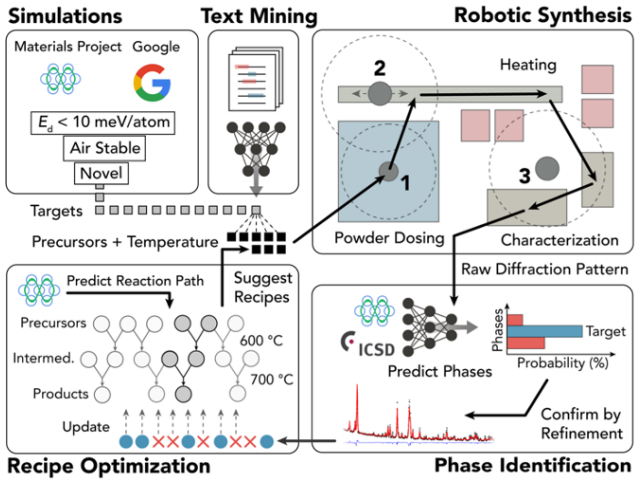

Figure 1. We have built an active learning algorithm to drive our autonomous solid state synthesis laboratory, with experiments inspired by simulation and text mining of the inorganic synthesis literature; this enables closed-loop operation for the targeted synthesis of new materials.

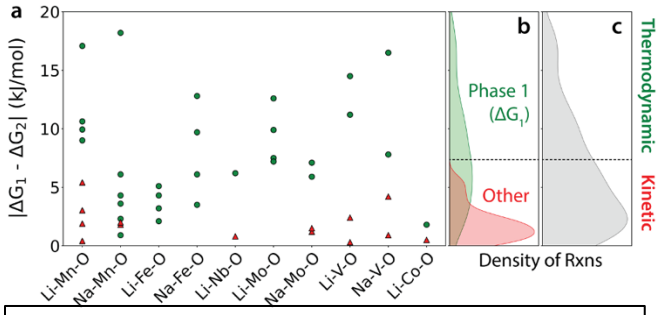

Figure 2. We tested 45 different pairwise reactions and identified the first product formed in each; A clear trend: thermodynamics dictates the first phase to form when its driving force is much larger than the competition

Recent Progress

We provide recent experimental data from 45 syntheses that support our ΔG_{max} hypothesis as well as an active learning framework to inform new experiments based on this hypothesis. Figure 2 illustrates the pairwise reactions conducted for this study, indicating that thermodynamics helps to predict which phase is the first to form.

Interrogating the validity of our hypotheses requires a wealth of data, so we highlight new autonomous laboratory setups for two materials synthesis methodologies: solid-state ceramics (A-Lab) and sol-gel thin films (SpinBot). These setups not only offer high-throughput experimental capabilities, but also include autonomous frameworks that intelligently inform future synthesis condition choices based on historical data. In addition to these high-throughput *ex situ* setups, we provide details on our advanced *in situ* XRD and TEM characterization capabilities, which provide mechanistic insights into synthesis pathways. We highlight an *in situ* diffraction study for $BiFeO_3$ thin films whose experiments were informed by text mining, illustrated in Figure 3. These results provide a comprehensive understanding of the crystallization pathway and, in combination with thermodynamic modeling, highlight the mitigating effects of including citric acid as a chelating agent on impurity phase formation.

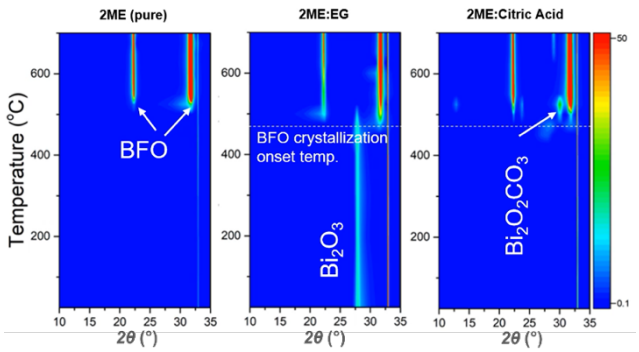

Figure 3. Synthesis & *In Situ* Characterization: Design experiments with text-mining knowledge and perform in situ XRD characterization to extract crystallization pathways. Here, solvent is varied from 2-methoxyethanol (2ME) to mixtures with ethylene glycol (EG), and citric acid resulting in different intermediate phases.

Future Plans

We plan to continue developing our current synthesis theories using this synergistic approach. The use of *in situ* TEM is a new development in this project. We describe our current capabilities and anticipated applications for resolving phase transformations at the microscale in complex oxide synthesis investigations. We also summarize our developing theory for preferred polymorph nucleation based on competing polymorph surface energies.

References

1. M. Bianchini, J. Wang, R. J. Clement, B. Ouyang, P. Xiao, D. Kitchaev, T. Shi, Y. Zhang, Y. Wang, H. Kim, M. Zhang, J. Bai, F. Wang, W. Sun, and G. Ceder, *The Interplay between Thermodynamics and Kinetics in the Solid-State Synthesis of Layered Oxides,* Nat. Mater. **19**, 1088 (2020)

2. A. Miura, C. J. Bartel, Y. Goto, Y. Mizuguchi, C. Moriyoshi, Y. Kuroiwa, Y. Wang, T. Yaguchi, M. Shirai, M. Nagao, N. C. Rosero-Navarro, K. Tadanaga, G. Ceder, and W. Sun, *Observing and Modeling the Sequential Pairwise Reactions That Drive Solid-State Ceramic Synthesis,* Adv. Mater. **33**, 2100312 (2021)

Publications

7. N. J. Szymanski, Y. Zeng, H. Y. Huo, C. J. Bartel, H. Kim and G. Ceder, *"Toward autonomous design and synthesis of novel inorganic materials"*, Materials Horizons 8 (8), 2169-2198 (2021)

8. M. Abdelsamie, K. Cruse, N. Tamura, G. Ceder, and C. M. Sutter-Fella, *Impact of processing conditions on the film formation of lead-free halide double perovskite Cs2AgBiBr6*, J. Mater. Chem. A, 37 (2022)

9. M. Abdelsamie, K. Hong, K. Cruse, C. J. Bartel, V. Baibakova, A. Trewartha, A. Jain, G. Ceder, and C. M. Sutter-Fella *"Combining text mining, in situ characterization and* ab initio *calculations to rationalize $BiFeO_3$ crystallization pathways"* (Submitted)

10. N. J. Szymanski, Y. Fei, B. Rendy, R. Kumar, G. Ceder, Y. Zeng, K. Persson, and A. Jain, *"Validating the synthesizability of inorganic materials with an autonomous laboratory"* (Submitted)

Nucleation and Self-Assembly of Hierarchical Materials: Predicting Pathways, Dynamics, and Experiment

Ying Chen, Jaehun Chun, James J. De Yoreo, Benjamin A. Legg, Dongsheng Li, Karl T. Mueller, Christopher J. Mundy, Peter J. Pauzauskie

Physical and Computational Sciences Directorate, Pacific Northwest National Laboratory, Richland, WA 99352, USA

Keywords: Nucleation, Oriented attachment, *in situ* TEM, *in situ* NMR, molecular modeling

Research Scope

The long-term vision of this project is to develop a predictive understanding of the physical principles connecting atomic-scale interactions to ensemble responses that control solution synthesis of crystalline materials via complex pathways not envisioned in classical theories (Fig. 1).[1] We are advancing that vision through four scientific objectives that target key knowledge gaps: (1) How do crystalline phases emerge along nucleation pathways that start from a dense liquid phase (DLP) and are accompanied by an evolution in chemical composition as crystallization proceeds?[2] (2) How does a shift in surface potential due to an applied electric field affect interfacial structure, surface speciation, and formation dynamics of nuclei?[3] (3) How do complexities of a particle system, including interfacial solution properties, anisotropies in particle shape, and solvent dielectrics, affect oriented attachment (OA) of nanocrystals?[4, 5] (4) How do surface-bound organic ligands and solution electrolytes affect interfacial solution structure and interparticle forces to enhance or hinder OA?[4, 5] Our approach combines synthesis of nanomaterials exhibiting non-classical pathways with characterization of pathways and dynamics using *in situ* TEM, NMR, and AFM-based methods, as well as theory and simulation of speciation, cluster evolution, interfacial structure, and interparticle forces. Through this approach, we seek to establish a predictive description of non-classical pathways by developing models of reduced complexity.

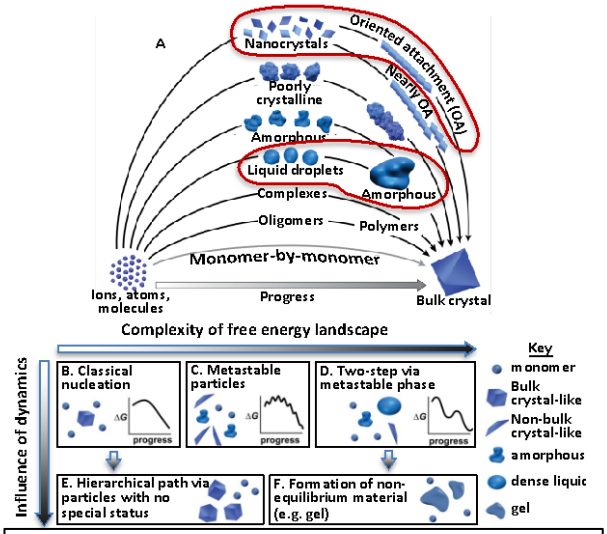

Fig. 1. Stable bulk crystals often form from species of higher order than monomers (A).[10] Pathways can be thermodynamic (B-D) or kinetic (E, F); (B) classical monomer-by-monomer addition; (C) metastable microscopic precursors; (D) metastable bulk precursors; (E) cluster/particle assembly; (F) kinetically trapped metastable or unstable products. Our research addresses the circled pathways in (A) corresponding to (D), (E), and (F).

Recent Progress

Nucleation via DLPs: To develop a comprehensive picture of nucleation via a DLP, we followed the development of $CaCO_3$ from isolated ions in a highly supersaturated solution to solid amorphous $CaCO_3$ (ACC) using a combination of *in situ* TEM, NMR, and FTIR (Fig. 2). Our results show that, at high supersaturations the initial step in nucleation is formation of a viscous bicarbonate-rich (DLP) comprised of $1Ca^{2+}$:$2HCO_3^-$:$7\pm2H_2O$, which then transforms into hollow hydrated ACC particles accompanied by the release of CO_2 and H_2O. The ACC then transforms to crystalline polymorphs either pseudomorphically or by dissolution-reprecipitation. Acidic proteins and polymers extend DLP lifetimes but otherwise leave the pathway and chemistry unchanged. A combination of simulations based on density functional theory (DFT) and a frustrated charge Ising model (FCI) in conjunction with all-atom molecular dynamics (MD) predict that the DLP forms via direct condensation of solvated $Ca^{2+}\bullet(HCO_3^-)_2$ complexes that react due to proximity effects in the confinement of DLP droplets and that droplets having the composition determined by NMR and TEM are both stable and exhibit diffusivities consistent with that of a dense liquid.

Results on two other systems – the laser cooling crystal $NaYF_4$ and the framework silicate cyclosilicate hydrate — also reveal pathways via DLPs that require an evolution in chemical composition to reach the final crystalline state. In the $NaYF_4$ system, an initially formed

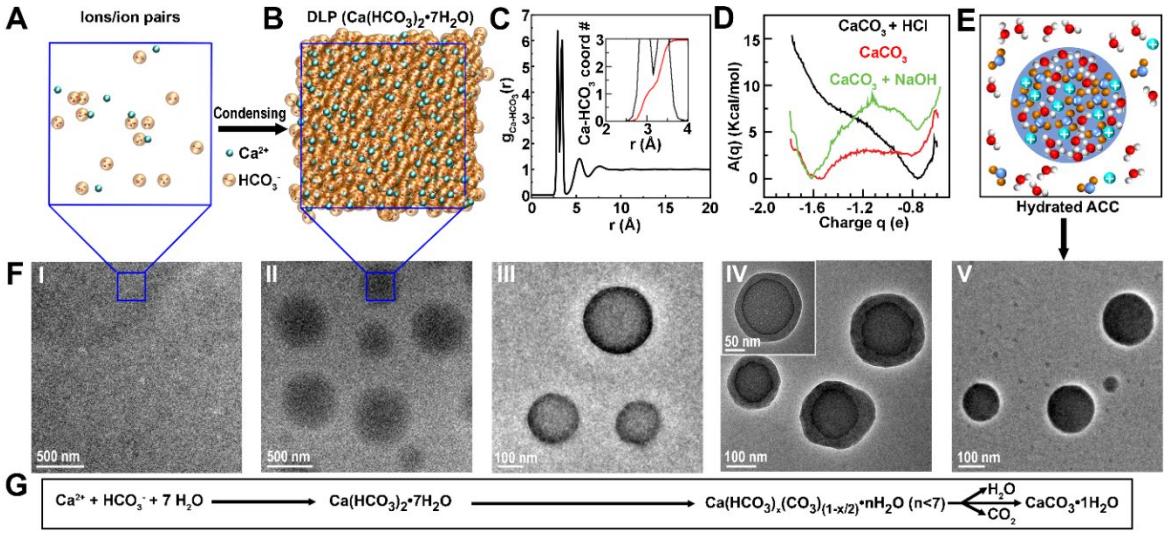

Fig. 2. Simulation of DLP structure in $CaCO_3$ system and observed formation and transformation process to solid ACC based on in situ TEM, ATR-FTIR and NMR measurements. (A) Ions and ion pairs in precursor solution. (**B**) All-atom MD model showing structure of bulk DLP with a composition of $1Ca^{2+}$:$2HCO_3^-$:$7H_2O$ based on the TEM and NMR data. (**C**) Radial distribution function between Ca^{2+} and C in HCO_3^-. Inset: red curve provides number of HCO_3^- around Ca^{2+} as a function of distance indicating a value between 2 and 3. (**D**) DFT calculations during numerical titration experiments. CO_3^{2-} free energy as a function of net charge state, A(q), determined at three notional pH values, ranging from "acidic" (black) to "neutral" (red) to "basic" (green). The global minimum in A(q) represents predicted stable charge state $q = 4 - 2n_O + n_H$, where n_X is the coordination of Ca with respect to the O within 1.90 Å and H coordinated to the central O within 1.20Å. (**E**) Schematic of hydrated ACC. (**F**) LP-TEM (I – III) and time-sequence of *ex-situ* TEM images (IV-V) showing formation and transformation of DLP droplets into solid hydrated ACC via core-shell particles. (**G**) NMR determined chemical reaction pathway during solid $CaCO_3$ formation via the DLP.

compositionally heterogeneous gel must undergo solid-state diffusion of Na^+ and F^- into the gel to before the stable cubic $NaYF_4$ phase forms. In the cyclosilicate hydrate system, the first step is assembly of cubic octameric silicate polyanions via cross-linking and polymerization of smaller silicate monomers and other oligomers. These so-called Q^3_8 units are stabilized by hydrogen bonds with surrounding H_2O and tetramethylammonium ions (TMA^+) to form atomically precise $[(TMA)_x(Q^3_8)\cdot nH_2O]^{(x-8)}$ pre-nucleation clusters (PNCs), which organize into a DLP comprising an interconnected network of the PNCs within which the cyclosilicate hydrate crystals then nucleate. Together these three systems demonstrate that crystal nucleation along pathways involving DLPs phases include continuous chemical evolution to reach the crystalline state, which is a phenomemon not considered within classical frameworks of nucleation.

Crystal growth by OA: To understand the forces and torques that lead to OA, we investigated Pd nanocube (NC) assembly into superlattices using *in situ* TEM and interpreted the results with a combination of MD simulations and continuum-based theory (Fig. 3). From the analysis of the TEM data, we extracted the van der Waals (vdW), Brownian, and ligand (i.e., steric hinderance) forces F_{vdW}, F_B, F_{sh}, respectively. The results show that the ligand interactions dominate over the other contributions and vdW forces and torques are the smallest, while anisotropic NC morphology introduces noticeable torques on the NCs. At regions with imperfect structures, such as line defects, the unbalanced forces and torques induce translational and rotational motions of the NCs, which are transmitted to neighboring NCs. This propagation of the motion prompts a "chain reaction" in the 2D network, leading to self-elimination of defects. MD simulations also predict that steric hindrance by the ligands provides the largest forces, however, attractive ligand-ligand interactions introduce a drag force between particles that enables rotations to propagate through the lattice and maintain alignment.

Results obtained on other systems have provided insights into other drivers of OA, as well as the underlying role of particle shape and roughness on vdW interactions and solution structure on hydration forces. For example, observations of OA dynamics by ZnO nanoparticles, which possess a permanent dipole, obtained in toluene complement results we published

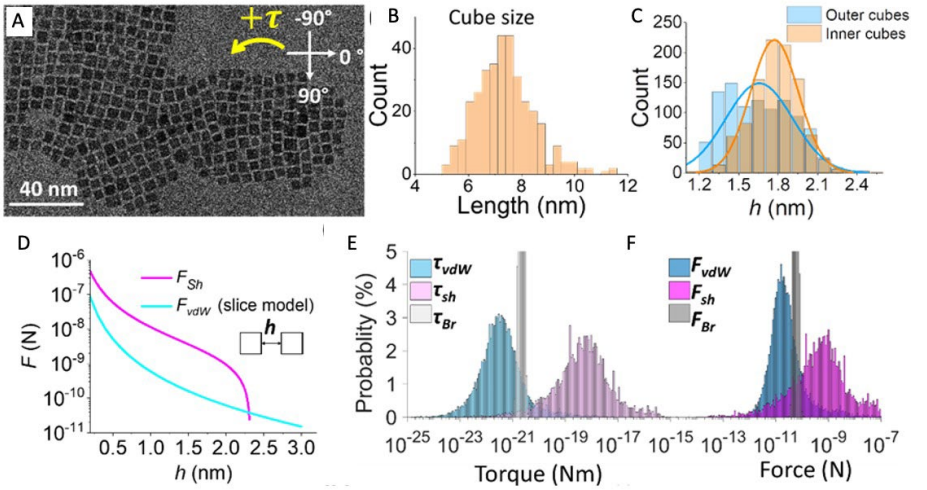

Fig. 3. Analysis of spacings, forces, and torques during self-assembly of a Pd NC superlattice. (A) Representative image from *in situ* TEM time series. (B) Particle size distribution of NCs in (A). (C) Separation (h) distributions of inner and outer NCs of superlattice in (A). (D) Theoretical calculation of F_{vdW} and F_{Sh} between two face-to-face NCs as a function of h. (E) F_{vdW}, F_{Sh}, and F_{Br} on all NCs observed by *in situ* TEM over time after attachment of two clusters, and (F) τ_{vdW}, τ_{Sh}, and τ_{Br} on all NCs observed by in-situ TEM after attachment of two clusters.

previously for ZnO in methanol, by showing that the decrease in dielectric constant results in a much stronger attractive interaction. Langevin dynamics simulations that incorporate the different dielectric constants correctly predict the increased rates of alignment and attachment expected for toluene.

Future Plans

Nucleation via DLPs: The phenomenon of condensation into a network of ions and/or clusters that define the DLP seen in the three systems described above, shares common features with the aluminum hydroxide ion networks seen during the formation of $Al(OH)_3$ films on mica.[3] There, charge frustration leads to barrier free formation of the clusters and defines their characteristic sizes. Due to our ability to both image this 2D system by high-speed AFM with molecular resolution and simulate it with FIC models, our work will focus on investigating the effect of both the surface potential and the identity of the cation (Al vs Mg and La) and building a predictive model that can account for the electrostatic stabilization that drives these systems.

Crystal growth by OA: While our work to date has enabled us to predict many aspects of particle assembly by OA, how the properties of ligands impact the individual force components is poorly understood. Consequently, our future work will address this knowledge gap by using a series of sequence defined polymers that have identical back bone chemistry but are constructed from a library of building units that allow us to systematically vary the length, rigidity, hydrophobicity, headgroup charge, and inter-ligand interactions. We will then determine these properties and the progression of OA nu combining *in situ* TEM measurements of particle assembly dynamics, 3D AFM mapping of solution structure, classical MD simulations of intermolecular interactions, and a continuum theory of interparticle forces and torques.

References

(1) De Yoreo, J. J.; Gilbert, P. U. P. A.; Sommerdijk, N. A. J. M.; Penn, R. L.; Whitelam, S.; Joester, D.; Zhang, H. Z.; Rimer, J. D.; Navrotsky, A.; Banfield, J. F.; et al. Crystallization by particle attachment in synthetic, biogenic, and geologic environments. *Science* **2015**, *349*, aaa6760

(2) Wallace, A. F.; Hedges, L. O.; Fernandez-Martinez, A.; Raiteri, P.; Gale, J. D.; Waychunas, G. A.; Whitelam, S.; Banfield, J. F.; De Yoreo, J. J. Microscopic evidence for liquid-liquid separation in supersaturated $CaCO_3$ solutions. *Science* **2013**, *341* (6148), 885-889.

(3) Legg, B. A.; Voitchovsky, K.; De Yoreo, J. J. Hydroxide films on mica form charge-stabilized microphases that circumvent nucleation barriers. *Sci Adv* **2022**, *8* (35). eabn7087

(4) De Yoreo, J. J.; Nakouzi, E.; Jin, B.; Chun, J.; Mundy, C. J. Spiers Memorial Lecture: Assembly-based pathways of crystallization. *Faraday Discuss.* **2022**, *235* (0), 9-35.

(5) Li, D. S.; Chen, Q.; Chun, J.; Fichthorn, K.; De Yoreo, J.; Zheng, H. M. Nanoparticle Assembly and Oriented Attachment: Correlating Controlling Factors to the Resulting Structures. *Chem. Rev.* **2023**, *123* (6), 3127-3159.

Publications

1. Jin, Y. Chen, J. Tao, K. Lachowski, M. E. Bowden, Z. Zhang, L. Pozzo, N. M. Washton, K. T. Mueller, **J. J. De Yoreo**, "Multi-step nucleation of a crystalline silicate framework via a structurally precise prenucleation cluster" *Angew. Chemie Int.* (In press)
2. M. Song, M. P. Prange, P. Ren, Z. Lu, J. Lee, J. Zheng, M. Engelhard, **J.J. De Yoreo**, P. V. Sushko, D. Li, "Transitional Structures with Continuous Variations in Atomic Positions from Anatase to Rutile Improve Photocatalytic Activity" *Adv. Mater. Interfaces* (In press).
3. Li, Q. Chen, J. Chun, K. Fichthorn, J.J. De Yoreo, H. Zheng "Nanoparticle Assembly and Oriented Attachment: Correlating Controlling Factors to the Resulting Structure" *Chem. Rev.* **123**, 3127 (2023).
4. B. A. Legg and J.J. De Yoreo, "Effects of Size and Shape on the Tolerances for Misalignment and Probabilities for Successful Oriented Attachment of Nanoparticles." *Langmuir* **39**, 2985 (2023).
5. E. Nakouzi, S. Kerisit, B. A. Legg, S. Yadav, D. Li, A. G. Stack, C. J. Mundy, J. Chun, G. K. Schenter, J. J. De Yoreo, "Solution structure and hydration forces between mica and hydrophilic versus hydrophobic surfaces" *J.*
6. C. Jia, G. Zhu, B. A. Legg, B. Guan and J. J. De Yoreo, "Bassanite Grows Along Distinct Coexisting Pathways and Provides a Low Energy Interface for Gypsum Nucleation" *Crys. Growth Des.* **22**, 6582 (2022).
7. B. A. Legg, K. Voïtchovsky, J. J. De Yoreo, "In-situ AFM reveals charge-stabilized nanostructures that circumvent crystal nucleation barriers" *Science Adv*. 8, eabn7087 (2022).
8. J.J. De Yoreo, E. Nakouzi, B. Jin, J. Chun and C. J. Mundy, "Assembly-based pathways of crystallization" *Faraday Disc*. **235**, 8 (2022).
9. B. Jin, Z. Liu, C. Shao, J. Chen, L. Liu, R. Tang, J. J. De Yoreo, "The Phase Transformation Mechanism of Amorphous Calcium Phosphate to Hydroxyapatite Investigated by Liquid-Cell TEM," *Cryst. Growth Des.* **21**, 5126 (2021).
10. E. Nakouzi, E, Yadav, S., Legg, B.A., Zhang, S., Tao, J., Mundy, C.J., Schenter, G.K., Chun, J., and De Yoreo, J.J. (In press) "Visualizing Solution Structure at Solid-Liquid Interfaces Using Three-Dimensional Fast Force Mapping", *JoVE*. **174**, e62585, (2021).

Electronic, Optical, and Electrochemical Properties of Doped Metal Oxide Epitaxial Films and Interfaces

Yingge Du[1], Le Wang[1], Steven Spurgeon[2], Peter V. Sushko[1], Scott A. Chambers[1], Tiffany C. Kaspar[1], Mark E. Bowden[1]

Pacific Northwest National Laboratory, Richland, Washington 99354

Keywords: perovskite oxides, epitaxial thin films, strain, defects, oxygen evolution reaction

Research Scope

Our project aims to *understand how the interplay between composition and structure (including defects) defines electronic transport, optical absorption, and electrochemical response in complex oxide heterostructures*. Complex oxides have the widest range of functional properties of any class of materials explored to date owing to their diverse structures and compositions. However, with many degrees of freedom come many possible outcomes. Consequently, controlled synthesis and processing of oxide materials, and ultimately achieving atomic precision, constitute grand challenges in materials science. To address these challenges, we leverage advanced synthesis techniques, including molecular beam epitaxy (MBE) and pulsed laser deposition (PLD), to attain precise control over the composition, phases, strain states, defects, and surface termination of these thin films. We strive to understand and control proximity effects brought about by the rational design of structural and compositional environments at controlled locations in the lattice of complex oxide heterostructures. This pursuit not only lays the groundwork for the scientifically informed synthesis of complex oxides but also serves as the cornerstone for their application in energy harvesting, conversion, and storage.

Recent Progress

Stabilize metastable phases through heteroepitaxy and tailored superlattices. Understanding phase stability and phase transitions is central to material synthesis and condensed matter physics. Sr doping in rare-earth nickelates has been extensively investigated as an effective strategy to tune their physical and chemical properties. In addition, the recent discovery of superconductivity in infinitely layered $Nd_{0.8}Sr_{0.2}NiO_2$ has motivated the synthesis of nickelates with higher Sr concentration. We explored the growth of $SrNiO_3$ using MBE and showed that spontaneous phase segregation occurs while targeting pure $SrNiO_3$ thin film fabrication on perovskite oxide substrates. Comprehensive studies revealed that two epitaxial, co-existing phases, Sr_2NiO_3 and $SrNi_2O_3$, form to balance the material's stoichiometry and stabilize the energetically preferred Ni^{2+} cation (Figure 1).[1] The formation of these co-existing phases explains the structural instability of nickelates with high Sr content. The unique, self-assembled nanocomposite structures result from an unusual kind of film nucleation, apparently driven by interfacial strain and the tendency of transition metal (TM) cations to form their most stable valence (i.e., Ni^{2+} in this case). These materials offer a fascinating testbed for understanding emergent phenomena in nickelates.

By using interface engineering in superlattices (SLs) of $[SrNiO_3]_m/[LaFeO_3]_n$ [2] (SNO_m/LFO_n) and $SNO_m/[SrTiO_3]_n$ (SNO_m/STO_n)[3], we show that $SrNiO_3$ can be stabilized at single unit cell thickness (Figure 1b). Higher SNO thicknesses lead to structural decay and amorphization. Our work shows that accurate control of material structure through superlattice engineering may be generally useful for the synthesis and discovery of metastable, layered functional materials. In addition, we have recently synthesized epitaxial hexagonal $BaNiO_3$ (BNO) thin films on STO(111) using MBE with dominant Ni^{4+} oxidation state observed. High quality X-ray absorption spectroscopy (XAS) spectra collected on these nickelate samples are summarized in Figure 1c.

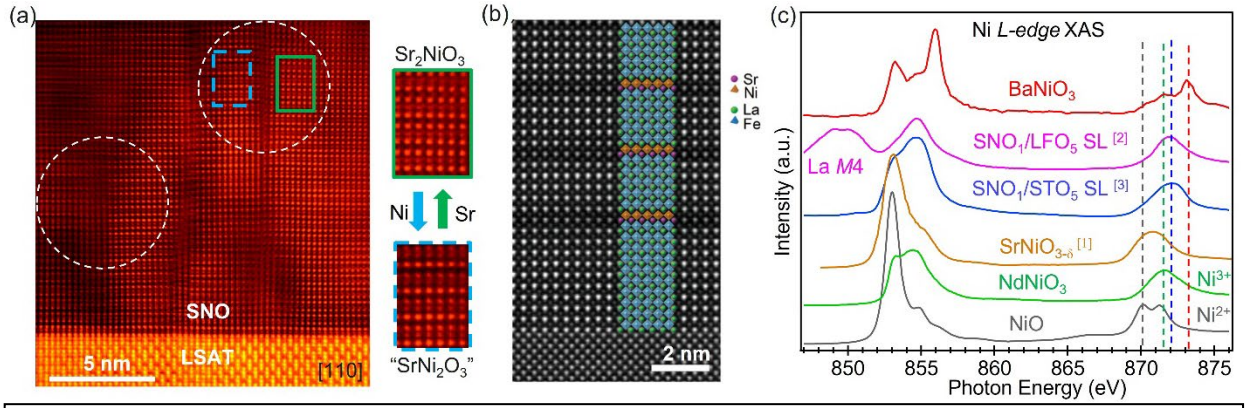

Figure 1. Tuning the structure of complex nickelates. (a) Cross-sectional STEM image of SNO/LSAT along the [110] LSAT direction. Dashed circles clearly show phase segregation. (b) Cross-sectional STEM image of the SNO_1/LFO_5 SL along the [100] substrate orientation. Structure assignments are also shown for comparison. (c) Ni *L*-edge XAS. The Ni L_2 edge peak position for BNO, SNO_1/LFO_5 SL, SNO_1/STO_5 SL, thick $SrNiO_{3-\delta}$, $NdNiO_3$, and NiO are marked by red, purple, blue, yellow, green, and grey dashed lines, respectively.

Tailor the electronic structure and electrochemical property of $LaNiO_3$ (LNO) by Fe doping. Cation doping is an effective design strategy to tune physicochemical properties of perovskite oxides. To understand how B-site doping influences the structural and electronic properties of LNO, we have synthesized a series of $LaNi_{1-x}Fe_xO_3$ (LNFO) films using MBE.[4] Scanning transmission electron microscopy (STEM) and X-ray diffraction (XRD) measurements reveal well-defined interfaces and high structural quality of these epitaxial LNFO films. By combining *in situ* X-ray photoemission spectroscopy (XPS) (Figure 2a) and *ex situ* soft and hard XAS with density functional theory (DFT) simulations, we show that Fe substitution for Ni in LNO induces electron transfer from Fe to Ni sites, reducing Ni from Ni^{3+} to Ni^{2+} and oxidizing Fe from Fe^{3+} to Fe^{4+}. The high-valent Fe^{4+} state resulting from Fe substitution makes significant contributions to the occupied and unoccupied density of states (DOSs) near Fermi level (E_F). These changes in turn increase the bandwidth of the total *TM* 3d states via Ni–O–Fe bridges and enhance *TM* 3d–O 2p hybridization (Figure 2b), boosting electrochemical oxygen evolution reaction (OER) activity (Figure 2c). Moreover, both Ni^{2+}/Ni^{3+} and Fe^{3+}/Fe^{4+} ratios increase with increasing Fe content in LNFO, leading to larger lattice parameters due to the longer Ni–O (Fe–O) bond lengths for Ni^{2+} (Fe^{3+}). The longer *TM*–O bond length primarily reduces the Ni 3d bandwidth and leads to

stronger Coulomb repulsion. The increased Coulomb repulsion induces a bandgap opening, reducing the *TM* 3d bandwidth and weakening the *TM* 3d/O 2p hybridization. Therefore, a volcano-like OER catalytic trend is observed with 37.5% Fe substitution in LNFO (Figure 2c) being the most active. This work offers new insights into design strategies for developing low-cost, Earth-abundant, and robust electrocatalysts for OER.

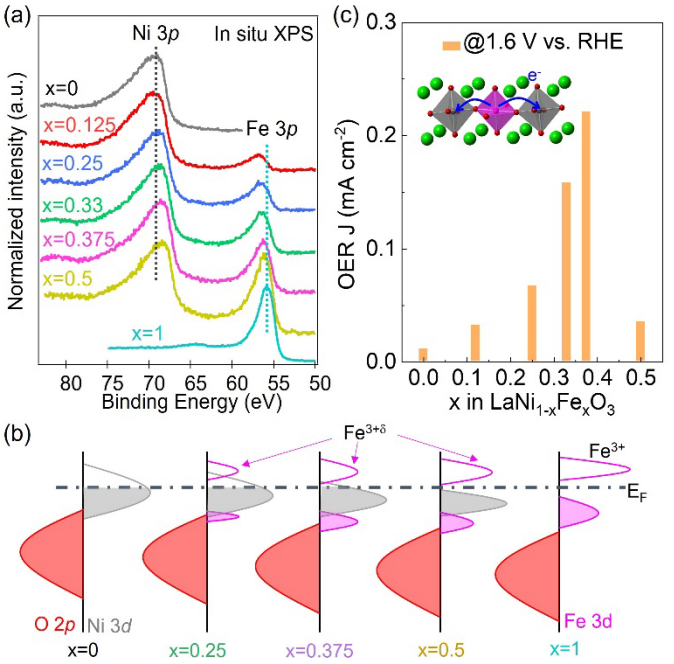

Figure 2. Fe doping enhances the *TM* 3d-O 2p hybridization and boosts the OER activity of LNO. (a) *In situ* Ni 3p and Fe 3p XPS spectra. The dashed lines denote the Ni 3p binding energy for $LaNi^{3+}O_3$ (x = 0) and Fe 3p binding energy for $LaFe^{3+}O_3$ (x = 1), respectively. (b) Schematic energy band diagram for LNFO with various x values. For simplicity, the *TM* 3d–O 2p hybridization is not shown here. (c) Comparison of the specific OER activities measured at 1.6 V vs reversible hydrogen electrode (RHE).

Correlate OER activity with surface compositional evolution. To understand how surface composition might evolve with OER cycling and in turn influence OER activity, we investigate a set of coherently strained, epitaxial $La_{0.5}Sr_{0.5}Ni_{1-x}Fe_xO_{3-\delta}$ (LSNFO) films grown by MBE.[5] We show that the OER activity of LSNFO films (x = 0–0.5) depends not only on bulk Fe content but also on the extent and window of electrochemical cycling. To directly assess changes in surface structure and composition, we characterized the x = 0.375 sample before (pristine) and after electrochemical cycling using high resolution XPS. After the OER test, the Ni 3p to Fe 3p area ratio is found to increase (Figure 3a), suggesting that there is Ni segregation on the surface after OER. Moreover, the decrease in Sr/La area ratio by XPS after OER cycling indicates that Sr-leaching occurs during OER. STEM images (Figure 3b) further reveal that the surface is smooth for the pristine sample, while the top 2 u.c. layer of the x = 0.375 sample becomes structurally amorphous after OER. Energy dispersive X-ray spectroscopy (EDS) maps show that the pristine sample is mostly uniform in composition, but after OER testing, Ni segregation is apparent, consistent with our XPS results. Our results highlight that a comprehensive understanding of the electrocatalysts is needed to reveal their intrinsic OER activity and long-term stability.

Future Plans

We will continue to investigate defect formation, clustering, and ordering phenomena during thin film deposition and post-processing using *in situ* tools to elucidate their impact on the materials' electronic, optical, and ion transport properties. In addition, we plan to explore complex oxide heterostructures with controlled nitrogen doping, seeking to understand the influence of N doping on the lattice, electronic structure, and physicochemical properties. Furthermore, we are interested in exploring the growth and characterization of high entropy perovskite oxides to evaluate how their enhanced thermal stability and corrosion resistance can be harnessed for energy conversion and storage. Finally, we remain interested in investigating the band-edge profiles for buried heterojunctions and superlattices using hard x-ray photoemission spectroscopy (HAXPES) to interpret and tune transport properties.

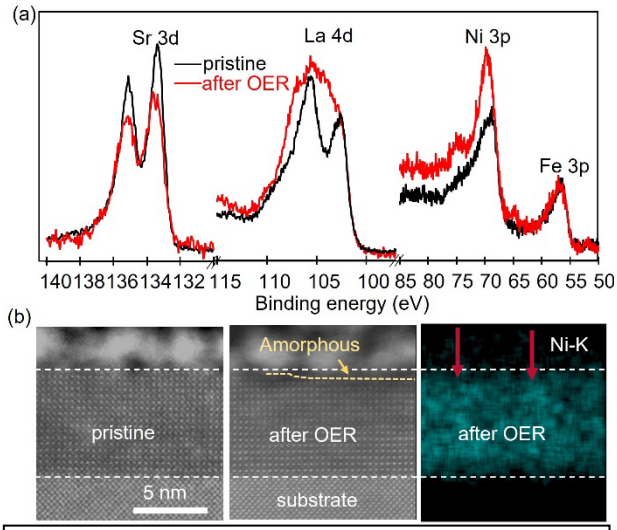

Figure 3. Surface evolution of an LSNFO film upon OER cycling. (a) Comparison of Sr 3d, La 4d, and Ni 3p & Fe 3p XPS core level spectra, and (b) cross-sectional STEM images and EDS maps for the LSNFO (x = 0.375) film before (pristine) and after OER.

References

1. L. Wang, Z. Yang, X. Yin, S. D Taylor, X. He, C. S. Tang, M. E. Bowden, J. Zhao, J. Wang, J. Liu, D. E. Perea, L. Wangoh, A. T. S. Wee, H. Zhou, S. A. Chambers, and Y. Du, *Spontaneous Phase Segregation of Sr_2NiO_3 and $SrNi_2O_3$ during $SrNiO_3$ Heteroepitaxy*, Sci. Adv. **7**, eabe2866 (2021).
2. L. Wang, Z. Yang, M. E. Bowden, J. W. Freeland, P. V. Sushko, S. R. Spurgeon, B. Matthews, W. S. Samarakoon, H. Zhou, Z. Feng, M. H. Engelhard, Y. Du, S. A. Chambers, *Hole-Trapping-Induced Stabilization of Ni^{4+} in $SrNiO_3/LaFeO_3$ Superlattices*, Adv. Mater. **32**, 2005003 (2020).
3. L. Wang, J. Zhao, C.-T. Kuo, B. E. Matthews, M. T. Oostrom, S. R. Spurgeon, Z. Yang, M. E. Bowden, L. W. Wangoh, S.-J. Lee, J.-S. Lee, E.-J. Guo, J. Wang, S. A. Chambers, and Y. Du, *Synthesis and Electronic Properties of Epitaxial $SrNiO_3/SrTiO_3$ Superlattices*, Phys. Rev. Mater. **6**, 075006 (2022).
4. L. Wang, P. Adiga, J. Zhao, W. S. Samarakoon, K. A. Stoerzinger, S. R. Spurgeon, B. E. Matthews, M. E. Bowden, P. V. Sushko, T. C. Kaspar, G. E. Sterbinsky, S. M. Heald, H. Wang, L. W. Wangoh, J. Wu, E.-J. Guo, H. Qian, J. Wang, T. Varga, S. Thevuthasan, Z. Feng, W. Yang, Y. Du, S. A. Chambers, *Understanding the Electronic Structure Evolution of Epitaxial $LaNi_{1-x}Fe_xO_3$ Thin Films for Water Oxidation*, Nano Lett. **21**, 8324-8331 (2021).
5. P. Adiga, L. Wang, C. Wong, B. E. Matthews, M. E. Bowden, S. R. Spurgeon, G. E. Sterbinsky, M. Blum, M.-J. Choi, J. Tao, T. Kaspar, S. A. Chambers, K. A. Stoerzinger, Y. Du, *Correlation between Oxygen Evolution Reaction Activity and Surface Compositional Evolution in Epitaxial $La_{0.5}Sr_{0.5}Ni_{1-x}Fe_xO_{3-\delta}$ Thin Films*, Nanoscale **15**, 1119-1127 (2023).

Publications

1. M.-J. Choi, L. Wang, K. A. Stoerzinger, S.-Y. Chung, S. A. Chambers, and Y. Du, *Epitaxial Design of Complex Nickelates as Electrocatalysts for the Oxygen Evolution Reaction*, Adv. Energy Mater. **13**, 2300239 (2023).
2. S. D Taylor, K. H Yano, M. Sassi, B. E Matthews, S. V Lambeets, S. Neumann, D. K Schreiber, L. Wang, Y. Du, S. R Spurgeon, *Resolving diverse oxygen transport pathways across Sr-doped lanthanum ferrite and metal-perovskite heterostructures*, Adv. Mater. Interfaces **10**, 2202276 (2023).
3. P. Adiga, L. Wang, C. Wong, B. E. Matthews, M. E. Bowden, S. R. Spurgeon, G. E. Sterbinsky, M. Blum, M.-J. Choi, J. Tao, T. Kaspar, S. A. Chambers, K. A. Stoerzinger, and Y. Du, *Correlation between Oxygen Evolution Reaction Activity and Surface Compositional Evolution in Epitaxial $La_{0.5}Sr_{0.5}Ni_{1-x}Fe_xO_{3-\delta}$ Thin Films*, Nanoscale **15**, 1119-1127 (2023).
4. L. Wang, M. Delower Hossain, Y. Du, and S. A. Chambers, *Exploring the potential of high entropy perovskite oxides as catalysts for water oxidation*, Nano Today **47**, 101697 (2022).
5. L. Wang J. Zhao, C.-T. Kuo, B. E Matthews, M. T Oostrom, S. R Spurgeon, Z. Yang, M. E Bowden, L. W Wangoh, S.-J. Lee, J.-S. Lee, E.-J. Guo, J. Wang, S. A Chambers, and Y. Du, *Synthesis and electronic properties of epitaxial $SrNiO_3/SrTiO_3$ superlattices*, Phys. Rev. Mater. **6**, 075006 (2022).
6. L. Wang, Z. Yang, W. S. Samarakoon, Y. Zhou, M. E. Bowden, H. Zhou, J. Tao, Z. Zhu, N. Lahiri, T. C. Droubay, Z. Lebens-Higgins, X. Yin, C. S. Tang, Z. Feng, L. F. J. Piper, A. T. S. Wee, S. A. Chambers, and Y. Du, *Spontaneous Lithiation of Binary Oxides during Epitaxial Growth on $LiCoO_2$*, Nano Lett. **22**, 5530-5537 (2022).
7. W. Samarakoon, J. Hu, M. Song, M. Bowden, N. Lahiri, J. Liu, L. Wang, T. Droubay, K. Koirala, H. Zhou, Z. Feng, J. Tao, and Y. Du, *Direct Imaging of the Structural and Morphological Evolution of Epitaxial LiCoO2 Films during Charge and Overcharge*, J. Phys. Chem. C **126**, 15882-15890 (2022).
8. L. Wang, P. Adiga, J. Zhao, W. S. Samarakoon, K. A. Stoerzinger, S. R. Spurgeon, B. E. Matthews, M. E. Bowden, P. V. Sushko, T. C. Kaspar, G. E. Sterbinsky, S. M. Heald, H. Wang, L. W. Wangoh, J. Wu, E.-J. Guo, H. Qian, J. Wang, T. Varga, S. Thevuthasan, Z. Feng, W. Yang, Y. Du, S. A. Chambers, *Understanding the Electronic Structure Evolution of Epitaxial $LaNi_{1-x}Fe_xO_3$ Thin Films for Water Oxidation*, Nano Lett. **21**, 8324-8331 (2021).
9. S. Akers, E. Kautz, A. Trevino-Gavito, M. Olszta, B. E. Matthews, L. Wang, Y. Du, and S. R. Spurgeon, Rapid and flexible segmentation of electron microscopy data using few-shot machine learning, npj Computational Materials **7**, 187 (2021).
10. L. Wang, Z. Yang, X. Yin, S. D Taylor, X. He, C. S. Tang, M. E Bowden, J. Zhao, J. Wang, J. Liu, D. E Perea, L. Wangoh, A. TS Wee, H. Zhou, S. A Chambers, and Y. Du, *Spontaneous phase segregation of Sr_2NiO_3 and $SrNi_2O_3$ during $SrNiO_3$ heteroepitaxy*, Sci. Adv. **7**, eabe2866 (2021).

Selective Interface Synthesis: Directing Atomic Structure at Defective Interfaces

Alex B. F. Martinson and Cong Liu (Argonne National Laboratory); Adam S. Hock (Illinois Institute of Technology)

Keywords: atomic layer deposition, interfaces, defect repair, targeted synthesis, calorimetry

Research Scope

We hypothesize that a precision approach to interface synthesis, based on control of well-defined atom *connectivity*, not crystallinity, will make possible non-epitaxial, polycrystalline, and amorphous material interfaces that exhibit uniform and predictable electronic properties. We aim to predict, design, and understand synthetic pathways that can selectively address and mitigate minority atom arrangements that produce electronic defects. To do so, we develop and leverage the science of *Selective Interface Reactions* (SIRs, **Figure 1**), an atomic layer deposition (ALD)-based synthesis approach, to deterministically direct vapor-phase surface reactions that are chemically tailored to selectively repair electronically unfavorable sites without compromising the integrity of desirable sites. Simultaneously we develop and leverage ALD calorimetry as a uniquely sensitive, time-resolved measurement of surface reaction heat in order to test computationally-predicted synthesis mechanisms. The outcome of such studies are design rules and advanced characterization methods that enable the synthesis of heterogeneous interfaces that forgo epitaxial perfection yet can still exhibit homogenous electronic properties.

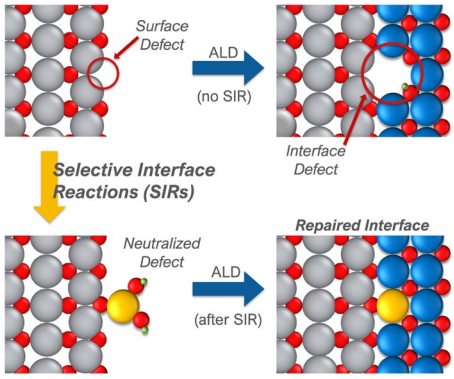

Figure 1. Idealized schematic of an SIR tailored to a defective surface site to repair an undesirable electronic state which would otherwise be buried at the interface.

Recent Progress

In the first phase of this FWP, we computationally predicted and experimentally corroborated a novel site-selective hydration strategy for metal oxides surfaces including rutile TiO_2 and bixbyite In_2O_3.[1-3] The basis for these SIRs is the thermodynamically favored formation of hydroxyl or aqua surface functionalization on only a subset surface sites. This conceptually simple approach provides a route to site-selective ALD at defects that strongly bind water when combined with metalorganic precursors that react exclusively at protonated surface sites. We show that the strategic choice of a less reactive metalorganic precursor, in combination with site-specific hydration, enables targeted, deterministic deposition.

Facet and Step Selectivity via Selective Hydration of Rutile Titanium Oxide. We first investigated the potential of a selective hydration strategy for rutile TiO_2. We targeted step edges as well as surface oxygen vacancies as the defects of interest. Comparing the thermodynamics of water adsorption between the terrace sites and the step edges of the (110) facet reveals the potential

for site-selectivity, as raising the temperature above 300 K is expected to favor water desorption from terrace sites while step hydration remains favorable until over 400K. Furthermore, free energy calculations of hydration of the TiO_2 (110) surface reveal a selectivity window of more than 700 K over which terrace hydroxylation is disfavored while oxygen vacancies (*vo*) and Ti interstitials (*Ti*$_i$) strongly favor hydroxylation, **Figure 2**.[1] We utilized a nominally less reactive alternative to TMA – diemethylaluminium isopropoxide (DMAI), hypothesizing that an improvement in selectivity may originate from a more strictly proton-mediated ligand exchange mechanism for DMAI. This hypothesis is supported by the striking absence of Al_2O_3 growth on a freshly fired, terraced TiO_2 surface for 50 ALD cycles of DMAI/H_2O, in contrast to a *hydrated* Si/SiO_2 surface. We further prepared TiO_2 crystals that present a range of surface *vo* densities that increase with high vacuum annealing temperature. In situ spectroscopic ellipsometry reveals that an increase in surface *vo* density is correlated to an increase in the Al_2O_3 ALD nucleation density, **Figure 3**, providing evidence for targeted growth at surface *vo* defects.[2]

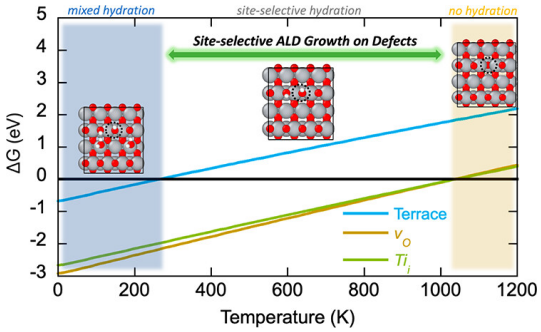

Fig. 2: Free energy of adsorption for terrace and point defects on the (110) facet.

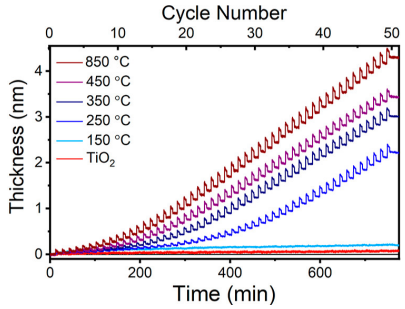

Fig 3: ALD Al_2O_3 nucleation depends upon the *vo* surface density, as controlled by TiO_2 substrate vacuum annealing temperature.

Facet and Step Selectivity via Selective Hydration of Indium Oxide. A related approach was applied to discriminate among distinct surface sites on bixbyite, In_2O_3. Using density functional theory (DFT), we predicted the discriminant hydration and hydroxylation of In_2O_3 terrace and step-edge sites that depends strongly on the substrate temperature at low water coverage.[3] The temperature at which hydroxylation of In_2O_3(111) terrace sites becomes unfavorable is 512 K. However, hydration of the step edge, which is modeled as a small In_2O_3(211) facet, remains hydroxylated until 1154 K. The computational study reveals a wide selective hydroxylation window larger than 600 K where hydroxylation is unfavorable on terrace sites but remains favored on step edges. As such, we hypothesize that nucleation/growth of the MgO ALD process will be hindered in the absence of In_2O_3 surface hydroxyls. In situ ellipsometric analysis of MgO ALD on polycrystalline (111)-textured In_2O_3 reveals nucleation/growth rates that are significantly lower than those for a SiO_2-terminated Si wafer. Steady-state growth (~0.12 nm/cycle) on itself (MgO) is achieved after 10 – 15 cycles on Si. In contrast, significantly lower growth rates characteristic of poor nucleation are observed on In_2O_3 in early cycles, and steady state growth is still not achieved after 20 cycles on In_2O_3. The very slow, but non-zero, nucleation suggests that a minority of "defective" surface sites (e.g. In_2O_3(211) step-edge sites) may remain to allow some foothold for MgO nucleation. Therefore, through this nucleation study, we have identified yet another ALD process that appears limited to the proton-mediated ligand release

mechanism required for our selective hydration strategy. The potential efficacy of defect repair was evaluated via examination of the DOS distribution of In_2O_3 surface sites to identify intragap states, which may act as electronic traps in optoelectronic devices. We hypothesized that wide band gap oxides including MgO, Ga_2O_3, and Al_2O_3 proximally bonded to In_2O_3 defect surface sites might modify the energy level of some electronic defects on the semiconductor surface to remove them from the bandgap. We calculated the DOS of a step edge In_2O_3(211) surface before and after reaction with three metalorganic precursors and predict Al and Ga SIR products may ameliorate mid-gap states , **Figure 4**.

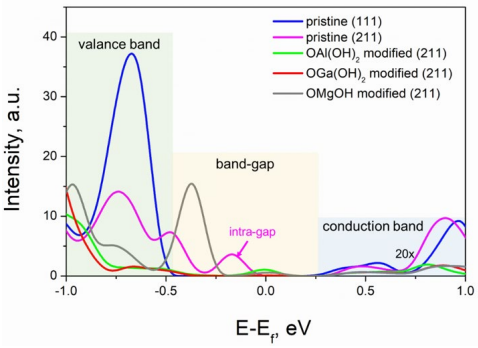

Fig. 4. The computed DOS of In_2O_3(111) terraces and step edges (211) before and after SIR.

Ultra-Sensitive, Time-Resolved Measurement of Surface Reaction Heat. We have developed in situ calibrated pyroelectric calorimetry as a probe of reaction heat evolved *during* the surface reaction.[4, 5] We have successfully designed and implemented an ALD calorimeter to measure the absolute heats and kinetics of ALD reactions on planar surfaces with thermal and temporal resolution down to 0.1 μJ/cm^2 (0.6 meV/nm^2) and 50 ns. The new benchmarks are orders of magnitude more sensitive and faster than complementary in situ measurement techniques typically employed in ALD research. We calibrated a pyroelectric capacitor that produces a voltage proportional to the crystal temperature change using a laser pulse to provide a known heat transfer.[4] The transient response was used to fit a mathematical model of the pyroelectric response, cooling rates, and electronic signal decay, **Figure 5**. In subsequent (dark) ALD surface reactions, we can then quantitatively convert the measured calorimeter voltage response to reaction heat generation per time. ALD calorimetry provides direct experimental access to the most rigorous output of first principles computation – reaction enthalpy – enabling comparison of our initial results to predictions based on computational mechanistic hypotheses. This unique design, implementation, calibration, and signal modeling for pyroelectric calorimetry of ALD enabled the first quantitative measurement of the TMA reaction heat, which we compared to computationally predicted reaction enthalpies.[5] The 50-micron thick crystal allows for a rapid heat transfer and pyroelectric response such that we resolved two equal TMA surface reaction heats as the traveling wave of precursor first arrives at the front and then back of the calorimeter crystal, **Figure 6**. As expected for the well-studied self-limiting reaction of TMA with a hydroxylated alumina surface, both the thickness (growth rate) and generated heat

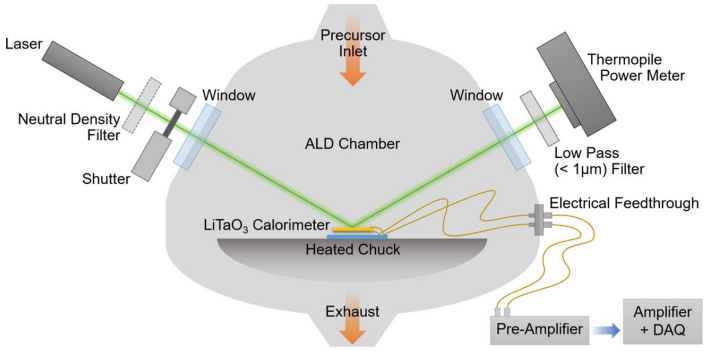

Fig. 5. Schematic of calorimeter installation in the ALD chamber.

are saturated with TMA dose times that are fractions of a second. Our calibrated calorimetric measurements of the TMA and H_2O reactions reveal absolute experimental heat that is in remarkable agreement with the standard enthalpy of formation. Furthermore, the measurements offered the first opportunity to benchmark the computational simulation of both complementary surface reactions in this prototypical ALD process. We demonstrate that the most rigorous computational models still deviate from our experimental calorimetry results, revealing that our understanding of the most ubiquitous ALD reactions remain incomplete.

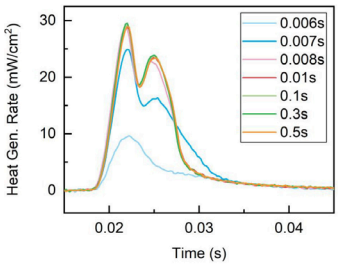

Fig. 6. The reaction heat generation for variable TMA dose times.

Future Plans

Addressing surface and buried recombination sites on oxide photoabsorbers: We will apply SIR design rules to the surface and buried interfaces of visible light absorbers. Targeted defect repair is necessary to reduce recombination without inhibiting charge carrier extraction.

Pioneering New SIR Strategies: Beyond Selective Hydration: DFT predicts a lack of selectivity through our selective hydration strategy for some low index facets of TiO_2. Therefore, we propose to improve the versatility of B-cycle selectivity by investigating the reactivity of small molecules.

Dedicated ALD Calorimetry Reactor Design, Modeling, and Data Handling: We will design, build, and benchmark an ALD reactor that significantly improves the accuracy and time-resolution of calorimetric measurements to reveal hidden mechanisms of multi-step surface reactions.

References

1. E. P. Kamphaus, J. C. Jones, N. Shan; A. B. F. Martinson, L. Cheng, *Site-Selective Atomic Layer Deposition on Rutile TiO_2: Selective Hydration as a Route to Target Point Defects,* J. Phys. Chem C **127** 1397 (2023).

2. J. C. Jones, E. P. Kamphaus, J. R. Guest, A. U. Mane, L. Cheng, A. B. F. Martinson, *Site-Selective Atomic Layer Deposition at Thermally Generated Surface Oxygen Vacancies on Rutile TiO_2,* Chem. Mater. **35** 2857 (2023).

3. N. Shan, J. C. Jones, C. Luo, A. S. Hock, A. B. F. Martinson, L. Cheng *Selective Hydroxylation of In_2O_3 as A Route to Site-Selective Atomic Layer Deposition*, J. Phys. Chem. C **126**, 10359 (2022).

4. A. R. Bielinski, E. A. Sprague-Klein, B. T. Phelan, A. B. F. Martinson, *Pyroelectric Heat Detection for Calibrated Measurement of Atomic Layer Deposition Reaction Heat*, Chem. Mater. **33**, 6176 (2021).

5. A. R. Bielinski, E. P. Kamphaus, L. Cheng, A. B. F. Martinson *Resolving the Heat of Trimethylaluminum and Water Atomic Layer Deposition Half-Reactions* J. Am. Chem. Soc. **144**, 15203 (2022).

Publications

1. A. R. Bielinski, E. A. Sprague-Klein, B. T. Phelan, A. B. F. Martinson, *Pyroelectric Heat Detection for Calibrated Measurement of Atomic Layer Deposition Reaction Heat*, Chem. Mater. **33**, 6176 (2021).

2. J. A. Dolan, H. Cai, L. Delalande, X. Li, A. B. F. Martinson, J. J. de Pablo, D. Lopez, P. F. Nealey, *Broadband Liquid Crystal Tunable Metasurfaces in the Visible: Liquid Crystal Inhomogeneities Across the Metasurface Parameter Space* ACS Photonics **8**, 567 (2021).

3. N. Shan, J. C. Jones, C. Luo, A. S. Hock, A. B. F. Martinson, L. Cheng, *Selective Hydroxylation of In_2O_3 as A Route to Site-Selective Atomic Layer Deposition*, J. Phys. Chem. C **126**, 10359 (2022).

4. A. R. Bielinski, E. P. Kamphaus, L. Cheng, A. B. F. Martinson, *Resolving the Heat of Trimethylaluminum and Water Atomic Layer Deposition Half-Reactions* J. Am. Chem. Soc. **144**, 15203 (2022). [Featured in JACS Spotlights]

5. E. P. Kamphaus, N. Shan, J. C. Jones, A. B. F. Martinson, L. Cheng, *Selective Hydration of Rutile TiO_2 as a Strategy for Site-Selective Atomic Layer Deposition* ACS Appl. Mater. Interfaces **14**, 21585 (2022).

6. Q. He, Y. Qiao, C. M. Jimenez, R. Hackler, A. B. F. Martinson, W. Chen, M. V. Tirrell, *Ion Specificity Influences on the Structure of Zwitterionic Brushes* Macromolecules **56**, 1945 (2023).

7. E. P. Kamphaus, J. C. Jones, N. Shan; A. B. F. Martinson, L. Cheng, *Site-Selective Atomic Layer Deposition on Rutile TiO_2: Selective Hydration as a Route to Target Point Defects,* J. Phys. Chem C **127**, 1397 (2023).

8. J. C. Jones, E. P. Kamphaus, J. R. Guest, A. U. Mane, L. Cheng, A. B. F. Martinson, *Site-Selective Atomic Layer Deposition at Thermally Generated Surface Oxygen Vacancies on Rutile TiO_2,* Chem. Mater. **35**, 2857 (2023).

9. A. R. Bielinski, E. P. Kamphaus, L. Cheng, A. B. F. Martinson, *Resolving the Heat Generated from ZrO_2 Atomic Layer Deposition Surface Reactions* Angew. Chem. Int. Ed. ASAP (2023).

Exploration and Design of Architected Polymers and Properties for Additive Manufacturing

Amit Naskar, Logan Kearney, Joshua Damron, Bobby G. Sumpter, and Amy Elliott, *Oak Ridge National Laboratory, Oak Ridge, TN 37830*
Frank Leibfarth, *University of North Carolina Chapel Hill, Chapel Hill, NC 27599*
Laurene Tetard, *University of Central Florida, Orlando, FL 32826*

Keywords: Additive Manufacturing, Operando characterization, Non-equilibrium dynamics, Architected polymers

Research Scope: In the pursuit of additive manufacturing (AM) modalities, 3D printed polymer platforms are already thriving and have substantial expectation of future growth and impact on many industries. Currently, there are no guidelines for the *a priori* design of polymers for high throughput AM that have the required flow properties for deposition while exhibiting desired mechanical properties in the product. The scope of this work is to gain a fundamental understanding of how the complex physical and chemical interactions between branched, network-forming, multi-dimensional macromolecules can be tuned to control bulk properties in AM. While the considerations for 3D printed polymers are analogous to traditional extrusion based thermoplastic or thermoset materials, they usually achieve only a fraction of the mechanical properties obtained through legacy methods. This is primarily due to the hurdles associated with the interplay of processability and the presence of non-equilibrium states which impede polymer interdigitation and bonding between layers. By expanding the dimensionality of the polymer with a rationally designed architecture, we hypothesize that the residual stress transverse to the printing direction can be modulated. We aim to synthetically target intermediately grafted polymers which can flow and achieve favorable interactions for deposition while retaining sufficient chain entanglement for property enhancement (**Fig. 1**). Property modulation can be further varied by using co-polymers of differing properties (stiffness, polarity, etc.) between mainchain and sidechain to tune phase morphologies and layer interactions. Beyond the manipulation of physical interactions, the incorporation of stimuli responsive chemistries (*e.g.,* thermal, light) on the sidechains to induce thermoset behavior will add an additional dimension to the design space. Elucidating these novel systems requires detailed characterization, including scattering, nuclear magnetic resonance (NMR), nano-Infrared (IR) Atomic Force Microscopy (AFM), theory and molecular dynamic simulations.

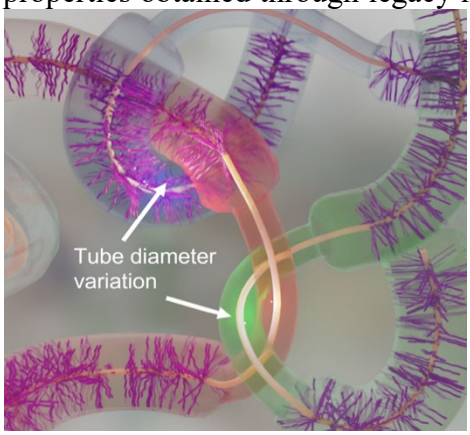

Figure 1. Variable mean-field depiction of branched, architected polymers.

Recent Progress: *Gel Phase Optimization.* To interrogate our hypothesis, we began with the identification of scalable synthesis routes to grafted polymeric morphologies and model macromolecular systems. To develop a detailed understanding of structure–property relationships, the dimensions of the ungrafted regions in our periodic graft co-polymers must be reliably controlled through the preparation of a heterogenous gel phase. In addition, the grafted side chain

concentration and length must be manipulable through controlled polymerization routes. We have prepared gels based on commodity polyethylene (PE) and polypropylene (PP) by varying the mass fraction of polymer and crystallization conditions to tune the resulting crystallite phase fraction and lamellar thickness. The contrast in free volume from the crystallites and the solvated amorphous regions allows the introduction of functional groups in a periodic configuration to encourage bulk toughening imparted by contributions from the exposed main chain. Low-field ^{1}H NMR relaxometry[1] showed excellent agreement with the calorimetry data and identified the appropriate temperature envelopes for functionalization of these gels.

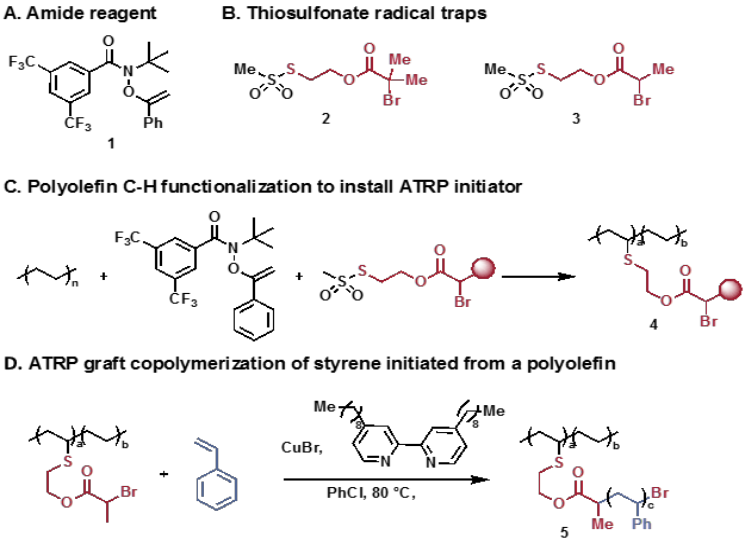

Figure 2. C–H functionalization of polyolefins for the synthesis of polyolefin graft copolymers.

Model system development. We have polymerized PE and d-PE between 50 to 150 kDa with PDIs < 1.1 via ionic polymerization. These enabled accurate determination of system dynamics without the complications that arise from highly disperse commodity polyolefin substrates. The d-PE is critical in isolating contributions from sidechain/mainchain in a controlled manner and allows for synergistic NMR and neutron scattering dynamic measurements to corroborate the scaling relationships within the chain conformations.

Polymer grafting synthesis. We recently identified an O-alkenylhydroxamate reagent[2] (**Fig. 2A)** whose steric demand around nitrogen and strong thermodynamic driving force for hydrogen atom transfer (HAT) results in selective and efficient functionalization, with an observed lack of chain coupling or scission events. We hypothesized that the amide reagent, when combined with a radical trap with fast chain-transfer kinetics, would provide a platform to access polyolefins with initiating sites for ATRP with discrete control over polymer structure. Additional synthetic steps are underway to introduce functional groups for subsequent controlled radical polymerization-based grafting from schemes to the prepared gels in suspension. In parallel, we have prepared graft copolymers as structural analogues. A key consideration was the suppression of radical initiated halogen transfer as a potential side-reaction during polyolefin functionalization that would remove the bromine from the ATRP initiator. It is expected that the electron deficient amidyl radical would be selective for HAT over halogen transfer due to polarity matching effects. We initially designed and synthesized the two thiosulfonate ATRP initiators based on α-halo esters (**Fig. 2B**). Initiator **2** is broadly applicable to ATRP but may be prone to dehalogenation during the C–H functionalization reaction due to the lower bond dissociation energy compared to the secondary bromide on initiator **3**. Using thiosulfonates **2** and **3 (Fig. 2B**), we found that initiator **3** performed better and attributed this to its *i)* higher functionalization efficiency and *ii)* limited dehalogenation compared to initiator **2** (10% vs. 25%). After successfully adding the ATRP initiator onto LLDPE, we sought to make a graft copolymer using copper catalyzed ATRP using CuBr–bipyridine as a catalyst–ligand combination (**Fig. 2D**). The functionalized LLDPE contained 2 mol% initiator, or

one ATRP initiating site for every 50 ethylene repeat units. We successfully grafted an average of 20 repeat units of styrene per grafting site. A preliminary survey into the polymer properties demonstrated that the graft-copolymer exhibited distinct thermal transitions. If successful, such grafting strategies would inform new polymer synthesis strategies including paths towards upcyling commodity polymers.

Vitrimeric welding for AM. To introduce thermoset-like side chain chemistry, we are exploring vitrimer or covalent adaptable network chemistry. These materials are promising for AM and can be reusable/recyclable due to their ability to bond exchange at their vitrimeric temperature (T_v). Using an ester-based transesterification chemistry, we synthesized a sustainable, reshapable vitrimer (**Fig. 3**) with excellent mechanical properties, potentially suited for an AM platform. Additional vitrimeric systems are being explored for their potential with grafted polymers. This is a promising approach which can help address the issues with layer-by-layer printing by incorporating a vitrimeric 'welding' within the printed layers. As a thorough exploration of this chemistry, we are developing sophisticated approaches to detect T_v, teasing out the subtleties between the onset of bond flipping events and those that are strictly from dynamics within the system. Using ^{1}H NMR, we detected transitions that align closely with the malleability point of this vitrimer (**Fig. 4**) and using state of the art nano-IR AFM[3] we probed site specific chemistry as a function of temperature (**Fig. 3**) that supported these conclusions. These efforts could provide impactful understanding in the field of vitrimeric chemistry and characterization.

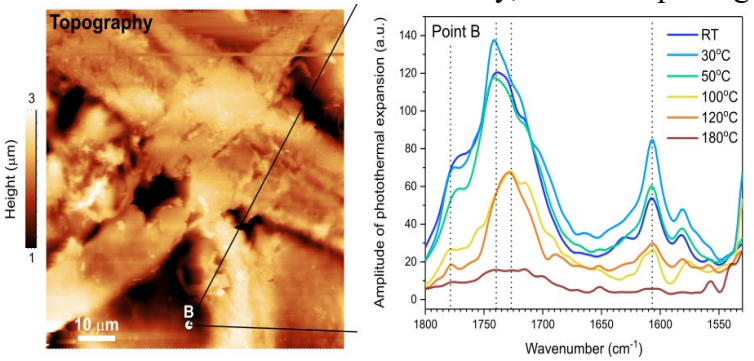

Figure 3. Temperature dependence of carbonyl resonances with site specific resolution using nanoIR AFM.

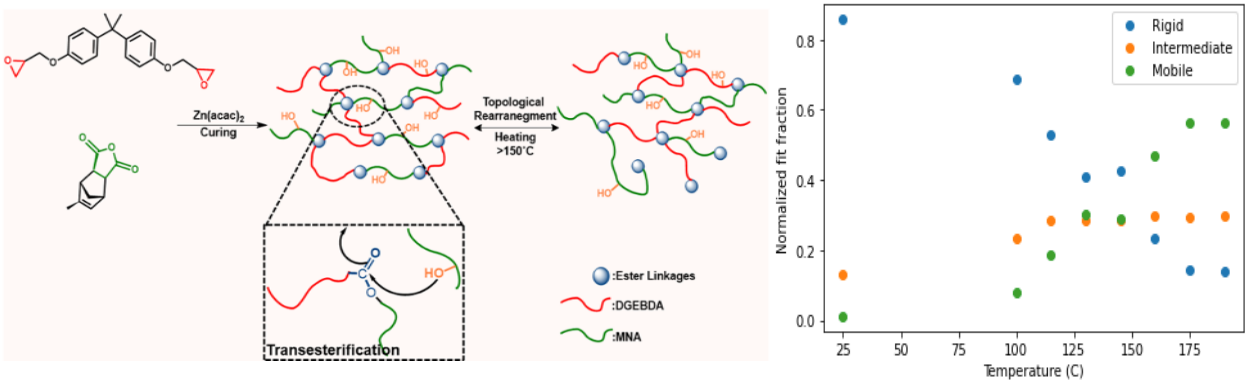

Figure 4. Left: Multi-layer vitrimer composite with reshapability at 150ºC. Right: phase fraction determination from ^{1}H low-field NMR.

Molecular Dynamics and Operando Characterization. Efforts to comprehend the physical behavior of sparsely grafted polymers are supported by molecular dynamics (MD) simulations. To concentrate on the physical factors, a coarse-grained representation of the polymer chain is employed, which disregards the chemical distinctions among coarse-grained beads. The zero-shear viscosity is being computed using equilibrium (Green-Kubo and Einstein methods) and non-equilibrium MD simulations to gain insights into the effect of chain architecture on polymer flow

properties (**Fig. 5**). Additionally, we are investigating the impact of phase morphologies by constructing models that explicitly consider phase separation. This is crucial for understanding the interplay between polymers with varying chemistries in terms of the main chain and sidechain, and it will contribute to the comprehension of the behavior in non-equilibrium phases, as we anticipate phase separation to occur within systems comprising different chemistries within the same polymer chain. This will be key in designing polymers with self-assembling interactions post printing. To directly visualize these effects, we are also developing purpose-built techniques capable of unraveling multi-scale attributes of materials. We commissioned a custom optical configuration for microscale tomographic reconstruction of polymeric 3D printed parts. Our initial sample sets included a printed composite containing reinforcing fiber (**Fig. 6**). We will continue to refine the image quality using resources within ORNL to study the effects of polymer architecture and residual stresses and crystallization induced void formation in model polymeric printed parts. In addition to direct microscale visualization, we have utilized our state-of-the-art benchtop x-ray source to spatiotemporally resolve structural changes in polymer melts *in operando* through wide angle and small angle x-ray scattering. The combination of approaches would provide actionable insight into the printing process enabling fundamental principles driven insight into AM.

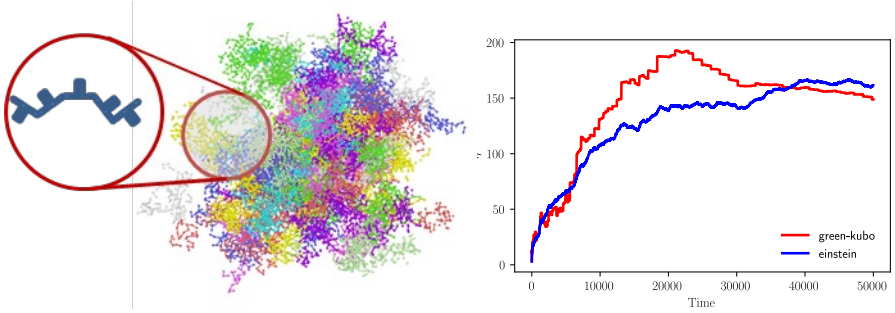

Figure 5. MD model of sparsely grafted polymer chain. Methodological verification is being achieved by computing viscosity with different methods.

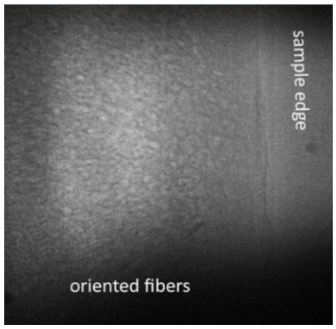

Figure 6. Internal structure of the oriented fiber in 3D printed composite.

Future Plans: We will continue to develop our synthetic schemes to interrogate the viability of sparsely branched polymer and thermoset chemistries for AM. Products from C-H gel-phase functionalization will be sequenced and studied for dynamic contrast through high field ^{13}C NMR. Functional end caps will be incorporated from the Br terminated side chains which can form reversible crosslink reactions. After the incorporation of dynamic covalent bonds in otherwise thermoplastic systems, we will explore aspects of controlled metastability by synthesizing di-block copolymers and slowly incorporate complexity from sidechains. These systems will serve to establish guiding principles for stimulus-induced structure development in evolving systems. Systems with suitable neutron contrast have been prepared and proposals for the next user cycle are in preparation built upon our initial data from x-ray scattering experiments. Of particular interest are phase separation kinetics and phase stability as a function of dynamic covalent bond concentration, block structure, and processing history.

References

1. Maus, A.; Hertlein, C.; Saalwächter, K. *A Robust Proton NMR Method to Investigate Hard/Soft Ratios, Crystallinity, and Component Mobility in Polymers*. Macromol. Chem. Phys., **207** (13), 1150–1158 (2006).

2. Fazekas, T. J.; Alty, J. W.; Neidhart, E. K.; Miller, A. S.; Leibfarth, F. A.; Alexanian, E. J. *Diversification of Aliphatic C–H Bonds in Small Molecules and Polyolefins through Radical Chain Transfer.* Science **80** (*375),* 6580 (2022).
3. Tetard, L.; Passian, A.; Farahi, R. H.; Thundat, T.; Davison, B. H. *Opto-Nanomechanical Spectroscopic Material Characterization*. Nat. Nanotechnol., **10** (10), 870–877 (2015).

Publications

1. Seo, J., Kearney, L.T., Toomey, M.D., Keum, J.K. and Naskar, A.K., *Polyester-based epoxy vitrimer integrating spent coffee ground as a natural filler*. Composites Part B: Engineering, **260**, p.110756. (2023)
2. Varadarajan, A., Kearney, L.T., Keum, J.K., Naskar, A.K. and Kundu, S., *Effects of Salt on Phase Behavior and Rheological Properties of Alginate–Chitosan Polyelectrolyte Complexes*. Biomacromolecules, **24(6)**, 2730-2740. (2023)
3. Nguyen, N.A., Bowland, C.C., He, L., Osti, N.C., Phan, M.D., Keum, J.K., Tyagi, M., Meek, K.M., Littrell, K.C., Mamontov, E. and Ankner, J., *A Sustainable Multi-Dimensional Printable Material*. Advanced Sustainable Systems, p.2300079. (2023)

Molecularly Organized Nanostructured Materials

Jun Liu, Maria Sushko, James De Yoreo, Praveen Thallapally, Jinhui Tao

Keywords: heteroepitaxy, layered heterostructures, van der Waals materials, in situ observation of nucleation and growth

Research Scope

The project aims to develop innovative approaches employing molecularly directed interfacial reactions to control crystallization and self-assembly of two-dimensional (2D) nanostructured materials that are becoming very important for energy and quantum information applications. The project addresses the challenge of developing scalable synthesis of 2D materials with structural control of sizes, crystallinity, morphology, surface, and interfacial chemistry. In particular, it focusses on exploring the hypothesis that the dimensionality and crystalline structure of the materials can be controlled by interfacial energies and solvation structure in the interfacial region within a few nanometers from the substrate (nucleation interphases). Several key synthetic strategies are being developed in which interfacial energies can be systematically manipulated using functional groups on the substrate, the solvation structure, nanoscale confinement in ordered surfactant templates, the strain energy between the crystal, and the substrate and electrochemical potentials. These effects are investigated using three material systems: (1) 2D nanosheets formed by metal oxides and metals that have three-dimensional (3D) crystalline structures, (2) 2D and 3D nanocomposites of metal chalcogenides and dichalcogenides, and (3) organic crystals whose lattice structures can be precisely tuned for epitaxial control from the substrate. A combination of state-of-the-art experimental and theoretical techniques are used to reveal nucleation mechanisms, nucleation pathways, and interfacial structures, and provide quantitative information about interfacial energies, the growth kinetics, and solid-liquid interfacial band structures.

Recent Progress

This project is demonstrating the potential of a general synthetic approach for multiscale structural control by manipulating the interfacial nucleation and growth pathways, developing an integrated theoretical and experimental approach, and developing and applying new in situ characterization tools. Recent studies focused on the understanding the driving forces for the morphological and dimensionality control in solution synthesis of layered and porous heterostructures. We identified the role of intermediate phases in directing the architecture and dimensionality of the growing organic crystals and hybrid heterostructures. The detailed studies of the interfacial forces at graphitic and metal surfaces revealed that interfacial forces can be finely tuned by the applied electric potential to drive nucleation into the interphase region and enhance the uniformity of the organic-crystal film. These studies also revealed that the applicability of the

classical theory of heteroepitaxy to van der Waals crystals is limited to materials with localized and semi-localized electron density.

Role of intermediate phases in directed synthesis of porous and layered architectures. Controlling the architecture and function of framework and layered materials, and their heterostructures requires a detailed understanding of the multistep pathways of their formation. By identifying intermediate coordination complexes, we gained insights into the complex role of a structure-directing agent (SDA) in the synthetic realization of a promising metal organic framework (MOF) material [1]. The formation of molecular complexes and larger coordination polymers observed in the SAXS spectra indicates that the role of the SDA goes beyond that of a benign pore-occupying guests or charge-balancing molecules (Fig. 1). Evidence of speciation in a ubiquitous solvent further corroborated the reactive pathway of the SDA and the metal toward the formation of the final framework. This conclusion was supported in the solvent-starved conditions present during in situ XRD data collection, where we observed the stabilization and crystallization of the molecular species $[In(HIm)_6](NO_3)_3$. Such behavior highlights the importance of in situ monitoring for the discovery of intermediate phases and understanding synthetic pathways.

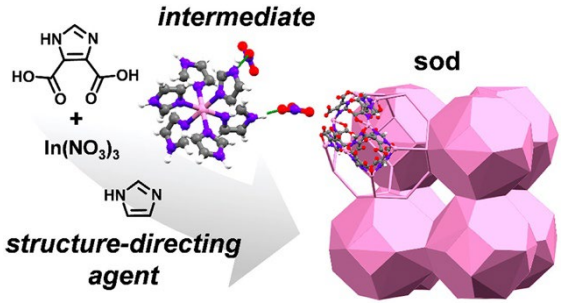

Figure 1. The role of the imidazole SDA was revealed by time-resolved in situ powder X-ray diffraction and small-angle X-ray scattering

Identifying the growth pathway of layered heterostructures further supported the generality of the conclusion about the reactivity of SDAs during solution synthesis. Like molecular SDAs, dispersed 2D flakes of van der Waals material were shown to play a dual role of 2D templates and \reactive intermediate phases in directing two-dimensional growth of materials that otherwise have three-dimensional structure [2]. In situ XRD observations indicated that the epitaxial layered heterostructure of ZnO-MoS_2 is formed through stabilizing intermediate states of $Zn(OH)_2$ on S-Mo-S-OH. The layered architecture of this heterostructure was confirmed using high resolution TEM and the EDS elemental analysis (Fig. 2). The developed synthetic approach furnishes a new general method for the scalable and reproducible synthesis of 2D layered heterostructures through stabilizing intermediate states. Furthermore, the hybrid heterostructures

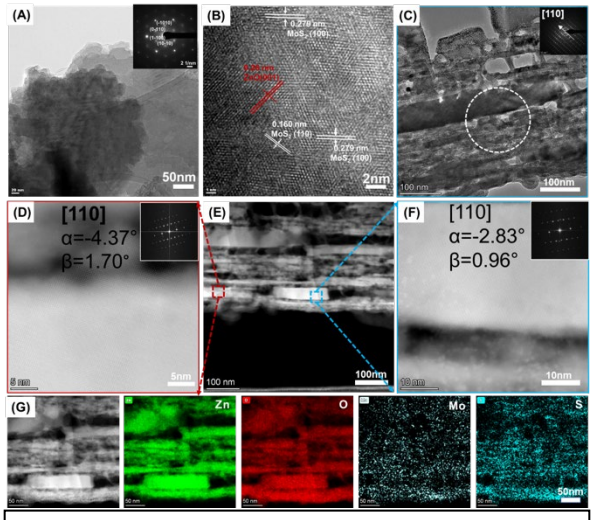

Figure 2. Scalable solution synthesis of epitaxial ZnO-MoS_2 heterostructures. TEM images (A-E) and EDS mapping (G) confirm the layered structure of interchanging ZnO and MoS_2 regions.

were shown to have emergent properties not observed in single components. The MoS_2 and ZnO layer alignment along [001] direction and strong interactions between MoS_2 and ZnO regions in the epitaxial heterostructure produced type II band alignment with the CBM associated with Mo 4d states of MoS_2, a VBM mostly with O 2p states of ZnO with a small contribution from Mo 4d. The bandgap of 1.33 eV facilitates efficient absorption of light in the visible range. The resulting quantum confinement and band alignment, that reduces recombination of photogenerated electrons and holes, was shown to improve the photocatalytic efficiency of the layered material by almost 50%, compared to the corresponding single-phase catalysts and mixtures.

Controlling interfacial structure through the flavor of van der Waals forces and applied potential. We demonstrated that the flavor of van der Waals interactions between the substrate and the growing film dictates whether the classical theory of heteroepitaxy is applicable. A combined experimental and theoretical study illustrated this concept using the nucleation of layered conductive MOF, Ni-CAT-1, on graphite and metal substrates [3]. We identified the electronic structure of the substrate as key to the growth pattern of the 2D MOF and showed that the nucleation and growth of Ni-CAT-1 MOFs at a solid/liquid interface is controlled by the type of van der Waals interactions between the substrate and p electrons of the linker molecules (Fig. 3). For graphite and copper substrates, substrate-linker interactions result in different interfacial layers but a parallel alignment of Ni-CAT-1 to the substrate surface and the MOF stacking into vertical columns. However, epitaxial matching with the substrate is only observed on graphite surface, which interacts with the linker via π-π interactions. The resulting MOF film has lower nucleation density and defects within the film, whereas π-metal interactions between the linker and the copper substrate dictate faster nucleation, higher nucleation densities, and the presence of extended defects. This work provides insights into the role of electron localization in the substrate in interfacial control over the growth of a 2D π-conjugated MOF film and other van der Waals heterostructures.

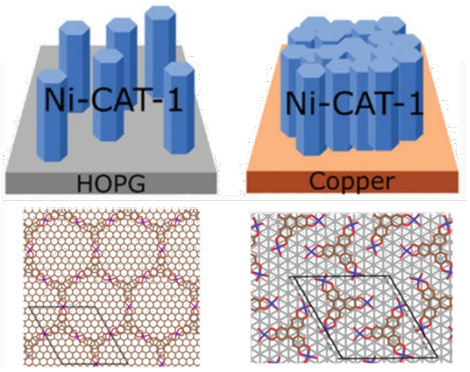

Figure 3. Electron localization in the substrate control the growth mode of a conductive 2D MOF through either epitaxy or non-specific templating.

Additional control over interfacial nucleation and the uniformity of the film can be gained by tuning the strength of van der Waals interactions between the film and the substrate by the applied potential. Reducing the strength of these interactions and modifying the structure of the electric double layer at electrified interfaces can shift nucleation into the interphase region. Under these conditions direct templating through van der Waals epitaxial coupling is replaced by non-specific physical templating [4]. Using these principles, we developed an anodic electrodeposition (AED) approach to fabricate a uniformly deposited 2D conducting MOF on nickel foam (Fig. 4). The mechanism of film formation was identified using simulations of the driving forces for ion accumulation in the electric double layer. Simulations predict that under electrochemical synthesis

conditions used in this study Ni^{2+} ions and NiPc-NH^{-} precursor molecules are driven toward the interface by ion correlation forces and accumulate 1.0 nm and 1.5 nm from the nickel foam surface, respectively. The large energy barriers at the electrode surface prevents Ni^{2+} and precursor deposition onto nickel foam surface creating ideal conditions for their coordination in the solvent-separated state. Because NiPc-MOF_{AED} nucleation takes place in the narrow region in the vicinity of the electrode and not directly on the nickel foam, a uniform particle size and uniform coverage is predicted.

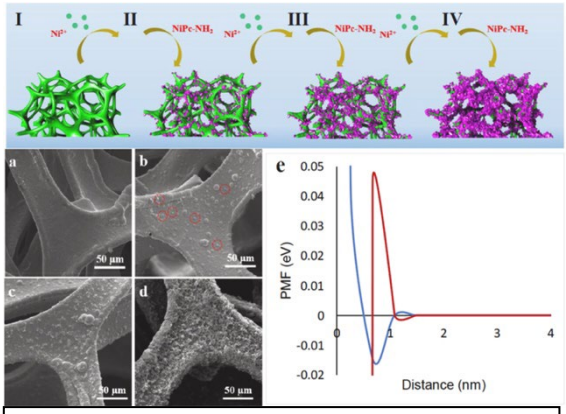

Figure 4. Electrodeposition mechanism of NiPc-MOF_{AED}@NF (I-IV) and corresponding SEM images (a-d). Simulated potential of mean force of Ni^{2+} (blue line) and NiPc-NH^{-} (red line) at nickel foam (NF) electrode favor nucleation ~1 nm from the substrate (e).

Overall, these studies identified the main interfacial factors controlling the nucleation and growth of van der Waals films and paved the way for the development of scalable solution synthesis of highly oriented functional materials.

Future Plans

Future research will continue to focus on understanding the principles of heteroepitaxy in van der Waals layered materials and the mechanisms of dimensionality control in solution synthesis of 2D layered heterostructures. New experimental capabilities will enable the shift in focus from studying the effects of mesoscale interactions at solid-liquid interfaces on growth pathways to the understanding of microscopic forces directing heterogeneous nucleation. We will use atomically precise CVD substrates and the developed in situ quantum capacitance measurements to elucidate free-energy landscape and transition pathways to ascertain whether growth of a new phase fits within the framework of classical heteroepitaxy. We will also aim to elucidate the role of defects and local fields in directing early stages of nucleation at electrified interfaces to gain insights into the driving forces for spherical and dendritic growth, and the transition between these two regimes.

References

1. M. A. Sinnwell, Q. Miller, L. Palys, D. Barpaga, L. Liu, M. E. Bowden, Y. Han, S. Ghose, M. L. Sushko, H. T. Schaef, W. Xu, M. Nyman, and P. K. Thallapally, *Molecular intermediate in the directed formation of a zeolitic metal-organic framework*, Journal of the American Chemical Society **142**,17598 (2020).
2. S. Shin, J. Tao, N. L. Canfield, M. E. Bowden, J. Heo, D. Li, J. J. De Yoreo, J. Liu, P. K. Thallapally, and M. L. Sushko. *Self-assembly and oriented growth of conductive Ni-CAT-1 metal-organic framework at solid-liquid interfaces*, Advanced Materials Interfaces **10**, 2202031 (2023).
3. L. Liu, P. Chen, X. Zhang, L. Kovarik, J. J. De Yoreo, J. Liu, and M. L. Sushko. *Scalable solution synthesis and photocatalytic activity of layered ZnO and MoS_2 heterostructures*, Advanced Materials Interfaces (in press).

4. H. Jia, X. Tao, S. Shin, M. L. Sushko, S. Lu, H. Matthew, P. K. Thallapally, J. Liu, and Z. Gu, *In situ anodic electrodeposition of 2D conductive MOF@nickel foam for high-performance flexible supercapacitor*, Journal of Power Sources **526**, 231163 (2022).

Publications

1. J. Hu, L. Li, E. Hu, S. Chae, H. Jia, T. Liu, B. Wu, Y. Bi, K. Amine, C. Wang, J. Zhang, J. Tao, and J. Xiao, *Mesoscale-architecture-based crack evolution dictating cycling stability of advanced lithium ion batteries*, Nano Energy **79**, 105420 (2021).

2. K. J. Kim, J. Culp, P. Ohodnicki, P. K. Thallapally, and J. Tao, *Synthesis of high-quality Mg-MOF-74 thin film via vapor-assisted crystallization*, ACS Applied Materials & Interfaces **13**, 35223 (2021).

3. R. G. Surbella, D. D. Reilly, M. A. Sinnwell, B. K. McNamara, L. E. Sweet, J. M. Schwantes, and P. K. Thallapally, *Multifunctional Two-Dimensional Metal–Organic Frameworks for Radionuclide Sequestration and Detection*, ACS Applied Materials & Interfaces **13**, 45696 (2021).

4. P. K. Thallapally and M. Kim, *Effective CH_4/N_2 Separation using NU-1000 at High Pressures,* Journal of Coordination Chemistry **74**, 216 (2021).

5. J. Wang, C. Shi, M. L. Sushko, J. Lan, K. Sun, J. Zhao, X. Y. Liu, and X. Yan, *Boost of the Bio-memristor Performance for Artificial Electronic Synapses by Surface Reconstruction*, ACS Applied Materials & Interfaces **13**, 39641 (2021).

6. X. Wu, S. Qui, Y. Liu, Y. Xu, Z. Jian, J. Yang, X. Ji, and J. Liu, *The Quest for Stable Potassium-Ion Battery Chemistry*, Advanced Materials **34**, e2106876 (2021).

7. H. Jia, X. Tao, S. Shin, M. L. Sushko, S. Lu, H. Matthew, P. K. Thallapally, J. Liu, and Z. Gu, *In situ anodic electrodeposition of 2D conductive MOF@nickel foam for high-performance flexible supercapacitor*, Journal of Power Sources **526**, 231163 (2022).

8. M. L. Sushko, *Crystallization pathways and interfacial drivers for the formation of hierarchical architectures*, Journal of Crystal Growth **600**, 126914 (2022).

9. S. Shin, J. Tao, N. L. Canfield, M. E. Bowden, J. Heo, D. Li, J. J. De Yoreo, J. Liu, P. K. Thallapally, and M. L. Sushko, *Self-assembly and oriented growth of conductive Ni-CAT-1 metal-organic framework at solid-liquid interfaces*, Advanced Materials Interfaces **10**, 2202031 (2023).

10. M. Kim, A. J. Robinson, M. L. Sushko, and P. K. Thallapally, *Aluminum-based microporous metal-organic framework for Xe/Kr separation*, Journal of Industrial Engineering Chemistry **118**, 181 (2023).

Design of structural inhomogeneities to control functional properties

Peter V. Sushko[1], Yingge Du[1], Dongsheng Li[1], Long Luo[2], Micah P. Prange[1], Kelsey A. Stoerzinger[1,3], Hua Zhou[4]

[1] Pacific Northwest National Laboratory, Richland, WA 99352, USA; [2] Wayne State University, Detroit, MI 48202, USA; [3] Oregon State University, Corvallis, OR 97331, USA; [4] Argonne National Laboratory, Lemont, IL 60439, USA

Keywords: nanomaterials, strain, critical materials, catalysis

Research Scope

The overarching goal of this project is to achieve predictive understanding of microscopic factors that control the coupling between deformations in hierarchical nanostructures and their stability and electronic properties. We aim to exploit the coupling between the lattice deformations and electronic properties to manipulate reaction pathways and stabilities of reaction intermediates and to develop strategies for controlling catalytic activity of materials formed by the platinum group elements (PGE), transition metals (TM), and transition metal oxides (TMO). We will achieve these goals by pursuing three interrelated objectives: (1) Reveal mechanisms of thermally-induced deformations in metastable polymorphs of TMO, learn to control the corresponding deformation fields, and establish the effect of these deformations on TMO band bending. (2) Establish the structure and properties of interfaces between PGE and PGE/TM nanoparticles, determine distribution of strain induced by these interfaces, and link the character of interfacial deformations to the mechanisms of surface reactions and energetics of hydride formation. (3) Reveal relationships between structure, composition, strain distributions, and chemical activity to develop principles for the design of novel materials needed to reduce the dependence on PGE.

Our approach combines synthesis of strained nanomaterials exhibiting distinct types of deformations, ex situ and in situ characterization of their structural and compositional inhomogeneities as well as their catalytic performance, and atomic-scale modeling with an emphasis on mechanistic aspects of interfacial interactions, atomic and electronic transfer, and the effect of deformations. The outcomes of this work will be understanding of how to apply physical and chemical controls to tailor deformations at the atomic level to direct the behavior of electrons and reaction intermediates, thereby providing new avenues for controlling catalytic properties.

Recent Progress

Physical and chemical properties of nanoparticles (NPs) can be controlled by varying their size and shape. However, the effects of deformations in NPs remained elusive due to challenges of applying external strain to nanomaterials. We developed a methodology that allows us to assemble NPs into open structures formed by quasi-one-dimensional chains of these NPs.

Our method utilizes electro-generated H_2 and localized high pH at the cathode to remove the ligands on NPs and promote random collisions of NPs in solution. This approach produces assemblies (Pt-gels) prominently displaying Pt NP interfaces with the form of a Σ3 (111) twin grain boundaries (GB). Structural characterization reveals that particles in Pt-gels have similar crystallite sizes as their NP precursors. While Pt-gels do not exhibit signs of global lattice strain, there is a clear signature of local structural disorder and corresponding microstrain at the Σ3 (111) twin GBs, that is absent in free Pt-NPs. We found that Pt-gels demonstrated extremely high activity for catalytic hydrogen oxidation in air, enabling room temperature catalytic hydrogen sensing.

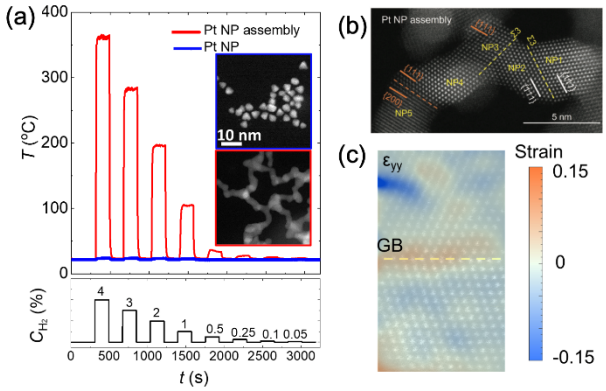

Figure 1. (a) Temperature readout of the H_2 sensors based on Pt NPs (blue) and Pt-gel (red) in response to stepwise decreasing H_2 concentrations (C_{H2}). Insets: isolated Pt NPs (top) and the same NPs assembled into a Pt-gel (bottom). (b) Structure of typical junctions in the Pt-gel. (c) Strain map near one of the twin GBs, demonstrating a distribution of tensile and compressive strains.

To examine how interactions between coupled NPs affect the rate of chemical reactions at their interfaces, we synthesized Pd/PdO_x material in a form of a network of interconnected nanodomains of Pd, PdO, and PdO_2 [Figure 2(a)]. Upon exposure of this system to 4% H_2, we discovered that PdO and PdO_2 were immediately (within ~1 sec) reduced to metallic Pd, as manifested by over a > 90% drop in electrical resistance. The 1-s response time of Pd/PdO_x under ambient conditions makes it a promising system for the rapid detection of H_2 gas leaks. On the basis of structural characterization and ab initio modeling, we generated a sequence of elementary processes that take place during the surface reduction: (i) metallic Pd at the Pd/PdO_2 interface enables fast H_2 dissociation to adsorbed H atoms along the Pd and PdO_2 surfaces; (ii) these H atoms interact with the outermost O atoms on the PdO_2 surface, thus forming H_2O and depleting the surface of oxygen; (iii) the surface Pd reorganize to form Pd-Pd bonds which leads to exposure of pristine PdO_2 surface and O out-diffusion; (iv) the formation of Pd skin-

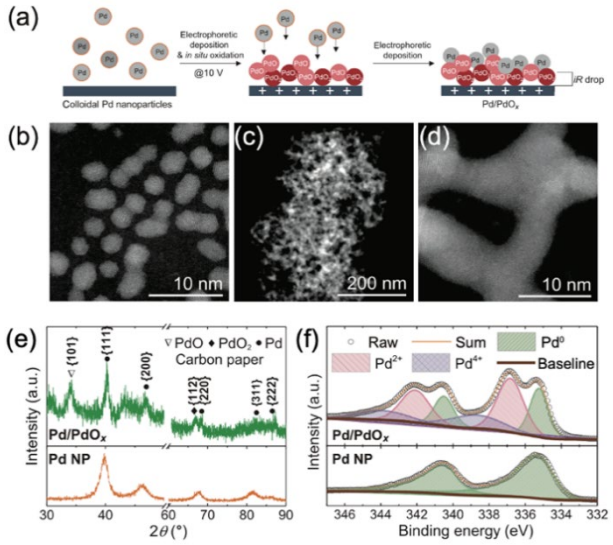

Figure 2. (a) Assembly of PdO_x films containing Pd, PdO, and PdO_2 nanodomains. (b-d) TEM images of Pd NPs (b) and Pd/PdOx systems (c,d). PXRD pattern (e) and XPS spectra (f) of Pd NPs and Pd/PdOx structures indicating the presence of Pd, PdO, and PdO_2.

layer suppresses out-diffusion of oxygen species from deeper in the sample, eventually burying the remaining oxygen under the skin of Pd metal. This study reveals that the Pd/PdO_2 interface in Pd/PdO_x is responsible for the ultrafast PdO_x reduction and suggests a path to lowering the amount of Pd used in H_2 sensor application via exploiting core-shell particle architectures.

Metal hydrides offer many possibilities in electrocatalysis, including unique reaction mechanisms involving the catalyst lattice and innovative reactor architectures, beneficial for applications in chemical transformations and energy. The presence of hydride phases can modulate reactivity via changes in electronic structure [1] or result in volume changes and embrittlement [2]. We discussed the identification of hydride formation under reaction conditions imperative for an understanding of electrocatalyst kinetics [Figure 3(a-c)] and examined the implications of hydride formation on electrochemical reactions in aqueous media, including the hydrogen evolution reaction and electrocatalytic hydrogenation reaction.

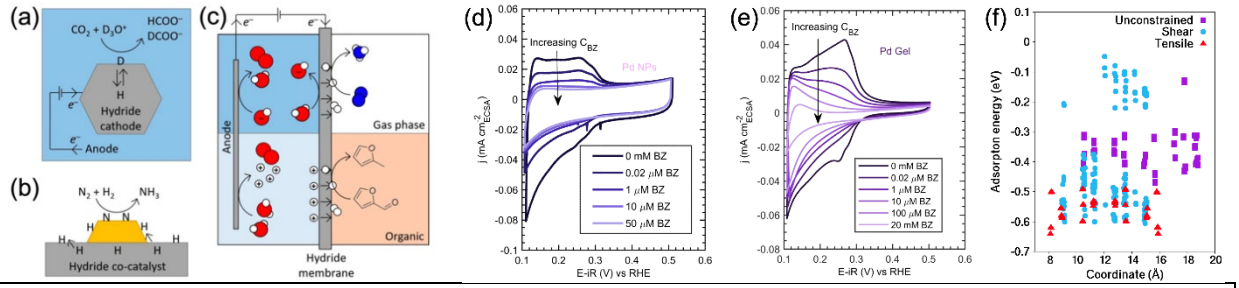

Figure 3. Electrochemically formed hydrides play key roles in catalytic processes including: (a) lattice hydride exchange, (b) spillover from a hydride catalyst, (c) an electrochemical-hydride membrane reactor. Cyclic voltammetry characterization: suppression of H adsorption and absorption in Pd-NP (d) and Pd-gel (e) samples occurs at BZ concentrations that differ by two orders of magnitude. (f) Calculated adsorption energies of H atoms on the surface of a model Pd-gel system in unstrained conditions and under shear and tensile load.

Finally, we investigated the effects of strains arrested during transformation of metastable phases of TiO_2 on their structural and electronic properties. Controlled heating of TiO_2-B [3] and anatase [4] nanoparticles induces continuous deformations that can span ~10 nm [Figure 4(a)]. Tests of photoinduced H_2O decomposition show that heat treatment increases photoactivity, suggesting that the spatial distribution and magnitude of deformations modulate key reaction steps. Using two-dimensional structure projections, obtained using high resolution transmission electron microscopy (HRTEM), as a guidance, we constructed a parametrized family of atomistic models of the deformed regions spanning from anatase (t=0) to rutile (t=1), where t is a deformation parameter. Our ab initio modeling shows that as t is increased from 0 to 1, the lattice structures split into two distinct categories: anatase-like (called anatise) and rutile-like. Comparison of the experimentally measured and calculated lattice parameters c and β shows that they vary within 0.5 Å and 5°, respectively [Figure 4(b)]. Since Ti-O bonds are ion-covalent, changes of both the interatomic distances and bond-bond angles affect the energetics of orbitals associated with Ti-O bonds. At the same time, since the supercell volume remains nearly constant regardless of the deformation magnitude up to t ~ 0.8 [Figure 4(c)], deformed regions may form without causing noticeable lattice mismatch. Spatial mapping of electronic density of

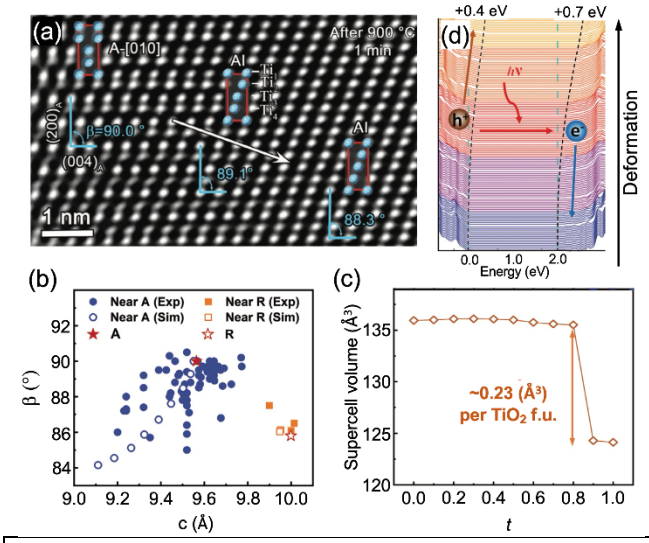

Figure 4. (a) Atomic gradient structure in thermally-treated anatase. The transition from anatase (A) to the intermediate anatise (AI) structure takes place over ~10 nm scale. (b) Comparison of the experimental (Exp) and simulated (Sim) lattice parameters for the anatase (A), anatise (near-A), rutile (R), and rutile-like (near-R) structures. (c) Calculated supercell volume along the A-R transformation path. (d) Band bending resulting from the atomic gradient structures for deformations from t=0.0 (blue) to t=0.8 (orange) promotes effective splitting of photo-induced electron-hole pairs.

states shows that as t is increased to 0.8, the valence and conduction band edges shift by ~0.4 and 0.7 eV, respectively [Figure 4(d)]. Such band bending profile promotes separation of photo-generated electron-hole pairs, which explains the observed enhancement of the photocatalytic H_2O splitting by heat-treated TiO_2.

Future Plans

We will examine the effect of strain on surface and subsurface diffusion of hydrogen and thermodynamic stability and electronic structure of hydrides in PGE gels and thin epitaxial films. We anticipate that by linking the magnitude and direction of deformation on the one side and diffusion barriers and the stability on the other, we will be able to construct predictive relationships guiding the formation of catalytically active hydrides. Our future work on the properties of the atomic gradient structures in TiO_2 will take two directions. First, we will investigate the linkages between the character of the lattice deformation and the direction and magnitude of band bending, which may allow us to control catalytic activity by controlling separation of the photoinduced electron-hole pairs. Second, we will examine the interaction between photoinduced charge carriers and PGE nanoparticles supported on the surface of TiO_2. We anticipate that photoinduced electrons and holes, separated by the atomic gradient structures, can be trapped at the supported PGE nanoparticles, thus changing their charge states, leading to structural reorganization and corresponding changes in their catalytic activity.

References

1. T. Chen, C. Foo, S. C. Edman Tsang, *Interstitial and substitutional light elements in transition metals for heterogeneous catalysis*, Chemical Science **12**, 517-532 (2021).
2. D. M. Soares, O. Teschke, I. Torriani, *Hydride Effect on the Kinetics of the Hydrogen Evolution Reaction on Nickel Cathodes in Alkaline Media*, J. Electrochem. Soc. **139**, 98. (1992).
3. P. Ren, Z. Lu, M. Song, J. Lee, J. Zheng, P. V. Sushko, D. Li, *Atomic gradient structure alters electronic structure in 3D across the bulk and enhances photoactivity*, Adv. Energy Mater. **11**, 2003548 (2021).
4. M. Song, M. P. Prange, P. Ren, Z. Lu, J. Lee, J. Zheng, M. Engelhard, J. J. De Yoreo, P. V. Sushko, D. Li, *Transitional Structures with Continuous Variations in Atomic Positions from Anatase to Rutile Improve Photocatalytic Activity*, Adv. Mater. Interfaces, 2202306 (2023).

Publications

1. X Geng, S. Li, J. Heo, Y. Peng, W. Hu, Y. Liu, J. Huang, Y. Ren, D. Li, L. Zhang, L. Luo, *Grain-Boundary-Rich Noble Metal Nanoparticle Assemblies: Synthesis, Characterization, and Reactivity*, Adv. Funct. Mater. **32**, 2204169 (2022).
2. X. Geng, S. Li, Z. Mei, D. Li, L. Zhang, L. Luo, *Ultrafast metal oxide reduction at Pd/PdO_2 interface enables one-second hydrogen gas detection under ambient conditions*, Nano Research **16**, 1149-1157 (2023).
3. S. K. M. Padavala, K. A. Stoerzinger, *Role of Hydride Formation in Electrocatalysis for Sustainable Chemical Transformations*, ACS Catal. **13**, 4544-4551 (2023).
4. M. Song, M. P. Prange, P. Ren, Z. Lu, J. Lee, J. Zheng, M. Engelhard, J. J. De Yoreo, P. V. Sushko, D. Li, *Transitional Structures with Continuous Variations in Atomic Positions from Anatase to Rutile Improve Photocatalytic Activity*, Adv. Mater. Interfaces, 2202306 (2023).
5. P. E. Evans, Y. Wang, P. V. Sushko, Z. Dohnálek, *Understanding Pd-Te Cluster Formation on WTe_2(001): From a Kinetically-Hindered Distribution to Thermodynamically Controlled Monodispersity*, PNAS Nexus (in press).

Band structure tuning of 2-d intercalated quantum materials and nanographenes

M.C.Tringides[1,2]. M. Kolmer[1] , Z. Fei[1,2], L.L. Wang[1]
[1]Ames National Laboratory, [2] Department of Physics-ISU, Ames IA 50011

I. Program scope

The goals of this FWP are the tunable synthesis and characterization of nanoscale structures with predictive control of their morphology and geometry, to realize novel types of 2-d quantum materials. Proposed work focuses on several graphene-based materials to establish the underlying principles for controlling their dimensions, structural uniformity, interface quality and interatomic interactions. Materials include: (i) on-demand metal-graphene heterostructures grown by targeted metal intercalation with precise experimental tuning of metal location[1-4] following the Synthesis BRN to "finally realizing the ability to link predictive design to predictive synthesis". (ii) Nanographene (NG) and graphene nanoribbons (NGR) generated by on-surface synthesis utilizing programmable chemical reactions of organic precursors[5,6]. The emerging electronic and magnetic properties depend critically on the quality of the grown structures, so detailed characterization of their morphology with surface diffraction and STM confirms atom bonding at pre-selected, sub-surface locations. Post growth characterization of the targeted band structures with spectroscopic techniques (STS, ARPES, optoelectronics microscopy SNOM) is used to confirm targeted electronic effects. DFT and modelling of the kinetics is applied to validate the expected band structure modifications. The proposed work also addresses priority directions in the Quantum Materials BRN "Harness Topological States for Groundbreaking Surface Properties".

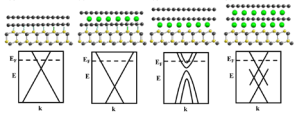

Fig. 1. Schematics showing how the intercalated metal location can modify the electronic band structure of single-layer-graphene

II. Previous work

Lead intercalation under Gr/SiC Pb is especially important for graphene intercalation because of its high Spin Orbit (SO) coupling and expected 2-d superconductivity[7]. With high resolution surface diffraction, we have studied Pb intercalation on a mixed surface of single layer graphene and bare buffer layer[8]. We found that the onset of intercalation is at the relatively low temperature ~200 °C, through domain boundaries between the two regions and with the most stable intercalated location under the buffer layer. Density Functional Theory (DFT) calculations of the band structure were carried out for different graphene thickness to map out band structure changes as a function of intercalated Pb location. These calculations have confirmed the richness of possible intercalated Pb phases, which are good candidates for topological effects [9]. DFT was used to assess aspects of the kinetics controlling Pb intercalation. We demonstrated that an intercalated Pb monolayer is initiated around a graphene step edge, which is aided by facile Pb mass transport, as seen experimentally[10-12].

Targeted Dy intercalation under Gr/SiC for tuning its electronic band structure Metal intercalation of graphene is a promising method to tune its band structure, but recent experiments in the literature of Ca intercalation under Gr/SiC have led to inconsistent assignment of the

intercalation location[13-16]. We have studied Dy intercalation under single layer graphene (SLG) on SiC using high resolution LEED (SPA-LEED) and STM[17]. The experimental work is complemented with DFT analysis. Because different diffraction spots originate from different sub-surface regions, it is possible to identify changes in the intercalation location, by monitoring the spot intensity as a function of growth conditions (temperature, time). DFT calculations of the chemical potential as a function of location, support the variation of the stability of the intercalated phase at different intercalated locations. The preferred location is also confirmed from STM studies showing the removal of the 6×6 moiré corrugation at the preferred location, observed at higher Dy coverage.

Band structure manipulation in Gd intercalated graphene heterostructure We synthesized Gd/graphene heterostructures under Gr/SiC with the metal intercalated at the bottom two pre-defined interlayer locations. The experimentally determined electronic structure is defined by the two topmost graphene layers. The band structure shows quantitative agreement between spectra measured globally with ARPES, measured locally with STM/STS and calculated by DFT[18]. The electronic properties reflect the highly anisotropic doping between the two topmost graphene layers, which generates a novel band structure topology. Initially parabolic energy bands characteristic of pristine surface become decoupled massless bands and shift in energy by a large amount ~1 eV confirming the large difference in doping. At the crossing points non-linear dispersion is observed indicating the reduced coupling between the two bands. Controlling the interlayer coupling between stacked layers is a very widely used method to engineer bands in heterostructures[19-22]. The control is commonly done with a transverse electric field by gating the voltage between exfoliated graphene layers[23]. However, phases generated by high displacement fields are elusive in this standard approach based on gating; our work shows this is possible with varying the Gd intercalated coverage, which introduces much larger effective displacement field by intercalation. The reduced interlayer coupling is also seen in high resolution density of states maps that show symmetry changes from 3-fold symmetry of bilayer graphene to 6-fold symmetry (see fig.2), characteristic of decoupled single layer graphene[24]. Multiprobe STM transport experiments confirm this and show that the intercalated system behaves truly as 2-d system with the substrate not contributing to the mesoscopic transport channels.

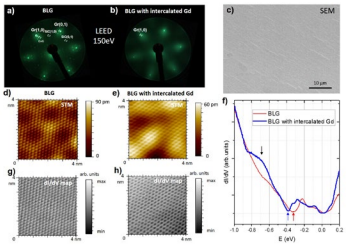

Fig. 2. Comparison of pristine with Gd intercalated graphene. (a-b) LEED (c) 4-probe transport (d-h) Change after intercalation from 3-fold to 6-fold symmetry in dI/dV maps. (f) STS spectra.

Unusual flat and extended morphology of intercalated Cu under MoS_2 A general method was developed in the FWP to intercalate metals under graphite through a controlled density of sputtered defects. Over last year it has been extended to the intercalation of Cu under MoS_2[25]. The characterization is carried out with XPS, SEM, EDS and AFM. Although the growth conditions needed for intercalation under graphite and MoS_2 are similar[26], the intercalated phases observed are very different. Each Cu island which nucleates on top of MoS_2 provides material that is transferred below MoS_2, through sputtered defects under the island base; this transfer results in a

uniform intercalated Cu "carpet" ≈30 layers thick that extends over the mesoscale. Following the practice of the FWP to predictively model growth[27], we have studied theoretically Cu intercalation under MoS_2[28]. DFT-based thermodynamic and kinetic analyses are used to interpret the observed Cu "carpet" intercalated under MoS_2. Cu transfer from Cu pyramids on top of MoS_2, through point defects to the "carpet", is driven by a slightly lower chemical potential for the latter. The competition between the energy gain for a thicker "carpet" and the cost of elastic stretching of the top MoS_2 layer explains the preferred "carpet" thickness of ≈30 layers.

Imaging stacking-dependent surface plasmon polaritons in trilayer graphene Nano-infrared (IR) imaging using s-SNOM of trilayer graphene (TLG) with both ABA and ABC stacking areas can be used to map the surface plasmon polaritons (SPPs)[29,30]. Through quantitative modeling of the plasmonic imaging data, we found that the plasmon wavelength of the ABA region is significantly larger than that of the ABC region. These differences of the two types of TLG are linked to differences in their band structures. Such experiments can assist the development of plasmonic responses in future applications using TLG and ABA/ABC junctions as components in planar IR nano-optics[31]. In a different experiment using IR imaging and spectroscopy we study hot-electron plasmons in graphene, which are excited by the sharp metallic tip with a mid-IR femtosecond pulsed laser. We found the average electron temperature can reach as high as Te~1100 °C. We monitored both the plasmon interference fringes and the hybrid plasmon-phonon resonances of graphene. When graphene is heavily doped, a higher Te leads to a smaller plasmon wavelength and a weaker plasmon-phonon resonance intensity. At lower doping, on the other hand, the plasmon-phonon resonance intensity is enhanced when Te increases[32]. With quantitative modeling we have shown that the plasmonic responses are determined by the temperature dependencies of chemical potential, electron scattering, and carrier generation.

III. Future Plans

Synthesis and multi-technique characterization of Nanographenes (NG) grown on insulating substrates. We will focus on answering two outstanding questions about NG growth: how to grow NG on insulating substrates and how to control the kinetics to increase their length from ~10 nm to ~100 nm. We will use the extensive experience of the FWP in predictive synthesis and modeling of nanoscale structures[33,34]. The FWP expertise is based on the systematic control of the growth parameters (coverage, temperature and time) to extract the key controlling barriers (diffusion, aggregation, reaction rates). Complementary FWP techniques will be applied to evaluate the NG grown quality and their dimensions. STM will be used to image the grown NG morphology with atomic scale resolution. STS and dI/dV maps will be used to measure the density of states at different locations of the NGs. Yield of reactions as a function of temperature will be measured with XPS. SPA-LEED will map out the length size distribution from the shape of the diffraction spots. Plasmonic effects in NGs will be imaged with SNOM. Multiprobe STM/STS characterization for electronic transport properties will be carried at DOE User Facilities.

Intercalated Pb under Gr/SiC ideal 2-d quantum material Some Pb work on topological phases (QSHE and Rashba effects) has been performed for metals under Gr/Ir(111), but there is limited work for Pb intercalated under Gr/SiC. This system offers more advantages because different

subsurface locations of Pb can be intercalated under Gr/SiC with more possibilities to observe novel electronic, magnetic and topological phases[35]. We plan to study Pb intercalation on different initial graphene thickness (zero-, single-, bi-layer graphene) to tune the band structure in exotic ways, i.e., develop edge states, spin polarized bands, etc. In addition, 2-d superconductivity should be present in intercalated Pb phases and be well protected from ambient conditions by graphene on top. Already over the last two years there are at least 12 publications studying Pb intercalation of Gr/SiC. The FWP will use quantitative diffraction for global characterization of the grown morphology and STM/STS for local mapping of the density of states. In addition, globally the band structure of the intercalated phases will be mapped in collaboration with the Complex States FWP using ARPES. Especially we will look for ordered structures of the intercalated Pb because it will show another way to introduce superlattice periodicities in the graphene 2-d electron gas. This will be a novel, promising system to grow novel materials controlled by Moiré physics [36].

SNOM and STM characterization of metal intercalated phases under Gr/SiC Plasmonic responses have been widely explored in graphene because many superior properties are possible, such as high field enhancement, strong field localization and tunability of the conductivity. One novel way to engineer plasmonic responses in graphene is by metal intercalation, which could change the doping level and potentially modify the graphene band structure. The in-house FWP synthesis capabilities and the detailed characterization of the intercalated phases with surface diffraction and STM, offer unique advantages in studying the intercalated heterostructures. We plan to perform systematic plasmonic studies of Gd-intercalated BLG by using s-SNOM. In these experiments we will perform nano-infrared imaging and spectroscopy to study their real-space transport properties and their coupling with the optical phonons in SiC. Through these studies, we expect to observe plasmons at relatively higher energies due to the metal-induced higher doping[18, 24]. Because of protection from likely topological phases, electronic and plasmonic excitations within the metal-graphene heterostructure will have longer lifetimes. The results will be compared to s-SNOM measurements of pristine graphene; because of intrinsic doping variations at locations of different thickness and/or stacking[37].

References

1 L. Daukiya et al., *Prog. Surf. Sci.* **94**, 1 (2019).
2 J. Wan et al., *Chem. Soc. Rev.* **45**, 6742 (2016).
3 N. Briggs et al., *Nanoscale* **11**, 15440 (2019).
4 S. Link et al., *Phys. Rev. B* **100**, 121407 (2019).
5 S. Clair et al., *Chem. Rev.* **119**, 4717 (2019).
6 L. Grill et al., *Nat. Chem.* **12**, 115 (2020).
7 B. Matta et al., *Phys. Rev. Res.* **4**, 023250 (2022).
8 S. Chen et al., *Phys. Rev. Mater.* **4**, 124005 (2020).
9 J. Wang et al., *Phys. Rev. B* **103**, 085403 (2021).
10 M. Hupalo et al., *Adv. Mater.* **23**, 2082 (2011).

11 A. Yurtsever et al., *Small* **12**, 3956 (2016).
12 Y. Han et al., *Carbon N. Y.* **205**, 336 (2023).
13 K. Kanetani et al., *Proc. Natl. Acad. Sci. U. S. A.* **109**, 19610 (2012).
14 S. Ichinokura et al., *ACS Nano* **10**, 2761 (2016).
15 H. Toyama et al., *ACS Nano* **16**, 3582 (2022).
16 J. C. Kotsakidis et al., *Chem. Mater.* **32**, 6464 (2020).
17 S. Chen et al., *Phys. Rev. B* **107**, 045408 (2023).
18 M. Kolmer et al., *J. Phys. Chem. C* **126**, 6863 (2022).
19 D. Marchenko et al., *Sci. Adv.* **4**, (2018).
20 L. Daukiya et al., *Phys. Rev. B* **97**, 035309 (2018).
21 K. S. Kim et al., *Nat. Mater.* **12**, 887 (2013).
22 P. Rosenzweig et al., *Phys. Rev. Lett.* **125**, 176403 (2020).
23 H. Zhou et al., *Science* **375**, 774 (2022).
24 M. Kolmer et al., *J. Phys. Chem. Lett.* **13**, 11571 (2022).
25 D. Jing et al., *Phys. Rev. Mater.* **6**, 094008 (2022).
26 A. Lii-Rosales et al., *J. Phys. Chem. C* **122**, 4454 (2018).
27 A. Lii-Rosales et al., *Nanoscale* **13**, 1485 (2021).
28 Y. Han et al., *J. Phys. Chem. Lett.* **13**, 6651 (2022).
29 J. Chen et al., *Nano Lett.* **13**, 6210 (2013).
30 Z. Fei et al., *Nature* **486**, 82 (2012).
31 Y. Luan et al., *Phys. Rev. Appl.* **18**, 024052 (2022).
32 Y. Luan et al., *Phys. Rev. B* **107**, 085414 (2023).
33 M. Kolmer et al., *Science* **363**, 57 (2019).
34 M. Kolmer et al., *Science* **369**, 571 (2020).
35 A. Vera et al., *arXiv preprint arXiv:2205.06859* (2022).
36 Y. Cao et al., *Nature* **556**, 43 (2018).
37 D. Momeni Pakdehi et al., *Adv. Funct. Mater.* **30**, 2004695 (2020).

Selected publications(10) by the FWP 2021-2023

[1] Y. Luan, M. Kolmer, M.C. Tringides, Z. Fei, "Nanoscale infrared imaging and spectroscopy of hot-electron plasmons in graphene", *Phys. Rev. B*. 107, 085414 (2023). https://doi.org/10.1103/PhysRevB.107.085414.

[2] Y. Han, M. Kolmer, M.C. Tringides, J.W. Evans, "Thermodynamics and kinetics of Pb intercalation under graphene on SiC(0001)", *Carbon N. Y.* 205, 336 (2023). https://doi.org/10.1016/j.carbon.2023.01.029.

[3] S. Chen, Y. Han, M. Kolmer, J. Hall, M. Hupalo, J.W. Evans, M.C. Tringides, "Targeted Dy intercalation under graphene/SiC for tuning its electronic band structure", *Phys. Rev. B*. 107, 045408 (2023). https://doi.org/10.1103/PhysRevB.107.045408.

[4] M. Kolmer, B. Schrunk, M. Hupalo, J. Hall, S. Chen, J. Zhang, C.-Z. Wang, A. Kaminski, M.C. Tringides, "Highly Asymmetric Graphene Layer Doping and Band Structure Manipulation in Rare Earth–Graphene Heterostructure by Targeted Bonding of the Intercalated Gadolinium", *J. Phys. Chem. C*. 126, 6863 (2022). https://doi.org/10.1021/acs.jpcc.2c01332.

[5] M. Kolmer, W. Ko, J. Hall, S. Chen, J. Zhang, H. Zhao, L. Ke, C.-Z. Wang, A.-P. Li, M.C. Tringides, "Breaking of Inversion Symmetry and Interlayer Electronic Coupling in Bilayer Graphene Heterostructure by Structural Implementation of High Electric Displacement Fields", *J. Phys. Chem. Lett.* 13, 11571 (2022). https://doi.org/10.1021/acs.jpclett.2c02407.

[6] Y. Luan, J. Qian, M. Kim, K.-M. Ho, Y. Shi, Y. Li, C.-Z. Wang, M.C. Tringides, Z. Fei, "Imaging Stacking-Dependent Surface Plasmon Polaritons in Trilayer Graphene", *Phys. Rev. Appl.* 18, 024052 (2022). https://doi.org/10.1103/PhysRevApplied.18.024052.

[7] D. Jing, Y. Han, J.W. Evans, M. Kolmer, Z. Fei, M.C. Tringides, "Unusual flat and extended morphology of intercalated Cu under MoS2", *Phys. Rev. Mater.* 6, 094008 (2022). https://doi.org/10.1103/PhysRevMaterials.6.094008.

[8] J. Wang, M. Kim, L. Chen, K.-M.M. Ho, M. Tringides, C.-Z.Z. Wang, S. Wang, M. C. Tringides, C.-Z.Z. Wang, S. Wang, "Manipulation of electronic property of epitaxial graphene on SiC substrate by Pb intercalation", *Phys. Rev. B*. 103, 085403 (2021). https://doi.org/10.1103/PhysRevB.103.085403.

[9] A. Lii-Rosales, Y. Han, D. Jing, M.C. Tringides, S. Julien, K.-T. Wan, C.-Z. Wang, K.C. Lai, J.W. Evans, P.A. Thiel, "Encapsulation of metal nanoparticles at the surface of a prototypical layered material", *Nanoscale*. 13, 1485 (2021). https://doi.org/10.1039/D0NR07024F.

[10] M. Petrović, F.J. Meyer zu Heringdorf, M.H. Hoegen, P.A. Thiel, M.C. Tringides, "Broad background in electron diffraction of 2D materials as a signature of their superior quality", *Nanotechnology*. 32, 505706 (2021). https://doi.org/10.1088/1361-6528/ac244f.

MINES – Minerals for Energy Storage Synthesis

Mark Asta, Gerbrand Ceder, Martin Kunz, Raluca Scarlat, Michael L. Whittaker

Keywords: lithium, battery, molten salt, spodumene, automated synthesis

Research Scope

The multidisciplinary MINES program establishes fundamental science for the synthesis of battery materials from natural resources, enabling a new 'separation-by-synthesis' paradigm for energy storage manufacturing. We address outstanding knowledge gaps related to synthesis in multicomponent systems with a minimum of seven or more elements, for which manifold component interactions control driving forces and transformation pathways in complex ways, and governing relationships are impossible to visualize or intuit in their entirety. We demonstrate the scientific basis for 'separation-by-synthesis' by synthesizing a new class of impurity-tolerant high entropy disordered rocksalt (DRX) lithium cathode materials directly from lithium ores. This novel approach to battery material synthesis reactions bypasses nearly all the purification steps that contribute to the current carbon footprint of conventional battery cathode manufacturing. We select molten fluoride salts among many potential synthesis media, both because they enable excess lithium and fluorine chemistry that can improve the performance of cathodes and because they offer many orthogonal degrees of freedom to control synthesis via temperature, composition, kinetics, and electrification. Our interdisciplinary expertise and existing collaborative partnerships in each aspect of the proposed work is amplified by clearly defined and highly motivating scientific outcomes, resulting in rapid and influential progress towards material- and energy efficient low-carbon manufacturing for energy storage.

Recent Progress

The MINES program is divided into three Thrusts focusing on 1) molten fluoride salts, 2) mineral precursors and 3) cathode materials. Work in Thrust 1) has shown that machine-learned (ML) potentials for molten salts are capable of reproducing key aspects of binary phase diagrams in the LiF-NaF-KF system. Experimental calorimetric data supports melting points, densities, and phase boundaries determined computationally, and suggests that computational exploration of synthesis pathways in molten salts may be a viable approach. ML potentials increase the simulation timescales by up to three orders of magnitude with essentially no loss in accuracy and allow for the exploration of long-lived configurations such as ionic oligomers (e.g, Li-F-O chains) that may impact species activities in the melt.

We have also discovered novel LiF polymorphs during melt crystallization *in silico*, some of which appear to have experimental analogs in synchrotron single-crystal X-ray diffraction. We will test

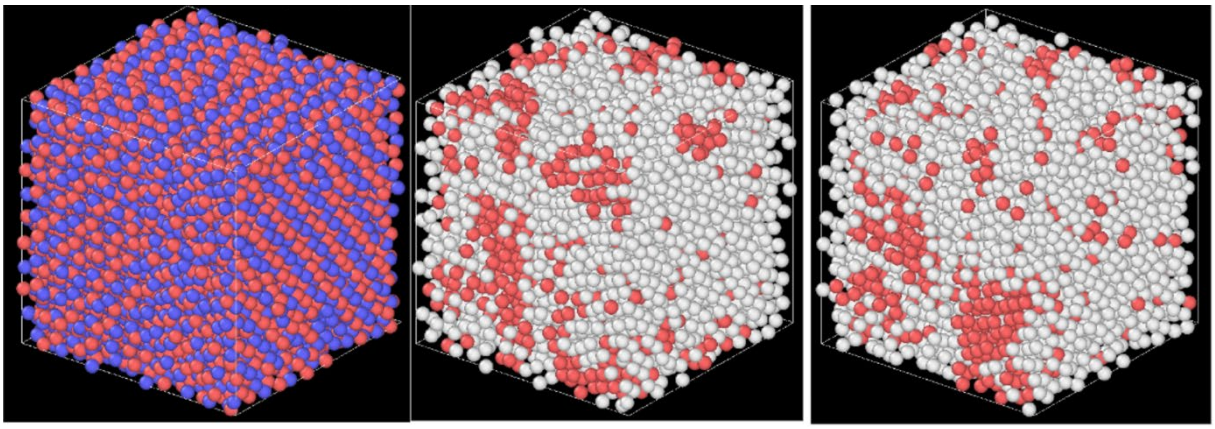

Figure 1: Molecular dynamics simulation of metastable LiF crystal quenched from the melt. (Left) Red=fluorine and blue-lithium. (Middle) Fluorine removed, showing hexagonally close packed (HCP) domains within a crystal of unknown structure. (Right) Lithium removed, showing HCP domains within crystal of unknown structure

the hypothesis that these metastable polymorphs, and expected metastable polymorphs of NaF and KF, can be used to influence cathode material synthesis in molten fluoride salts.

Specifically, we hypothesize that controlled rapid quenching of FLiNaK melts will precipitate non-equilibrium LiF/NaF/KF solids, in order to enrich the melts with compositions that are controlled by the cooling rate and not the equilibrium liquidus composition. This may allow for the transient enrichment of the melt with, e.g., Na, at a time when rapid ion exchange with Li in precursor mineral spodumene (LiAlSi2O4) is particularly favorable, as explained below.

Thrust 2) has shown that a novel nondisplacive phase transition in the spodumene may enable the rapid extraction, via ion exchange, of lithium at temperatures far lower than conventional processing routes (Figure 2). Although subtle in laboratory *in situ* XRD, some Bragg reflections transiently and simultaneously shift and then return to their previous locations over a narrow (~25 ^{o}C) temperature window. In other pyroxene-type framework silicates this type of transient structural reorganization is associated with ferroelastic phase transition[1] that disorders the lithium M1 site. It is anticipated that this transition is accompanied by a change in lithium diffusivity and may therefore enhance ion exchange with a surrounding molten salt medium. This transition temperature can be influenced by the cation on the M2 site, including with Mn^{2+} and Fe^{2+}, suggesting that naturally abundant cathode precursor minerals already present in the reaction mixture may additionally serve to assist in the lithium ion exchange step.

We also established the experimental framework we call Reaction Solution Calorimetry (RSC) to answer the following question: can the phase diagrams of mineral-melt systems be predicted from known phase diagrams of lower-order chemical spaces, such as the FLiNaK (pseudo)ternary system and oxyfluoride melts determined in Thrust 1, and the LiO-AlO-SiO (pseudo)ternary system? RSC is capable of determining the melting, mixing, and reaction enthalpies of specific

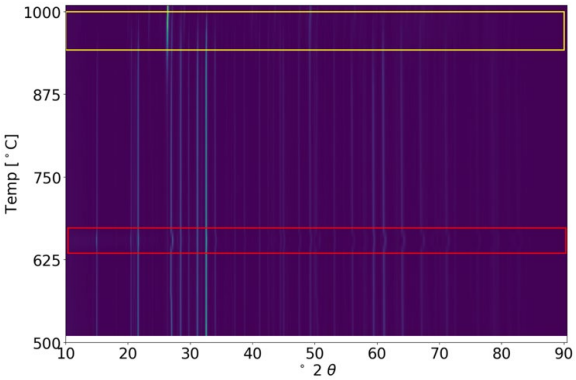

Figure 2: *In situ* X-ray diffraction of spodumene ($LiAlSi_2O_4$) reacting with manganese oxide precursors to form spinel ($LiMn_2O_4$, yellow box). A nondisplacive and reversible transformation in the spodumene at low (~660º C) temperature suggests a potential alternate pathway for lithium extraction via ion exchange at temperatures below the conventional $\alpha \rightarrow \beta$ transition near ~1000º C.

fluoride precursors. Extending this procedure to oxide precursors will provide high quality thermochemical data on specific transition metal oxide systems of interest to battery material synthesis, and will confirm whether existing thermochemical data is able to recapitulate the observed energetics of complex chemical spaces.

Building on progress in Thrust 2), Thrust 3) has shown that high-throughput computational prediction of reactions between spodumene and cathode precursors such as manganese and titanium oxides results in successful synthesis of targeted cathode materials in a single pot reaction (Figure 2). This avoids nearly all of the most carbon intensive steps in the current lithium extraction process and results in an electrochemically active product, as opposed to a precursor material that must be subsequently re-transformed. Future work in Thrust 3) will now focus on efficient separation of the active material from the reaction byproducts and electrochemical testing the material in coin cells.

Future Plans

Future plans for MINES include upcoming synchrotron X-ray beamtimes at the Advanced Light Source (ALS) for single crystal diffraction of synthesis precursors and products, including the fluoride salts (LiF, NaF, KF, FLiNaK eutectic) and high-temperature in situ powder diffraction and pair-distribution function analysis for validating liquid densities, structures, and speciation. *In situ* diffraction experiments at ALS will complement laboratory *in situ* XRD to provide a detailed look at the putative ferroeleastic phase transition that may dramatically decrease the necessary reaction temperature for extracting lithium from spodumene. Simultaneous neutron/X-ray tomography of spodumene single crystals will help elucidate the lithium distribution within naturally-occurring mineral precursors. This work will lay the foundation for examining lithium transport *in situ* during the transformation of spodumene, possibly via ion exchange. Computational and experimental analysis of lithium ion diffusivity in spodumene structures will help determine the feasibility of extracting lithium at far lower temperatures than conventional processing routes, and using that lithium to directly form active cathode materials.

References

1. Camara, F., Iezzi, G. and Oberti, R. HT-XRD study of synthetic ferrian magnesian spodumene: the effect of site dimension on the P 2 1/c→ C 2/c phase transition. *Physics and Chemistry of Minerals*, **2003** 30, pp.20-30.

Nonequilibrium synthesis and processing approaches to tailor the heterogeneity of 2D materials

Kai Xiao,[1] David B. Geohegan[1], Alex Puretzky,[1] Mina Yoon,[2] Gerd Duscher,[3] Christopher M. Rouleau,[1] Gyula Eres,[2] Sumner Harris,[1] Seokjoon Yun[1], Austin Houston[3]

[1]Center for Nanophase Materials Sciences and [2]Materials Science and Technology Division, Oak Ridge National Laboratory, Oak Ridge, TN 37831
[3]Dept. of Materials Science and Engineering, Univ. of Tennessee, Knoxville, 37996

Keywords: heterogeneity, *in situ* diagnostics, stacking, 2D materials, chemical vapor deposition

Research Scope: This project addresses key priority research directions in synthesis science and quantum materials for the development of *in situ* diagnostic-based understanding and control of non-equilibrium processes that can capture novel states of matter. The goal of this project is to identify and understand the dynamic pathways and interactions involved in the assembly of functional nanostructures, focusing on atomically thin 2D materials that are crucial to DOE's energy mission. This project emphasizes the development of real-time methods to induce and probe chemical and physical transformations away from thermodynamic equilibrium, in order to controllably synthesize 2D materials with emerging quantum states resulting from metastable phase and structures. The approach integrates non-equilibrium synthesis and processing methods and *in situ* diagnostic measurements to understand and control the crystalline pathway and interactions for growing predetermined quantum nanostructures. Advanced *in situ* probes will be used to reveal evolution of the "building blocks" and the kinetics of 2D material during synthesis and transformation by non-equilibrium processing approaches, to provide real-time adaptive control for developing automated platforms toward autonomous synthesis.

Recent Progress

Two-dimensional quantum materials offer unique opportunities for microelectronics and quantum information science. However, it is still a grand challenge to control heterogeneities such as defects, phases, and stacking in these materials and grow them scalably with good properties. Their growth mechanisms and crystallization pathways are poorly understood, which results in a lack of control over their synthesis and processing for integration and manufacturability. To better understand the evolution of heterogeneities in 2D crystals during synthesis and processing, including strain, phase, and stacking and their emergent functionalities, we have recently developed in situ diagnostics both at the microscale using optical imaging and laser spectroscopy, and at the atomic scale using electron microscopy and spectroscopy. Here we will present our recent progress on how to develop non-equilibrium CVD approaches to enable the heterogeneity control during synthesis, including the selective formation of antisite defects and metastable phases of 2D materials, and stacking control in bilayer crystals.

Antisite defects are emerging as an extremely important point defect in 2D materials that can induce many new optical and magnetic properties. However, antisite defects do not appear as frequently as other point defects during the growth since they tend to have much higher formation energies and are thus thermodynamically unfavorable. Recently, as shown in **Figure 1a**, we employed a non-equilibrium CVD approach to selectively formed S_W and $S2_W$ antisite defects during the growth of WS_2 monolayers. A dilute W-Au alloy (W less than 0.1at%) was used as the substrate to maintain W-poor (S-rich) growth conditions that were predicted to significantly reduce the formation energy of antisite defects by first-principles calculations (**Fig. 1b**). The high-density S_W and $S2_W$ (~5.0%) antisite defects were observed in the obtained WS_2 MLs (**Fig. 1c**) and confirmed by scanning transmission electron microscope (STEM) and electron energy loss spectroscopy (EELS) characterizations (**Fig. 1d**). Scanning tunneling microscopy/ spectroscopy (STM/S) combined with theoretical calculations revealed the clove- and trefoil-like structures of the antisite defects and corresponding localized defect states in the bandgap of monolayer WS_2 (**Fig 1e-f**). Tuning the chemical potential of reactants during growth as a nonequilibrium synthesis strategy to form specific defects is generally applicable to

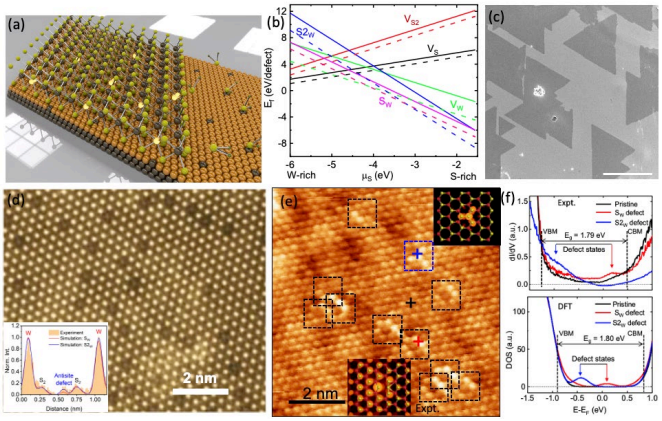

Figure 1. Non-equilibrium synthesis of antisite defects in monolayer WS_2. (a) A schematic illustrating a growth strategy to selectively form antisite defects in ML WS_2. The low density of W atoms that dissolve in gold substrates ensures a S-rich environment that favors the antisite defect formation. (b) Calculated formation energies in the freestanding WS_2 (solid line) and on Au (111) (dashed line). (c) A SEM image of ML WS_2 grown on Au coated W foil. (d) A STEM image of a WS_2 ML shows high-density antisite defects. Inset: intensity line profiles of the antisite defect. (e) A STM image shows two distinct structures, S_W (black frame,) and $S2_W$ (blue frame). Insets show simulated STM images of antisite defects. (f) The *dI/dV* spectra and corresponding calculated total density of states of S_W and $S2_W$. (K. Wang, *et al., Adv. Mater.* **34**, 2106674 (2022)).

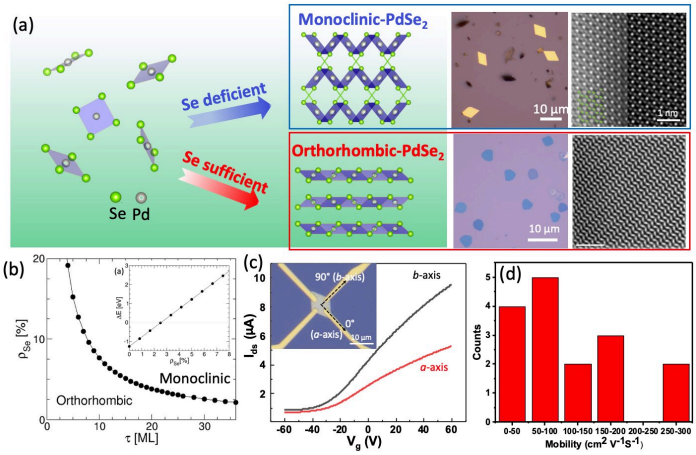

Figure 2. Defect stabilized growth of the monoclinic metastable phase of 2D $PdSe_2$. (a) A schematic demonstrates the polymorphs of 2D $PdSe_2$ in orthorhombic (O-) and monoclinic (M-) phases. Both can be selectively synthesized by tuning the Se supply through defect-mediated CVD. (b) Phase diagram delineating two phases as a function of thickness and Se vacancy density (ρ_{Se}). Inset shows total energy difference between O- and M-phases of $PdSe_2$ as a function of ρ_{Se}. (c) Transfer curves of the device along the *a*- and *b*- axes of an M-$PdSe_2$ crystal. Inset is an optical image of an M-$PdSe_2$ device, (d) Statistics of mobility in M-$PdSe_2$ transistors measured at room temperature. (Y. Gu, *et al., ACS Nano* **16**, 13900 (2022)).

tailor the electronic and optical properties of a wide variety of atomically thin 2D materials for designed functionalities, such as local magnetism, long-lifetime quantum emission and novel electronics.

Defects in 2D materials are not only crucial to enable new optical and electronic properties, but also to stabilize the metastable phases during growth. Recently as shown in **Figure 2a**, we directly synthesized a metastable monoclinic phase of 2D $PdSe_2$ under the Se deficient conditions using an ambient-pressure chemical vapor deposition method. DFT calculations revealed that Se vacancies reduce the free energy of the thermodynamically stable orthorhombic phase of $PdSe_2$ (**Fig. 2b**), providing an explanation for the emergence of the metastable monoclinic phase under Se-deficient growth conditions. Z-STEM and polarized Raman spectroscopy identified their unique quasi-2D structure and corresponding in-plane optical anisotropy. Most importantly, the as-synthesized 2D M-$PdSe_2$ crystals exhibit the high electron mobility up to 294 $cm^2\ V^{-1}\ s^{-1}$ (**Fig. 2d**) and a strong in-plane electron mobility anisotropy of ~1.9 (**Fig. 2c**) in prototype field effect transistor devices. The development of bottom-up approaches to directly grow metastable phase of 2D materials opens the door to exploration of their applications in electronics and quantum information science.

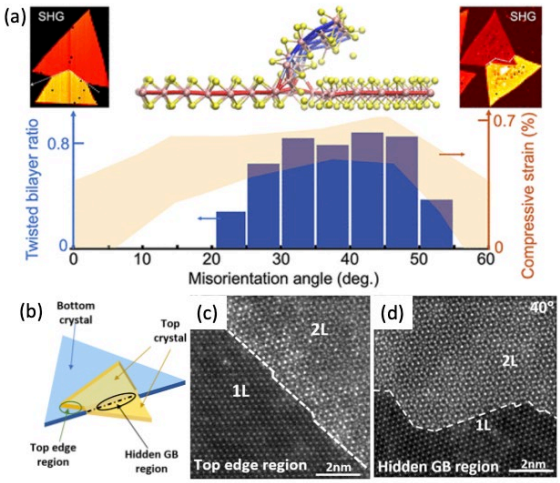

Figure 3. Strain-induced growth of MoS_2 twisted bilayers. (a) Upper: Atomistic MD simulations reveal how bilayers form at GB when two triangular MoS_2 crystals meet during growth. The crystal orientations are mapped in different colors by SHG. Lower: Strain induced in the crystals (orange shaded region) is discovered to be dependent on the relative angle (q) between the colliding crystals. Sufficient strain (for $q > 20°$) is important to facet GB segments to align nuclei for the growth of bilayers with the wide variety of observed twist angles in the graph. (b) Schematic illustration of a TB and its crystalline alignment with one of the two colliding crystals originating at a GB. STEM images of the top edge region (c) and the hidden GB region (d) with the white dashed lines outlining their borders. (Y. Yu, *et al.*, *ACS Nano* **15**, 4504 (2021)).

Tailoring the grain boundaries (GBs) and twist angles between 2D crystals is a crucial synthetic challenge for their emerging properties such as moiré excitons, magnetism, or single photon emission. As shown in **Figure 3a**, we reveal how twisted 2D bilayers can be synthesized from the collision and coalescence of two growing monolayer MoS_2 crystals during CVD growth and the important role strain plays in the process. The twisted bilayer (TB) moiré angles are found to preserve the misorientation angle (θ) of the colliding crystals. Optical spectroscopy measurements reveal a θ-dependent long-range strain in crystals with stitched grain boundaries (SGBs), and a sharp ($\theta > 20°$) threshold for the appearance of TBs which relieve this strain. Reactive molecular dynamics (MD) simulations explain this strain from the continued growth of the crystals during coalescence due to the insertion of atoms at unsaturated defects along the GB – a process that self-terminates when the defects become saturated. The simulations also reproduce atomic-resolution electron microscopy

observations of faceting along the GB, which are shown to arise from the growth-induced long-range strain. These facets align with the axes of the colliding crystals to provide favorable nucleation sites for second-layer growth of TB with twist angles that preserve the misorientation angle θ. Interplay between strain and TBs' formation provides a way to synthetically control stacking angles in 2D heterostructures for continuously tunable optoelectronic and quantum properties.

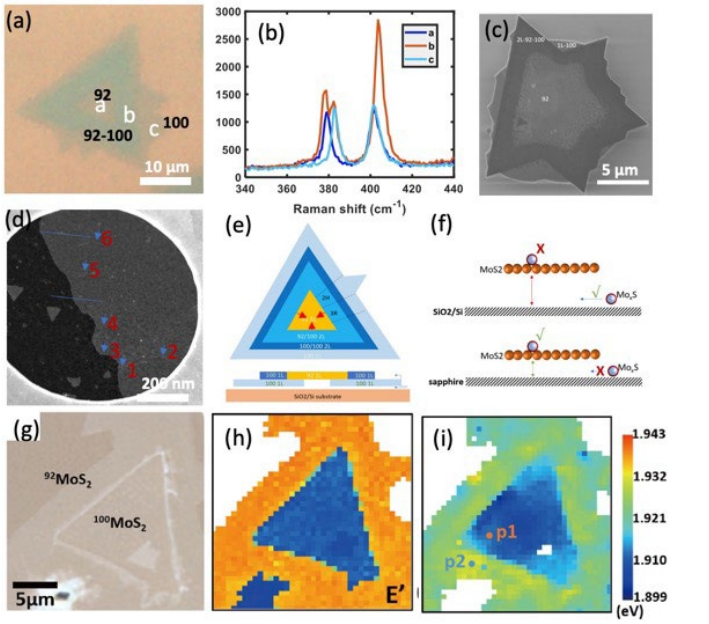

Figure 4. Sequential growth of isotopic MoS_2 vertical and lateral structures. (a) Optical image of an isotopic MoS_2 bilayer grown by a two-step CVD. (b) Raman spectra taken from the positions indicated in (a). (c) A SEM image of MoS_2 with partial bilayer region shows the $^{100}MoS_2$ from the 2nd growth is below the $^{92}MoS_2$ monolayer from the 1st growth. (c) Low-magnitude TEM image shows the confined growth of oriented small domains of $^{100}MoS_2$ from the 2nd growth. (e) and (f) Schematics of the sequential growth process of bilayers on the substrates using isotope labeling. (g-h) Optical image, Raman map of E' mode, and free exciton PL peak map of a monolayer $^{100}MoS_2$-$^{92}MoS_2$ lateral structure on sapphire reveal anomalous isotope effect on the excitonic properties of ML MoS_2 comparing to conventional semiconductors due to strong exciton-phonon coupling. (Y. Yu, *et al., submitted).*

Understanding the growth sequence of bilayer crystals using two-step CVD is very important to construct heterostructures and bilayer crystals with well-defined stacking. However, the growth mechanisms remain unclear, for example, does the 2nd layer grow above or below the 1st layer? How do the precursors directly feed bilayer growth? Which layer in bilayers modifies its lattice orientation to form the domain boundary in the stack? Current characterization techniques including Raman spectroscopy and TEM cannot normally distinguish the stacking order. Recently we investigated the two-step CVD growth of bilayer MoS_2 on SiO_2/Si and sapphire substrates using Mo isotope labeling during growth, and subsequent laser thinning combined with Raman spectroscopy, TOF-SIMS, and Z-STEM imaging. As shown in **Figure 4**, our results show that the growth of $^{100}MoS_2$ adlayers follows sequential modes with their top layer $^{92}MoS_2$ from the first growth. We discovered new microscopic steps governing the growth of the 2nd MoS_2 layer below the 1st layer as the diffusion of precursor between the 1st layer and SiO_2/Si substrate, which does not occur on the sapphire substrate because the precursors have the weaker binding interactions with SiO_2 substrate comparing to sapphire that enables the large gap between the 1st layer and SiO_2 surface. In addition, the 2nd MoS_2 layer follows the 1st layer, forming the AA and AB bilayers with antiphase domain boundaries below the single crystal 1st layer. By changing the growth condition, the isotopic lateral structures of monolayer $^{100}MoS_2$-$^{92}MoS_2$ are also synthesized on sapphire substrate that mitigates the effects of heterogeneities. This enables us to observe an anomalous isotope effect on optical band gap energy

shift in 2D materials comparing to that in conventional semiconductors due to the strong exciton-phonon coupling in 2D semiconductors (**Fig. 4g-i**). This study provides fundamental insights into understanding the growth mechanism of bilayers and heterostructure using isotope labeling and opens new opportunities in tailoring their electronic and optical functionalities by isotope engineering.

Future Plans

Efforts will continue to develop *in situ* diagnostic approaches for the rapid discovery, precision synthesis, and functional optimization of atomically-thin 2D materials that are guided by theory. To understand established non-equilibrium CVD and PLD synthesis and processing approaches that control heterogeneity, we will explore the kinetics, intermediates, and pathways involved in crystallization, phase transformations, and defect evolution through *in situ* diagnostic-coupled synthesis environments at multiple length scales from the macroscale, to microns-scale driven by laser heating and characterization within optical microscopes, to similar nanoscale measurements within STEM. We will continue to explore how strain changes the nucleation and crystallization pathway of 2D materials to form moiré stackings to localize excitons in 2D materials for the fabrication of uniform, array of single photon emitters, using patterned microspheres and highly strained industrial glass substrates. Novel approaches integrating with laser crystallization and nozzle-based CVD methods will be developed to explore the wafer-scale synthesis of single crystal 2D materials on a variety of practical substrates for microelectronics.

Publications

1. S. B. Harris, Y.-C. Lin, A. A. Puretzky, L. Liang, O. Dyck, T. Berlijn, G. Eres, C. M. Rouleau, K. Xiao, D. B. Geohegan, *Real-Time Diagnostics of 2D Crystal Transformations by Pulsed Laser Deposition: Controlled Synthesis of Janus WSSe Monolayers and Alloys*, ACS Nano **17**(3), 2472-2486 (2023).
2. K. Wang, L. Zhang, G. D. Nguyen, X. Sang, C Liu, Y. Yu, W. Ko, R. R. Unocic, A. A. Puretzky, C. M. Rouleau, D. B. Geohegan, L. Fu, G. Duscher, A.-P. Li, M. Yoon, K. Xiao, *Selective antisite defect formation in WS_2 monolayers via reactive growth on dilute W-Au alloy substrates*, Adv. Mater. **34,** 2106674 (2022).
3. K. Xiao and D. B. Geohegan, *Laser synthesis and processing of atomically thin 2D materials*, Trends Chem. **4**, 769 (2022).
4. Y. Gu, L. Zhang, H. Cai, L. Liang, C. Liu, A. Hoffman, Y. Yu, A. Houston, A. A. Puretzky, G. Duscher, P. D Rack, C. M. Rouleau, X. Meng, M. Yoon, D. B Geohegan, K. Xiao, *Stabilized synthesis of 2D Verbeekite: Monoclinic $PdSe_2$ crystals with high mobility and in-plane optical and electrical anisotropy*, ACS Nano **16**, 13900 (2022).
5. T. Zheng, Y.-C. Lin, N. Rafizadeh, D. B. Geohegan, Z. Ni, K. Xiao, H. Zhao, *Janus Monolayers for ultrafast and directional charge transfer in transition metal dichalcogenide heterostructures*, ACS Nano **16**, 4197 (2022).
6. D. B Geohegan, K. Xiao, A. A Puretzky, Y.-C. Lin, Y. Yu, C. Liu, *Chapter 8: Nonequilibrium synthesis and processing approaches to tailor heterogeneity in 2D materials*, Editor(s): R. Addou, L. Colombo, In Materials Today, *Defects in Two-Dimensional Materials*, Elsevier, 221-258 (2022).
7. Y. Yu, G. S. Jung, C. Liu, Y.-C. Lin, C. M Rouleau, M. Yoon, G. Eres, G. Duscher, K. Xiao, S. Irle, A. A Puretzky, D. B Geohegan, *Strain-induced growth of twisted bilayers during the coalescence of monolayer MoS_2 crystals*, ACS Nano **15**, 4504 (2021).
8. C. Liu, Y.-C. Lin, M. Yoon, Y. Yu, A. A. Puretzky, C. M. Rouleau, M. F. Chisholm, K. Xiao, G. Eres, G. Duscher, D. B. Geohegan, *Understanding substrate-guided assembly in van der Waals epitaxy by in situ laser crystallization within a transmission electron microscope,* ACS Nano **15,** 8638 (2021).

9. Y.-C. Lin, R. Torsi, D. B. Geohegan, J. A. Robinson, K. Xiao, *Controllable thin-film approaches for doping and alloying transition metal dichalcogenides monolayers*, Adv. Sci. **5**, 2004249 (2021).
10. T. Zheng, Y.-C. Lin, Y. Yu, P. Valencia-Acuna, A. A. Puretzky, R. Torsi, C. Liu, I. N Ivanov, G. Duscher, D. B Geohegan, Z. Ni, K. Xiao, H. Zhao, *Excitonic dynamics in Janus MoSSe and WSSe monolayers*, Nano Lett. **21**, 931 (2021).

Transforming PLD as an explorative synthesis tool to understand growth mechanism and head toward autonomous synthesis

Sumner Harris,[1] Kai Xiao,[1] Alex Puretzky,[1] Mina Yoon,[2] Gerd Duscher,[3] Christopher M. Rouleau,[1] Gyula Eres,[2] Seokjoon Yun[1], Austin Houston[3], David B. Geohegan[1]

[1]Center for Nanophase Materials Sciences and [2]Materials Science and Technology Division, Oak Ridge National Laboratory, Oak Ridge, TN 37831
[3]Dept. of Materials Science and Engineering, Univ. of Tennessee, Knoxville, 37996

Keywords: pulsed laser deposition, *in situ* diagnostics, laser heating within TEM, automation, 2D materials

Research Scope: This project addresses key priority research directions in synthesis science and quantum materials for the development of in situ diagnostic-based understanding and control of non-equilibrium processes that can capture novel states of matter. The goal of this project is to identify and understand the dynamic pathways and interactions involved in the assembly of functional quantum nanostructures, focusing on atomically thin 2D quantum materials that are crucial to DOE's energy mission. This project emphasizes the development of real-time methods to induce and probe chemical and physical transformations away from thermodynamic equilibrium, to controllably synthesize quantum materials with emerging quantum states resulting from metastable phase and structures. The approach integrates non-equilibrium synthesis and processing methods and *in situ* diagnostic measurements to understand and control the crystalline pathway and interactions for growing predetermined quantum nanostructures. Advanced *in situ* probes will be used to reveal evolution of the "building blocks" and the kinetics of 2D quantum material during synthesis and transformation by non-equilibrium processing approaches, to provide real-time adaptive control for developing automated platforms toward autonomous synthesis.

Recent Progress

Precision synthesis of nanostructures and thin films requires identification of the reaction pathways, key precursors, and assembly kinetics on different time and length scales. Here we describe recent progress in the controlled precision synthesis and processing of atomically-thin two-dimensional (2D) materials employing real-time *in situ* diagnostic techniques in pulsed laser deposition (PLD). PLD is a nonequilibrium pulsed plasma process capable of rapid exploration of novel materials and metastable phases. By adjusting the processing conditions, a variety of precursor "building blocks" and kinetic energy regimes can be accessed. Here we couple diagnostics of

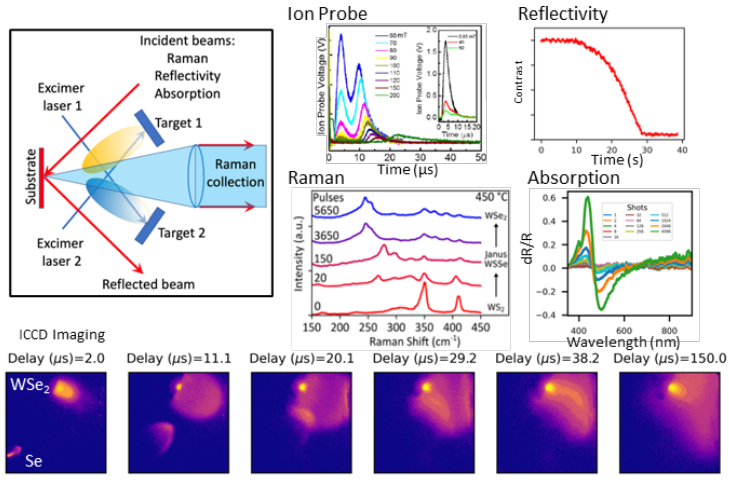

Figure 1. In situ diagnostics enable precise control of the PLD environment with real-time feedback of material response during growth and processing. The system features the option of two independent PLD plumes to explore on-the-fly stoichiometry adjustment (e.g., chalcogen enrichment). Intensified-CCD imaging and ion probes are used to control the kinetic energy and plume expansion dynamics. The sample is probed with optical spectroscopies to extract growth kinetics and enable precise real-time process control, including Raman spectroscopy, photoluminescence, laser reflectivity, and white-light absorption.

both the gas-phase plasma conditions with optical spectroscopy of the evolving 2D crystal on the substrate (**Fig. 1**) to provide real-time control of novel quantum materials such as Janus monolayers. A PLD system with fully automated processing parameters and data acquisition is described for this purpose. The approach simultaneously addresses priority research directions in synthesis and processing science, quantum materials, and transformative manufacturing by developing automated control over in situ diagnostic-guided precision synthesis and feedback suitable for autonomous exploration and discovery. While generally applicable to film growth, we focus on atomically-thin materials because of their sensitivity to remote monitoring (layer number, vibrational modes, PL for crystal quality and defects, etc.). We use the 2D materials to understand aspects of the PLD process that have not been understood before, for example the effects of kinetic energy on the damage of evolving films. We correlate the effects of growth conditions and *in situ* diagnostic measurements with atomistic characterization in the STEM by doing correlated depositions on suspended crystals on TEM grids.

We employ the kinetic energies (KE) of species inherent to PLD (typically < 100 eV/atom) to explore the formation processes of metastable phases and alloys of 2D crystals in a key processing regime that is difficult by other techniques. Background gas collisions are used to tune the KE of plume species arriving at the substrate. We previously showed that Se species tuned within a window of 3-5 eV/atom can selectively implant only the top-side chalcogen sites in monolayer TMD's to form 2D Janus TMDs (**Fig. 2a-b**).[1] To understand the mechanism and kinetics of the conversion of a monolayer of WS_2 to WSe_2 by Se implantation, and to explore and isolate metastable states, we recently employed real-time Raman spectroscopy coupled with *ex situ* electron microscopy and modeling. The evolution of the vibrational spectrum showed that WS_2 undergoes a layer-by-layer conversion mechanism in which the top S layer is totally replaced by Se before proceeding to replace the bottom layer (**Fig. 2c-d**). This general

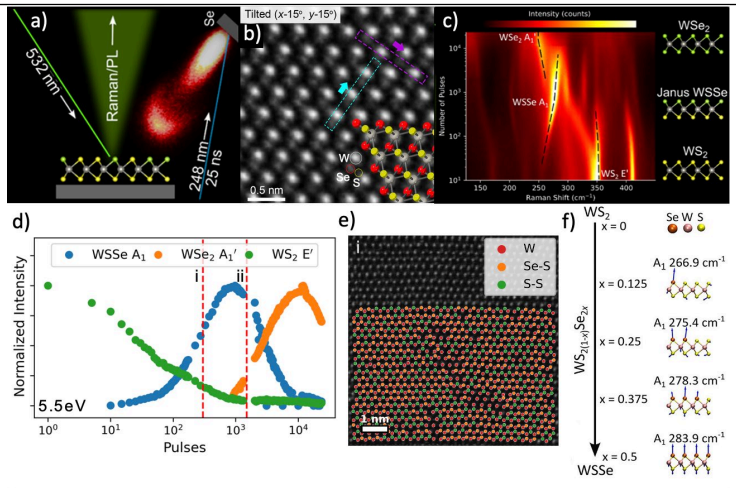

Figure 2. Real-time Raman spectroscopy reveals the formation dynamics of metastable 2D materials with pulsed laser deposition enabling their precision synthesis. a) The Raman spectrum of WS_2 is monitored in real-time during low energy Se implantation with pulsed laser deposition as it converts first to Janus WSSe and then WSe_2. b) Tilted HAADF-STEM image of Janus WSSe monolayer. c) Raman spectra collected at 1Hz map the kinetic shifts in Raman frequencies d) Intensity map of the prominent Raman peaks shown in c) reveal a layer-by-layer substitution mechanism with metastable Janus WSSe as an intermediate state as confirmed by e) HAADF-STEM imaging. f) Theoretically predicted Raman spectra allow calibration of the Raman modes, allowing precisely monitoring of the stoichiometry of the metastable fractional Janus $WS_{2x}Se_{2(1-x)}$ layer during synthesis in real-time. (Harris et al., ACS Nano 17, 2472 (2023)).

mechanism is independent of the KE below ~42 eV/atom while the kinetics, the rate of substitution with a given flux, increase with KE. The metastable, partially-substituted top-layer intermediate states we term fractional Janus alloys. Using *in situ* control to stop the conversion after evolution to particular Raman modes predicted by first principles calculations, HAADF STEM imaging confirmed the layer-by-layer growth mechanism (**Fig. 2e-f**). With the mechanism confirmed, we used XPS to calibrate the Raman mode frequency vs. at.% Se, which matched well with DFT predictions. We also discovered that *in situ* photoluminescence provided a sensitive probe of defect-healing dynamics after implantation and determined the energy barriers for fast and slow recovery mechanisms. These results and the general real-time feedback approach demonstrate a means to adjust the structure and quality of materials grown by PLD and enable precision synthesis of metastable 2D materials.

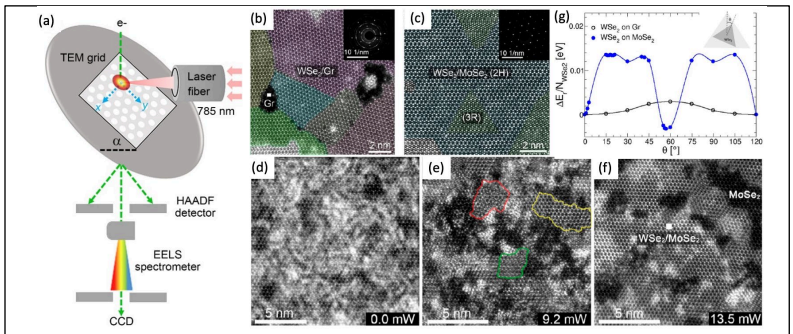

Figure 3. Understanding vdW epitaxy from amorphous WSe_2 'building blocks' deposited by PLD. (a) Illustration of the *in situ* observation arrangement within the HRTEM incorporating laser processing. (b) Z-STEM of polycrystalline WSe_2 on ML graphene, and (c) epitaxial WSe_2 on ML $MoSe_2$ grown directly by PLD at 600°C. (d) Z-STEM of amorphous WSe_2 clusters deposited on suspended ML $MoSe_2$ by PLD at room temp. (e) Crystalline nanoflakes of 2D WSe_2 flakes with different twist angles emerge after laser crystallization in the STEM. (f) Assembled large domains with single epitaxial orientation after further annealing reveal a variety of non-classical crystallization pathways by flake rotation and grain boundary elimination, which were witnessed by *in situ* imaging and SAED. (g) First principles studies yield extra energy per WSe_2 unit due to misalignment from epitaxial registry, reveal the significant driving force for alignment for a WSe_2 flake on $MoSe_2$, but not graphene. (C. Liu, *et al.*, ACS Nano **15**, 8638 (2021)).

To understand the mechanisms and kinetics of 2D materials crystallization and assembly on substrates, we utilized in situ laser-heating within a TEM (**Fig. 3a**) to reveal how 2D substrates can guide the crystallization and coalescence of amorphous precursors into vdW epitaxial heterostructures. We found amorphous precursors of WSe_2 that were deposited by PLD at 600°C could directly form epitaxial heterostructures on $MoSe_2$ substrates and only polycrystalline domains on graphene, as shown in **Fig. 3b-c**. These precursors were deposited by PLD at room temperature onto TEM grids (**Fig. 3d**) then subjected to *in situ* pulsed laser heating within a TEM for stepwise crystallization. We found the vertically aligned intermediate nanophases that were transformed to planar crystalline nanoflakes with lasing heating. These nanoflakes were preferentially aligned for $MoSe_2$ and randomly aligned for graphene substrates. The lattice-matched $MoSe_2$ substrates play a guiding role in the formation of large-domain, heteroepitaxial vdW $WSe_2/MoSe_2$ bilayers both during the crystallization process via templating and other classical mechanisms, and after crystallization via assisting the coalescence of the nanosized domains through non-classical particle attachment pathways by directed diffusion, domain rotation, and grain boundary migration **(Fig. 3f).** The favorable energetics for domain rotation

induced by lattice-matching with the $MoSe_2$ substrate were understood from first principles calculations shown in **Fig. 3g.** These *in situ* TEM studies of pulsed laser-driven non-equilibrium crystallization phenomena represent a transformational tool for the rapid exploration of synthesis and processing pathways that may occur on extremely different length and time scales and lend insight to the growth of 2D crystals by PLD and novel laser crystallization processing.

The development of our automated PLD platform in the above work enables a variety of AI/ML-guided synthesis experiments in numerous materials systems. For instance, we showed that Gaussian Process Regression (GPR) with Bayesian optimization can be used to effectively approximate complex process-property relationships for a material across a broad parameter space with sparse sampling, accelerating the understanding of the synthesis space 10x. **Figure 4b-c** shows the predicted crystallinity, the "*score*" based on the *in situ* Raman spectrum after growth, of ultrathin WSe_2 films grown by PLD in a 4D parameter space, which was calculated by sampling only 0.25% of the total parameter space. Combined with automated synthesis and characterization, we can rapidly gain a more complete picture of the synthesis process/environment to directly challenge broad theoretical predictions and enable simultaneous refinement of both the experiments and theoretical models.

Future Plans

Using the real-time Raman spectroscopy that we developed (**Fig. 2**), we are investigating strain and substrate effects on the implantation mechanism and kinetics of 2D TMD crystals. We plan to tune the strain and substrate binding energy of a TMD by creating bilayer stacks with well-defined twist angles and implant them with Se to determine the influence of these effects on the substitution mechanism. The substitution rates that are experimentally determined will be used to inform and directly compare with atomistic simulations to reveal the underlying physics of implantation. Also using the real-time Raman system, we plan to monitor and study the encapsulation of existing 2D materials or amorphous precursor films with protective BN films without inducing defects in the crystal or

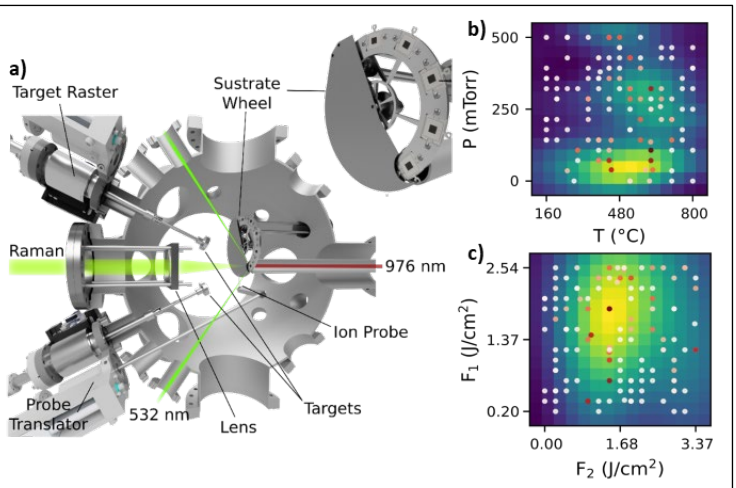

Figure 4. AI-guided PLD synthesis experiments enable rapid exploration of broad parameter space with sparse sampling. (top) The GPR surrogate prediction of the crystallinity (score) of WSe_2 as a function of synthesis parameters provides a full view of the process-property relationship with a small number of samples (0.25% of the parameter space explored). (bottom) Sample crystallinity vs sample number during AI-guided synthesis showed a gradual improvement in sample quality during parameter space exploration. (*in preparation)*

crystallizing the amorphous layer. Encapsulation of materials in this manner enables further studies in confined growth or crystallization with *in situ* laser processing within the HRTEM or by using a heated stage in a STEM to achieve atomic resolution of the crystallization process. By encapsulating an amorphous precursor with a well-defined stoichiometry, the kinetics of crystallization are accessible within a fixed chemical environment by preventing evaporation chemical species like we observed our study (**Fig. 3**). By tuning the composition of the encapsulated precursor, we hope to learn how the chemical environment can be manipulated to achieve directed growth of metastable phases or drive crystal phase changes. Finally, we plan to incorporate AI-driven experiments in each of the areas to accelerate discovery and glean a greater depth of understanding by machine-learning complex relationships between the growth mechanisms, process, structure, and properties.

References

11. Y,-C. Lin, C. Liu, Y. Yu, E. Zarkadoula, M. Yoon, A. A. Puretzky, L. Liang, X. Kong, Y. Gu, A. Strasser, H. M. Meyer III, M. Lorenz, M. F. Chisholm, I. N. Ivanov, C. M. Rouleau, G. Duscher, K. Xiao, D. B. Geohegan, *Low Energy Implantation into Transition-Metal Dichalcogenide Monolayers to Form Janus Structures*, ACS Nano **14**(4), 3896-3906 (2020).

Publications

1. S. B. Harris, Y.-C. Lin, A. A. Puretzky, L. Liang, O. Dyck, T. Berlijn, G. Eres, C. M. Rouleau, K. Xiao, D. B. Geohegan, *Real-Time Diagnostics of 2D Crystal Transformations by Pulsed Laser Deposition: Controlled Synthesis of Janus WSSe Monolayers and Alloys*, ACS Nano **17**(3), 2472-2486 (2023).
2. K. Wang, L. Zhang, G. D. Nguyen, X. Sang, C Liu, Y. Yu, W. Ko, R. R. Unocic, A. A. Puretzky, C. M. Rouleau, D. B. Geohegan, L. Fu, G. Duscher, A.-P. Li, M. Yoon, K. Xiao, *Selective antisite defect formation in WS_2 monolayers via reactive growth on dilute W-Au alloy substrates*, Adv. Mater. **34,** 2106674 (2022).
3. K. Xiao and D. B. Geohegan, *Laser synthesis and processing of atomically thin 2D materials*, Trends Chem. **4**, 769 (2022).
4. Y. Gu, L. Zhang, H. Cai, L. Liang, C. Liu, A. Hoffman, Y. Yu, A. Houston, A. A. Puretzky, G. Duscher, P. D Rack, C. M. Rouleau, X. Meng, M. Yoon, D. B Geohegan, K. Xiao, *Stabilized synthesis of 2D Verbeekite: Monoclinic $PdSe_2$ crystals with high mobility and in-plane optical and electrical anisotropy*, ACS Nano **16**, 13900 (2022).
5. T. Zheng, Y.-C. Lin, N. Rafizadeh, D. B. Geohegan, Z. Ni, K. Xiao, H. Zhao, *Janus Monolayers for ultrafast and directional charge transfer in transition metal dichalcogenide heterostructures*, ACS Nano **16**, 4197 (2022).
6. D. B Geohegan, K. Xiao, A. A Puretzky, Y.-C. Lin, Y. Yu, C. Liu, *Chapter 8: Nonequilibrium synthesis and processing approaches to tailor heterogeneity in 2D materials*, Editor(s): R. Addou, L. Colombo, In Materials Today, *Defects in Two-Dimensional Materials*, Elsevier, 221-258 (2022).
7. Y. Yu, G. S. Jung, C. Liu, Y.-C. Lin, C. M Rouleau, M. Yoon, G. Eres, G. Duscher, K. Xiao, S. Irle, A. A Puretzky, D. B Geohegan, *Strain-induced growth of twisted bilayers during the coalescence of monolayer MoS_2 crystals*, ACS Nano **15**, 4504 (2021).

8. C. Liu, Y.-C. Lin, M. Yoon, Y. Yu, A. A. Puretzky, C. M. Rouleau, M. F. Chisholm, K. Xiao, G. Eres, G. Duscher, D. B. Geohegan, *Understanding substrate-guided assembly in van der Waals epitaxy by in situ laser crystallization within a transmission electron microscope,* ACS Nano **15,** 8638 (2021).
9. Y.-C. Lin, R. Torsi, D. B. Geohegan, J. A. Robinson, K. Xiao, *Controllable thin-film approaches for doping and alloying transition metal dichalcogenides monolayers*, Adv. Sci. **5**, 2004249 (2021).
10. T. Zheng, Y.-C. Lin, Y. Yu, P. Valencia-Acuna, A. A. Puretzky, R. Torsi, C. Liu, I. N Ivanov, G. Duscher, D. B Geohegan, Z. Ni, K. Xiao, H. Zhao, *Excitonic dynamics in Janus MoSSe and WSSe monolayers*, Nano Lett. **21**, 931 (2021).

University
Abstracts

Electrodeposition of metals in viscoelastic liquid electrolytes

Lynden A. Archer and Donald L. Koch, School of Chemical & Bimolecular Engineering, Cornell University

Program Scope

Electrodeposition is a scalable, cost-effective process used to create metal coatings on conductive substrates. The process plays an important role in rechargeable batteries, where it must be carefully managed to facilitate stable and safe recharge of battery cells that use metals as anodes. The method's conceptual simplicity — metal ions in solution are driven to the substrate under the action of diffusion and electromigration where they are reduced to form the desired coating— belies its fundamental complexity.[1-2] **F**irst, the metal coatings are crystalline materials with symmetry features that may be fundamentally at odds with those imposed in the coating geometry.[3] **S**econd, the deposition can lead to a morphological instability that produces non-planar deposits (loosely termed *dendrites*) because of the Mullins-Sekerka instability in which ions are preferentially transported by diffusion and electromigration toward high points on the metal surface due to enhanced electric field and concentration gradients at the peaks.[4] **F**inally, above the diffusion limit, the depletion of anions near the electrode leads to an *extended space charge layer* (ESCL).[5-6] Electro-osmotic forces in this layer drive the hydrodynamic instability termed electroconvection that greatly enhances the deposit growth rate at certain locations by preferentially convecting cations toward the fastest growing features.

Understanding the physico-chemical processes that drive such instabilities and how they in-turn impact the morphology of metal electrodeposits is the motivation for our studies. Using a combination of experiment, linear stability analysis, and phase-field numerical simulations we previously reported that viscoelasticity of liquid electrolytes containing modest amounts of high molecular weight polymers suppress both the morphological and hydrodynamic instability by variety of mechanisms.[7-9] The work discussed in the poster and associated presentation summarizes our recent experimental and theoretical studies which show that interphases formed at metal electrodes can be as effective ad high molecular weight polymers in stabilizing electrodeposition of metals. It is shown that interphases stabilize electrodeposition by one or more of the mechanisms illustrated in **Fig. 1**: **(a)** Elastic forces produced by a porous polymer membrane that spans the inter-electrode gap; **(b)** a separator with a thin fluid layer (with and without dissolved polymers) near the anode regulates the ion flux to the interface; and **(c)** a polymer solution with a thin layer of adsorbed or cross-linked polymer at a cation-selective metal electrode or membrane surface exerts a restoring force that prevents disturbance of the ad-layer.

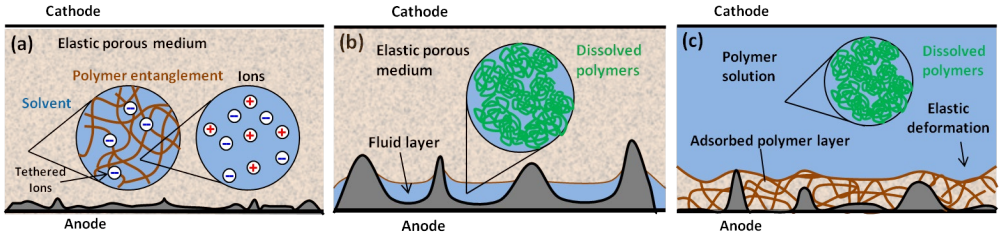

Fig 1. (a) An elastic porous medium model for the entangled polymer electrolyte. The solvent flows inside the pores of the porous structure and the ions are carried by the solvent, the polymers may carry immobilized anions on them. (b) Near the electrode surface, a thin layer of fluid is formed due to surface roughness and non-uniform deposition. (c) A polymer solution above a thin layer of an adsorbed polymer.

Recent Progress

II.1 Linear stability analysis of electrodeposition across an adsorbed polymer coating.

As illustrated in **Fig. 1c**, irrespective of molecular weight, an interfacial polymer coating can limit the ion flux to hot spots on an electrode by passivating sites at which electroreduction might occur. We analyzed this using a linear stability analysis of an adsorbed polymer layer on a metal electrode.[10] It is known that coating a thin polymer layer of any molecular weight on a metal electrode surface can change the ion reaction rate and help to stabilize the electrodeposition. We model this effect trivially using the Butler-Volmer condition to describe the ion flux at an electrode with a finite reaction rate, $I = 2Da(c^+e^{\alpha_c\Phi} - e^{-\alpha_a\Phi})$. The condition is applied at the inner edge of the space charge layer, which requires the additional condition, $\boldsymbol{n}\cdot\nabla c^+ = \boldsymbol{n}\cdot\nabla c^-$.

Through a linear stability analysis, we studied the effects of the Damköhler number (Da = exchange current density/limiting current density) on the morphology and hydrodynamics during metal deposition. Reducing Da is found to increase the critical voltage for the onset of the electroconvective instability (**Fig. 2a**) by effectively increasing the potential drop across the space charge layer Φ_s. The neutral stability curves are all found to converge when the variable $V - \Phi s$ is used for the y-axis —evidence that the instability is not sensitive to the potential drop across the space charge layer. The analysis also revealed that the salt concentration (primarily through its effect on the double layer thickness d), increases V_c at all Da values and that the classical extension of the diffusion-limiting regime, $\Delta V \sim Pe^{-1/2}$ is valid in a small, low-Pe range, that becomes smaller still as Da is lowered. Here $Pe \equiv \frac{\varepsilon_0\varepsilon_r}{2t^+}\left(\frac{RT}{zF}\right)^2(\eta D^-)^{-1}$ is the Peclet number and h, D, and t^+ respectively the viscosity, ambipolar diffusion coefficient, and cation transference number of the electrolyte.

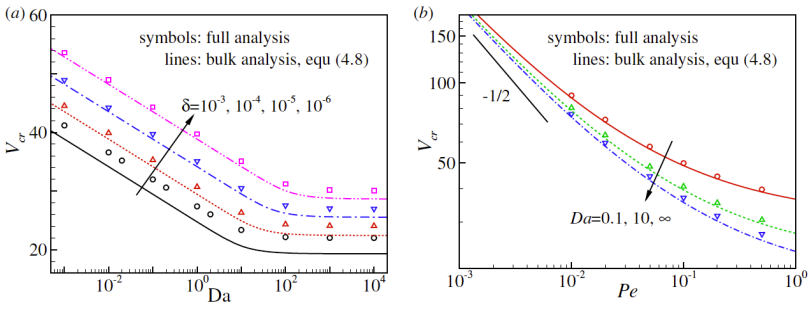

Fig 2. (**a**) The dependence of the critical voltage V_{cr} on the Damkohler number Da at Pe = 0.5. (**b**) The critical voltage V_{cr} vs Pe for $\delta = 10^{-5}$.

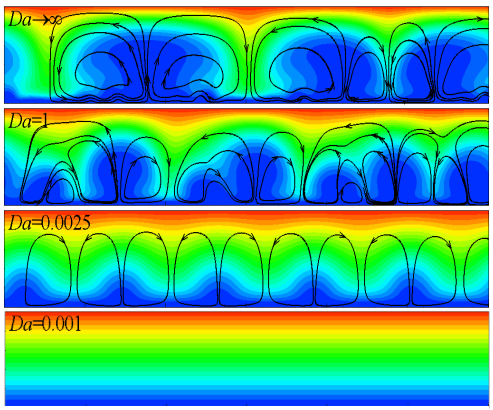

Fig 3. The cation concentration distribution (red: high concentration, blue: low concentration) in the electrolyte at V=40 at different Da. The lines are the streamlines.

We complemented the linear stability analysis with direct numerical simulations and experiments to study the effects of Da on the structure of the electroconvective flow. The simulations show that vortex rolls create downward and upward flows and lead to a large concentration variations. Decreasing Da gradually reduces and ultimately eliminates, the hydrodynamic contribution (**Fig. 3**). We note further, that at small Da, the lateral gradient of the surface potential Φ_s create a lateral ion flux, which drives the cations away from high cation concentration regions and helps smooth the deposition. This effect is absent at large Da because the gradient of Φ_s is in the unfavorable direction. Our results therefore indicate that a blocking

coating of essentially any chemistry that reduces the electroreduction rate of metal ions would be effective in stabilizing both the hydrodynamic and morphological instability.

II.2 Adsorbed polymer chains delay the onset of electroconvection.

We experimentally studied the onset of the electroconvective instability in liquid electrolytes containing low-molecular weight, methyl terminated polyethylene glycol (PEG300: PEG with M_w 300Da). These polymers are intentionally chosen with molecular weights below the entanglement threshold to eliminate effects of elastic forces in the bulk, which are also able to counter the electroosmotic drag that drives electroconvection. The voltammetry results in **Fig. 4a** were obtained from linear voltage sweep measurements in a three-electrode cell (RDE, Pine Research) in which Zn is the counter electrode, Ag/AgCl is the reference, and a stationary Nafion-coated glassy carbon (GC) is the working electrode.

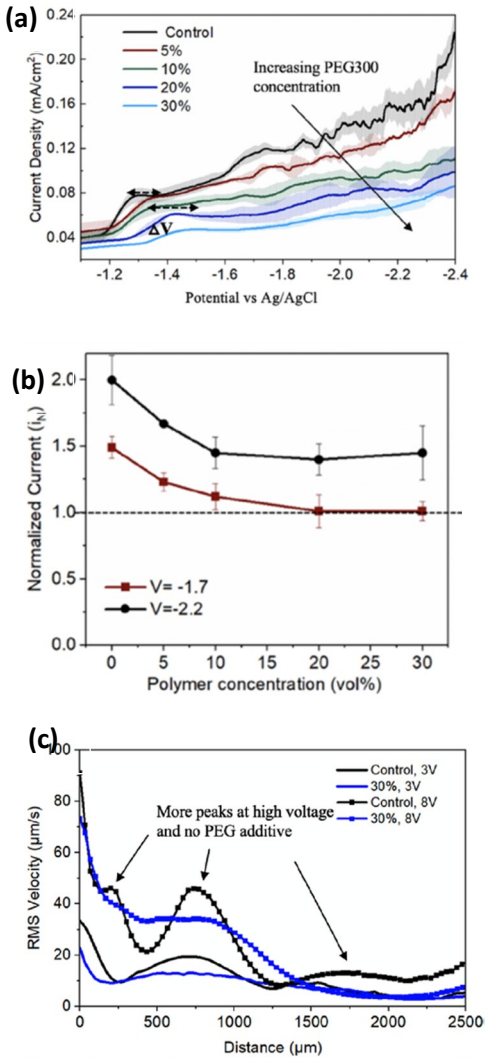

Fig 4. (a) Current-voltage response in a 3-electrode Zn||Nafion-GC cell containing 1mM ZnO4(aq) electrolyte with PEG oligomers (Mw = 300Da) at varying polymer volume fraction. **(b)** Normalized over-limiting current vs polymer volume fraction. **(c)** Velocity distribution measured in a Zn||Nafion-Zn visualization cell near the Nafion electrolyte interface in electrolytes with or without (control) PEG. [11]

The results in **Fig. 4a,b** show that as the polymer concentration rises, the limiting- and overlimiting ($i_N = \frac{i}{i_{lim}} = \frac{current}{limiting\ current}$) currents are reduced, and the overlimiting transport regime pushed out to higher voltages.[11-13] **Fig. 4b** shows the normalized over-limiting current. The extent to which the overlimiting current regime is delayed and electroconvection is suppressed at an oligomer concentration of 20% is comparable to what we reported previously in studies of more viscous electrolytes containing much higher molecular weight polymers (M_w = (1.3-10) x 10^6 Da) in electrolytes of different chemistry. The experimental results also show that oligomers are most effective in suppressing electroconvection at moderate concentrations and that the effect saturates at higher oligomer concentrations.

FluoSpheres, carboxylate-modified microspheres (diameter = 500 nm), dispersed as tracer particles in the electrolyte were used to quantify the time-dependent root mean squared velocity distribution near ion-select interfaces. These experiments allowed us to determine the detailed effects of PEG oligomers on electroconvection —from its onset state to achievement of steady state. The results reported in **Fig. 4c** show that the largest effects are on the intensity of the near-wall velocity and size of the mixing layer.[11]

To understand the source of these behaviors, we studied the interphases formed on metal electrodes in electrolytes containing PEG300. Measurements using quartz crystal microbalance (QCM) and spectroscopic ellipsometry revealed that the thickness of the ad-layer saturates with polymer concentration, explaining the origin of the effects seen in the current-voltage response reported in **Fig. 4b**.

Future Plans

Our future studies will take advantage of the experimental, theoretical, and numerical simulations framework developed in the prior work to further our understanding of electrodeposition in two contexts: 1) reversible and epitaxial electrodeposition of metal coatings in electrochemically reactive liquid electrolytes; and 2) electrodeposition of metal alloy coatings. Work in the first area is motivated by a recent discovery by the Archer group[14] that textured coatings composed of a crystalline material with low lattice mismatch for metal electrodeposits are effective in driving reversible electroreduction of metals in crystal symmetries set by the coating. This discovery is on the one hand a significant advance in the effort to limit out-of-plane electrodeposition at metal anodes in rechargeable batteries, but on the other is challenged by the propensity of metals of contemporary interest as battery anodes (e.g., Li, Na, Al, Zn) to form a solid electrolyte interphase (SEI) that limit the effectiveness of the epitaxial coating layer. By explicitly accounting for the reaction kinetics of electrolyte components in the stability analysis outlined in **Section II.1**, the goal is to develop design principles for achieving stable and reversible epitaxial electrodeposition of reactive metals in electrolytes prone to form SEI. Work in the second area is motivated by another discovery — namely, that gradients in composition and charge transport at a metal alloy-liquid interface introduce new modes of instability. Our goal is to understand these instabilities and to on that basis develop methods to limit their influence on metal electrodeposit morphology.

References

1. Tikekar, M.D., Choudhury, S., Tu, Z. and Archer, L.A. (2016) Design principles for electrolytes and interfaces for stable lithium-metal batteries. *Nature Energy* **1**, 6-12
2. Zheng, J., Kim, M.S., Tu, Z., Choudhury, S., Tang, T. and Archer, L.A. (2020) Regulating electrodeposition of lithium: Towards commercially relevant secondary Li metal batteries. *Chemical Society Reviews* **49,** 2701
3. Zheng, J. and Archer, L.A. (2022) Crystallographically textured electrodes for rechargeable batteries: symmetry, fabrication, and characterization. *Chem. Rev.* **122**, 14440
4. Mullins, W.W. and Sekerka, R.F. (1964) Stability of a planar interface during solidification of a dilute binary alloy. *Journal of Applied Physics* **35**, 444.
5. Rubinstein, I., Zaltzman, B. and Lerman, I. (2005) Electroconvective instability in concentration polarization and nonequilibrium electro-osmotic slip. *Physical Review E* **72**, 011505.
6. Mani, A. and Wang, K.M. (2020) Electroconvection near electrochemical interfaces: Experiments, modeling, and computation. *Annual Review of Fluid Mechanics* **52**, 509-529
7. Wei, S., Cheng, Z., Nath, P., Tikekar, M.D., Li, G. and Archer, L.A. (2018) Stabilizing electrochemical interfaces in viscoelastic liquid electrolytes. *Science Advances* **4**, 6243
8. Li, G., Archer, L.A. and Koch, D.L. (2019) Electroconvection in a viscoelastic electrolyte. *Phys. Rev. Lett.* **122**, 124501
9. Tikekar, M. D., Li, G., Archer, L.A. and Koch, D.L. (2018) Electroconvection and morphological instabilities in potentiostatic electrodeposition across liquid electrolytes with polymer additives. *J. Electrochemical Society* **165**, A3697-A3713
10. Li, G., Townsend, A., Archer, L.A. and Koch, D.L. (2022) Electroconvection near an ion-selective surface with Butler–Volmer kinetics. *Journal of Fluid Mechanics* **930**, A26.

11. Sharma, A., Mukherjee, A., Warren, A., Jin, S., Li, G., Koch, D.L., and Archer, L.A. (2023) Electroconvective Flow in Liquid Electrolytes Containing Oligomer Additives, Langmuir **39**, 92
12. Jin, S., Yin, J., Gao, X., Sharma, A., Chen, P., Hong, S., Zhao, Q., Zheng, J., Deng, Y., Joo, Y-L., Archer, L.A. (2022) Production of fast-charge Zn-based aqueous batteries via interfacial adsorption of ion-oligomer complexes. *Nature Communications* **13**, 2283
13. Jin, S., Deng, Y., Chen, P., Hong, S., Garcia-Mendez, R., Sharma, A., Utomo, N.W., Shao, Y., Yang, R., Archer, L.A. (2023) Solid-Adsorbed Polymer-Electrolyte Interphases for Stabilizing Metal Anodes in Aqueous Zn and Non-Aqueous Li Batteries, Angewandte Chemie e202300823
14. Zheng, J., Yin, J., Zhang, D., Li, G., Bock, D. C., Tang, T., Zhao, Q., Liu, X., Warren, A., Deng, Y., Jin, S., Marschilok, A.C., Takeuchi, E.S., Takeuchi, K.J., Rahn, C.D., and Archer, L.A. (2020) Spontaneous and field-induced crystallographic reorientation of metal electrodeposits at battery anodes, *Science Advances* ***6***, eabb1122

Directing C On-Surface

Michael S. Arnold, Department of Materials Science and Engineering, University of Wisconsin-Madison Formation

Keywords: 2D materials, anisotropy, heteroepitaxy, kinetics, hierarchy

Research Scope

When one- and two-dimensional materials are confined to a surface, their interactions with that surface profoundly affect their synthesis. New growth mechanisms arise. New opportunities for controlling synthesis with previously unobtainable precision emerge. As a result, novel materials behaviors can be obtained. With these opportunities come challenges: How do we understand these new synthetic mechanisms? How can we manipulate and control them to our benefit? To answer these questions, this project focuses on the chemical vapor deposition (CVD) based synthesis of graphene and graphene nanostructures and heterostructures (e.g., with hexagonal boron nitride, h-BN) on substrates (e.g., Ge) that strongly and directionally influence their nucleation and kinetics. The project is understanding synthetic mechanisms unique to low-dimensional materials confined on surfaces and learning how to exploit them to control shape, size, aspect ratio, and crystallographic orientation – with atomic precision.

Recent Progress

Towards this end, recent progress is reported in 3 areas: (1) Directional growth of graphene in the nanometer-scale limit; (2) Crystallographic orientational control of graphene monolayers (i.e., towards single crystal graphene); and (3) Precise graphene-h-BN lateral heteroepitaxy in the strongly kinetically frustrated regime.

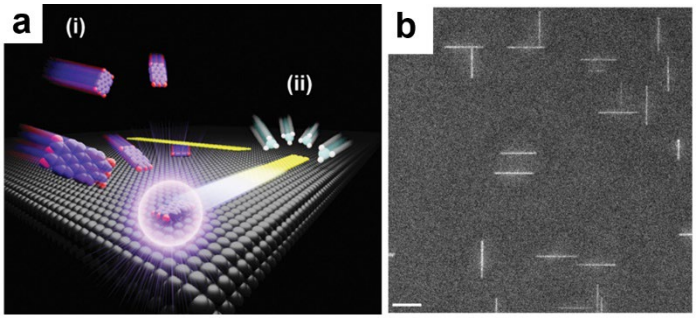

Fig. 1. Nanoribbon synthesis from molecularly derived seeds. (a) Schematic of two stages: (i) polyaromatic hydrocarbon molecules (red = O, purple = C, H not shown) are deposited at low temperature onto Ge(001) (grey) from vapor phase to form seeds. (ii) CH_4 (light blue = C and white = H) drives anisotropic growth via CVD and extends the seeds selectively along one direction, at high temp., to yield narrow, armchair graphene nanoribbons. In reality, most nanoribbons evolve in both directions from seed. **(b)** SEM image of nanoribbons initiated from PTCDA-derived seeds after 173 min of CH_4 exposure. Scale bar = 200 nm.

(1) Directional growth of graphene in the nanometer-scale limit.

Our work has revealed the existence of strong edge - substrate interactions that occur at particular combinations of graphene edge type, edge orientation, and substrate lattice orientation. These interactions are so powerful, especially on Ge(001), that growth kinetics are almost entirely frustrated along specific directions but not others.

In the past, we leveraged this kinetic frustration to synthesize highly anisotropic graphene nanoribbons via CH_4 CVD [Refs. 1-4]. Most recently, we have discovered (Fig. 1) how to launch this directional growth from the peripheries of molecular-scale seeds to realize nanoribbons with tunable, uniform widths as narrow as 2.6 nm [Ten Selected Publications 1-2]. Our research is elucidating the molecule-to-nanoribbon transformation (e.g., via STM) and uncovering fundamentals underpinning seeded and directional growth in the nm-scale limit, bridging the worlds of organic chemistry and the CVD of materials. These studies are important because they provide a pathway to realizing semiconducting, armchair-faceted nanoribbons directly on technologically relevant Ge(001) and Ge-on-Si wafers. U.S. Patent 11,618,681 has been issued as of Apr. 4, 2023 (2023), on this idea, as well.

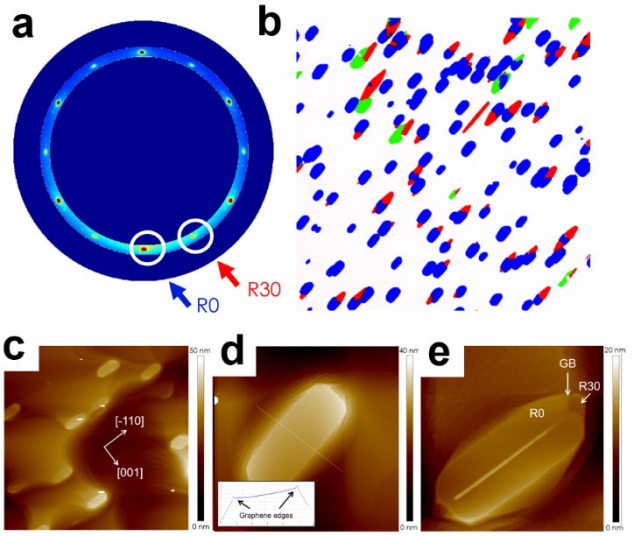

Fig. 2. Characterization of graphene island crystallographic orientation, prior to "single crystal" coalescence, on Ge(110) via LEED **(a)** and dark-field LEEM **(b)**, which superimposes dark-field images created from R0˚ (blue), R30˚ (red), and other, 5-25˚, (green) diffraction. R30˚ (red) and R5-25˚ (green) primarily nucleate off or near the ends of R0˚ domains. Secondary nucleation occurs after R0˚ domains reach a particular size or after a particular duration. **(c-e)** AFM height maps of graphene islands on Ge(110). **(c)** 10×10 μm^2. **(d)** 3.3×3.3 μm^2, **(e)** 1.4×1.4 μm^2. Each graphene island lies in shallow ~ 1 nm deep depression, elevated on a Ge mound (b insert). **(e)** exhibits R30˚ domain nucleated off / near long end of the R0˚ graphene island. GB = grain boundary.

(2) Crystallographic orientational control of graphene monolayers (i.e., towards single crystal graphene).

While initial reports indicated that graphene is single-crystalline when grown on the technologically important substrates Ge(110) and epitaxial Ge on Si(110) [Ref. 5], conflicting studies by us (in preparation) and others have revealed polycrystallinity. We have conducted crystal growth studies and used LEEM/LEED analysis (conducted by collaborators in the group of Michael Altman at the Hong Kong University of Science and Technology) to begin to understand why. Our data show that shortly after nucleation, the lattices of most graphene islands are indeed globally aligned in a single direction (Fig. 2a,b). However, as growth progresses, we have discovered that misoriented domains nucleate from or near the edges of the aligned islands (Fig. 2a-e). Our studies point to a likely culprit that facilitates this secondary nucleation: the Ge topography, which is simultaneously evolving during the synthesis due to surface tension effects and sublimation. We are now using this understanding to work towards truly synthesizing single-crystal graphene on Ge(110) via CVD [manuscript in preparation].

(3) Precise graphene-h-BN lateral heteroepitaxy in the strongly kinetically frustrated regime.

Graphene - substrate interactions in concert with fine-control of precursor supersaturation are capable of frustrating graphene crystal growth kinetics along particular edge facets to observed rates < 0.05 nm min^{-1} on substrates such as Ge, affording unparalleled control over graphene nanostructure dimensions. We have now coupled anisotropic graphene growth with h-BN synthesis on Ge(001). Highlights include: the first synthesis of h-BN on Ge from borazine [Ten Selected Publications 3] and an understanding of the interplay among Ge surface topography, Ge sublimation, and h-BN island evolution [Ten Selected Publications 3].

4) Other

- Published a huge, 14000-word perspective article that presents (i) an extensive review of progress to-date on the synthesis and processing of graphene nanoribbons and (ii) in-depth perspective regarding challenges and potential solutions. [Ten Selected Publications 4]
- Investigated nano-faceting & surface reconstruction at Ge-graphene interfaces (Fig. 4). [Ten Selected Publications 5]
- Created state-of-the-art graphene samples to enable collaborative advances in single crystal nanomembrane synthesis via remote- and lateral overgrowth epitaxy. [Ten Selected Publications 6-10]

Future Plans

We are particularly excited about beginning the study of two ideas:

(1) Exploring the fundamentals of creating metallic and semiconducting graphene - h-BN superstructures with unparalleled, atomic-scale control over dimensions.

(2) Studying the fundamentals underpinning a promising possible synthetic pathway to bilayer graphene with controlled twist angle.

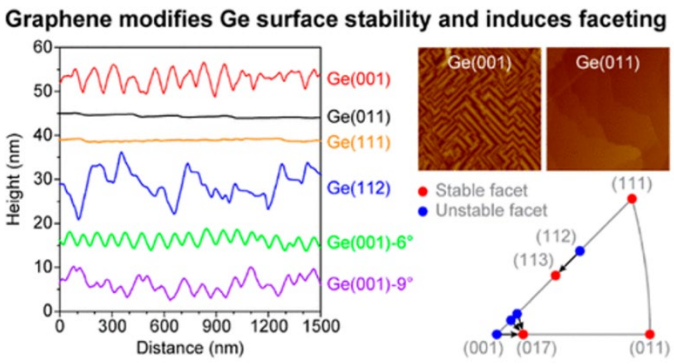

Fig. 4. Restructuring of Ge surface due to presence of graphene. (a-b) Surface topography after graphene monolayer synthesis on various Ge facets. **(c)** Phase diagram of the graphene-Ge interface.

References

1. R. M. Jacobberger, B. Kiraly, M. Fortin-Deschenes, P. L. Levesque, K. M. McElhinny, G. J. Brady, R. Rojas Delgado, S. Singha Roy, A. Mannix, M. G. Lagally, P. G. Evans, P. Desjardins, R. Martel, M. C. Hersam, N. P. Guisinger, M. S. Arnold, *Direct oriented growth of armchair graphene nanoribbons on germanium*. Nature Communications **6**, 8006 (2015).
2. A. J. Way, V. Saraswat, R. M. Jacobberger, M. S. Arnold, *Rotational self-alignment of graphene seeds for nanoribbon synthesis on Ge(001) via chemical vapor deposition*. APL Materials **8**, 091104 (2020).

3. V. Saraswat, Y. Yamamoto, H. J. Kim, R. M. Jacobberger, K. R. Jinkins, A. J. Way, N. P. Guisinger, M. S. Arnold, *Synthesis of Armchair Graphene Nanoribbons on Germanium-on-Silicon*. The Journal of Physical Chemistry C **123**, 18445-18454 (2019).
4. R. M. Jacobberger, V. Thapar, G.-P. Wu, T.-H. Chang, V. Saraswat, A. J. Way, K. R. Jinkins, Z. Ma, P. F. Nealey, S.-M. Hur, S. Xiong, M. S. Arnold, *Boundary-directed epitaxy of block copolymers*. Nature Communications **11**, 4151 (2020).
5. J. H. Lee, E. K. Lee, W. J. Joo, Y. Jang, B. S. Kim, J. Y. Lim, S. H. Choi, S. J. Ahn, J. R. Ahn, M. H. Park, C. W. Yang, B. L. Choi, S. W. Hwang, D. Whang, *Wafer-Scale Growth of Single-Crystal Monolayer Graphene on Reusable Hydrogen-Terminated Germanium*. Science **344**, 286-289 (2014).

Ten Selected Publications (supported by BES in most recent 2 years)

1. A. J. Way, R. M. Jacobberger, N. P. Guisinger, V. Saraswat, X. Zheng, A. Suresh, J. H. Dwyer, P. Gopalan, M. S. Arnold, *Graphene nanoribbons initiated from molecularly derived seeds*. Nature Communications **13**, 2992 (2022). 10.1038/s41467-022-30563-6

2. V. Saraswat, A. J. Way, X. Zheng, R. M. Jacobberger, S. Manzo, N. Tiwale, J. H. Dwyer, J. K. Kawasaki, C.-Y. Nam, P. Gopalan, M. S. Arnold, *Bottom-up synthesis of mesoscale nanomeshes of graphene nanoribbons on germanium*. APL Materials 11, 041123 (2023). 10.1063/5.0134756

3. K. A. Su, S. Li, M. S. Arnold, *High-Vacuum Chemical Vapor Deposition of Monolayer Hexagonal Boron Nitride on Ge(001) from Borazine*. ECS Transactions **111**, 97 (2023). 10.1149/11102.0097ecst

4. V. Saraswat, R. M. Jacobberger, M. S. Arnold, *Materials Science Challenges to Graphene Nanoribbon Electronics*. ACS Nano **15**, 3674-3708 (2021). 10.1021/acsnano.0c07835

5. R. M. Jacobberger, D. E. Savage, X. Zheng, P. Sookchoo, R. Rojas Delgado, M. G. Lagally, M. S. Arnold, *Effect of Germanium Surface Orientation on Graphene Chemical Vapor Deposition and Graphene-Induced Germanium Nanofaceting*. Chemistry of Materials **34**, 6769-6778 (2022). 10.1021/acs.chemmater.2c00919

6. D. Du, T. Jung, S. Manzo, Z. LaDuca, X. Zheng, K. Su, V. Saraswat, J. McChesney, M. S. Arnold, J. K. Kawasaki, *Controlling the Balance between Remote, Pinhole, and van der Waals Epitaxy of Heusler Films on Graphene/Sapphire*. Nano Letters **22**, 8647-8653 (2022). 10.1021/acs.nanolett.2c03187

7. Z. H. Lim, S. Manzo, P. J. Strohbeen, V. Saraswat, M. S. Arnold, J. K. Kawasaki, *Selective area epitaxy of GaAs films using patterned graphene on Ge*. Applied Physics Letters **120**, 051603 (2022). 10.1063/5.0078774

8. S. Manzo, P. J. Strohbeen, Z. H. Lim, V. Saraswat, D. Du, S. Xu, N. Pokharel, L. J. Mawst, M. S. Arnold, J. K. Kawasaki, *Pinhole-seeded lateral epitaxy and exfoliation of GaSb films on graphene-terminated surfaces*. Nature Communications **13**, 4014 (2022). 10.1038/s41467-022-30563-6

9. H. Yoon, T. K. Truttmann, F. Liu, B. E. Matthews, S. Choo, Q. Su, V. Saraswat, S. Manzo, M. S. Arnold, M. E. Bowden, J. K. Kawasaki, S. J. Koester, S. R. Spurgeon, S. A. Chambers, B. Jalan, *Freestanding epitaxial $SrTiO_3$ nanomembranes via remote epitaxy using hybrid molecular beam epitaxy*. Science Advances **8**, eadd5328 (2022). 10.1126/sciadv.add5328

10. D. Du, S. Manzo, C. Zhang, V. Saraswat, K. T. Genser, K. M. Rabe, P. M. Voyles, M. S. Arnold, J. K. Kawasaki, *Epitaxy, exfoliation, and strain-induced magnetism in rippled Heusler membranes*. Nature Communications **12**, 2494 (2021). 10.1038/s41467-021-22784-y

Integrated Synthesis and Simulation of Zeolites: Engineering Defects and Crystallization Kinetics Via 3rd Route to Zeolite Formation

PIs: Scott Auerbach (PI)[1,2] and Wei Fan (Co-PI)[2]

[1]Department of Chemistry, [2]Department of Chemical Engineering, UMass Amherst

Keywords: Zeolites, Crystallization, Raman, Fluoride, DFT

Research Scope

Zeolites represent a major cornerstone of today's energy industry as the most used petrochemical catalyst in the world. However, the rational synthesis of zeolites with targeted framework structures, compositions, and defect properties, remains a grand challenge because of the complex interplay among synthesis parameters, and our poor understanding of zeolite crystallization mechanisms. Our research program is shedding new and much needed light on how zeolites form in solution – opening the door to innovations that support the clean energy transition such as producing biofuels and chemicals, and capturing carbon dioxide. Our research tightly integrates synthesis, spectroscopy, and DFT simulations, and has provided rigorous evidence for the structure-directing and charge-balancing roles played by fluoride (F^-) during the assembly of all-silica LTA (Si-LTA) zeolite. Our research has also led to a "3rd route" to zeolite formation that gives both (*i*) faster crystallization and (*ii*) the titration of controlled Si-OH/Si-O^- defects into Si-LTA materials by rational choices of organic structure-directing agents (OSDAs). Our research is yielding new zeolite synthesis protocols for tuning charge distributions in zeolites – facilitating green applications using hydrophobic nanopores with controlled hydrophilic patches.

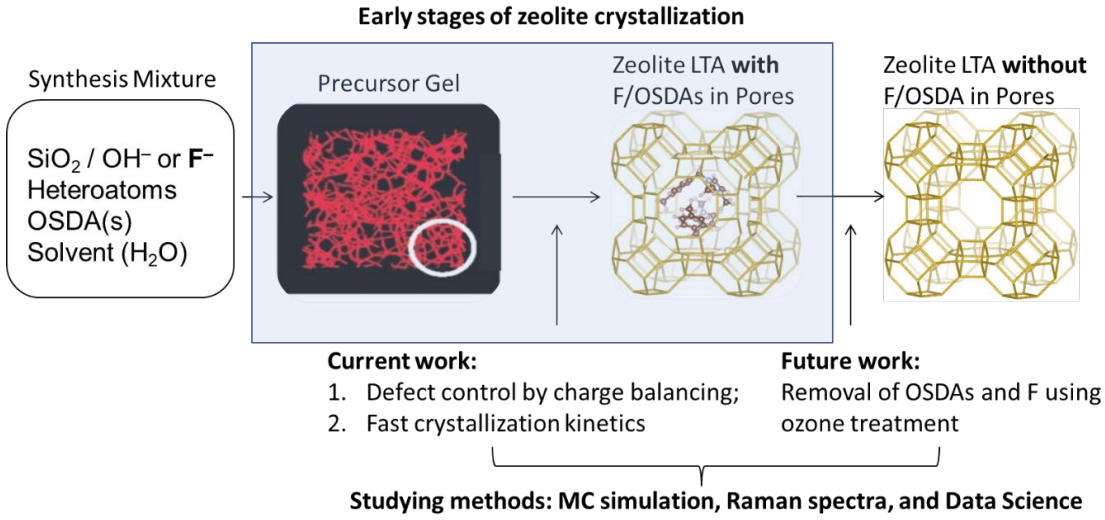

Figure 1. Project Scope – understanding early stages of zeolite crystallization for improved kinetics and defect control using charge-balancing principles.

Recent Progress

3rd Route to Zeolites for Precise Defect Control. Zeolites can be hydrothermally synthesized in alkaline or neutral media using hydroxide or fluoride, respectively, as a "mineralizing agent" for crystallization. Under alkaline conditions, negatively-charged framework defects (Si-O^-) are often formed in as-made zeolites (before applying heat to remove organic structure-directing agents or OSDAs) to balance positive charges from OSDAs and/or inorganic cations. In contrast, the fluoride synthesis route has led to a variety of new, defect-free zeolite materials – essentially high-silica or even all-silica zeolites. In addition to being a mineralizing agent, fluoride is hypothesized to act as a structure-directing agent, stabilizing small silicate rings and cages such as the double four-membered ring (D4R) in zeolites. Fluoride is also hypothesized to play a charge-compensating role, where F^- balances positive charges from OSDAs or inorganic cations used in zeolite synthesis, thereby producing low-defect or defect-free materials. Prior to our DOE-funded research, the conventional wisdom held that balancing of fluoride and OSDA amounts in the synthesis solution yields charge-balancing in the resulting zeolite crystal [1]. However, our research has challenged this assumption, generating a new paradigm in zeolite synthesis that we call the **3rd route to zeolites**. In particular, we have found that adding various amounts of a secondary OSDA (even in an excess of fluoride) influences both the speed of zeolite crystal formation and the presence of Si-OH/Si-O^- defects in otherwise hydrophobic nanopores. Here we indicate how our integrated synthesis and simulation approach has led to this breakthrough.

All-silica LTA (Si-LTA) zeolite was selected as a model synthesis system to investigate charge-balancing among a primary OSDA ("BULKY"), a secondary OSDA (TMA), F^- and defects. As shown in Fig. 2a, charge-balancing can be achieved with two BULKY cations, one TMA cation, and three F^- anions in each LTA unit cell. **One key discovery is that silanol defects (Si-O^-) can be titrated into LTA crystals by increasing TMA amounts in the synthesis solution**. Raman bands of zeolites were used to monitor the structure development during crystallization and to identify charge-balancing effects. In Si-LTA, two distinct Raman bands arise for D4R cages: empty D4Rs (yellow-shaded band in Fig. 2b) and D4Rs containing F^- (black-shaded band in Fig. 2b). Our accurate periodic DFT simulations of the Raman spectrum of as-made LTA containing both BULKY cations and F^- have led to the rigorous assignment of Raman bands from OSDA and the zeolite framework, allowing us to experimentally investigate the LTA crystallization process (Fig. 2b) and the titration of defects (Fig. 2c).

As shown in Fig. 2b, with increasing crystallinity (bottom to top), the ratio of Raman band intensities of F^-/D4R to empty D4R gradually decreases. Through our periodic DFT simulations, we have attributed this variation to the evolution of point defects in growing LTA-BULKY crystals. These defects were assigned as missing Si atoms in empty D4R units producing "silanol nests" – groups of Si-OH groups – consistent with solid-state ^{29}Si NMR data. Upon further crystallization, these defects become healed, leading to defect-free LTA zeolite crystals. The fact that defects were found in empty D4Rs but not in F^-/D4R provides the first **evidence during crystallization that F^- acts as a structure-directing agent for the formation of the D4R zeolite building block** – a breakthrough made possible by our integrated synthesis-simulation approach.

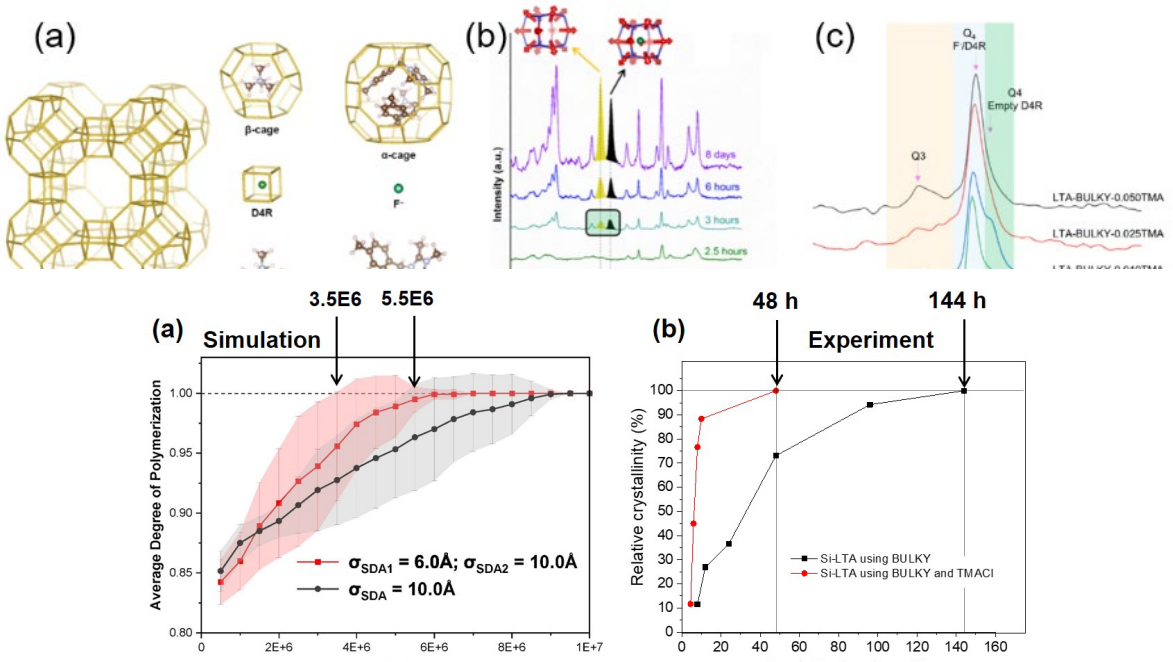

Figure 3. (a) Reaction Ensemble Monte Carlo of Si-LTA crystallization comparing 1 and 2 OSDAs, predicting a 60% speedup using 2 OSDAs; (b) Experimental syntheses find a 3-fold speedup; (c) Si-O-Si angle; (d) Analyses of Si-O-Si angular energies show more stable rings from packing the second OSDA into the system.

Furthermore, we have found that by varying the amount of TMA in the synthesis gel as a secondary OSDA, positive charge can be titrated into the resulting as-made Si-LTA. Surprisingly, greater TMA concentration does not pull more F^- into the resulting zeolite – in contrast to conventional wisdom in zeolite synthesis science. Our integrated spectroscopy and simulation studies indicate that this system has surpassed its capacity for F^- to balance OSDA positive charge, and that some positive charges are balanced by $Si\text{-}O^-$ framework defects (shown by solid-state ^{29}Si NMR data – Fig. 2c – and periodic DFT simulations). The number of defects in as-made Si-LTA was found to correlate with the amount of TMA, indicating our breakthrough ability to engineer novel charge distributions and defect densities in zeolites.

The 3rd route to zeolite synthesis paradigm – exploiting multiple OSDAs along with F^- – provides a novel and effective way to control defects and compositions in high-silica LTA zeolites. In ongoing research, we are expanding the 3rd route to other zeolite synthesis systems. We are also investigating ways to reduce and even eliminate F^- use, which would open important zeolites to industry-scale synthesis. For example, using these charge balancing ideas, we synthesized alumino-silicate LTA with a framework composition of Si/Al = 7 in the absence of F^-, which had not been done before (unpublished).

3rd Route to Zeolites for Faster Crystallization**.** Zeolite crystallization by hydrothermal treatment can take days to weeks depending on the targeted frameworks and synthesis conditions. Faster zeolite synthesis/production is highly desirable and could save significant amounts of energy. Despite substantial research on speeding up zeolite synthesis – mostly using novel heating methods

such as microwaves and rapid heat transfer – it still remains challenging to reduce synthesis times. In contrast, relatively little work has been done on understanding how combining different OSDAs can accelerate zeolite formation. This is akin to speeding up a reaction (i.e., zeolite formation) using a catalyst (i.e., an extra OSDA) instead of adding heat.

We have discovered that LTA crystallizes 3 times faster using the 3rd route synthesis. This discovery was initially predicted by our Reaction Ensemble Monte Carlo (RxMC) simulations of zeolite formation, which found a 60% speed up of crystallization when adding a second OSDA (Fig. 3a). Our experimental crystallization kinetics study to test this RxMC prediction found the speed up to be a factor of 3, from 6 days to 2 days (Fig. 3b). Our analysis of the RxMC trajectories indicate the surprising result that packing in the second OSDA actually stabilizes all the rings in the crystallizing system. We are studying how tuning charge balancing with dual OSDA systems may accelerate crystallization for other zeolite systems.

Future Plans

1. **Developing post-synthesis treatment for gentler, low-energy F^-/OSDA removal**. Applications of zeolites require removal of F^-/OSDA to open their nanopores; such removal is traditionally performed at high heat with oxygen, which is not a very controlled environment. We are studying the use of ozone for such post-synthesis treatment to save energy but also to exert control over defect structures that are formed in the 3rd route approach.
2. **Enhancing Monte Carlo simulations to treat structure-directing by F^-**. Our Raman studies (Fig. 2b) indicate a structure-directing effect from F^-, which is not accounted for in the present Reaction Ensemble Monte Carlo model. Making accurate predictions thus requires a major revision to the model; interpreting the trajectory datasets will require data science methods such as those reported in our recent publication on zeolite sorting by machine learning [2].
3. **Developing *ex situ* and *in situ* total X-ray scattering measurements**. Testing the predictions of the new Monte Carlo model discussed above will require detailed measurements of structure and order formation at medium-ranged length scales, provided by total X-ray scattering.

References

1. J. X. Jiang, J. H. Yu, and A. Corma, *Extra-Large-Pore Zeolites: Bridging the Gap between Micro and Mesoporous Structures*, Angew. Chem.-Int. Edit. **49**, 3120-3145 (2010).
2. B. A. Helfrecht, G. Pireddu, R. Semino, S. M. Auerbach, and M. Ceriotti, "*Ranking the Synthesizability of Hypothetical Zeolites via the Sorting Hat*," Digital Discovery **1,** 779-789 (2022).

Publications

1. S. Luo, T. Wang, J. Gulbinski, L. Qi, G. A. Tompsett, M. T. Timko, S. M. Auerbach, W. Fan, "*Identifying Order and Disorder in Double Four-membered Rings Via Raman Spectroscopy During Crystallization of LTA Zeolite*," Chemistry of Materials **33**, 6794-6803 (2021).
2. C. Bores, S. Luo, J. D. Lonergan, E. Richardson, A. Engstrom, W. Fan, and S. M. Auerbach, "*Monte Carlo Simulations and Experiments of Zeolite LTA Assembly Combining Structure-Directing Agents that Match Cage Sizes*," Phys. Chem. Chem. Phys. **24,** 142-148 (2021).
3. S. Luo, T. Wang, L. Qi, G. A. Tompsett, M. T. Timko, S. M. Auerbach, and W. Fan, "*Titrating Controlled Defects into Si-LTA Zeolite Crystals Using Multiple Organic Structure-Directing Agents*," Chemistry of Materials **34**, 1789-1799 (2022).

4. T. Wang, S. Luo, L. Qi, G. A. Tompsett, M. T. Timko, S. M. Auerbach, and W. Fan, "*Removing Fluoride from As-made Zeolite LTA Under Mild Conditions with Ozone*," in preparation.

Understanding and Controlling Nucleation in Atomic Layer Deposition for Materials Synthesis

Stacey F. Bent

sbent@stanford.edu
Department of Chemical Engineering
Stanford University, Stanford, CA 94305

Keywords: Atomic Layer Deposition (ALD); Nucleation; Precursors; Transition Metal Dichalcogenides (TMDC); Surfaces

Research Scope

Atomic layer deposition (ALD) is a materials synthesis technique with potential to produce the precise, nanostructured materials needed in emerging energy conversion and microelectronics technologies. This research program aims to obtain mechanistic information about ALD materials synthesis. We use a strategy of employing homologous series of precursors combined with careful control over surface functionality to separate and identify the precursor and surface properties that most strongly influence ALD nucleation. The research in this program focuses on understanding nucleation mechanisms in two technologically important materials systems: metal ALD on low surface energy dielectric substrates, and metal oxide ALD on transition metal dichalcogenides (TMDCs). We explore the use of precursor design, pre- and coadsorption of molecular species, and temperature to improve nucleation in ALD. New understanding will be used to develop deposition schemes in which better control over ALD nucleation can be achieved.

Recent Progress

Our recent studies are focused in three areas: influence of surface energy on ALD nucleation; using small molecular co-adsorbates to control ALD nucleation; and, ALD nucleation on TMDCs.

Effect of surface energy to influence noble metal ALD

Atomic layer deposition of noble metals on metal oxide surfaces is of interest in applications ranging from catalysis to microelectronics, but it typically suffers from nucleation delays which result in non-uniform and inhomogeneous thin films. The poor nucleation is usually attributed to sparse chemisorption sites on the substrate surface during the nucleation stage and poor material transport on the substrate surface during the growth stage. We are investigating the nucleation and growth of ruthenium (Ru) layers using ALD with $Ru(Cp)_2$ precursor and O_2 as a co-reactant. We explore the effects of pre-functionalizing the substrate surface with small organometallic molecules, such as trimethylaluminum (TMA) and diethylzinc (DEZ), on the nucleation and growth of Ru layers. Our results demonstrate a significant enhancement effect on the nucleation and growth of Ru as reflected in the larger average diameter and higher aerial density of the deposited Ru nuclei (Figure 1d). We hypothesize that the modified surface increases both the available chemisorption sites for nucleation and the surface free energy, which affects transport processes on the surface such as coalescence and nanoparticle diffusion. The scanning electron microscopy (SEM) images (Figure 1a-c) and coverage data shed light on the enhancement

mechanism and reveal notable differences between the non-, TMA-, and DEZ-pretreated substrates. Using a modification of the Johanson-Avrami-Mehl-Kolmagorov isothermal growth model [1-4], we attributed the enhanced growth to an increase in the surface diffusion of the Ru species on the substrate. This study contributes to the understanding of ALD processes and provides insights into how small organometallic molecules and changes in surface free energy can be used to enhance the nucleation and growth of thin films.

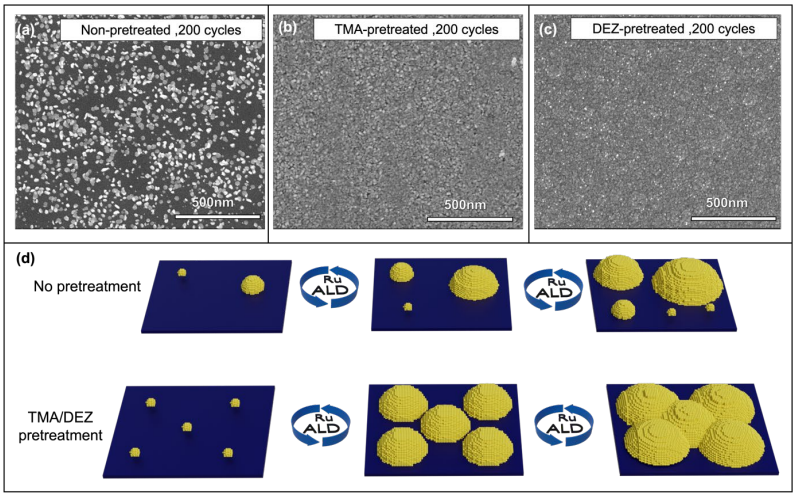

Figure 1. SEM images collected after 100 Ru ALD cycles on Si substrate (a) without organometallic pretreatment, (b) with TMA pretreatment, and (c) with DEZ pretreatment. (d) Illustration of the Ru ALD growth enhancement mechanism on Si substrate for the non-pretreated and TMA/DEZ pretreated cases.

Controlling ALD nucleation with small molecule co-adsorbates

In our studies of noble metal ALD on low-surface-energy metal oxide substrates, we also investigate another approach to enhancing nucleation. In these studies, we leverage our earlier experience with small molecule inhibitors developed for area-selective deposition and apply them to nucleation control in Pt ALD. In a first stage, we demonstrate blocking of the formation of new nuclei while still allowing deposition of material on existing nuclei, as illustrated in Figure 2a. The small molecule inhibitor trimethoxypropylsilane (TMPS) binds selectively on SiO_2 [5]. During the ALD of Pt on SiO_2, this adsorbate effectively prevents reaction of the Pt precursor (trimethyl(methylcyclopentadienyl)platinum or $MeCpPtMe_3$) with the SiO_2 surface, while the Pt precursor still can chemisorb on the existing Pt nuclei. The validity of this approach is demonstrated through an experiment in which 50 ALD cycles of $MeCpPtMe_3 + O_3$ results in an initial size distribution, which is then modified with an additional number of ALD cycles consisting of TMPS + $MeCpPtMe_3$ + O_3. (Figure 1b). The data show that the growth per cycle levels off when the TMPS dosing starts, indicating successful suppression of the formation of new nuclei. The effect of the inhibitor pulsing on the size distribution of nuclei is shown in Figure 1c. The distribution of nuclei sizes is being analyzed to understand the impact of the inhibitor on the ALD nucleation and growth processes.

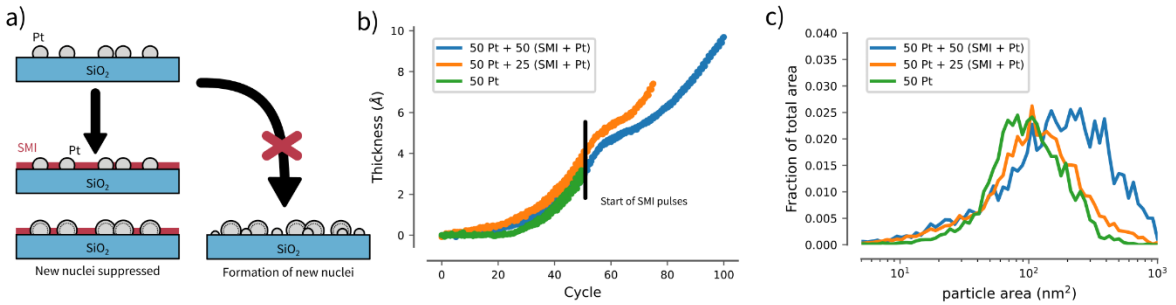

Figure 2. a) Schematic of the approach to nucleation control. b) In situ ellipsometry results. The first 50 cycles are identical, normal ALD cycles. From cycle 50, a different number of cycles containing TMPS are delivered. c) Particle area distribution for the different depositions, from an ensemble of SEM images.

ALD on 2D TMDC Materials

Recently, 2D TMDCs have received significant attention due to their unique optical and electrical properties, lending themselves to exciting applications such as microelectronics, sensing, catalysis, and photonics. Often, these materials need to be incorporated into material stacks for their intended application, e.g., transistor devices, requiring the deposition of materials such as metals and metal oxides on top of the TMDCs. Conventional methods for material deposition include various physical and chemical vapor deposition techniques. However, these 2D materials possess inert, low energy surfaces which tend to lead to material aggregation when material is deposited on top of them. Consequently, depositing uniform nanoscale thin films on 2D materials is challenging.

In this research, we are investigating the mechanisms of ALD on 2D TMDC materials and exploring ways to enhance nucleation. We are studying how ALD process parameters – such as temperature, purge time, and precursor type –can be tuned to alter the nucleation behavior of thin films on 2D materials. Our particular focus is on which process parameters strongly impact precursor physisorption on the 2D material and the subsequent reaction kinetics – thereby determining the nucleation and growth behavior.

We have been exploring various Al_2O_3 and HfO_2 ALD precursors to understand how changing the ligand type alters nucleation on TMDCs. In Figure 3(a) and (b), it is observed that using triethylaluminum (TEA) for Al_2O_3 deposition provides much better Al_2O_3 coverage on MoS_2 than trimethylaluminum (TMA). We hypothesize that this improvement arises from the longer ligands on TEA that can provide more van der Waals dispersion interactions with the surface, leading to better precursor wetting of the surface. In Figure 3(c) and (d), it can also be seen that tetrakis(dimethylamino)Hf (TDMAHf) provides better coverage than Hf(tertbutoxide). Furthermore, the change in HfO_2 precursor leads to different deposition morphologies: TDMAHf leads to the creation of fractal-like structures on the MoS_2 surface, whereas Hf(tertbutoxide) leads to more spherical particles on the surface. We postulate that the coverage and the morphology of the deposited HfO_2 are strongly affected by the kinetics and hypothesize that the TDMAHf reacts more quickly than the Hf(tertbutoxide) leading to less precursor desorption and higher nuclei formation. We plan to use these learning to select precursors that we expect will further improve nucleation and growth of films on TMDCs.

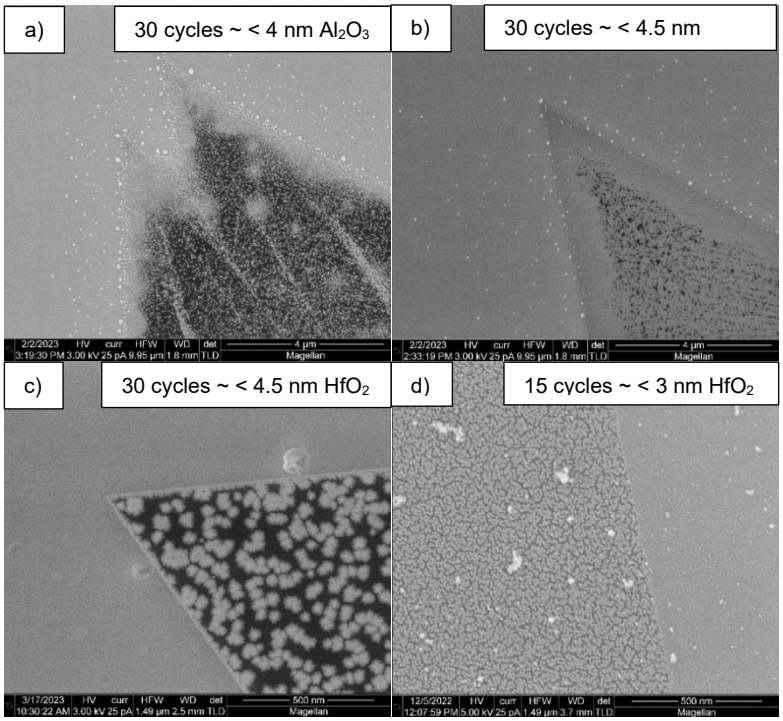

Figure 3. SEM of Al_2O_3 (a,b) and HfO_2 (c,d) deposited on monolayer MoS_2 by ALD using (a) TMA, (b) TEA, (c) Hf(tertbutoxide), and (d)TDMAHf at 100ºC.

Future Plans

We plan to complete the studies on Ru ALD as a function of molecular pretreatment and will model the growth behavior to delineate the roles of nucleation site density and surface free energy or diffusion. We will then explore ALD of Ru and other metals on substrates with different intrinsic surface free energies. In our nucleation control research, we will complete the study of Pt ALD using small molecule inhibitors that prevent growth on the SiO_2 substrate, and next explore use of different coadsorbates to block the growth on existing Pt nuclei to promote the formation of new nuclei. We have identified suitable candidate small molecule inhibitors that will be introduced in the following months. Finally, we will finish the studies of the role of precursor selection on metal oxide ALD on MoS_2 and will also explore the use of other process parameters such as substrate temperature to achieve enhanced nucleation and film coverage on TMDCs.

References

1. Avrami, M. *Kinetics of phase change. I General theory.* The Journal of Chemical Physics ***7*** (12), 1103-1112 (1939).

2. Avrami, M. *Kinetics of Phase Change. II Transformation-Time Relations for Random Distribution of Nuclei.* The Journal of Chemical Physics ***8*** (2), 212-224. (1940).

3. Johnson, W.; Mehl, R. American Institute of Mining and Metallurgical Engineers. *Transactions **135***, 416 (1939).

4. Kolmogorov, A. N. *Bulletin of Academic Science USSR **3***, 355 (1939).

5. Yarbrough J., F. Pieck, D. Grigjanis, I.-K. Oh, P. Maue, R. Tonner, and S. F. Bent, *Tuning molecular inhibitors and aluminum precursors for area-selective atomic layer deposition of Al_2O_3*, Chemistry of Materials, **34**(10), 4646-4659 (2022).

Publications

1. “Increased selectivity in area-selective ALD by combining nucleation enhancement and SAM-based inhibition,” C. de Paula, D. Bobb-Semple, and S. F. Bent, *J. Mater. Research*, 36 (2021) 582-591, 10.1557/s43578-020-00013-4.
2. “Identification of highly active surface iron sites on Ni(OOH) for the oxygen evolution reaction by atomic layer deposition,” J. G. Baker, J. R. Schneider, C. de Paula, A. J. M. Mackus, and S. F. Bent, *J. Catal.* **394** (2021) 476–485, 10.1016/j.jcat.2020.09.035.
3. "Mechanistic studies of nucleation and growth during the atomic layer deposition of metals", Camila de Paula Texeira, Ph.D. Thesis, Stanford University, 06/30/2021.
4. “The importance of decarbonylation mechanisms in the atomic layer deposition of high-quality Ru films by zero-oxidation state Ru(DMBD)$(CO)_3$,” J.R. Schneider, C. de Paula, J. Lewis, J. Woodruff, J.A. Raiford, and S.F. Bent, *Small* **18** (2022) 2105513, 10.1002/smll.202105513.
5. “Understanding and utilizing reactive oxygen reservoirs in atomic layer deposition of metal oxides with ozone,” J. R. Schneider, C. de Paula, N. E. Richey, J. G. Baker, S. T. Oyakhire, and S. F. Bent, *Chem. Mat*., **34** (2022) 5584–5597, 10.1021/acs.chemmater.2c00753.
6. “Elucidating reaction mechanism of atomic layer deposition of Al_2O_3 with a series of $Al(CH_3)_xCl_{3-x}$ and $Al(C_yH_{2y+1})_3$ precursors,” I.-K. Oh, T. Sandoval, T.-L. Liu, N Richey, N. C. Thang, B. U. Gu, H. B. R. Lee, R. Tonner-Zech and S. F. Bent, *J. Am Chem. Soc*., **144** (2022) 11757–11766, 10.1021/jacs.2c03752.
7. "Surface and subsurface reaction mechanisms in atomic layer deposition of metals and metal oxides", Joel R. Schneider, Ph.D. Thesis, Stanford University, 03/31/2022.
8. Tailoring the growth of ruthenium thin films through surface-diffusion control in atomic layer deposition, A. Rothman, A. W. Werbrouck, and S. F. Bent, in preparation.

Acoustic Modification of Crystallization and Dislocation Dynamics in Energy Materials

M. Bertoni - Arizona State Univ., D. Fenning - Univ. California San Diego, N. Alem - Pennsylvania State Univ.

Keywords: Crystallization, Dislocation Reduction, Ultrasound

Research Scope

In this program we propose to explore the use of high-intensity ultrasound (insonation) as a potentially transformative manufacturing approach to improve the crystal quality of a wide range of energy materials and manipulate dislocation dynamics, as an alternative to, or synergistic with, traditional thermal annealing. Specifically, for this workshop we will present on the crystallization and recovery in an exemplary halide perovskite alloy with a soft lattice and flexible substitution, $FAPbI_3$ [1]. We chose this lattice to explore the parameter space for insonation as well as the effects of electron beam dose during the development of a TEM protocol. We observe that the application of high-power ultrasound *during* or *after* perovskite crystallization show dramatic increases in photoluminescence quantum yield or external radiative efficiency (ERE).

Recent Progress

In the short period of time that we have been working on this project, we have deposited and characterized over 300 $FAPbI_3$ perovskite films for ultrasound modification. The films were fabricated by the Automated MAterials by Solution Synthesis (AMASS) robot developed by the Fenning group. Utilizing AMASS we fabricated the films which include a self-assembled monolayer (SAM) MeO-2PACz forming the hole transporting layer (HTL) and the organic-inorganic perovskite $FAPbI_3$ which were deposited on ITO substrates. After deposition several sets were annealed at UCSD and shipped to ASU with a set of unannealed sisters for insonation ex-situ and in-situ respectively. Note that the Bertoni group is building a replica of AMASS to easily transfer the chemistry developments by the Fenning group and minimize sample shipment.

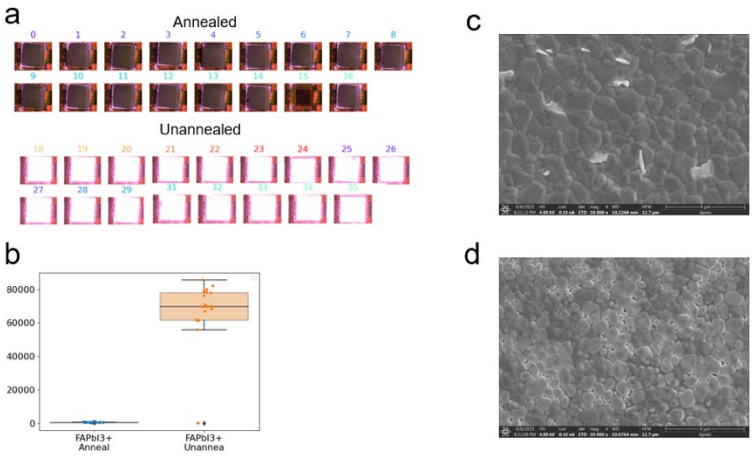

Figure 1: Characterization of a different batch of perovskite samples sent to ASU (a) PL images, (b) PL intensities, (c) SEM characterization an annealed $FAPBI_3$ film, and (d) SEM characterization of an unannealed $FAPBI_3$ film.

Figure 1a shows images of annealed samples and

unannealed samples before acoustic modifications. Figure 2b-d present the PL spectra taken by the automated characterization line and the complementary SEM images.

Figure 2 shows the results of the ex-situ (crystallized at UCSD) and in-situ (crystallized at ASU) insonation of the samples. We observe that the repletion rate is an important lever in achieving high quality crystals even when the application of ultrasound happens after crystallization.

Figure 3 presents the XRD of the films before and after ultrasound modification at ASU. The control samples that were not insonated are shown as A and B where the δ-phase $FAPbI_3$ is present at 2-theta = 11.6 for both. The in-situ samples treated with different insonation repetition show no δ-phase $FAPbI_3$ and only a strong 100 peak is present. Further studies on peak shifting and dislocations among the in situ and ex-situ samples are under way.

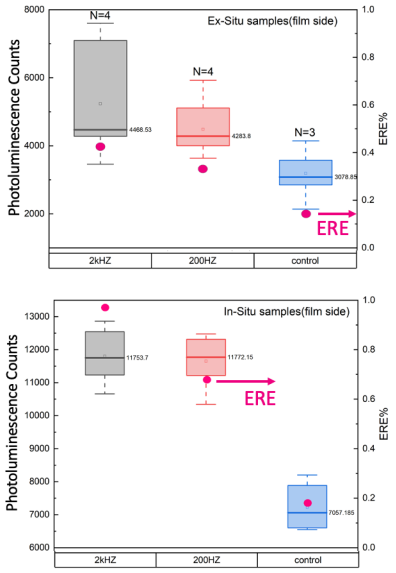

Figure 2: External Radiative Efficiency (ERE) and PL intensities for acoustic modification at different repetition rates in-situ and ex-situ.

The team at ASU has also focused on building the ultrasound platform and develop the fundamental understanding of how ultrasound interacts with the material. For example, in Figure 4 we show the time signal for a transmission measurement with a sender transducer and a receiver transducer sandwiching the specimens. The one layer sample is pure glass, and the two layer sample is glass plus film. The delay strongly depends on the layer's material properties and thicknesses.

The mean longitudinal velocities can be then calculated based on the time-of-flight of the peaks of each echo. We identified what seems an increase in mean longitudinal wave speed, but further reduction of the noise is needed to conclude on the evolution of the overall stiffness of the films.

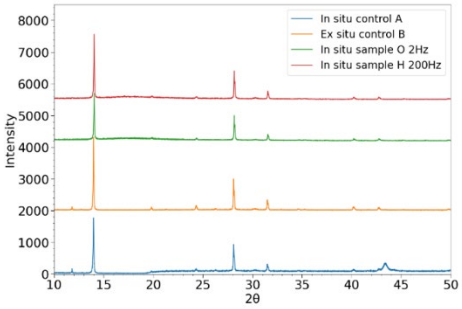

Figure 3: XRD characterization of the control $FAPbI_3$ films and the films modified with ultrasound.

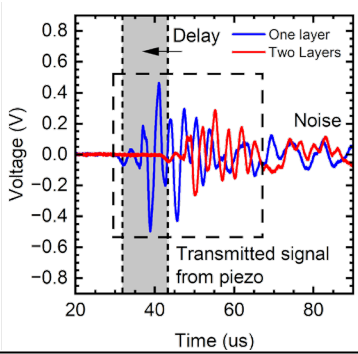

Figure 4: Measured ultrasonic signal throughout one layer (glass) and two layers (glass + perovskite solid film).

The Alem group have explored imaging techniques, i.e. Dark-field TEM (DFTEM) that allows us to reveal highly dense planar defects. To explore the damage mechanism and understand the role of the electron beam and the dose rate, we have recorded a series of TEM images a under continuous beam irradiation (Fig. 5). Massive holes appear at the intragranular planar defects and expand drastically as soon as the beam is exposed to the

$FAPbI_3$. In the first scan (Dose = 3.2 e/Å^2) the undamaged structure shows plenty of intragranular planar defects while in the second scan (Dose = 6.4 e/Å^2) cavities induced by electron beam occupies the defects rapidly. After extended irradiation, cavities evolve into aligned holes at defective region, leaving non-defective region less damaged. Our electron diffraction studies also confirm $FAPbI_3$ as defective polycrystalline, with discontinuous rings and extra streaks. DF-TEM imaging has also been acquired as a tool to investigate the defect structure, twins, stacking faults, or dislocations, in the films (Figs. 6 and 7)

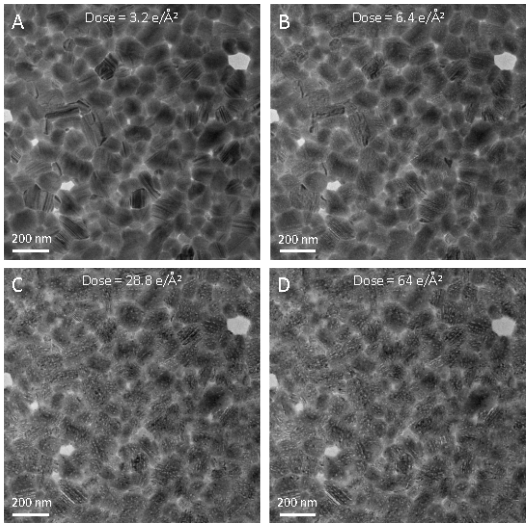

Figure 5: Damage mechanism of $FAPbI_3$ *under electron beam. (A-D)* A series of *TEM images* under continuous beam irradiation. Total electron dose is marked on the top of each figure.

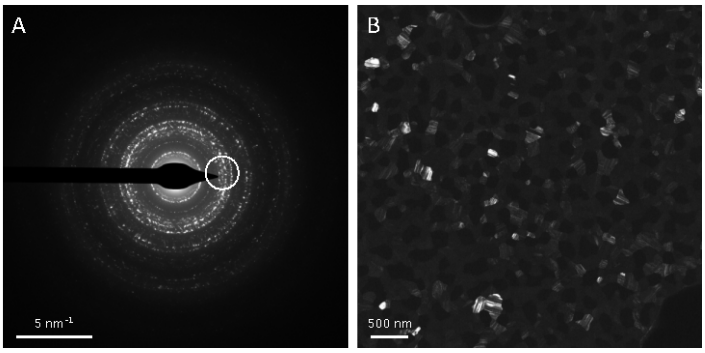

Figure 6: (A) Selected-area electron diffraction pattern of polycrystalline $FAPbI_3$. (B) Dark-field TEM by selecting diffraction spots in the white circle in Figure 2A.

Figure 7: Dark field TEM image of a dislocation array in an organic perovskite film. Low dose condition is applied. (Alem group, Unpublished)

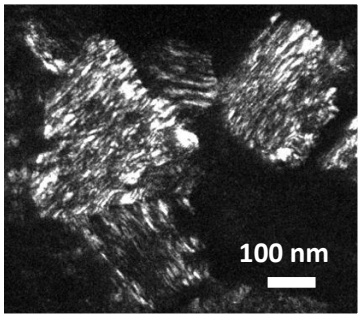

Future Plans

We plan to finalize tuning the ultrasonic setup and complete a first round of investigations on $FAPbI_3$ which include analysis of nanodiffraction data recently collected, and passivation of the top surface to eliminate the effect of surface recombination in the ERE. We also plan to perform GIWAXS during the summer to have a complete picture of the structural changes that the films are undergoing.

We will also continue to study the effect of adding acetate in the perovskite formulation and its effects on retarding the perovskite formation. First, we will continue to study the addition of formamidinium acetate precursor into the perovskite ink and analyze the effect of it in the perovskite film formation. We will also investigate the effect of adding lead acetate and compare

with the effect of formamidinium acetate modification. Then, after we formulate a set of acetate concentrations and know the basic characteristics of these modified films, we will investigate the effect of ultrasound in these amorphous perovskite films.
We will continue to improve the perovskite film deposition in TEM grids, for the study of the electron beam exposure effect on the perovskite. For this we will need to investigate the optimal concentration of the perovskite ink and the spin coating parameters. We need to optimize it in order to deposit a film on the TEM grid that is comparable, in terms of morphology and optoelectronic properties, to the ones deposited on glass and ITO substrates. Furthermore, we plan to track the progression of the nucleation mechanism induced by the ultrasound effects using in-situ photoluminescence microscopy, Raman spectroscopy, fast speed resistance measurements and supported as needed by in situ GIWAXS.
We plan to explore the pristine and transformed structure of the sample as a function of electron dose. For this step we will use low dose imaging techniques.
As indicated in the research progress, using dark field S/TEM imaging techniques, we will uncover the structure of the defects within the structure before and after the sample is treated with ultrasonic waves. At the moment we are in the process of developing machine learning algorithms to quantify the defect density in the acquired images. We will use these algorithms to qualify the defects to further assess the structure of the defects as a function of external trigger.
Finally, using electron energy loss spectroscopy (EELS), we will investigate the bonding and its evolution in the sample before and after ultrasonic treatment. In addition, EELS will be used to investigate the damage mechanism in the sample under the electron beam.

References

[1] Eperon, G. E.; Stranks, S. D.; Menelaou ,C.; Johnston, M. B.; Herz, L. M.; Snaith, H. J. Formamidinium Lead Trihalide: A Broadly Tunable Perovskite for Efficient Planar Heterojunction Solar Cells. *Energy Environ. Sci., 2014, 7, 982.* DOI: 10.1039/c3ee43822h

Publications

Y. Zhang, A. Bisht, S. Bachu, F. Rezaei, K. X. Vences, K. Kaushal, S. P. Dunfield, S. V. Gayathri Ayyagari, M. I. Bertoni, D. P. Fenning, N. Alem, *Damage Mechanism and Defect Evolution of Hybrid Perovskite FAPbI3 Under a Variable Dose Electron Beam,* Submitted to the microscopy and microanalysis proceedings. (2023)

Targeted Single Crystal Growth of Lanthanide Intermetallic Compounds Through Data Driven Synthesis and In-situ X-ray Diffraction

Julia Y Chan: Baylor University, Waco, TX 76798

Keywords: Targeted Synthesis, Intermetallic compounds, In-situ Synthesis and Diffraction

Research Scope

The proposal seeks to investigate the synthetic process of a new class of highly correlated intermetallic compounds $Ce_{n+1}Co_nGe_{3n+1}$ (n = 1 – 6). This family of compounds is attractive as members of the series consist of subunits found in quantum materials. With our efforts to grow single crystals, we will address the fundamental questions of 1) how do crystals that are built from subunits form during crystallization and 2) what determines how these subunits arrange**.** By understanding the assembly of subunits, strategies to affect process could emerge, which will ultimately lead to controlled heterostructural stacking of various subunits in the growth of bulk materials.

Our aim to answer the hypotheses of the growth processes of novel quantum materials will impact the synthesis and crystal growth intermetallics. We will perform (1) thermal analysis (DSC-TGA) to determine thermodynamic properties for each batch (2) in-situ synchrotron and neutron synthesis and structural characterization.

Recent Progress

Our research has exemplified the utility of heuristic methods such as tolerance factors to predict the stability of intermetallics. As a first stepping stone we have focused on the $Yb_3Rh_4Sn_{13}$- and $(Sn_{1-x}Er_x)Er_4Rh_6Sn_{18}$- structure types, part of the Remeika phases.[1] Intermetallics with the $Yb_3Rh_4Sn_{13}$ structure type consist of compounds with a stoichiometry of $A_3M_4X_{13}$ (A = alkali metals, Sc, Y, lanthanides, and actinides; M = transition metals from groups 8-10; and X = Si, Ge, In, Sn, and Pb). The $Yb_3Rh_4Sn_{13}$ structure type, also referred to as quasi-skutterudite, consists of a three-dimensional array of corner-sharing trigonal prism where the formed cuboctahedral and icosahedral cavities are filled by an electropositive and p-block elements, respectively (Figure 1). The $(Sn_{1-x}Er_x)Er_4Rh_6Sn_{18}$ structure type consists of similar structural motifs as shown in Figure 1 with a slight rearrangement of the

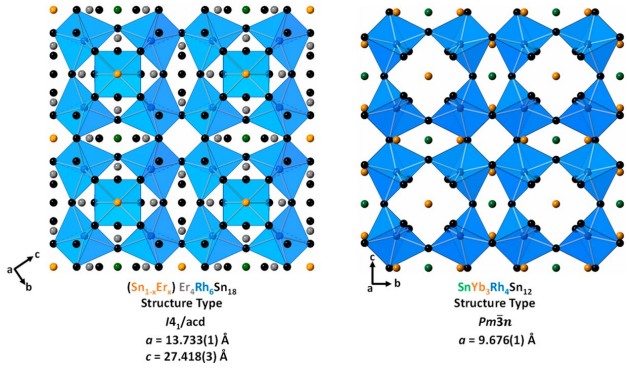

Figure 1. Structural comparison between the $(Sn_{1-x}Er_x)Er_4Rh_6Sn_{18}$ (left) and $Yb_3Rh_4Sn_{13}$ (right) structure types. The $(Sn_{1-x}Er_x)Er_4Rh_6Sn_{18}$ unit cell is partially shown to easy the comparison between both structures.

transition metal filled trigonal prisms. Figure 2 depicts the stability regions for the $Yb_3Rh_4Sn_{13}$- and $(Sn_{1-x}Er_x)Er_4Rh_6Sn_{18}$- structure types. The tolerance factor only requires the radii of the constituent elements. We have demonstrated the feasibility by synthesizing the predicted compound $Yb_5Ru_6Sn_{18}$ and provide insight to the property-structure relationship, where we have highlighted the correlation between valence fluctuation and tolerance factor value for the Ce and Yb analogues. For instance, both $Yb_3Ru_4Sn_{13}$ and $Yb_5Ru_6Sn_{18}$ are predicted to be stable depending on whether the Yb^{2+} or Yb^{3+} character is dominant, respectively.

To expand upon previous work using Ce, we have investigated the Pr analogue of the $Ln_{n+1}Co_nGe_{3n+1}$ (n = 1 – 5, ∞) homologous series, as our primary platform for in-situ synthesis. The $Pr_{n+1}Co_nGe_{3n+1}$ series are a family of systematically changing structures that, based on preliminary work, cannot be easily distinguished by changes in reactant composition. Instead, minor changes in the synthetic temperature profile and Sn flux concentration are critical in distinguishing the members.[2]

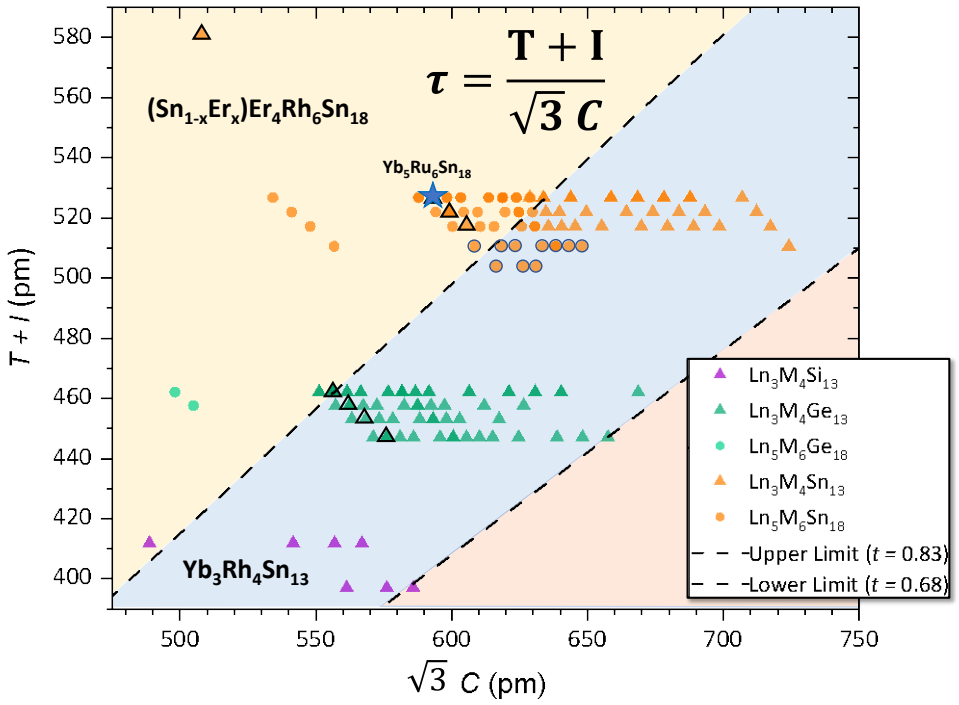

Figure 2. Graph of the calculated $T + I$ as a function of the calculated C for all of the reported $Yb_3Rh_4Sn_{13}$ (triangles) and $(Sn_{1-x}Er_x)Er_4Rh_6Sn_{18}$ (circles) structures and their respective hettotypes. The dotted lines correspond to the boundaries of stability regions, with t values of 0.83 and 0.68. Moving from the top left to the bottom right, the domain corresponds to $(Sn_{1-x}Er_x)Er_4Rh_6Sn_{18}$, $Yb_3Rh_4Sn_{13}$, and unsynthesized, respectively. The symbols are color-coded based on distinct X elements: purple for Si, green for Ge, and orange for Sn. The intensity of these colors is related to the overlap of the data points. The delimited triangles correspond to Yb and U analogues, capable of valence fluctuation, while those in concentered circles correspond to the A-(Fe, Os)-Sn family.

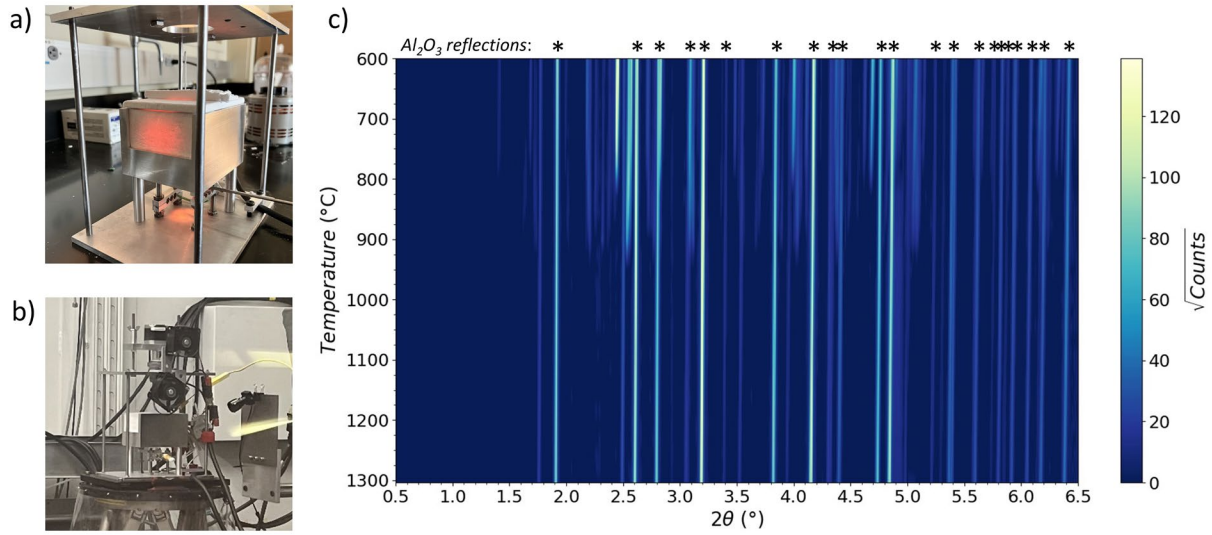

Figure 3. a) New high temperature in-situ furnace at temperatures more than 1200 °C. b) An in-situ flux growth experiment of Pr-Co-Ge-Sn performed at 11-ID-C with results (c) confirming temperatures of approximately 1300 °C using alumina as an internal standard. Data shown was collected at $\lambda = 0.1147$ Å.

Improving upon our previous in-situ furnace for flux growth synthesis,[3] we have developed a new model using silicon carbide heating elements and alumina insulation, while retaining the motorized vertical sample orientation favorable for liquid samples (Figure 3a, b). Additionally, the use of alumina capillaries allows for a low cost, inert sample environment that can be epoxy sealed under inert atmosphere. This choice allows for (1) an internal standard consistent across experiments and (2) creates an inert environment analogous to bulk flux growth synthesis that is not compromised during the experiment. Initial testing of the high temperature furnace was successful with the furnace easily achieving temperatures of 1300 °C, as illustrated in Figure 3c, and with temperatures as hot as 1450 °C in miscellaneous testing. This furnace marks a significant milestone in the flux growth community, providing an easy-to-use format with samples that can be prepared in the home lab for optimum experimental control. Work is ongoing to characterize experiments performed at the 11- ID-C beamline at the Advanced Photon Source of Argonne National Laboratory using Sn flux as a medium to grow praseodymium cobalt germanides.

In the meantime, synthesis studies aimed at improving the growth of $Pr_{n+1}Co_nGe_{3n+1}$ have led to the growth of two polymorphs of $Pr_2Co_3Ge_5$,[4,5] and subsequently the identification of a high temperature phase transformation associated with a shift in Pr valence from Pr^{3+} in the high temperature orthorhombic polymorph of $Pr_2Co_3Ge_5$ to a dominantly Pr^{4+} state in the room temperature monoclinic polymorph (see Figure 4). A highlight of this work is that a valence state this near to Pr^{4+} has not previously been observed in an intermetallic compound, making *m*-$Pr_2Co_3Ge_5$ a particularly unique example for studies concerning the itinerancy of 4*f* electrons.

Future Plans

Our group seeks to predict and synthesize new quantum materials by dictating the geometrical and electronic factors as a strategic first step. We foresee understanding both the electronic and structural factors of intermetallic compounds can lead to not only predict new phases but search for those in the verge of instability, which could lead to emergent states. We have recently synthesized another predicted compound, $Zr_5Ru_6Sn_{18}$. Current work focuses on solving single crystal X-ray data and measuring properties for both the Yb and Zr analogues. In combination with in-situ flux growth synthesis, made possible by our new high-temperature furnace, we now have a platform to target structure types of particular interest and employ an optimal synthetic method. In combination with future work using differential scanning calorimetry, we will employ an approach using multiple analytical methods to predict and optimize the crystal growth of Remeika phases.

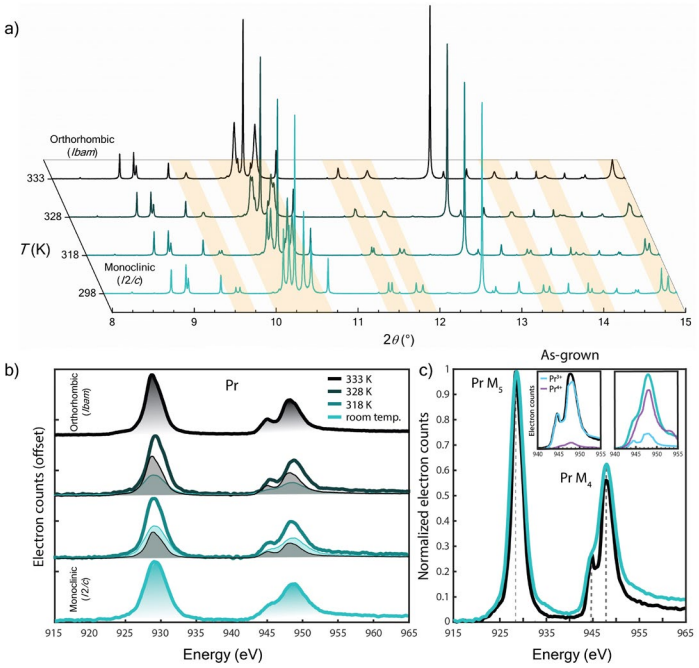

Figure 4. Temperature dependent powder X-ray diffraction (a) of *m*-$Pr_2Co_3Ge_5$ performed at 11-BM illustrating a structural phase transformation in tandem with (b) a valence changes in Pr determined by electron energy-loss spectroscopy at the Molecular Foundry. The shift in Pr valence corresponds well with that observed from room temperature measurements (c) on *m*-$Pr_2Co_3Ge_5$ and *o*-$Pr_2Co_3Ge_5$.

Improving control over reaction products through in-situ synthesis will shed light towards the mechanism of crystal growth and tuning of microstructural changes. The infrastructure developed here will generate a feedback loop between prediction and in-situ synthesis, creating a model that can be extended to other families of quantum materials driving the discovery of technologically relevant intermetallic compounds towards a "materials by design" approach.

References

1. Dominguez Montero, A.; McCandless, G. T.; Oladehin, O.; Baumbach, R. E.; Chan, J. Y., *Development of a Geometric Descriptor for the Strategic Synthesis of Remeika Phases,* Chem. Mater. **35**, 2238-2247 (2023).
2. Kyrk, T. M.; Bravo, M.; McCandless, G. T.; Lapidus, S. H.; Chan, J. Y., *Investigating the $A_{n+1}B_nX_{3n+1}$ Homologous Series: A New Platform for Studying Magnetic Praseodymium Based Intermetallics,* ACS Omega **7**, 19048-19057 (2022).
3. Weiland, A.; Frith, M. G.; Lapidus, S. H.; Chan, J. Y., *In Situ Methods for Metal-Flux Synthesis in Inert Environments,* Chem. Mater. **33**, 7657-7664 (2021).

4. Kyrk, T. M.; Scheifers, J. P.; Thanabalasingam, K.; McCandless, G. T.; Young, D. P.; Chan, J. Y., *It Runs in the $BaAl_4$ Family: Relating the Structure and Properties of Middle Child $Ln_2Co_3Ge_5$ (Ln = Pr, Nd, and Sm) to its Siblings $LnCo_2Ge_2$ and $LnCoGe_3$,* lnorg. Chem. **60**, 15343-15350 (2021).
5. Kyrk, T. M.; Galeano-Cabral, J.; Kennedy, E. R.; Wei, K.; McCandless, G. T.; Scott, M. C.; Baumbach, R. E.; Chan, J. Y., *Anisotropic Magnetic and Transport Properties of Orthorhombic o-$Pr_2Co_3Ge_5$,* J. Phys. Mater. **5**, 044007 (2022).

Publications

1. Kyrk, T. M.; Bravo, M.; McCandless, G. T.; Lapidus, S. H.; Chan, J. Y., *Investigating the $A_{n+1}B_nX_{3n+1}$ Homologous Series: A New Platform for Studying Magnetic Praseodymium Based Intermetallics,* ACS Omega **7**, 19048-19057 (2022).
2. Kyrk, T. M.; Galeano-Cabral, J.; Kennedy, E. R.; Wei, K.; McCandless, G. T.; Scott, M. C.; Baumbach, R. E.; Chan, J. Y., *Anisotropic Magnetic and Transport Properties of Orthorhombic o-$Pr_2Co_3Ge_5$,* J. Phys. Mater. **5**, 044007 (2022).
3. Dominguez Montero, A.; McCandless, G. T.; Oladehin, O.; Baumbach, R. E.; Chan, J. Y., *Development of a Geometric Descriptor for the Strategic Synthesis of Remeika Phases,* Chem. Mater. **35**, 2238-2247 (2023).
4. Wang, Y.; Wu, H.; McCandless, G.T.; Chan, J.Y.; Ali, M.N., *Quantum Sates and Intertwining Phases in Kagome Materials*, Nat. Rev. Phy. **Re-submitted**, (2023) https://arxiv.org/abs/2303.03359
5. Kennedy, E.; Kyrk, T.M.; McCandless, G.T.; Ophus, C.; Chan, J.Y.; Scott, M.C., *Variations in EELS Fine Structure Along $Sm_2Co_3Ge_5$ Grain Boundaries*, **Submitted** (2023)
6. Kyrk, T.M.; Kennedy, E.; McCandless, G.T.; Baumbach, R.E.; Scott, M.C.; Chan, J.Y., *Structural Phase Transformation Induced Pr Valence Instability in Intermetallic m-$Pr_2Co_3Ge_5$*, **In Preparation** (2023)w

Understanding Flash Sintering for Highly Conductive High Temperature Ceramics

Zhe Cheng, Andriy Durygin, Vadym Drozd - Florida International University (FIU)
Keywords: High temperature ceramics, Flash sintering, Conductive ceramics, Synchrotron, *In situ* characterization

Research Scope

In the past decade or so, many studies have been carried out on flash sintering (FS) of various oxides such as Y_2O_3-stabilized ZrO_2 (YSZ), ZnO, and others. To carry out flash sintering, electrical current is forced through the sample, which leads to Joule heating. For oxides like YSZ that show a rapid (often "exponential") increase in conductivity when temperature rises, Joule heating causes the sample resistance to drop. As a result, under the applied (often constant) voltage, reduced resistance causes current and heating to increase further, producing additional drop in sample resistance. The process becomes self-accelerating, which eventually leads to the *flash* or the drastic increase in current and power dissipation and rapid densification of ceramics within minutes or even seconds [1].

On the other hand, for highly conductive high temperature ceramics (HTC), their *bulk* conductivity behaves differently: it would *decrease* with increasing temperature, which, in principle, would *work against* the principle for flash sintering. Yet, flash sintering has been demonstrated for several highly conductivity HTC materials such as ZrN and WC, and the underlying mechanism is *not* clear.

The central objectives of this project are to ***investigate the fundamental mechanism for flash sintering of highly conductive high-temperature ceramic (HTC) materials using materials such as zirconium nitride (ZrN) as examples and reveal the interrelationships between those materials' microstructure, defect and surface characteristics, transport properties, and their behaviors in flash sintering***. The scope of the project will include (i) systematically characterizing the flash sintering behaviors for highly conductive HTC materials s ZrN, (ii) revealing the origin for the observed flash sintering phenomena for these materials, and (iii) establishing the relationships between defects, materials transport properties (e.g., electrical conductivity), and observed flash sintering behaviors.

Recent Progress

In the past two years since the project's start in Aug 2021, progress has been made in the several areas, as briefly outlined below.

- Characterization of ZrN flash sintering behavior

The flash sintering behavior for ZrN powder has been systematically studied with the aim to characterize the influence of various processing parameters including electrical field (or voltage), voltage ramp rate (constant voltage versus different linear ramp rates), external mechanical pressure, post-flash holding time, powder milling, choice of electrode material, and sample history. Using commercial ZrN powder, it was found that voltage (or electrical field) had a non-linear effect on triggering the flash event, meaning flash only occurred when the applied voltage exceeded a certain critical value (e.g., ~5 V or 20 V/cm in the current setup for ZrN, see Figure 1(a)), while the voltage ramp rate did *not* significantly impact the onset of the flash event (see Figure 1(b)). Higher mechanical pressure lowered the critical voltage (see Figure 1(c)), but also made the flash, the sudden drop in resistance, less dramatic or abrupt (see Figure 1(d)). In terms of post-flash holding time, as expected, longer holding improved densification and sample

mechanical properties (e.g., hardness, see Figure 1(e)). Mechanical milling of the commercial ZrN powder facilitated flash sintering, leading to higher maximum current (see Figure 1(f)) and lower

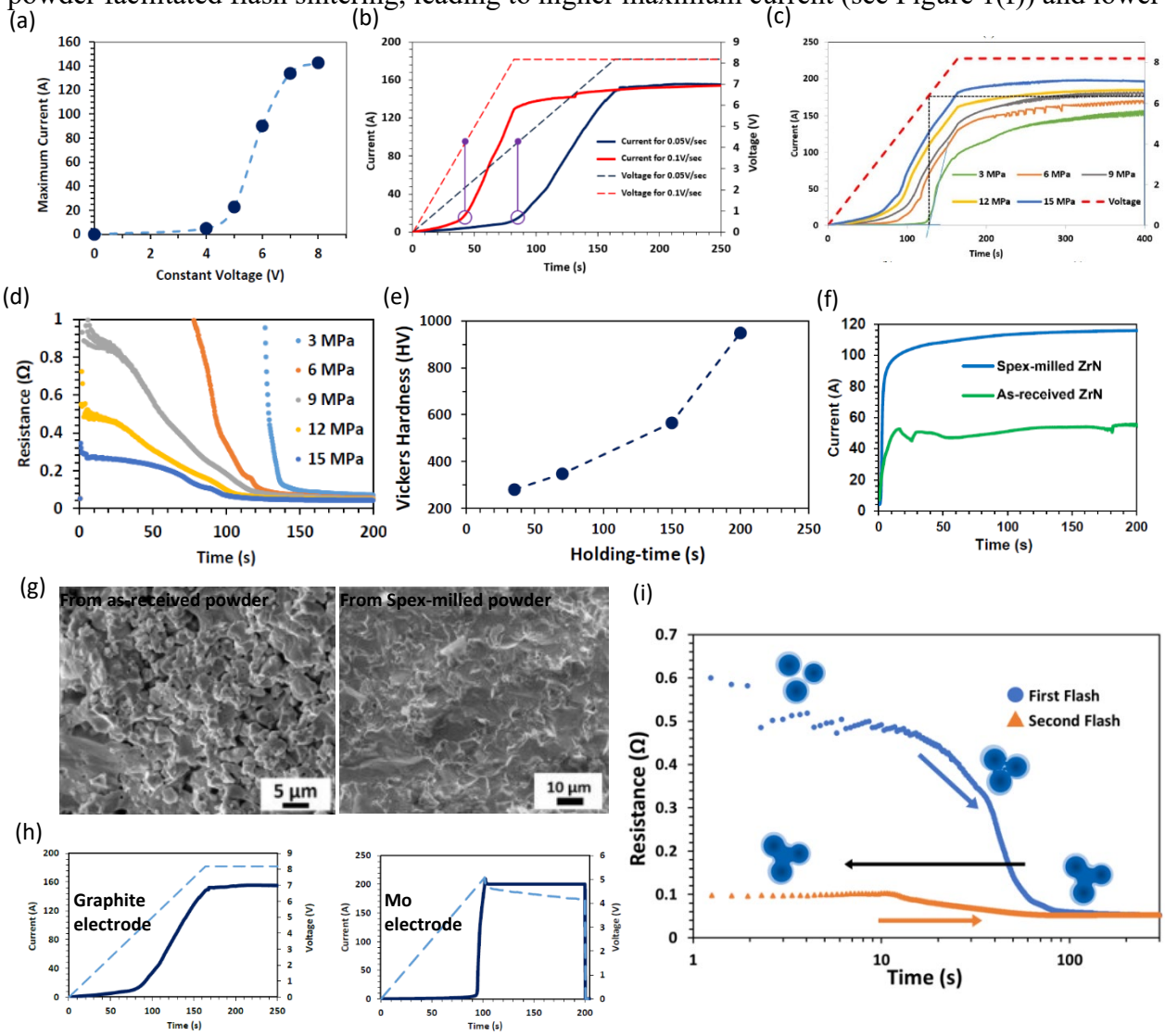

Figure 1 Plots showing the influence of various processing parameters on the flash sintering behavior for a highly conductive high temperature ceramics of ZrN: (a) influence of applied constant voltage; (b) influence of voltage ramp rate of 0.1 V/s vs. 0.05 V/sec; (c and d) influence of mechanical pressure on current (c) and resistance (d) during flash sintering; (e) influence of post-flash holding time on sample Vickers hardness; (f) influence of powder Spex milling on flash behavior (under the same constant voltage); (g) SEM images showing microstructure of flash sintered ZrN using either as-received commercial powder (left) or Spex-milled powder (right); (h) influence of electrode material (left: graphite; right: molybdenum); (i) influence of repeat application of electrical field.

porosity (see Figure 1(g)). Even electrode choice influenced the observed flash behavior, with the flash more dramatic when using molybdenum (Mo) electrodes instead of graphite electrodes (see Figure 1(h)). Finally, there did *not* appear to be an obvious second flash when the same voltage (or field) was applied again to the same ZrN sample that had been flash sintered in a first cycle (see Figure 1(i)): the current vs. time response in the *second* cycle was same as that for two graphite electrodes directly touching each other without ZrN powder compact between the two electrodes.

The observed flash sintering behavior for ZrN suggests that it shares similarity as well as difference from conventional oxides such as YSZ. The mechanism for flash sintering of highly conductive HTC like ZrN is likely due to improved contacts and breakage/breakdown of the oxide shell over ZrN surfaces, which lead to significantly reduced *effective* resistivity upon heating/compaction. Future modeling and experiments are needed to distinguish the contributions by particle packing from oxide shell breakdown.

- Use of *in situ* synchrotron for real time study of (reaction) flash sintering behavior

Apart from systematically characterizing the flash sintering behaviors for highly conductive HTC like ZrN, to gain deeper understanding about the process, preliminary *in situ* synchrotron experiments had been carried out at the Advanced Photon Source (APS) of the Argonne National Lab (ANL) to characterize the changes in real time *during* flash sintering. In particular, reaction flash sintering (RFS) had been carried out for two related systems: one is TiN-ZrN with both phases highly conductive, and the other is TiN-AlN with TiN highly conductive but AlN insulating. Figure 2(a) and (b) show the plots of voltage and power versus time for the systems of TiN-ZrN and TiN-AlN, respectively, both starting as a two-phase mixture. The voltage was ramped up from zero at 0.1 V/s, while the pressure was kept constant at 15 MPa. For the TiN-ZrN equimolar mixture, the flash was gradual. In comparison, for the TiN-AlN mixture with TiN conductive but AlN insulating, the flash was delayed, but much more abrupt and dramatic.

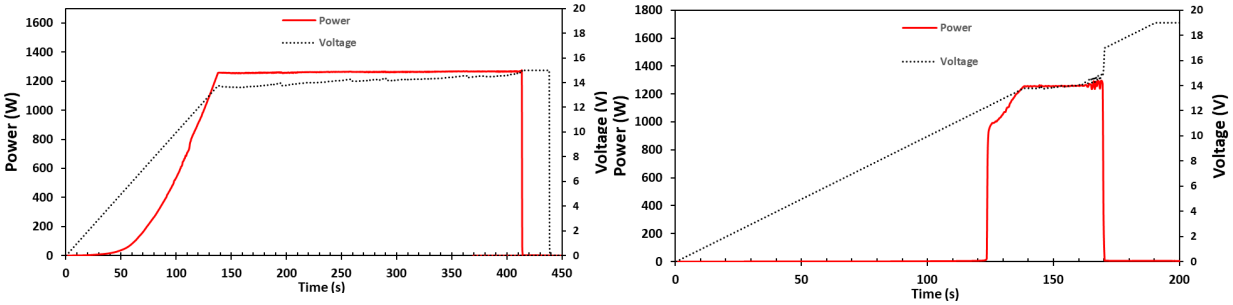

Figure 2 Plots of voltage and power versus time for the *in situ* synchrotron RFS experiment for equimolar mixtures of (a) TiN-ZrN and (b) TiN-AlN. Note that in both cases, the voltage was linearly ramped up from 0 V at a rate of 0.1 V/s with applied constant pressure of 15 MPa. For (a) TiN-ZrN system, the power spiked up non-linearly from ~40 s, reaching the max power of ~1.2 kW (max current of 90 A), and then stabilized. For (b) the power displayed the *incubation* before ~123 s, the *flash* at ~123-125 s, and the *post-flash steady state* after ~125 s, also reaching a max power of ~1.3 kW. Later at ~170 s, electrodes failed and power/current dropped to zero.

Figure 3 gives an example of the results from an *in situ* synchrotron RFS experiment for the TiN-ZrN system. It includes 2D X-ray scans before and after the experiment showing the shrinkage of the sample (Figure 3(a and b)), changes in lattice parameter for various phases (Figure 3(c)), as well as selected diffraction patterns capturing the gradual formation of (Ti, Zr)N single-phase solid solution from the starting TiN and ZrN phases in the RFS process (Figure 3(d and e)). Although many questions still remain, the *in situ* synchrotron experiment provided greater details about RFS that had been unavailable or elusive in conventional *ex situ* studies.

Future Plans

Future planned work for this project include: (i) systematic characterization of the flash sintering behavior for the another highly conductive HTC material of ZrB_2; (ii) simulation (e.g., by COMSOL) and detailed material electrical property and microstructure characterizations to understand the effects of materials intrinsic conductivity, powder packing/porosity/particle contact area, as well as surface oxide shells on the flash sintering behaviors; (iii) combination of theoretical

calculation (e.g., by DFT) and advanced characterization (e.g., by synchrotron) to understand changes in defects and atoms diffusion/migration during the (reaction) flash sintering process.

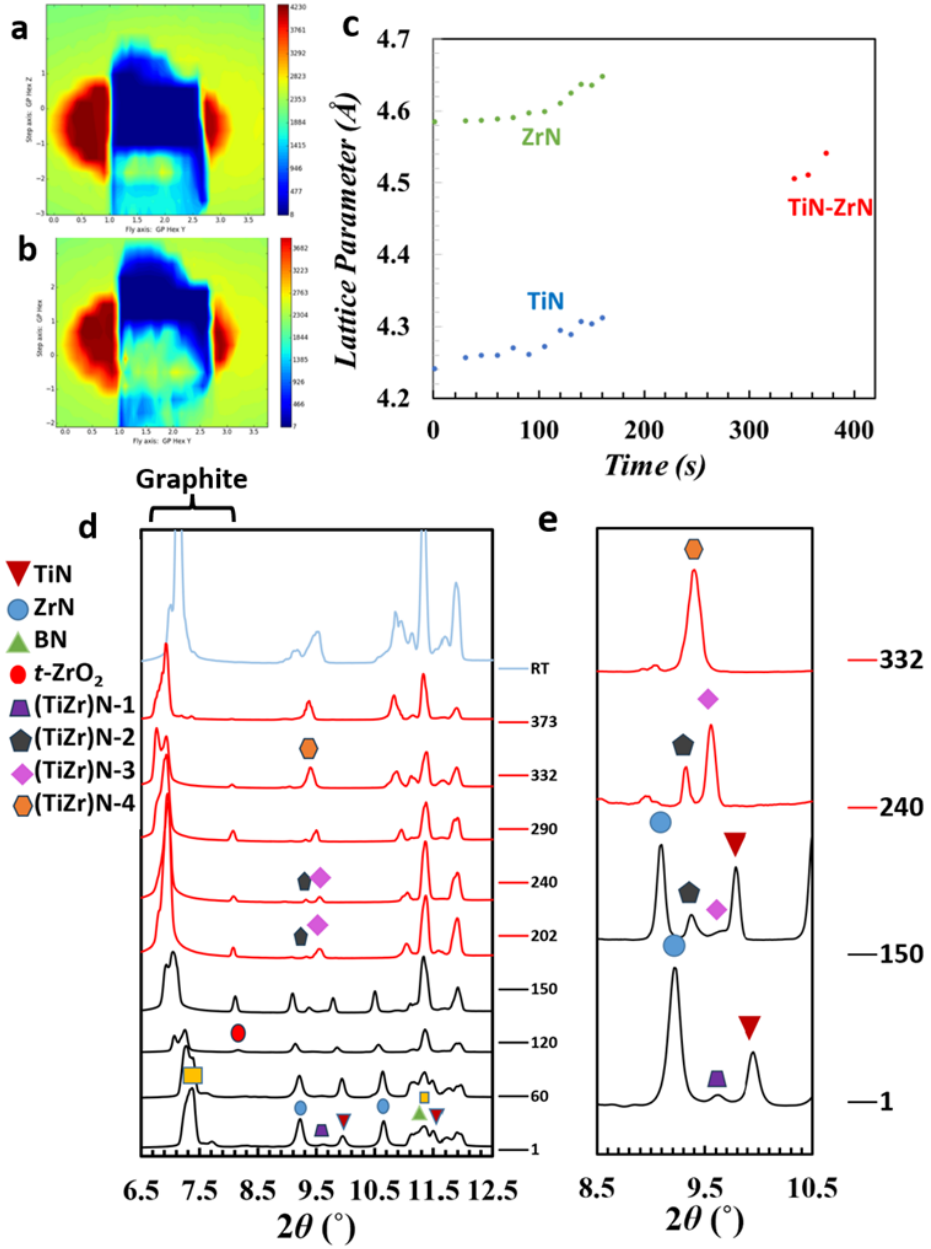

Figure 3 (a and b) 2D X-ray scans of the reaction flash sintering cell (RFS) assembly loaded with TiN-ZrN equimolar powder mixture before (a) and after (b) RFS. (c) Change in lattice parameter of parent TiN and ZrN as well as (Ti, Zr)N product with time during RFS. (d) Selected integrated 1D *in situ* synchrotron XRD patterns of the TiN-ZrN mixture during RFS at different time (in seconds) after the beginning of the experiment. (TiZr)N-1 represents the solid solution formed in Spex milling; (TiZr)N-2 and (TiZr)N-3 correspond to solid solutions formed during the heating stage of the RFS; (TiZr)N-4 corresponds to the final single-phase nitride solid solution formed after RFS. (e) Zoomed-in section for selected XRD patterns at different time showing gradual changes in the (111) peak for TiN, ZrN, and related (Ti, Zr)N solid solution in the 2θ range of 8.5-10.5º. Note the gradual disappearance of individual TiN and ZrN peaks and the appearance of peaks for (Ti, Zr)N solid solutions.

References

1. M. Cologna, B. Rashkova, R. Raj, "Flash sintering of nanograin zirconia in <5 s at 850°C," *Journal of American Ceramic Society*, **93** 3556–3559 (2010). https://doi.org/10.1111/j.1551-2916.2010.04089.x

Publications

1. Suprabha Das, Diego Dubois, Md Shariful Islam Sozal, Yusuf Emirov, Borzooye Jafarizadeh, Chunlei Wang, Vadym Drozd, Andriy Durygin, Zhe Cheng, "Synthesis and flash sintering of zirconium nitride powder," *Journal of the American Ceramic Society*, **105** (6), 3925-3936 (2022). https://doi.org/10.1111/jace.18421
2. Amirali Eskandariyun, Suprabha Das, Diego Dubois, Andriy Durygin, Vadym Drozd, Zhe Cheng. "Effects of processing conditions on flash sintering of commercial ZrN," manuscript written, to be submitted soon.
3. Suprabha Das, Andriy Durygin, Vadym Drozd, Md Shariful Islam Sozal, Zhe Cheng. "Reaction Flash Sintering of TiZrN and TiAlN Ternary Metal Nitrides", manuscript written, to be submitted soon.

In-situ Visualization of Microstructure Evolution in Metallic Alloys under Additive Manufacturing Conditions

A.J. Clarke, Colorado School of Mines (Principal Investigator)

A. Karma, Northeastern University (Co-Principal Investigator)

Keywords: Rapid solidification, phase-field modeling, additive manufacturing, in-situ characterization, absolute stability

Research Scope

There are many potential benefits to using additive manufacturing (AM) - also known as three-dimensional (3D) printing - for making metal parts, rather than conventional manufacturing processes. AM is highly customizable, can produce complex structures, and can economically produce low numbers of metal components. To achieve the strict specifications needed for some applications, the microscopic structure of printed metal objects must be controlled. However, 3D printing is still in its infancy. There is also a need for new approaches that combine AM with other processing methods to provide flexible architectural control over a wide range of length scales, from the nanoscale to the macroscale, of AM builds. Here we seek to enhance our understanding of structure-processing relationships under AM conditions through novel experiments performed in the laboratory and at U.S. DOE national user facilities and by modeling to visualize microstructural development.

Our aim is to gain new insights into the fundamental mechanisms of microstructure formation and grain texture evolution under far-from-equilibrium AM conditions by the development of experimentally validated, computational approaches that can reliably predict the microstructures of 3D printed metals. We are examining binary Al alloys in the high velocity range near the absolute stability limit that remains poorly understood and ternary Ni-Mo-Al alloy single crystals. We have developed a new, quantitative phase-field (PF) formulation for rapid solidification that quantitatively reproduces banded microstructures - a hallmark of microstructural pattern formation near the absolute stability - in metallic alloy thin-films. We are also using this model to investigate non-equilibrium effects on dendrite orientation transitions (DOTs) in binary Al alloys and the non-trivial dynamic coupling of microstructure and grain texture evolution near the absolute stability limit. Experimental validation utilizes not only thin-film sample geometries, but also bulk samples, and novel in-situ imaging of solidification dynamics by dynamic transmission electron microscopy (DTEM) and during simulated AM at the Advanced Photon Source (APS) at Argonne National Laboratory (ANL). Another aim is to unambiguously determine the genesis of grain refinement (e.g., by constitutional supercooling during solidification and/or by eutectoid formation during solid state thermal cycling) in Ti-Cu alloys designed for AM.

Recent Progress

New quantitative PF model of rapid alloy solidification and experimental validation: A major accomplishment during the present grant period was the development of a new PF formulation of rapid alloy solidification and its experimental validation (Ji et al., 2023). A distinguishing feature of this new model is that it quantitatively incorporates well-known non-equilibrium effects at the solid-liquid interface over a very wide range of interface velocities, V, for a computationally tractable interface thickness, W. In particular, the model quantitatively reproduces velocity (V)-

dependent forms of the partition coefficient $k(V)$ and liquidus slope $m(V)$ over a several orders of magnitude V-range that spans the moderate V regime, with near-equilibrium solute partitioning at the interface, all the way up to the high-V, far from equilibrium regime with complete solute trapping (Fig. 1). As a result, simulations of this model were able to reproduce banded microstructures, consisting of an alternation of microsegregation-patterned bands, i.e. bands with cellular/dendritic microstructures, and microsegregation-free bands, produced by rapid solidification for the first time. The modeling results also shed light on the mechanism of band formation by identifying a new dynamical instability of dendrite tip growth driven by solute trapping at velocities approaching the absolute stability limit. In addition, they revealed the importance of incorporating latent heat rejection at the interface to quantitatively predict measured band spacings in rapidly solidified Al-Cu thin-films.

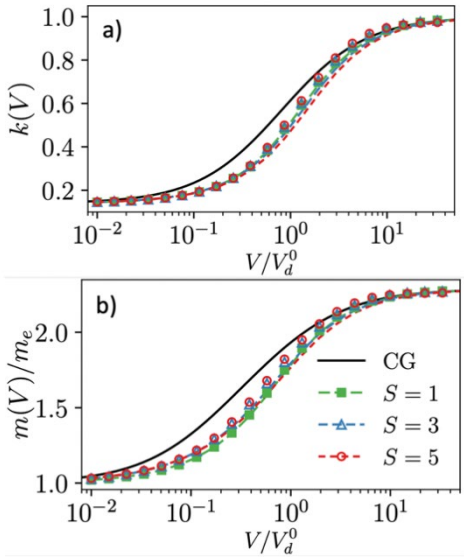

Fig. 1. Comparison of PF (symbols) and continuous growth (CG) model predictions of $k(V)$ and $m(V)$ curves for different ratios $S = W/W_0$ of PF-model interface thickness W and reference physical thickness $W_0 = 1$ nm. The curves are nearly independent of S, showing that solute trapping properties are quantitatively reproduced by this model for a computationally tractable interface thickness. Dashed lines are approximate semi-analytical solutions.

Fig. 2 shows a quantitative comparison of banded microstructures simulated with latent heat produced in a thin-film re-solidification experiment, where a short laser pulse was used to create an elliptical melt pool in an Al-9wt.% (Al-4at.%) Cu alloy. Based on DTEM measurements of interface velocity, the isotherm velocity was increased in the simulations linearly from 0.3 to 1.8 m/s over a time of 30 μs. As shown in Fig. 2, the resulting band spacing in the simulations (~ 400 nm) agrees remarkably well with the experiment. A peer-reviewed *Physics Review Letters* article has been published based upon this work (Ji et al., 2023).

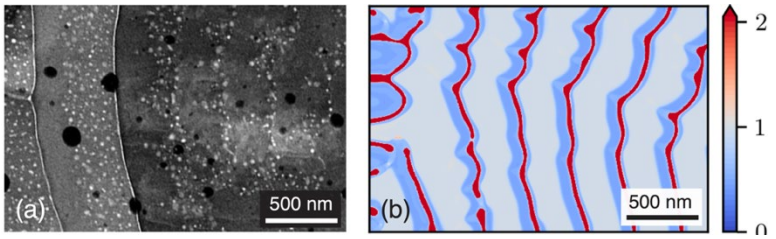

Fig. 2. Comparison of experimental (a) and simulated (b) banded microstructures for an Al-9wt.%Cu resolidified thin film where the concentration field normalized by the nominal alloy composition is shown in (b).

Microstructure development and absolute stability in ternary Ni-Mo-Al alloy single crystals: Ternary alloy single crystals with the chemistry Ni-22.2Mo-2.8Al (wt.%) were selected to study the absolute stability limit and validity of one of the most widely used models for rapid solidification found in the literature by Kurz, Giovanola, and Trivedi, i.e., the KGT model (Kurz et al., 1986). This model was utilized to determine the solidification modes that would correspond to different temperature gradients (G) and growth velocities (V) for the alloy studied. Thermophysical parameters for the alloy were assessed from thermodynamic equilibrium calculations (CALPHAD method). Values for parameters such as diffusivity and solid-liquid (S-

L) interfacial energy and kinetic coefficient of the interface were assumed based upon values available in the literature.

Approximately 200 µm-thick single crystal samples were prepared for directional solidification experiments during simulated AM, keeping the <100> direction along the sample thickness and either the <100> or <110> crystallographic direction perpendicular to the sample top surface. Samples were subjected to laser spot melting (1 ms dwell time) at powers ranging from 104 to 260 W at the APS Sector 32-ID-B at ANL (Fig. 3) and real-time synchrotron x-ray imaging was performed of the melt pool dynamics and solidification progression. Solidification velocities were directly obtained by measuring the propagation of the S-L interface between the images, fitting these data to an ellipse, and then using fitted functions to estimate the velocities in the direction parallel to the <100> crystal orientation. Velocities were found to increase from the bottom to the tops of the melt pools (e.g., see the results for 104 W for the <100> and <110> crystal orientations), and the KGT-predicted absolute stability limit was determined to be ~0.15 m/s.

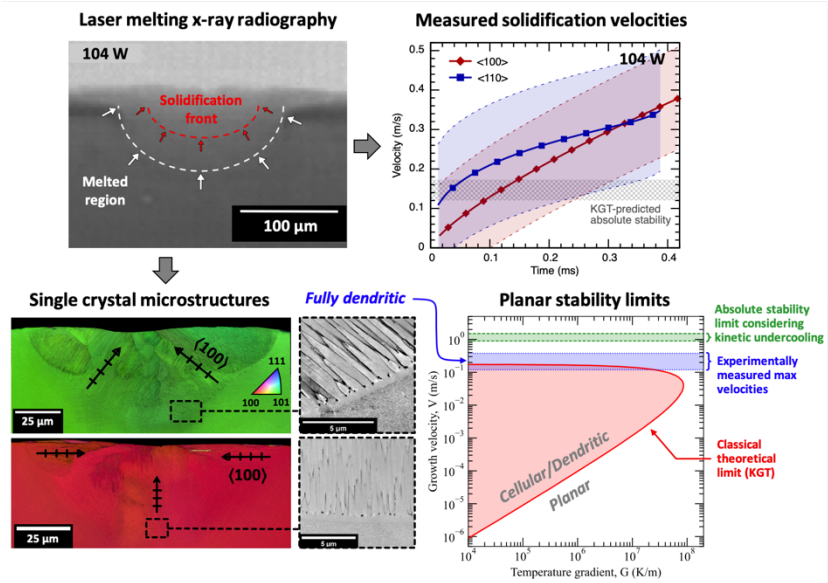

Fig. 3. Synchrotron x-ray radiography, highlighting the progression of the solid-liquid interface during simulated LPBF at the APS at ANL, measured solidification velocities for two Ni-Mo-Al ternary alloy single crystals from real-time imaging and the KGT-predicted absolute stability limit, ex-situ SEM and EBSD of APS melt pools, showing fully dendritic microstructures, and planar stability limit calculations compared to experiments, highlighting that further considerations like kinetic undercooling are needed to match absolute stability limit predictions to experimental outcomes.

An initial region of planar growth is seen at the bottom of the melt pools, followed by a transition to cellular and columnar dendritic patterns with increasing solidification velocity. Electron backscatter diffraction (EBSD) inverse pole figure (IPF) and image quality (IQ) maps (Fig. 3) reveal most of each melt pool has the same crystallographic orientation as the substrate, and the main growth direction of cells or dendrites (annotated with black) clearly correspond to <100> directions, as expected for dendrites, but not cells. No indication of re-stabilization of a planar interface at the melt pool tops was found, as predicted by the classical theoretical limit (KGT), proving that further theoretical developments (e.g., incorporation of kinetic undercooling) and accurate assessments of key thermophysical parameters are needed to fully elucidate the cause of these discrepancies to pave the way for the prediction and control of microstructure selection under rapid solidification conditions. A peer-reviewed journal article was recently published in *Acta Materialia* (Tourret et al., 2023).

Ti-Cu grain refinement under AM conditions: Constitutional supercooling has been reported to explain the observed microstructural refinement (Zhang et al., 2019) in Ti-Cu alloys produced by

AM. Zhang et al. proposed that columnar-to-equiaxed transition (CET) occurred in these alloys by the formation of a large zone of supercooled liquid ahead of the solid-liquid interface, producing equiaxed grains during solidification of the melt. But another plausible scenario for the creation of the fine-scale, equiaxed grains is their formation during solid state thermal cycling during AM of the initially martensitic or eutectoid (α-Ti + Ti_2Cu) microstructure (Clarke, 2019).

To explore if solid state thermal cycling could explain the previously observed microstructures attributed to solidification during AM, a series of controlled dilatometric heat treatments were employed to thermally cycle eutectoid Ti-Cu in the solid state. We demonstrated that thermal cycling of eutectoid Ti-Cu forms new β-Ti parent grains upon reheating, producing finer grains of eutectoid product upon cooling. The parent β-Ti grain size can successfully be reset by thermal cycling, meaning as-solidified microstructures produced by AM are likely *completely* removed. Given that thermal cycling occurs naturally during an AM build, refined microstructures in Ti-Cu can be guaranteed. Grain growth kinetics of the parent β-Ti phase were also assessed using ideal grain growth assumptions, where the grain growth slows considerably with increasing hold times above the eutectoid temperature. A peer-reviewed journal article is under review in *Additive Manufacturing*. Another peer-reviewed journal article on observed orientation relationships between the parent β-Ti phase and eutectoid or martensitic products was also published in *Materials Characterization*.

Future Plans

AM frequently results in the formation of complex microstructures during the solidification of structural alloys. While grain competition has been extensively investigated under slow growth rate conditions, the examination of grain texture selection during AM, where an alloy undergoes rapid solidification, is comparatively less explored. Moreover, although conventional solidification in cubic structures typically presents a <100> primary dendritic growth direction, several studies in various alloy systems have revealed that solute additions can modify the primary growth direction, producing the so-called dendrite orientation transition (DOT). Current and future work involves a combined experimental and computational study of grain texture selection during the rapid solidification of Al-Si thin-films subjected to laser melting and DTEM, allowing for real-time imaging and tracking of the solid-liquid interface. Complementary ex-situ microstructure characterization is also performed at the nanoscale to assess the crystallographic textures produced by solidification. To interpret the statistically significant results observed in the experiments, we employed a quantitative PF model of rapid binary alloy solidification that incorporates nonequilibrium effects at the solid-liquid interface. Our computational study elucidates the mechanism underlying the grain texture selection behavior and guides future similar studies of other binary alloys. Additional DOT experiments and modeling are also underway for Al-Ag and Al-Ge alloys, in addition to banding studies to confirm the prediction that absolute stability can be reached at moderate velocities less than a m/s in hypo-eutectic Al-Ag alloys.

References

1. K. Ji, E. Dorari, A.J. Clarke, A. Karma, "*Microstructural pattern formation during far-from-equilibrium alloy solidification*", Physical Review Letters, 2023, **130**:026203
2. W. Kurz, B. Giovanola, R. Trivedi, "*Theory of microstructural development during rapid solidification*", Acta Metallurgica, **34**:823-830, 1986
3. D. Tourret et al., "*Morphological stability of solid-liquid interfaces under additive manufacturing conditions*", Acta Materialia, 2023, **250**:118858

4. D. Zhang, D. Qiu, M.A. Gibson, Y. Zheng, H.L. Fraser, D.H. StJohn, M.A. Easton, "*Additive manufacturing of ultrafine-grained high strength titanium alloys*", Nature, **576**:91-95, 2019
5. A. Clarke, "Fine-grained metals from 3D printing", Nature, **576**:41-42, 2019

Publications

1. A.I. Saville, O.W. Hesmondhalgh, N.A. Compton, G.A. Thompson, M. Sanders, J. Klemm-Toole, K.D. Clarke, H.L. Fraser, M.J. Kaufman, A. Karma, A.J. Clarke, "*Mechanism of fine-grained Ti-Cu microstructures in additive manufacturing*", Additive Manufacturing, 2023, in review
2. D. Tourret, J. Klemm-Toole, A. Eres-Castellanos, B. Rodgers, G. Becker, A. Saville, B. Ellyson, C. Johnson, B. Milligan, J. Copley, R. Ochoa, A. Polonsky, K. Pusch, M. Haines, K. Fezzaa, T. Sun, K. Clarke, S. Babu, T. Pollock, A. Karma, A. Clarke, "*Morphological stability of solid-liquid interfaces under additive manufacturing conditions*", Acta Materialia, 2023, **250**:118858
3. K. Ji, E. Dorari, A.J. Clarke, A. Karma, "*Microstructural pattern formation during far-from-equilibrium alloy solidification*", Physical Review Letters, 2023, **130**:026203
4. A.I. Saville and A.J. Clarke, "*Reconstructing parent microstructures in martensitic and pearlitic Ti-Cu*", Materials Characterization, 2023, **196**:112569
5. A.J. Clarke, "*Unusual microstructures by 3D printing*", Nature Materials, 2022, **21**:1223-1224

In Situ Studies of Charge Transfer Phenomena in Complex Oxide Heterostructures

Ryan Comes, Auburn University, Department of Physics; Wencan Jin, Auburn University, Department of Physics

Keywords: Complex oxides, molecular beam epitaxy, iridates, X-ray spectroscopy, interfacial phenomena

Research Scope

Complex oxide thin films exhibit a wide range of unique phenomena that have been investigated for use in technologies ranging from renewable energy, data storage, and quantum information processing. Perovskite oxides with the formula ABO_3 represent a particularly interesting class of complex oxides because of the wide array of transition metal ions that can occupy the *B* site of the material. To date, most research has focused on 3*d* transition metals on the *B* site, such as cobalt. However, emerging work focused on 5d transition metal *B* site ions has shown that these materials exhibit stronger spin-orbit coupling and a wide array of correlated electronic phenomena. Many of these properties are modulated through charge transfer across epitaxial interfaces or between cations in ordered phases. In this EPSCOR-State/National Laboratory Partnership project, we are focused on the use of *in situ* techniques to examine the role of charge transfer processes in epitaxial oxide superlattices and ordered double perovskite thin films. Partners include Argonne National Laboratory, Brookhaven National Laboratory, and Pacific Northwest National Laboratory.

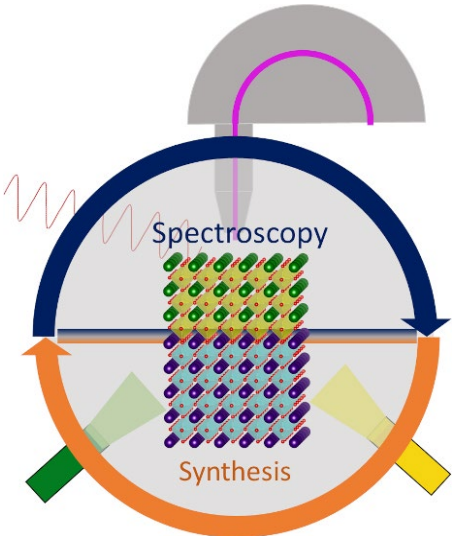

Figure 1: Feedback loop of in situ characterization of oxide thin films, providing feedback to improve the synthesis process. Taken from Thapa, et al.[1]

In this project, we employ hybrid metal-organic molecular beam epitaxy for the delivery of refractory tantalum and iridium cations and examine charge transfer to cobalt. Through systematic studies of interfaces and superlattices that combine the three B site cations, we are examining models governing charge transfer in oxide systems. Current *in situ* experiments at Auburn and planned experiments at the Advanced Photon Source are used to measure charge transfer in films during the growth process using X-ray photoelectron[1] and absorption spectroscopy. Ultrafast optical spectroscopy will be employed to examine the electronic structure and induced polarization in these materials that results from interfacial charge transfer. Films and heterostructures synthesized in this work will also be examined to probe emergent electronic and magnetic topological phenomena. Collectively, this work will advance our synthesis capabilities and provide

a fundamental understanding of interfacial charge transfer in complex oxides. Both results are key goals for the Department of Energy Basic Energy Sciences roadmap for development and control of new materials for quantum information technologies and renewable energy.

Recent Progress

Initial work on the project has focused on the synthesis of $SrCoO_3$ and $SrIrO_3$ thin films via molecular beam epitaxy. $SrCoO_3$ is grown using a high temperature effusion cell for delivery of Co in a highly oxidizing environment (~10^{-5} Torr oxygen with RF plasma), while $SrIrO_3$ is grown using an iridium acetylacetonate solid metal-organic source from a low temperature effusion cell. High quality films of both materials have been achieved. An example of the *in situ* RHEED pattern for $SrCoO_3$ is shown in Figure 2(a).

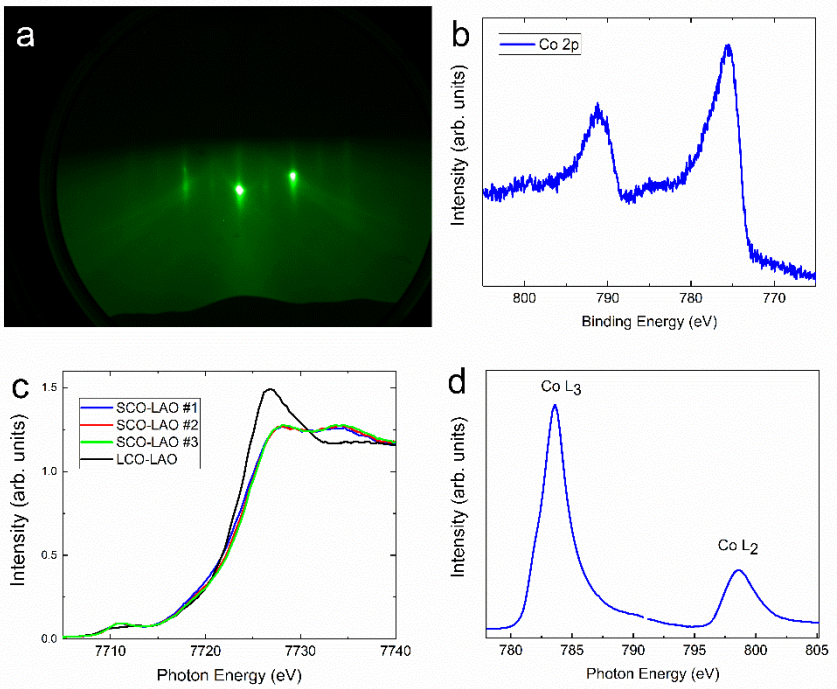

Figure 2: $SrCoO_3$ film characterization. (a) *In situ* RHEED image showing high quality film surface after growth on $LaAlO_3$, (b) *In situ* Co 2p XPS data consistent with Co^{3+} or Co^{4+} valence; (c) Co K edge XANES for $LaCoO_3$ and three $SrCoO_3$ samples showing Co valence greater than 3+; (d) Co L edge XAS.

Post-growth characterization on $SrCoO_3$ has focused on spectroscopic studies to determine the formal charge of the Co ions to determine oxidation conditions for the films. *In situ* XPS (Figure 2(b)) showed that the Co charge state was consistent with either 3+ or 4+, but could not delineate between the two[1]. Co K edge X-ray absorption near edge spectroscopy (XANES) was performed at the Advanced Photon Source and showed that the $SrCoO_3$ films have a higher oxidation state than reference $LaCoO_3$ with a 3+ formal charge. This was corroborated by Co L edge XAS at Brookhaven National Laboratory (Figure 2(d)). Samples have also been characterized by scanning transmission electron microscopy to examine homogeneity and determine if any brownmillerite phase is present[2]. These measurements set the stage for further materials characterization to examine magnetic and electronic properties of the materials. They also lay the groundwork for understanding of charge transfer from Ir to Co at interfaces and in double perovskite films, which are part of our ongoing work.

Temperature-dependent transport measurements have been performed on $SrIrO_3$ films to determine how electronic transport is affected by epitaxial strain. $LaAlO_3$, (La,Sr)(Al,Ta)O_3 (LSAT), and $SrTiO_3$ apply compressive strain with decreasing strain values, while $GdScO_3$ applies a small tensile strain. Reciprocal space maps show that, except for $LaAlO_3$, films on other substrates are clamped to and commensurate with the underlying substrate lattice parameter. In terms of transport response, films on $GdScO_3$ shows semiconducting behavior whereas other films show a largely metallic behavior down to some specific temperature, and then shows a slight upturn in resistivity. The cause of this upturn is under investigation. The film grown on $SrTiO_3$ shows the "best" characteristics in terms of resistivity and mobility. The carrier density of the films at 10 K is ~10^{20} carriers/cm^3. These results are shown in Figure 3 and are comparable to previously reported values[3,4]. Ir L edge XAS measurements have also been performed at Argonne National Laboratory to serve as reference spectra for comparison with $SrIrO_3$/$SrCoO_3$ superlattices and double perovskite films.

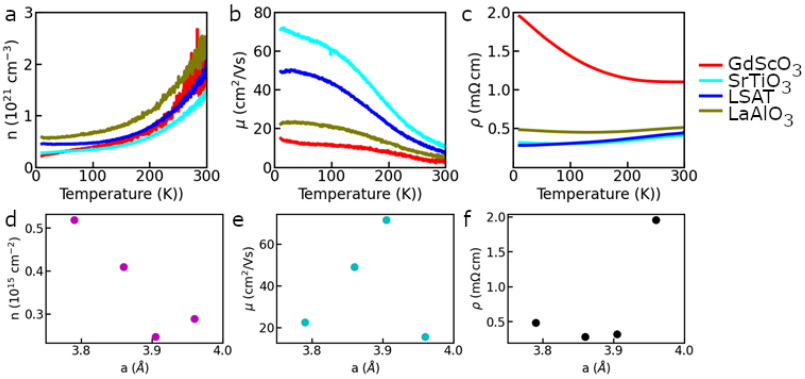

Figure 3: Temperature-dependent transport data of $SrIrO_3$ films grown on various substrates. (a) Carrier concentration; (b) Mobility; (c) Resistivity. 10 K (d) Carrier concentration; (e) Mobility; and (f) Resistivity versus substrate lattice parameter.

Future Plans

Future work at Auburn will focus on the continued development of $SrIrO_3$/$SrCoO_3$ and $SrTaO_3$/$SrCoO_3$ superlattices to characterize interfacial charge transfer in these systems. Ultrafast pump-probe spectroscopy and second harmonic generation measurements will be performed in the Jin lab to examine polar distortions in these materials due to charge transfer. Temperature-dependent vibrating sample magnetometry (VSM) will be performed to determine the effect of heterostructuring and charge transfer on the ferromagnetic Curie temperature of $SrCoO_3$. Electronic and magnetotransport measurements will be performed to examine possible topological Hall effect due to magnetic skyrmions at the interface between ferromagnetic $SrCoO_3$ and $SrIrO_3$/$SrTaO_3$, metals with high spin-orbit coupling. Through the laboratory partnership program, scanning transmission electron microscopy (STEM) measurements will be performed at Pacific Northwest National Laboratory. Soft X-ray absorption and photoemission measurements will be performed at Brookhaven National Laboratory at the National Synchrotron Light Source II.

Double perovskite Sr_2IrCoO_3 and Sr_2TaCoO_3 will also be examined to determine if cation ordering is present and how charge transfer mediates the growth process of these phases. Initial growths of alloy Sr(Ta,Co)O_3 are underway and we are working to determine the optimal conditions for the

stoichiometric double perovskite. *In situ* XPS will be used to determine the stable chemical valence of these materials, as there is controversy in the literature as to whether Co takes on a 2+ or 3+ charge state, with Ir in a corresponding 6+ or 5+ state, in Sr_2IrCoO_3. These materials will be characterized by XRD, VSM, and STEM as well. Our eventual goal is to conduct *in situ* growth at the upgraded Advanced Photon Source at Argonne National Laboratory in 2024 and 2025. We performed our first *in situ* XRD experiments at Argonne in April 2023 through collaborations with Pacific Northwest National Laboratory focusing on the growth of $SrFeO_x$ films. This allowed us to benchmark the capabilities of the *in situ* growth system to allow us to prepare for future experiments. To complement this work, we are also developing a vacuum suitcase that will allow us to transfer samples from Auburn to the synchrotrons at Argonne and Brookhaven National Labs so that films grown on campus can be characterized without atmospheric exposure. This system is expected to be completed in fall 2023.

References

1. S. Thapa, R. Paudel, M. D. Blanchet, P. T. Gemperline, and R. B. Comes, *Probing surfaces and interfaces in complex oxide films via in situ X-ray photoelectron spectroscopy*, Journal of Materials Research, **36**, 26-51 (2021).
2. H. Jeen, W. S. Choi, M. D. Biegalski, C. M. Folkman, I-C. Tung, D. D. Fong, J. W. Freeland, D. Shin, H. Ohta, M. F. Chisholm & H. N. Lee, *Reversible redox reactions in an epitaxially stabilized SrCoOx oxygen sponge*, Nature Materials **12**, 1057–1063 (2013).
3. A. Biswas, K.-S. Kim, and Y. H. Jeong, *Metal insulator transitions in perovskite $SrIrO_3$ thin films*, Journal of Applied Physics **116**, 213704 (2014).
4. J. Liu, J.-H. Chu, C. Rayan Serrao, D. Yi, J. Koralek, C. Nelson, C. Frontera, D. Kriegner, L. Horak, E. Arenholz, J. Orenstein, A. Vishwanath, X. Marti, and R. Ramesh, *Tuning the electronic properties of J_{eff} = ½ correlated semimetal in epitaxial perovskite $SrIrO_3$*, arXiv:1305.1732 (2013).

Publications

1. S. Nair, Z. Yang, D. Lee, S. Guo, J.T. Sadowski, S. Johnson, A. Saboor, R.B. Comes, W. Jin, K.A. Mkhoyan, A. Janotti, and B. Jalan. *Engineering Metal Oxidation using Epitaxial Strain*, Nature Nanotechnology, **18**, (2023).

Structure and stability of multicomponent vapor-deposited organic glasses

Mark Ediger, University of Wisconsin-Madison

Keywords: vapor-deposition, glass, structure, organic semiconductor

Research Scope

Using molecules applicable to organic electronics, we investigate three fundamental issues about glasses prepared by physical vapor deposition (PVD) with relevance both for their practical use and for a broader understanding of amorphous materials. Our objectives: 1) We seek to control phase segregation in glasses prepared by co-deposition of organic semiconductors. For a given pair of molecules, we attempt to use PVD to obtain glasses that range from well-dispersed to mesoscale component-segregated. 2) We seek to understand what controls interface composition and structure in co-deposited PVD glasses of organic semiconductors. Structure near the interface can influence charge transport and glass stability. 3) We seek to understand the conditions under which co-deposited PVD glasses can exhibit the very high stability of single-component PVD glasses. Highly stable glasses are useful as they inhibit chemical and physical degradation that leads to a loss of device performance. These three objectives are investigated with grazing-incidence small angle x-ray scattering, polarized resonant soft x-ray reflectivity, spectroscopic ellipsometry, and calorimetry. We find that the surface equilibration mechanism (interface-controlled assembly) that has been useful for understanding single-component PVD glasses can also predict the properties of multicomponent systems.

Recent Progress

The stability of multicomponent vapor-deposited glasses of organic semiconductors. We wish to understand the conditions under which co-deposited PVD glasses can exhibit the very high stability of single-component PVD glasses. The technological context is this: the light-emitting layer in organic light-emitting diodes (OLEDs) is generally a glassy mixture of organic semiconductors prepared by PVD. Recent studies have indicated that OLEDs comprising highly stable glass layers show extended device lifetime[i,ii]. Previous work has identified the conditions for preparing ultrastable single-component PVD organic glasses, however, little is known about the stability of vapor-deposited glass mixtures. In our current work[iii], we studied the stability of binary PVD glasses of the organic semiconductors, TPD (N,N'-

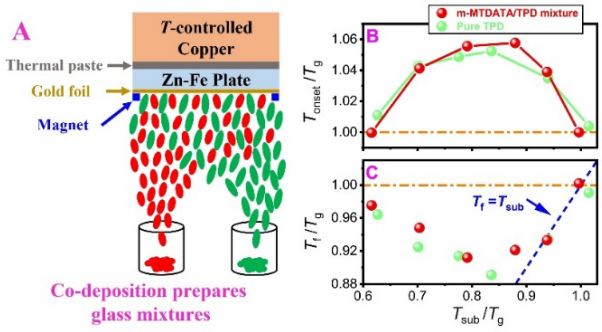

Figure 2. Scheme for preparing glass mixtures by co-deposition for DSC measurements (panel A); and the trend of T_{onset}/T_g (panel B) and T_f/T_g (panel C) as a function of T_{sub}/T_g for deposited m-MTDATA/TPD mixtures and pure TPD glasses.

Bis(3-methylphenyl)-N,N'-diphenylbenzidine) and m-MTDATA (4,4',4"-Tris[phenyl(m-tolyl)amino]triphenylamine) using differential scanning calorimetric (DSC) measurements and also spectroscopic ellipsometry. The stability of these films is quantified by using the onset temperature (T_{onset}) and the fictive temperature (T_f). A glass with greater kinetic stability will have a higher T_{onset}. A glass with lower enthalpy will have a lower T_f. We found that the most stable glass mixtures of m-MTDATA/TPD (with the highest T_{onset} and lowest T_f) are obtained when deposited at T_{sub}/T_g=0.78-0.90. The trend of T_{onset}/T_g (or T_f/T_g) as a function of T_{sub}/T_g for deposited m-MTDATA/TPD glass mixtures is the same as that for single-component PVD organic glasses, as shown in the accompanying Figure 1B and 1C. This is consistent with the surface equilibration mechanism.

Structure of co-deposited TCTA and Ir(ppy)$_3$ glass mixtures. Another goal is to control component segregation in glasses prepared by co-deposition of organic semiconductors. In an initial effort, we make use of Ir(ppy)$_3$, one of the most common light emitters in organic light emitting diodes (OLEDs) due to its high quantum efficiency; light emitters are typically dispersed in a host material for this application. Understanding the properties of Ir(ppy)$_3$ in thin glassy films is crucial because it impacts the light out-coupling and lifetime of the devices. To study its dispersion within a host, we selected TCTA, commonly used as a host material in OLEDs, as a pair with Ir(ppy)$_3$. Although light-emitting layers in OLEDs are typically glass mixtures prepared by physical vapor deposition (PVD), studies of fundamental structure in co-deposited mixtures are rare. PVD glasses of TCTA and Ir(ppy)$_3$ were characterized by grazing incidence wide angle X-ray scattering (GIWAXS) at SSRL. Vapor-deposited glasses of pure Ir(ppy)$_3$ show a broad signature peak along Q_z, coming from a weak periodicity of Ir atoms in the vapor-deposited glass. We prepared PVD glass mixtures with different mass composition and substrate temperatures. Figure 2 is the GIWAXS scattering patterns of the studied samples. The results for pure TCTA are displayed in the top panel. The signature peak of Ir(ppy)$_3$ becomes more pronounced as its concentration increases from 0% to 50%, indicating component segregation of TCTA and Ir(ppy)$_3$ in PVD glasses. (This peak can only occur in clusters of Ir(ppy)$_3$ molecules.) In addition, at a fixed composition, the intensity of this signature peak increases with the substrate temperature. Substrate temperature has a strong effect on molecular mobility and so we interpret this result to indicate

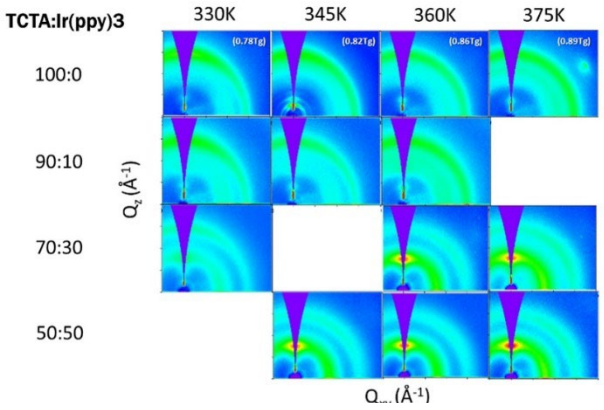

Figure 3. GIWAXS patterns of TCTA:Ir(ppy)$_3$ PVD glasses. The composition and substrate temperature are written on left and top panel, respectively. Red indicates higher intensity whereas the blue color means lower intensity.

increasing component segregation at higher concentrations of $Ir(ppy)_3$. Future work aims to quantify the size of the domains present in these glassy mixtures.

Structure of co-deposited TPD and DO37 glass mixtures. In collaboration with the DeLongchamp group at NIST, we have used polarized resonant soft X-ray scattering (P-RSoXS) to measure the size of component-segregated domains in vapor-deposited mixtures of TPD and DO37. The first evidence for component segregation in co-deposited glasses for this pair of molecules came from ellipsometry experiments which indicated that the sample showed two glass transitions upon heating. We interpreted this to indicate that there were domains rich in TPD (the high T_g component) and domains rich in DO37 (the low T_g component). A much more definitive understanding of these co-deposited glasses is provided by P-RSoXS, with preliminary results shown in Figure 3. This soft X-ray technique clearly shows peaks related to domains that are rich in TPD and DO37. At the lowest substrate temperature, the domains are roughly 20 nm, while at the highest substrate temperatures, they are 120 nm. This trend is reasonable, since surface mobility is higher at higher substrate temperatures, allowing the component molecules (which arrive randomly at the surface) more opportunity to separate into domains. Bulk measurements show that this mixture is immiscible, and this provides the driving force for phase segregation. This is the first example in which the size of domains in co-deposited PVD glasses has been systematically manipulated through the deposition conditions. The 120 nm length scale observed for deposition at 325 K is amazingly large, considering that co-deposition occurs randomly, directly into the glassy state, and that all of the component segregation must occur within just a few seconds during the deposition process. This is a direct result of the highly mobile surfaces of organic glasses.

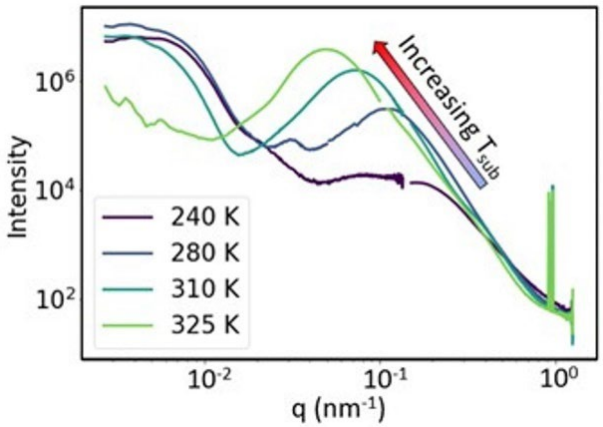

Figure 4. P-RSoXS data on co-deposited glassy thin films of TPD and DO37. The peaks near the center of the figure show phase-segregated domains. The domains are larger at higher substrate temperatures.

Composition and structure at organic/organic interfaces in vapor-deposited glasses. We also want to understand what controls interface composition and structure in co-deposited PVD glasses of organic semiconductors. In OLEDs for example, there are many such interfaces, and structure near the interface can influence charge transport and glass stability. While we know that physical vapor deposition can prepare birefringent molecular glasses with tunable bulk molecular packing, it remains unclear how this anisotropic structure becomes perturbed at buried interfaces. To address this nanoscale characterization challenge, we utilized polarized resonant soft X-ray reflectivity (P-RSOXR) to determine the depth dependence of composition and molecular

orientation simultaneously in a series of glassy bilayers composed of the semiconducting molecules aluminum-tris(8-hydroxyquinoline) (Alq_3) and 1,4-di-[4-(N,N-diphenyl)amino]styryl-benzene (DSA-Ph) [iv]. We determined the orientation of DSA-Ph intermixed with Alq3 at a buried heterointerface. In Figure 4, the upper panel shows that the composition changes from pure Alq3 to pure DSA-Ph over roughly 2 nm, for each of the three substrate temperatures utilized. The bottom panel shows that the molecular orientation of the DSA-Ph also changes across the interface, in a manner that depends strongly upon the substrate temperature utilized. Our results reveal that the surface equilibration mechanism controls molecular orientation in multicomponent blends, even when the composition is changing rapidly over of 1-2 nm!

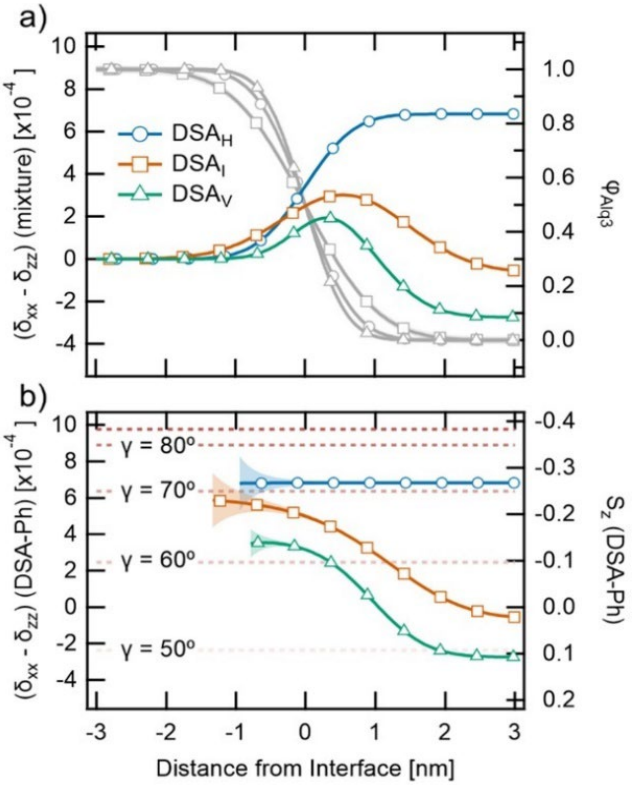

Figure 5. Composition (panel a) and molecular orientation of DSA-Ph (panel b) at the interface of Alq3 and DSA-Ph glasses, prepared by physical vapor deposition.

Future Plans

We will investigate the kinetic stability and phase segregation in a number of co-deposited PVD glasses comprised of organic semiconductors, to test the generality of the results that we have obtained to date. We have found a way to predict molecular orientation in co-deposited PVD glasses of organic semiconductors, and we are assembling a data base to test this idea. p-RSoXs measurements are being performed with the DeLongchamp group at NIST to characterize the spatial extent of component segregation in these systems.

References

[1]. Ràfols-Ribé, J., Will, P. A., Hänisch, C., Gonzalez-Silveira, M., Lenk, S., Rodríguez-Viejo, J., and Reineke, S. High-performance organic light-emitting diodes comprising ultrastable glass layers. *Sci. Adv.*, 4, eaar8332 (2018).

[1]. Bangsund, J. S., Van Sambeek, J. R., Concannon, N. M., and Holmes, R. J. Sub-turn-on exciton quenching due to molecular orientation and polarization in organic light-emitting devices. *Sci. Adv.* 6, eabb2659 (2020).

[1]. Cheng, S., Lee, Y., Yu, J., Yu, L., and Ediger, M. D. Surface equilibration mechanism controls the stability of a model co-deposited glass mixture of organic semiconductors. *J. Phys. Chem. Lett.* 14, 4297-4303 (2023).

[1]. Ferron, T. J., Fiori, M. E., Ediger, M. D., DeLongchamp, D. M., and Sunday, D. F. Molecular Orientation of Birefringent Organic Glasses at Heterointerfaces. *JACS Au.* 2023 (submitted).

Publications supported by DOE BES

1. Cheng, S., Lee, Y., Yu, J., Yu, L., and Ediger, M. D. Surface equilibration mechanism controls the stability of a model co-deposited glass mixture of organic semiconductors. *J. Phys. Chem. Lett.* 14, 4297-4303 (2023).

2. Ferron, T. J., Thelen, J. L., Bagchi, K., Deng, C., Gann, E., de Pablo, J. J., Ediger, M. D., Sunday, D. F., and DeLongchamp, D. M. Characterization of the interfacial orientation and molecular conformation in a glass-forming organic semiconductor. *ACS Appl. Mater. Interfaces* 14, 2, 3455 (2022).

3. Fiori, M. E., Bagchi, K., Toney, M. F., and Ediger, M. D. Surface equilibration mechanism controls the molecular packing of glassy molecular semiconductors at organic interfaces. *Proc. Natl. Acad. Sci. U.S.A.* 118, e2111988118 (2021).

4. Bagchi, K., Fiori, M. E., Bishop, C., Toney, M. F., and Ediger, M. D. Stable Glasses of Organic Semiconductor Resist Crystallization. *J. Phys. Chem. B* 125, 461-466 (2021).

DFT-Based Kinetic Monte Carlo Framework for the Growth of Multiphase Thin Films

(Project Title: Achieving Long Range Ordering in Oxide-Metal Hybrid Materials —A Combined Experimental and Modeling Approach)

Anter El-Azab (Purdue University, aelazab@purdue.edu); Modeling lead
Haiyan Wang (Purdue University, hwang00@purdue.edu); Experimental lead

Keywords: Epitaxial thin film, Kinetic Monte Carlo (kMC), Two-phase ordering, Vertically aligned nanocomposite (VAN).

Research Scope

Great success has been reported on the growth of multiphase thin films with pillar-in-matrix configuration experimentally [1,2]. Yet, a complete theoretical understanding of the formation of these vertically aligned nanocomposites thin film remains a challenging task. The self-organization of pillars in these films occurs in such a way that the system seeks to minimize its sum of chemical, elastic and interfacial energies [3,4]. However, kinetic factors such as the deposition/coverage rate (pulse rate and magnitude) and substrate temperature can significantly impact the final configuration of phases in the film [5]. In this project, we have developed a multi-scale framework that describes the growth of multiphase heteroepitaxial systems using the kinetic Monte Carlo (kMC) scheme. A density-functional theory (DFT) approach has been used to parameterize the bonding energies and kinetic barriers required for the implementation of this kMC scheme. Since the structure of lattice mismatch is believed to have an impact on the configurational microstructure of the multiphase system, it is important to understand such an elastic strain field impacts the diffusion of adatoms [6]. For that reason, we have developed a 3D elastic model to compute the nanoscale stresses in multiphase films. In one implementation of this elastic scheme, we have accounted for the mechanical effects of the interfacial energy in the system. Another implementation is based on a homogenization scheme for heterogeneous elastic media with lattice and modulus mismatches, which is used in conjunction with the kMC method to assess the effect of local strain at the nanoscale on adatom diffusion on the surface.

Recent Progress

Our major achievements on the modeling side include:

1) Development of a thermodynamic model based on elastic, interfacial and chemical energy of multi-phase films. The model has been used to explore the minimum energy configurations of pillars in the film.
2) Development of a highly-parallelized synchronous kMC framework for the simulation of the growth of multi-phase films on mismatched substrates.
3) Development of a homogenization scheme to solve for the elastic strain in heterogeneous oxide-metal films using Fast Fourier Transform (FFT).
4) Coupled the kMC framework with FFT-mechanics solver and to account for the elastic strain effect on the activation barrier for adatom diffusion.

In 1), the modeling approach solves for the elastic strain field due to lattice mismatch while taking into consideration the capillarity forces arising from interfacial energies at the pillar/matrix, pillar/substrate and matrix/substrate interfaces. The model involves interfaces and a

contact line which is an intersection of interfaces as shown in Fig. 1(a-d). The model was used to compute the total elastic energies of representative volume elements (RVEs) for different microstructural configuration patterns, square, hexagonal and random as shown in Fig. 1(e-g) [3].

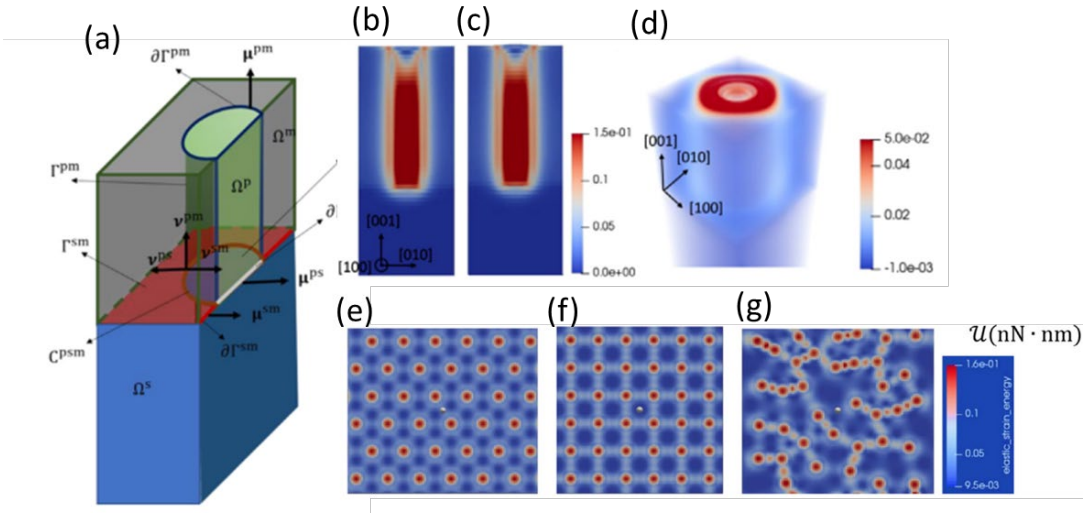

Fig. 1. (a) The control volume for the boundary value problem. Elastic strain energy density in the (b) reference and (c) deformed configurations. (d) 3D solution of the elastic strain energy density of single pillar simulation domain. Elastic energy density of (e) hexagonal, (b) square (c) and random nanopillars patterned microstructural configurations [3].

In 2), we developed a highly-parallelized kMC algorithm that is specific to modelling to multiphase thin film growth based on previously developed parallelized scheme for 3D Ising lattice by Martinez *et al* [7]. The model is refined to atomic scale of fcc lattice of metals. The model is fully guided by nudged elastic band (NEB) simulations using DFT for the estimation of the kinetic barriers. We used the kMC-diffusion model to study the effect of deposition parameters such as pulsed-laser frequency, substrate temperature, ratio of multi-adatoms arriving, and coverage rate, on the growth nano-clustering and phase separation. An example of the effect of frequency is shown in Fig. 2.

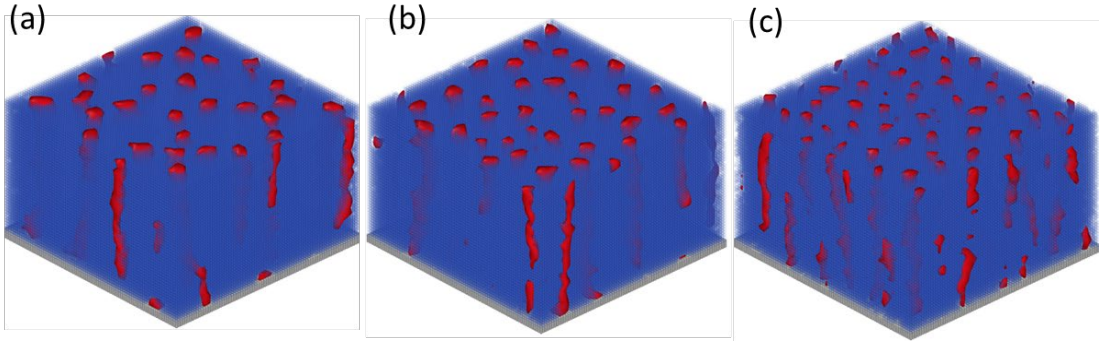

Fig. 2. Mutliphase thin microstructure evolution at fixed temperature 600 °C and different pulsed laser frequencies (a) 2 Hz, (b) 5 Hz and (c) 10 Hz using kMC simulations. The coverage rate is set to 0.1 ML/s and the ratio of Au:CeO2 adatom arriving is 0.15:1 [5].

In 3) and 4), a homogenization scheme for the elastic solution of heterogeneous thin films was developed accounting for lattice, thermal, and modulus mismatch in the multiphase film. This

scheme solves for the elastic strain throughout the system, of which the value sat the free surface are coupled to the adatom diffusion to account for the bias caused by the elasticity of the film. The homogenization scheme is solved using FFT under the augmented lagrangian algorithm. Obtaining the solution using FFT is both feasible and more desirable for coupling with the kMC framework. An elasto-diffusion model of adatoms is then implemented using kMC-FFT framework. The overall algorithm is illustrated in Fig. 3. DFT parameterization is done via software the VASP package, fed into kMC, where the parallelized output is analyzed and visualized through Ovito. The atomistic structure is approximated to continuum scale where the lattice-mismatch eigen-strain BVP is solved using Homogenization scheme. The elastic strain solution is projected onto the surface where it will be fed into the kMC model to modify the activation energy barrier. Therefore, we try to show how the surface elastic strain field will add an additional biased term to the activation energy barrier for an adatom to hop from one place to another. The effect of elastic strain on the growth was found to be significant, which will be shown during the meeting.

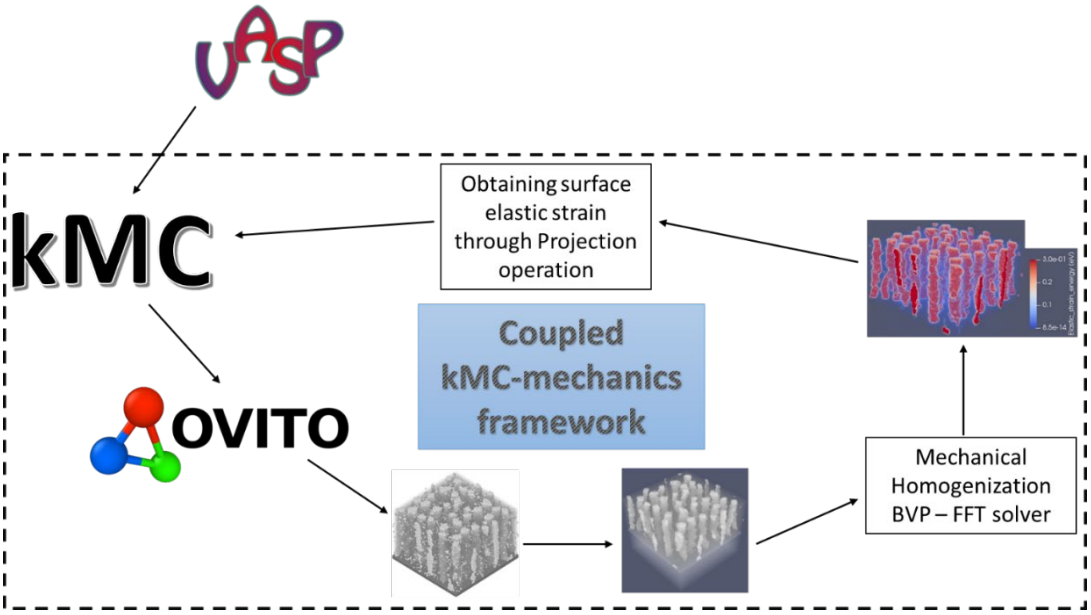

Fig. 3. A generalized 3D framework of film growth using surface deposition.

Future Plans

In the next fiscal year, the modeling framework will be compared with the experimental findings. It will also be used to design experiments for templated growth. The parametrization will be extended for multiple systems to enable the exploration of combination of phases for film design.

References

[1] Juanjuan Lu, Robynne L. Paldi, Yash Pachaury et al, *Ordered Hybrid Metamaterial of La0.7Sr0.3MnO3-Au Vertically Aligned Nanocomposites Achieved on Templated SrTiO3 Substrate*, Materials Today Nano, **15**, 100121 (2021).

[2] Juanjuan Lu, Di Zhang, Robynne L. Paldi et al, *Abnormal In-plane Epitaxy and Formation Mechanism of Vertically Aligned Au Nanopillars in Self-Assembled CeO_2-Au Metamaterial System,* Materials Horizons, (2023).

[3] Kyle Starkey, Ahmad Ahmad, Juanjuan Lu, et al, *A generalized 3D elastic model for nanoscale, self-assembled oxide-metal thin films with pillar-in-matrix configurations*, Acta Materialia 228, 117779 (2023).

[4] Rayaprolu Goutham Sreekar Annadanam, Ahmad Ahmad et al, *Energetics of nanoscale films with self-assembled oxide/metal pillars in nitride matrix*. Materialia, under revision (2023).

[5] Ahmad Ahmad, Jie Peng, Khaled Abdelaziz et al. *A DFT-based kinetic Monte Carlo simulation of multiphase oxide-metal thin film growth*, To be submitted, Journal of Applied Physics, 2023.

[6] Zhengzheng Chen and Nasr Ghoniem, *Biaxial strain effects on adatom surface diffusion on tungsten from first principles*, Physical Review B, **88**, 035414 (2013)

[7] E. Martinez, P. Monasterio, J. Marian, *Billion-atom synchronous parallel kinetic Monte Carlo simulations of critical 3D Ising systems*, Journal of Computational Physics, **230**, 1359 (2011).

Publications

[1] Kyle Starkey, Ahmad Ahmad, Juanjuan Lu, et al, A generalized 3D elastic model for nanoscale, self-assembled oxide-metal thin films with pillar-in-matrix configurations. Acta Materialia **228**, 117779 (2023).

[2] Rayaprolu Goutham Sreekar Annadanam, Ahmad Ahmad et al, *Energetics of nanoscale films with self-assembled oxide/metal pillars in nitride matrix*. Materialia, under revision (2023).

[3] Ahmad Ahmad, Jie Peng, Khaled Abdelaziz et al. *A DFT-based kinetic Monte Carlo simulation of multiphase oxide-metal thin film growth*, To be submitted, Journal of Applied Physics, 2023.

Extending the reach and breadth of nanofabrication to atomic-scale precision in three dimensions using area-selective and self-limited deposition processes

James R. Engstrom (P.I.), School of Chemical and Biomolecular Engineering, Cornell University

Robert A. DiStasio Jr. (co-P.I.), Department of Chemistry and Chemical Biology, Cornell University

Keywords: Atomic layer deposition, Area-selective deposition, Competitive interactions, Nanofabrication, Density functional theory

Research Scope

We assert that competition can provide mechanisms to achieve area-selective substrate-composition-dependent deposition. Essential to our approach is the use of multiple species *simultaneously*, such that competition can occur between the species **[1,2]**. If species are introduced sequentially, there is no competition. While CVD makes use of simultaneous exposure of a substrate to at least two reactant species, ALD has traditionally required that no two species be present simultaneously. Thus, introducing multiple species simultaneously *runs against the orthodoxy of ALD*, and represents a great opportunity to develop a fundamentally new approach to ASD. Such a strategy must be well thought out, however. In our approach, the choice of the co-adsorbate(s) must factor in potentially deleterious direct interactions between it and the thin film precursor, as well as it and the co-reactant. The range of possible species is vast, and much is to be learned by a broad, fundamentally based investigation of multiple systems of interest.

In the second year of our project, we focused on systems in involving the selective deposition of dielectrics on another dielectric (DoD) and a metal (DoM). We are using a combination of experiments and high-level quantum chemical calculations to make progress on increasing our fundamental understanding of these systems. We have considered two examples of dielectric-on-dielectric (DoD): (i) self-limiting deposition of Al_2O_3 on SiO_2 (the growth surface, GS); and (ii) self-limiting deposition of ZrO_2 on SiO_2 (GS). We have also considered one example of dielectric-on-metal (DoM): self-limiting deposition of Al_2O_3 on Co (GS) and Cu (GS).

In the DoD system, we are investigating two thin film systems: Al_2O_3 and ZrO_2. Concerning the former, in our year one report we described initial calculations concerning the reaction of a nitrogen containing-aluminum precursor (NcAP)—that forms an intermolecular Lewis acid-base complex—with a hydroxyl terminated SiO_2 surface [e.g., -OH(*a*) on the GS]. We performed a series of gas-phase and solid-state quantum chemical calculations to analyze this gas-surface interaction and found that the chemisorption of NcAP if favorable on SiO_2, with an overall reaction energy of ~ -36 kcal-mol^{-1}. In year two we examined the deposition of Al_2O_3 using NcAP as the thin film precursor, including studies of two heteroatom co-adsorbate species. Since the fundamental surface chemistry of this species is essentially unknown, we seek to develop a detailed

mechanistic picture concerning how this species interacts with surface functional groups [e.g., -OH(*a*) on the GS] and with potential co-adsorbate species on the surface and in the gas phase.

Concerning the ZrO_2 system, we have investigated ALD growth using a heteroleptic thin film precursor, $(Cp)Zr[N(CH_3)_2]_3$. Although this precursor has been examined in ALD, the fundamental surface chemistry of this species is essentially unknown, and as with NcAP, we seek to develop a detailed mechanistic picture of the chemisorption of this precursor and how it might interact with potential co-adsorbate species on the surface and in the gas phase.

For the DoM system, we examined the deposition of Al_2O_3 on Cu and Co, using two thin film precursors [NcAP, and trimethylaluminum (TMA)], and multiple co-reactants (H_2O and ROH). Here the emphasis is on developing an understanding of reactions at the interface between the depositing dielectric and the underlying metallic substrate. For example, for which process chemistries and conditions does oxidation of the underlying metallic substrate occur?

Recent Progress

DoD: Nitrogen-containing-aluminum precursor (NcAP) on SiO_2

We have examined the deposition of Al_2O_3 using NcAP as the thin film precursor, including studies of two heteroatom co-adsorbate species. We used our viscous flow QCM-based system to quantify the ALD process and supplemented these *in situ* real-time results with *ex situ* measurements using X-ray photoelectron spectroscopy (XPS), spectroscopic ellipsometry (SE), and atomic force microscopy (AFM). Here is a summary of our major findings:

- ALD of Al_2O_3 with NcAP as the thin film precursor and H_2O as the co-reactant occurs over the temperature range, T = 120-285 °C, and the thickness deposited per cycle decreases from ~ 1.0 to 0.6 Å-cycle^{-1} over this range. *Ex situ* XPS indicates near stoichiometric Al_2O_3, with minimal incorporation of C or N.
- Mass changes in each ALD cycle monitored with the QCM indicate significant loss of mass with the co-reactant (H_2O) half-cycle. This is consistent with a ligand exchange reaction with the adsorbed NcAP species, releasing a large molecular weight amido ligand.
- Co-adsorption of NcAP with an oxygen-containing co-adsorbate produced a suppression of the growth rate, decreasing to ~ 40% of the unattenuated value, which is constant for each cycle. This is consistent with no direct reaction between NcAP and the co-adsorbate, but competition for adsorption sites.
- Co-adsorption of NcAP with a nitrogen-containing co-adsorbate produced an increase in the growth rate (> factor of 2), and this effect also increased with the length of the time of co-exposure. This observation indicates that this co-adsorbate produced CVD-like growth.

DoD: Growth of ZrO_2 on SiO_2 using a heterolyptic thin film precursor.

We have investigated the ALD growth of ZrO_2 using a heteroleptic thin film precursor, $(Cp)Zr[N(CH_3)_2]_3$. We used our viscous flow QCM-based system to quantify the ALD process and supplemented these *in situ* real-time results with *ex situ* measurements using X-ray photoelectron spectroscopy (XPS), spectroscopic ellipsometry (SE), and atomic force microscopy (AFM). Here is a summary of our major findings:

- ALD of ZrO_2 with $(Cp)Zr[N(CH_3)_2]_3$ as the thin film precursor and H_2O as the co-reactant occurs over the temperature range, T = 120-285 °C, and the thickness deposited per cycle increases from ~ 0.4 to 0.7 Å-cycle^{-1} over this range. XPS shows considerably more C in the films grown at T = 120 °C. Growth of ZrO_2 with O_2 as the co-reactant was minimal at T = 120 °C, but growth was observed at T = 285 °C.
- Mass changes in each ALD cycle monitored with the QCM indicate modest loss of mass with the co-reactant (H_2O) half-cycle. From DFT we predict that the Cp ligand will be the last to be removed in the ALD process.

DoM: ALD of Al_2O_3 on Cu and Co.

We examined the deposition of Al_2O_3 on Cu and Co, using two thin film precursors [NcAP, and trimethylaluminum (TMA)], and multiple co-reactants (H_2O and ROH). Here the emphasis was on developing an understanding of reactions at the interface between the depositing dielectric and the underlying metallic substrate. Here is a summary of our major findings:

- Concerning growth on Co substrates, we have observed a strong effect of the co-adsorbate, based on results from XPS. With the TMA and H_2O ALD process, we observe oxidation of the underlying Co, at T = 120 and 285 °C. In contrast, ALD with TMA and ROH, results in no oxidation of the underlying Co at T = 285 °C (ALD with this process at T = 120 °C is minimal).
- Concerning growth on Cu substrates, we find that neither process, TMA and H_2O at T = 120 and 285 °C , or TMA and ROH, at T = 285 °C results in oxidation of the underlying Cu. This suggests that the thermodynamic driving force for oxidation may play a role in whether or not the underlying substrate is oxidized.

Key Outcomes

- ALD growth of Al_2O_3 using NcAP results in near stoichiometric thin films over a wide range of substrate temperatures, similar to those produced in the TMA and H_2O process.
- Two small molecule co-adsorbates produce dramatically different effects. An oxygen containing molecule produces a suppression in the rate of growth and no direct reaction with the thin film precursor. A nitrogen containing molecule produces an increase in the rate of growth, strongly indicating CVD-like growth.
- Interfacial oxidation of the underlying metallic substrate can be eliminated by use of an alternative co-reactant. We observed this effect when examining Al_2O_3 ALD on Co with TMA and H_2O (at T = 120 and 285 °C), and TMA and ROH (at T = 285 °C), with the latter process producing no oxidation of the underlying Co.

Future Plans

We are planning several new sets of experiments for the third year of the contract. We will continue our studies of the NcAP, including studies involving introducing co-adsorbates to direct deposition of Al_2O_3 on SiO_2, but not on Cu. Our work to date using oxygen- and nitrogen-containing co-adsorbates, where different effects were observed, is worthy of more in depth study. Concerning selectivity, we will significantly expand our studies of NcAP, including studies involving introducing co-adsorbates to direct deposition of Al_2O_3 on SiO_2, but not on Cu. This work will involve a closely coupled effort involving experiments and high-level quantum chemical calculations.

In addition to the DoD and DoM studies we have completed to date, we will launch a new study of MoM growth. In particular, we plan to investigate the ASD deposition of refractory metals on other metals, but not dielectric. An application could include bottom-up gap fill in high-aspect ratio features, where growth is initiated by a seed metal at the bottom of the trench but does not occur on the dielectric sidewalls. The refractory metal could be Mo (W has been studied more extensively), the growth surface (GS) could be TiN, while the dielectric could be SiO_2, Al_2O_3 or low-κ. Metals such as Mo often require high deposition temperatures, where using small molecules for recombination reactions may be a superior approach (i.e., not as blocking molecules). Again, this work will involve a closely coupled effort involving experiments and high-level quantum chemical calculations.

References

1. T. Suh, Y. Yang, P. Zhao, K. U. Lao, H.-Y. Ko, J. Wong, R. A. DiStasio Jr., and J. R. Engstrom, *Competitive Adsorption as a Route to Area Selective Deposition*. ACS Appl. Mater. Interfaces, **12**, 9989 (2020).

2. T. Suh, Y. Yang, H. W. Sohn, R. A. DiStasio Jr., and J. R. Engstrom, *Area-Selective Atomic Layer Deposition Enabled by Competitive Adsorption*. J. Vac. Sci. Technol. A **38**, 062411 (2020) (an Editor's Pick).

Presentations:

James R. Engstrom, *From atomic-scale characterization to atomic-scale control of thin film deposition processes*, Keynote Lecture, Materials Science and Technology Technical Meeting (MS&T22), Pittsburgh, PA, October 2022. **INVITED**

James R. Engstrom, *Area-selective deposition: An assessment of current approaches and challenges*, Micron, Boise, ID, March 2023. **INVITED**

James R. Engstrom, *Area-selective deposition: An assessment of current approaches and challenges*, IEEE Workshop on Microelectronic Devices, Boise, ID, March 2023. **INVITED**

[i]. Ràfols-Ribé, J., Will, P. A., Hänisch, C., Gonzalez-Silveira, M., Lenk, S., Rodríguez-Viejo, J., and Reineke, S. High-performance organic light-emitting diodes comprising ultrastable glass layers. *Sci. Adv.*, 4, eaar8332 (2018).
[ii]. Bangsund, J. S., Van Sambeek, J. R., Concannon, N. M., and Holmes, R. J. Sub-turn-on exciton quenching due to molecular orientation and polarization in organic light-emitting devices. *Sci. Adv.* 6, eabb2659 (2020).
[iii]. Cheng, S., Lee, Y., Yu, J., Yu, L., and Ediger, M. D. Surface equilibration mechanism controls the stability of a model co-deposited glass mixture of organic semiconductors. *J. Phys. Chem. Lett.* 14, 4297-4303 (2023).
[iv]. Ferron, T. J., Fiori, M. E., Ediger, M. D., DeLongchamp, D. M., and Sunday, D. F. Molecular Orientation of Birefringent Organic Glasses at Heterointerfaces. *JACS Au.* 2023 (submitted).

Publications supported by DOE BES

1. Cheng, S., Lee, Y., Yu, J., Yu, L., and Ediger, M. D. Surface equilibration mechanism controls the stability of a model co-deposited glass mixture of organic semiconductors. *J. Phys. Chem. Lett.* 14, 4297-4303 (2023).
2. Ferron, T. J., Thelen, J. L., Bagchi, K., Deng, C., Gann, E., de Pablo, J. J., Ediger, M. D., Sunday, D. F., and DeLongchamp, D. M. Characterization of the interfacial orientation and molecular conformation in a glass-forming organic semiconductor. *ACS Appl. Mater. Interfaces* 14, 2, 3455 (2022).
3. Fiori, M. E., Bagchi, K., Toney, M. F., and Ediger, M. D. Surface equilibration mechanism controls the molecular packing of glassy molecular semiconductors at organic interfaces. *Proc. Natl. Acad. Sci. U.S.A.* 118, e2111988118 (2021).
4. Bagchi, K., Fiori, M. E., Bishop, C., Toney, M. F., and Ediger, M. D. Stable Glasses of Organic Semiconductor Resist Crystallization. *J. Phys. Chem. B* 125, 461-466 (2021).

Synthesis of Electronic-Grade Quantum Heterostructures by Hybrid PLD

Chang-Beom Eom - University of Wisconsin-Madison

Keywords: Thin Film Synthesis, Quantum Heterostructures, Electronic-Grade, Heterointerfaces, Superconductivity

Program Scope

Quantum materials such as unconventional superconductors, interfacial 2D electron gases (2DEGs), and multiferroics have been fertile ground for new discoveries. Our overarching theme is developing novel synthesis routes to create a new generation of epitaxial quantum thin film heterostructures for studies of fundamental science and development of new applications. These heterostructures can be of comparable or higher quality than available bulk single crystals, but these novel systems are usually sensitive to constraints of thin film heterostructures, including interaction with the substrate, the difficulty in controlling stoichiometry and point defects, and the challenge of forming atomically perfect interfaces.

Our hypothesis is that designing substrate interactions, controlling and identifying point defects, the creation of atomically perfect interfaces and fabricating and stacking of free-standing single crystal membranes will reveal new phenomena in complex oxides and unconventional superconductors, and will discover fundamental intrinsic properties of quantum materials arising from dimensionality, anisotropy, and electronic correlations. We have already demonstrated static strain engineering of the Fe-based superconductor $BaFe_2As_2$, made the first direct observation of the two-dimensional hole gas (2DHG) at an oxide interface, are developing a hybrid pulsed laser deposition, and have begun to understand a route to new discoveries through control of highly perfect and defect free films and heterostructures and free-standing membranes. This approach overcomes conventional thin film growth limitations of epitaxial and orientational lattice match, and the clears the way for nearly limitless possibilities in materials design. The **thrusts** of our proposed work expand into new materials systems with synthesis and experimental measurements:

Fabrication of Novel Quantum Material Platforms

Novel Hybrid PLD Synthesis Route - builds on our chemical PLD process but with expanded capabilities for stoichiometry and point defect control in electronic grade quantum heterostructures involving elements with a very large vapor pressure mismatch

Complex oxide membranes **-** free-standing membranes of complex oxides films and heterostructures for assembling stacked and twisted heterostructures that expand quantum heteromaterials, allowing for dynamic strain control

Fundamental Science of Novel Quantum Materials Platform

$LaAlO_3$ / $KTaO_3$ interface superconductivity **–** a strong spin-orbit superconducting system with not yet understood orientation dependence, studied with hybrid PLD heterostructures.

$Ba(Pb_xBi_{1-x})O_3$ superconducting films and membranes with strong spin-orbit coupling **–** our recently discovered spin hall effect in this unusual superconducting system has implications for the microscopic mechanism, and offers opportunities for superconducting spintronics.

Strain-controlled pnictide superconducting free-standing membranes **–** investigation of fundamental magnetic, nematic, structural, and superconducting properties by dynamic strain manipulation, building on our epitaxial strain results.

Recent Progress

The discovery of interfacial superconductivity at $KTaO_3$ (111) heterointerfaces offers fresh insights into the interplay of quantum paraelectricity, strong spin-orbit coupling, and superconductivity. Future progress relies on innovations in the synthesis of ever-cleaner samples to investigate the intrinsic quantum phenomena free of extrinsic effects due to crystalline imperfections. Recently, we reported superconducting heterostructures based on electronic-grade epitaxial (111) $KTaO_3$ thin films grown by a novel hybrid synthesis route that synergistically combines thermal evaporation of K_2O suboxide and pulsed laser deposition of Ta_2O_5 facilitated by an ultrathin $SmScO_3$ template. The two-dimensional electron gas at the heterointerface between $LaAlO_3$ and the $KTaO_3$ thin film exhibits significantly higher electron mobility, superconducting transition temperature and critical current density than those in bulk single crystal $KTaO_3$-based heterostructures. Cross-sectional STEM shows a lower density of point defects and cleaner interface in heteroepitaxial $KTaO_3$ thin films in contrast to bulk single crystal $KTaO_3$ substrates. Our hybrid approach opens new synthesis routes to epitaxial growth of other alkali metal-based oxides that lie beyond the capabilities of conventional approaches.

Fig. 1a shows the calculated stability phase diagram of K-Ta-O near the stoichiometric $KTaO_3$ as a function of K partial pressure and temperature; here, the oxygen (O_2) partial pressure is fixed at 10^{-6} Torr based on the potential phase diagram as a function of K and O_2 partial pressures. We used commercially available potassium oxide (K_2O) as K source due to the unstability of elemental K. We estimate the source temperatures for achieving stoichiometric $KTaO_3$ synthesis by calculating partial pressures of all gas species (Fig. 1b) at source temperatures from 500-1000 K. We identify three major gas species as O_2, K_2O_2, and K with the calculated equilibrium partial pressures $\approx 1.7\text{x}10^{-3}$, $9.2\text{x}10^{-7}$, and $3.9\text{x}10^{-7}$ Torr, respectively, at a source temperature of 750 K. These values set the upper limits for the partial pressures of gas species.

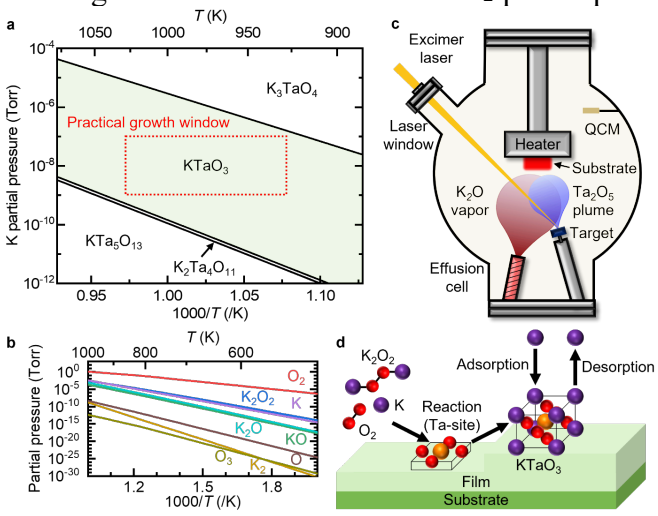

Fig. 1 | Thermodynamics-guided epitaxial growth of $KTaO_3$ thin films by hybrid PLD. a, Phase region of $KTaO_3$ as a function of K partial pressure and temperature at fixed O_2 partial pressure of 10^{-6} Torr. Practical experimental parameters within the $KTaO_3$ growth window are marked by a red box. **b**, Vapor pressure of gas species in the K-O system. **c**, Schematic illustrating the hybrid PLD method for $KTaO_3$ thin film growth. QCM: quartz crystal microbalance. **d**, Schematic illustrating the adsorption-controlled growth of $KTaO_3$ thin films.

These analyses indicated that the practical growth window of $KTaO_3$ should be in the range of 10^{-7}-10^{-9} Torr K partial pressure and 950-1000 K substrate temperatures (red box, Fig. 1a). Fig. 1c schematically depicts the hybrid PLD experimental setup. As with MBE, K is supplied by thermal evaporation of a K_2O effusion cell directed at the substrate. In contrast, Ta is supplied by ablating a ceramic target of tantalum pentoxide (Ta_2O_5) with a pulsed excimer laser as in PLD. Fig. 1d schematically illustrates the adsorption-controlled growth of $KTaO_3$. In adsorption-controlled growth, the volatile species (K in this case) is provided with sufficiently large overpressure to avoid for K deficiency while excess K readily evaporates from the K-terminated surface.

We grew ≈8-10 nm thick epitaxial $KTaO_3$ thin films on single crystal substrates of $SrTiO_3$ (001), $SrTiO_3$ (111), $KTaO_3$ (111), and on $KTaO_3$ (111) with an ≈1 nm-thick $SmScO_3$ template layer. An increased substrate temperature of 1023 K enhances stoichiometry, but results in surface roughening. To address these issues, we grew a thin $SmScO_3$ template on $KTaO_3$ (111) substrates, and grew stoichiometric and smooth $KTaO_3$ thin films at low substrate temperature. The $SmScO_3$ template serves three purposes (i) stabilizing the $KTaO_3$ surface by suppressing K evaporation from the $KTaO_3$ substrate surface at high temperature and high vacuum, (ii) inhibiting the migration of native defects from the $KTaO_3$ substrate to the film that may deteriorate the superconductivity and (iii) suppressing the leakage of charge carriers from the film to the substrate area where more disorder is expected.

We characterized the interfacial structure with scanning transmission electron microscopy High-angle annular dark field (HAADF). Cross-sectional images of the heterostructures confirm atomically-sharp interfaces of $SmScO_3/KTaO_3$ (111) substrate and $LaAlO_3/KTaO_3$ (111) thin film, which means that thin $SmScO_3$ template could protect the unstable (111) surface of the KTO substrate under the highly reducing atmosphere of $\approx 10^{-6}$ Torr at 973 K. The $KTaO_3$ thin film is fully epitaxial to the $KTaO_3$ substrate through the underlying $SmScO_3$ template without any misfit dislocations, facilitated by a small 2.6% lattice mismatch between $SmScO_3$ and $KTaO_3$ (111). The crystal structure of ≈1 nm-thick $SmScO_3$ film appears to adopt a (psuedo-)cubic structure. This allows the $KTaO_3$ (111) thin film to be coherently grown with the desired cubic structure due to the (pseudo-)cubic $SmScO_3$ template.

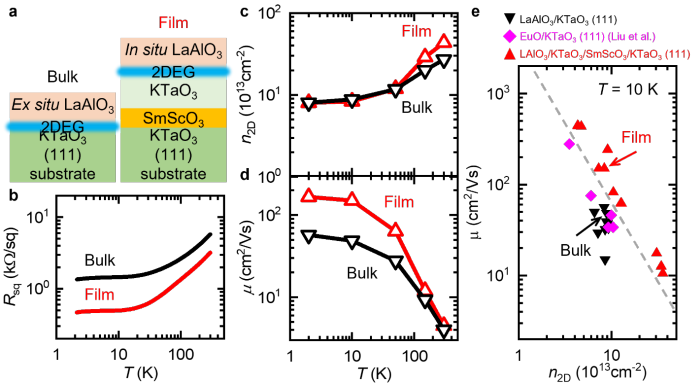

Fig. 2 | Electrical transport measurements of $KTaO_3$ (111). a, Schematic illustrating the structures of the measured samples. In the bulk case, the $LaAlO_3$ overlayer is always grown *ex situ*, which inevitably creates the 2DEG in the first few nm of $KTaO_3$ with high defect density. In the case of $KTaO_3$ thin film, the $LaAlO_3$ layer is grown *in situ* and the surface of $KTaO_3$ has low defect density, which results in enhanced μ. **b-d**, Temperature dependence (2-300 K) of **b**, R_{sq}, **c**, n_{2D}, **d**, μ of $LaAlO_3/KTaO_3$ (111) (Bulk) and $LaAlO_3/KTaO_3/SmScO_3/KTaO_3$ (111) (Film) heterostructures. The measurements in **b-d** are performed in a Van der Pauw geometry. **e**, Distribution of μ and n_{2D} estimated from Hall measurements at $T = 10$ K. The samples shown in **b-d** marked with arrows. Purple diamonds are data at $T = 10$ K from different growth conditions of EuO.

These lower defect concentrations improve the normal state and superconducting state properties of the 2DEG at the $LAlO_3/KTaO_3$ interface. We compared two different heterostructures: $LaAlO_3/KTaO_3$ (111) substrate (denoted as "Bulk") and $LaAlO_3/KTaO_3/SmScO_3/KTaO_3$ (111) substrate (denoted as "Film") (Fig. 2). As shown in Fig. 2a, 2DEGs are created at the $LaAlO_3/KTaO_3$ interface. The amorphous $LaAlO_3$ layer is grown *in situ* in the case of $LaAlO_3/KTaO_3/SmScO_3/KTaO_3$ (111) heterostructures to produce clean $LaAlO_3/KTaO_3$ interface. Fig. 2b shows the R_{sq}-T data of the "Bulk" and "Film" samples. The Film sample shows much lower R_{sq} in the normal state (Fig. 2b) despite having nearly the same n_{2D} as the Bulk sample at 10 K (Fig. 3c). We attribute the lower R_{sq} to the high carrier mobility (μ) of the Film sample (≈150 cm^2/Vs at 10 K) compared to the Bulk sample (≈48 cm^2/Vs at 10 K). We tested multiple samples with the similar structures and summarize their properties at 10 K in a μ-n_{2D} diagram (Fig. 2e). This clearly demonstrates that the $LaAlO_3/KTaO_3/SmScO_3/KTaO_3$ (111) (red up-triangles, Fig. 2e)

samples generally possess higher μ within the same n_{2D} range compared to the $LaAlO_3/KTaO_3$ (111) samples (black down-triangles, Fig. 2e). We attribute the differences in μ to the lower point defect concentrations, which control the low temperature mobility.

We patterned Hall bars along the [11-2] and [1-10] on the Bulk and Film samples to investigate the superconductivity in $KTaO_3$. Fig. 3a shows the R_{sq} vs. T data at $T < 2$ K along the [11-2]. The Film sample shows a $T_c \approx 1.5$ K, which is 25% higher than the $T_c \approx 1.2$ K exhibited by the Bulk sample. The V-I curves at $T = 0.5$ K (Fig. 3b) confirm the enhanced superconductivity in the Film sample with a critical current I_c (≈12.3 μA), substantially larger than I_c of the Bulk sample (≈3.9 μA) possessing the same n_{2D}. The R_{sq}-T, V-I data suggests that reduced disorder (*i.e.*, higher μ) eliminates signatures of disorder-induced inhomogeneities[41] observed in the superconductivity of $KTaO_3$ (111) such as anisotropic transport, residual resistance, and step-like V-I curves which appear to be highly sensitive to μ.

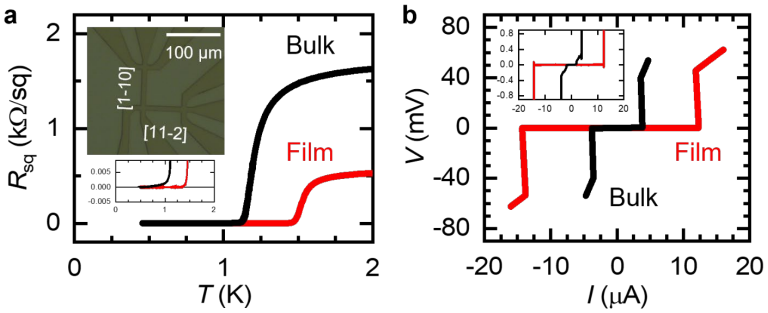

Fig. 3 | Superconductivity of $KTaO_3$ (111). a, Temperature dependence of R_{sq} along the [11-2] on Hall bars. The insets show an optical micrograph of Hall bars (top) and a magnified view near the transition (bottom). **b**, V-I curves along the [11-2] measured at $T = 0.5$ K on Hall bars. The inset shows a magnified view near the transition.

Future Plans

(1) Fabrication of freestanding membranes made of electronic-grade $KTaO_3$

We plan to fabricate freestanding membranes made of electronic-grade $KTaO_3$ (KTO) grown by hybrid PLD. We choose 001- and 111-orientations as the model systems to examine the complex interplay of dynamic (or static) strain, dimensionality, and doping. Our findings will have implications on the understanding of i) the detailed processes through which superconductivity emerges in the KTO system, ii) the interplay of ferroelectricity, spin-orbit coupling, and superconductivity and the resulting phase diagrams, and iii) novel applications derived from therein. This task will be achieved by employing a judiciously chosen composition of sacrificial and reaction barrier layers, namely $0.15Ba_3Al_2O_6$-$0.85Sr_3Al_2O_6$ (BSAO) (BSAO) and $0.3BaZrO_3$-$0.7SrTiO_3$ (BSZT), during the growth of $KTaO_3$ (001) and (111) heterostructures.

(2) Nonreciprocal transport in BPBO (Diode effects and Spin Orbit Torque),

Our observation of giant spin-orbit torque (SOT) in the normal state of $BaPb_{1-x}Bi_xO_3$ (BPBO), a known superconductor, demonstrated its potential for spintronics and hinted at a hidden spin-orbit coupling (SOC). But a triplet superconducting state must be induced for superconducting BPBO to produce a net torque which could be accomplished with a ferromagnetic interface. Such interfaces, as well as unit cell-level distortions can lead to nonreciprocal responses, which we will investigate through spin orbit torque and superconducting diode effects in which current in one direction shows no voltage drop, while current in the opposite direction (opposite polarity) shows a finite, non-zero voltage[2]. We intend to extract the nonlinearities from sensitive IV curves, as we did in our previous work. Our plan for next year is to isolate the detailed nonreciprocal transport dependencies on BPBO. The current results are a convolution of superconducting diode effects in the longitudinal resistance and torque driven dependence on the anomalous Hall effect. We first intend to evaluate any superconducting diode effects in isolated BPBO thin films.

Publications (which acknowledge DOE support)

1. Kitae Eom, Muqing Yu, Jinsol Seo, Dengyu Yang, Hyungwoo Lee, Jung-Woo Lee, Patric Irvin, Sang Ho Oh, Jeremy Levy, Chang-Beom Eom, "Electronically reconfigurable complex-oxide heterostructure free-standing membranes" *Science Advances*, **7**, eabh1284 (2021) https://doi.org/10.1126/sciadv.abh1284
2. S. Ryu, H. Zhou, T. R. Paudel, N. Campbell, J. Podkaminer, C. W. Bark, T. Hernandez, D. D. Fong, Y. Zhang, L. Xie, X. Q. Pan, E. Y. Tsymbal, M. S. Rzchowski, and C. B. Eom "Electronic reconstruction at the polar (111)-oriented oxide interface", accepted for publication in *APL Materials* (2022) https://arxiv.org/abs/2110.02305
3. Kitae Eom, Hanjong Paik, Jinsol Seo, Neil Campbell, Evgeny Y. Tsymbal, Sang Ho Oh, Mark Rzchowski, Darrell G. Schlom, and Chang-Beom Eom, "Oxide two-dimensional electron gas with high mobility at room-temperature" *Advanced Science,* 2105652 (2022). https://doi.org/10.1002/advs.202105652
4. Megan Briggeman, Hyungwoo Lee, Jung-Woo Lee, Kitae Eom, François Damanet, Elliott Mansfield, Jianan Li, Mengchen Huang, Andrew J. Daley, Chang-Beom Eom, Patrick Irvin and Jeremy Levy, "One-dimensional Kronig–Penney superlattices at the $LaAlO_3/SrTiO_3$ interface" *Nature Physics*, **17**, 782 (2021). https://doi.org/10.1038/s41567-021-01217-z
5. Lu Guo, Shun-Li Shang, Neil Campbell, Mark Rzchowski, Zi-Kui Liu, and Chang-Beom Eom, "Searching for a route to *in situ* synthesis of epitaxial $Pr_2Ir_2O_7$ thin films guided by thermodynamic calculations" *npj Computational Materials*, **7**, 144 (2021) https://doi.org/10.1038/s41524-021-00610-9
6. J.H. Kang, Philip J. Ryan, Jong-Woo Kim, Jonathon Schad, Jacob P. Podkaminer, Neil Campbell, Joseph Suttle, Tae Heon Kim, Liang Luo, Di Cheng, Yesusa G. Collantes, Eric E. Hellstrom, Jigang Wang, Robert McDermott, Mark S. Rzchowski, and Chang-Beom Eom, "Local Atomic Configuration Control of Superconductivity in the Undoped Pnictide Parent Compound $BaFe_2As_2$" *ACS Appl. Electron. Mater.* **4**, 1511 (2022) https://doi.org/10.1021/acsaelm.2c00291
7. S. Lindemann, J. Irwin, G.-Y. Kim, B. Wang, K. Eom, J. J. Wang, J. M. Hu, L. Q. Chen, S. Y. Choi, C. B. Eom, M. S. Rzchowski, "Low-Voltage Magnetoelectric Coupling in Membrane Heterostructures" *Science Advances* **7,** eabh2294 (2021) https://doi.org/10.1126/sciadv.abh2294
8. "Quantum Coherence Tomography of Lightwave–Controlled Superconductivity" L. Luo, M. Mootz1, J. H. Kang, C. Huang, K. Eom, J. W. Lee, C. Vaswani, Y. G. Collantes, E. E. Hellstrom, I. E. Perakis, C. B. Eom and J. Wang, *Nature Physics*, (2022) https://doi.org/10.1038/s41567-022-01827-1
9. C. Vaswani, J. H. Kang, M. Mootz, L. Luo, X. Yang, C. Sundahl, D. Cheng, C. Huang, R. H. J. Kim, Z. Liu, Y. G. Collantes, E. E. Hellstrom, I. E. Perakis, C. B. Eom & J. Wang, "Light quantum control of persisting Higgs modes in iron-based superconductors" *Nat. Commun.* **12**, 258 (2021). https://doi.org/10.1038/s41467-020-20350-6
10. Michael Patton, Gautam Gurun, Ding-Fu Shao, Gahee Noh, Joseph A. Mittelstaedt, Marcel Mazur, Jong-Woo Kim, Philip J. Ryan, Evgeny Y. Tsymbal, Si-Young Choi, Daniel C. Ralph, Mark S. Rzchowski, Tianxiang Nan, Chang-Beom Eom, "Symmetry Control of Unconventional Spin-Orbit Torques in IrO_2", *Advanced Materials*, ***in press*** (2023)

Formulation Engineering of Energy Materials via Multiscale Learning Spirals

PI: **Lara A. Estroff**, Cornell University; co-PIs: **Josh J. Choi**, University of Virginia; **Paulette Clancy** and **Rigoberto Hernandez**, Johns Hopkins University; **John Marohn**, Cornell University; **Rebecca Lindsey**, U Michigan; **David Moore**, NREL; and **Jinhui Tao**, PNNL

Keywords: Crystallization, Bayesian Optimization, Atomic Force Microscopy, Electric Force Microscopy, Machine Learning Models

Research Scope

SPIRAL (**S**cience & **P**rocessing **I**nformed by **R**ational **A**lgorithmic **L**earning) aims to provide a blueprint for accelerate the optimization of the formulation and manufacturing of solution-processed crystalline materials for energy applications. Solution processing represents a major opportunity to reduce cost and increase throughput of device fabrication, but the compositional and processing complexity is overwhelming. Our premise is that the fabrication of device-quality materials can be achieved through a comprehensive understanding of, first, how these materials grow and, second, the impact of growth pathways on materials properties, device performance, and reproducibility. We are applying new and existing machine learning (ML) tools to accelerate the optimization of solution-processed, solid-state energy materials. Our strategy eschews end-to-end black-box optimization and, instead, views the process from reagents to devices as a set of three interrelated "learning spirals" that are iteratively improved towards target objectives: ***Learning Spiral #1***: Deciphering the crystallization pathways as a function of solution chemistry, processing variables, and substrate; ***Learning Spiral #2***: Designing materials with tailor-made electronic and ionic conductivities; and ***Learning Spiral #3***: Designing efficient, stable, reproducible, and scalable devices. To test our proposed design process, we have chosen metal halide perovskites (MHPs) including their 2D, Ruddlesden-Popper phases. Our objectives are: 1) design functional MHP electronic materials using multiscale modeling and active ML integrated with experiment, bridging 10 to 15 orders of magnitude in space and time; 2) learn new connections between materials formulations and processing conditions and crystallization pathways using on-the-fly ML techniques as a means to yield thin film materials with desired structures and electronic/ionic properties; and 3) develop new data-science tools by leveraging our domain data, thereby better interrogating metadata to yield user-defined optoelectronic properties and device performance. We will integrate the resulting knowledge and tools into a more directed synthesis and formulation process that will tame the otherwise daunting compositional and processing complexity of MHP materials and devices. The spiral feedback process and the ML tools we are developing are broadly applicable, in principle, to any solution-processed materials. This work will accelerate the adoption of renewable energy systems through the development of stable and reproducible devices from low-cost, high-throughput, solution processes using earth-abundant components.

Recent Progress. In data science methods development, we have extended our previous Physical Analytics pipeLine (PAL) to allow it to search for the best correlations of physico-chemical properties that match a given target property, and we have formulated nested autoencoders aimed at addressing multiscale molecular, materials and devices properties. In Spiral 1, we have made progress towards linking solution speciation to aspects of crystal nucleation and growth. In Spiral 2, we have laid the groundwork for increasing throughput of the vacuum electric force microscope for MHP analysis. Finally, in Spiral 3 we have demonstrated reliable perovskite solar cell manufacturing based on an automated gas quenching process.

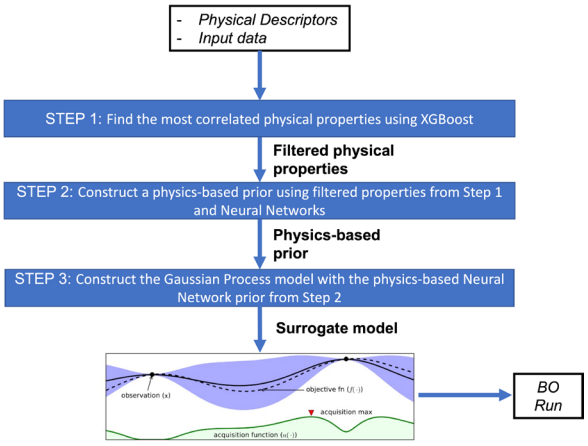

Fig. 1. Workflow for the Bayesian optimization code, PAL 2.0.

Data Science Methods Development. We have developed a new physics-informed Bayesian optimization (BO) algorithm, PAL 2.0 (Fig. 1). We tested its robustness and transferability for systems of carbon dots (for LEDs) and thermoelectric materials, and for solvent selection to solubilize lead salts and the role of the organic cation in crystallization.[1] Our models generally outperform other BO approaches. PAL 2.0 predicts which combination of physically relevant properties, with quantitative weights between properties, shows the best correlation with the test function. We have a *predictive* surrogate model that allows us to use the same models for optimization in different situations. It can be used to test hypotheses and hence provide information about the chemistry of the materials system. This is a unique capability amongst competing BO algorithms and is a hugely exciting avenue for us to explore in the coming year.

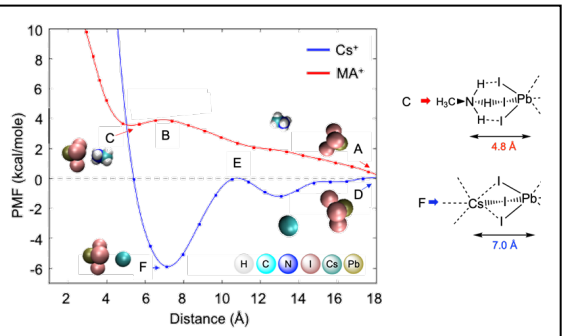

Fig. 2: The potential of mean force (PMF) shows that solvated MA^+ (point A) has a high barrier (B) to approach PbI_3^- because partial desolvation of H-bonded MA^+ is required to form an adduct (C). Solvated Cs^+ (D) has a low barrier (E) to approach PbI_3^-, benefitting from weak solvation energetics, to form an adduct (F). Energies for coordination of MA^+ or Cs^+ with PbI_3^- show the latter to be more stable by ~9 kcal/mole in DMF.

We have also developed nested autoencoders (nestedAEs) using artificial neural networks (ANNs) coupled at multiple scales with inputs from the latent spaces of lower scales entering as features in ANNs at higher scales.[2] We have demonstrated the efficacy of nestedAEs using synthetic and established databases as a proof of concept. In parallel, we are developing a database

with multiple-scale features and labels for MHPs taking advantage of additional observables that are selected according to gaps uncovered in the nestedAE optimization.

Cesium-Iodoplumbate Complexation in Solution Has Implications for Perovskite Crystallization: Cs salts are known to beneficially affect crystallization of the desired phase of the perovskite and can result in A-site incorporation in "triple cation" materials. Critically missing is both an analysis of the role that Cs plays in solution compared to other commonly used cations, methylammonium (MA) and formamadinium (FA). While we can assess H-bonding of MA or FA with Pb-I complexes in solution, envisioning analogous ones for Cs is more subtle. We have identified the role of Cs as a key player in formation of solvated Pb-I species that will eventually become 'perovskite' nuclei.[3] This involved the DFT, *ab initio* molecular dynamics, and MD simulations to capture the impact of the A-site cation and solvent interactions on the formation of PbI_3-A species (Fig. 2). Experimental (NMR) and computational results revealed that organic cations like MA and FA prefer to interact with the solvent (e.g., DMF), which may hinder the formation of these species. Conversely, Cs does not interact as strongly with the solvent and is allowed to interact with PbI_3^- to more readily form A-PbI_3.

Thermodynamic and Kinetic Modulation of Methylammonium Lead Bromide Crystallization. We have performed the first *in situ* AFM growth study of MHPs, which provides quantitative information on the kinetics of $MAPbBr_3$ growth on steps produced by screw dislocation spirals.[4] By tuning the temperature to change solution supersaturation, we observe growth hillocks on the {100} facet and track the growth/dissolution dynamics in the spiral growth regime. Temperature-dependent step velocity measurements demonstrate that increasing concentration of formic acid (FoA) decreases both the solubility of $MAPbBr_3$ and the kinetic coefficient (b) of step movement. Moreover, solution ^{1}H-NMR measurements show that the tumbling motion of the MA ions is inhibited by FoA. Our findings establish a direct correlation between the mesoscale crystal growth kinetics and the molecular-scale interactions between organic additives and constituent ions, providing unprecedented insights for developing predictive syntheses of MHP crystals.

Design of New Microscopy Probe Head for Electric Force Microscope. We increased microscope throughput from 1-2 to an estimated 6-9 samples/day by: (1) adding a second turbomolecular pump; (2) adding a large-range translation stage and probe mounted camera; and (3) inventing a new microscope probe head (Fig. 3) with a 1600x lower noise, (50 fm)^2/Hz. This new stage enables fast cantilever exchange, rapid manual alignment of the cantilever to a fiber-optic interferometer, and rapid piezoelectric optimization of the fiber/cantilever spacing. The

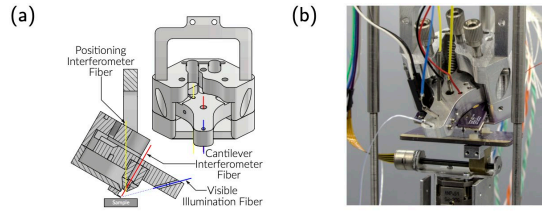

Fig. 3. An electric force microscope with dramatically improved throughput, sensitivity, and stability. (a) Schematic of the microscope's 1.75-inch-wide scanning probe head. (b) Photograph showing probe head atop a sample, sample-swapping translation platform, and scanning stage.

probe head includes a downward- pointing optical-fiber for feedback stabilization of tip-sample separation, improving stability and reproducibility.

Improved Reproducibility of Metal Halide Perovskite Solar Cells. We have demonstrated an automated gas quenching (GQ) system to improve perovskite solar cell reproducibility at the lab-scale.[5] We used *in-situ* photoluminescence (PL) to monitor perovskite film formation as a function of glove box atmosphere and conclude that antisolvent quenching is more sensitive to lingering precursor solvents than the GQ method. We observed better reproducibility with GQ than antisolvent quenching because it maintains a more consistent atmosphere in the glove box. The automated GQ process leads to high-performing devices, reproducible both batch-to-batch and researcher-to-researcher. Insights into GQ film formation as a function of solvent atmosphere and quench velocity will inform future studies on large scale fabrication systems.

Future Plans. Learning Spiral 1 will tackle the self-assembly of metal halide perovskites in solution into critically sized nuclei. We will use PAL 2.0 to search for the strongest binding $MAPbI_3$ and $CsPbI_3$ "oligomers" and then use *ab initio* Molecular Dynamics to determine the optimal configuration and electronic properties (e.g., density of states) for these important organic and inorganic cation iodoplumbates. This work will be complemented by experimental measurements of solution speciation. We will extend the *in situ* AFM experiments to mixed A-site and X-site MHPs and use the resulting crystallization metrics with the BO to target formulations with specific properties. Learning Spiral 2 will develop higher throughput vacuum electric force microscopy capabilities to analyze MHP samples: 1) measuring conductivity vs. halide ratio in $CsPb(I_xBr_{1-x})_3$ in the dark and under illumination – a first systematic study probing the dependence of total conductivity on stoichiometry; 2) developing methods to quantify local sample conductivity and dielectric constant; 3) estimating activation energies for the recombination of photo-generated vacancies; and 4) measuring transient electronic conductivity in MHPs using phase-kick electric force microscopy. Learning Spiral 3 will demonstrate the use of nestedAEs to optimize the selection of measurable properties of MHP across scales and accelerate the selection of next-generation materials and processes. The nestedAEs will learn from data sets (e.g., SEMs, X-ray scattering patterns, AFM images, UV/Vis spectra, etc.) added to our multi-scale perovskite database. Use of reinforcement learning and nested AEs will help select features from this database through a 'spiral feedback.'

References: 1) M.S. Priyadarshini, O.V. Romiluyi, Y. Wang, K. Miskin, P. Clancy, *A new approach to incorporate physical domain knowledge for Bayesian optimization searches in high-dimensional chemical materials system*, to be submitted. 2) N. Thota, M. S. Priyadarshini, R. Hernandez, *Bridging Molecular and Material Scales Using Nested Autoencoders*, to be submitted 3) Y. Eatmon*, O.V. Romiluyi*, C. Ganley, R. Ni, I. Pelczer, P. Clancy, B. Rand, J. Schwartz, *Untying the Cesium "Not:" Cesium- Iodoplumbate Complexation in Solution Has Implications for Perovskite Crystallization*, J. Phys Chem Lett, **13**, 6130, (2022). 4) A. Ortoll-Bloch, Y. Chen, N.M. Washton, K.T. Mueller, J.J. De Yoreo, J. Tao, L.A. Estroff, *"Thermodynamic and kinetic modulation of methylammonium lead bromide crystallization revealed by in situ monitoring",* to be submitted. 5) S.C. Kaczaral, D.A. Morales Jr., S.W. Schreiber, D. Martinez, A.M. Conley, R. Herath, G.E. Eperon, J.J. Choi, M.D. McGehee, D.T. Moore, *Improved*

Reproducibility of Metal Halide Perovskite Solar Cells via Automated Gas Quenching, ACS Applied Materials and Interfaces, in revision.

Publications Supported by BES 2021-2023

1. Y. Eatmon*, O.V. Romiluyi*, C. Ganley, R. Ni, I. Pelczer, **P. Clancy**, B. Rand, J. Schwartz, *Untying the Cesium "Not:" Cesium- Iodoplumbate Complexation in Solution Has Implications for Perovskite Crystallization*, J. Phys Chem Lett, **13**, 6130, (2022)

2. S. C. Kaczaral, D. A. Morales Jr., S. W. Schreiber, D. Martinez, A. M. Conley, R. Herath, G. E. Eperon, **J. J. Choi**, M. D. McGehee, **D. T. Moore**, *Improved Reproducibility of Metal Halide Perovskite Solar Cells via Automated Gas Quenching*, ACS Applied Materials and Interfaces, in revision (2023).

Radiolytic Redox Interplay Defines E-Beam Direct-Writing of Nanomaterials in Liquids

Andrei G. Fedorov, School of Mechanical Engineering, Georgia Tech, Atlanta, GA 30332

Keywords: Additive Nanomanufacturing; Atomic Scale Control.

Research Scope

Synthesis of topologically-complex and functionally-endowed 3D nano/meso/micro-structures is of great practical importance in the field of nanosciences and engineering, leading to transformative opportunities and new methods of materials synthesis and manufacturing. The emerging technology of Focused Electron Beam-Induced Processing (FEBIP), including Deposition (FEBID) and Etching (FEBIE) processes, provides an opportunity to create such structures with control of shape and phase as well as chemical composition (**Fig. 1**). In the past, it has been demonstrated that directing appropriate energy electrons to a deposition location can lead to a wide range of chemical and phase change processes. While FEBIP is a promising route to atom-by-atom growth of complex 3D structures, its utility has been constrained by slow growth rates (largely due to low precursor density), a limited selection of precursors, and structural heterogeneity/ porosity along with a lack of control over topology. As we discussed in a recent review, electron/ion-beam based deposition methods have the potential for full control of structure atomic arrangement and bonding in three dimensions (**Fig. 2**); yet the practical realization of this tantalizing possibility has been elusive, with only

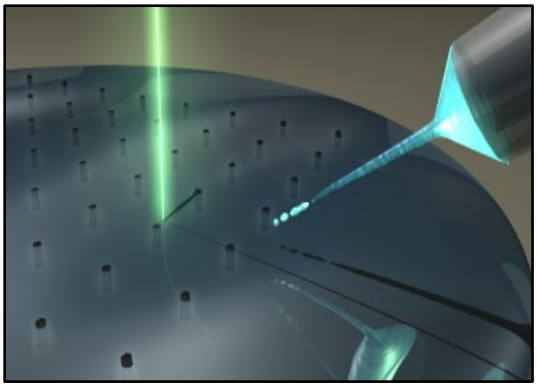

Fig. 1: Schematic of FEBIP, involving nanoelectrospray delivery of electrically energized liquid phase precursor to the substrate where it interacts with an e-beam, resulting in the formation of nanoscale deposits.

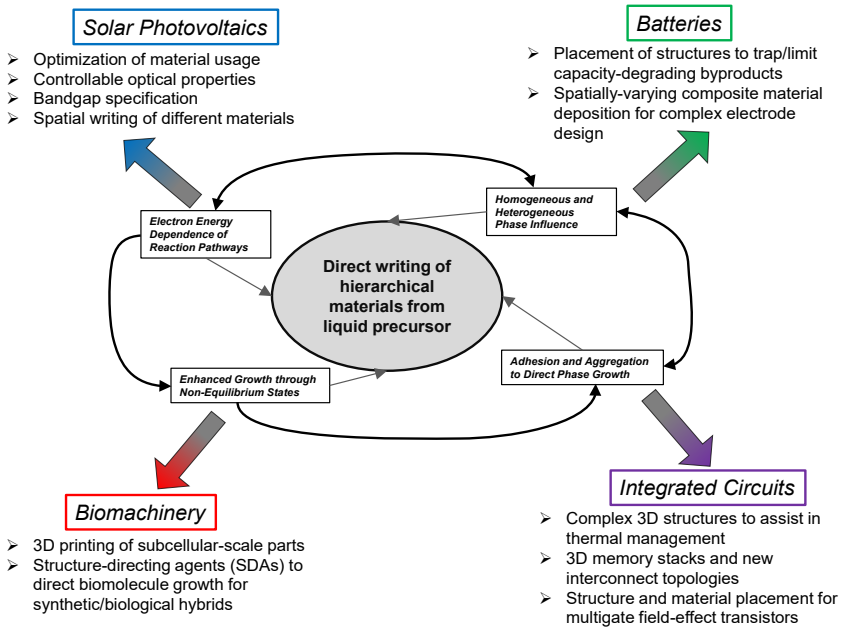

Fig. 2: Research questions that should result in establishment of the scientific foundation for FEBIP as a powerful tool for "direct write" nanofabrication of hierarchical materials with impact on a broad range of important applications.

limited success confined to gas-phase precursors. [1] With DOE BES support, we have pioneered a family of multi-mode energized micro/nano-jet techniques as a method of local precursor delivery in an excited state, which aims to resolve both fundamental process control issues and to expand the range of useful precursors for FEBIP. [2-5] Out-of-equilibria states for material nucleation and growth are established via thermally energized gas modulation of adatoms and electrokinetic separation of ionic precursors in liquid phase. Our ongoing program focuses on establishing a fundamental understanding of nanomaterials and meso-scale materials created from the electrically-energized liquid phase precursors under far from equilibrium conditions. In this work, we present fundamental advances on these two new methods, facilitated by the use of electrospray nano-jets and supersonic gas micro-jets, we pioneered for delivery of energized precursor molecules into a vacuum environment of the FEBIP chamber. The results of complementary experiments and multiscale modeling on high intensity thermal and electric field gradients associated with the energized multiphase jet delivery are presented leading to discovery of fundamental mechanisms of electron-precursor interactions and transport in the course of material synthesis with implications to FEBIP deposit growth rate, topology, phase and compositional purity. Energized micro/nano-jets provide unique capabilities for excitation of the far-from-equilibrium precursor-to-substrate molecular interactions, thus establishing a locally controlled deposition/etching/doping site for focused electron-beam induced processing (FEBIP). Not only does this expands FEBIP to a wider range of precursor materials and new phases of synthesized nanomaterials, but also affords tuning of sticking coefficients and adsorption/desorption activation energies of participating molecules to controlling the deposition chemistry. The latter is especially critical for FEBIP on substrates which are sensitive to doping, such as graphene and other 2D materials, whose electronic properties change by adsorption of different molecules. [1]

Recent Progress

Significant advances have been made towards the project goals in the areas of (1) determination of the role of solvent mediated redox chemistry in deposition control, and (2) spray-induced gas jet formation for film morphology manipulation. In the first area, Nano Electrospray Assisted Focused Electron beam Induced Deposition (NESA-FEBID) experiments and simulations have been employed to analyze the use of water-ammonia as an

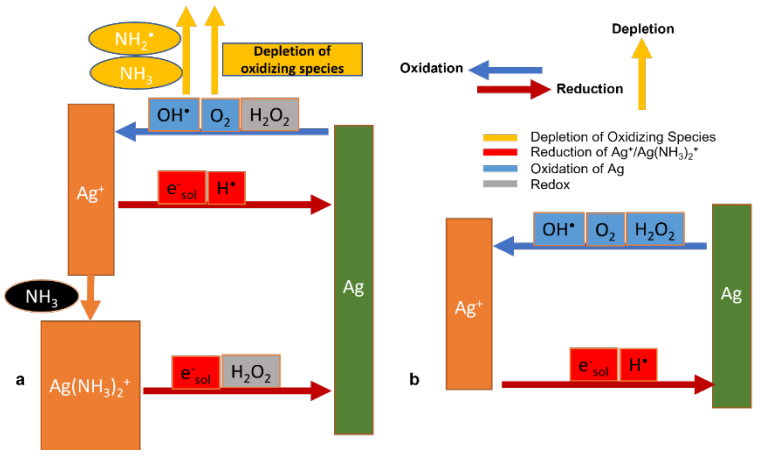

Fig. 3: Important radiolysis products and their roles as oxidizing and reducing species involved in Ag deposition from an $AgNO_3$ precursor in (a) water-ammonia vs (b) pure water solvents. In the presence of NH_3, Ag^+ ions can form the diamine silver complex, enabling additional reduction pathways. The role of H_2O_2 is altered from purely oxidizing in water to both oxidizing Ag and reducing in water-ammonia. Furthermore, reactions with NH_3 and $NH_2^{\bullet}$ deplete O_2 and $OH^{\bullet}$ suppressing the oxidation rate of Ag.

agent focusing on growth of silver nanostructures from dissolved silver nitrate precursor at the desired location (beam impingement point), while suppressing off-target parasitic deposition. Large ammonia concentrations (~30%) increase the growth rate of both desired and off-target parasitic deposits by creating a highly reducing environment over a large area within the precursor film, while lower concentrations (<1%) suppress the creation of off-target deposits by increasing the concentration of oxidizing species outside the e-beam impingement region without sacrificing localized growth at the target site. We have identified a range of ammonia concentrations which supports formation of high aspect ratio deposits and have elucidated the chemistry that yields high growth rates at the desired location while suppressing off-target growth (**Fig. 3**). In the second area, the induced gas jet structure, strength, and controlling parameters for effective gas jet formation have been determined as they are critical to achieve control of precursor-loaded dispersed liquid phase and film formation. Gas jets of 10s of m/s can be formed by nano-electrospray in the presence of sufficient surrounding gas. These jets weaken quickly beyond ~ 1mm from the spray emitter. The most effective method to increase gas jet strength is through reduction of droplet size (vs increasing the electric field).

Higher ammonia concentrations lead to a high growth rate of deposits due to a highly reducing environment resulting from the addition of a reducing pathway via H_2O_2 and depletion of oxidizing species. Figure 4 shows the topological details (obtained with AFM) of selected deposits created in these experiments. These results provide greater information about deposit resolution than the SEM images (from which height data is difficult to accurately extract) which is presented in terms of aspect ratio, defined as the ratio of pillar height to half width (**Fig. 4 f**). There is an increase in aspect ratios of the deposits as the initial concentration of ammonia decreases from 30% to 15%. At the highest concentrations of ammonia, the growth rate is very high due to the highly reducing environment within the entire liquid film, leading to significant off-target peripheral deposition. On the other hand, at a lower range of ammonia concentrations, the high growth rate is localized to the center of domain while the growth rate further away is suppressed due lower rate of reduction and higher rate of oxidation as ammonia concentration

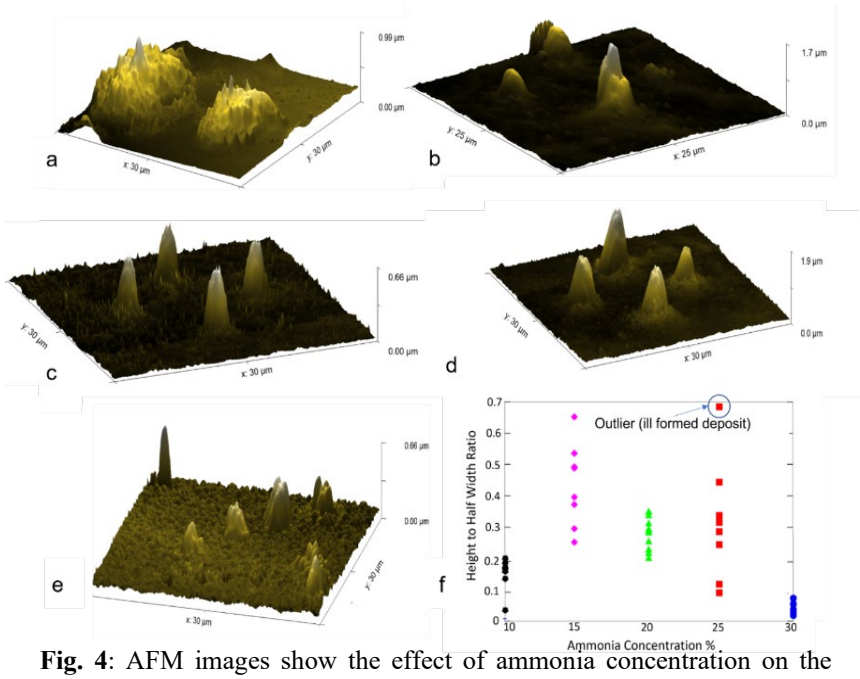

Fig. 4: AFM images show the effect of ammonia concentration on the quality of deposits created using 100µmol/L $AgNO_3$ in water-ammonia with concentrations of (a) 30%, (b) 25%, (c) 20%, (d) 15% and (e) 10%. All deposits are created by irradiation with a 30kV e-beam.

reduces. This leads to higher aspect ratios and hence higher resolution deposits. However, there is a limit to the benefit obtained from ammonia concentration reduction. The aspect ratio falls when the concentration is reduced from 15% to 10%, due to reduced growth rates at the beam impingement site. Simulations of coupled precursor species transport, electrochemical reactions, and electron beam radiolytic interactions with the liquid precursor provide an explanation of the dynamic behavior observed in experiments (**Fig. 5**). Both simulation and experiments lead to the conclusion that at lower concentrations, ammonia acts as a "chemical lens" to focus desired electrochemistry at the electron beam impingement site only, thus enabling the promise of the extreme deposit resolution of FEBIP.

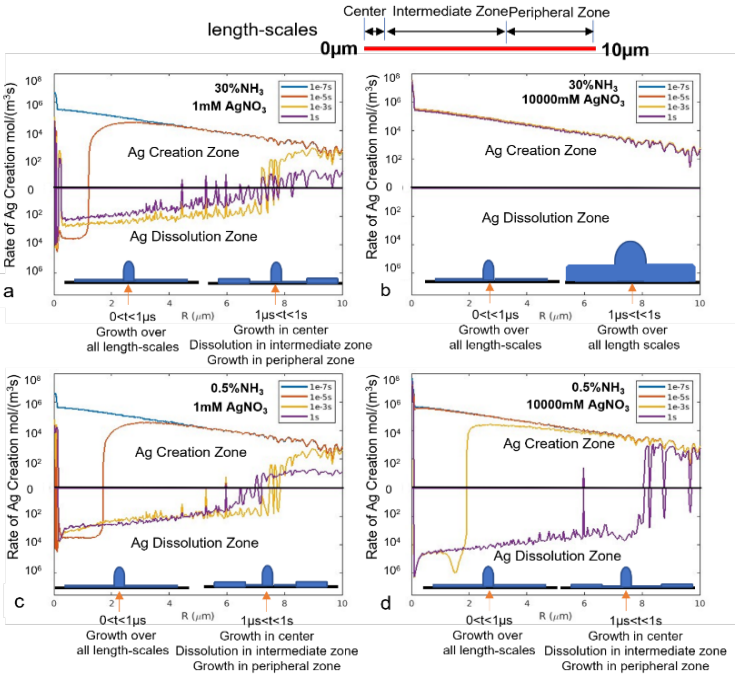

Fig. 5: The predicted spatial distribution of the net Ag creation rate on the e-beam irradiated substrate shown at different times.

Future Plans

Future work will focus on: (1) discovery of the reaction and growth pathways, resulting in formation of pure metal nanostructures with unique phases and crystalline structures by NESA-FEBIP from liquid-phase precursors under an influence of a strong local electric field; (2) discovery of new processing capabilities and fundamental understanding for the formation of nanostructures via e-beam activated droplet-to-deposit (D2D) FEBIP mode, and (3) establishment of experimentally-validated modeling framework for NESA-FEBIP enabled by controlled energy multi-phase precursor jets at a precisely controlled thermodynamic states.

References

1. Kim, S. and Fedorov, A.G., FEBIP for functional nanolithography of 2D nanomaterials, *Nanofabrication: Nanolithography Techniques & Their Applications*, J. M. De Teresa (Editor), Institute of Physics, UK, 2020.
2. Henry, M. and Fedorov, A. G., Adaptive simulations enable computational design of electron beam processing of nanomaterials with supersonic micro-jet precursor, *Computational Materials Science*, **186**, 109993 (2021).
3. Henry, M., Kim, S., and Fedorov A. G., Non-equilibrium adatom thermal state enables rapid nanomanufacturing, *Phys. Chem. Chem. Phys.,* **21**: 10449 (2019).
4. Fisher, J., Kottke, P. A., and Fedorov A. G., Synthesis of crystalline metal nanomonoliths by e-beam reduction of negatively-electrified jets, *Materials Today Physics*, **5**, 87-92 (2018). **Featured by Research Insights as 2018 influential contribution article.**

5. Fisher, J., Kottke, P. A., Kim, S., and Fedorov A. G., Rapid electron beam writing of topologically complex 3D nanostructures using liquid phase precursor, *Nano Lett.*, **15** (12), 8385–8391 (2015).

Publications

1. Kim, S. and Fedorov, A.G., FEBIP for functional nanolithography of 2D nanomaterials, *Nanofabrication: Nanolithography Techniques & Their Applications*, J. M. De Teresa (Editor), Institute of Physics, UK, 2020.
2. Kim, S., Jung, S., Lee, J., Kim, S., and Fedorov, A. G., High resolution three-dimensional sculpting of two-dimensional graphene oxide by e-beam direct write, *ACS Appl. Mater. Interfaces,* **12** (35), 39595-39601 (2020).
3. Henry, M. and Fedorov, A. G., Adaptive simulations enable computational design of electron beam processing of nanomaterials with supersonic micro-jet precursor, *Computational Materials Science*, **186**, 109993 (2021).
4. Ahmed, A., Boyle, E. C., Kottke, P. A., and Fedorov, A. G., Radiolytic redox interplay defines nanomaterial synthesis in liquids, *Science Advances*, **7** (51), 1-7 (2021).
5. Prabhakaran, V., Romo, J., Bhattarai, A., George, K., Norberg, Z. M., Kalb, D., Aprà, E., Kottke, P. A., Fedorov, A.G., El-Khoury, P.Z.., Johnson, G. E., and Laskin, J., Integrated photoelectrochemical energy storage cells prepared by benchtop ion soft-landing, *ChemComm - Journal of the Chemical Society D: Chemical Communication*, 58, 9060-9063 (2022). Inside Front Cover.
6. Chapman J. D., Kottke P. A., Fedorov, A. G., Droplet-gas interactions in nanoelectrospray multiphase flow, *International Journal of Multiphase Flow*, submitted (2023).
7. Chapman J. D., Kottke P. A., Fedorov, A. G., Thermodynamic analysis of nanoelectrospray induced gas jet, *International Journal of Multiphase Flow*, submitted (2023).
8. Fedorov, A. G., *"Systems and Methods for Electron Beam Induced Processing"*, U.S. Patent No. 11,583,875, Issued 02/2023.
9. Fedorov, A. G., Boyle, E. C., Ahmed, A., Kottke, P.A., *"Electron Beam Induced Deposition of Nanomaterials from Dispersed Liquid Precursors"*, US Patent Application (June 2023).
10. Wall Street Journal Front Page story "The Nanotechnology Revolution Is Here—We Just Haven't Noticed Yet" (*https://www.wsj.com/articles/the-nanotechnology-revolution-is-herewe-just-havent-noticed-yet-11642827640?redirect=amp*) and the WSJ print edition story 'The Next Miniature Marvels".

Science of Shape-Selective Nanocrystal Synthesis

Kristen A. Fichthorn

Dept. of Chemical Engineering; The Pennsylvania State University; University Park, PA 16802

Keywords: Metal nanocrystal, Molecular Dynamics, Monte Carlo, Density-Functional Theory

Research Scope

A significant challenge in the development of functional nanomaterials is understanding the growth and transformations of colloidal metal nanocrystals. From a practical perspective, a knowledge of how to selectively synthesize desired metal nanocrystal sizes and shapes would benefit numerous applications in energy technology, as well as enhance energy efficiency. For example, nanocrystal synthesis science is playing an increasingly prominent role in catalysis, solar-cell technologies, photothermic desalination based on plasmonic nanocrystals, wearable triboelectric generators, energy storage devices, and electrochromic smart windows. For these and many other applications, the science of shape-selective nanocrystal synthesis has been advancing at an increasingly rapid pace, with numerous recent reports on the synthesis of various beneficial nanocrystal morphologies. These and many more studies indicate that nanocrystal synthesis science will play an important role in achieving a sustainable energy future. Despite ample demonstrations that it can be highly beneficial to tune nanocrystal morphologies for specific applications and despite the tremendous strides made in nanocrystal synthesis science, it is still difficult to achieve high, selective yields in most synthesis protocols. Many fundamental aspects of these complex syntheses remain poorly understood and empiricism still runs rampant. This research targets three key gaps in the fundamental understanding of these syntheses:

1. Understanding the equilibrium structures and kinetics of fcc-metal nanocrystal seeds from an atomistic point of view using replica exchange molecular dynamics and hyperdynamics simulations.
2. Understanding the kinetics of crystal growth using kinetic Monte Carlo.
3. Understanding the structures of solid-liquid interfaces relevant for crystal growth using ab initio grand canonical Monte Carlo.

This work will help to move the field of nanostructure growth from its current empirical state to one that builds on the fundamentals of materials science and surface chemistry.

Recent Progress

In the current funding cycle, we focused on understanding minimum free-energy shapes of small nanocrystals using the parallel tempering variant of replica-exchange molecular dynamics (REMD), as well as partial REMD (PREMD) simulations of small (100-200 atoms) Ag, Cu, and Au nanocrystals described by embedded-atom method (EAM) potentials. We compared the temperature dependent structures of Ag nanocrystals in three different environments: vacuum, ethylene glycol (EG), and EG+PVP – a common solvent-capping agent combination in polyol synthesis of Ag nanostructures. We classified the structures of these crystals using common-neighbor analysis (CNA). **Figure 1** shows the characteristic shapes observed in our study, with the bulk atoms that distinguish them highlighted. Our studies yielded a veritable treasure trove of results, with one paper submitted, one to be submitted shortly, and one to hopefully be submitted by the end of the summer.

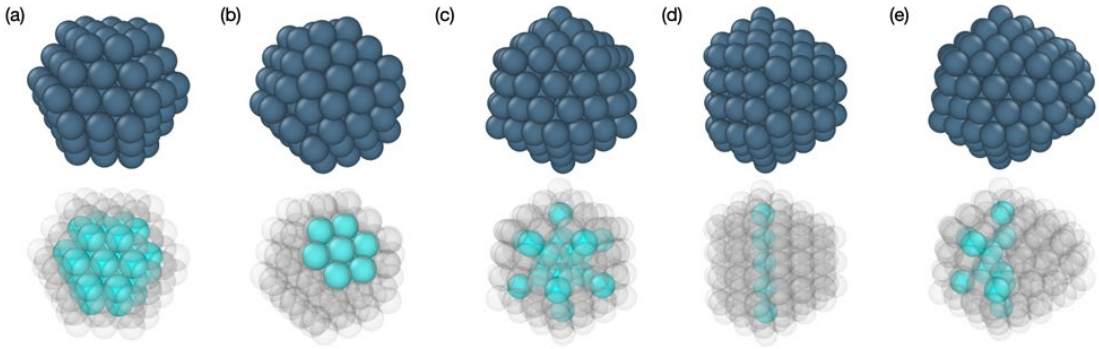

Figure 1. Representative structures of Ag clusters. (a) Single crystal (FCC), (b) single crystal with stacking faults (SCSF), (c) icosahedron (Ih), (d) decahedron (Dh), (e) structure having mixed features of both a decahedron and icosahedron (Dh-Ih). The top panel shows all the atoms as opaque and in the bottom panel, bulk atoms from characteristic environments from each shape are turquoise, while all other atoms are shown as semi-transparent.

Figure 2 shows shape fractions for Ag nanocrystals containing 100-200 atoms in each of the three environments at 450 K. The MD snapshots depict Ag nanocrystals in each environment. In vacuum, we saw dramatic changes in nanocrystal shapes with relatively small changes in size – for example, in nanocrystal sizes going from 116 to 117 atoms in vacuum, we see a mixture of SCSF, Ih, and Dh at 116 atoms, but almost all Dh at 117 atoms. However, we see more gradual shape changes in a solution environment because the shape changes are the result of energetically unfavorable surface atoms that are passivated in a solution environment.

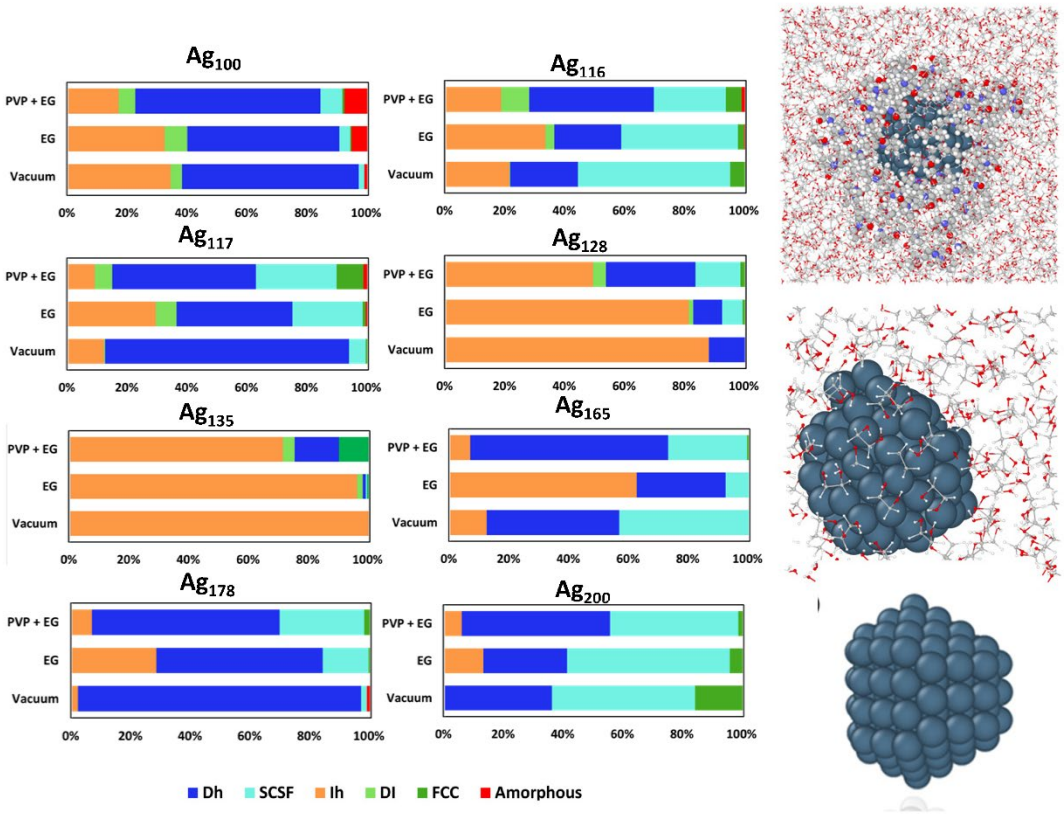

Figure 2. Fractions of characteristic shapes observed for Ag nanocrystals of different sizes in PVP+EG solution, EG solution, and vacuum at 450 K. The leftmost panel shows snapshots of Ag nanocrystals in each of the three environments.

Another trend that emerges when we compare the shapes of nanocrystals in EG and EG+PVP is that nanocrystals in EG+PVP exhibit a higher fraction of Dh than nanocrystals in EG for all sizes studied. This trend can be attributed to the higher binding energy of PVP to Ag(100) than to Ag(111), as Dh possess a non-negligible fraction of {100} surfaces and the expression of Dh morphologies is favored by surface energies. It is also evident that nanocrystals in EG exhibit a higher fraction of Ih than nanocrystals in EG+PVP for all sizes studied. This trend indicates that EG favors the {111} facets because perfect Ih are {111}-faceted. Though EG binds slightly stronger to Ag(100) than to Ag(111), MD simulations indicate that EG exhibits a tighter binding network on Ag(111) than Ag(100), so EG-EG interactions dominate at this interface. Thus, stronger EG-EG interactions on Ag(111) favor {111}-faceted Ih.

We also investigated the shapes of Cu nanocrystals in the 100-200 atom size range in vacuum. **Figure 3** shows phase diagrams on the small end of the size scale we investigated and highlights a new shape introduced by our group: the Dh-Ih.

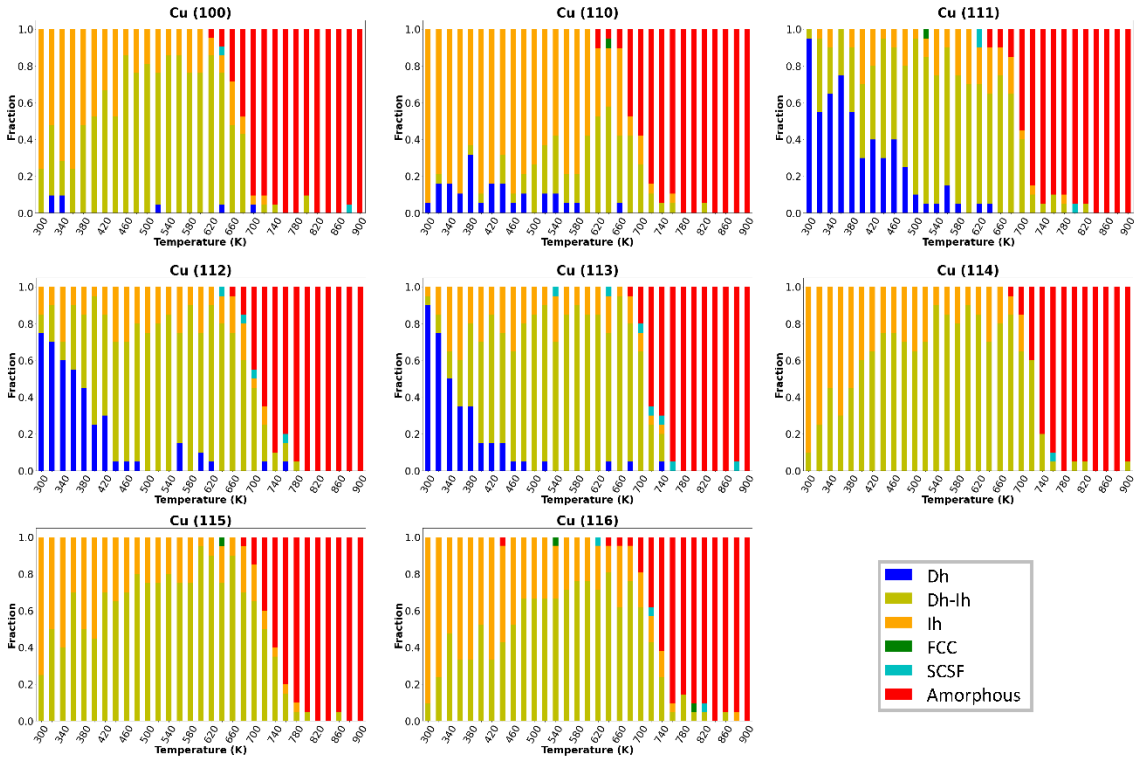

Figure 3. Phase diagrams of the fraction of shapes as a function of temperature for various sizes of Cu nanocrystals.

As shown in **Figure 1(e)**, the Dh-Ih is an intermediate structure between a Dh and an Ih. Only Ih have the so-called Ih center atom, but as shown in **Figure 1(c)**, they have a large fraction of Ih spine atoms. Dh clusters have no Ih center and they also have a single, linear axis consisting of Ih spine atoms. Dh-Ih have no Ih center and they have a collection of disordered Ih spine atoms. Though such species are a minority for Ag, they are abundant in Cu – especially for the small sizes. Associated with the Dh-Ih are many new atom types in CNA classification, which in prior studies would have led to classification of these structures at amorphous.

Future Plans

Many studies are in the works in our group. We are preforming REMD studies of Au nanoparticles using an EAM potential that appears to have the accuracy of much slower machine-learning potentials. Work on our kinetic Monte Carlo code for predicting kinetic nanocrystal shapes is well underway. Our studies of the kinetics of nanocrystal shape transitions using hyperdynamics simulations are yielding tantalizing results. Finally, work on ab initio grand-canonical Monte Carlo simulations is in full swing. Here, we are using the new capabilities of the VASP code to fit machine-learning potentials to DFT results to facilitate these simulations.

Publications

1. K. A. Fichthorn, Z. Chen, Z. Chen, R. M. Rioux, M. J. Kim, and B. J. Wiley **(Invited Feature Article)**, "Understanding the Solution-Phase Growth of Cu and Ag Nanowires and Nanocubes from First Principles", *Langmuir* **37**, 4419–4431 (2021).
2. T. Yan and K. A. Fichthorn, "Self-Assembly of a Linear Alkylamine Bilayer around a Cu Nanocrystal: Molecular Dynamics", *J. Phys. Chem. B* **125**, 4178-4186 (2021).
3. Z. Chen and K. A. Fichthorn, "Adsorption of Ethylenediamine on Cu Surfaces: Attributes of a Successful Capping Molecule Using First-Principles Calculations", *Nanoscale* **13**, 13529-13537 (2021).
4. Z. Chen and K. A. Fichthorn, "Adsorption of Alkylamines on Cu Surfaces: Identifying Ideal Capping Molecules Using First-Principles Calculations", *Nanoscale* **13**, 18536-18545 (2021).
5. J. Kim, J. Cui, and K. A. Fichthorn, "Solution-Phase Growth of Cu Nanowires with Aspect Ratios Greater than 1000: Multi-Scale Theory", *ACS Nano* **15**, 18279-18288 (2021).
6. J. Kim and K. A. Fichthorn, "The Influence of Iodide on the Solution-Phase Growth of Cu Microplates: A Multi-Scale Theoretical Analysis from First Principles", *Faraday Discussions* **235**, 273-288 (2022).
7. V. Mastronardi, J. Kim, M.Veronesi, T. Pomili, F. Berti, G. Udayan, R. Brescia, J. Diercks, J. Herranz, T. Bandiera, K. A. Fichthorn, P. Pompa, and M. Moglianetti,, "Green chemistry and first-principles theory enhance catalysis: Synthesis and 6-fold catalytic activity increase of sub-5 nm Pd and Pt@Pd nanocubes", *Nanoscale* **14**, 10155 (2022).
8. H. Xu, Z. Chen, S. Hao, K. A. Fichthorn, and B. J. Wiley, "Modulating the Facet-Selective Binding of PVP with Chloride to Control the Anisotropic Growth of Ag Nanocrystals", *Nanoscale* **15**, 5219-5229 (2023).
9. D. Li, Q. Chen, J. Chun, K. A. Fichthorn, J. De Yoreo, and H. Zheng, "Particle Assembly and Oriented Attachment: Controlling Factors and the Resulting Structures", *Chemical Reviews* **123**, 3127 (2023).
10. K. A. Fichthorn "Theory of Anisotropic Metal Nanostructures", *Chemical Reviews* **123**, 4146-4183 (2023).

Two-Dimensional Materials for Thin Film and Interface Manipulation in Solar Energy Conversion Devices

Nicolas Gaillard (PI),[1] Mitchel McLean, [1] Chad Junkermeier,[2] Ezekiel Domingo,[2] Clemens Heske (Co-PI),[3] Mary Blankenship,[3] Tadashi Ogitsu,[4] and Christopher Muzzillo.[5]

[1] University of Hawaii, Hawaii Natural Energy Institute.
[2] University of Hawaii, Department of Physics and Astronomy.

[3] University of Nevada Las Vegas, Department of Chemistry and Biochemistry.

[4] Lawrence Livermore National Laboratory
[5] National Renewable Energy Laboratory

Keywords: 2D materials, polycrystalline thin films, interface properties, photovoltaics.

Research Scope

The University of Hawaii (UH) and the University of Nevada, Las Vegas (UNLV) have partnered with the Lawrence Livermore National Laboratory (LLNL) and the National Renewable Energy Laboratory (NREL) to expand the concept of 2D material-assisted thin film exfoliation from III-V monocrystalline to polycrystalline materials, focusing on the chalcopyrite semiconductor class and transition metal dichalcogenides (TMDCs, e.g., MoS_2 and $MoSe_2$) 2D interfacial layers that can naturally form when sulfur- or selenium-containing semiconductors are deposited onto transition metal (TM) substrates. The overarching goal of the project is not only to discover 2D TMDCs that can facilitate exfoliation of a variety of polycrystalline materials, but also to tune the physical and chemical structures of 2D TMDCs to transfer a predetermined number of 2D layer(s) with the polycrystalline materials and thus create controllable and optimized interface energetics. We employ a *theory-synthesis-characterization feedback loop* based on a multi-disciplinary methodology that has been established and refined by over a decade of collaboration between theorists at LLNL, the synthesis groups at HNEI and NREL, and the characterization team at UNLV, to accelerate the developments of promising 2D TMDCs and advance the knowledge and ability to control properties in interface material science.

Recent Progress

As interfacial layers, 2D $MoSe_2$ in chalcopyrite technologies are an inevitable consequence of the integration process rather than a deliberate incorporation. Their benefit for chalcopyrite solid-state devices has been demonstrated many times.[1–3] However, controlling their properties, such as thickness, composition, defect chemistry or electronic properties, is rather complex. The primary motivation for year 1 was to study the chemical properties of the chalcopyrite / $MoSe_2$ interface to better understand how they impact energetics and the mechanical exfoliation process.

XPS analysis of the chalcopyrite/2D TDMC interface: During year 1, UNLV focused on the initial characterization of an exfoliated AZO/i-ZnO/CdS/Cu(In,Ga)Se_2/Mo/glass sample using lab-based XPS. The absorber films were fabricated at NREL using a three-stage growth process on a Mo back contact, which was DC-sputtered onto a soda lime glass substrate (SLG). A RbF post-deposition treatment (PDT), with an NH_3- and deionized (DI) water-based rinse were applied to the Cu(In,Ga)Se_2 (CIGSe) absorber. Afterwards, a CdS buffer layer was deposited onto the CIGSe

surface using chemical bath deposition, and i-ZnO/AZO window layers were RF-sputtered onto the thin film stack. A generic representation of the exfoliation process is presented in Figure 1. First, the CIGSe solar cell was bonded onto a SLG substrate using epoxy. Once bonded, the samples were placed in a nitrogen-filled glove box, and exfoliation was performed by inserting a razor blade cutting edge between the two SLG substrates until delamination at the CIGSe/$MoSe_2$ interface. Upon visual confirmation of successful exfoliation, both the "CIGSe back" and "Mo front" samples were sealed and shipped to UNLV for monochromated and non-monochromated XPS analysis.

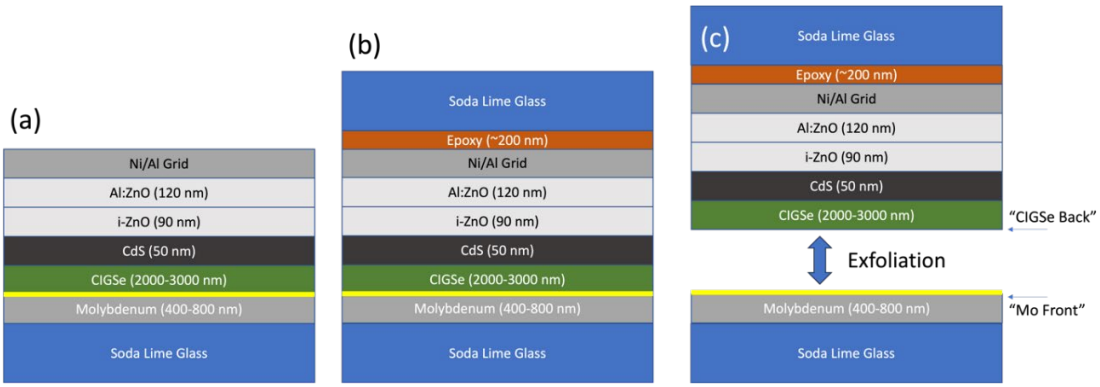

Figure 6. (a) The composition of a CIGSe cell as provided by NREL. Note the inherent $MoSe_2$ layer in yellow. (b) CIGSe cell bonded to a soda lime glass substrate with epoxy. (c) The CIGSe cell post-exfoliation, with the top stack exposing the CIGSe back surface, while the bottom stack exposes the Mo front surface.

An XPS survey spectrum for the Mo front surface, measured with a non-monochromatized Mg Kα x-ray source, is shown in Figure 2a. The most prominent photoelectron and Auger lines are labeled. The Mo front survey features strong molybdenum and selenium-related peaks. The survey spectrum also shows small signals of gallium and indium; however, no indication of copper-related peaks can be identified, implying that the entire CIGSe layer has been successfully transferred as a result of the exfoliation process. In addition, trace signals of F (1s) and Rb (3d) are also observed on the surface of the Mo front. Both oxygen- and carbon-related peaks are present in the spectrum, with much greater intensity of the C 1s peak. The intensity of the C 1s may give initial indication of a "C-rich layer" formation, as found in previous XPS studies of chalcopyrite and kesterite absorber/Mo interfaces.[4,5] An additional Al Kα survey measurement (not shown here) indicates that only trace amounts of Na are present at the surface of the Mo front.

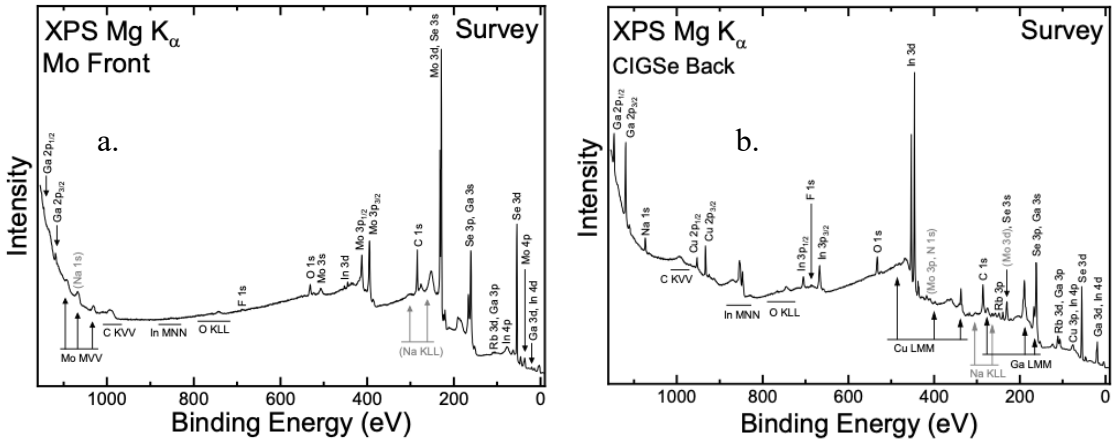

Figure 7. (a) Mg Kα XPS survey spectra of the Mo front surface cleaved at the CIGSe/Mo interface. (b) Mg K_α XPS survey spectra of the CIGSe back surface cleaved at the CIGSe/Mo interface.

Figure 2b shows a Mg Kα survey spectrum of the CIGSe back surface. The spectrum indicates high signals of indium and gallium, as well as selenium-related peaks and smaller signals of copper-related lines (as expected). There may be some trace signals of molybdenum-related peaks, however Mo 3d and Mo 3p lines are at similar energies as other CIGSe-related peaks, making it difficult to discern the true presence of molybdenum without additional detailed region measurements. There does appear to be higher intensity of Na 1s present at the CIGSe back than the Mo front, likely due to diffusion to that surface after exfoliation. Rb 3d and F 1s signals are also seen on the CIGSe back surface, with possible traces of a N 1s signal.

Raman study of exfoliated 2D TDMC layers from commercial bulk crystals: During year 1, the UH team learned 2D materials manipulation and characterization using commercially available samples. After discussion with experts in the field (including the Island group at UNLV), we decided to acquire graphite, $MoSe_2$ and MoS_2 bulk crystals from 2D Semiconductors. These samples were further processed using the mechanical exfoliation method described by Novoselov and Geim,[6] and regularly employed at the Island group, to yield single or few layers of graphene and TDMCs. Flakes of both types were delaminated from bulk seed crystals by stamping a transfer strip to them, followed by folding the tape on itself a predetermined amount of times to further delaminate the remaining crystals, then deposited on the polished side of (100) SSP 700 μm silicon wafers with a 1 μm SiO_2 layer. The resulting Raman microscopy analysis in Figure 3a shows regions where MoS_2 monolayers are expected to be present. Fringing effects around the edges of larger crystals can be seen as false-positive results, while isolated shaded regions are assumed to contain monolayer MoS_2.

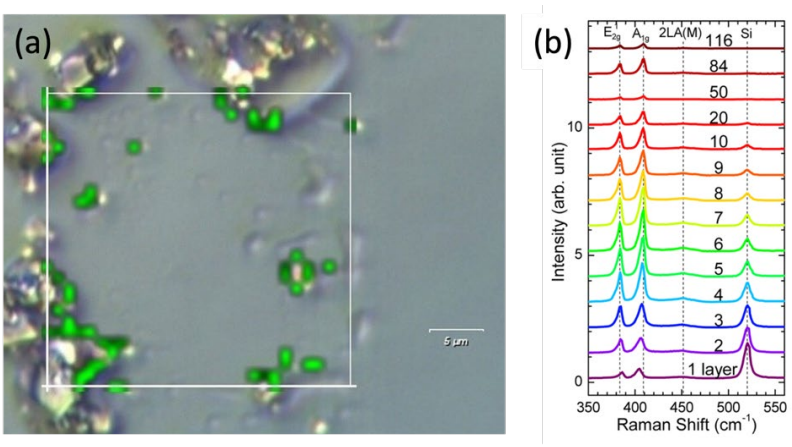

Figure 8. Raman and optical analysis of MoS_2 crystals on 15 mm x 15 mm Si/SiO_2 substrate. Note the small crystal lateral dimensions as a result of a high (60) exfoliation count. Crystals can be seen surrounded by adhesive. Areas shaded in green depict the presence of mono- and few-layer MoS_2 as detected by Raman analysis. (b) Raman spectra showing the E_{2g} and A_{1g} MoS_2 mode intensity relative to silicon peak intensity as a function of MoS_2 layer height. The relationship between the intensity peaks of MoS_2 and silicon can be used to determine the layer number. Adapted from Ref. [7].

A method to determine mono- and few-layer MoS_2 via Raman spectroscopy was adapted from the litterature.[7] Figure 3b shows the characterization of MoS_2 layer height by peak intensity. The method used to generate Figure 3a assumes that the intensity of the MoS_2 E^1_{2g} and A_{1g} peaks increase with single digit layer height, while the silicon peak at 520.5 cm^{-1} is reduced by having been covered by MoS_2. Following this, the ratio of MoS_2 peaks to silicon peak can be used to predict areas of interest. Using this methodology, analysis was performed on a single MoS_2 crystal to determine the number of layers present. Figure 4 shows the resulting Raman spectra for points on a crystal, which were then used to determine the number of MoS_2 layers at each point.

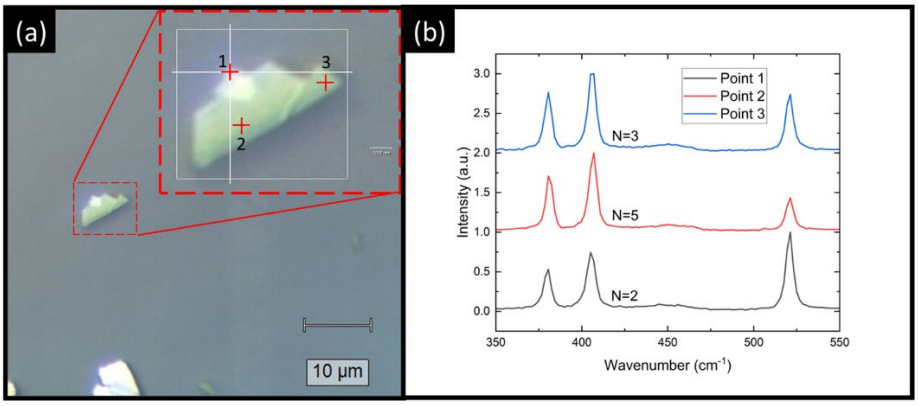

Figure 9. (a) An example MoS_2 crystal of variable thickness, with analysis points shown inset. (b) Raman spectra of the analysis points shown in (a). The ratio between MoS_2 and silicon peaks is used to determine the number of MoS_2 layers present.

Future Plans

Future work includes developing DFT-based models of strain-energy curves for 2D $MoSe_2$ systems, which will provide insight into the effects of localized strain on the optoelectronic properties of 2D $MoSe_2$. These models will be particularly important when 2D TDMCs will be interfaces with rough polycrystalline CIGSe layers. Refinements in Raman microscopy techniques with correlations provided by atomic force microscopy will be used to better characterize 2D materials by their layer number. The results will allow for larger-scale automated mapping of samples to identify areas of interest. Improvements in synthesis and exfoliation methods will be pursued to allow for interfacing 2D TMDCs with chalcopyrite absorbers to further study novel interface energetics. Further refinements in characterization techniques using XPS, ultraviolet photoemission spectroscopy (UPS), and inverse photoemission spectroscopy (IPES) will allow for detailed information on the chemical and electrical properties of the chalcopyrite/2D TMDC interface.

References

1. Sun,H.; Li,P.; Xue,Y.; *et al. Optoelectron. Lett.* **15**, 428 (2019).
2. Hsiao,K. J.; Liu,J. Da; Hsieh,H. H.; *et al. Phys. Chem. Chem. Phys.* **15**, 18174 (2013).
3. Al-Thani,H. A.; Hasoon,F. S.; Young,M.; *et al.* in *Conf. Rec. IEEE Photovolt. Spec. Conf.* 720 (2002). doi:10.1109/pvsc.2002.1190666
4. Hauschild,D.; Wachs,S. J.; Kogler,W.; *et al. IEEE J. Photovoltaics* **11**, 658 (2021).
5. Weinhardt,L.; Blum,M.; Bär,M.; *et al. Thin Solid Films* **515**, 6119 (2007).
6. K. S. Novoselov et al. *Science (80-.).* **306**, 666 (2004).
7. Li,S. L.; Miyazaki,H.; Song,H.; *et al. ACS Nano* **6**, 7381 (2012).

A Unified Model for Epitaxy of Metastable Crystal Polytypes at the Nanoscale

Rachel S. Goldman and Liang Qi, University of Michigan; Judith C. Yang, University of Pittsburgh and Brookhaven National Laboratory

Keywords: crystal, epitaxy, polytype, nanoscale**,** nitride

Research Scope

It has been hypothesized that metastable nanowire (NW) polytype selection is governed by surface/interface energies, surface diffusivities, and/or droplet angles that determine ABC vs. AB stacking of atomic planes, resulting in zincblende (ZB) or wurtzite (WZ) polytypes. For ZB-polytype-preferring materials, such as III-As and III-P, ZB vs. WZ polytype selection has been described by empirical "contact angle" models, enabling the design and fabrication of NW polytype superlattices. However, for GaN, a WZ-polytype preferring material, the "contact angle" models for NW polytype selection, using literature values for WZ and ZB GaN surface energies, predict ZB polytype formation, across contact angles, even though WZ GaN NWs are most frequently reported in the literature.

The purpose of this work is to develop the fundamental materials science to controllably synthesize NWs with meta-stable polytypes, stable polytypes, or some combination of both, through coordinated synthesis, in situ atomic-scale characterization, and multi-scale simulations. We will utilize multi-scale simulations to construct a physics-based atomistic model for nanoscale epitaxy of metastable crystal polytypes and iteratively verify its nucleation and growth components via experiments in chemical environments using both molecular-beam epitaxy (MBE) and environmental TEM (E-TEM). Although GaN is selected as a model system, these results will be widely applicable to systems that have multiple metastable polytypes. The new knowledge generated will significantly broaden our capabilities to produce nanowires of complex materials composed of multiple polytypes, with properties of interest for various functional devices.

Recent Progress

Visualization of droplet epitaxy of InN quantum dots via E-TEM The formation of InN QDs during nitridation of indium droplet arrays was examined using ETEM and HRTEM. For these studies, indium nanoparticles were deposited on (001)-oriented silicon thin-film TEM grids using MBE and were exposed to ammonia gas in the E-TEM at the CFN at BNL. During the nitridation process, as the substrate temperature increases, the nanoparticle (NP) sizes decrease, while their density increases; meanwhile, moiré pattern formation suggests the formation of coherently strained InN/In2O3 interfaces. At the lowest nitridation temperatures, the smallest NPs primarily exhibited 2D moiré fringes suggesting ZB InN formation. At the highest nitridation temperatures, larger NPs primarily exhibited 1D moiré fringes. These results reveal a higher probability for nucleation of ZB (WZ) polytypes from smaller (larger) indium nanoparticles. In both cases, In_2O_3 layer formation on InN is observed, and warrants further study.

Determined the role of excess silicon on the nucleation of ZB vs. WZ GaN nanowires We recently discovered a Ga metal-mediated molecular-beam epitaxy (MBE) process to selectively nucleate ZB GaN films and/or nanowire ensembles, or WZ NW ensembles directly on silicon (Si). Key to this process is a Ga pre-deposition step, in which Ga droplet arrays are formed prior to film or NW growth. For the ZB films and NW ensembles, reflection- high energy electron diffraction and x-ray diffraction reveal ZB-to-WZ transformations at thicknesses ~ 20 nm. High-angle annular dark-field scanning transmission electron microscopy (HAADF-STEM) reveals ZB NWs with the close-packed (111) planes oriented ~37° from the Si [001] surface normal, i.e. [001]-oriented ZB NWs. Interestingly, the NW axis orientation remains fixed as it transforms to the WZ polytype. On the other hand, for pure WZ NWs, the close-packed (0001) planes are oriented along the Si [001] surface normal, i.e. [0001]-oriented WZ NWs. We hypothesize that Si incorporation into Ga droplets influences the polytype selection during film and NW growth. Preliminary Energy Dispersive Spectroscopy (EDS) measurements suggest a higher concentration of Si within the ZB NWs.

Meanwhile, density-functional theory (DFT) calculations show that ~8 at% substitutional Si in the Ga sublattice makes ZB GaN thermodynamically more stable than WZ GaN. Kinetically, it would be difficult to add these substitutional Si in the Ga sublattice by solid-state reactions. However, when Si substrate temperature was fixed in the range of 1050-1130 K during the synthesis, the Ga-Si liquid phase can incorporate up to more than 10 at% of Si. Hence when a high Ga flux was applied in the pre-deposition process, a considerable amount of Si atoms dissolve into the liquid Ga. During the nitridation process, this high solubility of Si would introduce a large quantity of substitutional Si atoms onto the GaN lattice. Consequently, this Si-rich environment makes the ZB phase more thermodynamically favorable.

Nucleation of high-density arrays of ultra-small Ga droplets via molecular-beam epitaxy In preparation for E-TEM studies of GaN QD formation during nitridation of Ga droplet arrays, we have developed a process of nucleation of high density arrays of ultra-small Ga droplets via MBE. The MBE process involves Ga droplet deposition at low temperatures followed by surface Ga evaporation via a brief high temperature annealing step. Using this approach, we have achieved arrays of ~10 nm diameter Ga droplets, with densities of 1.4×10^{11} cm^2. We are currently in the process of adapting this approach for deposition directly onto (001)-oriented silicon thin-film TEM grids.

Built a small ex situ reactor vacuum chamber that is compatible with the TEM heating holder for quasi-in-situ experiments in the E-TEM A portable vacuum chamber has been built with multiple ports and a viewing port. The ports allow for vacuum pumps and different gasses or plasma source to be attached to this chamber. One of the ports is dedicated to the TEM heating holder. Three different flanges were made for this port to be compatible with Thermo-Fisher, JEOL, and Hitachi TEM heating holders. The CFN as well as U. Pittsburgh houses microscopes from these three TEM manufacturers, thus increasing the versatility of this chamber. The ETEM

at CFN is a Thermo-Fischer and the ETEM at U. Pittsburgh is a Hitachi. The chamber itself is small and portable to be placed in the same room as the electron microscopes. An image of this ex situ reactor chamber is shown below.

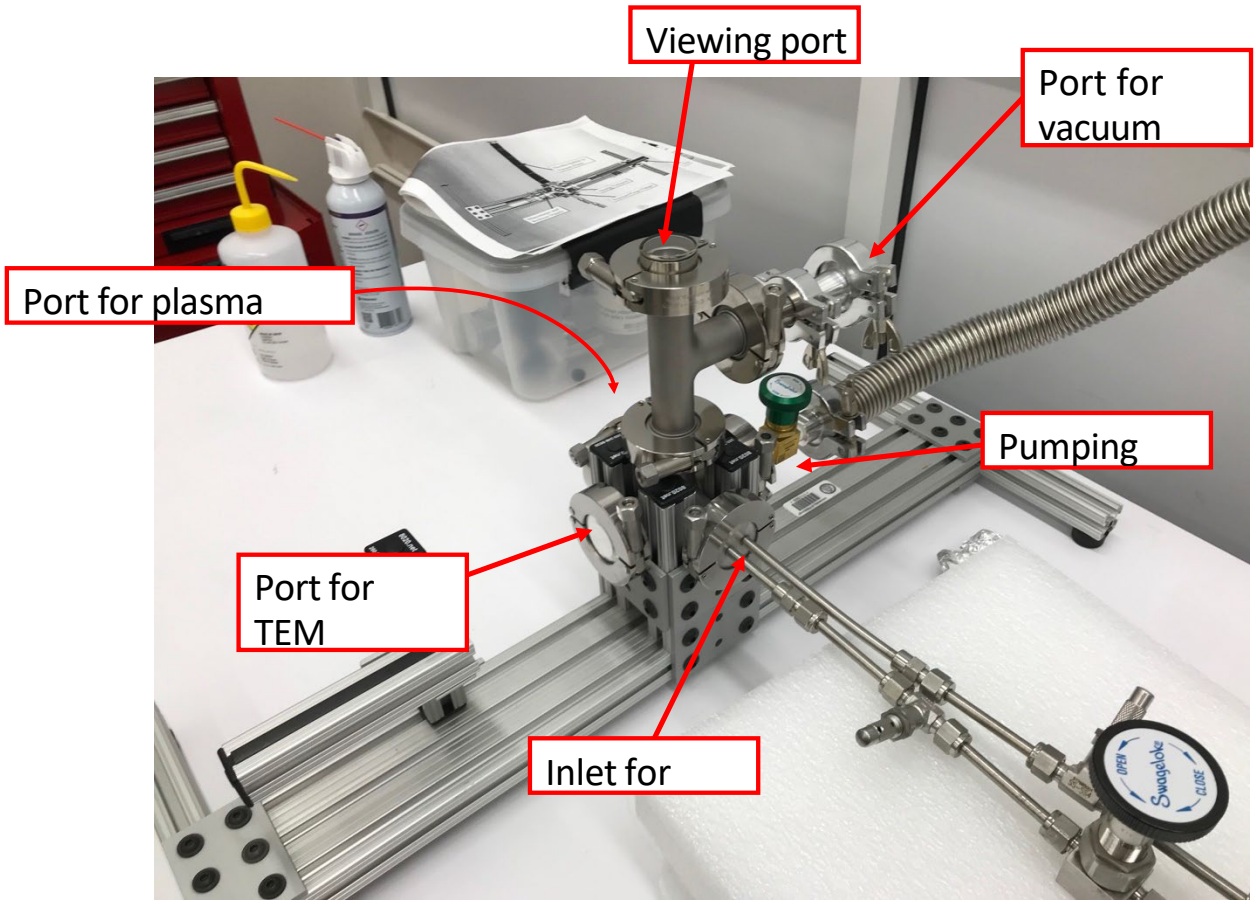

Future Plans Our Future plans include the following:

- We are currently developing a special MBE-TEM sample holder to enable MBE of droplets directly onto TEM sample grids.
- We are pursuing high throughput DFT calculations to search other possible alloying elements to change the ZB-WZ stability of bulk GaN
- We are constructing kinetic Monte Carlo simulation codes to study diffusion and phase transformation in GaN. Atomistic simulations based on classical and machine learning interatomic potentials will be applied to investigate surface and interface structures and energies of GaN.
- We will purchase and install a nitrogen plasma source onto the ex-situ reactor chamber at BNL-CFN for quasi-in situ observations of nanowire nucleation and growth. In particular, Ga droplets deposited onto TEM grids will be placed onto the TEM heating holder, placed into the reaction chamber for nitridation, followed by transfer into the ETEM for visualization. In this way, the parameters for growth, such as temperature, nitrogen source,

distance between nitrogen source and sample, can be probed and identified for subsequent ETEM modification for direct in situ observations.

Publications

Invited Presentations by PIs

1. "Tailoring semiconductor polytype selection during molecular beam epitaxy", AVS-MI Spring Symposium, June 7, 2023 (Ann Arbor MI)

2. "Tailoring semiconductor polytype selection during molecular beam epitaxy", Center for Functional Nanomaterials Seminar, Brookhaven National Laboratory, May 4, 2023 (Upton, NY)

3. "Tailoring semiconductor polytype selection during molecular beam epitaxy", Materials Science and Engineering Seminar, Georgia Tech, December 5, 2022 (Atlanta, GA)

4. "Tailoring semiconductor polytype selection during molecular beam epitaxy", Materials Research Society Fall 2022 Annual Meeting, November 29, 2022 (Boston MA)

Publications/Presentations

1. F. E. Camino, A. Rua, D. M. Piñero Cruz, F. E. Nieto-Fernandez, A. Perez, K. Kisslinger, and J. C. Yang, “Remote Operation of Instruments for Education and Research”, Microscopy and Microanalysis 2023 (Minneapolis, MN)

2. A. Liu, H. Lovelace, Z. Xi, T Borrely, H. Lu, D. Zakharov, J.C. Yang, L. Qi, and R.S. Goldman, “Influence of Excess Silicon on the Nucleation of Zincblende vs. Wurtzite GaN Nanowires", Microscopy & Microanalysis 2023 (Minneapolis, MN)

3. L. Qi, A. Liu, and R.S. Goldman, "Mechanisms for Polytype Selection during the growth of self-catalyzed GaN Nanowires", EMC Meeting 2023 (Santa Barbara, CA).

4. A. Liu, H. Lu, and R.S. Goldman, "Formation, structure, and properties of GaN nanowire polytype heterostructures", APS Meeting 2023 (Las Vegas NV).

5. H. Lu, S. Moniri, C. Reese, S. Jeon, A. Katcher, T. Hill, H. Deng, L. Qi, R.S. Goldman, "Tailoring Nanoscale Crystal Polytype Selection for Quantum Confinement Engineering", Defects in Semiconductors GRC (2022).

Local Crystal Orientation of THF Hydrates in Cylindrical Nanoconfinement by In-situ Polarized Raman Spectroscopy and Microfluidics

Ryan L Hartman[1*] (PI) and Carolyn A Koh[2] (co-PI)

[1] Department of Chemical & Biomolecular Engineering, NYU Tandon School of Engineering, Brooklyn, NY, USA 11201

[2] Center for Hydrate Research, Department of Chemical & Biological Engineering, Colorado School of Mines, Golden CO, USA 80401

Keywords: Polarized Raman Spectroscopy, Glass microfluidics, Anodic Aluminum Oxide, THF hydrate crystal orientation, Melting point depression.

Research Scope

Gas hydrates crystallize in confined media at high pressure and low temperature in marine sediments and permafrost regions. Despite forming in nanoconfinement, gas hydrates have been extensively studied only in bulk. The hydrate formation is a nucleation and growth phenomenon where heterogeneous nucleation is a dominant process in natural and synthetic hydrates. Understanding nucleation and growth of gas hydrates in nanoporous confinements can help create ways for storage and utilization as a future energy source. We propose understanding the single crystal nucleation and evolution of different structure types in highly ordered nanopores inside glass microfluidics. The primary objective of this research is to discover a fundamental molecular-to-pore-based multiscale understanding of the hydrates crystallization mechanism in confinement. We hypothesize that the nature of the nanopores determines the gas hydrate nucleated in nanoconfinement, their resultant structure type, cage occupancy, and their crystallization and dissociation kinetics.

Recent Progress

Along the lines of the proposed research, we bring out the method for studying crystal orientation/tilt during Tetrahydrofuran (THF) hydrate crystallization under the influence of nanoconfinement using Polarized Raman spectroscopy as a test case. It has been known that though THF and methane hydrates are different, THF can be a substitute for laboratory studies of methane hydrates. THF hydrates form at moderate conditions, and studies for the THF hydrates can be used to forecast the issues regarding the analysis of Methane hydrates. Here, uniform cylindrical nanometer size pores of Anodic Aluminum Oxide (AAO) are used as nanoconfinement, and hydrate is crystallized in AAO inside a glass microfluidics device for controlled and rapid hydrate formation and analysis via in-situ Polarized Raman spectroscopy. Also, to extend this methodology for natural gas hydrates, we have devised a new high-pressure glass microfluidics fabrication method that can be used for Natural Gas hydrates crystallization under confinement.

1. Understanding crystal tilt using Polarized Raman spectroscopy for THF hydrates

The ability to analyze crystals, either ex-situ or in-situ, is crucial for understanding crystallization under confinement. Various methods, such as microscopy, tomography-based methods, calorimetry, Nuclear Magnetic Resonance, X-ray diffraction, and neutron diffraction, can be employed based on the scale, confinement medium, and crystal properties. One such method for determining crystal orientation is Polarized Raman Spectroscopy. The theory of Polarized Raman spectroscopy is well-developed and implemented for various crystal classes. Polarized Raman Spectroscopy has been used extensively in literature for understanding local crystal orientation for solids and molecules in liquid under confinement. However, for crystallization under high-pressure and low-temperature conditions, such as hydrates, specifically designed experimental set-up with in-situ analytical techniques becomes crucial.

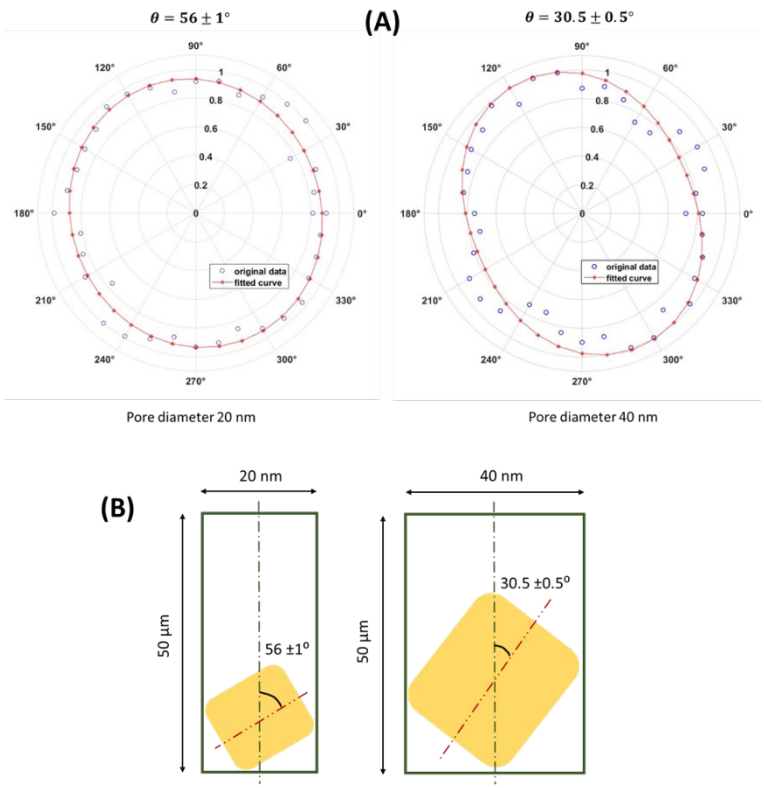

Figure 1. (A) least square curve fit to the obtained intensity values; (B)Crystal tilt measured using Polarized Raman Spectroscopy for 20 and 40 nanometer nanoconfinement

The irreducible representation of the space group of the crystal lattice is the result of the different symmetry of vibration in a crystal corresponding to the different phonon branches. By using standard group theoretical methods and the interaction of crystal with polarized light, we can determine the Raman active phonon modes of the crystal. Raman polarizability tensor depends on the position of atoms and directions of bonds in a molecule. For 32 crystal classes, the Raman tensor forms have already been determined and tabulated in literature. THF hydrate crystals are octahedral, belonging to the O_h, ***m3m*** point, and ***Fd3m*** space group. So, for crystals fixed in space Raman tensor can describe the crystal symmetry and orientation relative to the direction and polarization of the incident and collected light. Using the Raman tensor pertaining to the unique crystal structure, it is possible to obtain the series of independent equations which can be used to investigate the crystallographic plane and for the determination of the orientation of crystal in space. The Raman tensor is unique for each Raman-active mode, and the given peak intensity can be characterized as a function of incident and scattered polarization.

Based on the crystal symmetry and its alignment with the incident polarized light, the equations were formulated for the THF hydrates crystal class. The data was collected for the known rotation of the crystal on the rotational stage, and obtained intensity values were fitted to the formulated equation **(fig. 1A)**. The effect of single crystal orientation on observed spectra was studied and utilized for obtaining crystal tilt inside 20 and 40-nanometer-size AAO pores. It was observed that for 40nm diameter crystal tilt is 30.5 ± 0.5° whereas, for 20nm pores, the tilt is 56 ± 1°. Crystal tilt observed in 20 and 40-nanometer-size pores were proportional to the pore diameter resulting in lower tilt relative to the axis of the confinement in larger-diameter pores **(fig. 1B)**.

Nanoconfinement can also help stabilize the different polymorphs of the material depending on the interaction, which can affect the growth rate and the observed properties, such as melting point. It has been shown in the literature that the tilt inside the confinement can have significant implications on the melting point of the crystal compared to the bulk of the system, which can be dictated by the Gibbs-Thomson equation. Based on the Gibbs-Thomson equation, the melting point usually decreases with the decrease in the pore size or the confinement medium. The general Gibbs-Thomson equation is given below.

$$\frac{\Delta T_m\,(r)}{T_{m,bulk}} = -\frac{2M}{\Delta H^{fus}\rho r}\gamma_{nl}cos\theta$$

Here ρ is the crystal density, M is the molar mass, γ_{nl} is the surface tension between the crystal and the fluid surrounding it, θ is the interfacial angle between the condensed phase and the confined media on which it may have nucleated and ΔH^{fus} is the molar heat of fusion in bulk. Where nuclei do not wet the pore walls, the contact angle may be taken as 180º; however, in the case of THF hydrates in AAO where AAO is hydrophilic, crystal tilt is crucial for calculating the melting point depression. After determining the tilt experimentally, the Gibbs-Thomson equation was used to calculate the melting point depression and based on the literature values of the data for other parameters and observed crystal tilt, the observed melting point depression is 1.6-1.8º compared to the bulk of the THF hydrates.

2. Fabrication of high-pressure glass microfluidic device

Conventional photolithography and etching techniques were optimized to fabricate high-pressure glass microfluidic devices. However, this technique is laborious and takes weeks for device fabrication. An alternate technique called laser ablation for microfluidic chip fabrication was followed and optimized to speed up the process. The laser ablation technique was slightly altered for consistency and reproducible results. In the modified technique, the glass slide is taped on both sides with acid-resistant tape (**fig. 2A**). The microfluidic channel patterns are created using a commercially available laser engraver. After patterning, the slides were etched in the hydrofluoric acid solution for 1 hour to etch the irradiated portion of the tape. The tape was then removed, and holes were drilled at the inlet and outlet section of the channel using standard drilling techniques. The slides were then bonded to the blank slide via an optimized fusion bonding technique in an oven at 620ºC for 6 h (**fig. 2B**). The bonded microfluidic chips were then tested for pressure ratings. Through successive improvements, fabricated microfluidic chips were shown to withstand 75 bar pressure (**fig. 2C**).

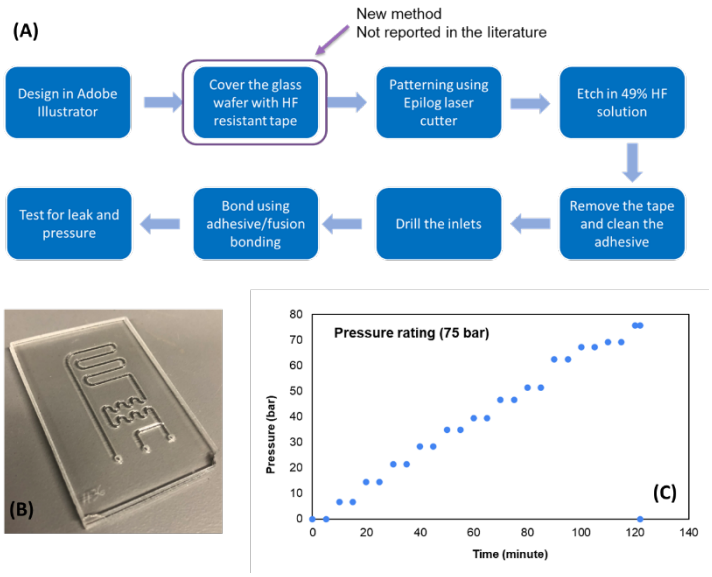

Figure 2. (A) New Laser ablation method for the high-pressure glass microfluidic device fabrication; (B) Fabricated glass microfluidic device using new technique; (C) Pressure test of the fabricated device

Future Plans

The validation of predicted melting point depression using DSC studies at CSM is in progress. We think that the proposed methodology can be easily extended for the natural gas hydrates to understand crystallization kinetics and behavior of crystals inside nanoconfinement using a high-pressure glass microfluidic device. The new fabrication method allows known-sized nanoporous AAO to be placed inside created channels before bonding and crystallization can be observed for the methane hydrates. In parallel, to perform the high-pressure experiment in NMR, a high-pressure NMR rotor is also being fabricated at NYU. The aim is to fabricate an NMR cell in non-magnetic material for a magic angle spinning experiment. Preliminary samples have been created, and the rotor is being refined.

Once validated, this technique will be extended for the methane hydrates to study the project's original proposed objective listed as **1.** Discover why the nanopore geometry controls the ice polymorph, the nucleated hydrate structure type, and the resultant cage occupancy of CH_4; **2.** Reveal the cage-type occupancy for varying natural gas compositions, structure types, and the

resultant hydrate kinetics; **3.** Elucidate why the nanopore hydrophobicity controls the ice polymorph, the nucleated hydrate structure type, its resultant cage occupancy of CH_4, and the kinetics; **4.** Discover why different salt ions (*e.g.*, mono- and di-valent, NaCl, and $CaCl_2$) influence hydrate crystallization in nanoconfinement; **5.** Determine whether confinement affects long-range crystallization, i.e., subsequent growth beyond the pore exits; **6.** Use of machine learning techniques with experimental data to validate first principal models.

References

1. Loudon, R., The Raman effect in crystals. *Advances in Physics* 1964, ***13*** **(52)**, 423-482.
2. Mossbrucker, J.; Grotjohn, T., Determination of local crystal orientation of diamond using polarized Raman spectra. *Diamond and related materials* 1996, ***5*** **(11)**, 1333-1343.
3. Zhu, W.; Pezzotti, G., Tensor and spatially resolved analysis of microscopic stress fields in polycrystalline alumina by polarized Raman spectroscopy. *physica status solidi (a)* 2011, ***208*** **(5)**, 1141-1150.

Publications

1. Sharma, M. K.; Hartman, R. L., Perspectives on Microfluidics for the Study of Asphaltenes in Upstream Hydrocarbon Production: A Minireview. *Energy & Fuels* 2022**,** ***36*** **(16)**, 8591-8606.
2. Sharma, M. K.; Hartman, R. L., Perspectives on Polyolefin Catalysis in Microfluidics for High-Throughput Screening: A Minireview. *Energy & Fuels* 2022, ***37*** **(1)**, 1-18.
3. Sharma, M. K.; Koh, C. A. and Hartman, R. L., Insights into local crystal orientation of THF hydrates in tailored confined media using microfluidics through In-situ Polarized Raman spectroscopy *(In preperation)*

Modeling and synthesis of heavy-element xenes

PI: Jennifer Hoffman (Harvard, Dept. of Physics);
co-PIs: Julia Mundy (Harvard, Dept. of Physics),
Boris Kozinsky (Harvard, Division of Materials Science & Mechanical Engineering),
Taylor Hughes (University of Illinois at Urbana-Champaign, Dept. of Physics)

Keywords: Xene, quantum spin Hall, molecular dynamics, molecular beam epitaxy

Research Scope

Atomic-layer honeycomb materials (Xene, where "X" may stand for a number of different elements) present a promising platform to stabilize distinct quantum states. When X is a heavier element such as Sn or Bi, the strong spin-orbit coupling (SOC) can open a large inverted band gap, giving rise to quantum spin Hall or even novel quantum valley Hall edge states that may be stable at room temperature. The size of the gap and nature of the edge states depend sensitively on the substrate coupling, lattice buckling, and adatom decoration, suggesting the potential for highly tunable device geometries at the nanoscale. Here we describe the simulation of xene synthesis via Machine-Learning Molecular Dynamics, and prediction of Zn adatom decoration to realize the quantum spin Hall – quantum valley Hall (QSH/QSV) transition in stanene. We report our progress towards the synthesis and characterization of bismuthene on hydrogen-decorated SiC, using molecular beam epitaxy (MBE) and scanning tunneling microscopy (STM).

Recent Progress (Theoretical)

Predicting functionality: Proposals for topological electronic, spintronic, and valleytronic devices rely on applying *local* perturbations, including electric fields and proximity magnetism, to induce topological phase transitions in xenes. However, these techniques lack control over the geometry of interfaces between topological regions. Kozinsky and Hughes groups collaborated to seek specific adatom decoration strategies for engineering atomically precise topological edge modes in xenes. Our first-principles calculations show that decorating stanene with Zn adatoms exclusively on one of two sublattices induces a topological phase transition from the quantum spin Hall (QSH) to quantum valley Hall (QVH) phase. We calculate the existence of spin-valley polarized edge modes propagating at QSH/QVH interfaces.

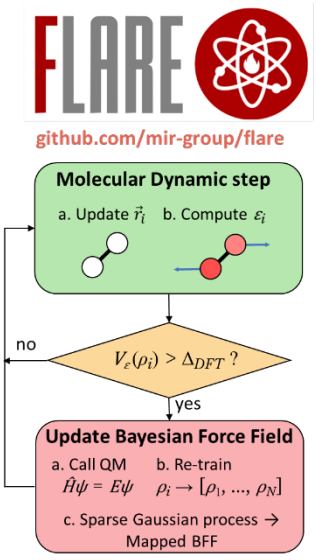

Fig 1: FLARE workflow

Synthesis science: To aid the time-consuming and expensive task of synthesizing and decorating new materials, we aim to simulate growth mechanisms to inform experimental parameter choices. However, first-principles simulation of the trajectories of $>10^{12}$ atoms in a single macroscopic xene film is not feasible. Through this grant, we are developing machine-learning methods, in a code-base called FLARE, that intelligently insert new first-principles DFT calculations only at critical time steps in

molecular dynamics simulations. For example, we demonstrated a several-order-of-magnitude speed-up in modeling pressure-induced phase transitions of silicon carbide (SiC), a crucial substrate for bismuthene. The resulting model exhibits close agreement with both ab initio calculations and experimental measurements. The active learning workflow readily generalizes to a wide range of material systems.

Recent Progress (Experimental)

Synthesizing bismuthene: Monolayer Bismuth arranged in a honeycomb lattice (bismuthene) requires the use of hydrogen passivated silicon carbide - SiC(0001) as a substrate [1-4]. The hydrogen atoms bond to the surface silicons of SiC(0001), protecting the substrate from undergoing the $\sqrt{3}\times\sqrt{3}$-Si reconstruction that prevents bismuthene growth. To grow bismuthene, we need to desorb hydrogen atoms slowly, while depositing bismuth on the SiC substrate. In an ideal scenario, the bismuth atoms occupy 2/3 of the lattice sites on Si-terminated SiC, and the remaining 1/3 are occupied by hydrogen atoms at the center of the bismuth honeycomb [1]. The literature on preparing an atomically flat, Si-terminated, and H-passivated SiC substrate is limited and inconsistent [1, 2].

Here we outline the challenges and progress that we have made towards the synthesis of bismuthene on atomically flat SiC passivated with atomic hydrogen. We designed and built an ultra-high vacuum system (Fig. 2a) for annealing SiC in an ultra-pure (part per billion impurity) hydrogen and helium mixed gas environment. The purity of the mixed gas is crucial to realize the H-Si-terminated surface of SiC substrate. Previous attempts using as-received hydrogen gas lead to a formation of silicate adlayers, which can be seen as a large oxygen peak (O 1s) from our X-ray photoelectron spectroscopy (XPS) experiment (red curve in Fig. 2d).

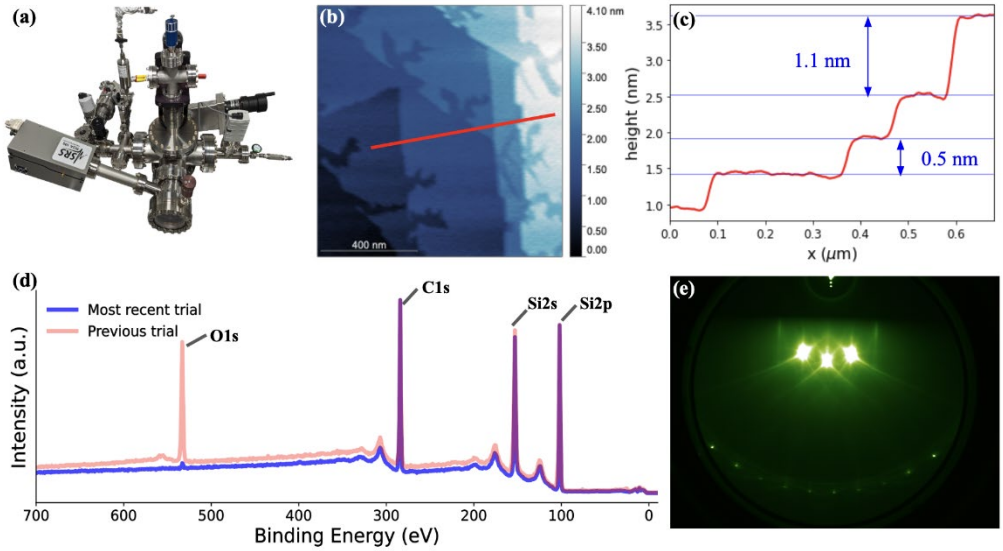

Fig 2: (a) photo of the hydrogen chamber used to anneal SiC at high temperature and ultra-pure hydrogen/helium environment. **(b)** AFM image for the 4H-SiC(0001) substrate annealed at 1180°C. **(c)** line cut in **(b)**, the height trace shows atomically flat terraces. The terrace's height is either 0.5 nm or around 1nm, which matches the lattice constant for 4H-SiC. **(d)** XPS survey for the previous trial and the most recent trial with annealing in different hydrogen purity. Surface oxygen (O1s peak) is barely seen in the most recent trial. **(e)** RHEED image for the same substrate as in **(b)**, clear 1×1 diffraction spots are another support for hydrogen passivation on the surface.

We dramatically improved the system by adding an extra gas purifier and direct current heating, which lead to a promising hydrogen passivated SiC surface. As shown in Fig. 2d (blue curve), the oxygen peak is barely visible which is a good indication of a clean surface. Atomic force microscope (AFM) confirms an atomically flat substrate surface with sharp terraces (Fig. 2b,c) that are integer multiples of a single Si-C bilayer height (0.25 nm). Reflective high energy electron diffraction (RHEED) shows that this well-prepared SiC substrate does not have the destructive $\sqrt{3}\times\sqrt{3}$-Si reconstruction (Fig. 2e). Our most recent results clearly demonstrate that we have succeeded in growing an atomically flat SiC surface with hydrogen passivation that is needed for growing high-quality bismuthene.

The next step is bismuthene growth. Our preliminary results demonstrated that epitaxial bismuth can be grown on SiC above 500°C, which is consistent with the results in the literature. After bismuth deposition, the RHEED patterns show sharp streaks with a $\sqrt{3}\times\sqrt{3}$ reconstruction, indicating good crystallinity in the bismuth layer, though not distinguishing between the honeycomb bismuthene, α-Bi(111) and β-Bi(111) phases [2]. Our XPS data further confirmed that bismuth is indeed on the SiC surface (Fig. 3). A fine scan within the Bi 4f energy range shows the energy split due to the Bi-O state. More interestingly, we still observe the pure Bi peak, which demonstrates that the monolayer Bi that bonded with Si atoms is more robust against oxidation [1]. The STM image shows a rough surface (Fig. 3d). The next step is to optimize the parameter space for desorbing atomic hydrogen and evaporating bismuth in a perfect stoichiometric ratio to realize large domains of bismuthene for STM studies.

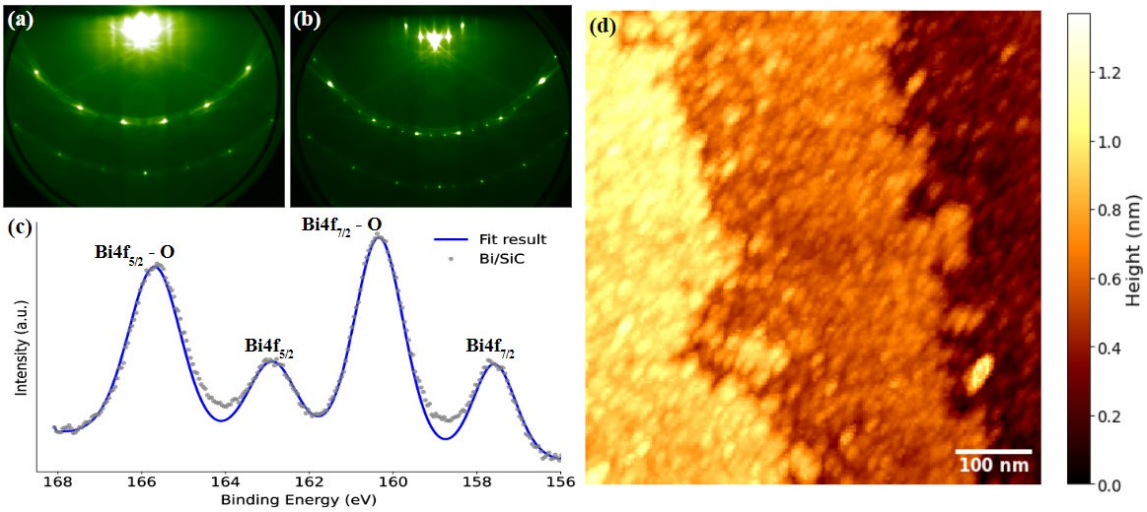

Fig 3: (a-b) RHEED image before **(a)** and after **(b)** Bi deposition. **(c)** XPS of Bi on SiC after brief exposure in air. The Bi spectrum shows oxidation states in addition to the pure Bi state. **(d)** STM image on the epitaxial Bi grown on SiC (0001). (Current setpoint: 30 pA, sample bias: -2 V)

Future Plans

Our long-term vision is the development of reconfigurable edge current channels in Xenes by controllable adatom decoration using scanning tunneling microscopy (Fig. 4a). Kozinsky and Hughes groups are predicting adatom configurations, while Hoffman and Mundy labs are working towards reproducible bismuthene synthesis. Hoffman lab has already demonstrated controlled STM manipulation of single Bi atoms on a topological surface (Fig. 4b-c).

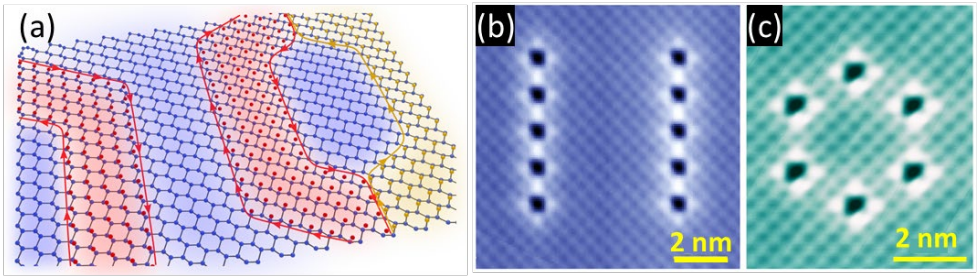

Fig 4: (a) Long-term vision: development of reconfigurable edge currents in Xenes, using adatoms to define regions of different bandgap. **(b-c)** Controlled Bi adatom decoration of topological CeBi, using Hoffman's STM.

References

[1] F. Reis, G. Li, L. Dudy, M. Bauernfeind, S. Glass, W. Hanke, R. Thomale, J. Schäfer, and R. Claessen, *Bismuthene on a SiC substrate: A candidate for a high-temperature quantum spin Hall material,* Science **357**, 287-290 (2017).

[2] K. Yaegashi., K. Sugawara, T. Kato, T. Takahashi, and T. Sato, *Selective Fabrication of Bismuthene and α-Bi on Hydrogen-Terminated SiC(0001)*, Langmuir **38**, 13401-13406 (2022).

[3] R. Stühler, F. Reis, T. Müller, T. Helbig, T. Schwemmer, R. Thomale, J. Schäfer and R. Claessen, *Tomonaga–Luttinger liquid in the edge channels of a quantum spin Hall insulator,* Nature Physics **16**, 47-51 (2020).

[4] R. Stühler, A. Kowalewski, F. Reis, D. Jungblut, F. Dominguez, B. Scharf, G. Li, J. Schäfer, E. M. Hankiewicz and R. Claessen, *Effective lifting of the topological protection of quantum spin Hall edge states by edge coupling,* Nature Comminication **13**, 3480 (2022).

Publications

(1) Jennifer Coulter, Mark R. Hirsbrunner, Oleg Dubinkin, Taylor L. Hughes, Boris Kozinsky, "Engineering ideal helical topological networks in stanene via Zn decoration." arxiv:2203.15800. Under second round review at Nature Communications (2023).

(2) Cameron J. Owen, Steven B. Torrisi, Yu Xie, Simon Batzner, Jennifer Coulter, Albert Musaelian, Lixin Sun, Boris Kozinsky, "Complexity of Many-Body Interactions in Transition Metals via Machine-Learned Force Fields from the TM23 Data Set." arxiv:2302.12993. Submitted to npj Computational Materials (2023).

(3) Yu Xie, Jonathan Vandermause, Senja Ramakers, Nakib H. Protik, Anders Johansson, Boris Kozinsky, "Uncertainty-aware molecular dynamics from Bayesian active learning: Phase Transformations and Thermal Transport in SiC." npj Comp. Materials **9**, 36 (2023).

(4) Jonathan Vandermause, Yu Xie, Jin Soo Lim, Cameron J. Owen, Boris Kozinsky "Active learning of reactive Bayesian force fields: Application to heterogeneous hydrogen-platinum catalysis dynamics." Nature Communications **13**, 5183 (2022).

(5) Lixin Sun, Jonathan Vandermause, Simon Batzner, Yu Xie, David Clark, Wei Chen, Boris Kozinsky, "Multitask Machine Learning of Collective Variables for Enhanced Sampling of Rare Events." J. Chem. Theory Comput. **18**, 2341 (2022)

(6) Yulia Maximenko, Yueqing Chang, Guannan Chen, Mark R. Hirsbrunner, Waclaw Swiech, Taylor L. Hughes, Lucas K. Wagner & Vidya Madhavan, "Nanoscale studies of electric field effects on monolayer 1T′-WTe_2." npj Quantum Materials **7**, 29 (2022).

(7) Nicola Molinari, Yu Xie, Ian Leifer, Aris Marcolongo, Mordechai Kornbluth, Boris Kozinsky, "Spectral Denoising for Accelerated Analysis of Correlated Ionic Transport." Phys. Rev. Lett. **127**, 025901 (2021)

Lattice engineered single crystal architecture in glass

PI: Himanshu Jain. Co-PI: Volkmar Dierolf. Lehigh University, Bethlehem, PA USA
Keywords: Radiation processing; single crystal; lattice engineering; crystal growth atomistics; glass-crystal metastructures

Research Scope

Previously, we reported the discovery of a new type of metamaterials, called rotating lattice single (RLS) crystals, which were fabricated by a solid → solid transformation of glass using controlled laser heating. These hierarchical structures possess a lattice that rotates in a specific manner, which can be engineered by controlling the laser processing parameters. We have sought to fully characterize the nature of lattice rotation and establish its atomistic origin both experimentally and by molecular dynamics simulations, with the hope of designing the lattice and ultimately the properties of RLS crystal architecture in glass.

The dominant source of lattice rotation appears to be densification upon crystallization of glass, which introduces stresses at the growth front that are then relieved by ordered introduction of dislocations. Our working hypothesis is that the magnitude of Burgers vector of dislocations normal to rotation axis and their mobility on preferred slip planes are the two most important characteristics that determine lattice rotation rates (Θ °/μm). Further, the spatial profile of viscosity, which determines the rate of stress relaxation, of glass at the growth front is another important property for determining Θ. We have explored the role of glass structure in lattice formation, with a hypothesis that the formation and the orientation of a seed are determined by the local structure of glass and dynamic interactions between the crystals and the glass.

Using in situ, real-time characterization techniques we are assessing whether the mechanism of crystal growth by solid → solid transformation is substantially different from that in a liquid (melt or solution) as the interactions between atomic size units are much stronger for the former. MD simulations are being performed to determine at what stage formation of two separate crystals seeds in close vicinity is no longer random but is determined by mutual interaction mediated by the highly viscous (essentially solid) glass. We are expanding the scope of the laser fabrication process and the resulting metamaterial by fabricating RLS crystal architecture using X-ray and electron beams and observing in real time the respective diffraction patterns. These complementary tools for providing energy locally are helping us understand the glass → RLS crystal transformation at the earliest observable stage. Thus, we are seeking to observe the 'birth' of an order within fully disordered glass.

Recent Progress

1. First demonstration of e-beam fabrication of lattice engineered crystals in glass (Evan Musterman)

Laser heating is well-established to impart optical functionality into glass by local modification and crystallization. However, the minimum size of crystal is limited by the diffraction limit of the laser, thereby excluding practical use in high-resolution structures for micro-nano photonics. Electron beam heating in scanning and transmission microscopes was successfully demonstrated as an alternative for fabricating architectures of arbitrary shapes, as seen in Fig. 1 for the local crystallization of Sb_2S_3 in Sb-S-I glasses as our model. It expanded morphological

control of crystal cross-section significantly, producing nanoscale (~50 nm) single crystal (see Fig. 2) with feature sizes much smaller than possible with the laser-fabrication method.

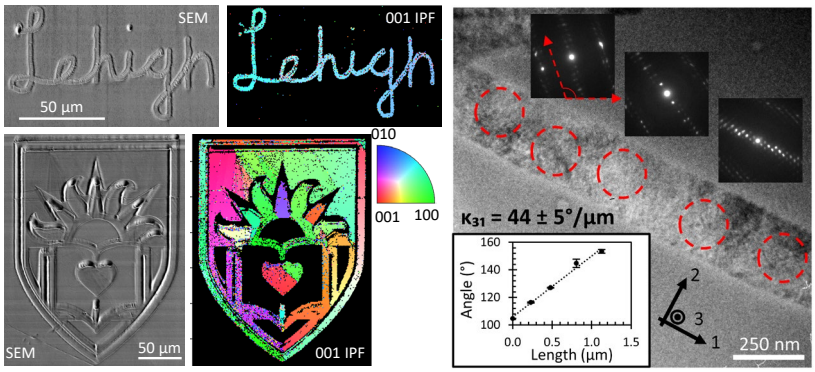

Fig. 1 (left): Examples of Sb_2S_3 RLS crystal architecture patterned on the surface of Sb-S-I glass in SEM by scanning the e-beam. (Left) SEM image and (right) inverse pole figure maps. **Fig. 2 (right):** An Sb_2S_3 RLS crystal line written in a TEM with its orientation from diffraction patterns. (inset).

2. <u>In situ observations of glass → crystal transformation: earliest stages of crystal growth</u> (Courtney Au-Yeung, Evan Musterman)

We have observed in situ transformation of glass to crystal in real time using X-ray and electron beams at the earliest stage experimentally possible. Figure 3 shows the formation and evolution of a crystal formed by an e-beam. Kikuchi diffraction is observed after an incubation time that varies randomly. The seed orientation changes almost exclusively about axis 2 for the first few seconds before reaching a stable state. A similar variation is observed during crystallization with a white X-ray beam at Advance Light Source synchrotron. Indeed, in situ observation of *laser* crystallization probed by a low power monochromatic X-ray beam at NSLS-II shows the same phenomenon, confirming that it is a universal feature of crystal formation in glass. This rotation has been modeled assuming a spherical rigid body embedded in a high viscosity medium (i.e. low Reynolds number), which is growing with time under a constant torque. The fit to the model is very good as shown in Fig. 3.

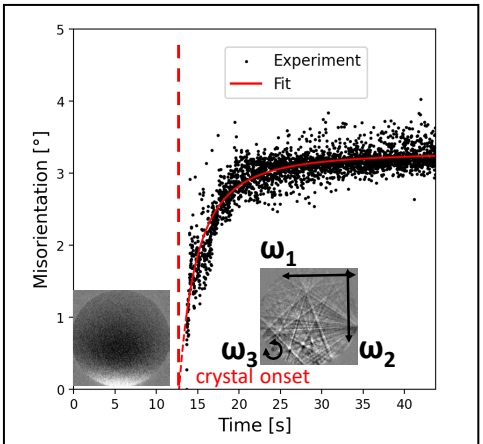

Fig. 3: In situ observation of early stage reorientation of a Sb_2S_3 crystal formed in Sb-S-I glass by e-beam in an SEM.

3. <u>Characteristics of RLS crystal</u> (Evan Musterman, Jack Kaman)

Initially, the RLS crystals were fabricated by forming an Sb_2S_3 seed near the surface of Sb-S-I glass with a laser beam and then scanning it in a straight line. The lattice of these linear crystals rotates at a rate Θ, typically up to a few °/µm, producing component κ_{21} in Nye's curvature tensor when the 1-axis is defined as the crystal growth direction, typically parallel to the laser scanning direction, the 3-axis is the direction typically normal the glass surface and opposite the laser propagation direction, and the 2-axis is orthonormal to the 1- and 3-axes to create a right-handed coordinate system.[P6] A question remained: what happens to the rotation as the crystal continues to grow? This question is now answered in Fig. 4 by fabricating much longer lines, where an additional 'macro' periodicity is superimposed on the finer, previously reported 'micro' rotation. The macro period of crystal lines increases with increasing laser scanning rates and powers, or conversely the lattice curvature decreases with increasing laser parameters, thus providing a mechanism for engineering the lattice rotation. In fact, we discovered two distinct macro

periodicities for the Sb_2S_3 RLS crystal lines fabricated in Sb_2S_3 glass depending on whether the rotation is about <001> for shorter or <010> axis for longer periods. The relative fraction of crystal lines rotating about the <001> or <010> crystal axes also change with laser parameters. As laser scanning rate and power is increased, the alignment is biased towards rotation about the <001> crystal axis. From a more detailed analysis using the higher spatial resolution of electron microscopes, we have discovered weaker, secondary rotations superimposed on primary rotation (κ_{21}), which act to align the RLS crystals during initial growth by rotation about the two other axes (κ_{11} and κ_{31}).

To extend the knowledge of the structure of RLS crystals to their physical properties, we have started characterizing their ferroelectric and piezoelectric properties since the emerging stibnite (Sb_2S_3) crystals have been reported to be weakly ferroelectric at room temperature. Our goal is to confirm these reports and then also establish how ferroelectricity would be modified by confinement by glassy matrix and by lattice curvature. Accordingly, the first piezo-response force microscopy (PFM) experiments have been performed at CNMS/ORNL in collaboration with Neus Domingo and Kyle Kelley. The results in Fig. 5 show a clear difference between the response of the RLS crystal and the glass matrix. The former shows a hysteresis loop characteristic of a ferroelectric response. However, this response decays with time exponentially, indicating a highly unusual quasi-ferroelectric response.

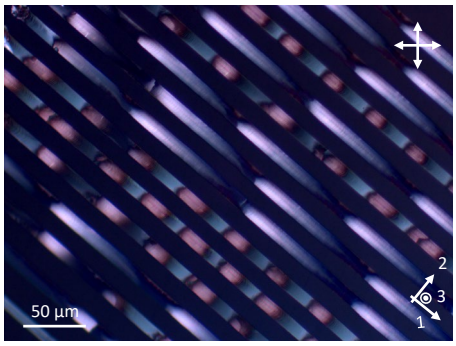

Fig. 4: Polarized optical micrograph of macroperiodic Sb_2S_3 RLS crystals fabricated in glass of same composition, showing two macro periodicities with different crystallographic origins.

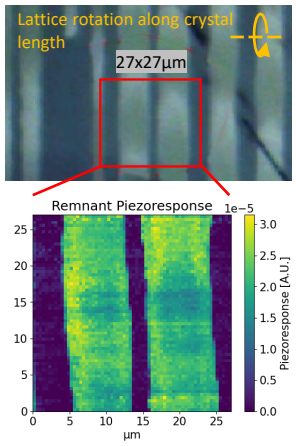

Fig. 5: Electromechanical response of crystal lines (top), and the map of piezoresponse due to remnant polarization.

4. Mechanisms of lattice rotation in RLS crystals (Evan Musterman)

We postulated that the observed lattice rotation results from the introduction of edge dislocations to accommodate stresses from density change at the growth front upon crystallization of glass. This hypothesis was proven by direct observation of edge dislocations. The magnitude of rotation closely agreed with the value calculated from the Burgers vector and observed density of dislocations, thus suggesting minimal contribution from elastic strain gradient [P1]. This mechanism has been extended to explain the crystallographic dependencies of the lattice curvature components based on the limited available slip systems of Sb_2S_3. The predominant lattice curvature component, κ_{21}, is maximized when growing along the <100> crystal direction, matching the maximum geometric contribution of the predominant ½[100] dislocations. Increases in dislocation density result in periodic changes in dislocation structure, tending towards an ordered series of low-angle (1 – 6°) grain boundaries forming lamellae (50 – 100 nm wide). Entirely disordered dislocation arrangement is expected for crystal lines with overall lower lattice curvatures [P1].

5. Atomistic description of seeded crystal growth in glass (Wei Sun, Rajendra Thapa)

To model incongruent crystal growth used in most applications using molecular dynamics (MD) simulations, a $LiNbO_3$ crystal seed was sandwiched between two lithium niobosilicate (LNS) glass slabs. We established that seed crystal growth is strongly affected by the orientation of the seed, temperature, and the SiO_2 concentration in the LNS glass matrix [P8]. Following atomistic insights were gained: (i) The orientation of $LiNbO_3$ seed surface with larger interplanar distance results in a relatively slower crystal growth. (ii) The addition of SiO_2 to the LNS system significantly decreases the crystal growth, which primarily occurs in the region devoid of Si - see Fig. 6 where dashed black lines represent approximate boundaries between the crystal growth from the seed and the glassy LNS matrix. At low silica LNS glass, there are large Si-free regions where the crystallization of $LiNbO_3$ is promoted. For ten times higher silica LNS glass, crystalline structures containing Nb and O form are still observed in certain places of glass without Si atoms. (iii) The suppressive effect of SiO_2 on growth rate can be traced to the existence of a [Si_{Nb}-V_{Nb}] defect complex. (iv) These defect pairs form both in the amorphous and crystallizing regions of the interface next to the seed. Such a defect complex is capable of existing in $LiNbO_3$ crystal only at low silica concentration. These defects polymerize the surrounding structures that prevent the crystal growth.

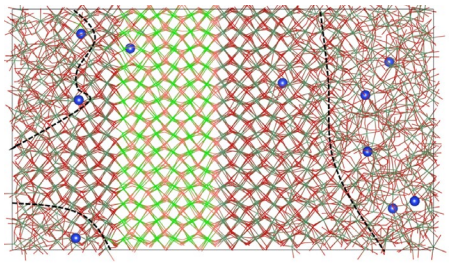

Fig. 6: Snapshots of seeded crystal growth of $LiNbO_3$ in LNS glasses containing 10 mol% SiO_2. Wireframe: Nb–O bonds; large blue spheres: Si atoms. Li atoms are hidden, since they do not participate in the growth process.

To establish the origin of early stage seed reorientation reported in the previous section, atomistic simulation of the impact of one seed on the growth of a neighboring seed was initiated. The model simulated the growth of a 15 Å radius spherical $LiNbO_3$ seed embedded in glass of the same composition using ~10^5 atoms. The growth of this seed is compared when a second seed of 10Å radius and same orientation was placed with a 29 Å of glass between them. The growth of the first seed is significantly enhanced by the presence of the second seed. It appears that the presence of a seed promotes order within the glass ahead of crystal formation. The addition of a second seed accelerates this process in the surrounding glass, thereby enhancing the growth rate of the first seed.

Future Plans

In view of the discoveries made recently and the overall goals of the project, in the next period we plan to focus on three main questions: 1. What is the nature and cause of crystal rotation that occurs within the first few seconds of the identifiable crystal? For this, we will perform extensive experiments to establish any correlation between the lattice rotation and seed orientation relative to (a) surface and (b) a neighboring seed, and simulate the same by MD. 2. How does a glass prepare itself for crystallization? In situ time-resolved micro-extended x-ray absorption fine structure (TR-μEXAFS) method, which has been already designed and established at NSLS-II, will be followed toward this goal. 3. What are the nature and origin of the unusual 'ferroelectric' behavior exhibited by stibnite RLS crystals? PFM along with Kelvin probe and other scanning probe microscopy at ORNL will be the principal tool employed to answer this question.

Publications 2021-2023

Full articles in archival journals

P1. E. J. Musterman, D. Savytskii, V. Dierolf, and H. Jain, The source of lattice rotation in rotating lattice single (RLS) crystals, Scripta Mat.193 (2021) 22-26. https://doi.org/10.1016/j.scriptamat.2020.10.027

P2. C. Au-Yeung, D. Savytskii, K. Veenhuizen, V. Dierolf, and H. Jain, Effect of Laser Beam Profile on Rotating Lattice Single Crystal Growth in Sb_2S_3 Model Glass, Crystals 11, no. 1 (2021) 36. https://doi.org/10.3390/cryst11010036

P3. W. Sun, V. Dierolf, and H. Jain, Molecular dynamics simulation of the effect of cooling rate on the structure and properties of lithium disilicate glass, J. Non-cryst. Solids, 569 (2021) p.120991 (11 pages). https://doi.org/10.1016/j.jnoncrysol.2021.120991

P4. C. Au-Yeung, D. Savytskii, K. Veenhuizen, S. McAnany, H. Jain, and V. Dierolf, Polarization and Surface Effects on the Seed Orientation of Laser-Induced Sb_2S_3 Crystals on Sb-SI Glass, Cryst. Growth & Des. (2021). https://doi.org/10.1021/acs.cgd.0c01230

P5. W. Sun, K. Veenhuizen, J. Marsh, V. Dierolf, and H. Jain, Determination of the structure of lithium niobosilicate glasses by molecular dynamics simulation with a new Nb-O potential, Computational Mat. Sci. 207 (2022) 111307 (11 pages). https://doi.org/10.1016/j.commatsci.2022.111307

P6. E. J. Musterman, V. Dierolf, and H. Jain, Curved lattices of crystals formed in glass, Int. J. Appl. Glass Sci. 13(3) (2022) 402-419. http://doi.org/10.1111/ijag.16574

P7. E. J. Musterman, V. Dierolf, and H. Jain, Electron beam heating as a tool for fabricating lattice engineered crystals in glass, Opt. Mater. Exp. 12(8), pp.3248-3261. July 2022. https://doi.org/10.1364/OME.462724

P8. W. Sun, V. Dierolf, and H. Jain, Molecular dynamics simulation of seeded crystal growth in glass, J. Non-crystalline Solids–X, 15 (2022) 100113, August 2022. https://doi.org/10.1016/j.nocx.2022.100113

Navigating Atomically-Precise Synthesis of Functional Oxides using Source Chemistry

Bharat Jalan, Department of Chemical Engineering and Materials Science, University of Minnesota, Twin Cities

Keywords: Thin Films, oxidation kinetics, membranes, molecular beam epitaxy, epitaxial strain

Research Scope

The overall goal of this project is to understand the fundamental factors responsible for determining crystal growth of perovskite oxides of select "stubborn" metals. Our objectives are three-fold: *(i)* to develop hybrid molecular beam epitaxy (MBE) approaches for single-crystalline films of perovskite stubborn-metal-based oxides with atomic-level control over thickness; structural perfection; cation and oxygen stoichiometry; and low defect concentration; *(ii)* to exploit the growth of metastable and artificial-layered structures by exploiting chemistry of source materials; *(iii)* to develop "remote" epitaxy and lateral epitaxy overgrowth approaches to exploit strain relaxation and surface adatom diffusivity towards defect-managed complex oxide membranes. It is hypothesized that the light illumination, or the use of two-dimensional Van der Waal (vdW) materials have tremendous influence on both thermodynamics and kinetics of functional oxide growth via controlling adatom mobility, and their chemical potential. We are investigating the growth of metastable and artificial-layered structures by exploiting chemistry of source materials during growth. Ultimately, we also plan to investigate growth kinetics – defect – structure – electroactive response (ferroelectricity) relationships in these films.

Recent Progress

Revealing record-high dielectric constant in thin films of $SrTiO_3$ through mechanistic understanding of film/metal interfaces [1]. The study of subtle effects on transport in heterostructures requires high-quality epitaxial structures and interfaces with low defect density. Despite over 60 years of research, the dielectric constants of the well-known complex oxide $SrTiO_3$ thin films have consistently been measured to be lower than that of bulk $SrTiO_3$. In this study, we demonstrates that the intrinsic dielectric constants of unstrained $SrTiO_3$films exceed 25,000 at low temperature which is well above that of bulk $SrTiO_3$ single crystals (Fig. 1). We reveal using hybrid molecular beam epitaxy method that there are low capacitances at the buried n-$SrTiO_3$/undoped $SrTiO_3$ interfaces in heterostructures despite it being homoepitaxially grown that affect the measured value of the intrinsic low-temperature dielectric constant, thereby addressing the long-standing question of why the dielectric constants of thin films have consistently been measured to be lower than that of bulk $SrTiO_3$.

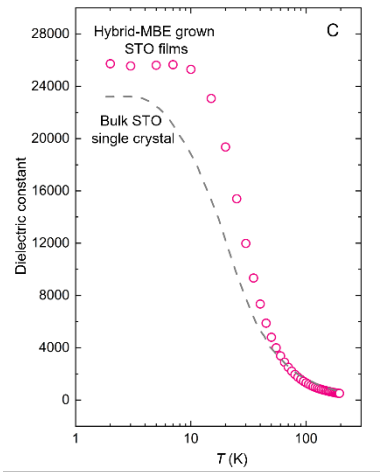

Figure 1: T-dependent dieelctric constant of $SrTiO_3$ thin films and that of the bulk single crystals [1].

***Investigation* of "remote" epitaxy using hybrid MBE approach for creating $SrTiO_3$ membranes *[2]*.** We have now laid the groundwork for understanding of growth mechanism(s) in remote epitaxy process. In collaboration with the PNNL team, we have extended our hybrid MBE growth for the synthesis of oxide membranes (see Fig. 2). We demonstrated that graphene oxidation can be completely eliminated by supplying oxygen via a molecular moiety that also contains Ti. We successfully used a metal-organic chemical precursor of Ti (titanium tetraisopropoxide) which contains four O atoms per Ti atom, thereby eliminating the need for a separate oxygen source. This discovery will influence synthesis of a broad range of oxides via remote epitaxy, generating novel pathways for the synthesis of large-area nanomembranes without damaging the graphene template. We further show that the use of an oxygen-containing molecular precursor yields nanomembranes with self-regulating cation stoichiometry control, enabling for the first-time adsorption-controlled growth of oxide nanomembranes [2].

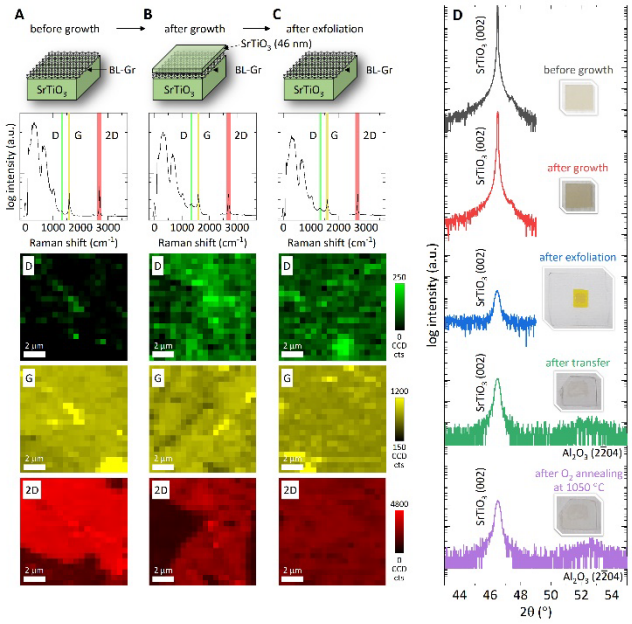

Figure 2: Demonstration of hybrid MBE-grown $SrTiO_3$ nano-membranes. (A-C) Confocal Raman spectroscopy and microscopy of BL-Gr/$SrTiO_3$(001) before growth (A), the resulting $SrTiO_3$/BL-Gr/$SrTiO_3$(001) after growth (B), and the restored BL-Gr/$SrTiO_3$(001) via exfoliating the grown film (C). Each Raman micrograph shows the integrated intensity from one graphene peak scanned over the surface of the sample. (D) High-resolution X-ray diffraction (HRXRD) 2θ-ω coupled scans of the sample before growth, and after growth, exfoliation, and then transfer to an r-plane Al_2O_3 substrate.

Discovering the key role of epitaxial strain in engineering metal oxidation during synthesis [3-5]. A major synthesis breakthrough of the current DOE support came through the discovery of the role of epitaxial strain in engineering metal oxidation. In a highly collaborative work involving two DOE national labs (Argonne National Lab and Brookhaven National Lab), and two other academic institutions (Auburn University and University of Delaware), we have shown how epitaxial strain can be used to navigate synthesis of atomically precise oxides of "stubborn" metals. To provide a context, the oxides of platinum group metals are promising for future electronics and spintronics due to their unconventional properties. However, their synthesis as thin films remains challenging due to their low vapor pressures and low oxidation potentials. In this work, we show how epitaxial strain can be used as a control knob to enhance metal oxidation. Using Ir as an example, we demonstrate the use of epitaxial strain in engineering its oxidation chemistry, enabling phase-pure Ir or IrO_2 films despite using identical growth conditions. The observations are explained using a DFT-based modified formation enthalpy framework, which highlights the important role of metal/substrate epitaxial strain in governing the oxide formation enthalpy. We

also validated the generality of this principle by demonstrating epitaxial strain effect on Ru oxidation. The IrO_2 films studied in our work, further revealed quantum oscillations, attesting to the excellent film quality. Our work provides new dimension to our understanding of epitaxial strain on oxidation chemistry and can have profound implications in enabling growth of oxide films of hard-to-oxidize elements using strain engineering.

Future Plans

(1) Novel solid-source metal-organic MBE (SSMOMBE) synthesis route for advances in oxide films and heterostructures. We are continuing to develop the novel SSMOMBE method that is showing significantly lower concentration of point defects in oxide thin films. One of the future goals is to understand the mechanism by which chemical precursor decomposes and reacts during MBE synthesis. One natural outcome of this work is growth of epitaxial films and heterostructures of 4d- and 5d-metal oxides enabling new science using unexplored quantum materials.

2) Strain control of oxidation kinetics during growth: As illustrated above, we have recently discovered an important role of epitaxial strain on oxidation kinetics during film growth. It was discovered that epitaxial strain can enhance the oxidation of Ir and Ru metal, which are otherwise harder to oxidize under the UHV conditions. Strain relaxation yielded the formation of metallic island of different shape and size. It is however still unclear what governs the shape and size of these islands? Can epitaxial template be used to tailor metallic island distribution, their shape and size? This question can particularly be important in the context of designing metallic support on oxides for catalytic applications. We will investigate how nucleation and growth of metallic islands take place as a function of substrate orientation, and film thickness. Topography, orientation, and distribution will be mapped out.

3) Understanding the growth mechanisms of complex oxide growth on vdW materials. Our recent study confirms the growth of epitaxial oxide nanomembrane on graphene-coated substrate. However, the underlying growth mechanism remains elusive. Understanding the growth mechanism is one of major goals of the future investigation.

4) Real-time tuning of chemical potential and adatom mobility during synthesis using light illumination. Finding novel knobs to control thermodynamics and kinetics can have profound impact on synthesizing defect-managed materials. We will use hybrid MBE to investigate growth mechanisms of functional oxides under light illumination of different wavelengths.

References

1. Z. Yang, D. Lee, J. Yue, J. Gabel, T.-L Lee, R. D. James, S. Chambers, and B. Jalan, **"Epitaxial $SrTiO_3$ films with dielectric constants exceeding 25,000"** *Proc. Natl. Acad. Sciences **119**, e2202189119 (2022)*
2. H. Yoon, T. K. Truttmann, F. Liu, B. E. Matthews, S. Choo, Q. Su, V. Saraswat, S. Manzo, M. S. Arnold, M. E. Bowden, J. K. Kawasaki, S. J. Koester, S. R. Spurgeon, S. A. Chambers and B. Jalan, "Free-Standing Epitaxial $SrTiO_3$ Nanomembranes via Remote Epitaxy using Hybrid Molecular Beam Epitaxy" *Sci. Adv. **8**, eadd5328 (2022)*
3. S. Nair, Z. Yang, D. Lee, S. Guo, J. T. Sadowski, S. Johnson, A. Saboor, R. B. Comes, W. Jin, K. A. Mkhoyan, A. Janotti, and B. Jalan, **"Engineering Metal Oxidation using Epitaxial Strain"** *Nat. Nanotechnol. (2023).* https://doi-org.ezp3.lib.umn.edu/10.1038/s41565-023-01397-0

4. P. Adiga, W. Nunn, C. Wong, A. K. Manjeshwar, S. Nair, B. Jalan, and K. A. Stoerzinger, **"Breaking OER and CER scaling relations via strain and its relaxation in RuO_2 (101)"** Materials Today Energy **28**, *101087* (2022).
5. R. Choudhary, S. Nair, Z. Yang, D. Lee, and B. Jalan, **"Semi-metallic $SrIrO_3$ films using solid-source metal-organic molecular beam epitaxy"**, *APL Materials **10**, 091118 (2022)*

Publications (last 2 years)

1. H. Yoon, T. K. Truttmann, F. Liu, B. E. Matthews, S. Choo, Q. Su, V. Saraswat, S. Manzo, M. S. Arnold, M. E. Bowden, J. K. Kawasaki, S. J. Koester, S. R. Spurgeon, S. A. Chambers and B. Jalan, "Free-Standing Epitaxial $SrTiO_3$ Nanomembranes via Remote Epitaxy using Hybrid Molecular Beam Epitaxy" *Sci. Adv. **8**, eadd5328 (2022)* (Primarily funded by DOE)
2. Z. Yang, D. Lee, J. Yue, J. Gabel, T.-L Lee, R. D. James, S. Chambers, and B. Jalan, **"Epitaxial $SrTiO_3$ films with dielectric constants exceeding 25,000"** *Proc. Natl. Acad. Sciences **119**, e2202189119 (2022)* (Primarily funded by DOE)
3. S. Nair, Z. Yang, D. Lee, S. Guo, J. T. Sadowski, S. Johnson, A. Saboor, R. B. Comes, W. Jin, K. A. Mkhoyan, A. Janotti, and B. Jalan, **"Engineering Metal Oxidation using Epitaxial Strain"** *Nat. Nanotechnol. (2023).* https://doi-org.ezp3.lib.umn.edu/10.1038/s41565-023-01397-0 (Primarily funded by DOE)
4. P. Adiga, W. Nunn, C. Wong, A. K. Manjeshwar, S. Nair, B. Jalan, and K. A. Stoerzinger, **"Breaking OER and CER scaling relations via strain and its relaxation in RuO_2 (101)"** Materials Today Energy **28**, *101087* (2022). (Partially funded by DOE)
5. R. Choudhary, S. Nair, Z. Yang, D. Lee, and B. Jalan, **"Semi-metallic $SrIrO_3$ films using solid-source metal-organic molecular beam epitaxy"**, *APL Materials **10**, 091118 (2022)* (Partially funded by DOE)
6. S. A. Chambers, D. Lee, Z. Yang, Y. Huang, W. Samarakoon, H. Zhou, P.V. Sushko, T. K. Truttmann, L. W. Wangoh, T-.L. Lee, J. Gabel, B. Jalan, **"Probing electronic dead layers in homoepitaxial *n*-$SrTiO_3$(001) films"** *APL Materials **10**, 070903 (2022)* (Primarily funded by DOE)
7. J. Yue, Y. Ayino, T. K. Truttmann, M. N. Gastiasoro, E. Persky, A. Khanukov, D. Lee, L. R. Thoutam, B. Kalisky, R. M. Fernandes, V. S. Pribiag, and B. Jalan, **"Anomalous transport in high-mobility superconducting $SrTiO_3$ thin films"** *Sci. Adv. 8, eabl5668 (2022)* (Partially funded by DOE)
8. D. Lee, F. Liu, T. K. Truttmann, S. A. Chambers, and B. Jalan, **"Stoichiometry-dependent surface electronic structure of $SrTiO_3$ films grown by hybrid molecular beam epitaxy"** *Appl. Phys. Lett. 120, 121604 (2022)* (Primarily funded by DOE)
9. W. S. Samarakoon, P. V. Sushko, D. Lee, B. Jalan, H. Zhou, Y. Du, Z. Feng, S. A. Chambers, "Transient electron scavenger drives carrier modulation at a polar/nonpolar perovskite oxide heterojunction" *Phys. Rev. Mater. 6, 103405 (2022) (Editor's pick)* (Primarily funded by DOE)
10. William Nunn, A. Kumar, R. Zu, B. Nebgen, S. Yu, A. K. Manjeshwar, V. Gopalan, J. M. LeBeau, R. D. James, and B. Jalan **"Sn-modified $BaTiO_3$ thin film with enhanced polarization"** *J. Vac. Sci. Technol. A, 41, 022701 (2023)* (Primarily funded by DOE)

A Mechanistic Approach to Solid State Synthesis by Controlling Interfacial Reactions in Designed Precursors

David C. Johnson
Department of Chemistry and Materials Science Institute,
University of Oregon

Keywords: interfaces, metastable compounds, nucleation, x-ray reflectivity, energy landscape

Research Scope

The goal of this project is to enable the synthesis new compounds predicted to be stable by the Materials Genome Initiative (and similar projects) that cannot be prepared using conventional synthesis approaches. To accomplish this goal, the reaction conditions required to direct a reacting system through the energy landscape to a targeted metastable compound, avoiding stable compounds as reaction intermediates, needs to be discovered. The proposal initially focuses on investigating the initial stages of reacting interfaces between elemental layers. The goals are to understand how interfaces evolve using a precursor consisting of a repeating sequence of elemental layers to increase the percent of "interface" in the sample. Our hypothesis is that the layers will interdiffuse, forming an amorphous region at the interface that spans the entire composition range between the elements (Fig. 1). Since different compositions will have different free energies of formation and different inter diffusion rates for the elements, the shape of the amorphous composition as a function of distance will evolve as the sample is annealed at low temperatures. Our hypothesis is that the developing composition profile determines which compound nucleates first at the reacting interfaces. The developing interfacial composition profile will be characterized using a combination of techniques (X-ray reflectivity (XRR), X-ray diffraction (XRD), scanning transmission electron microscopy (STEM), and STEM-energy-dispersive X-ray spectroscopy). The information gained by investigating the evolution of composition gradients in binary A|B diffusion couples as a function of layer thickness and composition will enable the design of ternary, elementally layered precursors that avoid the formation of binary compounds at reacting interfaces.

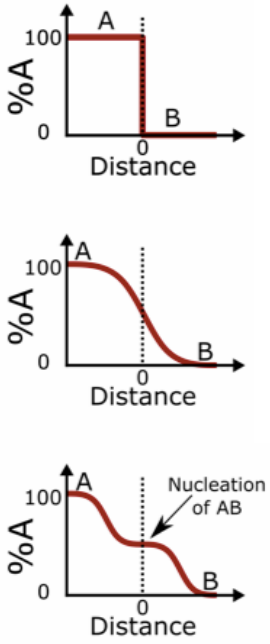

Fig 1: How interfaces evolve on the path to nucleating the first crystalline compound.

Our second hypothesis is that by systematically varying layer thicknesses, the ratio of layer thicknesses and the sequence of reacting layers, it will be possible to change what compound nucleates first and/or inter diffuse the elemental layers before nucleating any crystalline compound. The hypothesis is based on four well-known principles, derived from general thermodynamic and kinetic considerations, that have been established through many decades of research. The starting precursors are designed to enhance the kinetic stability of targeted reaction

intermediates and the final targeted metastable materials against transformation to the thermodynamic ground state. Since diffusion rates decrease exponentially as temperature decreases, low temperature annealing of the precursors kinetically favor products with nanoarchitectures similar to the designed precursor. Rather than having to mix reactants during the reaction to form desired products as in conventional synthesis approaches, minimal diffusion needs to occur to transform the designed precursors deposited with sub nanometer thick elemental layers into ternary and higher order products. To form thermodynamically stable binary products, MER precursors must unmix! This is consistent with Oswald's rule of stages, which is based on the idea that reaction pathways are determined by the fastest reduction in Gibbs free energy. By depositing elements onto unheated substrates and controlling the deposition sequence and layer thicknesses in our designed precursors, we create uniquely structured, mostly amorphous initial reactants. Since diffusion rates in solids at low temperatures are very small, we favor intermediate metastable phases that can form with minimal diffusion during low temperature annealing - because this results in the fastest reduction of the Gibbs free energy. Finally, nucleation depends on both the difference in Gibbs free energy between the existing state and potential products and the magnitude of the rearrangements required. The free energy difference generally is proportional to the extent of undercooling of the metastable state. The designed structure of the precursor requires less rearrangement to form the targeted compound because the local composition and nanoarchitecture match the targeted compound rather than the thermodynamic ground state, which is often mixtures of binary compounds. At low temperatures, disproportionation of a ternary amorphous intermediate is limited by low diffusion rates and the formation of binary compounds should be frustrated by the presence of additional elements. The local structure and overall composition of the homogenous amorphous intermediates should control what compounds nucleate, a kinetic phenomenon.

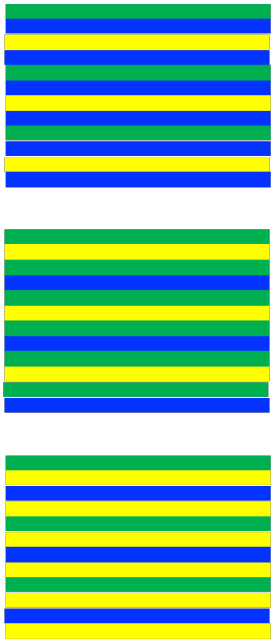

Fig. 2. The sequence of deposited ultrathin elemental layers controls the reaction pathway.

Recent Progress

Our initial project focused on discovering how the reaction between the binary couples in the Pb-Fe-Se system depended on the layer thicknesses and compositions of layered precursors. We used this knowledge to prepare new ternary compounds by avoiding binary compounds as reaction intermediates. Before our investigation, the only compounds in the Pb-Fe-Se ternary phase diagram were the binary compounds → PbSe, tetragonal β-FeSe, NiAs structured δ-FeSe, several NiAs defect structures such as Fe_7Se_8, and two polymorphs of $FeSe_2$, marcasite and pyrite. Although several ternary compounds were predicted to be stable, they could not be synthesized using conventional high temperature reaction of the elements or via molecular beam epitaxy investigations.

Our investigation of the binary systems revealed drastic differences in how the elements reacted. Pb and Se nucleated PbSe grains during the deposition, regardless of the thickness of the layers or the average composition in a broad composition range around a 1 to 1 ratio of the elements. Se deposited on Fe did not react, but Fe deposited on Se interdiffused during deposition to form a mostly amorphous alloy up to a composition near 1 to 1 Fe to Se. If more Fe was deposited, it formed a layer of crystalline Fe on the amorphous 1 to 1 alloy. Most of the reported Fe-Se compounds formed as internediates during annealing of the precursors. We also detected the presence of a new hexagonal compound with close to a 1 to 2 ratio of Fe to Se that formed during deposition and decomposed on annealing at low temperatures (150°C).

Using the information gained from the study of the binary systems, we attempted to prepare the ternary compounds predicted to be stable. We were not successful perhaps due to the complex unit cells of the predicted compounds, which may make their nucleation challenging. We did result in the formation of a new cubic $Pb_{1-x}Fe_xSe$ compound which does not have a rock salt structure. We also showed that it was possible to prepare heterostructures containing intergrowths of PbSe and a 1T structured $FeSe_2$, $(PbSe)_m(FeSe_2)_n$. The values of m and n can be controlled by the structure of the deposited precursor. Fig. 3 contains a HAADF-STEM image of $(PbSe)_1(FeSe_2)_2$ and a STEM-EDS line profile showing the location of Pb, Fe and Se planes. Searching to stabilize this new hexagonal phase of $FeSe_2$, we used previously published data on the dependence of the reaction between V and Se on the thickness and thickness ratios, to prepare substitutional transition metal alloys $V_{1-x}Fe_xSe_2$ with x greater than 0.8 and alloy heterostructures $(PbSe)_m(V_{1-x}Fe_xSe_2)_n$ with $0 < x < 1$ and m and n values determined by the structure of the precursor. The second Ph.D graduate produced from this project, who defended on June 1, is finishing papers on these Pb-V-Fe-Se investigations.

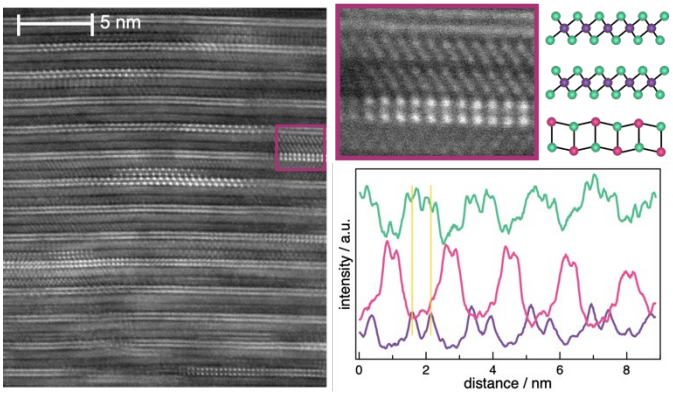

Fig. 3. HAADF STEM cross section of a $(PbSe)_1(FeSe_2)_2$ sample, a close-up showing zone axes, and a STEM-EDS data line scan collected across several unit cells.

Future Plans

The results discussed above clearly demonstrate the ability to prepare new compounds that cannot be prepared using either conventional solid state synthesis approaches. This results from the ability to prepare precursors with designed structures that favor the formation of targeted structures due to the short diffusion lengths and the small diffusion rates during the self-assembly of the crystalline phases at low temperatures. The low diffusion rates during the low temperature processing prevent the precursor from exploring much of the energy landscape. The most rapid way for the system to decrease its free energy is to self-assemble into the most stable phase that

has the composition profile of the precursor. A precursor at place X on the landscape at low temperatures can only explore the local free energy landscape within the local free energy basin containing X due to limited diffusion. This is distinctly different from other synthesis approaches, where the higher diffusion rates enable the system to explore a much larger area of the free energy landscape, favoring the formation of thermodynamically stable products.

We are extending our investigations to include new binary systems (Nb-Se, Sr-Se, Sn-Se and La-Se) binary diffusion couples to understand how the reactions to form binary compounds are impacted by layer thicknesses and composition. There is a rapid growth of the number of ternary and higher order systems where the design of precursors can be informed by knowledge of the binary reaction pathways. While for 7 elements there are 21 binary A|B combinations to be explored, we expect that the M-Se couples are the most important due to the low melting point of Se. The resulting knowledge of how to avoid binary selenides can be used to explore 35 possible ternary, 35 possible quaternary, 21 possible penternary and 7 possible hexaternary systems. We will measure the changing composition gradients at reacting interfaces as a function of temperature and time to understand how tunable nanoarchitecture of a precursor (absolute and relative layer thicknesses, layer order, etc…) can be used to avoid the formation of binary compounds as reaction intermediates. We will limit the extent that the system can explore the free energy landscape as the ultra-small diffusion lengths allow self-assembly of crystalline products at low annealing temperatures for short times. *Our overarching goal is to develop a set of unifying principles describing how to prepare metastable compounds through the design of precursors that avoid the nucleation of more stable compounds as reaction intermediates.*

We will attempt the synthesis of predicted ternary and higher order compounds with energies only slightly above the energy hull of mixtures of binary compounds. We will also attempt the synthesis of heterostructures predicted to be kinetically accessible by our theory collaborator, Sven Rudin at LANL. His approach is to test the stability of nuclei of binary and ternary constituent structures by relaxing islands of these structures sandwiched between layers of the other heterostructure constituent. In the Nb-Fe-Se system, he has predicted that tetragonal β-FeSe should be stable between $NbSe_2$ layers. Our initial probe of this system indicated that we could not make the three predicted ternary Nb-Fe-Se compounds but have been able to make ternary and quaternary PbSe-$FeSe_2$-$NbSe_2$ heterostructures and $NbSe_2$-FeSe heterostructures.

The knowledge being discovered to both understand and control interfacial reactions will advance diverse technologies and tremendously impact fundamental research aimed at the discovery of new materials. The ability to follow solid-state reaction at interfaces through changes X-ray reflectivity of ordered sequences of layers as a function of temperature provides critical information on the initial stages of interdiffusion leading to nucleation of compounds. The experimental parameters associated with the elementally layered precursors (layer thicknesses and layer sequence) enable local composition to be controlled. These parameters can be used to guide reactions through specific intermediates – which is revolutionizing our ability to the search for predicted compounds and new function materials.

Publications

1. D. Bardgett, R. N. Gannon, D. M. Hamann, D. M. Roberts, S. R. Bauers, P. Lu and D. C. Johnson, *Understanding the reactions between Fe and Se binary diffusion couples*, Chem. Mater., **33**, 2585– 2592, 2021. doi.org/10.1021/acs.chemmater.1c00303

2. R. N. Gannon, M. M. Choffel, H. R. Blackwood, N. Wolff, A. Lotnyk, L. Kienle, and D. C. Johnson, *Growth of Crystallographically Aligned PbSe of Controlled Thickness on Amorphous Substrates*, Z. Anorg. Allg. Chem., **648**, e202200015, 2022. doi.org/10.1002/zaac.*202200015*

3. A. M. Miller, M. Lemon, M. Choffel, S. Rich, F. Harvel and D. C. Johnson, *Extracting information from x-ray diffraction patterns containing Laue oscillations*, Z. Naturforsch. B, *77*, 313-322, 2022. doi.org/10.1515/znb-2022-0020

4. F. G. Harvel, M. M. Lemon, R. N. Gannon, D. Bardgett, M. Humphrey, and D. C. Johnson, *Investigation of the Pb-Fe-Se Ternary System and the Synthesis of a New $Pb_{1-x}Fe_xSe$ Phase.* Chem. Mater., **34***,* 6339−6344, 2022. doi.org/10.1021/acs.chemmater.2c00799

5. M. Lemon, F. G. Harvel, R. N. Gannon, P. Lu, S. P. Rudin, and D. C. Johnson, *Targeted synthesis of predicted metastable compounds using modulated elemental reactants*, J. Vac. Sci. Technol. A, **41**, 022203, 2023. doi. org/10.1116/6.0002260

6. M. Lemon, F. G. Harvel, R. N. Gannon, P. Lu, S. P. Rudin, and D. C. Johnson, *1T-$FeSe_2$ Layers in $(PbSe)_{1+\delta}(FeSe_2)_n$ – An Interlayer Stabilized 2D Structure*, Accepted pending minor revisions, Chem. Mater., 2023.

7. M. Lemon, P. Lu, and David C. Johnson, *Trapping metastable transition metal dichalcogenide alloys, $Fe_x(Fe_yV_{1-y}Se_2)$, using slow solid state diffusion rates*, in preparation, 2023.

8. M. Lemon, P. Lu, and David C. Johnson, *Controlling the local and global structure of quaternary heterostructures $[PbSe]_m[Fe_x(Fe_yV_{1-y}Se_2]_n)$, using designed precursors*, in preparation, 2023.

ChIMES: Enabling an Agile Atomistic Simulation Capability for Complex, Inherently Multiscaled Systems

Rebecca Lindsey, University of Michigan

Keywords: Interatomic Models, Atomistic Simulation, Multiscale Modeling, Machine Learning

Research Scope: The *Formulation Engineering of Energy Materials via Multiscale Learning Spirals* SPIRAL team led by PI Lara A. Estroff at Cornell University aims to provide a blueprint for accelerated formulation and manufacturing optimization of solution-processed crystalline materials for energy applications, from reagents to devices. Focusing on metal halide perovskites (MHPs) as a testbed system, this goal necessitates an ability to predict and decipher crystallization pathways as a function of solution chemistry, processing variables, and substrate, which is currently intractable through experiment alone. Simulations provide an ideal means of obtaining this information, but users are currently forced to choose between highly predictive yet computationally expensive first principles (FP) methods, and parametric "force field" approaches affording greater computational efficiency at the expense of accuracy and predictive power. Neither of these approaches afford the balance of accuracy and efficiency necessary for describing nucleation and growth in complex (i.e., many atom-type) MHP materials. But now, modelers have a third option in machine learned interatomic potentials (ML-IAP), which can yield approximations of quantum-based potential energy surfaces at a fraction of the computational expense. These ML-IAPs have had a transformative effect by enabling "quantum accurate" simulations on previously inaccessible scales on the order of 1 micron and 100s of ns that ultimately help bridge the simulation/experiment divide in characterizable phenomena. However, these ML-IAPs remain significantly more computationally intensive than classical "force field" models, and development for systems of more than a few atom types (especially those for which phenomena including chemistry and/or nucleation involved) necessitates enormous sets of high expense training data, generation of which is (1) only tractable for a small subset of the community with access to commensurate computing resources, and (2) impractical for formulation and manufacturing optimization endeavors. To meet this challenge, we are extending the uniquely structured ChIMES ML-IAP and generation framework to enable (1) generating high accuracy models for complex reacting systems with a fraction of the data needed by more ubiquitous ML-IAP approaches and (2) model extension to new chemical spaces without the need for retraining. Ultimately, these capabilities will enable agile deployment of accurate yet efficient simulations for complex, inherently multiscaled materials.

Recent Progress: ML-IAPs aim to provide computationally efficient proxy models predicting how potential energy of a system changes as a function of atomic position, and typically learned on data from FP calculations or simulations. The vast majority of ML-IAPs make use of highly non-linear descriptors and basis functions that necessitate an *a-la-carte* approach to model development, that is, parameter sets are system composition-specific such that introduction of a new atom type necessitates completely refitting the model. Previously, we developed ChIMES[1-3],

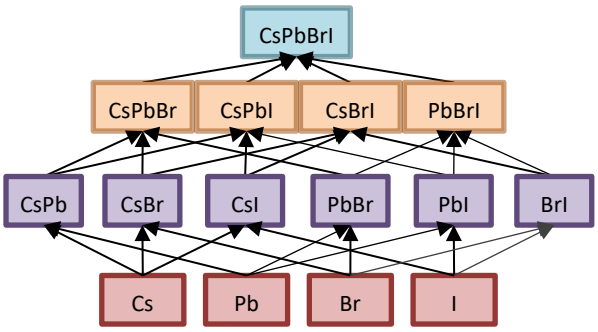

Figure 10: Sample ChIMES parameter hierarchy for $CsPb(I_xBr_{1-x})_3$ MHPs. Each block represents all parameters necessary to describe interactions between atoms of the indicated type. Parameter block in the same row can be fit in parallel, independent of one another.

parametrically linear ML-IAP and semi-autonomous fitting framework[4] capable of equivalent accuracy with orders of magnitude fewer parameters[5] (and hence, training data) than non-linear, e.g., neural network-based approaches.

ChIMES has been shown capable of describing complex processes including reactive phase nucleation on scales overlapping with experiment[6,7]. Here, we demonstrate that the unique underlying ChIMES form enables generation of *chemically transferable and extensible* models, toward application to MHP systems. We show that this makes generating models for high atomic-complexity systems tractable by decomposing the fitting problem into "bite sized" portions that can be fit independently and later combined (See Fig. 1). Ultimately, this allows generation of more trustworthy models that can be continually built upon (Fig. 2).

Future Plans: With our new transfer-learning approach implemented, verified, and validated, we will apply it first to determine how halide distribution and structure changes as a function of composition in $CsPb(I_xBr_{1-x})_3$ MHPs to contextualize experimentally observed changes in conductivity, photostability and mechanical stability. This model will then be extended to investigate unexpectedly favorable solvation observed in methylamine and acetonitrile mixtures, to establish governing solvent/ion, solvent/colloid, and/or solvent nuclei structures toward establishing design principles for other candidate low-viscosity solvents.

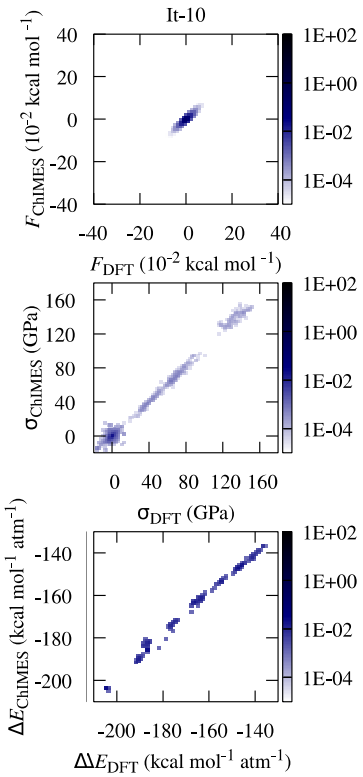

Figure 11: Sample accuracy for the first transfer learned ChIMES model. The top, middle, and bottom plots give provide ChIMES versus FP (DFT) predicted values for per atom forces, and overall configuration stress tensor and energies. Configurations were taken from DFT molecular dynamics simulations.

References:

1. R.K. Lindsey, L.E. Fried, N. Goldman *JCTC 13, 6222 (2017)*
2. R.K. Lindsey, L.E. Fried, N. Goldman *JCTC, 15, 436 (2018)*
3. R. K. Lindsey S. Bastea, N. Goldman, L.E. Fried, *JCP* (2021)
4. R.K. Lindsey, L.E. Fried, N. Goldman, S. Bastea *JCP,* **153** 134117 (2020)
5. C. H. Pham, R.K. Lindsey, N. Goldman, L.E. Fried, *JPC Lett.* (2022)
6. R.K. Lindsey, N. Goldman, L.E. Fried, S. Bastea*, *Nat. Commun.* **13**, 1424 (2022).
7. M.R. Armstrong, R.K. Lindsey, N. Goldman, M.H. Nielsen, E. Stavrou, L.E. Fried, J.M. Zaug, S. Bastea, *Nat. Commun.* **11** 353 (2020)

Atomic Substitution Approach for the Synthesis of non-vdW 2D Crystals

Xi Ling, Department of Chemistry, Division of Materials Science and Engineering, Boston University

Keywords: MoS_2, Metal nitrides, Epitaxial, Edge conversion, Surface conversion

Research Scope

The overarching goal of this program is to develop an *in situ* atomic substitution in van der Waals (vdW) 2D crystals with comprehensive atomic level understanding about the process to realize ultrathin and thickness tunable non-vdW 2D crystals such as metal nitrides, creating a new platform for unprecedented properties and building blocks for cutting-edge device applications. Conventional 2D materials, whose bulks are van der Waals layered materials, have been realized through top-down mechanical exfoliation and self-limited bottom-up growth using chemical vapor deposition (CVD), thanks to the weak binding between layers in their bulks. Such 2D materials possess rational area and quality for electronic and optoelectronic devices. However, metal nitrides,[1] as well as the majority materials in nature, are atomically bonded in three dimensional mode. Synthesizing atomically thin 2D crystals of these materials using the conventional synthetic strategies remains a great challenge. The atomic substitution approach developed in PI Ling group is a new strategy for many synthetically challenging and brand new 2D quantum materials such as the Janus monolayers, new phases, and lateral and vertical junctions between vdW and non-vdW 2D crystals with desired quality for ubiquitous electronics. This approach utilizes an existing vdW 2D crystal as surface confined reactors and converting it to a different material with maintained morphology and crystallinity. Using the conversion from MoS_2 to MoN_x as a model system, this program unveils the conversion process and mechanisms and characterizes the electrical and phonon properties of the obtained new 2D materials.

Recent Progress

Developing new type of two-dimensional (2D) materials remains highly desirable given their versatile properties and applications.[2] Compared to the numerous studies on various vdW 2D materials, the properties and applications of non-vdW 2D materials are rarely studied. The main reason is the lack of effective synthesis methods to access them. In early 2020, we demonstrated an atomic substitution approach to convert vdW MoS_2 layers to ultrathin non-vdW Mo_5N_6. Detailed investigations on the conversion process and mechanism, properties and applications of the obtained Mo_5N_6 are not well studied, which however, are essential for the further development of the approach and the materials. In our recent progress, we dived deeper into the reaction mechanisms of the conversion reaction from few-layer MoS_2 to ultrathin MoN through a comprehensive TEM characterization. We also performed systematic electrical and Raman spectroscopy studies of the obtained ultrathin Mo_5N_6. Moreover, we further applied the approach to synthesize other important ultrathin non-vdW 2D materials such as GaN. Below are the progresses with more details on these topics.

1. Investigation of the conversion process and mechanism from MoS_2 to MoN_x

The crystal structure of molybdenum nitride can be viewed as the molybdenum atoms forming hexagonal close-packed structure and the nitrogen atoms occupying the interstitial sites.[3,4] Depending on the occupancy rate of the interstitial sites, different stoichiometric ratios in forming TMNs were reported. Mo_5N_6 and d-MoN are two commonly reported phases. Although the crystal structure of MoS_2 differs significantly from that of MoN_x, the molybdenum atoms in each layer of MoS_2 also form a hexagonal lattice, but "loose-packed" between the layers. This structural similarity between MoS_2 and MoNx could pay an important role in preserving the crystalline integrity of the material during the conversion process.

We performed nitridation reactions on MoS_2 at different temperatures and obtained two phases: Mo_5N_6 and d-MoN. To investigate the conversion process, we characterize the sample at different stages of the conversion reaction. When the conversion starts at the edge of the MoS_2 flake, lateral heterostructure between MoS_2 and MoN are obtained. On the contrary, when the conversion initiates on the surface of the MoS_2 flake, only a portion of the surface area is converted, forming the MoN/MoS_2 vertical heterostructure. These two conversion mechanisms (Figure 1), named as edge conversion and surface conversion, respectively, are both observed in our experiments. Importantly, the crystal orientation of the converted MoN remains the same as the MoS_2 precursor in both edge and surface conversion pathways. This was evidenced by the aligned selective area electron diffraction (SAED) patterns of the two materials and the Moiré superlattice formed by MoS_2 and MoN with 0° twist angle. These results suggest the atomic substitution process follows an epitaxial mechanism.

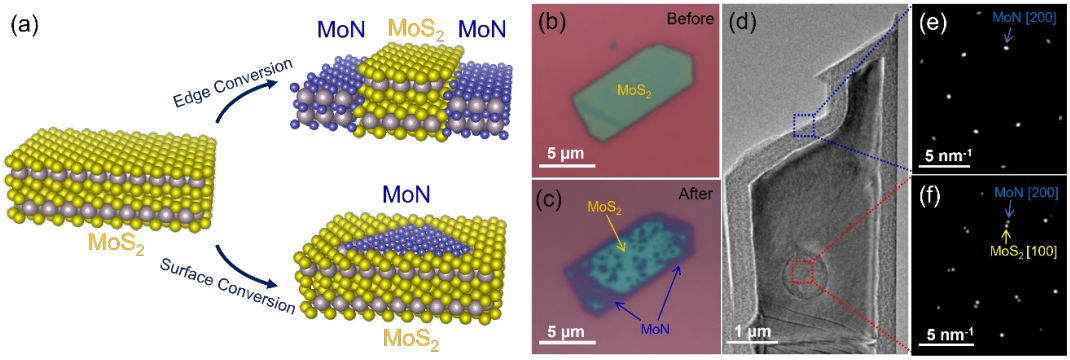

Figure 1. Schematics, optical images, and TEM characterizations of MoS_2-MoN lateral heterostructure from edge conversion, and MoN/MoS_2 vertical heterostructure from surface conversion.

We further conducted a detailed investigation into the reaction kinetics of the edge and surface conversion, utilizing TEM images at different stages (Figure 2). Our findings revealed that edge conversion occurred at a relatively constant rate, while surface conversion exhibited a slower initial rate, followed by a rapid increase in reaction rate. Based on our observations, we proposed potential atomic schemes for the two conversion mechanisms, as shown in Figure 2(g). Edge conversion initiated at the dangling sulfur atoms along the flake's edges, which are typically more reactive compared to fully bonded sulfur atoms. In contrast, surface conversion likely involved point defects such as molybdenum vacancies or line defects like localized strained edges, which

provided active reaction sites. After desulfurization, ammonia molecules attached to exposed molybdenum atoms, forming Mo-N bonds. The reaction progressed as nitrogen atoms replaced inner sulfur atoms, leading to the formation of MoN crystal structures in the converted region. Early edge conversion mainly stemmed from the pre-existing dangling atoms at the edges, whereas surface conversion relied more on intrinsic defect levels. However, as the conversion reaction proceeds, thermal effects and nitrogen diffusion within the MoS_2 generates additional active sites for surface conversion. In contrast, the active sites for edge conversion at the MoS_2-MoN lateral heterostructure interface remains relatively stable. This explains the steady reaction rate of edge conversion, and the increasing rate of surface conversion over time.

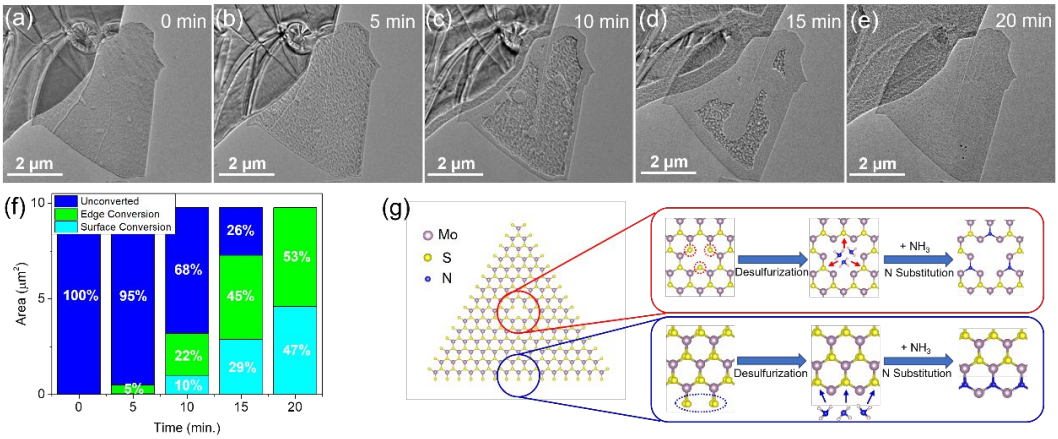

Figure 2. TEM characterization of the conversion reaction progress, and proposed reaction schemes for surface and edge conversion.

2. Electrical properties and applications of the ultrathin MoNx.

Bulk MoNx has long been recognized as a highly conductive material and has been used as electrode materials. One advantage of the atomic substitution approach is that MoNx with tunable thicknesses can be easily obtained by using MoS_2 with different number of layers as the precursor. We measured the electrical conductivity of the two phases of MoNx with different thicknesses. The electrical measurements show that both Mo_5N_6 (229.6 S cm^{-1}) and δ-MoN (3126 S cm^{-1}) exhibit high electrical conductivity down to a few nanometers and remain stable under ambient condition for at least four weeks. To showcase the potential of MoN_x as electrodes for 2D electronics, we first synthesized a MoS_2-MoN lateral heterostructure with an atomically bonded interface through a mask-assisted atomic substitution approach. In this structure, MoS_2 functions as a semiconductor channel material, while MoN serves as a metallic electrode material. We fabricated Au electrodes on MoS_2 and MoN in this structure and performed electrical measurements at various temperatures to determine the Schottky barrier height (SBH) at the junction (Figure 3). Compared

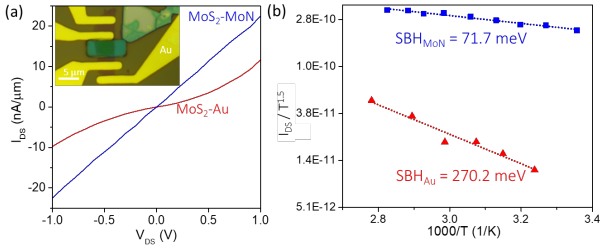

Figure 3. MoS_2–MoN lateral heterostructure by mask-protected conversion and its electrical properties.

to the MoS_2−Au junction, the I-V transport curve of the MoS_2-MoN based device exhibited better linearity and higher current density, indicating the improved contact condition for MoS_2−MoN heterojunction. The SBH for MoS_2−MoN heterojunction was about 70 meV, significantly lower than that of the MoS_2−Au heterojunction (270 meV). This fundamental study on the electrical properties highlights the promise of using atomically bonded MoN as contacts in MoS_2 based electronic devices.

3. Raman spectroscopy study of ultrathin MoN_x.

Raman spectroscopy is a valuable tool for studying the structural and phonon characteristics of materials, especially in the context of 2D materials with distinct properties from their bulk counterparts. However, the Raman spectra and modes of MoN_x have received limited attention in previous research. To address this gap, we conducted a comprehensive study on the Raman spectra of MoNx with different thicknesses. We focused on the Mo_5N_6 and used the theoretical calculations and angle-dependent Raman spectroscopy to assign the observed Raman modes. We then measured the Raman spectra of Mo_5N_6 with varying thicknesses, revealing a significant redshift of the peak at ~210 cm^{-1} when the thickness dropped below 15 nm. These findings motivate further exploration of thickness dependent-properties in MoN_x.

4. Synthesis of other ultrathin non-vdW crystals using the atomic substation approach.

Expanding the application of our approach to other material systems not only enables the creation of new 2D materials, but also enhances our understanding of conversion mechanisms and materials chemistry. In line with this objective, we performed nitridation atomic substitution reactions on several layered materials including GaS, WS_2, WSe_2 and WTe_2, and realized ultrathin GaN and WN_x. Our approach offers advantages such as low-temperature processes and the ability to achieve different thicknesses. Through UV-excited photoluminescence spectroscopy, we observed a blueshift in the band gap of GaN as its thickness decreased. These results demonstrate the successful engineering of GaN band gaps using our atomic substitution method.

Future Plans

In the current program, we made an intriguing observation regarding the dynamics and kinetics of the nitridation reaction of MoS_2, which strongly depend on the stacking configuration and thickness of the MoS_2 layer. Building upon this finding, our future plans aim to unravel the underlying mechanisms behind the discovery. Our hypothesis is that the Moire potential in the stacked 2D structures tailors the chemical reactivity, leading us to introduce a concept of "Moire Chemistry". To test this hypothesis and demonstrate this concept, our focus will be on investigating the nitridation chemical reactivity in a range of 2D homostructures and heterostructures, with particular attention to twisted MoS_2 layers, twisted WS_2 layers, and twisted MoS_2/WS_2 layers known for their rich Moire physics.[5] To characterize the materials at different stages of the reaction, we will employ spectroscopic techniques such as Raman spectroscopy and X-ray photoelectron spectroscopy (XPS), as well as electron microscopy techniques like TEM and EDS. Through these investigations, we anticipate establishing a relationship among the chemical reactivity, structural parameters (such as twist angle), and Moire potential. Additionally, we will collaborate with theorists to complement our experimental observations and findings.

References

1. Toth, L. E. *Transition metal carbides and nitrides*. (Academic Press, 1971).

2. Frisenda, R. *et al.* Recent progress in the assembly of nanodevices and van der Waals heterostructures by deterministic placement of 2D materials. *Chem. Soc. Rev.* **47**, 53–68 (2018).

3. Salamat, A., Hector, A. L., Kroll, P. & McMillan, P. F. Nitrogen-rich transition metal nitrides. *Coord. Chem. Rev.* **257**, 2063–2072 (2013).

4. Luo, Q., Lu, C., Liu, L. & Zhu, M. A review on the synthesis of transition metal nitride nanostructures and their energy related applications. *Green Energy Environ.* S246802572200108X (2022)

5. van der Zande, A. M. *et al.* Tailoring the Electronic Structure in Bilayer Molybdenum Disulfide via Interlayer Twist. *Nano Lett.* **14**, 3869–3875 (2014).

Publications (2021-2023)

1. T. Li, J. Cao, H. Gao, Z. Wang, M. Geiwitz, K. S. Burch, and X. Ling, "*Epitaxial Atomic Substitution for MoS2–MoN Heterostructure Synthesis*", ACS Appl. Mater. Interfaces, **14** (51) 57144–57152 (2022)
2. H. Gao, J. Cao, T. Li, W. Luo, M. Gray, N. Kumar, K. S. Burch, and X. Ling, "*Phase-Controllable Synthesis of Ultrathin Molybdenum Nitride Crystals Via Atomic Substitution of MoS_2*", Chemistry of Materials, **34** (1), 351–357 (2022)
3. R. Li, X. Ma, J. Li, J. Cao, H. Gao, T. Li, X. Zhang, L. Wang, Q. Zhang, G. Wang, C. Hou, Y. Li, T. Palacios, Y. Lin, H. Wang and X. Ling, "*Flexible and High-Performance Electrochromic Devices Enabled by Self-Assembled 2D TiO2/MXene Heterostructures*", Nature Communications, **12**, 1587 (2021)
4. Q. Tan, W. Luo, T. Li, J. Cao, H. Kitadai, X. Wang, and X. Ling, "*Charge-transfer-enhanced d–d emission in antiferromagnetic $NiPS_3$*", Applied Physics Reviews, **9** (4), 041406 (2022)
5. Luo, A. Puretzky, B. Lawrie, Q. S. Tan, H. Z. Gao, Z. F. Chen, A. Sergienko, A. Swan, L. B. Liang and X. Ling, "*Deterministic Localization of Strain-induced Single-photon Emitters in Multilayer GaSe*", ACS Photonics, 2023, Accepted

Electric field driven precision material synthesis

PIs: Chong Liu[1], Shirley Meng[1], Shuolong Yang[1]
[1]Pritzker School of Molecular Engineering, University of Chicago, Chicago, IL 60637

Keywords: Electric Field, Angstrom Resolution Nanopore, Ultrathin Membrane, Scanning Transmission Electron Microscopy, Molecular Beam Epitaxy

Research Scope

Membranes are a key component of energy devices that determines energy efficiency and stability. Angstrom resolution nanopores synthesis on ultrathin films (nanometer scale) opens new avenues towards realizing high selectivity and high conductivity membranes for critical energy devices[1–3]. Methods that can fabricate uniformly distributed nanopores with pore size down to angstrom resolution with controllable surface pore density on any given substrate are still lacking.

The goal of the project is to enable a new method, a non-invasive remote electric field, to create high-density nanopores on ultrathin films, therefore realizing a remote electric field as a general tool for precision material synthesis. The team aims to pinpoint the fundamental mechanisms of materials transformation under an electric field and finally achieve inverse design via the control of materials characteristics (such as composition, crystal structure, electronic structure, thickness, grain size, exposed facets, and defect level), electric field (strength, duration, and wavefunctions), and electrolyte (composition and conductivity). We aim to understand the effect of each tuning knob (materials characteristics, electric field, and electrolytes) and reveal the reaction pathway via (1) the creation of defined starting material states; (2) in situ characterization of reactions and materials evolutions; (3) atomic resolution characterization of the final material states; and (4) validation via computation and modeling.

Recent Progress

This is the first year of the collaborative project. We have made important progress on three fronts: 1) Our team has demonstrated successful in situ pore generation driven by an electric field, which is the key method proposed in the project; 2) Our team has successfully developed an electron microscopy (EM) characterization method to allow location-tracking thickness measurement and atomic resolution imaging for pore origin identification which will be critical for us to unveil the pore creation mechanism; 3) Our team has developed a wafer-scale molecular beam epitaxy (MBE) film liberation technique that broadens the library of materials with defined electronic structures for membrane synthesis.

1. Electric field driven in situ pore generation on polycrystalline MoS_2 thin films.

An electrochemical system is constructed to probe the electric field driven synthesis process. An ultrathin material of interest is suspended in the electrochemical cell with both surfaces exposed to the electrolytes. An electric field is applied on this barrier ultrathin material using two remote

electrodes. With the electric field, cations and anions are accumulated across the barrier (**Fig. 1a**). This accumulation induces an electric double-layer gating effect. Two critical effects of electric field-matter interaction need to be understood as well as the interplay of these two effects, the electrostatic effect and the electrochemical effect, for us to achieve controllable synthesis[4,5].

Few-layer polycrystalline MoS_2 films were grown via chemical vapor deposition (CVD). This growth method can create a high density of grain boundaries. Upon the application of an electric field across the polycrystalline thin films, we measured a dramatic increase in the ionic conductance of the film (**Fig. 1a**), indicating the creation of pores. After pore generation, the film was imaged by scanning transmission electron microscopy (STEM), identifying the largest pores, and establishing an upper bound for the pore size, which we controlled to be <1.5 nm (**Fig. 1b**). This is the first time that electric field gating was successfully used for high density pore generation with pore dimensions of less than 2 nm. We performed the same tests with mechanically exfoliated MoS_2 and found that, due to the absence of grain boundaries, pore creation occurred at much higher voltages, and the rate of pore creation is significantly more difficult to control, which results in large pores. This proves the importance of material characteristics control, especially grain boundaries (**Fig. 1c**) in this case, to achieve precise nanopores. A critical test of the efficacy of nanoporous membranes is their selectivity towards small species of similar size. Our measurements demonstrated the efficacy of our membrane and, paired with molecular dynamics simulations, provided insight into ion dynamics at the nanometer scale.

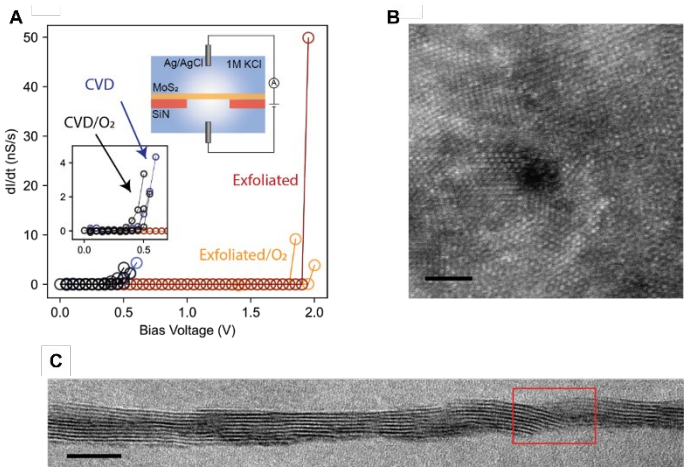

Figure 1. Electrochemical pore creation on polycrystalline MoS_2 thin films. **A**, Change in ionic conductance as a function of applied voltage. Curves for both mechanically exfoliated and CVD-grown MoS_2 are shown. Partial oxidation does not have a significant effect on the pore creation behavior. The inset shows the schematic of the electrochemical device employed. **B**, STEM image of a ~1 nm pore on the polycrystalline MoS_2 thin film formed via electric field gating. **C**, Cross section view of few-layer polycrystalline MoS_2 thin film. A grain boundary is highlighted in red. Scale bar in **B** is 2 nm, scale bar in **C** is 10 nm.

2. Location-tracking thickness measurement and atomic resolution imaging by transmission electron microscopy.

Atomic resolution TEM is critical to characterize the morphology, size, density, and chemistry of nanopores, therefore correlating the material characteristics to pore origin and generation mechanism. Our team employs cryo-EM combined with spectroscopic analysis (Electron Energy

Loss Spectroscopy, EELS) to quantify the pore size distribution and defects chemistry around the pore region for different model compounds. Thus far, we have initially characterized pristine MoS_2 films to establish the ideal imaging conditions. Importantly, we developed the EELS log-ratio method for thickness measurement and established a calibration curve that will permit simplified characterization of porous films and the nanopore aspect ratios from top-view TEM samples. This method can be developed with a location-tracking capability using markers that allows us to compare the MoS_2 thin films before and after pore generation to identify the physical location for pore generation and extract materials' properties correlated to pore formation.

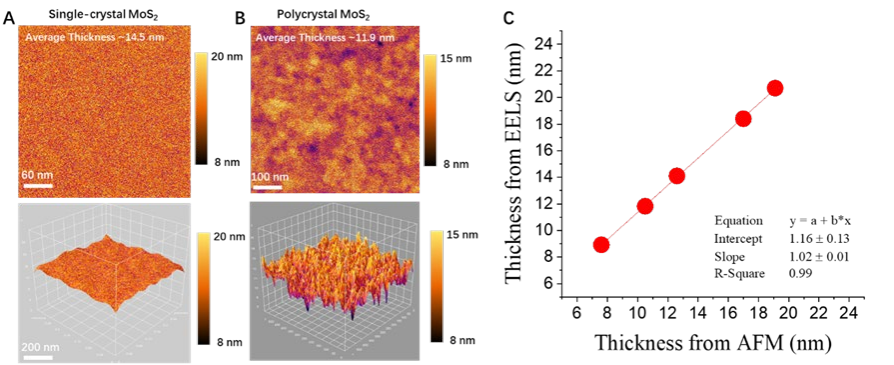

Figure 2. The EELS 2D thickness distribution of single-crystal MoS_2 (**A**) and polycrystal MoS_2 (**B**). **C**, Calibration of low loss EELS thickness measurement based on the AFM-EELS thickness curve to predict more accurate MoS_2 thickness.

The MoS_2 thin film was measured by both Atomic Force Microscope (AFM) and EELS Log-Ratio method. Film thickness measured using EELS Log-Ratio method is consistently larger than AFM measurements. It is generally accepted that the accuracy of the EELS method for material thickness measurement is within 10% and that the source of error arises in cases where the film is too thin for inelastic scattering events to occur, causing the film thickness to be overestimated[6]. In order to correct this error, we collected the thickness of multiple MoS_2 samples to generate a calibration curve. From **Fig. 2C**, with the fit thickness correlation, we can now prescribe the result of future EELS thickness measurements to the AFM-EELS thickness curve. As shown in **Fig. 2A** and **Fig. 2B**, we can obtain the thickness 2D distribution of single-crystal MoS_2 (**Fig. 2A**) and polycrystal MoS_2 **(Fig. 2B)** at a high spatial resolution (0.2 nm) by the Log-Ratio method and the fitted linear AFM-EELS thickness equation. The pore generation mechanism study using location-tracking thickness measurement and atomic resolution imaging is in progress.

3. Wafer-scale molecular beam epitaxy film liberation technique

Materials characteristics are one of the most important tuning knobs for achieving nanopores synthesis. The materials' characteristics include the composition, crystal structure, electronic structure, thickness, grain size, exposed facets, and defect level, which determine the valence and reactivity of the elements, electron and hole reaction pathways (the electronic structure), and solid migration barriers. Our team will use MBE to grow starting materials with defined characteristics to control and correlate pore generation under an electric field. Our team has substantially improved our wafer-scale film liberation technique. We were able to transfer wafer-scale Bi_2Se_3

films, with thicknesses down to 3 nm, from $SrTiO_3$ substrates to 50 μm apertures. As shown in **Fig. 3**, we performed systematic characterizations using optical microscopy, angle-resolved photoemission spectroscopy (ARPES), and TEM. Most interestingly, the TEM image shows that the membrane can have anisotropic strains. Our preliminary result illustrates up to 5% tensile strain along one lattice vector, and 1% compressive strain along another. The anisotropic strain varies between different local domains. This result not only demonstrates the possibility for local strain tuning on a suspended film, but also provides a great platform for nanopore creation using wafer-scale liberated films.

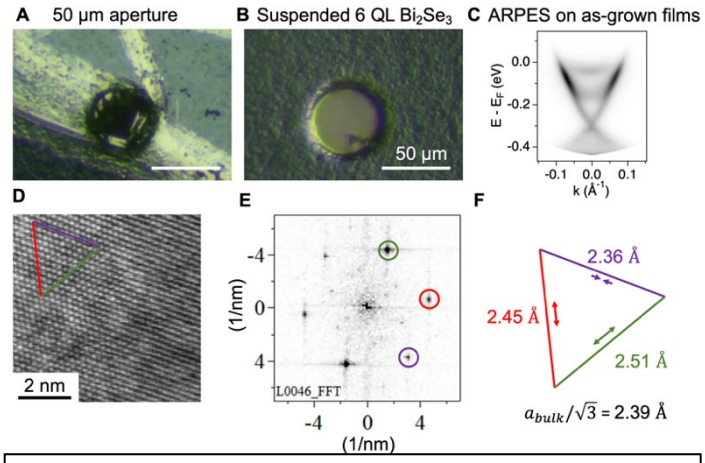

Figure 3. Fabrication and characterization of 6 quintuple layer (QL) suspended Bi_2Se_3 membranes. **A, B,** Optical microscopy images on (**A**) a bare 50-μm aperture and (**B**) an aperture covered by 6 QL Bi_2Se_3. **C,** Angle-resolved photoemission spectroscopy (ARPES) on the as-grown film. **D,** TEM image of the suspended film. **E**, Fourier transform of the TEM image. **F,** Extracted surface-projected lattice constants.

Future Plans

There are two key directions for our future work. The *first* is to unveil the pore generation mechanism, and the *second* is to demonstrate optimized pore size and density generation to the thin film materials of interest. Our team will keep developing methods for materials characteristics control, including establishing the new MBE growth capability of $MoSe_2$, WSe_2, and WTe_2, the introduction of defects or heterogeneities into single crystal MoS_2, assembly and manipulation of thin film (twist and creation of heterostructure). In parallel, we will keep optimizing our location-tracking thickness measurement and atomic resolution imaging method to pinpoint the pore generation mechanism and validate the mechanism to multiple similar transition metal chalcogenides material systems.

References

1. Feng, J., Graf, M., Liu, K., Ovchinnikov, D., Dumcenco, D., Heiranian, M., Nandigana, V., Aluru, N. R., Kis, A. & Radenovic, A. Single-layer MoS2 nanopores as nanopower generators. *Nature* **536,** 197–200 (2016).

2. Wang, L., Boutilier, M. S. H., Kidambi, P. R., Jang, D., Hadjiconstantinou, N. G. & Karnik, R. Fundamental transport mechanisms, fabrication and potential applications of nanoporous atomically thin membranes. *Nature Nanotech* **12,** 509–522 (2017).

3. Garaj, S., Hubbard, W., Reina, A., Kong, J., Branton, D. & Golovchenko, J. A. Graphene as a subnanometre trans-electrode membrane. *Nature* **467,** 190–193 (2010).

4. Leighton, C. Electrolyte-based ionic control of functional oxides. *Nature Mater* **18,** 13–18 (2019).

5. Welborn, V. V., Ruiz Pestana, L. & Head-Gordon, T. Computational optimization of electric fields for better catalysis design. *Nat Catal* **1,** 649–655 (2018).

6. Zhang, H.-R., Egerton, R. F. & Malac, M. Local thickness measurement through scattering contrast and electron energy-loss spectroscopy. *Micron* **43,** 8–15 (2012).

Publications (project started on September 1, 2022)

1. Eli Hoenig, Yu Han, Mingzhan Wang, Chong Liu. Electric field driven in situ (sub)nanometer nanopores generation in few-layer MoS_2 membranes for ion separations. *In preparation (2023).*
2. Jess Chi-Ian Ip, Qiang Gao, Khanh Duy Nguyen, Ian Gangbin Yan, Chenhui Yan, Hossein Rokni, Eli Hoenig, Thomas Marchese, Minghao Zhang, Shirley Meng, Chong Liu, and Shuolong Yang. Wafer-scale liberation of topological insulator ultrathin films. *In preparation (2023).*
3. Woojoo Lee, Haoran Lin, Khanh Duy Nguyen, Yichao Zhang, Yufei Zhao, Hengxin Tan, Jianchen Dang, Tongyao Wu, Ian Gangbin Yan, Thomas Marchese, Minghao Zhang, Shirley Meng, Chong Liu, Chao-Xing Liu, Xiao-Xiao Zhang, Binghai Yan, Pinshane Huang, and Shuolong Yang. Topological electronic structure engineering via layer-by-layer atomic-scale Lego game. *In preparation (2023).*

Boron-Rich Compounds for Applications in High-Density Energy Conversion Devices

Bin Liu, James Edgar, Tim Taylor Department of Chemical Engineering, Kansas State University, Manhattan, KS 66506

Jeffrey Comer, Department of Anatomy and Physiology, Kansas State University, Manhattan, KS 66506

Keywords: Icosahedral boron synthesis, crystal nucleation mechanism, first-principles modeling, molecular dynamics simulation, data-driven experiment design

Research Scope

Icosahedral boron compounds (IBCs), such as boron suboxide (B_6O), display extreme hardness and multiple unusual electrical properties [1]. It has also been demonstrated that many IBCs possess the extraordinary self-healing ability to repair the lattice defects generated from exposure to high-energy irradiation [2]. Such unique behaviors enable these boron-rich compounds to be deployed in nuclear battery devices for space or deep-sea exploration applications when coupled with their high hole mobility. Synthesis and control of the stoichiometry of IBCs remain the key technical challenge. Thus far, the highest quality B_6O crystals were only obtained from high-pressure, high-temperature (~1700°C, 4~5 GPa) experiments using mixed boron and boron oxide powders. The overarching goal of this project is to establish tunable synthesis protocols to produce high-quality B_6O crystals at reduced pressures for intended applications.

The research scope encompasses the acquisition of structural, thermodynamic, and electronic data to determine the stability and phase transition of IBC crystals under synthesis conditions, complemented by experimental crystal growth and characterizations in the lab. Density functional theory (DFT), combined with classical molecular dynamics simulations, has been employed as the primary tool for investigating molecular mechanisms to aid and accelerate experimental synthesis design. This poster highlights recent breakthroughs achieved over the past two years.

Recent Progress

First-principles modeling and data generation. First-principles modeling based on density functional theory (DFT) calculations was employed (by Liu's group) to reveal the fundamental relationships between the structural, electronic, and thermodynamic stabilities of compounds of B_6O with its interstitial elements and point defects. Figure 1a presents the energy band diagrams of semiconducting IBCs [3]. A systematic screening of α-boron compounds also revealed that a simple octet rule offers a consistent explanation for the variations in the computed electronic structures. Thermodynamic calculations (Figure 1b) predicted that the lowest ΔG_f corresponds to the stoichiometric B_6O, indicating the overall stability of this IBC. For defective structures, $B_{5.5}O_{1.5}$ and $B_{5.5}O$ are thermodynamically favored below 500K, even though the phonon dispersions suggest that both compounds are dynamically unstable. The formation energy of $B_{5.5}O_{1.5}$ remains

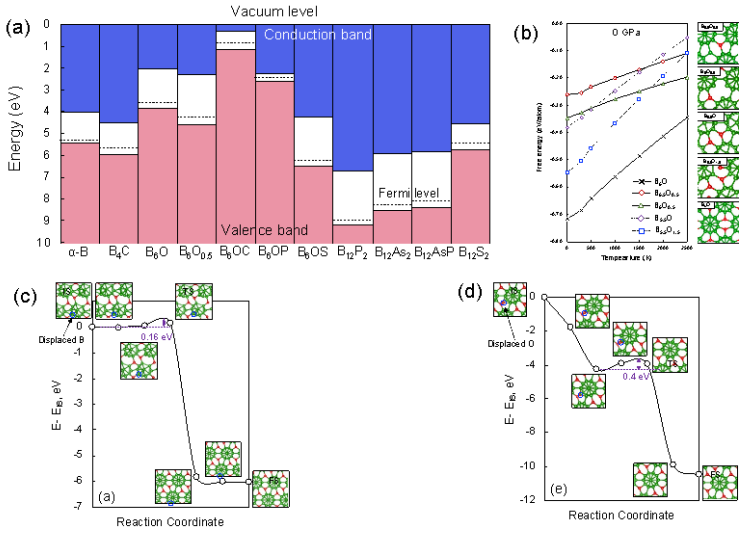

Figure 1. (a) Energy band diagram of semiconducting IBCs. (b) Formation energy of B_6O and representative defective structures (0~2500K) at 0 PGa. (c) Lowest barrier path for displaced boron atom to repair the B point defect. (d) Lowest barrier path for displaced oxygen atom to repair the O point defect. These results are adapted from Ref. [3].

lower than other defective structures up to 1800 K due to the strong B–O bond. At even higher temperatures, the O-deficient structures (e.g., $B_6O_{0.5}$) become thermodynamically favored because the formations of B–O bonds are penalized due to high O_2 entropy cost. At 2500 K, $B_{6.5}O_{0.5}$, with the lowest O content, also overtakes $B_{5.5}O_{1.5}$ and $B_{5.5}O$ and becomes the second thermodynamically stable structure (next to $B_6O_{0.5}$). The nudged elastic band (NEB) method was employed to identify the minimum energy pathways for the diffusions of dislocated B and O atoms. The diffusion of the displaced icosahedral B atoms has an energy barrier as low as 0.16 eV (Figure 1c), confirming that B point vacancies can be repaired with little kinetic limitation. The displaced interstitial O point vacancies can also be easily repaired with a barrier of 0.4 eV (Figure 1d).

Understanding icosahedral boron nucleation with classical molecular dynamics. Reactive molecular dynamics (MD) simulations with a frozen *core* were performed by Comer's group to gain insights into the initial crystal nucleation process using the ReaxFF force field. For the first time, we can gain a molecular perspective on the formations of the boron icosahedra (B_{12}) motif and the energetic profile. Using the data produced from first-principles modeling, the original ReaxFF force field parameters for boron structures, provided by the van Duin group, were updated for icosahedral boron nucleation simulations. Benefiting from a close collaborative relationship with the van Duin group, we adopted an iterative approach to constantly improve and reconcile potential discrepancies between DFT and ReaxFF in the structures generated from MD simulations (Figure 2). Our initial training, based on regular boron and B_6O crystal structures, yields a potential that predicts boron atoms favor the hexagonal borophene-like lattices after 10 ns of simulation. We attribute this behavior to the overstabilization of sp^2 B–B bond formation. To correct the overstabilization, core-shell structures

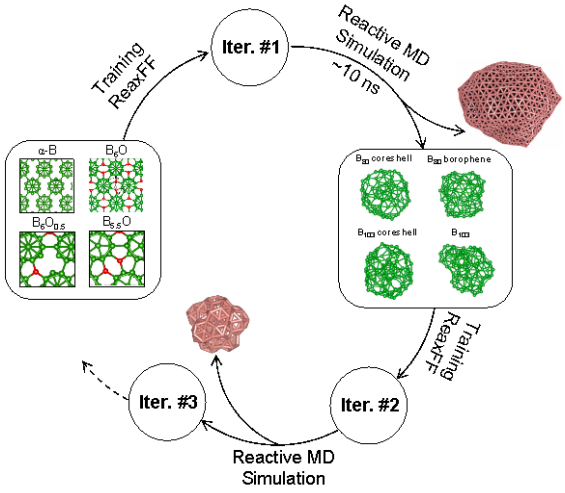

Figure 2. The workflow that describes iterative ReaxFF force field development and reactive molecular dynamics (MD) simulations of icosahedral boron nucleation. Representative training set structures are illustrated in the boxes, and predicted boron structures are shown in pink.

representing B_{80} and B_{103} clusters were added to refine the force field. In the next iteration, MD simulations showed the growth of icosahedral boron structures, which was not observed with the original parameters. As shown in Figure 2, after two iterations, numerous boron clusters exhibiting partial icosahedral character are observable. Continuing efforts are needed until MD predictions fully reconcile with the quantum mechanical calculations.

Quantifying the icosahedrality of boron structures. To analyze our simulations of the growth of icosahedral boron compounds, a robust algorithm has been developed by Comer's group to identify whether each atom is icosahedrally coordinated (locally resembling B_{12} icosahedra) based on the bond topology. This algorithm returns a value of 1.0 for the α phase of pure boron and an ideal B_6O crystal. The β phase of pure boron yields a value of 0.86 owing to the presence of "fused" icosahedra that have atoms with non-icosahedral local environments. As shown in Figure 3a, we observed a greater fraction of "icosahedral" atoms with the new ReaxFF parameters compared to the original ReaxFF parameters in simulations of liquid boron supercooled to 1800 K at atmospheric pressure. The amount of "icosahedrality" appears to increase with decreasing temperature, but we see little dependence on pressure (Figure 3b,c).

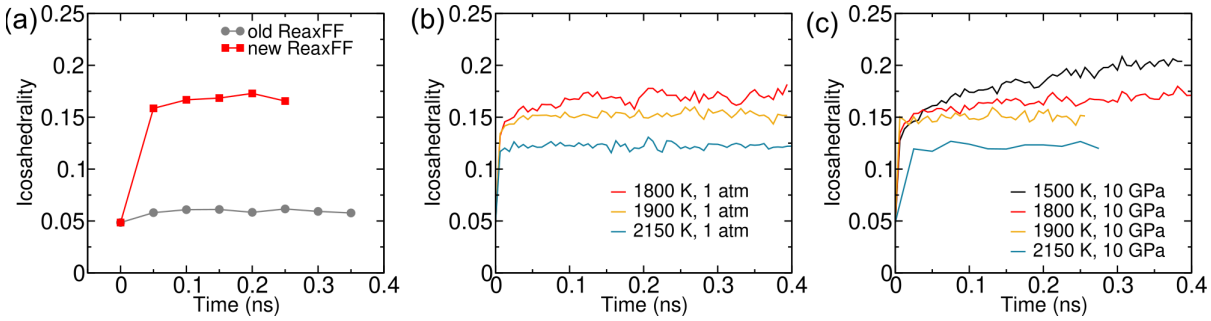

Figure 3. Quantification of the amount of icosahedral boron structure in supercooled liquid boron. (a) Much more icosahedral structure is formed with the reoptimized ReaxFF parameters than the original parameters (1800 K, 1 bar). (b) The amount of the icosahedrality formed within 0.4 ns increases with decreasing temperature using the new parameters. (c) No significant amounts of icosahedral structure was observed at 10 GPa.

Machine-learning inter-atomic potentials. The iterative force field development described above can be time-consuming. Data collected from first-principles modeling can be directly utilized to generate mathematical inter-atomic potentials. In the past two years, Liu's group adopted two approaches, i.e., artificial neural network (ANN) [4] and sparse Gaussian Process (GP), to train machine-learning potentials to study IBC properties. ANN potential training is relatively straightforward. A large data set can be quickly generated from standard DFT calculations or *ab initio* MD simulations. Figure 4 presents the estimation of thermal expansion coefficients of bulk B_6O, which show excellent agreement with experimental values [5]. Nevertheless, ANN potentials fail to predict phase transitions. Current research focuses on the active learning

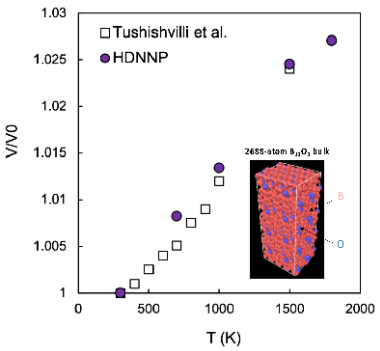

Figure 4. Thermal expansion coefficients predicted by ANN potential and comparison with experimental results, Ref. [5].

enabled by the sparse GP technique, an efficient approach better adapted to predicting structure evolutions.

Flux-based bulk B_6O crystal synthesis. Many solvents, e.g., Fe, would reduce B_6O formed in the solution because metal oxides have significantly lower energy than B_6O. Nickel oxide thermodynamically favors B_6O formation, but nickel complexes heavily with boron, preventing B_6O from precipitating from the molten flux. In this project, copper was chosen as the solvent. The synthesis and crystal growth experiments proceeded as follows. A mixture of boron powder, copper, and copper oxide is heated to 1300°C-1500°C (at 1 bar) until a homogeneous solution is formed. The solution is held at this temperature for 24 hours and then slowly cooled at 2°C /hour to precipitate boron suboxide from the copper flux.

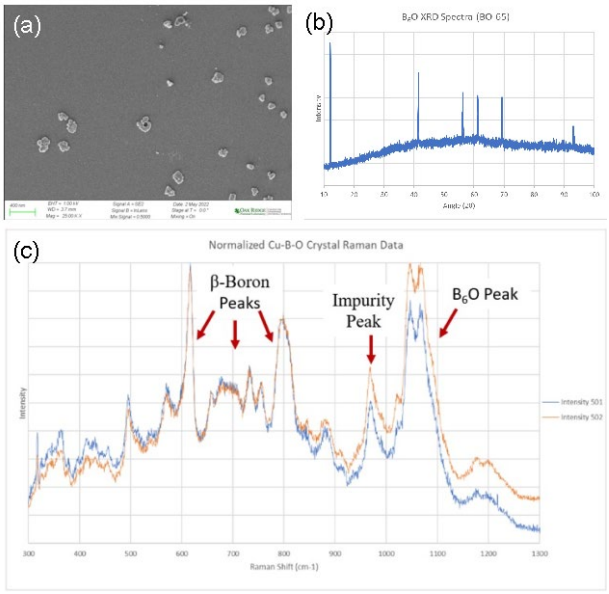

Figure 5. (a) SEM image of a B_6O crystal surface with copper microparticles. (b) XRD spectra, whose narrow peaks indicate highly crystalline behavior. (c) Raman data outlining the different peaks present in this crystal system.

The precipitated crystals (embedded in the copper flux) are displayed in Figure 5a. The XRD (Figure 5b) and Raman (Figure 5c) measurements confirmed the boron suboxide phase in these samples. Different crucible materials, primarily alumina, and hBN, were used to precipitate B_6O from a molten metal flux. hBN crucibles severely inhibit crystal precipitation, resulting in smaller crystallites and a significantly smaller total precipitated mass. Experiments have moved forward using alumina crucibles. Other crucible materials are expected to be tested in the future.

Future Plans

Future research will focus on establishing accurate, reliable inter-atomic potentials for large-scale molecular simulations of icosahedral boron nucleation and growth. The success will reveal the critical thermodynamic and composition factors to control IBC growth. More importantly, these molecular insights will allow us to better guide experiment design to improve the size and quality of boron suboxide crystals.

The successful synthesis will also be accompanied by further characterizations to test metal flux compositions to improve material stoichiometry, including SEM, EDS, TEM, Raman spectroscopy, and XRD.

References

[1] D. Emin, *Unusual properties of icosahedral boron-rich solids*, Journal of Solid State Chemistry, **179** (2006) 2791-2798.

[2] S.P. Huber, E. Gullikson, C.D. Frye, J.H. Edgar, R.W.E. van de Kruijs, F. Bijkerk, D. Prendergast, *Self-healing in $B_{12}P_2$ through mediated defect recombination*, Chemistry of Materials, **28** (2016) 8415-8428.
[3] B. Liu, D. Evans, H. Deng, J. Edgar, *Structure, Stability, and Electronic Properties of Boron Suboxide: A Density Functional Theory Study*, The Journal of Physical Chemistry C, **126** (2022) 16050-16060.
[4] H. Deng, J. Comer, B. Liu, *A high-dimensional neural network potential for molecular dynamics simulations of condensed phase nickel and phase transitions*, Molecular Simulation, **49** (2023) 263-270.
[5] M.C. Tushishvili, G. Tsagaresihvili, D.S. Tsagareishvili, *Thermoelastic Properties of Boron Suboxide in the Range 0-1500 K*, Journal of Hard Materials(UK), **3** (1991) 225-233.

Publications

[1] B. Liu, D. Evans, H. Deng, J. Edgar, *Structure, Stability, and Electronic Properties of Boron Suboxide: A Density Functional Theory Study*, The Journal of Physical Chemistry C, **126** 16050-16060 (2022).

[2] H. Deng, J. Comer, B. Liu, *A high-dimensional neural network potential for molecular dynamics simulations of condensed phase nickel and phase transitions*, Molecular Simulation, **49** 263-270 (2023).

[3] H. Deng, D. Evans, B. Liu, *Predicting phase stability of boron suboxides using inter-atomic potentials from active learning*, (*in preparation*).

[4] Ahmadisharaf, A., Comer, J., *Molecular simulation of icosahedral boron nucleation based on the ReaxFF force field study* , (*in preparation*).

Leveraging metastability in high entropy alloy design for grain refinement in additive manufacturing

Atieh Moridi, Cornell University

Keywords: Additive manufacturing, phase metastability, solidification, synchrotron X-ray diffraction

Research Scope

Despite the advantages of additive manufacturing (AM) such as mechanical design freedom and short lead times, anisotropic properties and scatter in mechanical performance of printed parts currently impede greater adoption of AM. The property anisotropy arises due to formation of columnar grains along build direction, and the inconsistency in performance is caused by the stochastic nature of process-induced defects. We hypothesize that a single alloy design criterion focused on phase metastability design could concurrently address the challenges. In particular, metastable alloys could undergo multiple phase transformations induced by intrinsic heat-treatment in the layer-wise AM process and develop fine-grained microstructures with reduced crystallographic textures. Such metastable alloys can also trigger phase transformation or other additional deformation mechanisms in the vicinity of defects upon loading and can retard their growth by providing localized work hardening.

While metastable alloys have been successfully processed using AM, there is currently no fundamental knowledge about the effect of varying metastability on 1) solidification pathways, 2) grain morphology and 3) defect tolerance in AM parts. We are explicitly studying this gap in this project. To systematically vary the degree of metastability, we place focus on FeMnCoCr high entropy alloy system. The metastability of this alloy system can be modified by changing its composition (i.e., Mn and Fe content). To investigate the solidification pathway of these different metastable alloys under AM processing conditions, we leverage our custom AM setup designed for integration at synchrotron facilities. Solidification pathways are correlated with the solidified microstructure using electron microscopy imaging. Finally, microstructural evolution upon loading especially around manufacturing defects will be studied by conducting tensile experiments inside a scanning electron microscope (SEM).

Recent Progress

During the current award year, we are beginning to achieve the first goal of understanding the complex relationship between phase metastability and solidification microstructure using HEAs composed of FeMnCoCr. In the rapid cooling of AM, solute segregation and formation of metastable phases that are not in the equilibrium solidification pathway can occur. Scheil-Gulliver solidification model [1] predicts the phases and compositions using a thermodynamic description of the phases in a system. The main assumptions in the Scheil-Gulliver model are that the composition of the liquid is homogeneous while the back-diffusion in the solid phase(s) is negligible. Since the Marangoni flow in AM mixes the melt pool well [2], the assumptions made in the model is justified, and agreement between simulations and experimental results have been

documented in literature [3]. Fig. 1 shows the calculated Scheil solidification diagrams for $Fe_{40}Mn_{40}Co_{10}Cr_{10}$, $Fe_{35}Mn_{45}Co_{10}Cr_{10}$, and $Fe_{30}Mn_{50}Co_{10}Cr_{10}$, which will henceforth be referred to as Mn40, Mn45, and Mn50, respectively. In both Mn40 and Mn45, liquid phase is projected to begin solidifying into fcc at 1308 ˚C and 1282 ˚C, respectively. However, in Mn50, the solidification model predicts a metastable bcc phase to first appear from liquid at 1278 ˚C, and at 45% solid, the fcc phase is projected to appear.

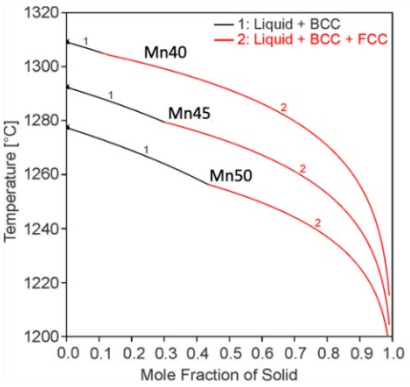

Fig. 1. Scheil solidification plot of Mn40, Mn45, and Mn50.

To validate the solidification simulation, operando X-ray diffraction studies were conducted at Cornell High Energy Synchrotron Source (CHESS) to observe the solidification pathway of each material. The experiment used a custom setup developed by the Laboratory for Advanced Materials and Manufacturing. A high-energy monochromatic hard X-ray beam with 61.332 keV energy, and square cross-section of 0.750 mm X 0.750 mm was used in transmission mode. A CdTe Eiger 500k area detector and a GE 51-RT+ area detector were placed at a sample-to-detector distance of 899 mm as calibrated by a CeO_2 standard reference powder material. A frame rate of 100 Hz and 4 Hz were found to be the maximum temporal resolutions attainable without deterioration of the signal-to-noise ratio for the Eiger detector and GE detector, respectively. Laser power of 200 W, scanning velocity of 4.5 mm/s, and layer height of 2 mm were determined to be the best parameter to acquire the XRD data during the print in Argon atmosphere.

The diffracted rings acquired on the Eiger detector were integrated along the azimuth and plotted against time, as shown in Fig. 2. All materials initially have three peaks associated with fcc. As the material goes through heating and melting, the peaks shift towards a lower 2θ, reflecting the increase in temperature and consequent expansion of the crystal lattice. While Mn40 and Mn45 only have three peaks throughout the process, Mn50 shows an intermediate peak appear and disappear immediately after melting. This peak is indexed as a metastable bcc phase (δ(211) peak marked by an arrow). The experimental results disagree with Scheil simulation since only Mn50 goes through a bcc-to-fcc solidification pathway. This is because Scheil simulation often overpredicts the bcc phase fraction when applied to AM

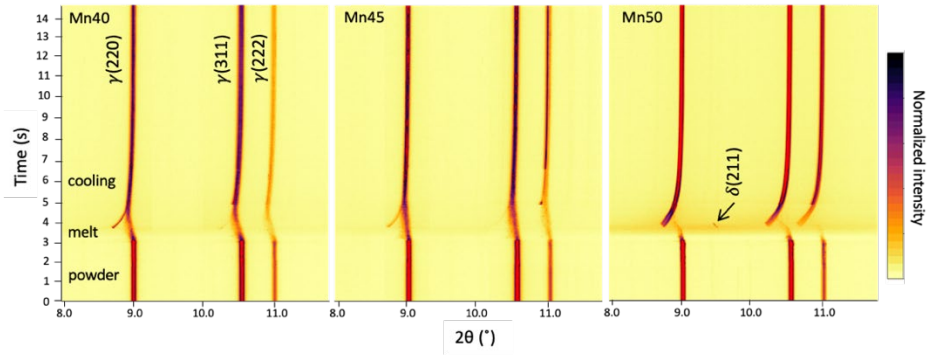

Fig. 2. 2θ vs time plot of Mn40, Mn45, and Mn50 in operando synchrotron X-ray diffraction studies at Cornell High Energy Synchrotron Source (CHESS).

conditions; thus, the trend still stands that there is an increase in bcc content from Mn40 and Mn45 to Mn50.

In Fig. 3, the BSE images of the cross-section of the bead shows significant grain refinement in Mn50 compared to Mn40 and Mn45. In addition, the elongated nature of the grains in Mn40 and Mn45 are broken down into finer, more equiaxed grains. There is a small amount of retained ferrite in Mn50, which show up as white spots in BSE images as presented in the inset of Fig. 3.

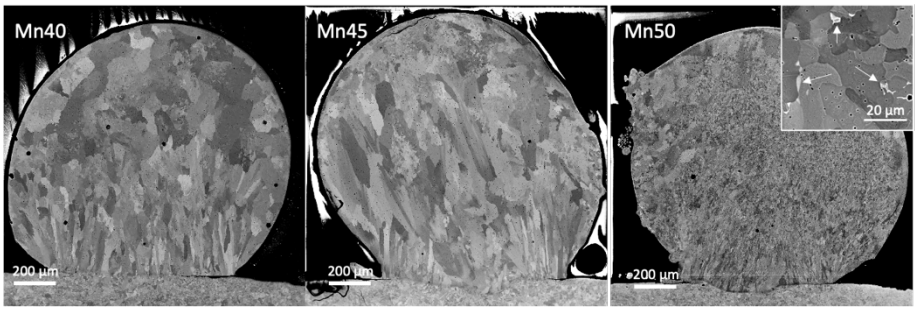

Fig. 3. Backscatter images of cross sections of single beads acquired at CHESS

The three compositions were printed in a FormAlloy X2 direct energy deposition (DED) system equipped with an IPG Nd:YAG continuous wave fiber laser with 500 W maximum power with a spot size of 1.2mm. Blocks of 26 mm x 10 mm x 6 mm (WxLxH) were printed in an inert Ar atomsphere on a stainless steel 304L substrate with 0.2 mm layer height. All were printed under the same nominal processing conditions (laser power of 250 W, scanning speed of 800 mm/min, powder feed rate of 0.5 rpm). These samples were cross sectioned using a high-speed diamond saw parallel to the build direction and polished down to 0.08 µm colloidal silica for compositional and microstructural evaluation. Imaging was conducted on a Tescan Mira3 field-emission scanning electron microscope (FE-SEM) equipped with a backscattering detector. Electron backscatter diffraction (EBSD) was acquired on a QUANTAX EBSD for grain morphology and phase makeup evaluation at a pixel size of 1.2 µm for Mn40 and Mn45 and 0.6 µm for Mn50 (Bruker, Billerica, MA). The measurements were processed using ATEX open-source software (Metz, France).

Multilayer printed microstructure shows the same trend as single beads, with notable grain refinement as well as the breakup of epitaxial crystallographic growth, as shown in the Inverse Pole Figure (IPF) maps in Fig. 4. The grains are elongated along and across layer boundaries in Mn40 and Mn45, but grain refinement is observed in Mn50 with a nearly 80% decrease in average grain size (191.6±140.8 µm for Mn40 and 41.6±27.8 µm

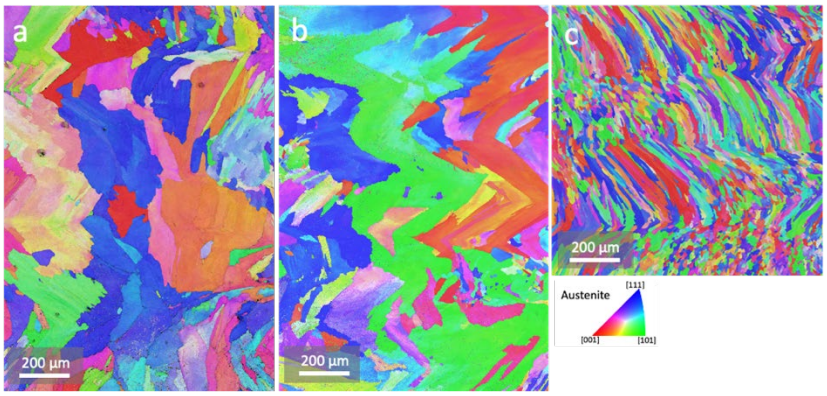

Fig. 4. Inverse Pole Figure (IPF) maps of (a-c) Mn40, Mn45, and Mn50, respectively.

for Mn50). The mechanism for grain refinement is hypothesized to be dendrite fragmentation of bcc during transformation, pinning of grain boundaries by the secondary phase, or a combination of both.

Future Plans

Future plans include the mechanical testing of the printed specimens to study the deformation mechanism and damage tolerance of the materials. We will conduct an interrupted mechanical testing on the fully dense samples of the three compositions to understand the work-hardening and deformation behavior using a micro tensile stage, digital image correlation (DIC) for strain measurement, and EBSD. In addition, thermodynamic simulations will be conducted to reveal the compositional trends of solidification pathways amongst HEAs composed of 3d transition metals and other common elements such as Al. While the potential of HEAs has been well demonstrated in literature, the vast compositional space renders the alloy development a daunting task. For a smart screening of the possible combinations of HEAs, we will employ thermodynamic simulations using ThermoCalc to determine phase metastability before investing time, money, and effort into atomizing a custom powder, performing print parameter optimization, and conducting in-situ synchrotron XRD studies for every possible composition. For this study, we will screen a combination of 3d transition metals (Ti, V, Cr, Mn, Fe, Co, Ni, Cu) as well as other elements with larger atomic radii such as Al, Nb, and Ta using the Scheil solidification model to investigate the combinations of elements that may solidify with an intermediate phase. Since the prediction of intermediate phase formation alone is insufficient (as demonstrated in the current HEA system), we will look for an increasing trend in bcc formation in materials systems. The standing questions are the following:

1. What is the underlying mechanism for bcc formation with increasing Mn content?
2. What is the effect of solidification rate on metastable phase formation?
3. How does additive manufacturing affect the materials properties compared to conventionally processed HEAs?

These questions will be answered through a systematic study of phase metastability to uncover the complex relationship between composition, process, microstructure, and properties in AM. These findings will inform the design guidelines for a metastable HEA for AM.

References

[1] F. Scaglione, S. Arnaboldi, C. Viscardi, M. Baricco, M. Palumbo, Solidification Calculations of Precious Alloys and Al-base Alloys for Additive Manufacturing, Metals (Basel). 12 (2022).

[2] T. DebRoy, H.L. Wei, J.S. Zuback, T. Mukherjee, J.W. Elmer, J.O. Milewski, A.M. Beese, A. Wilson-Heid, A. De, W. Zhang, Additive manufacturing of metallic components – Process, structure and properties, Prog. Mater. Sci. 92 (2018) 112–224.

[3] B. Bocklund, L.D. Bobbio, R.A. Otis, A.M. Beese, Z.K. Liu, Experimental validation of Scheil–Gulliver simulations for gradient path planning in additively manufactured functionally graded materials, Materialia. 11 (2020).

Publications

[1] A. Wakai, A. Das, J. Bustillos, A. Moridi, Effect of solidification pathway during additive manufacturing on grain boundary fractality, Addit. Manuf. Lett. 6 (2023).

[2] S. Alipour, A. Moridi, F. Liou, A. Emdadi, The Trajectory of Additively Manufactured Titanium Alloys with Superior Mechanical Properties and Engineered Microstructures, Addit. Manuf. V 60, Part A, 103245 (2022).

Synthesis of layered square planar nickelates

Julia A. Mundy, Department of Physics, Harvard University

Keywords: molecular-beam epitaxy, thin films, superconductivity, soft chemistry, strain

Research Scope

Since the discovery of high-temperature superconductivity in copper oxide materials, there have been sustained efforts to both understand the origins of this phase and discover new cuprate-like superconducting materials. One prime materials platform has been the rare-earth nickelates and, indeed, superconductivity was recently discovered in the doped compound $Nd_{0.8}Sr_{0.2}NiO_2$ (ref. [1]). Undoped $NdNiO_2$ belongs to a series of layered square-planar nickelates with chemical formula $Nd_{n+1}Ni_nO_{2n+2}$ and is known as the 'infinite-layer' ($n = \infty$) nickelate. Our research has developed the synthesis of the full family of $Nd_{n+1}Ni_nO_{2n+2}$ thin films. We begin with the reactive oxide molecular-beam epitaxy of the Ruddlesden-Popper $Nd_{n+1}Ni_nO_{3n+1}$ materials which are reduced to form $Nd_{n+1}Ni_nO_{2n+2}$. Our work discovered superconductivity with $T_c \sim 13$ K in the undoped $Nd_6Ni_5O_{12}$ compound. We also determine the limits to the strain-engineering of these materials.

Recent Progress

The discovery of superconductivity in infinite-layer $Nd_{0.8}Sr_{0.2}NiO_2$ thin films reignited an interest in the nickelates as cuprate analogues. More broadly, the infinite-layer nickelates are the $n = \infty$ member of a homologous series of 'layered square-planar nickelates', $R_{n+1}Ni_nO_{2n+2}$ or $(RNiO_2)_n(RO_2)$, where R = trivalent rare-earth cation and $n > 1$. These compounds host n quasi-two-dimensional NiO_2 planes separated by $(RO_2)^-$ spacer layers, as illustrated in Fig. 1. Mapped onto the cuprate phase diagram, the bulk stable $n = 3$ compound, $Nd_4Ni_3O_8$, lies in the overdoped regime with a formal electron count of $3d^{8.67}$. The $n = 5$ compound, $Nd_6Ni_5O_{12}$, has a formal electron count of $3d^{8.8}$ aligned with optimal doping. The layering n also tunes the out-of-plane electronic dispersion: density-functional theory (DFT) calculations suggest that, despite their similar d electron fillings, the electronic structure of $Nd_6Ni_5O_{12}$ is more two-dimensional, and thus more cuprate-like, than that of the hole-doped infinite-layer nickelates. Layered square-planar nickelate thin films thus form an exciting platform to investigate the role of dimensionality, epitaxial strain, and chemical doping in nickelate superconductivity.

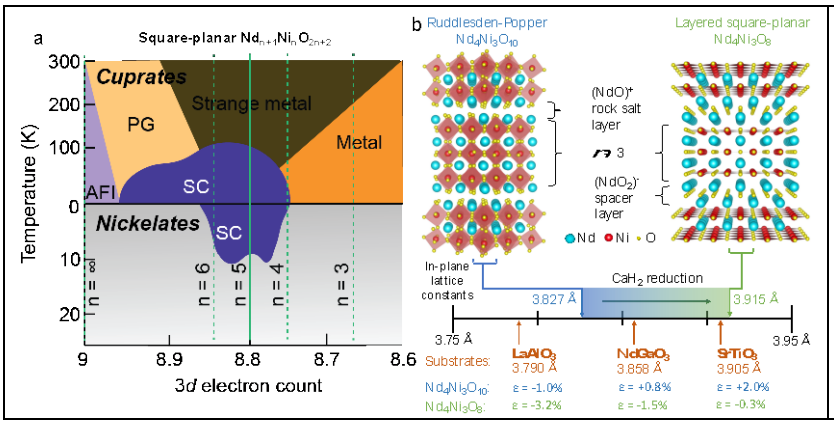

Fig 1. Synthesis of square planar nickelates. a) The layered square-planar nickelates $R_{n+1}Ni_nO_{2n+2}$ can be mapped onto the cuprate phase diagram where the n = 5 has the optimal filling. b) Synthesis of these compounds involves competing requirements for the as-grown and reduced phases.

The synthesis of square-planar nickelate thin films, however, remains an immense challenge. Due to their low decomposition temperatures, infinite-layer and layered square-planar nickelates are accessible only via low temperature topotactic reduction of the perovskite RNiO$_3$ ($n = \infty$) or Ruddlesden–Popper $R_{n+1}Ni_nO_{3n+1}$ ($n > 1$) parent compounds, respectively. Furthermore, the absence of superconductivity in reduced nickelate powders and bulk single crystals to date suggests that external stabilization by a substrate may be required to yield superconductivity. The synthesis of reduced nickelate thin films, however, is complicated by the large ~2–3% increase in the in-plane lattice parameter upon reduction. To minimize compressive strain in the reduced phase, the parent compound must be synthesized under tensile strain, as shown in Fig. 1. Therefore, understanding the strain-dependent stability of both the parent Ruddlesden–Popper and reduced square-planar phases is essential to optimize the synthesis of layered square-planar nickelate thin films.

Using reactive oxide molecular-beam epitaxy, we have synthesized the targeted Nd$_6$Ni$_5$O$_{16}$ compound on NdGaO$_3$ substrates which provide slight tensile strain to the as-grown phase; these materials were reduced to the Nd$_6$Ni$_5$O$_{12}$ square-planar structure. We demonstrate superconductivity with a T_c of ~13 K. Our square-planar layered compounds possess similarities to the doped infinite-layer nickelates, but notably have positive Hall coefficients up to room temperature, which is indicative of a more single-band-like picture. This, in tandem with our theoretical description, suggests that the quintuple-layer Nd$_6$Ni$_5$O$_{12}$ compound possesses an electronic structure that is qualitatively intermediate between that of the cuprates and infinite-layer nickelates, and tunable by the dimensionality of the system.

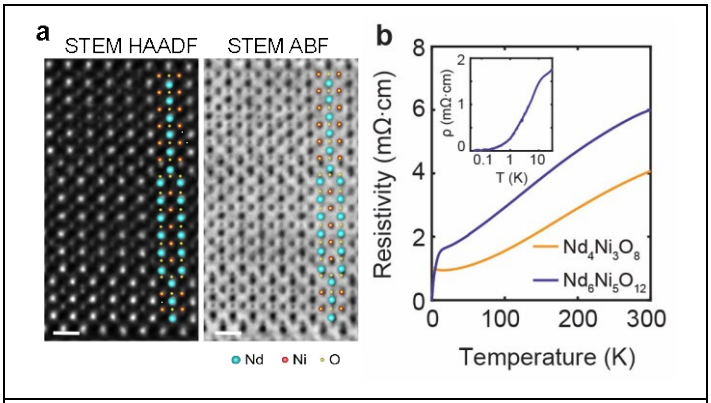

Figure 2. Superconductivity in the $n = 5$ compound. a) Electron microscopy images of the ordered phase after the chemical reduction. b) We observe the onset of superconductivity at 13 K in the $n = 5$ compound. The overdoped $n = 3$ compound is fully metallic.

We also explore the competing requirements for the synthesis and oxygen deintercalation of $Nd_4Ni_3O_{10}$ thin films on $LaAlO_3$ (001), $NdGaO_3$ (110), and $SrTiO_3$ (001). We focus on the $n = 3$ Ruddlesden–Popper compound because both the oxidized $Nd_4Ni_3O_{10}$ and reduced $Nd_4Ni_3O_8$ compounds have been synthesized as bulk single crystals, allowing us to benchmark the strain states with bulk lattice constants. We present the molecular beam epitaxy (MBE) synthesis of $Nd_4Ni_3O_{10}$ on the three substrates. We show that $Nd_4Ni_3O_{10}$ on $SrTiO_3$ exhibits a high degree of disorder characterized by a near-equal density of vertical and horizontal rock salt faults; consequently, we do not consider these films for reduction. When synthesized under lesser tensile strain on $NdGaO_3$, a smaller density of vertical rock salt faults forms while maintaining relatively high-quality Ruddlesden–Popper ordering. By contrast, $Nd_4Ni_3O_{10}$ on $LaAlO_3$ exhibits coherent ordering of horizontal rock salt layers with very few extended defects. Next, we reduce $Nd_4Ni_3O_{10}$ to the square-planar phase, $Nd_4Ni_3O_8$, on $LaAlO_3$ and $NdGaO_3$. In $Nd_4Ni_3O_8$ on $LaAlO_3$, we observe regions with pristine square-planar ordering along with disordered regions where the c-axis cants locally by as much as 7°, likely a compressive strain relaxation mechanism. However, all reduced films on $LaAlO_3$ are insulating. On the other hand, $Nd_4Ni_3O_8$ and $Nd_6Ni_5O_{12}$ on $NdGaO_3$ are metallic and superconducting, respectively. Our study thus demonstrates a pathway to the synthesis of a superconducting compound and sets limits on the ability to strain-engineer $R_{n+1}Ni_nO_{2n+2}$ thin films via epitaxy.

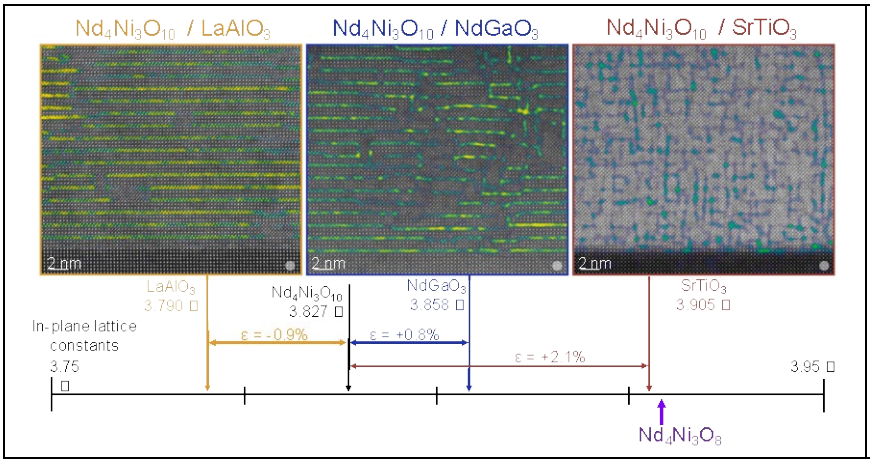

Figure 3. HAADF-STEM images of $Nd_4Ni_3O_{10}$ compounds synthesized as a function of strain. While we can synthesize high quality films on compressively strained $LaAlO_3$ substrates, tensile strain generates rock salt defects that disrupt the intended layering.

Future Plans

In revealing superconductivity in a new layered nickelate compound, we unlock the rare-earth nickelates as a family of superconductors beyond the doped infinite-layer compound. While the nickelates are their own class of superconductors distinct from the cuprates, it is intriguing that the cuprate-motivated predictions of optimal $d^{8.8}$ filling have yielded superconductivity, whether achieved through chemical doping or layering dimensionality. Our work opens up future avenues in which chemical doping and artificial layering may be harnessed in concert to map out and optimize superconductivity. In this vein, we suggest that exploring the phase diagram around optimal $d^{8.8}$ filling by using Sr^{2+} or Ce^{4+} to chemically dope a layered nickelate may be an exciting route to further expand the family of nickelate superconductors.

Publications

1. G. A. Pan et al. "Superconductivity in a quintuple-layer square-planar nickelate." *Nature Materials* 21(2), 160-164 (2022).

2. G. A. Pan, Q. Song et al. “Synthesis and electronic properties of $Nd_{n+1}Ni_nO_{3n+1}$ Ruddlesden-Popper nickelate thin films.” *Physical Review Materials*, *6*(5), 055003 (2022).

3. G. Grissonnanche et al. "Seebeck coefficient in a nickelate superconductor: electronic dispersion in the strange metal phase." *arXiv:2210.10987* (2022).

4. D. Ferenc Segedin, B. H. Goodge et al. "Limits to the strain engineering of layered square-planar nickelate thin films." *Nature Communications* 14(1), 1468 (2023).

Model Construction and Material Realization of Electronic Flat Bands

Feng Liu - University of Utah

Keywords: flat-band materials, electron topology, excitonic insulator

Program Scope

This project, titled "Construction and Quantum States of Single and Yin-Yang Flat Bands", encompasses a comprehensive study of physical mechanisms that lead to formation of exotic many-body quantum electronic states associated with topological flat bands (FBs) in lattice models and FB materials. It consists of three correlated research topics: (1) Orbital design of 2D/3D single and yin-yang flat bands and search of FB materials; (2) Complete population inversion between yin-yang FBs; (3) Fractional excitonic insulator state. The common theme of the proposed research is to improve our fundamental understanding of topological FBs, demonstrate novel and exotic many-body quantum phases arising from single and yin-yang FBs, and discover new classes of topological FB materials.

Our theoretical/computational project will employ a multiscale approach, combining several state-of-the-art theoretical and computational techniques, ranging from single-particle first-principles density-functional-theory (DFT) electronic structure calculations to tight-binding (TB) model Hamiltonian calculations and analyses, and to calculations and solutions of many-body Hamiltonian. Specifically, open-source package of DFT method combined with many-body GW and Bethe-Salpeter equation (e.g. Berkley-GW) and our newly developed in-house package of exact diagonalization (ED) method for solving many-body TB Hamiltonian will be used to study various excitonic states arising from photoexcitation, including fractional excitations, between yin-yang FBs. Topological properties of single-particle electronic states will be analyzed using conventional methods of calculating (spin) Chern numbers, while topology and fractional statistics of many-body quantum states will be analyzed using ED calculations of spectral flow, quasi-hole excitation and particle-cut entanglement spectra.

Our studies will significantly improve our fundamental understanding of the nature and underpinning of many-body quantum states in association with single and yin-yang FBs, in terms of lattice symmetry and dimension, electron-electron Coulomb vs. exchange interaction and screening, and fractional statistics of band population. Both the continuations and new initiatives of the proposed research will significantly not only improve our fundamental understanding of the construction of topological FBs and realization of FBs-enabled many-body quantum states, but also expand the scope of topological FB materials and FB physics. They will provide useful guidelines for future experimental efforts in synthesis and characterization of new 2D and 3D topological FB materials. They will also have direct technological impact on advancing quantum materials and devices for energy applications, to fulfill the mission of the Department of Energy.

Recent Progress

During the last two years, we have published 25 journal papers fully or partially supported by this DOE grant, including 5 Physical Review Letters, 6 Nano Letters, and one invited review arttcle. Three postdoctoral research associates and two graduate students have been fully or partially supported by this DOE project. The PI gave 6 invited talks at national/international conferences, and 5 departmental colloquium/seminar presentations. Below is a brief summary of four topics of research achievements pertaining to this project.

(1) **Flat-Band-Enabled Triplet Excitonic Insulator in a Diatomic Kagome Lattice:**[1] The excitonic insulator (EI) state is a strongly correlated many-body ground state, arising from an instability in the band structure toward exciton formation. Recently, we show that the flat valence and conduction bands of a semiconducting diatomic Kagome lattice, as exemplified in a superatomic (trianglene) graphene lattice, can possibly conspire to enable an interesting triplet EI state, based on density-functional theory calculations combined with many-body GW and Bethe-Salpeter equation. Our results indicate that massive carriers in flat bands with highly localized electron and hole wave functions significantly reduce the screening and enhance the exchange interaction, leading to an unusually large triplet exciton binding energy (~1.1 eV) exceeding the GW band gap by ~0.2 eV (Fig. 1) and a large singlet-triplet splitting of ~0.4 eV, which point to spontaneous formation of multiple triplet excitions. Our findings enrich once again the intriguing physics of flat bands and extend the scope of EI materials. Excitingly, both our proposal of the superatomic (trianglene) graphene lattice and our thereotical theoretical predictions of spontaneously formation of excitons have been supported by the latest experiments.[2]

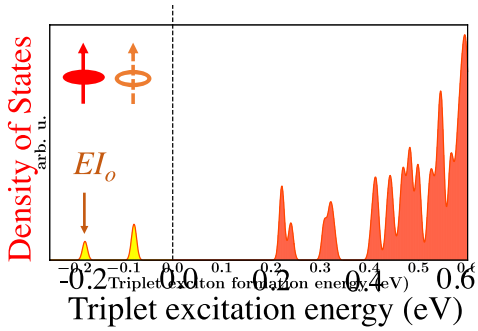

Fig. 1. DOS for triplet excitons obtained by solving Bethe-Salpeter equation of a superatomic (trianglene) graphene lattice. It clearly shows the presence of excitons with negative formation energy (EI_0), indicative of spontaneous formation of excitons.

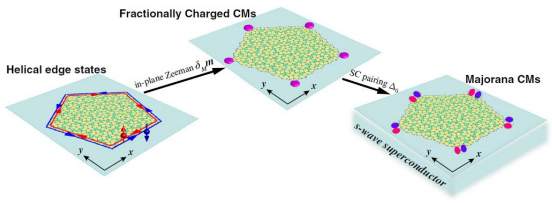

Fig. 2. Schematic illustration of the Zeeman-field-induced topological phase transitions in a 2D pentagonal quasicrystal. Starting from a TI phase with helical edge states, the quasicrystal is driven to a HOTI phase with five charged corner modes (CMs) by an in-plane Zeeman field. Furthermore, in proximity with an s-wave superconductor, Majorana CMs can be generated by tuning the Zeeman field and chemical potential.

(2) Effective Model for Fractional Topological Corner Modes in Quasicrystals:[3] High-order topological insulators (HOTIs), as generalized from topological crystalline insulators, are characterized with lower-dimensional metallic boundary states protected by spatial symmetries of a crystal, whose

theoretical framework based on band inversion at special k points cannot be readily extended to quasicrystals because quasicrystals contain rotational symmetries that are not compatible with crystals, and momentum is no longer a good quantum number. We have developed a low-energy effective model underlying HOTI states in 2D quasicrystals for all possible rotational symmetries (Fig. 2). By implementing a novel Fourier transform developed recently for quasicrystals and approximating the long-wavelength behavior by their large-scale average, we construct an effective $k \cdot p$ Hamiltonian to capture the band inversion at the center of a pseudo-Brillouin zone. We show that an in-plane Zeeman field can induce mass kinks at the intersection of adjacent edges of a 2D quasicrystal TIs and generate corner modes (CMs) with fractional charge, protected by rotational symmetries. Our model predictions are confirmed by numerical tight-binding calculations. Furthermore, when the quasicrystal is proximitized by an s-wave superconductor, Majorana CMs can also be created by tuning the field strength and chemical potential. Our work affords a generic approach to studying the low-energy physics of quasicrystals, in association with topological excitations and fractional statistics.

(3) High-Temperature Fractional Quantum Hall State in Floquet-Kagome Flat Band:[4] Fractional quantum Hall effect (FQHE) has been predicted in Chern FB by single-particle band structure combined with phenomenological theory or solution of many-body lattice Hamiltonian with fuzzy parameters. A long-standing roadblock towards realization of FB-FQHE is lacking the many-body solution of specific materials under realistic conditions. We have demonstrated a combined study of single-particle Floquet band theory with exact ED of many-body Hamiltonian. We show that a time-periodic circularly polarized laser inverts the sign of second-nearest-neighbor hopping in a Kagome lattice and enhances spin-orbit coupling in one spin channel, to produce a Floquet FB with a high flatness ratio of bandwidth over band gap (Fig. 3), as exemplified in metalorganic monolayer $Pt_3C_{36}S_{12}H_{12}$. The ED of the resultant Floquet-Kagome lattice Hamiltonian gives a one-third-filling ground state with a laser-dependent excitation gap of FQH state, up to an estimated temperature above 70 K. Our findings pave the way to explore the alluding high-temperature FB-FQHE.

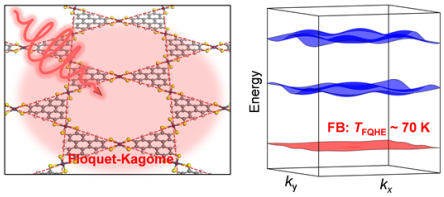

Fig. 3. Left: Schematics of Floquet-Kagome lattice with a laser shining on a 2D Kagome material. Right: Calculated Floquet-Kagome band structure showing a bottom FB with large flatness ratio exhibiting high-temperature FQHE.

(4) Structural Amorphization-Induced Topological Order:[5] Electronic properties of crystals are inherently pertained to crystalline symmetry, so that amorphization that lowers and breaks

symmetry is detrimental. One important crystalline property is electron band topology which is known to be weakened and destroyed by structural disorder. We reported a counterintuitive theoretical discovery that atomic structural disorder by amorphization can in fact induce electronic order of topology in an otherwise topologically trivial crystal (Fig. 4). The resulting nontrivial topology is characterized by a nonzero spin Bott index, developed by us in the last funding cycle for defining electronic-state topology in real space,[6,7] associated with robust topological edge states and quantized conductance. The underlying topological phase transition (TPT) from a trivial crystal to a topological amorphous is analyzed by mapping out a phase diagram in the degree of structural disorder using an effective medium theory. The atomic disorder is revealed to induce topological order by renormalizing the spectral gap toward nontriviality near the phase boundary. As a concrete example, we further show such TPT in amorphous stanane by first-principles calculations. Our findings point to possible observation of an electronic ordering transition accompanied by a structural disorder transition.

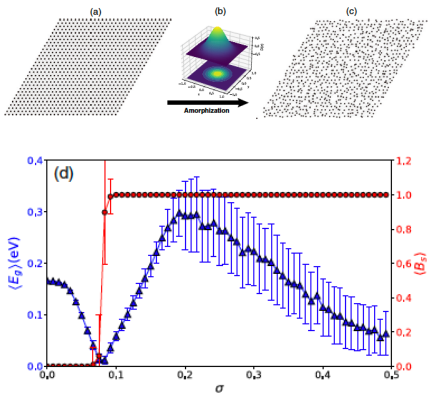

Fig. 4. Amorphization induced topological phase transition. (a) The initial triangular lattice. (b) Gaussian distribution of atomic displacements. (c) The lattice after amorphization. (d) Energy gap (blue) and spin Bott index (red) as functions of atomic displacement (σ).

Future Plans

We plan to expand our current studies in the following areas:

(a) Anomalous bilayer quantum Hall effect
(b) p-wave excitonic Bose-Einstein condensation
(c) High-order topological point states
(d) Ferroelectric topological superconductor
(e) Excitonic insulator state in hydrogen-bond organic framework
(f) Continuing the efforts of experimental collaborations

References

1. G. Sethi, Y. Zhou, L. Zhu, L. Yang, and Feng Liu, *Flat-Band-Enabled Triplet Excitonic Insulator in a Diatomic Kagome Lattice*, Phys. Rev. Lett. **126,** 196403 (2021)**.**
2. A. Delgado, C. Dusold, J. Jiang, A. Cronin, S. G. Louie, F. R. Fischer, *Evidence for excitonic insulator ground state in triangulene Kagome lattice*, arXiv:**2301**.06171 (2023)**.**
3. C. Wang, Feng Liu, and H. Huang, *Effective Model for Fractional Topological Corner Modes in Quasicrystals*, Phys. Rev. Lett. **129,** 056403 (2022).
4. H. Liu, G. Sethi, D. N. Sheng, Y. Zhou, J.-T. Sun, S. Meng, and Feng Liu, *High-temperature fractional quantum Hall state in the Floquet kagome flat band*, Phys. Rev. B **105**, L161108 (2022)**.**
5. C. Wang, T. Cheng, Z. Liu, Feng Liu, and H. Huang, *Structural Amorphization -Induced Topological Order*, Phys. Rev. Lett. **128,** 056401 (2022)**.**

6. H. Huang and Feng Liu, *Quantum Spin Hall Effect and Spin Bott Index in a Quasicrystal Lattice*, Phys. Rev. Lett. **121,** 126401, Editor's Suggestion, (2018); *Theory of spin Bott index for quantum spin Hall states in nonperiodic systems*, Phys. Rev. B, **98**, 12513, Editor's Suggestion,(2018).

Publications

1. "Effective Model for Fractional Topological Corner Modes in Quasicrystals", C. Wang, Feng Liu, and H. Huang, *Phys. Rev. Lett*. **129**, 056403 (2022).
2. "Excited quantum anomalous and spin Hall effect: dissociation of flat-bands-enabled excitonic insulator state", Y. Zhou*, G. Sethi*, H. Liu, Z. Wang, and Feng Liu, *Nanotech*. **33**, 415001 (2022).
3. "High-temperature fractional quantum Hall state in the Floquet kagome flat band", H. Liu, G. Sethi, D. N. Sheng, Y. Zhou, J.-T. Sun, S. Meng, and Feng Liu, *Phys. Rev. B* **105**, L161108 (2022).
4. "Orbital design of flat bands in non-line-graph lattices via line-graph wave functions", H. Liu, G. Sethi, S. Meng, and Feng Liu, *Phys. Rev. B* **105**, 085128 (2022).
5. "Structural Amorphization-Induced Topological Order", C. Wang, T. Cheng, Z. Liu, Feng Liu, and H. Huang, *Phys. Rev. Lett.* **128**, 056401 (2022).
6. "Generic Orbital Design of Higher-Order Topological Quasicrystalline Insulators with Odd Five-Fold Rotation Symmetry", H. Huang, J. Fan, D. Li, and Feng Liu, *Nano Lett*. **21**, 7056 (2021).
7. "Screening two-dimensional materials with topological flat bands", H. Liu, S. Meng and Feng Liu, *Phys. Rev. Mat*. **5**, 084203 (2021).
8. "Flat-Band-Enabled Triplet Excitonic Insulator in a Diatomic Kagome Lattice", G. Sethi, Y. Zhou, L. Zhu, L. Yang, and Feng Liu, *Phys. Rev. Lett.* **126**, 196403 (2021).
9. "Exotic Topological Bands and Quantum States in Metal–Organic and Covalent–Organic Frameworks", W. Jiang, X. Ni, and Feng Liu, *Acc. Chem. Res*. **54**, 416 (2021) (**Invited review**).
10. "Realization of an Antiferromagnetic Superatomic Graphene: Dirac Mott Insulator and Circular Dichroism Hall Effect", Y. Zhou and Feng Liu, *Nano Lett*. **21**, 230 (2021).

Atomistic understanding of ion conduction and interfacial processes in emerging sodium batteries

Principle Investigators: Badri Narayanan (co-PI), Hui Wang (PI) (Mechanical Engineering, University of Louisville, Kentucky)

Keywords: Na-ion chalcogenide conductors, Sodium batteries, Interfacial chemistry, Quantum chemical calculations, Molecular Dynamics

Research Scope: The major goal of this project is to understand the cation/anion doping effect on the structure, ion transport, and reactivity (towards Na-metal) of novel sodium (Na) superionic conductors ($Na_{3-x}A_xSbS_{4-y}X_y$) from the Na_3SbS_4 (NSS) family by integrating density functional theory (DFT) calculations, *ab initio*/classical molecular dynamics (AIMD/CMD), synthesis, *in situ* neutron diffraction experiments, and electrochemical characterization. Specifically, we aim to understand (a) thermodynamic phase stability and reactivity of NSS towards sodium metal with different dopants, (b) the effect of size, valence, and nature of cation/anion dopants on ion-conduction pathways in NSS, and (c) investigate the atomic-scale interfacial processes between NSS and Na-metals in solid-state Na batteries, as well as identify routes enhance stability of the interface. In addition, we also investigate the interplay between ion-solvation, lattice oxygen, and structural water, as well their collective impact on structural stability of layered metal oxide cathodes in aqueous sodium ion storage. Our team is working in collaboration with Oak Ridge National Laboratory (ORNL) and the neutron diffraction experiment is being conducted in Spallation Neutron Source (SNS, a DOE user facility).

Recent Progress. In this abstract, we summarize the key accomplishments of our atomistic simulation efforts. The findings from our synthesis, *in situ* neutron diffraction, and electrochemical characterization are provided in a separate abstract. On the atomistic simulation front, we found that (a) Na^+ ion conduction in NSS can be significantly enhanced by substitutional doping of Na with multivalent cations, owing to activation of new pathways (that are dormant in pristine NSS), (b) partial substitution of S with larger chalcogen anions (e.g., Se) enables fast Na^+ diffusion via lattice expansion, impacts the relative stability of cubic and tetragonal polymorphs (with cubic polymorph becoming more stable for $Na_3SbS_{4-x}Se_x$ at x >3), and (c) identified the key mechanisms underlying the efficiency of ionic-liquid interlayers in enhancing the stability of Na/NSS interface in Na-battery. In addition, we also highlight our work on aqueous Na batteries, wherein, we find that Ni-doping of layered birnessite (MnO_2) induces charge depletion of lattice oxygen, which in turn, facilitates immobilization of structural water in (Ni)MnO_2 and prevents lattice collapse in deep charge states. Below, we mainly briefly describe these results.

1. Enhancing sodium ion diffusion in solid-state Na_3SbS_4 conductors by cation doping. Na_3SbS_4 (NSS) is a promising solid electrolyte for Na-batteries owing to its good chemical stability under ambient conditions, low flammability, and favorable Na^+ conductivity (~1 mS cm^{-1}).[1] At room temperature, it exhibits a tetragonal (*t*) crystal structure (space group: $F\bar{4}3m$) made up of

SbS_4 motifs, wherein, Na atoms occupy two inequivalent set of sites, namely Na1 and Na2, arranged in a zigzag manner (Fig. 1(a)).[1] Na^+ conduction in NSS occurs via a vacancy-mediated mechanism composed of two types of elementary Na^+ hops between neighboring Na-sites, i.e., Na1-Na1 (P_a) and Na1-Na2 (P_b). Controlled introduction of charge-compensating Na-vacancies in NSS via multi-valent cation dopants (e.g., Ca^{2+}, La^{3+}) can significantly enhance ion-conductivity, as

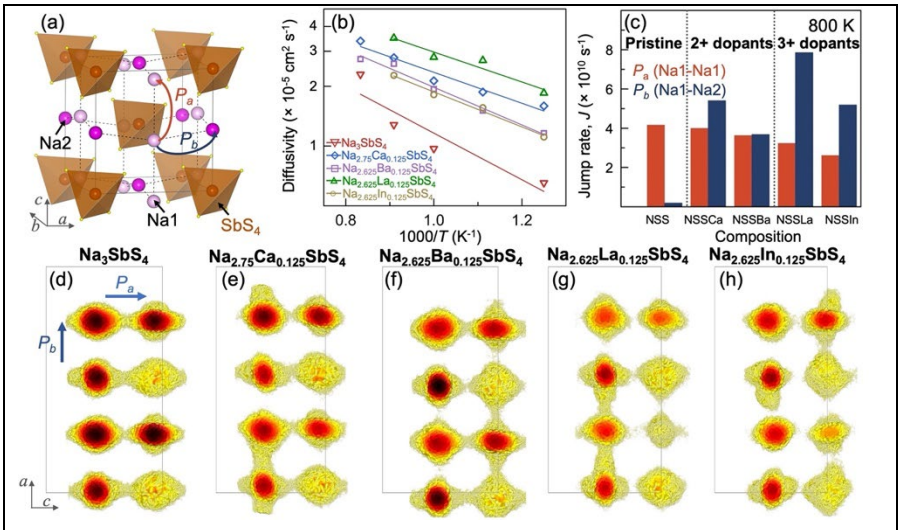

Figure 1. Understanding effect of cation dopants on Na^+ conduction in cation-doped Na_3SbS_4 conductor using AIMD simulations. (a) Schematic representation of a unit cell of *t*-Na_3SbS_4 ($F43m$) containing SbS_4 tetrahedra (tan), and Na occupying two sets of unique sites, namely Na1 (purple), and Na2 (magenta); (b) Arrhenius plot of Na^+ diffusivity in Na_3SbS_4 with various cation dopants (alongside charge compensating vacancies) obtained from AIMD trajectories; (c) Jump rates for two distinct types of hops (P_a: Na-Na1, and P_b: Na1-Na2) illustrated in panel (a) as arrows (P_a: tan, P_b: blue). Probability distribution maps of Na (red: high, yellow/white: low) over a typical 100 ps-long AIMD trajectory in (d) Na_3SbS_4, (e) $Na_{2.75}Ca_{0.125}SbS_4$, (f) $Na_{2.75}Ba_{0.125}SbS_4$, (g) $Na_{2.625}La_{0.125}SbS_4$, and (h) $Na_{2.625}In_{0.125}SbS_4$.

demonstrated by our AIMD simulations (Fig. 1(b)). Careful analysis of AIMD trajectories reveal that Na^+ diffusion in pristine NSS occurs primarily via Na1-Na1 hops, which contribute ~96% of the Na^+ diffusion in NSS (Fig. 1(c)). This largely restricts the conduction channels along the crystallographic *c*-direction, and limits ion conductivity (Fig. 1(d)). Partial replacement of Na with multi-valent cations introduces charge-compensating Na-vacancies, which activate Na1-Na2 pathways, and in turn, enhance Na^+ conductivity significantly (Fig. 1(b-h)). Note that although 2+ cations occupy Na-sites, 3+ cations may either substitute Na or Sb in the NSS lattice. For instance, our DFT calculations show that Ga^{3+}, Ce^{3+}, and Bi^{3+} prefer to substitute Sb^{5+} instead of Na (with accompanying S^{2-} vacancy) owing to the lower formation energy (~20 – 40 meV/atom) of these phases as compared to that formed by replacing Na (alongside charge-compensating Na-vacancies); in contrast, La^{3+} and In^{3+} ions show favorable energetics for Na-substitution (~10 – 30 meV/atom lower than Sb-substitution). Interestingly, we found that in divalent-cation-doped NSS ($Na_{2.75}A_{0.125}SbS_4$; A = Ca^{2+}, Ba^{2+}), the contributions of Na1-Na1 and Na1-Na2 hops to Na^+ diffusion are nearly equal Figure 1(c,e,f). On the other hand, partial replacement of Na with trivalent cations in NSS ($Na_{2.625}A_{0.125}SbS_4$; A = La^{3+}, Ba^{3+}) enables Na1-Na2 hops to emerge as the dominant contributor to ion transport (~66% of Na^+ diffusion occurs via Na1-Na2 hops as shown in Figure 1(c,g,h). Notably, the ions with similar ionic radius as Na^+ (i.e., La^{3+}: $r_{La^{3+}}/r_{Na^+}$=1.01, Ca^{2+}: $r_{Ca^{2+}}/r_{Na^+}$=0.98) show the highest improvement in conductivity (Fig 1(b)). For cation dopants whose size deviate significantly away from Na (i.e., In^{3+}: $r_{In^{3+}}/r_{Na^+}$=

0.78, Ba^{2+}: $r_{Ba^{2+}}/r_{Na^{+}}$= 1.32), the local strain impedes the Na-hop pathways in the immediate vicinity of the dopant, yielding low ionic conductivities despite the charge-compensating Na-vacancies.

2. Effect of ionic liquid interlayer on interfacial stability of Na_3SbS_4 conductors against sodium-metal. Our DFT calculations using the grand potential phase diagram approach[2] show that NSS is unstable against Na-metal; and when used as solid electrolyte (SE) in Na-batteries, will decompose at the Na || SE interface into a combination of metallic (Na_3Sb) and insulating (Na_3SbS_4: Na_2S), adversely impacting cycle life and capacity retention. To enhance the stability of Na_3SbS_4 solid electrolyte (SE) against the Na-metal, we investigated the effect of introducing $PYR_{14}TFSI$ ionic liquid (IL) as an interlayer between Na and SE. Our *ab initio* molecular dynamics (AIMD) simulations showed that the IL does not react with SE, and shields it from reductive decomposition against Na-metal; thus, the IL acts as a physical barrier between Na and SE, inhibiting parasitic reactions between Na and SE. At the Na/IL interface, the PYR_{14}^{+} cations remain intact (Fig. 2(a,b)), while the $TFSI^{-}$ anions interact strongly with Na and decompose quickly (Fig. 2(c)) to form a solid-electrolyte interphase (SEI) containing Na-F bonds and -CF_3 complexes (consistent with our XPS experiments). Careful analysis of the atomic coordination in the SEI indicated a high fraction of NaF, which is well-known to enhance the electrochemical stability of SEI. Additionally, the good wettability of (PYR/Na)TFSI electrolyte can facilitate intimate contact which (a) reduces the resistance at the Na_3SbS_4/electrode interfaces and promotes a proper interface for fast ion transport from SE to electrodes; and (b) enables uniform Na electrodeposition, thereby, suppressing Na dendrite formation/growth. Indeed, all these beneficial effects of IL-interlayer enable stable long-term cycling of FeS_2||Na_3SbS_4||Na cells, holding a specific capacity of ~103 mAh g^{-1} after 330 cycles at high current density (100 mA g^{-1}).

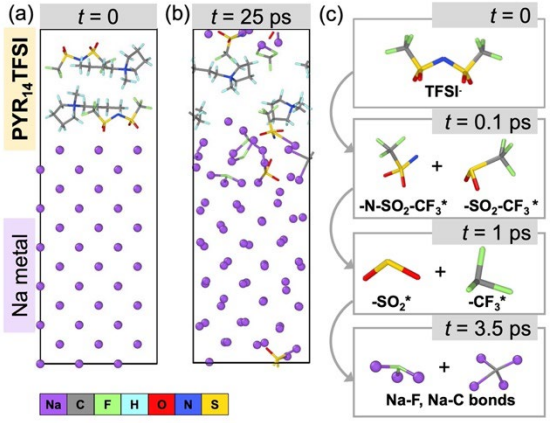

Figure 2. Structural evolution of Na anode/$PYR_{14}TFSI$ interface obtained from *ab initio* molecular dynamics simulations under ambient conditions. (a), (b) The equilibrated atomic-scale structures of the interface at 0 and 25 ps, respectively. (c) $TFSI^{-}$ decomposition sequence over the simulation time (*represents complexes).

3. Role of structural water in mitigating lattice collapse of Ni-MnO_2 birnessite cathodes at deep charge states in aqueous Na-ion batteries. Layered transition-metal oxide cathodes (such as MnO_2) hold tremendous promise for alkali-ion (e.g., Na^{+}) storage in aqueous electrolytes.[3] However, at deep charge states (high voltage), these electrode materials undergo an abrupt lattice collapse in the *c*-direction;[4] likely, due to co-removal of Na^{+} and structural water (that exist as part of strong hydration shells around Na^{+}) during deep charging. We employed a combination of in situ X-ray diffraction experiments (by X. Teng's group at U. New Hampshire), DFT calculations,

and classical molecular dynamics (CMD) simulations to assess the suitability of Ni-doping in mitigating this lattice collapse. Our DFT calculations on the representative $Na_{0.17}MnO_2.0.833H_2O$ model (Fig. 3(a)) for deep-charge state (lean-Na conditions) show that substitutional doping of Mn with Ni results in charge depletion on lattice oxygens (Fig. 3(b)) owing to high electronegativity of Ni as compared to Mn. This charge reduction, in turn, yields a significant decrease in electrostatic repulsion between the oxygens (O_w-O) belonging to lattice and structural water (Fig. 3(c)). CMD simulations based on atomic charges obtained from DFT elucidate that Ni-doping facilitates immobilization of structural water (with concurrent increase in diffusivity of intercalating Na^+ ions) in (Ni)MnO_2 and prevents lattice collapse upon Na-ion removal (Fig. 3(d,e)), consistent with *in situ* XRD and *ex situ* XANES experiments. (Ni)MnO_2 exempted from lattice collapse shows an improved storage capacity (96 mAh g^{-1} at 1 A g^{-1}) relative to MnO_2 (47 mAh g^{-1}) with similar cycling stability.

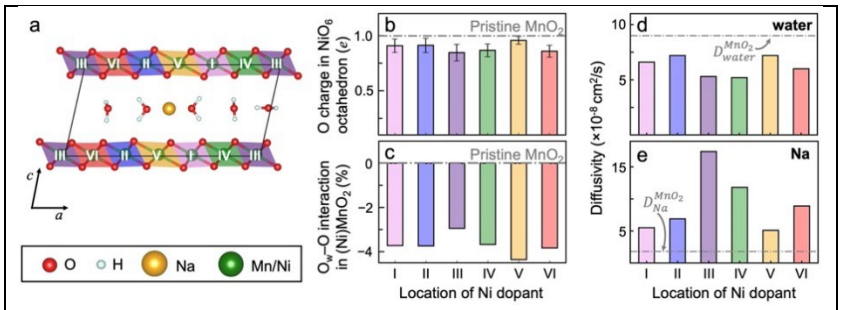

Figure 3. Atomic-scale simulations to understand interactions between lattice oxygen and structural water in (Ni)MnO_2 under deep charge conditions. (a) Equilibrium atomic configuration of pristine Na-birnessite under Na-lean conditions (deep charge) with composition $Na_{0.17}Ni_{0.17}Mn_{0.83}O_2.0.833H_2O$ obtained from total energy DFT calculations. (b) Bader charge on the O atoms belonging to the NiO_6 octahedron for different locations of Ni dopant (marked as I-VI in panel(a)), and (c) Percentage change in the electrostatic repulsion between the oxygen atoms belonging to lattice (O) and structural water (O_w) in Ni(Mn)O_2 as compared to that in pristine MnO_2 for different location of Ni-dopant. Room temperature diffusivity of (d) structural water, and (e) Na^+ ion in for different locations of Ni dopant obtained from CMD simulations.

Future Plans. We will employ a combination of AIMD simulations and DFT calculations to gain a fundamental understanding of (a) the effect of size, valence, and nature of cation dopants on reactivity against Na-metal, (b) links between structure of high-symmetry grain boundaries (using bi-crystal models), segregation of dopants, and ionic conduction, and (c) dynamical evolution of the SEI between Na and Na_3SbS_4 (with a variety of dopants that hold promise for fast Na^+ conduction). All these works will be performed in synergy with our synthesis, *in situ* neutron diffraction, and *ex situ* spectroscopy/microscopy experiments (detailed in a separate abstract).

References

1. H. Wang, Y. Chen, Z. Hood, G. Sahu, A. Pandian, J. Keum, K. An, and C. Liang, *An air-stable Na_3SbS_4 superionic conductor prepared by a rapid and economic synthetic procedure,* Angewandte Chemie, **128**, 8693-8697 (2016)
2. S.P. Ong, L. Wang, B. Kang, and G. Ceder, *Li-Fe-P-O_2 phase diagram from first principles calculations*, Chemistry of Materials, **20**, 1798-1807 (2008)
3. N. Zhang, M. Jia, Y. Dong, Y. Wang, J. Xu, Y. Liu, L. Jiao and F. Cheng, *Hydrated layered Vanadium Oxide as a highly reversible cathode for rechargeable aqueous zinc batteries*, Advanced Functional Materials, **29**, 1807331 (2019)
4. X. Shan, F. Guo, D. Charles, Z. Lebens-Higgins, S. Razek, J. Wu, W. Xu, W. Yang, K. Page, J. Neuefeind, M. Feygenson, L. Piper, and X. Teng, *Structural water and disordered structure promote aqueous sodium-ion energy storage in sodium-birnessite*, Nature Communications **10**, 4975 (2019)

Publications

1. S. Halacoglu, S. Chertmanova, Y. Chen, Y. Li, M. Rajapakse, G. Sumanasekera, B. Narayanan and H. Wang, *Visualization of Solid-State Synthesis for Chalcogenide Na Superionic Conductors by in-situ Neutron Diffraction*, ChemSusChem, **14**, 5161-5166 (2021).
2. S. Halacoglu, Y. Li, W. Arnold, V. Shreyas, X. Guo, J. B. Jasinski, B. Narayanan and H. Wang, *Solvent-free and low temperature synthesis of chalcogenide Na superionic conductors for solid-state batteries*, Chemical Engineering Journal, **468**, 143624 (2023).
3. Y. Li, S. Halacoglu, V. Shreyas, W. Arnold, X. Guo, Q. Dou, J. B. Jasinski, B. Narayanan and H. Wang, *Highly efficient interface stabilization for ambient-temperature quasi-solid-state sodium metal batteries,* Chemical Engineering Journal, **434**, 134679 (2022).
4. Y. Li, W. Arnold, S. Halacoglu, J. B. Jasinski, T. Druffel and H. Wang, *Phase-Transition Interlayer Enables High-Performance Solid-State Sodium Batteries with Sulfide Solid Electrolyte*, Advanced Functional Materials, **31**, 2101636 (2021).
5. F. Guo, S. Jagadeesan, R. Pidathala, S.-W. Kim, X. Shan, N. Deskins, M. Abeykoon, G. Kwon, D. Olds, B. Narayanan, X. Teng. *Revitalizing Iron Redox by Anion-Insertion-Assisted Ferro- and Ferri-Hydroxides Conversion at Low Alkalinity*. Journal of American Chemical Society, **144**, 11938–11942 (2022)
6. X. Shan, R. Pidathala, S.-W. Kim, W. Xu, M. Abeykoon, G. Kwon, D. Olds, B. Narayanan and X. Teng. *Exemption of lattice collapse in Ni–MnO_2 birnessite regulated by the structural water mobility.* Journal of Materials Chemistry A 9, 23459 (2021)

Tailoring Grain-boundaries by Electro-Nano-Pulsing (ENP)

Eugene Olevsky (PI), Wenwu Xu (Co-PI), Department of Mechanical Engineering, School of Engineering, San Diego State University

Keywords: Electro Nuno-Pulsing, Grain Boundaries, Tailoring

Research Scope

The major goal of the project is to develop a new electric current assisted materials processing to enable the nanoscale control and tailoring of grain boundaries (GBs) and interfaces in materials. This may be achieved by incorporating a nanopulsing system that can send intense electrical DC current through the conductive samples. The nanoseconds (ns) pulsing of intense electrical current is expected to result in heterogeneous heating in the sample. We expect significant heat localization at GBs and large temperature gradient across the GB regions, similar expectation for particle interfaces (Fig. 1). As a result, the GB structures and properties may be modified locally while the rest of the material is not affected. The hypothesis is that the, at the atomic level, the GBs are "damaged or even melted" resulting in an atomistic level reconfiguration of GBs. Due to the extremely short nanopulsing time, atomic diffusivities and melting at each nanopulse duration is very limited to the GB or interfacial regions, thus, this structural change is mostly localized at the GB regions.

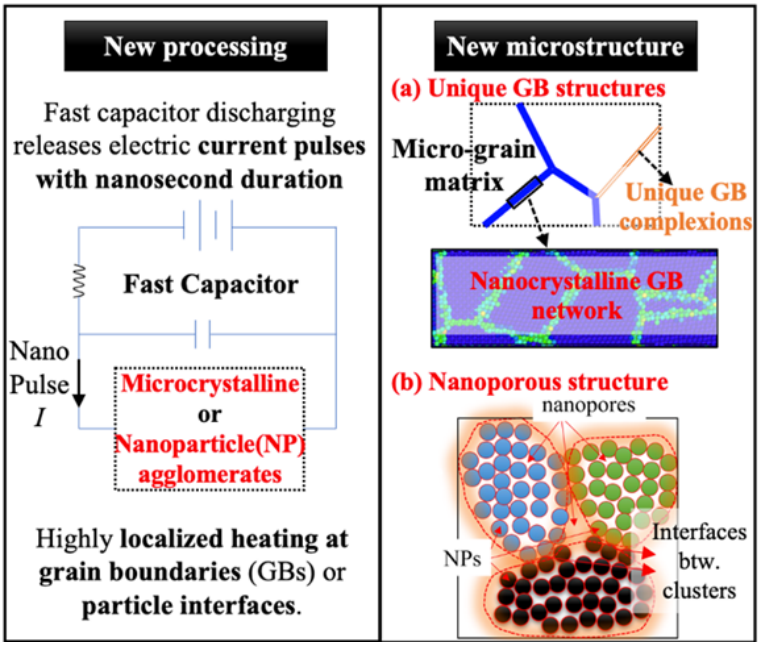

Fig. 1 Electro-nano-pulsing processing to locally tailor the GBs in polycrystalline materials and the interfaces between nanoparticles.

Recent Progress

Experimental progress:

Experimental apparatus. We successfully constructed and completed the comprehensive system testing for a new electro-nano-pulsing (ENP) system which can generate intense electrical DC current with nanosecond durations from 100ns to 2000ns at different frequencies (up to 100,000Hz). Fig. 2 shows the built ENP system setup. A DC power supply is used to charge the

supercapacitors within the Integrated Power Module (IPM) unit, which is the core of the ENP system. The SDSU customized IPM enables output of intense DC electric current pulses with a single pulse duration as short as 100 nanoseconds (ns) (Fig. 2).

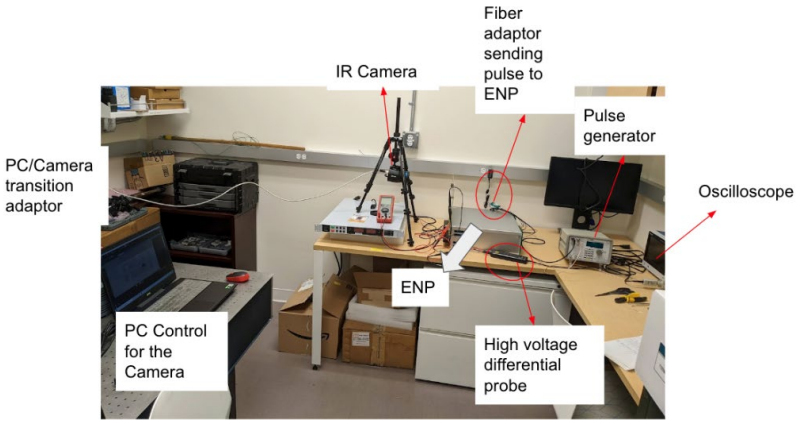

Fig. 2. Electro-nano-pulsing (ENP) experimental setup.

The pulsation is controlled by a nanopulse generator and monitored by an advanced ossilocsope. The IPM customization uses a pair of Cu feed plates, to which a specimen is electrically connected. It allows fleaxible installation of specimen with either rod or disk shape. The maximum voltage and single pulse current of the IPM are 1,200V and 10,000A, respectively. With the ENP system, the current in specimen climbs up to several thousands of Amps within a few 100ns. This is calcualted based on a metal rod sample with diameter of 2mm and lengh of 8mm, and at a chargiing voltage of 600V.

Depending on the size of the sample, the current density can be as high as several 10^{11}A/m^2, which is ~4-5 magnitudes higher than that in a typical spark plasma sintering experiment. In addition, a high-resolution infrared (IR) camera is used to monitor the sample's temperature during processing.

Preliminary experimentation. We used the built system and conducted several series of preliminary experiments for pure metals Zn and Al, as well as the superalloy Nichrome 80 (80% Ni, 19.5%Cr, 1.45% Si). The variety of samples used to explore and test the ENP setup's capability. There are in general, three types of samples in terms of the sample's diameter: large (>2mm), median (0.4-2mm), and small (<0.4mm). Different levels of electric current density can be achieved in these three types of samples, which are on the order of <10^9A/m^2, ~10^{10}A/m^2, and >10^{11}~10^{12}A/m^2, for the large, median, and small diameter samples, respectively. In experimental, when passing through one 1000ns-pulse to the large diameter sample, no appreciable heating takes place. When passing through one 1000ns-pulse to the median sample, significant heat (up to several hundreds of ^{o}C) will be generated in the sample. When passing through one 1000ns-pulse in the small diameter sample, metal wires melted. For example, we have melted the superalloy Nichrome 80 (melting point of 1400^{o}C) wire by using just one such nanopulse current. The IR camera shows that this wire was melted within one time frame (33.3ms), which is limit time frame capability of this IR camera. Our preliminary estimation of the actual duration of heating until melting is probably <~10ms by observing IR camera detections. This gives the range of heating rate achieved in this sample of about 40,000K/s to 100,000K/s.

Microstructure and GB characterization. We characterized the microstructure in several selected as-processed samples using the optical and scanning electron microscopic methods. More comprehensive transmission electron microscopic characterization at the nanoscale and atomistic scale are being conducted. This was achieved by just one nanopulse with duration of 1000ns. Our latest experiments also showed that one 500ns pulse can also melt the 36-gauge superalloy wire. It is not supersizing to see the equiaxed polycrystalline structure formed after the solidification.

Then, following standard metallurgical sample preparation and chemical etching treatment, we

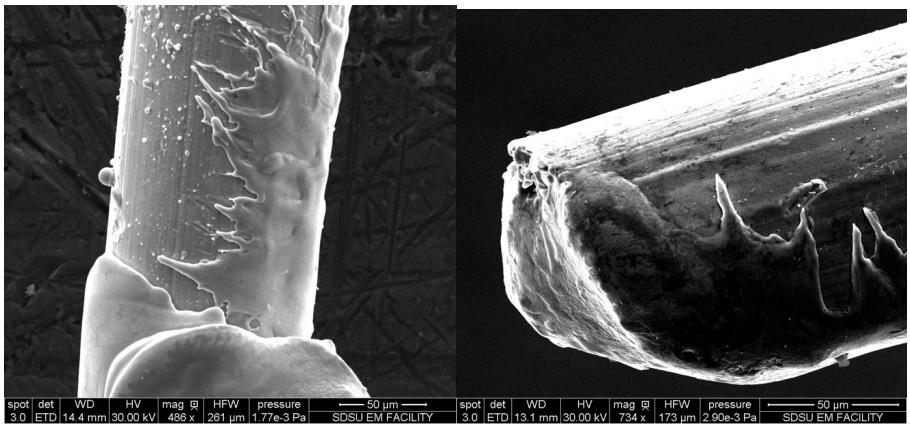

Fig. 3. Melted superalloy wire (Nichrome 80, gauge 36, 0.127mm diameter) by one nanopulse.

were able to visualize the internal (cross-sectional area) microstructure of the sample on a region that is immediately close to the melted zone. We expect in those un-fully melted regions the samples' part is hot enough to melt/change the GB only, while the grains are remained solid and crystal. From the optical images in Fig. 3, it seems like the microstructure of sample has changed, as shown by the comparison images before and after the ENP treatment (36-gauge Nichrome 80). We further conducted SEM imaging analysis to inspect the as-processed Nichrome 80 wires. This is consistent with the internal microstructure inspected by optical microscopy. Interestingly, some GBs seem to show different (grayer and "thick") contrast with a width of less than ~100-200nm. We suspect those GBs are probably melted and crystallized, and the melted zone might spread across a couple of hundreds of nanometers. This is in good agreement with our theorical analysis explained in the proposal. The ENP can heat the polycrystalline metal heterogeneously, GBs are heated more rapidly as compared with grain interiors. As a result, relative heat localization can be achieved at GBs, it is even possible to melt the GBs across a localized region when optimized processing parameters of ENP are achieved. SEM does not have sufficient resolution to examine the detailed structures of those grayer GB regions. TEM imaging is being conducted, which is expected to provide more understanding.

Modeling progress.

Method. We have preliminarily established a suitable method (Reactive Molecular Dynamics, RMD) and software platform (Amsterdam Modeling Suite with ReaxFF module) to model the influence of the nanopulse electric field on the grain boundary and interface structures of materials during electro-nano-pulsing (ENP) processing. We started the modeling for sintering of YSZ nanoparticles for two reasons. One, the PIs recently developed the classical MD modeling to study the E-field effect on YSZ system, it is naturally for the PIs to extend this modeling in the framework of RMD. Second, sintering of nanoparticles using ENP processing is also an important part of the proposed work in the proposal.

ReaxFF Issue. After comprehensive testing RMD simulations, we found out that all the reported reactive force fields (ReaxFF) for RMD modeling of YSZ systems do not predict the high temperature stability of crystal structure of the YSZ model. This means that all the existing reactive force fields underestimated the melting point of YSZ. For example, all the reported reactive force

fields for YSZ systems predicted the melting temperature of 8YSZ to be about <1500K, which is ~3000K from experimental measurement.

Preliminary modeling. Since the ReaxFF of YSZ systems need to be re-optimized, we use ZrO_2 as our preliminary testing model. This is because that the reported reactive force field of ZrO_2 can predict the melting point of ZrO_2 reasonably well. First of all, we created atomistic bi-particle models of ZrO_2 (with the equivalent amount of vacancy concentration to the 8YSZ system (Fig. 4)), then we carried out a series of RMD modeling of the initial sintering process of ZrO_2 models at the electric field up to 1000V/cm at different temperatures of 1500K and 1700K.

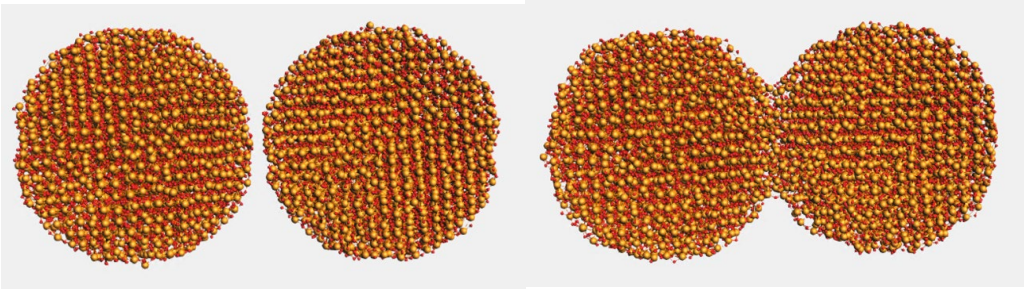

(a) Initial (b) Necking after 75ps RMD time

Fig. 4. Bi-particle (5nm diameter of each particle) model of ZrO2 (with equivalent amount of vacancy concentration as in the 8YSZ): (a) initial model; (b) significant necking formation at 1500K in the absence of electrical field.

Future Plans

We will conduct systematical TEM observations and analysis of the seemly melted GBs. We will also conduct several series of ENP processing experiments on other proposed metals in the proposal and inspect their potential GB and microstructure changes due to the ENP treatment. Then, by adjusting the ENP processing parameters, the optimize conditions for maximizing the GB modifications will be studied systematically. In the meantime, the thermal and nonthermal effect of the intense nanopulsing current will also be investigated by using the small and large samples, respectively.

W will extend the RMD modeling to investigate the nanopulsing electrical field effect on interfacial and grain boundary structures during the consolidation of chosen material systems proposed in the proposal, including a couple of metals and the YSZ systems. One major effort will be re-optimizing the ReaxFF of YSZ models and/or for chosen metal systems if necessary. One of the main parameters to be studied will be the atomistic diffusivity at the grain boundaries and interfaces as a function of electrical field strength during ENP processing.

Publications

W. Xu, R. Jiang, E.A. Olevsky, Tailoring Grain-boundaries by Electro-Nano-Pulsing (ENP), Acta Materialia, *submitted*

E.A. Olevsky, W. Xu, R. Jiang, A. Maksymenko, E. Torresani, Quasi-instantaneous Materials Processing Technology via High-intensity Electrical Nano Pulsing, Nature Comm., *in preparation*

Nanomaterials Synthesis Discovery with Parallel Electrodeposition Arrays

PI: Michelle L. Personick, Wesleyan University

Keywords: electrodeposition, nanomaterials, metals, surface structure, catalysis

Research Scope

The FOA (TA7, Critical Materials and Minerals) identifies a need for establishing "hypothesis-driven materials design and synthesis approaches for enhanced functional materials that reduce or eliminate the use of REE [rare earth elements], PGE [platinum group elements], or other critical elements." This project responds to this need for fundamental principles for materials design to replace PGE by addressing the gap in understanding of how to precisely control the surface structure of nanoscale materials composed primarily of non-PGE such as nickel (Ni), copper (Cu), cobalt (Co) and iron (Fe). In addition, the project responds to the related challenge of reducing the use of PGE by developing strategies for synthesizing nanoscale catalyst materials in which an underlying non-PGE core controls the atomic arrangement of a monolayer of a PGE at the surface of the material. These goals will be achieved using an integrated electrochemical approach to metal nanoparticle synthesis pioneered by the PI's research group, in which real-time, *in situ*, electrochemical measurements bridge colloidal and electrochemical materials synthesis to elucidate the fundamental chemical principles that direct metal nanoparticle growth. Designing routes for the synthesis of these precision materials and establishing their structure-function relationships in key (electro)chemical transformations is critical to the advancement of the objectives of TA4 (Energy Storage), particularly the development of sustainable and scalable catalysts for the interconversion of electrical and chemical energy. Specifically, priority research direction (PRD) 4, "Design Catalysts for Efficient Electron-driven Chemical Transformations," from the related report Basic Research Needs for Catalysis Science highlights a need for transformative approaches to synthesizing architecturally complex catalysts in order to tailor the catalyst surface to meet the complex requirements of important electrochemical conversions.

The supported work is organized around the following specific aims:

Aim 1: Direct the development of electrochemical and colloidal syntheses for non-PGE nanoparticles with well-defined shapes by applying detailed mechanistic insight from *in situ* electrochemical measurements.

Aim 2: Push boundaries in the shape control of non-PGE nanoparticles by harnessing the unique tunability of electrochemical synthesis.

Aim 3: Enable the epitaxial deposition of PGE onto non-PGE nanoparticle cores by using halide-free surfactants, control of solubility, and manipulation of diffusion in colloidal growth.

Efforts in the first partial year of the grant have enhanced capacity for pursuing Aim 2 by developing an innovative, high throughput, parallel approach to synthetic discovery for electrodeposited nanoparticles.

Combinatorial colloidal synthesis approaches are powerful and highly successful methods for materials synthesis discovery but they have been less successful for non-platinum-group materials, where identification of innovative reaction conditions is required. Electrochemical nanomaterials synthesis, such as techniques developed in the PI's research group, expands the toolbox of available synthetic handles to include both electrochemical and chemical parameters.[1-3] It also provides quantitative information about the dynamic chemical environment of the reaction during nanoparticle growth (solution potentials), enables "arbitrary" and precise tuning of these values, and provides access to control over synthetic conditions in ways that are not possible in colloidal nanoparticle growth. For example, an oscillating square wave potential can be applied in which growth conditions switch from more reducing to more oxidizing. More generally, reaction potentials can be tuned over the time course of a nanoparticle growth process to tune reduction kinetics at key points in nanoparticle shape development. This provides capacity to synthesize nanostructured materials that are not accessible via colloidal growth. However, electrochemical materials synthesis (electrodeposition) is inherently serial, limiting throughput and preventing widespread implementation. Increasing throughput with existing electrochemical deposition approaches would require purchasing a large number of potentiostats, which is prohibitively expensive and thus not scalable. Overcoming this limit on throughput will vastly accelerate synthetic development for nanostructured electrode materials.

Recent Progress

To address this need for enhanced electrodeposition throughput to enable materials discovery, during the first part of the reporting period we have developed a *parallel* approach to the electrodeposition of metal nanoparticles, which for the first time enables electrochemical synthetic development and discovery with an experimental bandwidth that is equivalent to that of colloidal synthesis. This advance makes use of an instrument known as the "Legion" potentiostat, which was recently developed by the research group of Prof. Lane Baker at Texas A&M University. Prof. Baker hosted PI Personick for a research-based sabbatical leave from January to May 2023. Designed around the geometry of a 96-well plate, the Legion potentiostat uses a single large glassy carbon electrode (110 x 73 mm) and 96 quasi-reference counter electrodes (QRCEs) to conduct 96 parallel electrochemical experiments, each in one of 96 separate wells (Fig. 1). This enables variation of both chemical and electrochemical parameters in each well, along with measurement of the current during the reaction. During her sabbatical, PI Personick developed methodology for expanding the capabilities of the Legion potentiostat beyond analytical measurement to include electrodeposition of metal nanoparticles for synthetic discovery in electrochemical nanomaterials synthesis.

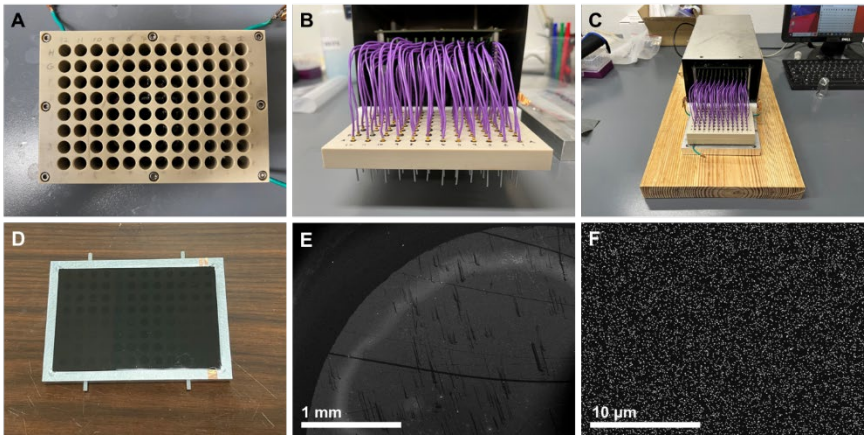

Figure 1. Photographs of the experimental setup (A-C): (A) assembled 96-well plate with glassy carbon electrode at the bottom of the wells; (B) Ag quasi-reference counter electrodes and leads; (C) fully assembled Legion instrument. (D) Photograph of the glassy carbon electrode in a custom holder for SEM. Dark circles are electrodeposited particles from each well. (E-F) SEM images of electrodeposited Pd nanoparticles in a single well, highlighting the uniform coverage of the electrodeposition process.

Each Legion deposition array was composed of 24 experimental conditions (electrochemical and/or chemical variations of the nanoparticle deposition environment) along with four replicates of each condition, for a total of 96 experiments. For example, some conditions selected for variation in a single array included: square wave vs. constant potential deposition, deposition potential (or upper and lower potentials for square wave synthesis), surfactant concentration, and metal precursor concentration. With three standard potentiostats and nine electrodes, this same number of experiments would take almost a month to complete. In contrast, the Legion experiment takes about four hours for setup and one hour to run the electrodeposition, followed by time for imaging with scanning electron microscopy (SEM). This significantly accelerates the synthetic discovery process, and also allows multiple possible synthetic avenues to be pursued simultaneously and efficiently in a single experiment. This ability to simultaneously probe an expanded scope of experimental parameters will be of great importance as we move forward to metals such as Cu and Fe, and especially Co and Ni, where few successful conditions for shaped nanoparticle synthesis are available.

To demonstrate the utility of this approach, we have shown that we can use this parallel experimental design to: (1) identify chemical capping agents that result in shape control for electrodeposited polyhedral nanoparticles; (2) simultaneously optimize the electrochemical parameters and chemical conditions required for synthesis of a particular shape; and (3) tune the nucleation step of nanoparticle growth to dictate nanoparticle defect structure while concurrently optimizing parameters of the subsequent nanoparticle growth step. The examples below highlight how the capabilities gained from this development can be implemented in a way that will advance the discovery-based design of electrochemical syntheses for shaped metal nanoparticles.

In an initial synthesis discovery array focused on the deposition of palladium (Pd) nanoparticles, 24 different electrochemical deposition conditions were explored, including varying the lower (reducing) and upper (oxidizing) potentials of a square wave deposition protocol, the frequency of the oscillation between the two potentials, and constant potential deposition at a range of potentials. We also tested different electrolytes and capping molecules within the array. This rapid

survey of such a large range of synthetic conditions is not possible using any existing technique and is critical to identifying novel conditions for syntheses of materials such as non-platinum-group elements where close iteration around existing synthetic conditions is unlikely to lead to the successful formation of shaped nanoparticles. In the present experiment, we identified the most promising chemical composition and applied potential waveform for the electrodeposition of Pd cubes.

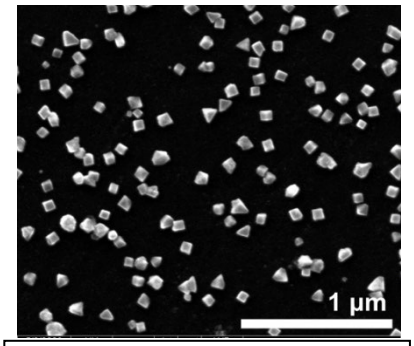

Figure 2. Electrodeposited cubes synthesized with identified optimal deposition conditions.

We then used the electrodeposition array platform to optimize the synthesis to improve the quality and increase the size of the cubes. Focusing on a square wave potential profile, two key parameters to optimize are the upper potential (E_U), at which the growing particles can be oxidized, and the lower potential (E_L), which controls the rate of metal ion reduction and thus nanoparticle growth. These particular conditions were optimized using a subset of wells in the array: seven distinct conditions with four replicates each for 28 total wells. The parallel deposition arrays also show good consistency across multiple wells with the same deposition conditions and chemical growth solution composition, providing built-in replicate experiments as part of the array. The optimal conditions identified from the array described above yielded larger well-defined cubes (Fig. 2).

Future Plans

Because the work described above is the first demonstration of this parallel approach to electrochemical synthetic development, Pd was used as a starting point for proof of concept. However, beginning during the remainder of the present reporting period (June-August 2023), the next experiments will focus on applying this approach to the development of synthetic conditions for shaped copper (Cu) nanoparticles. This synthesis development work will be coupled with real-time electrochemical measurements of the limited number of existing colloidal syntheses of shaped Cu nanoparticles, using *in situ* measurement approaches developed by the PI.[1] These measurements will direct the synthesis development efforts, as described in the original proposal. Other aspects of the proposed work will proceed as described in the original proposal.

References

1. S. P. McDarby, C. J. Wang, M. E. King, M. L. Personick, *An Integrated Electrochemistry Approach to the Design and Synthesis of Polyhedral Noble Metal Nanoparticles,* J. Am. Chem. Soc. **142**, 21322 (2020).
2. G. C. Halford, M. L. Personick, *Bridging Colloidal and Electrochemical Nanoparticle Growth with In Situ Electrochemical Measurements*, Acc. Chem. Res. **56**, 1228 (2023).
3. S. P. McDarby, M. L. Personick, *Potential-Controlled (R)Evolution: Electrochemical Synthesis of Nanoparticles with Well-Defined Shapes*, ChemNanoMat **8**, e202100472 (2022).

Publications : None to report yet.

Integrated Materials Platform for Topological Quantum Computing Devices

PIs: Vlad Pribiag (University of Minnesota), Paul Crowell (University of Minnesota), Sergey Frolov (University of Pittsburgh), Noa Marom (Carnegie Mellon University), Chris Palmstrøm (University of California Santa Barbara)

Keywords: topologically-protected quantum information, ferromagnet-semiconductor-superconductor hybrid materials, interface discovery, in-situ interface growth, low-temperature transport

Research Scope

Majorana zero modes (MZMs) are the leading candidate for developing quantum bits that are intrinsically protected from decoherence by quantum state topology and which also enable topologically-protected quantum gates based on the braiding of non-Abelian anyons. This project focuses seeks to develop a robust and scalable platform for manipulating MZMs and other exotic odd-parity superconductor states through the systematic integration of magnetic materials with semiconductors and superconductors. The project leverages the experimental and computational insights and capabilities developed by the team so far to broaden the space of candidate interfaces to screen while simultaneously steering clear of systems our work to date has revealed to be unviable. The experiments required to synthesize and fabricate high-quality interfaces and devices are costly and time consuming. Therefore, it is unfeasible to explore the space of possible structures and compositions by conventional experimental means alone. To this end, this project consists of an inter-disciplinary effort that combines materials synthesis with *in-situ* characterization and device fabrication, integrated with a computational approach based on lattice matching, genetic algorithm (GA) optimization, and machine learning. Experimental verification is carried out for the most promising candidates identified by first-principles calculations. Lattice matching is used for initial screening of a large number of candidate structures, with a focus on interfaces with Heusler compounds. The team leverages these novel one- and two-dimensional materials platforms to assess the presence of predicted topological excitations and seeks to demonstrate topological quantum systems with robust functionality.

Recent Progress

Integrated 1D and 2D quantum nanostructure growth: We have been optimizing the growth of superconductor on InAs shallow quantum well structures (QW structures) for planar Josephson devices and nanowires. Emphasis has been on improving the growth of InAs and InGaAs quantum wells for multi-terminal Josephson junctions devices and the subsequent growth of Al superconductor films. In order to ensure that there was no parallel conduction from the substrate,

Fe-doped InP(001) substrates were used. The carrier mobilities are in excess of 377,000 cm^2/Vs. In addition, we have developed growth of magnetic materials on III-V semiconductors. For example, using MBE growth on GaSb (001) substrates and adopting 3 nm LuSb as a buffer layer, we have achieved first epitaxial films of PtMnSb (001) single phase (Fig. 1). PtMnSb is one of the first predicted half-metals with high Curie temperature above room temperature and has been known to exhibit record-high magneto-optic Kerr effect. While PtMnSb is considered as a promising material for magnetic applications owing to the broken inversion symmetry and large spin-orbit coupling, its film research has been rare, limited to low-crystallinity quality films grown on oxide substrates. The PtMnSb exhibits an in-plane easy axis, a saturation moment of 4 mB/formula unit as expected from the Slater-Pauling rule of half Heusler compounds, and an anomalous increase of magnetization at low temperature associated with the development of a half-metallic gap. We have also continued working on the growth and study of the hexagonal ferromagnet, MnSb. Thin films can be grown on $In_{0.27}Ga_{0.73}Sb$ with minimal substrate-film intermixing, showing diffraction patterns that depend on the substrate temperature.

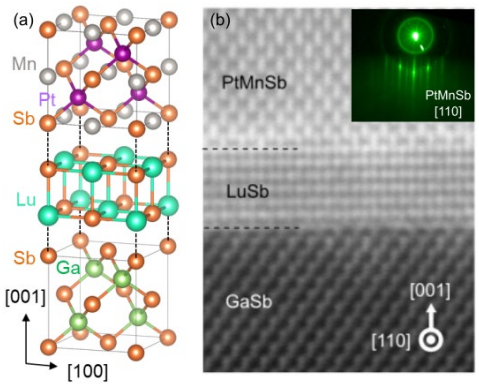

Figure 1. Structural characterization of PtMnSb(001) films. (a) Crystal structure; (b) transmission electron microscope image of the PtMnSb/LuSb/GaSb(001) heterostructure. Inset is the RHEED image of the PtMnSb taken from [110] azimuthal angle.

DFT calculations of Heusler compounds and interfaces with III-V semiconductors relevant for MZM experiments: We have undertaken a systematic study of the electronic structure and magnetic properties of 23 Heusler compounds observed or predicted to be lattice matched to either InAs or InSb. We compared the results of DFT using the semi-local PBE functional and the hybrid HSE functional to many-body perturbation theory within the quasiparticle self-consistent GW (QPGW) scheme. We use QPGW as the reference for machine learning the U value in PBE+U for these compounds by Bayesian optimization (BO). We have found that the proximity-induced spin polarization around the Fermi level of the semiconductor largely depends on the degree of spin polarization around the Fermi level of the Heusler, regardless of the Heusler's total magnetic moment [1]. Based on this criterion, we find that the Fe-based, Co-based, and Ru-based Heuslers are the most promising materials for MZM experiments because they have the highest spin polarization around the Fermi level. In addition, we have adapted the Ogre interface code to predict the structure of interfaces between ionic materials. We have tested this new method for an epitaxial interface of the lead sulfohalide $Pb_4S_3Br_2$ on top of the lead halide perovskite $CsPbBr_3$. The results of lattice matching demonstrate good agreement between the new score function and DFT calculations for the interfacial distance and the in-plane registry between the substrate and film for one possible configuration of the $CsPbBr_3(100)$/ $Pb_4S_3Br_2(010)$ interface.

Zero-bias conductance peaks in semiconductor nanowire – superconductor – ferromagnet nanostructures: As part of this project, we have recently demonstrated hybrid superconductor-semiconductor devices integrated with micromagnets, a new type of platform that combines three diverse materials families. The team have now achieved the first experimental devices and measurements [2]. The results show the possibility to control superconductivity in a thin shell of Sn or Al superconductor, as well as induced superconductivity in an InAs or InSb nanowire using remote but nearby micromagnets (Fig. 2).

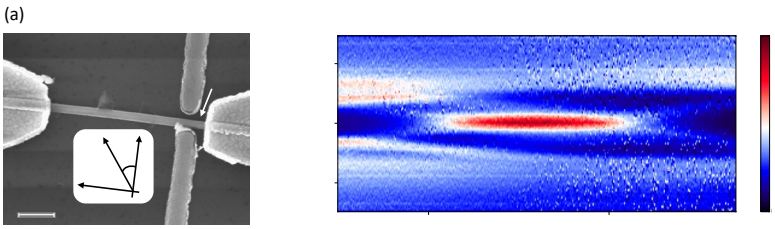

Figure 2. ***(a) SEM image of device based on Al-InAs nanowire with CoFe magnets. (b) Conductance as function of bias voltage (V) vs. side-gate voltage (V_{sg1}) at zero applied magnetic field. The CoFe strips are magnetized in the opposite direction of $\theta = 0^o$.***

Mitigating disorder in integrated materials platforms for topological studies: Disorder is an ubiquitous challenge faced by many quantum information materials platforms, including MZMs [3], because the materials requirements for quantum information systems are extremely stringent compared to those for classical computing. Importantly, to observe clear topological features it is not enough to have high-quality as-grown materials; the final *processed* material *system* must itself have sufficiently low disorder. Therefore, we are taking a dual approach; while part of the team has been working on improving growth of nanowires and quantum wells, another part has developed new ways to process the materials. To this end, we have explored the integration of InSb nanowires with van der Waals (vdW) materials. Hexagonal boron nitride (hBN) is a pristine single-crystalline dielectric, which should minimize disorder from charged impurities in our devices. The use of a few-layer graphite (FLG) further ensures that the entire gate structure is atomically flat, reducing surface roughness scattering, and provides enhanced screening of remaining charged defects. We have successfully created the world's first fully integrated FLG/hBN/nanowire materials structure, which shows robust conductance quantization in an external field, the signature of one-dimensional ballistic quantum transport. This quantization persists even in zero external applied field, suggesting that our system is remarkably clean, and enabling us to perform low field ballistic measurements as are required for MZM studies.

Over the past year, PbTe nanowires have emerged as a promising new materials platform for realizing MZMs, complementary to the III-V platforms (InSb and InAs). Our collaborators in the Bakkers group (Eindhoven) have recently demonstrated growth of clean PbTe SAG nanowires [4] by MBE, which enables the highest possible purity. In addition to strong spin-orbit coupling (necessary for MZMs), these PbTe nanowires have a high dielectric constant, which could enable new electrostatic functionalities, and they can be grown in networks, which is essential for scaling up to MZM circuits. In preliminary work, we have seen extremely encouraging results in these

nanowires, in particular, well-defined conductance quantization plateaus, even at zero applied magnetic field. This points to their high quality and low disorder, which are essential attributes.

Non-reciprocal superconducting effect: In a very recent work we reported a novel superconducting effect: non-reciprocal superconductivity in InAs-Al quantum wells structured as a multi-terminal Josephson junction [5]. These results are very timely due to the enormous interest in non-reciprocal superconductivity that has arisen in the past couple of years. Among of the most intriguing implications of this work are the potential to use such structures for topologically-stabilized superconducting circuits and for hybrid neuromorphic circuits for AI.

Future Plans

Having made significant improvements on deeper InAs quantum wells, the aim is now to start growing shallower wells without too much loss in mobility. In addition, the development of in-situ shadow masking techniques (for pristine interfaces), selective area-growth of InAs and InGaAs nanowires, and the growth and study of the hexagonal ferromagnet, MnSb on $In_{0.27}Ga_{0.73}Sb$ will continue. With regards to interface discovery, we plan to finish the study of the electronic and magnetic properties of Heusler compounds, and of interfaces of Fe-based, Co-based, and Ru-based Heuslers with InAs. We also plan to complete the structure prediction of ionic interfaces and complete the development, publication, and release of a new major version of Ogre (Ogre 3.0). Time-permitting, preliminary work will be initiated to explore the fundamental electronic properties of PbTe and related IV-VI nanowires, and identify promising interfaces with superconductors and magnets. Characterization of materials structure will leverage several new approaches proposed in recent theory work. The focus will be on using these new approaches to detect the helical state and MZMs. We will explore the usability of micromagnets and the dipole fields they generate in circuit QED experiments that include semiconductor nanowires, for use in either parametric amplifier circuits or hybrid quantum bits. This research has the potential of alleviating the need to operate superconductor microwave electronics at large magnetic fields, as required for spin qubit as well as topological qubit experiments. Based on our very encouraging preliminary results, we will complement InAs and InSb with IV-VI materials (especially PbTe quantum wells and selective-area grown nanowires).

References

[1] B. Heischmidt, M. Yu, D. Dardzinski, J. Etheridge, S. Moayedpour, V. S. Pribiag, P. A. Crowell, and N. Marom, *First Principles Study of the Electronic Structure of the Ni2MnIn/InAs and Ti2MnIn/InSb Interfaces*, Phys. Rev. Mater. **7**, 026203 (2023).

[2] Y. Jiang, M. Gupta, C. Riggert, M. Pendharkar, C. Dempsey, J. S. Lee, S. D. Harrington, C. J. Palmstrøm, V. S. Pribiag, and S. M. Frolov, *Zero-Bias Conductance Peaks at Zero Applied Magnetic Field Due to Stray Fields from Integrated Micromagnets in Hybrid Nanowire Quantum Dots*, ArXiv:2305.19970 (2023).

[3] S. Ahn, H. Pan, B. Woods, T. D. Stanescu, and S. Das Sarma, *Estimating Disorder and Its Adverse Effects in Semiconductor Majorana Nanowires*, Phys. Rev. Mater. **5**, 124602 (2021).

[4] J. Jung, S. G. Schellingerhout, M. F. Ritter, S. C. Ten Kate, O. A. H. Van Der Molen, S. De Loijer, M. A. Verheijen, H. Riel, F. Nichele, E. P. A. M. Bakkers, J. Jung, S. G. Schellingerhout, O. A. H. Van Der Molen, S. De Loijer, M. A. Verheijen, E. P. A. M. Bakkers, M. F. Ritter, S. C. Ten Kate, H. Riel, and F. Nichele, *Selective Area Growth of PbTe Nanowire Networks on InP*, Adv. Funct. Mater. **32**, 2208974 (2022).

[5] M. Gupta, G. V. Graziano, M. Pendharkar, J. T. Dong, C. P. Dempsey, C. Palmstrøm, and V. S. Pribiag, *Gate-Tunable Superconducting Diode Effect in a Three-Terminal Josephson Device*, Nat. Commun. **14**, 3078 (2023).

Publications (10 most relevant, supported by BES):

1. B. Heischmidt, M. Yu, D. Dardzinski, J. Etheridge, S. Moayedpour, P. A. Crowell, V. S. Pribiag, and N. Marom, *First Principles Study of the Electronic Structure of the $Ni_2MnIn/InAs$ and $Ti_2MnIn/InSb$ interfaces*, Phys. Rev. Materials **7**, 026203 (2023).
2. Y. Jiang, M. Gupta, C. Riggert, M. Pendharkar, C. Dempsey, J. S. Lee, S. D. Harrington, C. J. Palmstrøm, V. S. Pribiag, S.M. Frolov, *Zero-bias conductance peaks at zero applied magnetic field due to stray fields from integrated micromagnets in hybrid nanowire quantum dots*, arXiv:2305.19970 (submitted for peer review) (2023).
3. Mohit Gupta, Gino Graziano, Mihir Pendharkar, Jason T. Dong, Connor P. Dempsey, Chris Palmstrøm, and Vlad S. Pribiag, *Gate-Tunable Superconducting Diode Effect in a Three-terminal Josephson Device*, Nature Communications **14**, 3078 (2023).
4. M. J. A. Jardine, D. Dardzinski, M. T. Yu, A. Purkayastha, A. H. Chen, Y. H. Chang, A. Engel, V. N. Strocov, M. Hocevar, C. Palmstrøm, S. M. Frolov, and N. Marom, *Assessment of CdTe as a Tunnel Barrier at the α-Sn/InSb Interface*, ACS Applied Materials & Interfaces **15**, 16288 (2023).
5. G. V. Graziano, M. Gupta, M. Pendharkar, J. T. Dong, C. P. Dempsey, C. J. Palmstrøm, and V. S. Pribiag, *Selective Control of Conductance Modes in Multi-terminal Josephson Junctions*, Nature Communications **13**, 5933 (2022).
6. Z. Yang, P. A. Crowell, and V. S. Pribiag, *Spin-Helical Detection in a Semiconductor Quantum Device with Ferromagnetic Contacts*, Physical Review B **106**, 11541 (2022).
7. D. Dardzinski, M. Yu, S. Moayedpour, and N. Marom, *Best Practices for First-Principles Simulations of Epitaxial Inorganic Interfaces*, J. Phys. Condensed Matter **34**, 233002 (2022).
8. S. Moayedpour, D. Dardzinski, S. Yang, A. Hwang, N. Marom, *Structure Prediction of Epitaxial Inorganic Interfaces by Lattice and Surface Matching with Ogre*, J. Chem. Phys. **155**, 034111 (2021).
9. M.J.A. Jardine, J.P.T. Stenger, Y. Jiang, E.J. de Jong, W. Wang, A.C. Bleszynski Jayich, S. M. Frolov, *Integrating micromagnets and hybrid nanowires for topological quantum computing*, SciPost Phys. **11**, 090 (2021).
10. M. Yu, S. Moayedpour, S. Yang, D. Dardzinski, C. Wu, V. S. Pribiag, N. Marom, *Dependence of the electronic structure of the EuS/InAs interface on the bonding configuration*, Phys. Rev. Mater. **5**, 064606 (2021).

Elucidating Pathways of Zeolite Crystallization: Cooperative Effects of Inorganic and Organic Structure-Directing Agents

Jeffrey D. Rimer and Jeremy C. Palmer

Chemical and Biomolecular Engineering, University of Houston, 4226 Martin Luther King Blvd., S222 Engineering Building 1, Houston, TX 77401 USA

Keywords: zeolite, nonclassical crystallization, structure direction, crystal engineering

Research Scope

Critical challenges in zeolite synthesis stem from an inability to a priori tune crystal properties and limited, often phenomenological, understandings of fundamental pathways of crystallization. The goal of our DOE project is to develop a fundamental understanding of zeolite crystallization, and to use this knowledge as a versatile platform for tailoring their physicochemical properties. These studies are motivated by opportunities and practical needs to implement rational design in zeolite synthesis, while also addressing aspects of nonclassical crystallization that may prove to be applicable to a broader class of crystalline materials. The research scope of this project includes three specific aims. The first specific aim is the elucidation of zeolite crystallization mechanisms wherein we seek to understand the physical phenomena that underlie complex processes of nucleation and growth, focusing on several industrially-relevant zeolites. High temperature atomic force microscopy (AFM) is being used as a unique tool to monitor zeolite growth *in situ* under realistic synthesis conditions. Our work is uncovering multiple pathways of zeolite crystal growth, including nonclassical crystallization by particle attachment. A major thrust of this specific aim is to identify critical variables influencing pathway selection with an intent to use this information to engineer high performance materials.

The second specific aim involves controlled elemental siting through the use of divalent structure-directing agents (SDAs). In zeolite synthesis the ability to control the spatial distribution of framework aluminum is nontrivial; however, the strategic placement of Al sites in close proximity can impact their performance in applications such as adsorption and catalysis. In this project, we are developing new methods to control Al siting by the introduction of divalent cations in zeolite syntheses to promote paired Al sites, drawing inspiration from natural zeolites comprised of alkaline earth metals. To achieve fundamental understandings of controlled Al siting, we are using a computational platform that employs hybrid Monte Carlo – molecular dynamics methods and accurate deep neural network force fields trained on density functional theory reference data.

In the third specific aim, we are developing new approaches in zeolite synthesis based on the use of cooperative inorganic/organic structure direction. Preliminary studies in our group have

revealed that certain combinations of SDAs control the Si/Al ratio of zeolites (i.e. total acidity), gradients (or zoning) of aluminum and/or silicon through the interior and exterior regions of zeolite crystals, and can lead to alterations in crystal habit and number of defects. Recently, we have shown that the judicious selection of two or more inorganic cations can dramatically reduce the crystallization time of zeolite chabazite (CHA type) by more than 10-fold (Figure 1) compared to conventional methods. This is accomplished using lithium as a minor SDA, noting that Li has traditionally been viewed as a strong inhibitor of zeolite growth. These unique pairings of SDAs can also lower synthesis temperature, which reduces energy requirements. Moreover, the concept of using cooperative SDAs is a relatively new advancement in the rational design of zeolites. To this end, our project is leveraging expertise in zeolite synthesis, state-of-the-art characterization, and molecular modeling to identify the mechanisms underlying SDA cooperativity.

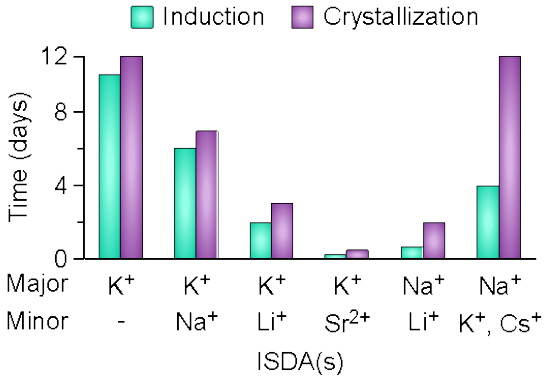

Figure 1. Zeolite CHA crystallization times for nucleation (cyan) and crystal growth (purple). Comparisons are made for different major/minor combinations of inorganic structure-directing agents (ISDAs) compared to the convention K^+ synthesis.

Recent Progress

A common objective of zeolite crystal engineering is to overcome the inherent mass transport limitations of nanopores, often through the design of nanosized or hierarchical materials [1]; however, the complex nonclassical pathways of zeolite nucleation and crystal growth involving heterogeneous media comprised of both solid (gel) and solution states (Figure 2a) make it difficult to control the physicochemical properties of zeolitic materials for energy-related applications. In this presentation, we will highlight key advancements in our DOE project over the past two years with respect to understanding zeolite crystallization and developing new synthetic and computational methods to achieve materials with enhanced properties. To this end, we have leveraged tools such as high-temperature AFM to elucidate mechanisms of zeolite crystallization, from which we have identified a broad range of nonclassical

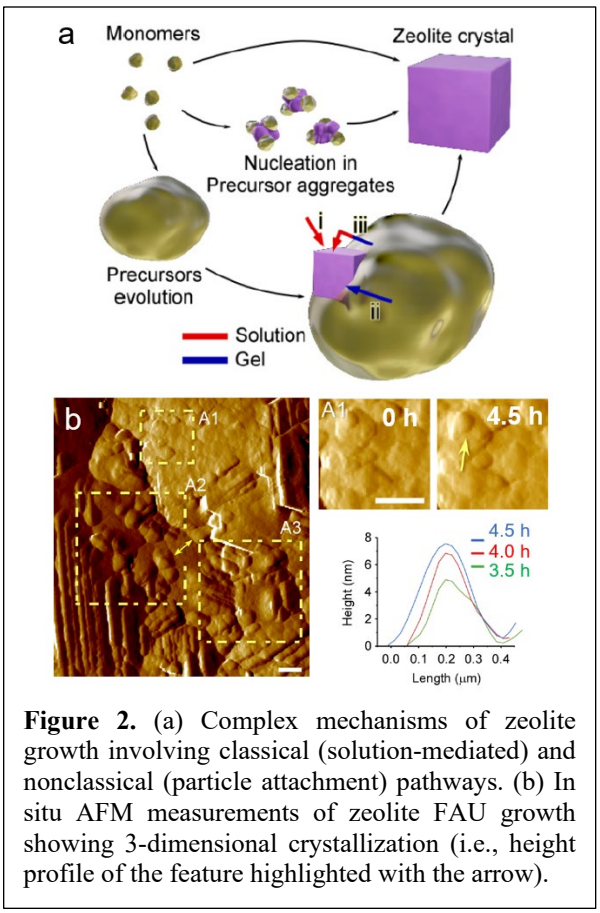

Figure 2. (a) Complex mechanisms of zeolite growth involving classical (solution-mediated) and nonclassical (particle attachment) pathways. (b) In situ AFM measurements of zeolite FAU growth showing 3-dimensional crystallization (i.e., height profile of the feature highlighted with the arrow).

pathways [2]. *In situ* AFM studies of zeolites surface growth have been coupled with time-resolved characterization of amorphous precursor evolution to identify generalizable methods to control zeolite crystallization [3]. Examples include the analysis of commercial zeolite faujasite (FAU type) where our findings revealed that growth is dominated by the solid state via the disorder-to-order transition of amorphous precursors. For conditions where the solution phase contributes to zeolite FAU crystallization, we observed a unique 3-dimensional growth of surface features (Figure 2b) by the addition of soluble species – a process that deviates from classical 2-dimensional birth and spreading of layers commonly reported in literature.

One of the major thrusts of this DOE project has been the development of new synthetic methods employing cooperative inorganic and organic structure-directing agents to achieve zeolite products more efficiently (e.g., reduced time and energy, as shown in Figure 1) and to access materials properties, such as crystal size and morphology, that cannot be achieved by conventional methods [4]. This presentation will highlight these design approaches along with synthesis strategies using crystal growth modifiers [5] to achieve hierarchical zeolites that outperform state-of-the-art materials in applications (e.g., catalytic reactions) by dramatically reducing internal diffusion limitations. Collectively, our findings have demonstrated how the synergistic combination of experimental and computational approaches lead to more fundamental understandings of zeolite crystallization as a platform for materials design.

Future Plans

During the next period of our DOE project, we are expanding *in situ* AFM studies to investigate the nature of zeolite intergrowths. This topic has been garnering significant attention in the materials community owing to the hierarchical structures produced from intergrowths, which increases surface area, introduces mesoporosity, and produces nano-sized domains with reduced mass transport limitations. Our preliminary work has focused on intergrowths of zeolites FAU and EMT where our group and others have shown that these structures exhibit pillared and branched nanosheet architectures (Figure 3a). We are using both experimental and computational efforts to identify cooperative inorganic/organic SDA pairs that promote intergrowths. In addition, we are examining organic structure-directing agents that lead to unique growth pathways and produce ultra-small zeolites. Examples include the synthesis of zeolite AEI using an organic that directs the formation of nanosheets (Figure 3b) through a pathway involving interzeolite transformation of FAU-to-AEI, with hierarchical intermediates that resemble those of FAU/EMT intergrowths. The overarching goals of these studies are to control zeolite crystal size/morphology and aluminum

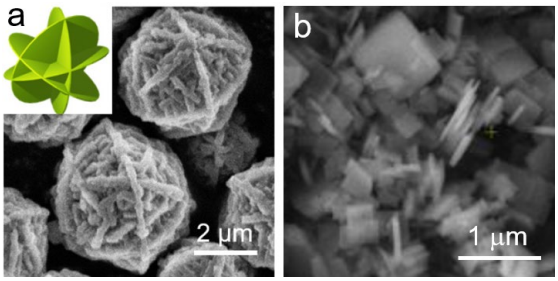

Figure 3. (a) Intergrowths of zeolites FAU and EMT with a pillared morphology. (b) OSDAs can direct the formation of zeolite AEI nanosheets.

siting by directing intergrowth (defect) formation, which is a powerful tool for the design of hierarchical zeolites with dramatically reduced diffusion limitations.

Publications

1. A.J. Mallette, S. Seo, and J.D. Rimer, *Synthesis Strategies and Design Principles for Nanosized and Hierarchical Zeolites*, Nature Synthesis **1**, 521-534 (2022).
2. R. Jain, Z. Niu, M. Choudhary, H.A. Bourji, J.C. Palmer, and J.D. Rimer, *In Situ Imaging of Faujasite Surface Growth Reveals Unique Pathways of Zeolite Crystallization*, J. Am. Chem. Soc. **145**, 1155-1164 (2023).
3. D. Parmar, Z. Niu, Y. Liang, H. Dai, and J.D. Rimer, *Manipulation of Amorphous Precursors to Enhance Zeolite Nucleation*, Faraday Discuss. **235**, 322-342 (2022).
4. A. Chawla, A.J. Mallette, R. Jain, N. Le, F.C. Robles-Hernandez, and J.D. Rimer, *Crystallization of Potassium-Zeolite in Organic-Free Media*, Micropor. Mesopor. Mater. **341**, 112026 (2022).
5. D. Parmar, A.J. Mallette, T. Yang, X. Zou, and J.D. Rimer, *Unique Role of GeO_2 as a Noninvasive Promoter of Nano-sized Zeolite Crystals*, Adv. Mater. **34**, 2205885 (2022).

Fundamentals of Scalable Nanoparticle Assembly in Engineering Polymers

Linda S. Schadler, Department of Mechanical Engineering, College of Engineering and Mathematical Sciences, University of Vermont, Burlington, Vermont

Sanat Kumar, Chemical Engineering Department, Columbia University, New York, NY

Brian C. Benicewicz, Chemistry and Biochemistry Department, University of South Carolina, Columbia, SC

Keywords: Polymer, crystallization, nanoparticle ordering, external fields, design maps

Research Scope

We have developed a fundamental understanding of the kinetic mechanisms that can be used to manipulate and control the organization of nanoparticles (NP) in semicrystalline polymers. This particular NP ordering is controlled by the polymer crystallization process. We postulated and verified that the ability to organize is controlled by the spherulitic growth rate and NP diffusion coefficient, which together define a dimensionless Peclet numbers. This understanding allows us to develop an apparently universal design map that permits us to quickly articulate the conditions under which we can achieve the desired level of NP ordering, and hence system properties, apparently independent of the specific chemical identity of the system constituents.

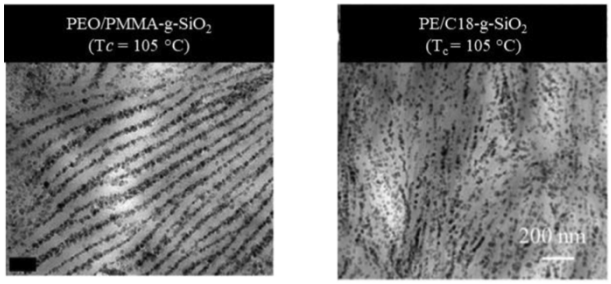

Figure 1. Cryo-microtomed TEM images of: Left) PEO/PMMA-g-SiO_2 PNC crystallized at low undercooling. Right) PE/C18-g-SiO_2 PNC crystallized at low undercooling.

Specifically, *in situ* monitoring of NP motion using AFM, x-ray photon correlation spectroscopy, optical microscopy and modeling demonstrated definitively that the nanoparticles are being rejected from the growing lamella and selectively placed in the amorphous regions of the semicrystalline morphology resulting in the desired ordered morphology, e.g., Figure 1. The spherulite growth rate can be easily manipulated by the extent of supercooling, while the NP diffusion can be controlled through variations in interactions between the particle and matrix, e.g., through grafting polymer brushes of different length and density on the NP. Building on this understanding we demonstrated that the critical spherulite growth rate of optimal organization is when the Peclet Number (in this case a ratio of the characteristic time for diluent diffusion over the corresponding spherulite growth time) is equal to 1, apparently providing a system-independent description of the underlying physics in these situations. Additionally, we have developed a zone annealing technique that allows large scale directional ordering of both nanoparticles and compatible polymer mixtures. We are currently using micro-Raman spectroscopy to probe the impact of these new morphologies on the micromechanical behavior.

Recent Progress

We previously demonstrated that quiescent, isothermal crystallization can be used to synthesize semicrystalline polymer composites with carefully controlled NP ordering, i.e., where the inorganic NPs are selectively placed in the amorphous regions of the semicrystalline morphology (Figure 1). The result, especially in the case of polymer nanocomposites, is a locally layered, but overall disordered, morphology that reflects the underlying space filling spherulitic arrangement of the polymer. This discovery of NP ordering has exciting potential for a variety of applications relying on improved mechanical [1] and dielectric properties.

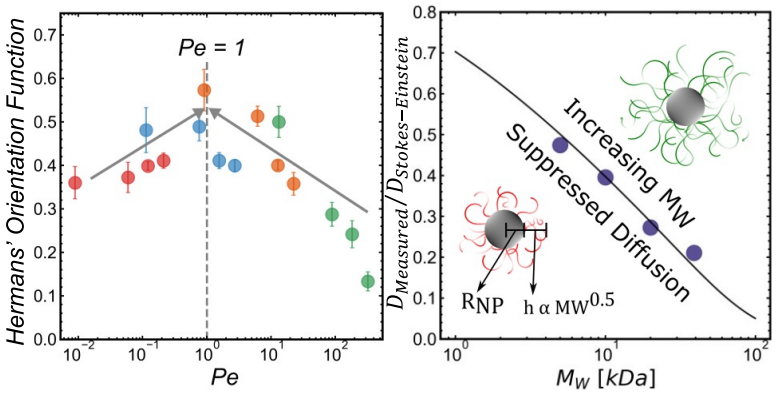

Figure 2 (Left) Hermans' Orientation Function calculated from 2D SAXS images as a function of *Pe* with demarcation behavior shown at *Pe = 1*. Right) Measured silica NP diffusion coefficients normalized by Stokes-Einstein calculated diffusion coefficients plotted as a function of matrix M_W.

We have demonstrated that this ability to organize NPs represents a competition between diluent motion and the polymer crystallization rate, and only occurs over long timescales because of the slow filler (or more generally diluent) dynamics. In short, the critical crystallization rate, G_c, can be obtained when a characteristic Peclet number $Pe = \tau_D/\tau_G = \frac{a^2/D}{a/G} = \frac{aG}{D} \equiv 1$ [2]. τ_D is the characteristic time for diluent diffusion, τ_G is the corresponding crystal growth time; a is the characteristic length scale in the problem (crystal unit cell dimension), D is the diluent diffusivity, and G is the crystal growth rate. When the crystallization time scales, τ_G, are longer than the diluent diffusion times, τ_D, then we get local segregation of the defects and hence the results seen in Figure 2. This is essentially a design criterion for predicting this behavior in other systems. Pe was quantified through independent measurements of both spherulite growth rate (G) and NP diffusion (D). Spherulite growth rate was measured using polarized optical microscopy across a range of low undercooling crystallization temperatures. NP diffusion was quantified using x-ray photon correlation spectroscopy (XPCS) measurements where the observed relaxation times were found to scale with $\tau \propto q^{-2}$ indicating hydrodynamic diffusion.

In addition, we have used *in situ* AFM to monitor the motion of the nanoparticles during crystallization. In order to probe this process further and begin to understand the fundamental mechanism, we used a Cypher AFM to monitor particle migration *in situ*. The AFM has a precision hot stage with control of 1.0 ºC/s heat rate as well as scan speeds of up to 40Hz, enabling *in-situ* capturing of fast-growing crystals and mobile particles. This set up was utilized to image

migration of bare silica nanoparticles into the interlamellar zone of a growing polyethylene oxide (PEO). This investigation was carried out on NPs of three different sizes small (14nm), medium (26nm) & large (50nm) in PEO (M_w=46k), using *in-situ* Atomic Force Microscopy, previously proven to undergo organization under isothermal crystallization temperatures. These studies verify the conjectures presented above in a detailed manner.

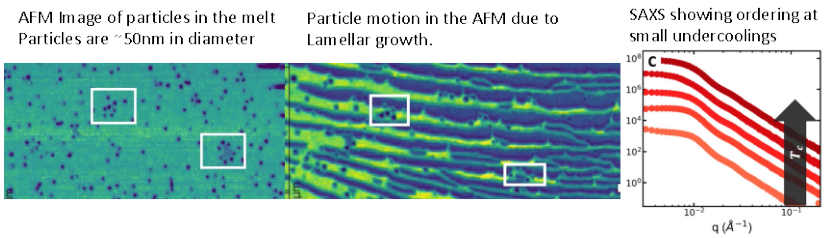

Figure 3. AFM images showing the movement of particles, and scattering profiles as a function of undercooling

Our theoretical work (with Chris Durning, Columbia and Sumesh Thampi, IIT Madras) has focused on developing the underpinning macroscale physics of the zone annealing protocol. The work is closely tied with experiments and is able to critically explain the underpinning molecular basis of the result that the velocity at which the sample is pulled through the zone equals the polymer's spherulite growth rate. We are also able to rationalize why these highly non-isothermally crystallized samples have structures analogous to an isothermally crystallized sample. This is because the sample crystallizes over a very narrow temperature range, a result that naturally occurs because polymers are poor thermal conductors. While these are important insights, these works do not include the lamellar semicrystalline morphology which is critical to the prediction of NP ordering – this is a key issue we shall address in future work.

We have demonstrated that the nucleation mechanisms and crystallization kinetics can be tailored in grafted brush nanocomposites by using grafted chains that are amorphous or capable of crystallizing. For example, PMMA grafted silica NPs did not significantly alter nucleation or growth of PEO (fully miscible), compared to bare particles. On the other hand, polyethylene grafted silica NPs significantly changed the nucleation and growth of neat polyethylene with which they were mixed. These changes were (strong) functions of the graft chain length and graft density of the polyethylene on the NPs – i.e., by controlled changes in brush morphology.

Additionally, Our results show that in grafted brush NP nanocomposites the extent of "interpenetration" of the matrix and the graft, which also determines NP morphologies [3], critically controls nucleation kinetics. Heterogeneous nucleation is enhanced in nanocomposites where the brushes are the least interpenetrated by the matrix (typically higher graft densities and lower molecular weights); this is likely because the oriented graft chains are more easily able to epitaxially favor polymer crystallization. On the other hand, increased wetting and interpenetration from the neighboring monomer units of the matrix (which can be achieved for specific combinations of graft density and chain length) suppress nucleation well below the matrix nucleation rate despite the graft being crystallizable.

In summary, we have a detailed understanding of the mechanisms controlling this non-equilibrium NP assembly, and this understanding is driving our decision to focus on external field driven

assembly in the proposed work. In particular, we know we need to enhance diluent mobility and drive directionality in the NP ordering to achieve a length and time scale that could have impact in the context of transformative manufacturing of these nanocomposites. Our fundamental understanding of these issues also gives us confidence that this approach can be extended to polymeric mixtures of sustainable or recycled polymers. In addition, the coupling of this kinetically driven assembly mechanism with external fields opens up the opportunity to develop further fundamental understanding of material behavior in highly non-equilibrium situations. We can thus learn how we can control these ordering processes on a length and time scale more applicable for production.

Future Plans

In future work we will explore a highly non-equilibrium processing space where internal self-assembly (crystallization) and externally driven assembly interact, potentially synergistically, to create large scale highly ordered/layered polymeric materials. To create large scale directional ordering, we propose to combine directional zone annealing with other external drivers (acoustic fields, followed by electric fields and potentially shear, time permitting, as we learn more) to facilitate the ordering of nanocomposites and miscible polymer blends into layered structures. An integrated program involving a tight coupling of experiments and theory is proposed with the ultimate goal of creating a design space which can allow us to synthesize these hierarchically ordered structures with desired properties. While much of the future work will focus on miscible systems (either with NPs or with amorphous polymers), we can also extend these ideas to immiscible polymer blends following ideas presented in a very new manuscript [4] – here, we add dynamic crosslinkers that compatibilize immiscible polymer mixtures. Presumably, this idea can also port over to NP/polymer mixtures. We shall, time permitting, examine such dynamically compatibilized systems to consider the application of these ideas to immiscible systems.

References

[1] R. A. Register, "A 'Layered Look' for Spherical Nanoparticles in Semicrystalline Polymers," *ACS Cent. Sci.*, vol. 3, no. 7, pp. 689–691, Jul. 2017, doi: 10.1021/acscentsci.7b00277.

[2] D. Zhao *et al.*, "Tunable Multiscale Nanoparticle Ordering by Polymer Crystallization," *ACS Cent. Sci.*, vol. 3, no. 7, pp. 751–758, Jul. 2017, doi: 10.1021/acscentsci.7b00157.

[3] P. Akcora *et al.*, "Anisotropic self-assembly of spherical polymer-grafted nanoparticles," *Nat. Mater.*, vol. 8, no. 4, pp. 354–359, Apr. 2009, doi: 10.1038/nmat2404.

[4] R. Clarke, "Dynamic crosslinking compatibilises polymer mixtures," *Nature*, vol. in press, 2023.

Publications

Nicholas F. Mendez, Deboleena Dhara, Qingteng Zhang, Suresh Narayanan, Linda S. Schadler, Alejandro J. Müller, and Sanat K. Kumar, *Nanoparticle Diffusion in Miscible Polymer Nanocomposite Melts,* **Macromolecules,** https://doi.org/10.1021/acs.macromol.3c00490 (2023).

N. F. Mendez, A. S. Altorbaq, A. J. Müller, and S. K. Kumar, *Organizing Nanoparticles in Semicrystalline Polymers by Modifying Particle Diffusivity*, ACS Macro Lett., **11(7)**, 882–888 (2022).

Kamlesh Bornani, Nicholas F. Mendez, Abdullah S. Altorbaq, Alejandro J. Müller, Yueqian Lin, Eric Zhonghang Qu, Kai Zhang, Sanat K. Kumar and Linda S. Schadler, *In-situ AFM tracking of Nanoparticle Migration in Semicrystalline Polymers*, ACS Macro Letters**, 11**, 818-824 (2022).

C. J. Durning, A. Purushothaman, S. Adhikari, S. K. Kumar, and S. Thampi, *Physics of Directional Polymer Crystallization*, ACS Macro Lett., **11(9)**, 1102–1106 (2022).

A. S. Altorbaq, H. Alkhodairi, N. F. Mendez, L. S. Schadler, A. J. Müller, and S. K. Kumar, *Crystallization Kinetics and Mechanical Properties of Miscible Polymer Blend Nanocomposites: Linear versus Grafted Systems*, Macromolecules, **55(18)**, 8210–8221 (2022).

K. Bornani, M. A. Rahman, B. Benicewicz, S. Kumar, and L. Schadler, *Using Nanofiller Assemblies to Control the Crystallization Kinetics of High-Density Polyethylene*, Macromolecules, **54**(12) 5673–5682, (2021).

A. A. Krauskopf, A. M. Jimenez, A. S. Altorbaq, A. J. Müller, and S. K. Kumar, *Quantifying Nanoparticle Ordering Induced by Polymer Crystallization*, ACS Nano, **15(9)**, 14430–14443 (2021).

S. Adhikari, A. Purushothaman, A. A. Krauskopf, C. Durning, S. K. Kumar, and S. P. Thampi, *Modeling polymer crystallisation induced by a moving heat sink*, Soft Matter, **17(9)**, 2518–2529 (2021).

S. Adhikari, A. A. Krauskopf, S. K. Kumar, S. P. Thampi, and C. J. Durning, *Boundary layer description of directional polymer crystallisation*, Soft Matter, **17(3)**, 7755–7768 (2021).

Coupling real-time experiments with molecular simulations to visualize the dynamics of quasicrystalline interfaces

Ashwin J. Shahani and Sharon C. Glotzer, University of Michigan

Keywords: quasicrystals, interfaces, solidification, x-ray imaging, molecular dynamics

Research Scope

Quasicrystals (QCs) possess long-range positional order but non-crystallographic orientational order. Their classically 'forbidden' symmetry has long attracted the interest of scientists worldwide. Despite their frequent observation in both metal alloys[1] and soft matter structures[2] in the 35 years since their discovery, little is known about how QCs evolve from a liquid, amorphous, or crystalline precursor. Here, we seek to resolve the enigma of QC self-assembly through a combined experimental and computational program. Particular attention in Y1 of our renewal is focused on the dynamics of QC interfaces, including solid-liquid and solid-solid (grain boundaries, GBs). The Shahani group employs *in situ* synchrotron X-ray tomography (XRT)[3] to peer into the solidification of QCs in a liquid. In parallel, Glotzer's team develops new simulation models incorporating phasonic defects[4] — which are unique to QCs — and used this model to investigate the growth of QC grains, closely mimicking the experimental conditions.

While QCs remain exceptional structures, most compounds in the realm of intermetallics adopt non-trivial geometries. In fact, only around 6% of phases are comprised of the simplest sphere packings that researchers so readily associate with metals.[5] State-of-the-art knowledge of phase transformations at the outset of this collaborative project did not encompass the remaining 94% of intermetallic compounds that possess complex and aperiodic structure types. Therefore, we anticipate that outcomes from Y2 and Y3 of this project will have immediate and profound impact on synthesis and processing science: our efforts will be used to not only explain the growth dynamics of QCs but also complex intermetallics more broadly.

Recent Progress

One of the highlights of our collaboration is the discovery of grain coalescence in QCs, *i.e.*, the relaxation of a poly-quasicrystalline aggregate to a single crystal state (see publication #1). Our work presents the first-ever *in situ* experimental evidence of grain coalescence in QCs and uses simulation to elucidate how stress is redistributed when two QC grains collide.

Fig. 1 depicts the time-evolution of multiple decagonal (*d*-)QCs before and after collisions in an alloy of composition $Al_{79}Co_6Ni_{15}$, upon slow cooling (1 °C/min.) from above the liquidus (~1026 °C) to below. The solid *d*-QCs show a decaprismatic morphology with a long axis parallel

to <00001> (along z), representing the fast-growing periodic direction. Perpendicular to this direction is the aperiodic plane {00001}. As the *d*-QCs grow, they interact with each other through soft impingements (overlapping diffusion fields) and hard impingements (collisions). We selectively focus on two different cases of hard collisions between *d*-QCs with (i) parallel long axes (**Figs. 1(a-b)**) and (ii) non-parallel long axes (**Figs. 1(c-d)**). When the long axes of *d*-QCs are parallel, we observed multiple coalescence events, the culmination of which is the formation of a *single d*-QC. The formation of a single *d*-QC is further evidenced by the absence of a GB groove (where the GB intersects the solid-liquid interfaces) as well as the presence of ten facets on the coalesced structure at the final time-steps, as shown in **Fig. 1(b)**. On the other hand, in the case where the two long axes are non-parallel to each other, we observed the persistence of a 'V'-shaped GB groove (**Figs. 1(c-d)**), signifying the formation of a stable GB between the two QC grains. Since contrast in XRT stems from differences in photo-absorption between the phases, we can only capture the *external* solid-liquid interfaces. To peer inside the QCs, we turn to molecular dynamics (MD).

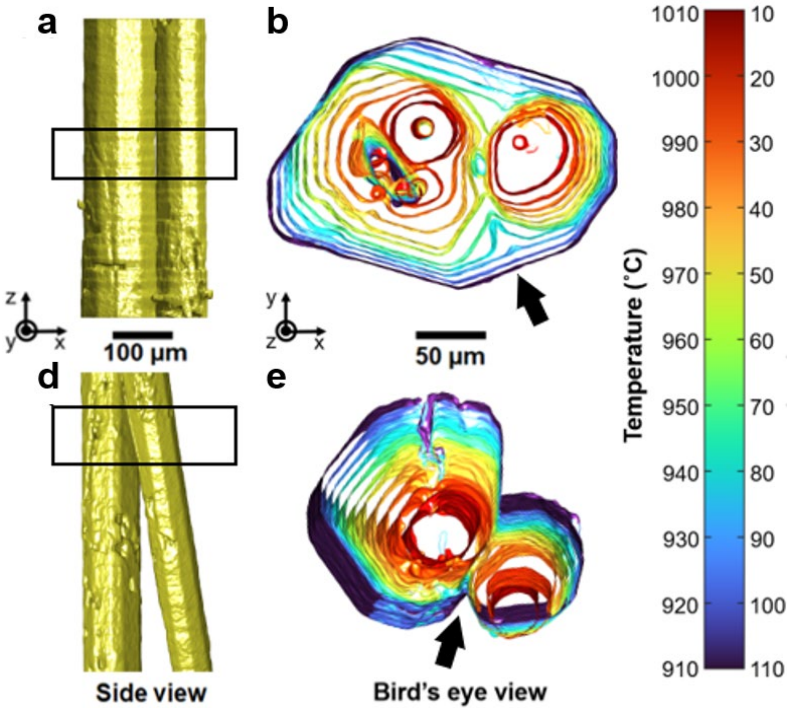

Fig. 12. Tracking grain impingements in QCs via XRT. Top row shows d-QC grains with parallel long axes, and bottom row the converse. 3D structures shown from two perspectives: side (a,d) and bird's eye (b,e) views. Solid-liquid interfaces colored to indicate passage of time.

We systematically examined the effects of misorientation on grain behavior in *d*-QCs using seeded MD simulations with an isotropic, single-component pair potential. We focused on misorientations within the aperiodic plane {00001}, since the above XRT experiments provide evidence for coalescence when the long axes are parallel (**Fig. 1(a-b)**). We used the decatic order parameter to determine the alignment of the local bond configurations about each particle. We call this quantity the *local grain orientation* (LGO) and particles with local bond configurations that align with the reference basis have a LGO of $\theta = 0^{\circ}$. In **Fig. 2**, we map the LGOs of grains grown from two seeds with relatively low misorientation of 6°. At early timesteps (**Fig. 2(a-b)**), we observe two grains (labelled A and B) with good alignment to seed orientation (yellow-orange and blue regions, seeds A and B, respectively). Immediately after collision, grain A remains well aligned with seed A and a GB is clearly visible (**Fig. 2(b)**). Both grains tend to rotate and reduce misorientation (darkening of both grains, **Fig. 2(b-e)**) over the next 4.33×10^6 timesteps. The GB

grooves (**Fig. 2(b-c)**, arrows) disappear during grain rotation. After coalescence (**Fig. 2(e)**), a gradient between the grains is still visible. This confirms the formation of a single grain, analogous to the experimental results (**Fig. 1**). In comparison, results from a simulation of fcc grains with 6° misorientation (not pictured) show GB grooves at all stages of the growth process, suggesting unresolved phonon strain due to the incommensurate distances between fcc lattices.

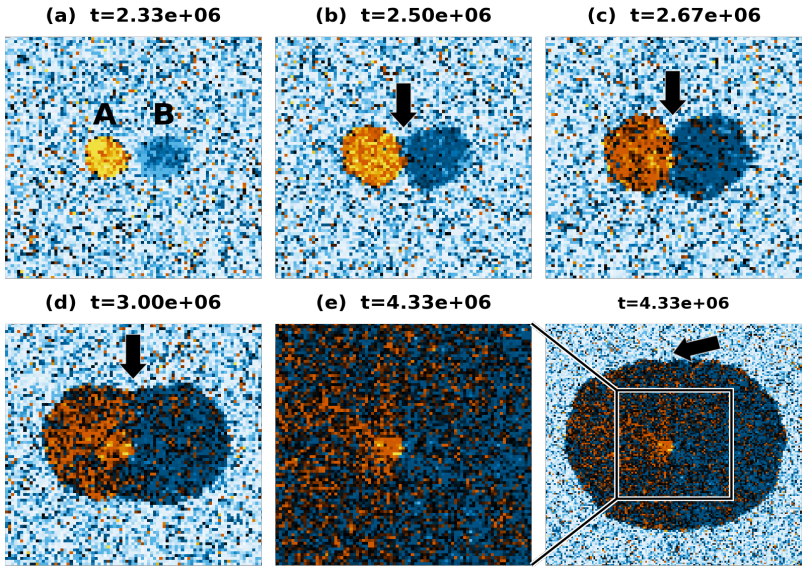

Fig. 13. Simulation results of the growth of a single d-QC from two seeds, labelled A and B in (a), with 6° initial misorientation. Images of aperiodic {10000} plane show LGOs of d-QC grains at various time-steps. Data are coarse-grained such that one pixel represents ~20 particles. Contiguous regions of white are the liquid. Arrows point to GB groove.

Although GBs were not observed in the physical space of our QCs, we found evidence of translational mismatches in the form of residual phason strain in the crystal. This observation supports the notion that the presence of multiple tiling motifs, which arise due to additional phasonic degrees of freedom in QCs, introduces additional lattice configurations that allow for grain coalescence in the presence of a translational mismatch, a highly unexpected result. Such configurational variations are impossible in periodic crystals due to restrictions imposed by a single, unique unit cell. Broadly, these insights provide a first glimpse into the remarkable self-healing behavior of QCs, with implications for the manufacture of single crystals.

Even more recently, we have sought to affirm the *generality* of the above observations, going beyond the above case of semi-solid sintering. Shahani's *in situ* XRT experiments also demonstrate the interaction between the QCs and a network of pores in the liquid. When these pores collide with the QC during solidification, they cause a disruption in the development of solid-liquid facets. However, as solidification proceeds, the growing QC grows around the pores, engulfs them, and gradually regains its facets, see **Fig. 3(a)**. This behavior is strikingly different from that of periodic crystals, *e.g.*, Si, which is known to develop twin boundaries upon colliding with, *e.g.*, a cluster of atoms (the so-called impurity-induced twinning phenomenon).

Corresponding MD simulations systematically explore the results observed in experiments. Ultimately, we aim to quantify phason and phonon strain along the *axis of grain coalescence* in these simulations, defined as the axis along which the QC completes growth towards and around the pore. Preliminary MD simulations show good agreement with experimental results. We ran simulations without pores as a reference system and some with pores where the pore aspect ratio matches that measured from the experiment. In both simulation and experiment, we see dislocation-free growth of *d*-QCs around pores, see **Fig. 3(b)**. A new automated, diffraction-based

analysis was developed to visualize phonon and phason fields in the QC. Results (not pictured) from this analysis show a phason trail along the axis of grain coalescence. Even so, we do not observe the formation of a GB or any significant increase in the dislocation density. These results open new research directions that we will pursue in the next reporting period.

Future Plans

Recognizing the limitations in spatial resolution of conventional x-ray tomography (1 μm/voxel), Shahani's team has developed expertise in synchrotron x-ray nanotomography (TXM). This imaging technique offers a 100× improvement in spatial resolution (10 nm/voxel),[3] allowing them to approach length-scales that can be simulated by MD. In addition, they have developed a two-zone heater at the TXM beam-line (National Synchrotron Light Source II at Brookhaven National Laboratory). With this apparatus, they can impose a thermal gradient across the sample (~5-20 C/mm), enabling them to sample temperature-dependent thermodynamics and kinetics. We intend to use this heater in the next reporting period for real-time TXM imaging of QCs during (1) directional solidification and (2) grain growth under non-isothermal conditions.

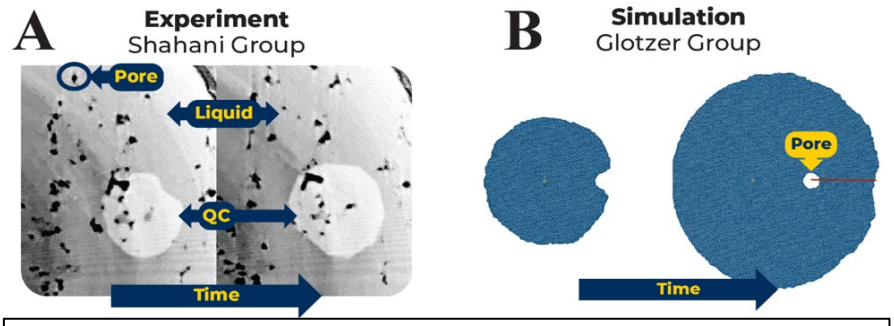

Fig. 3. Dislocation-free growth of d-QCs around pores, as observed in (a) synchrotron-based x-ray tomography (XRT) results from Al-Ni-Co QCs and (b) simulation results from a MD simulation run with 1 million particles and a single spherical pore. The red line indicates the axis of grain coalescence.

Separately, Glotzer's team will refine their analysis codes to quantify and detect phason trails. They will measure per-particle diffusion coefficients and compare it to local phonon and phason strain measurements. Then, they will measure how global and local phasons vary based on experimentally-relevant conditions (aspect ratio and relative distance between the pore and QC nucleation site), then run periodic simulations (diamond and/or fcc) with comparable parameters. They will measure phonon strain in these periodic systems and compare to QCs, where the periodic simulations act as a baseline to understand how the presence of phasons alters grain-pore interactions. Intuition gained from these simulations will deepen our understanding on how phasons contribute to the unusual grain growth behavior seen in the real-time experiments.

References

1. A. I. Goldman and M. Widom, *Quasicrystal Structure and Properties*, Annu. Rev. Phys. Chem. **42**, 685 (1991).
2. C. R. Iacovella, A. S. Keys, and S. C. Glotzer, *Self-assembly of Soft-matter Quasicrystals and their Approximants*, Proc. Natl. Acad. Sci. USA **108**, 20935 (2011).
3. A. J. Shahani, X. Xiao, E. M. Lauridsen, and P. W. Voorhees, *Characterization of Metals in Four Dimensions*, Mater. Res. Lett. **8**, 462 (2020).
4. P. J. Steinhardt, *Quasicrystals: A new phase of matter?* Science **238**, 1242-1247 (1987).
5. W. Steurer and J. Dshemuchadse, *Intermetallics*, Oxford University Press (2016).

Publications

1. I. Han, K. L. Wang, A. T. Cadotte, Z. Xi, H. Parsamehr, X. Xiao, S. C. Glotzer, and A. J. Shahani, *Formation of a Single Quasicrystal upon Collision of Multiple Grains*, Nature Comm. **12**, 5790 (2021).
2. K. Je, S. Lee, E.G. Teich, M. Engel, and S.C. Glotzer, *Entropic formation of a thermodynamically stable colloidal quasicrystal with negligible phason strain*, Proc. Natl. Acad. Sci. USA **118**, e2011799118 (2021).
3. I. Han, J. T. McKeown, L. Tang, C.-Z. Wang, H. Parsamehr, Z. Xi, Y.-R. Lu, M. J. Kramer, and A. J. Shahani, *Dynamic Observation of Dendritic Quasicrystal Growth upon Laser-induced Solid-state Transformation*, Phys. Rev. Lett. **125**, 195503 (2021).

The role of temperature in solid-state ceramic synthesis

Wenhao Sun, University of Michigan Ann Arbor

Keywords: Predictive synthesis, *ab initio* thermodynamics, CALPHAD, liquidus, metastability.

Research Scope

Temperature plays a fundamental role in solid-state synthesis, but there are currently no mechanistic theories to predict which temperature is best to carry out a solid-state ceramic reaction. It is often difficult to deconvolute whether temperature affects non-equilibrium phase evolution because of thermodynamics, $\Delta G = \Delta H - T\Delta S$; or kinetics, $k = k_0 \exp(-E_a/k_B T)$. This Early Career Award aims to elucidate the fundamental thermodynamic and kinetic principles for how temperature determines the reaction sequence, onset temperature, liquid formation, and metastable intermediates in a solid-state reaction. Specifically, we aim to build a theoretical framework that unifies classical thermodynamics, nucleation, diffusion, and crystal growth theories to calculate Temperature-Time-Transformation (TTT) diagrams for predictive solid-state ceramic synthesis.

Inspired by our recent *in situ* observations of fast solid-state reactions at subsolidus temperatures,[1,2] we hypothesize that a transient liquid phase form in the interfacial reactions between solid-state precursors, which provides a diffusion media for fast product formation. This liquid phase can be determined by the metastable eutectic formed by extending the liquidus curves into the solidus region (**Fig 1**), and sets the minimum onset temperature of a solid-state reaction. To evaluate this hypothesis, we are developing rapid and accurate *ab initio* predictions of G_{liquid}. We then collaborate with experimentalists who use *in situ* synchrotron XRD, nano-tomography, and high-throughput robotic synthesis to validate the role of this liquid in solid-state reactions.

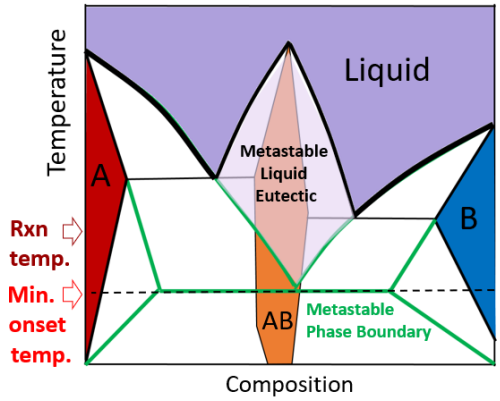

Fig 1. We hypothesize that a metastable liquid eutectic explains the reaction onset temperature and fast reaction kinetics in solid-state reactions

Recent Progress

In surveying a list of 100 oxide synthesis reactions, we find that the magnitude of ΔG is usually dominated by the ΔH contribution, rather than the $T\Delta S$ contribution. Because $\Delta G_{reaction}$ appears in the denominator of the classical nucleation barrier, as supersaturation in the JMAK theory of crystal growth, and as $d\mu/dx$ in Fick's first law of diffusion, we can use DFT-calculated ΔH to compare thermodynamic driving forces between different precursor sets without explicitly calculating diffusion barriers or surface energies for nucleation and growth analyses.

Based on these facts, we developed a thermodynamic strategy to design precursor compositions for high-purity synthesis of multicomponent oxide materials. Briefly: when 3 binary oxide precursors are mixed together, pairs of binary oxides react at a time, which can consume a

great deal of reaction energy, leaving little energy to complete a reaction (**Figure 2a**). However, in the high-dimensional phase diagrams of multicomponent oxides, there are often opportunities to find unconventional precursors that are both high in energy, and have compositions that circumvent low-energy undesired kinetic byproducts. For example, in Figure 2, a target material $LiBaBO_3$ is synthesized with much higher purity when starting from $LiBO_2$ + BaO than the simple oxide precursors B_2O_3 + BaO + Li_2O, which form low energy ternary intermediates that kinetically trap the reaction in an incomplete state.

For a set of 35 target quaternary oxides with chemistries representative of intercalation battery cathodes and solid-state electrolytes, we perform 224 reactions spanning 27 elements with 28 unique precursors. Our predicted precursors frequently yield target materials with higher phase purity than when starting from traditional precursors. (**Fig 2b**). Further details can be found in our paper 'Navigating Phase Diagram Complexity for Robotic Inorganic Materials Synthesis' on Arxiv.

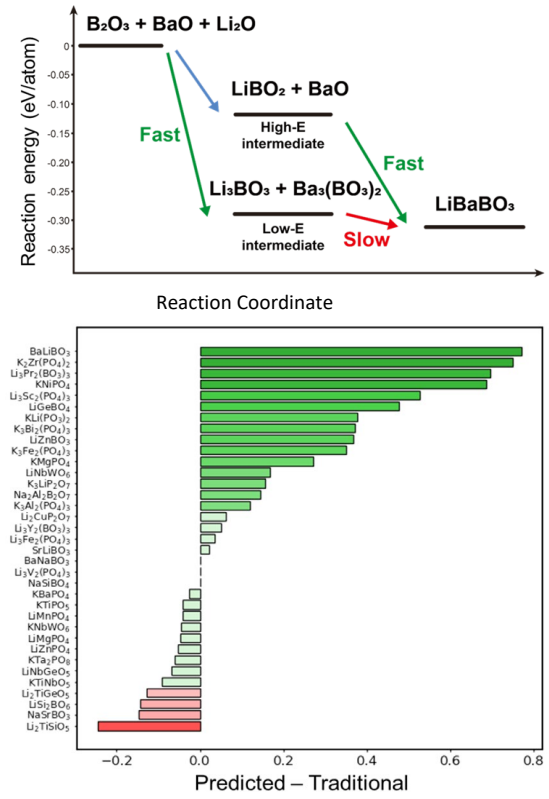

Figure 2.a) Pairs of precursors that avoid low-energy impurities while maximizing driving force can yield higher-purity samples. **b)** On a 35 materials validation set for ASTRAL, our designed precursors generally outperform simple oxide precursors.

Validating the metastable eutectic hypothesis

We are collaborating with Prof. Karena Chapman through the GENESIS EFRC, using *in situ* synchrotron XRD with a thermal gradient heater to capture the onset TTT behavior of a solid-state oxide synthesis reaction, which we are comparing against predictions of the metastable liquid eutectic temperature. **Figure 3** below shows an experimentally measured Temperature-Time-Transformation curve for the onset reaction of Fe_2O_3 + MoO_3 → $Fe_2(MoO_4)_3$. We believe that this represents the first experimentally-measured TTT curve of a solid-state oxide synthesis reaction at a temperature-and-time-resolution that can tell us fundamental aspects of solid-state reactions.

There are several important observations from the experimental data. First, the solid-state reaction is largely completed after 2 minutes; which is much faster than is typically assumed in the solid-state synthesis community where reactions take hours. Second, the solid-state reaction has a relatively sharp onset temperature of about 500°C, which is slightly above the CALPHAD predicted eutectic temperature of 395°C, as expected. The extremely fast nature of the reaction, combined with the fact that we have micrometer-sized precursor particles, suggests that this

reaction probably does not proceed via solid-state diffusion. Secondly, the very sharp onset temperature of the reaction, which is non-Arrhenius in its temperature dependence, suggests a critical phenomenon; possibly a first-order phase transition (like formation of a metastable liquid).

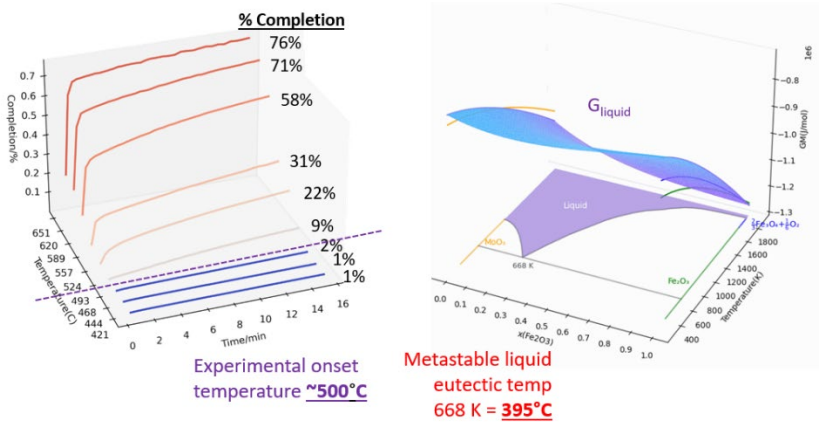

Figure 3. Left) *In situ* thermal gradient heater measurement of a TTT diagram for a solid-state oxide reaction. Reactions occur quickly (2 minutes) and initiate sharply at 500°C. Right) Metastable liquid eutectic in this system, calculated using G_{liquid}

To further characterize the role of a potential metastable liquid intermediate in facilitating diffusion, we next worked with Prof. Ashwin Shahani, who used *in situ* X-ray nanotomography (TXM) to characterize the morphology of the powder reactions before and after the reactions. From the TXM results, we can assess the spatially-resolved mass flux, J, with DFT-calculated driving forces $\Delta\mu$ as obtained from the Calphad assessment, to directly extract the diffusivity, D, of precursor species, from $J = Dc\, d\mu/dx$. We have found that the reaction proceeds far too quickly for diffusivity values that can be explained by solid-state vacancy-mediated diffusion, and can only be rationalized by the presence of a liquid diffusion-media. A metastable liquid eutectic hypothesis therefore explains both he observed reaction onset temperature, as well as the fast diffusion kinetics associated with a <2 minute reaction.

Fast and accurate *ab initio* estimation of G_{liquid}

To evaluate the metastable eutectic temperature, we need to be able to estimate G_{liquid} broadly across chemical space. Most thermodynamic databases do not have this G_{liquid} information readily and openly available. We developed a thermodynamic framework to construct a G_{liquid} for elemental solids that was referenced to the DFT convex hull, meaning we can integrate this G_{liquid} with DFT databases like the Materials Project. Using only 4 non-ideal interaction parameters, we can accurately and rapidly fit experimental liquidus curves on to DFT solid-state convex hulls. By machine-learning the non-ideal interaction terms across a large 25×25 matrix of elemental solids, we are able to predict binary and ternary liquidus curves for metal alloys over broad compositions.

Figure 4 illustrates the liquidus curve fitted from our model (purple) versus the liquid curve from the Materials Platform for Data Science (MPDS), which hosts the ASM phase diagrams. Importantly, the liquidus curves have been fit using our extremely simple G_{liquid} model and using only DFT convex hulls (no calculated entropies). This liquid fit is largely successful despite some

of the lower-temperature solid phases not being completely captured in DFT; this is because the liquidus curve can be thought of as a 'tent' that is held up by the very-stable high melting temperature phases, which are usually well captured in DFT.

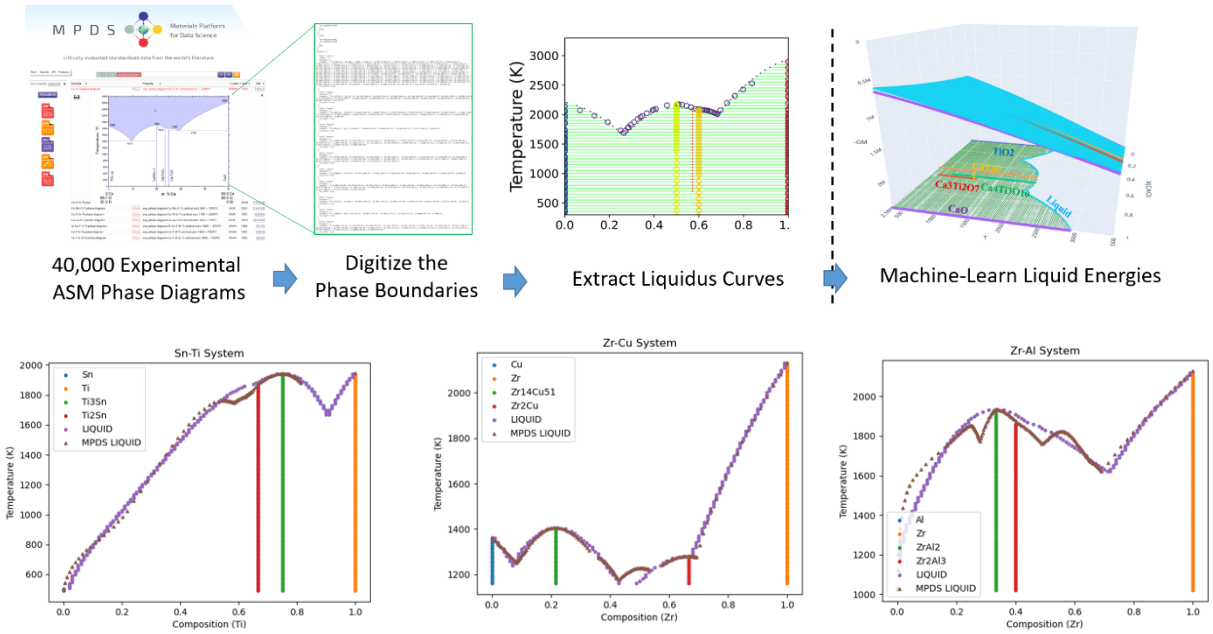

Figure 4. Scheme to fit DFT-referenced G_{liquid} against ASM phase diagram liquidus curves. We machine-learn the non-ideal mixing parameters to extrapolate our liquidus curves broadly across chemical space.

Future Work

Our goal this year is to publish our research results from the last two years. Our publication on the design of precursors based on DFT-calculated reaction enthalpies is out to review, and a pre-print is available on the Arxiv. Next, we aim to complete and submit our collaborative computational and EFRC-GENESIS experimental work on rationalizing the onset temperatures of solid-state reactions with the concept of the metastable liquid eutectic, and we are also preparing our work on *ab initio* predictions of G_{liquid}. We anticipate that these works will take our main effort this upcoming year.

Scientifically, our next objective is to begin designing synthesis recipes to enthalpically-stable 5-component oxides. Combinatorically speaking, 5-component oxides should be extremely abundant – however they comprise < 1% of known materials. We hypothesize that some of these high-component materials are difficult to synthesize because of slow reaction kinetics, rather than because they are intrinsically unattainable. With our new understanding of precursor selection and fast liquidus-mediated reactions, we believe we can rationally design synthesis routes to these high-component oxide materials.

References

1. A. Miura, C. J. Bartel, G. Ceder, **Wenhao Sun** *et al*. "Observing and Modeling the Sequential Pairwise Reactions that Drive Solid-State Ceramic Synthesis." *Advanced Materials* (2021).
2. M. Bianchini, J. Wang, **Wenhao Sun**[+], Gerbrand Ceder[+] *et al*. "The interplay between thermodynamics and kinetics in the solid-state synthesis of layered oxides." *Nature materials* (2020): 1088-1095.

Publications

S. Tan, J. Willwerth, **Wenhao Sun**, "Fast and efficient *ab initio* calculations of the liquidus free energy" *In preparation.*

S. Tan, G. Kamm, P. Chao, A. Shahani, K. Chapman, **Wenhao Sun** "Origin of the onset temperature in solid-state ceramic synthesis" *In preparation.*

J. Chen, S. R. Cross, L. J. Miara, J.J. Cho, Y. Wang, **Wenhao Sun**. "Navigating phase diagram complexity to guide robotic inorganic materials synthesis." *arXiv:2304.00743* (2023).

N. David, **Wenhao Sun**, C. W. Coley. *The promise and pitfalls of AI for molecular and materials synthesis*. Nature Computational Science: 1-3 (2023).

D. Evans, J. Chen, G. Bokas, W. Chen, G. Hautier, **Wenhao Sun**. *Visualizing temperature-dependent phase stability in high entropy alloys,* npj Computational Materials 7, 1: 151 (2021).

Synergistical computational and experimental study of synthesis mechanism and discovery of complex layered magnetic quantum materials

Zhiqiang Mao (PI)
Department of Physics, Pennsylvania State University, University Park, PA 16802
Jianwei Sun (co-PI)
Department of Physics and Engineering Physics, Tulane University, New Orleans, LA 70118

Keywords: Synthesis mechanism, layered magnetic quantum materials, non-centrosymmetric vdW ferromagnetic semiconductor, high-throughput computational screening, DFT.

Research Scope

Computational materials design has been playing an important role in discovering novel quantum materials such as topological materials. One of the major challenges in synthesizing computationally designed materials is that their thermodynamic stabilities are often unknown, which significantly reduces the rate of successful synthesis. Therefore, thermodynamic stability predictions for computationally designed materials are key to accelerating new quantum material discoveries. For complex quantum materials such as the ternary layered magnetic materials proposed in this project, their thermodynamic stability predictions are challenging, since this type of materials not only involves different kinds of chemical bonds ranging from the in-plane strong covalent bonds to weak interlayer van der Waals interactions, but also needs accurate treatments of thermal excitations from electronic, vibrational, and magnetic degrees of freedom, which makes first-principles-based thermodynamics calculations difficult. This proposed research aims to address this challenge through the integrated experimental and theoretical investigations of the synthesis mechanisms of ternary layered magnetic quantum materials which were predicted to host a rich variety of new quantum states. Most members of these material families were hypothetical, with unknown thermodynamic stability. Through this proposed research, the PIs anticipate making the synthesis of complex layered quantum materials more predictive.

Recent Progress

This project has been fruitful and led to 10 publications in the past 2 years (see the publication list). We first summarize the progress on computational method developments informed by experimental measurements, followed by high-throughput screening assisted experimental synthesis of a novel stable antiferromagnetic semiconductor. We also highlight a successful synthesis and study of a novel non-centrosymmetric van der Waals ferromagnetic semiconductor $Cr_{0.32}Ga_{0.68}Te_{2.33}$ that integrated computational and experimental efforts.

Progress in method development/calibration/application: Sun and his team introduced the strongly constrained and appropriately normed (SCAN) density functional in 2015, which demonstrated superior accuracy and transferability compared to traditional density functional (like LDA, PBE and PBEsol), yet had some limitations in numerical robustness. To overcome this, the r2SCAN density functional was developed. We undertook a systematic testing of r2SCAN focusing on lattice dynamics, which proved it to be more accurate, transferable and numerically stable than traditional models and slightly better than SCAN. This makes r2SCAN ideal for high

accuracy, efficiency demanding scenarios like lattice dynamics and high-throughput calculations. This finding was published in Chemistry of Materials [1]. Additionally, to evaluate r2SCAN's utility in solid-state thermodynamics, we tested it alongside SCAN and PBE using over 1000 solids, including two dispersion-corrected variants, SCAN+rVV10 and r2SCAN+rVV10. r2SCAN showed comparable accuracy to SCAN, even surpassing it in some areas. The predicted formation enthalpies errors decreased significantly with r2SCAN and SCAN meta-GGA, with r2SCAN showing improvements over SCAN for intermetallic systems. These findings, published in ACS Materials Au [2], make r2SCAN and r2SCAN+rVV10 reliable meta-GGAs for materials discovery. In an early work [**3**], we developed a set of first-principles-based methods to investigate the subtle metastability of $MnBi_2Te_4$, the first recognized intrinsic antiferromagnetic topological insulator. Our integrated experimental and theoretical analysis considered factors like spin-orbit coupling, van der Waals interactions, phonons, and magnons. We concluded that these variables not only enable emergent phenomena in layered materials but also determine their thermodynamic stability. This lays a groundwork for future computational synthesis of novel layered systems.

High-throughput screening assisted discovery of stable antiferromagnetic semiconductor: $CdFeP_2Se_6$: We have applied the knowledge we gained from the study of thermodyamic stability of $MnBi_2Te_4$ to predict and synethize new layered magnetic materials. The material system we have considered is the metal phosphorous trichalcogenides (MPTs) such as MPX_3 and $MM'P_2X_6$ where M and M' are transition metal, e.g., M = V, Cr, Mn, Fe, Co, Cu, Ag, In, Bi, Sb, or Sc; M'= Cd, Cu, or Ag; X = S or Se. Both 2D MPTs and $MM'P_2X_6$ have been of great interest in recent years, owing to their interesting electronic properties arising from quantum confinement. The diverse properties of these materials tunable by proper selection and combination of the M, M' and X elements make the $MM'P_2X_6$ materials an interesting platform for fundamental science and practical applications. However, only a few of these materials could be synthesized in lab, with thermodynamic stability cited as a major obstacle. Using the computational skills we obtained on $MnBi_2Te_4$ [3], we have done high-throughput computations to calculate chemical reaction energies for 43 different combinations of quaternary compounds with varying M, M' and X. Our computational results predict that 14 of the 43 compositions have negative chemical reaction energies, indicating that they are potentially synthesizable, as illustrated in Fig. 1. Following the predictions of these potential thermodynamically stable candidates, Mao's group synthesized three, including $AgVP_2S_6$, $CdFeP_2Se_6$, and $CdMnP_2S_6$. Among them, $CdFeP_2Se_6$ is found to be a

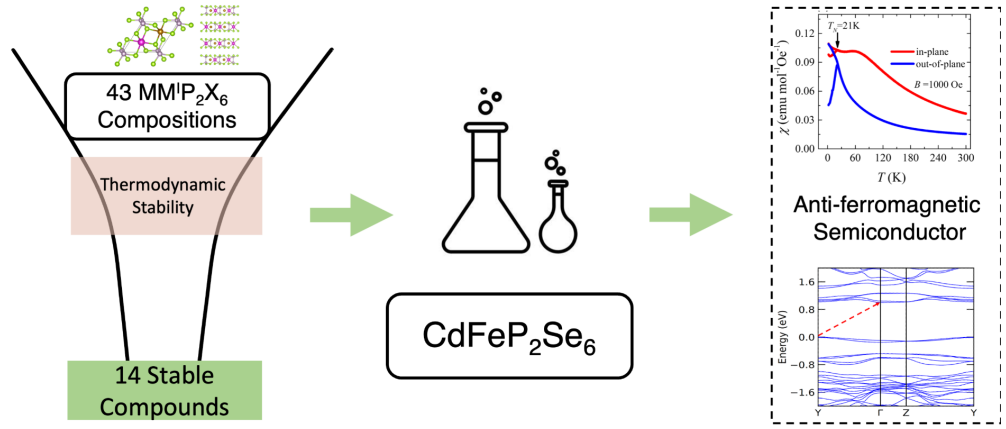

Figure 1: Synthesis of low-dimensional quaternary materials is challenging and remains rare. This is mainly due to thermodynamic stability as the most cited reason. Potentially stable MMIP2X6 quaternary compounds are screened using by DFT calculations, leading to successful synthesis of a stable semiconducting layered magnetic material $CdFeP_2Se_6$ that exhibits a short-range antiferromagnetic order at TN = 21 K with an indirect band gap of 2.23 eV

stable semiconducting layered magnetic material $CdFeP_2Se_6$ that exhibits a short-range antiferromagnetic order at $T_N = 21$ K with an indirect band gap of 2.23 eV (Note that the calculated gap shown in Fig. 1 is underestimated). This work was recently Published in Advanced Functional Materials [4].

Discovery of a novel non-centrosymmetric van der Waals ferromagnetic semiconductor $Cr_{0.32}Ga_{0.68}Te_{2.33}$: In our efforts of searching for new layered magnetic materials, we also discovered a novel layered semiconductor $Cr_{0.32}Ga_{0.68}Te_{2.33}$ with concurrent broken inversion symmetry and ferromagnetism. This material may realize a long-sought ferro-valley electronic state which features spontaneous valley polarization. Valleytronic state, characterized by spin-valley locking, was first predicted and demonstrated in group-VI transition-metal dichalcogenides such as MoS_2. Such an electronic state has attracted immense interest since its valley degree of freedom could be used as the information carrier. However, the valleytronic applications require spontaneous valley polarization, which is predicted to be accessible in ferrovalley materials featuring the coexistence of spontaneous spin and valley polarization. Although many atomic monolayer materials have been predicted to be ferrovalley materials, they have not been verified experimentally due to the difficulties in synthesizing these materials. Our systematic studies suggest $Cr_{0.32}Ga_{0.68}Te_{2.33}$ is a possible candidate of bulk ferrovalley material. This material exhibits several remarkable characteristics: (i) it crystalizes to a non-centrosymmetric trigonal structure with the space group of *P3*, forming a natural heterostructure between vdW gaps (Fig. 2a): quasi-

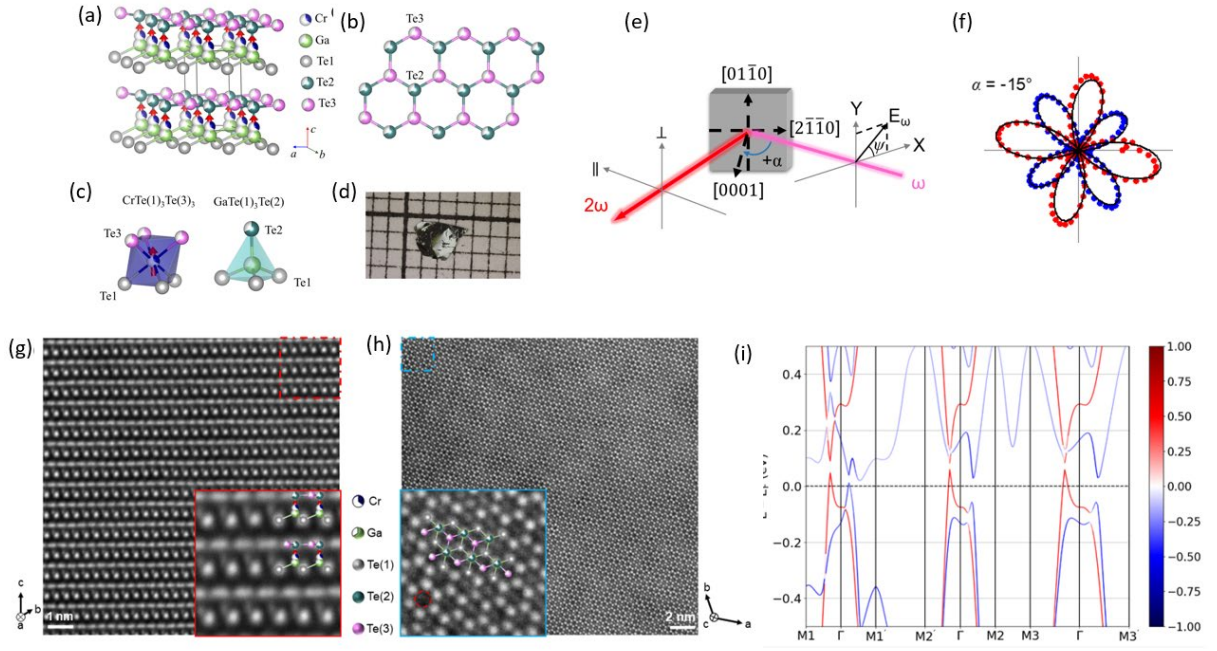

Figure 2: (a) Crystal and magnetic structure of $Cr_{0.32}Ga_{0.68}Te_{2.33}$. (b). honeycomb lattice formed by Te(2) and Te(3) atoms. (c). Octahedral environment of Cr and tetrahedral environment of Ga. (d). Picture of a typical $Cr_{0.32}Ga_{0.68}Te_{2.33}$ crystal. (e) Schematics of the SHG experiment. (f) Polar plots of $Cr_{0.32}Ga_{0.68}Te_{2.33}$ measured at the incident angle of -15°. HAADF-STEM images of the $Cr_{0.32}Ga_{0.68}Te_{2.33}$ acquired from the [100] zone axis (g) and [001] zone axis (h). The inset is the magnified images from the region highlighted by the dashed red box, with the crystal model from neutron diffraction superimposed. (i) Band structure of $Cr_{0.32}Ga_{0.68}Te_{2.33}$ with magnetic Sz projection.

two-dimensional (2D) semiconducting Te-honeycomb layers (Fig. 2b) are stacked on a 2D ferromagnetic (Cr, Ga)-Te layers with T_c=20K (Fig. 2a). Such crystal structural characteristics are revealed through neutron scattering and scanning transmission electron microscopy (STEM) (Fig. 2g-2h) experiments; the inversion symmetry breaking is confirmed by optical second harmonic generation (SHG, Fig. 2e & 2f) measurements. (ii) The 2D Te-honeycomb lattice yields a valley-like electronic structure near the Fermi level, which, in combination with inversion symmetry breaking, ferromagnetism, and strong spin-orbit coupling, creates a possible bulk spin-valley locked electronic state with valley polarization as suggested by DFT calculations (Fig. 2i). Further, this material can also be easily exfoliated to 2D layers and has a bulk band gap of 0.4 eV. Therefore, this material offers a unique platform to explore the physics of valleytronic state in both bulk and 2D atomic crystals. This work is published in JACS [5].

Future Plans

The future research plan of the team will center on precise control of crystal stoichiometry of chalcopyrite compounds using a double-crucible Bridgman crystal growth technique. This research aims to overcome the challenge of inhomogeneous and non-stoichiometric crystal growth, common in traditional techniques like Czochralski and Bridgman, by developing a novel growth protocol for precise composition control. The chosen candidate materials are chalcopyrite compounds with technologically beneficial properties. The researchers will employ a high-pressure double-crucible vertical Bridgman (HP-DCVB) method. This new crystal growth technique, integrated with computational studies on crystal defects, is expected to enable exact composition control and producing homogenous crystals with stoichiometric compositions. In addition, the properties of these crystals will be characterized using a variety of techniques, and computational studies will be conducted to understand the crystal composition control mechanisms. This project has considerable potential for advancing materials synthesis science and developing novel materials for use in energy harvesting and other advanced technologies.

References

1. J. Ning, J. W. Furness, and J. Sun, Reliable Lattice Dynamics from an Efficient Density Functional Approximation, Chemistry of Materials **34**, 2562 (2022).
2. M. Kothakonda, A. D. Kaplan, E. B. Isaacs, C. J. Bartel, J. W. Furness, J. Ning, C. Wolverton, J. P. Perdew, and J. Sun, Testing the r^{2}SCAN Density Functional for the Thermodynamic Stability of Solids with and without a van der Waals Correction, ACS Materials Au (2022). doi:10.1021/acsmaterialsau.2c00059
3. J. Ning, Y. Zhu, J. Kidd, Y. Guan, Y. Wang, Z. Mao, and J. Sun, Subtle metastability of the layered magnetic topological insulator MnBi2Te4 from weak interactions, npj Computational Materials **6**, 157 (2020).
4. M. Kothakonda, Y. Zhu, Y. Guan, J. He, J. Kidd, R. Zhang, J. Ning, V. Gopalan, W. Xie, Z. Mao, and J. Sun, High-throughput screening assisted discovery of a stable layered anti-ferromagnetic semiconductor: $CdFeP_2Se_6$, Adv. Funct. Mater. **33**, 2210965 (2023).
5. Y. Guan, L. Miao, J. He, J. Ning, Y. Chen, W. Xie, J. Sun, V. Gopalan, J. Zhu, X. Wang, N. Alem, Q. Zhang, and Z. M. Mao, Novel layered semiconductor $Cr0_{.32}Ga_{0.68}Te_{2.33}$ with concurrent broken inversion symmetry and ferromagnetism: a bulk ferrovalley material candidate, J. Am. Chem. Soc. **145**, 4683 (2023).

Publications

1. M. Algarni, C. Tan, G. Zheng, S. Albarakati, X. Zhu, J. Partridge, Y. Zhu, L. Farrar, M. Tian, J. Zhou, X. Wang, Z. Mao, and L. Wang, Tunable artificial topological Hall effects in van der Waals heterointerfaces, Physical Review B **105**, 155407 (2022). doi:10.1103/PhysRevB.105.155407
2. J. Ebad-Allah, S. Rojewski, Y. L. Zhu, Z. Q. Mao, and C. A. Kuntscher, In-plane and out-of-plane optical response of the nodal-line semimetals ZrGeS and ZrGeSe, Physical Review B **106**, 075143 (2022). doi:10.1103/PhysRevB.106.075143
3. Y. D. Guan, C. H. Yan, S. H. Lee, X. Gui, W. Ning, J. L. Ning, Y. L. Zhu, M. Kothakonda, C. Q. Xu, X. L. Ke, J. W. Sun, W. W. Xie, S. L. Yang, and Z. Q. Mao, Ferromagnetic $MnBi_4Te_7$ obtained with low-concentration Sb doping: A promising platform for exploring topological quantum states, Physical Review Materials **6**, 054203 (2022). doi:10.1103/PhysRevMaterials.6.054203
4. J. Y. Liu, J. Yu, J. L. Ning, H. M. Yi, L. Miao, L. J. Min, Y. F. Zhao, W. Ning, K. A. Lopez, Y. L. Zhu, T. Pillsbury, Y. B. Zhang, Y. Wang, J. Hu, H. B. Cao, B. C. Chakoumakos, F. Balakirev, F. Weickert, M. Jaime, Y. Lai, K. Yang, J. W. Sun, N. Alem, V. Gopalan, C. Z. Chang, N. Samarth, C. X. Liu, R. D. McDonald, and Z. Q. Mao, Spin-valley locking and bulk quantum Hall effect in a noncentrosymmetric Dirac semimetal $BaMnSb_2$, Nature Communications **12**, 4062 (2021). doi:10.1038/s41467-021-24369-1
5. A. Majed, M. Kothakonda, F. Wang, E. N. Tseng, K. Prenger, X. Zhang, P. O. Å. Persson, J. Wei, J. Sun, and M. Naguib, Transition Metal Carbo-Chalcogenide "TMCC:" A New Family of 2D Materials, Advanced Materials **34**, 2200574 (2022). doi:https://doi.org/10.1002/adma.202200574
6. R. Zhang, C.-Y. Huang, J. Kidd, R. S. Markiewicz, H. Lin, A. Bansil, B. Singh, and J. Sun, Weyl semimetal in the rare-earth hexaboride family supporting a pseudonodal surface and a giant anomalous Hall effect, Physical Review B **105**, 165140 (2022). doi:10.1103/PhysRevB.105.165140
7. J. Ning, J. W. Furness, and J. Sun, Reliable Lattice Dynamics from an Efficient Density Functional Approximation, Chemistry of Materials **34**, 2562 (2022). doi:10.1021/acs.chemmater.1c03222
8. M. Kothakonda, Y. Zhu, Y. Guan, J. He, J. Kidd, R. Zhang, J. Ning, V. Gopalan, W. Xie, Z. Mao, and J. Sun, High-throughput screening assisted discovery of a stable layered anti-ferromagnetic semiconductor: $CdFeP_2Se_6$, Adv. Funct. Mater. **33**, 2210965 (2023).
9. Y. Guan, L. Miao, J. He, J. Ning, Y. Chen, W. Xie, J. Sun, V. Gopalan, J. Zhu, X. Wang, N. Alem, Q. Zhang, and Z. M. Mao, Novel layered semiconductor $Cr0_{.32}Ga_{0.68}Te_{2.33}$ with concurrent broken inversion symmetry and ferromagnetism: a bulk ferrovalley material candidate, J. Am. Chem. Soc. **145**, 4683 (2023).
10. M. Kothakonda, A. D. Kaplan, E. B. Isaacs, C. J. Bartel, J. W. Furness, J. Ning, C. Wolverton, J. P. Perdew, and J. Sun, Testing the r^2SCAN Density Functional for the Thermodynamic Stability of Solids with and without a van der Waals Correction, ACS Materials Au (2022). doi:10.1021/acsmaterialsau.2c00059

PSCF+ and What We Have Done with It

Qiang Wang, Colorado State University

Keywords: Polymer self-consistent field calculations, Block copolymer self-assembly, Frank-Kasper phases, Graphics processing units.

Research Scope

The **overall goal** of our three-year, fundamental research project entitled "GPU-Accelerated Understanding and Design of Frank-Kasper Phases and Quasicrystals in Model Block Copolymers" is to enable rational design of the Frank-Kasper (FK) phases and quasicrystals (QCs)[1, 2] formed by linear diblock copolymer (DBC) A-B melts via understanding their formation mechanisms and the system fluctuation/correlation effects on them. This will be achieved by combining GPU-accelerated polymer self-consistent field (SCF) calculations and well-tempered metadynamics (WTM) simulations based on the same dissipative particle dynamics chain (DPDC) model[3]. We split our proposed work into three **Specific Aims** (SAs):

SA 1: We will extend the newly released open-source code (PSCFPP)[4] for real-space (RE) SCF calculations of the "standard" model for block copolymer (BCP) phase behavior on GPUs to include our DPDC model, and further improve its numerical performance. We will also develop similar open-source code for reciprocal-space (RC) SCF calculations of our DPDC model on GPUs.

SA 2: Using our code developed in SA 1, we will perform RE- and RC-SCF calculations of FK phases and QCs, respectively, of A-B melts and construct their phase diagrams at selected parameter values. Our focus here will be the stability of QCs and FK phases other than A15 and *s*, as well as the differences in the phase diagrams for the "standard" and DPDC models.

SA 3: Based on the SCF phase diagrams for the DPDC model constructed in SA 2, we will perform WTM simulations of selected FK phases, and directly compare our RE-SCF and WTM results without any parameter-fitting to unambiguously quantify the system fluctuation/correlation effects neglected by the SCF theory.

Recent Progress

We have made the following progress:

(1) We have extended PSCFPP[4] to include various discrete-chain models and improved its numerical performance in various aspects as proposed in SA 1. PSCFPP[4] provides a nice framework for GPU-accelerated RE-SCF calculations, but applies only to the "standard" model for BCP self-assembly (*i.e.*, an incompressible melt of continuous Gaussian chains (CGCs) with the Dirac *d*-function repulsions), which cannot be used in molecular simulations. We have therefore extended it to all possible combinations of either incompressible or

compressible melts of different chain-connectivity (including the CGC, discrete Gaussian chain (DGC), and freely jointed chain (FJC)) models with different non-bonded (including the Dirac *d*-function, Gaussian (G), DPD, and soft-sphere (SS)) potentials between polymer segments; the DPDC model, for example, corresponds to a compressible melt of the DGCs interacting with the DPD potential, and only compressible melts of a discrete chain model (*i.e.*, DGC or FJC) with the DPD or SS potential can be directly used in molecular simulations. Our work not only greatly extends the applicability of PSCFPP[4], but also provides the mean-field (SCF) reference for unambiguously quantifying, without any parameter-fitting, the fluctuation/correlation effects in such simulations, which will be used in our SA 3 later. We have also improved the numerical performance of PSCFPP[4] as described in SA 1. Our extended and improved open-source code is named PSCF+ and released at https://github.com/qwcsu/PSCFplus.

(2) Using PSCF+, we have performed RE-SCF calculations of the DPDC model of A-B melts.[3] We have considered in our calculations eight ordered phases, including three classical phases (*i.e.*, hexagonally packed cylinders (HEX), spheres arranged on a body-centered cubic lattice (BCC), and spheres arranged on a face-centered cubic lattice (FCC)) and five FK phases (*i.e.*, A15, *s*, C14, C15, and Z), as well as the disordered phase (DIS). The phase diagram is constructed in the *cN*-*e* plane (where *cN* and *e* characterize, respectively, the repulsion and the conformational asymmetry between the two blocks) at the A-block volume fraction f_A=0.2 and 0.3 for the copolymer chain length N=10; see Fig. 1 below. So far we have found that *s* is the only stable FK phase in our calculations.

(3) Using PSCF+, we have also performed RE-SCF calculations of the "standard" model of A-B melts. The corresponding phase diagrams are shown in Fig. 2 and can be compared with those

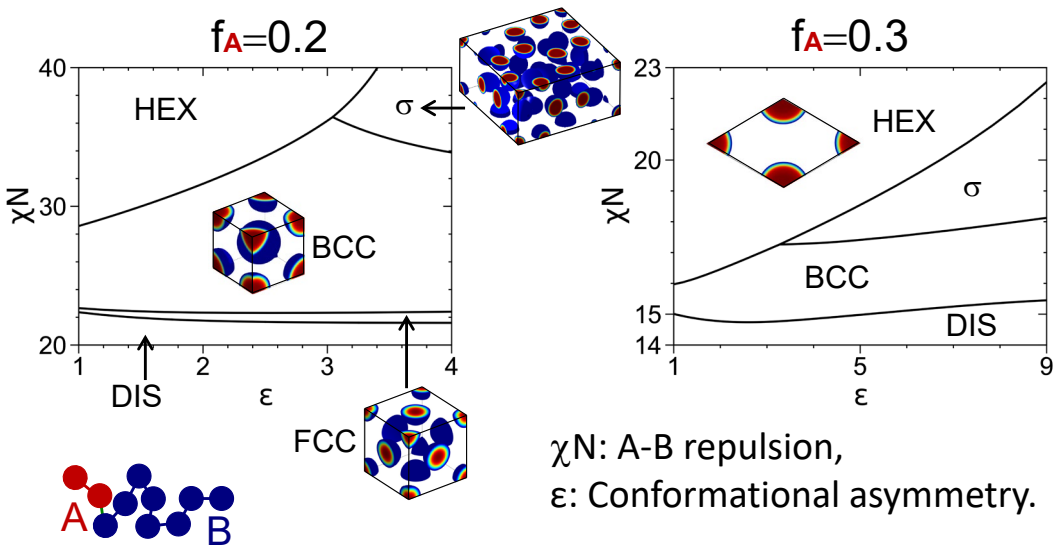

Fig. 1: Phase diagrams of conformationally asymmetric diblock copolymer A-B melts obtained from our self-consistent field calculations of the DPDC model at copolymer chain length N=10; see the main text for more details.

in Fig. 1; in particular, we find that A15 emerges as another stable FK phase, consistent with the SCF results of Fredrickson and co-workers[5]. This highlights the importance of model differences.

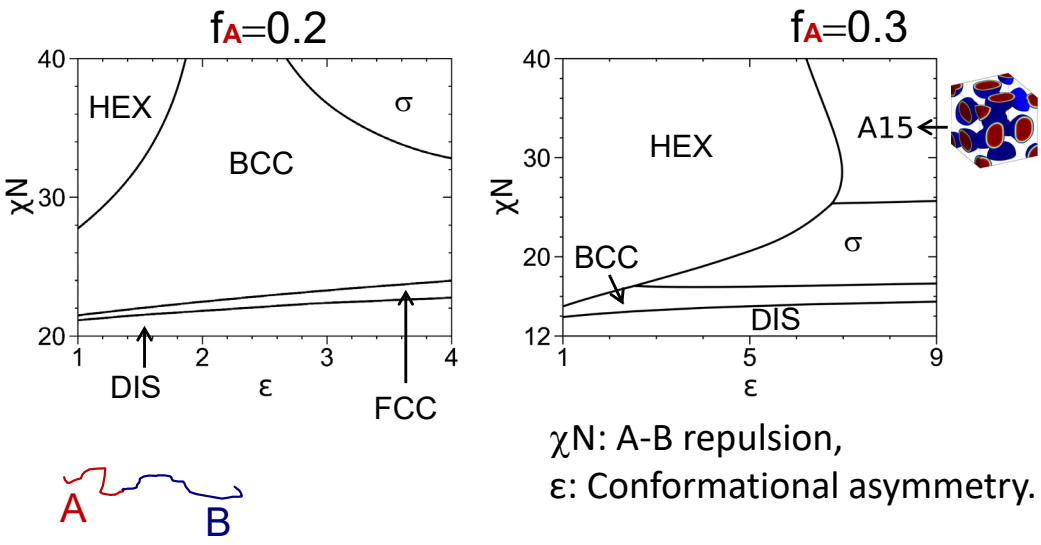

Fig. 2: Phase diagrams of conformationally asymmetric diblock copolymer A-B melts obtained from our self-consistent field calculations of the "standard" model; see the main text for more details.

Future Plans

(1) As proposed in SA 1, we plan to develop an open-source code for RC-SCF calculations, which will be included in PSCF+ for its release to the public.

(2) As proposed in SA 2, we plan to perform RC-SCF calculations to study QCs formed by A-B melts using PSCF+. We will also include more FK phases in our RE-SCF calculations, and continuously update the aforementioned phase diagrams based on our SCF results.

(3) We plan to start working on SA 3 of our proposal.

References

1. M. J. Huang, K. Yue, J. Wang, C. H. Hsu, L. G. Wang and S. Z. D. Cheng, Sci. China Chem. **61** (1), 33-45 (2018).
2. K. D. Dorfman, Macromolecules **54** (22), 10251-10270 (2021).
3. J. He and Q. Wang, Macromolecules **55** (19), 8931-8939 (2022).
4. G. K. Cheong, A. Chawla, D. C. Morse and K. D. Dorfman, Eur. Phys. J. E **43** (2), 15 (2020).
5. M. W. Bates, J. Lequieu, S. M. Barbon, R. M. Lewis, K. T. Delaney, A. Anastasaki, C. J. Hawker, G. H. Fredrickson and C. M. Bates, P. Natl. Acad. Sci. **116** (27), 13194-13199 (2019).

Publications

- *J. He and Q. Wang*, "Frank–Kasper Phases of Diblock Copolymer Melts Studied with the DPD Model: SCF Results", **Macromolecules 55**, 8931-8939 (2022); *ibid.*, 10243 (2022).
- https://github.com/qwcsu/PSCFplus (our open-source code PSCF+ described above).

Achieving Long Range Ordering in Oxide-Metal Hybrid Materials

—A Combined Experimental and Modeling Approach (DOE-BES DE-SC0020077)

Haiyan Wang (Purdue U., hwang00@purdue.edu)
Anter El-Azab (Purdue U., aelazab@purdue.edu)

Keywords: hybrid materials, oxide-metal nanocomposite, epitaxial thin film, self-assembly, multifunctionality

Research Scope

Ordered, high-density metallic nanopillars in oxide matrices offer nanoscale composites with applications in nanodevices such as nanophotonic and plasmonic devices, high-density magnetic storage devices and reader heads and in thermoelectrics. Nanostructures of this type are often fabricated through multiple steps involving laser patterning, e-beam lithography, or focused ion beam (FIB). These methods are limited to small patterning areas, low resolutions (typically in 50-100 nm), and slow speed. In this project, we use thin film epitaxy of two-phase nanocomposites, guided by computational modeling, to circumvent these limitations and achieve highly-ordered nanoscale metallic pillars in oxide matrixes. Specifically, we aim to achieve single-step, direct growth of self-assembled oxide-metal epitaxial nanocomposite systems with long-range in-plane ordering of metal nanopillars in an oxide matrix.

The impact of this research is multi-faceted. First, the fundamental understanding of the two-phase self-assembly process leads to the further development of the concept of thin film epitaxy, which allows the growth of large mismatch systems or the deposition of materials that are hard to grow epitaxially; Second, it will lead to development of guidelines for the design and processing of ordered oxide-metal hybrid materials a wide range of applications in optical, plasmonic, piezoelectric devices and catalysis. Finally, the computational models developed in conjunction with our experimental effort will have broader impacts extending to systems beyond oxide-metal nanocomposite systems, e.g., oxide-oxide and nitride-metal systems as well as battery systems.

Recent Progress

In the past funding period, we have made several major achievements/findings, including (1) various methods for ordering of the nanocomposite designs, (2) alloyed metal nanopillar designs for enhanced functionality, and (3) fundamental understanding and modeling tools for effective predicting the complex two phase self-assembly process.

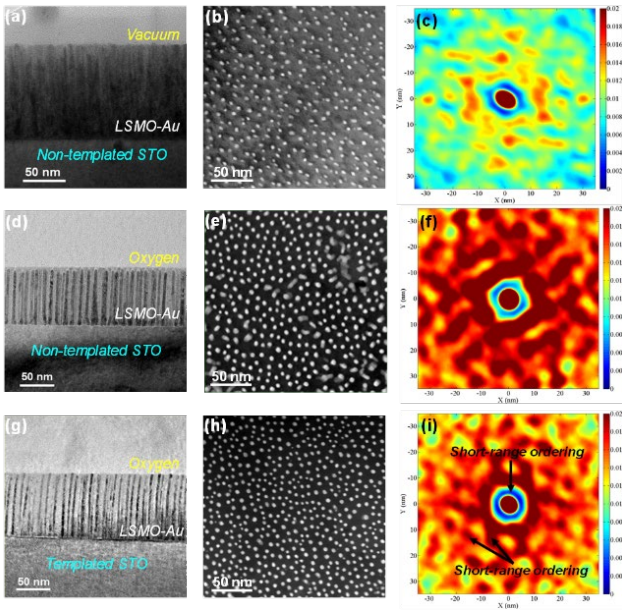

Fig.1 Microstructures and corresponding autocorrelation plots of: (a), (b) and (c) vacuum deposited, non-templated set of film; (d), (e) and (f) oxygen deposited, non-templated set of film; (g), (h) and (i) oxygen deposited, templated set of film. (a), (d) and (g) are their respective cross-section STEM images. (b), (e) and (h) are the corresponding plan-view STEM images. (c), (f) and (i) are the autocorrelation plots of Au nanopillars based on plan-view TEM images of each film. Long-range and short-range orderings are denoted by black arrows shown in (i). [1]

Some of the selected examples are summarized in the review talk.

(1) Achieving in-plane ordering: We have demonstrated the growth of complex hyperbolic metamaterial $La_{0.67}Sr_{0.33}MnO_3$ (LSMO)-Au vertically aligned nanocomposites (VAN) growth by using step-mediated growth via annealed $SrTiO_3$ substrate with ordered terminating terraces. The films were obtained by a one-step pulsed laser deposition method. Plasmon resonance on the oxide-metal interfaces as well as anisotropic magnetic properties by LSMO matrix were highlighted in this system along with its anisotropic optical performance. A long-range ordering of Au nanopillars inside LSMO matrix were achieved by a templated $SrTiO_3$ substrate. The improved orderings in this paper were visually demonstrated by a two-point correlation function analysis, supported by simulations based on plan-view TEM images. [1,2]

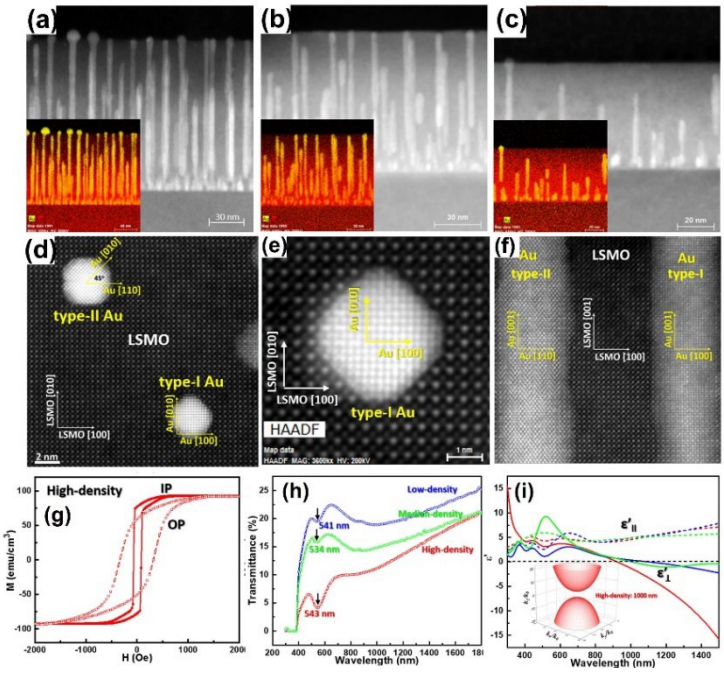

Fig. 2. Multifunctional $La_{0.67}Sr_{0.33}MnO_3$ (LSMO)-Au VAN system. (a-c) Cross-sectional STEM and EDS images (d, e) Plan-view HRSTEM images of type I and type II Au nanopillars. (f) HRSTEM cross-sectional images (g) M-H loops, (h) optical transmittance and (i) dielectric constants fitted.[2]

(2) Alloyed metal pillar designs for enhanced functionalities

Very recently, we have demonstrated that it is possible to incorporate multiple metals in one system as the alloyed nanopillars for strongly coupled multifunctionalities among the metals and the oxide matrix. As shown in **Fig. 3**, [3] unique core-shell metallic nanopillars can be formed with a Au-Cu alloyed shell and a Ni-Co alloyed core. Interestingly, this complex alloyed nanopillar system presents very strong coupled physical properties, such as strong magnetic anisotropy, as well as obvious magneto-optical coupling properties through magneto-optical Kerr effect (MOKE) measurements. These properties suggest that complex alloy nanopillar designs present enormous opportunities in multifunctionalities and coupled properties. We have also demonstrated multiple other alloyed pillar designs, including

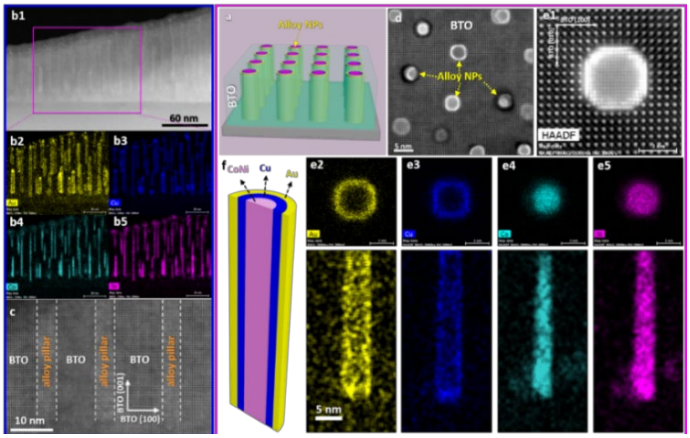

Fig.3. Microstructure study on the BTO-AuCuCoNi nanocomposite thin film. Cross-section/ plan-view TEM/STEM and EDX mappings demonstrate the interesting pillars with AuCu shell and CoNi alloy core epitaxially grown in BTO matrix.[3]

$ZnO\text{-}Ag_{61}Au_{39}$ with anisotropic dielectric response [4] and plasmon resonance and $BaTiO_3\text{-}Au_{0.4}Ag_{0.6}$ VANs with uniquely ordered "nanodomino-like" structures. [5]

(3) Fundamental understanding and modeling tools for effective predicting the complex two-phase self-assembly process

During this report period, related work has been added into the experimental reports, and several systematic theoretical works have been, or will be published. In CeO_2-Au system, we observed interesting abnormal epitaxial relationship between the matrix and the pillars despite the large mismatch. (**Fig.4**) [6] Another effort is building theoretical models based on the reported oxide-metal VAN thin films, considering the roles played by interfacial energies and elastic strain during the thin film deposition process. Finally, a kinetic Monte Carlo model has been developed to simulate the deposition processes of oxide-metal VANs, which helps the accurate prediction of microstructural designs with varying growth parameters. Details of the modeling efforts are summarized in a poster presentation at the meeting.

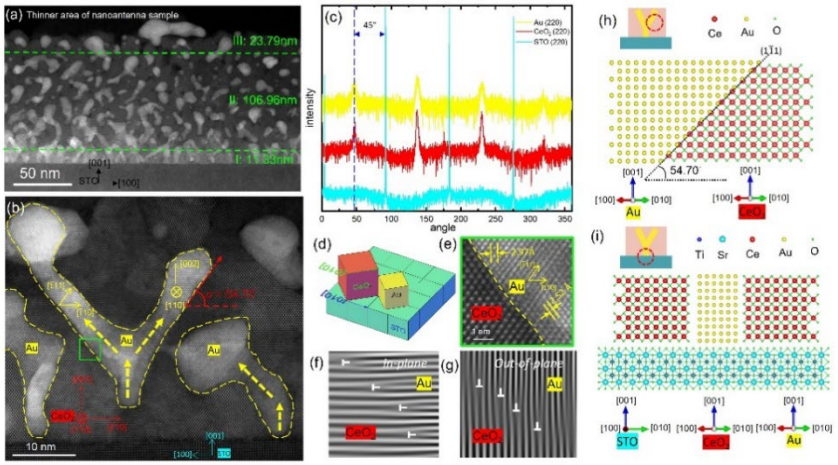

Fig.4. Abnormal epitaxy relationship in CeO2-Au on STO substrate suggests the importance of growth control of matrix to pillars. STEM and XRD analysis confirm the perfect cube-in-cube of CeO2 and Au with large lattice mismatch but a 45° in-plane rotation with the underlying substrate. [6]

Future Plans: In the next fiscal year, we plan to undertake the following tasks. We are working to explore substrate types and orientation effects on two phase epitaxy and nucleation, demonstrate free layer transfer of two -phase nanocomposite systems onto other substrates that could not achieve epitaxy, and complete the modeling framework for simulating the complex two-phase growth. In parallel, we are also trying several new approaches for achieving ordering, including the strain guided ordering, templated seeding, and patterning-based ordering.

References cited

1. Juanjuan Lu, Robynne L. Paldi, Yash Pachaury, Di Zhang, Han Wang, Matias Kalaswad, Xing Sun, Juncheng Liu, Xin Li Phuah, Xinghang Zhang, Anter A El-Azab, Haiyan Wang. Ordered Hybrid Metamaterial of La0.7Sr0.3MnO3-Au Vertically Aligned Nanocomposites Achieved on Templated SrTiO3 Substrate, ***Materials Today Nano***. https://doi.org/10.1016/j.mtnano.2021.100121.

2. Jijie Huang, Han Wang, Zhimin Qi, Ping Lu, Di Zhang, Bruce Zhang, Zihao He, and Haiyan Wang*, Multifunctional Metal-Oxide Nanocomposite Thin Film with Plasmonic Au Nanopillars Embedded in Magnetic La0.67Sr0.33MnO3 Matrix. ***Nano Lett.*** 21, 1032–1039 (2021). https://doi.org/10.1021/acs.nanolett.0c04213

3. Jijie Huang, Xin Li Phuah, Luke Mitchell McClintock, Prashant Padmanabhan, K. S.N. Vikrant, Han Wang, Di Zhang, Haohan Wang, Ping Lu, Xingyao Gao, Xing Sun, Xiaoshan Xu, R. Edwin Garcia, Hou Tong Chen, Xinghang Zhang, and Haiyan Wang, Core-Shell Metallic Alloy Nanopillars-in-Dielectric Hybrid Metamaterials with Magneto-Plasmonic Coupling, ***Materials Today***, 51. December (2021), 39–47 https://doi.org/10.1016/j.mattod.2021.10.024.

4. Robynne L. Paldi, Xuejing Wang, Xing Sun, Zihao He, Zhimin Qi, Xinghang Zhang, and Haiyan Wang, Vertically Aligned AgxAu1-x Alloyed Nanopillars Embedded in ZnO as Nanoengineered Low-Loss Hybrid Plasmonic Metamaterials. Nano Lett. 20, 3778–3785 (2020). https://doi.org/10.1021/acs.nanolett.0c00790.
5. Di Zhang, Shikhar Misra, Jie Jian, Ping Lu, Leigang Li, Ashley Wissel, Xinghang Zhang, and Haiyan Wang, Self-Assembled BaTiO3-AuxAg1-x Low-Loss Hybrid Plasmonic Metamaterials with an Ordered 'Nano-Domino-like' Microstructure. ACS Appl. Mater. Interfaces 13, 5390–5398 (2021). https://doi.org/10.1021/acsami.0c19108.
6. Juanjuan Lu, Di Zhang, Robynne L. Paldi, Zihao He, Ping Lu, Julia Deitz, Ahmad Ahmad, Hongyi Dou, Xuejing Wang, Juncheng Liu, Zedong Hu, Bo Yang, Xinghang Zhang, Anter A El-Azab, Haiyan Wang, Abnormal In-plane Epitaxy and Formation Mechanism of Vertically Aligned Au Nanopillars in Self-Assembled CeO_2-Au Metamaterial System, **Materials Horizons,** 2023. DOI: 10.1039/D3MH00233K.

10 Publications (selected from 36 journal publications from this project)

1. Rayaprolu Goutham Sreekar Annadanam, Ahmad Ahmad, Kyle R. Starkey, Zedong Hu, Juanjuan Lu, Haiyan Wang, Anter A. El-Azab. Energetics of nanoscale films with self-assembled oxide/metal pillars in nitride matrix. To be Resubmitted, ***Materialia***, 2023.
2. Ahmad Ahmad, Jie Peng, Khaled Nabil Shar Abdelaziz, Juanjuan Lu, Haiyan Wang, Anter A. El-Azab. A DFT-based kinetic Monte Carlo simulation of multiphase oxide-metal thin film growth. To be resubmitted, Journal of Applied Physics, 2023.
3. Di Zhang, Shikhar Misra, Jie Jian, Ping Lu, Leigang Li, Ashley Wissel, Xinghang Zhang, and Haiyan Wang, Self-Assembled BaTiO3-AuxAg1-x Low-Loss Hybrid Plasmonic Metamaterials with an Ordered 'Nano-Domino-like' Microstructure. ACS Appl. Mater. Interfaces 13, 5390–5398 (2021). https://doi.org/10.1021/acsami.0c19108
4. Robynne L. Paldi, Matias Kalaswad, Juanjuan Lu, James P. Barnard, Nicholas A. Richter, Mengwei Si, Nirali A. Bhatt, Peide D. Ye, Raktim Sarma, Aleem Siddiqui, Jijie Huang, Xinghang Zhang, Haiyan Wang, ZnO-Ferromagnetic Metal Vertically Aligned Nanocomposite Thin Films for Magnetic, Optical and Acoustic Metamaterials, ***Nanoscale Advances*****,** 5.1 (2022), 247–54 https://doi.org/10.1039/d2na00444e
5. Xuejing Wang and Haiyan Wang, Recent Advances in Vertically Aligned Nanocomposites with Tunable Optical Anisotropy: Fundamentals and Beyond, ***Chemosensors*****,** 9.6 (2021), 1–17. Invited review article.
6. Juncheng Liu, Xuejing Wang, Xingyao Gao, Han Wang, Bruce Zhang, Di Zhang, Matias Kalaswad, Jijie Huang, and Haiyan Wang, Integration of Self-Assembled BaZrO3-Co Vertically Aligned Nanocomposites on Mica Substrates toward Flexible Spintronics, ***Crystal Growth and Design***, 22.1 (2022), 718–25 https://doi.org/10.1021/acs.cgd.1c01227
7. Kyle Starkey, Ahmad Ahmad, Juanjuan Lu, Haiyan Wang, and Anter El-Azab, A Generalized 3D Elastic Model for Nanoscale, Self-Assembled Oxide-Metal Thin Films with Pillar-in-Matrix Configurations, ***Acta Materialia*****,** 228 (2022), 117779 https://doi.org/10.1016/j.actamat.2022.117779
8. Di Zhang, Matias Kalaswad, and Haiyan Wang, Self-Assembled Vertically Aligned Nanocomposite Systems Integrated on Silicon Substrate: Progress and Future Perspectives, ***Journal of Vacuum Science & Technology A***, 40.1 (2022), 010802 https://doi.org/10.1116/6.0001479. Invited review article.
9. Robynne L. Paldi, Juanjuan Lu, Yash Pachaury, Zihao He, Nirali A. Bhatt, Xinghang Zhang, Anter El-Azab, Aleem Siddiqui, and Haiyan Wang, ZnO-Au_xCu_{1-x} Alloy and ZnO-Au_xAl_{1-x} Alloy Vertically Aligned Nanocomposites for Low-Loss Plasmonic Metamaterials, ***Molecules*****,** 27(6).1785 (2022) https://doi.org/https://doi.org/10.3390/molecules27061785
10. Juncheng Liu, Xuejing Wang, Han Wang, Zhimin Qi, James P. Barnard, Bruce Zhang, and Haiyan Wang, Multiferroic Self-Assembled BaTiO3-Fe Vertically Aligned Nanocomposites on Mica Substrates toward Flexible Electronics, ***ACS Applied Electronic Materials*****,** 4.8 (2022), 4077–84 https://doi.org/10.1021/acsaelm.2c00712

Substantial Stability Improvements of Amorphous TiO_2 by Phase and Stoichiometry Control for Photoelectrode Protection

PI: Xudong Wang, Materials Science and Engineering, University of Wisconsin-Madison

Co-PI: Dane Morgan, Materials Science and Engineering, University of Wisconsin-Madison

Co-PI: Jinwoo Hwang, Materials Science and Engineering, Ohio State University

Keywords: Atomic Layer Deposition; Amorphous thin films; Stoichiometry; Intermediates; Photoelectrode protection

Research Scope

Photoelectrochemical (PEC) water splitting is considered as a promising sustainable energy path to hydrogen fuel generation. Silicon (Si) is a commonly used photoanode material that is expected to deliver the highest energy conversion efficiency owing to its appropriate band structure and excellent charge mobility. However, Si also exhibits a very short lifetime of only a few hours, as it would experience rapid corrosion or dissolution in alkaline electrolytes. To improve its lifetime, a prevailing strategy is to protect the reactive photoanode surfaces with a conformal and pinhole-free inert oxide coating by atomic layer deposition (ALD).[1-3] Despite the broad use of ALD for surface protection, the essential structure-property relationship that dictates the protection lifetime control is still largely missing. Typically, the amorphous ALD films are considered homogeneous. Their protection performances are primarily tuned by thickness and deposition temperature. Our previous project supported by BES revealed that structural inhomogeneity in the amorphous film (e.g. imbedded intermediate phases) could induce highly localized current through the amorphous film and facilitate pinhole formation.[4] While this discovery suggested a low-temperature crystalline-free amorphous film is preferable for achieving a long lifetime, the unreacted precursor ligands and byproducts are now found to be another inevitable issue associated with the low temperature ALD processes. These impurities could substantially change the film properties, such as electronic and ionic transport properties, mechanical stability, and chemical reactivity, which may open another pathway to breaking the current protection lifetime limit. This study is therefore to address the critical synthesis challenge that how to achieve a high stoichiometric TiO_2 ALD film without introducing any additional crystallization in the amorphous phase.

Recent Progress

Failure of Amorphous ALD TiO_2 coating in PEC protection. In a typical Si-based photoanode, the surface of n-type Si photoabsorber was coated by an ultrathin film of amorphous TiO_2 *via* ALD, followed by a layer of Ni acting as the oxygen evolution reaction (OER) catalyst. The conformal amorphous TiO_2 coating prohibits OH^- group diffusion thus protects the Si surface from chemical corrosion. The ALD TiO_2 layer can also passivate Si surface defect states to suppress charges recombination at the interface. Meanwhile, the ultrathin film still permits adequate hole transport through defect band conduction, allowing for unimpaired PEC efficiency. The as-deposited TiO_2

films deposited at 100 °C showed a uniform morphology, which was free of any particles (**Figure 1a**). The nano-diffraction pattern of the TiO_2 film indicated a completely amorphous phase without any crystalline phases (Inset of **Figure 1a**). However, X-ray photoelectron spectroscopy (XPS) survey spectrum showed appreciable Cl signal in addition to the Ti and O signals.

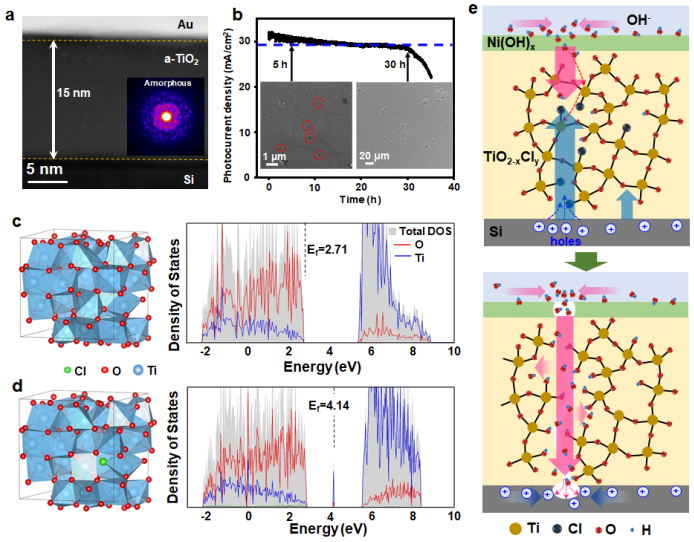

Figure 1. a, Cross-sectional STEM image of Si/TiO_2. Inset is a nano-diffraction pattern taken from the TiO_2 region. **b,** Chronoamperometry test of Si/TiO_2/Ni photoanode. Blue line marks 90% of the original J_{ph} value. Insets show Si/TiO_2/Ni surfaces after 5 h (left) and 30 h (right) chronoamperometry test. **c, d,** Structure (left) and density of states (left) of the melt-quenched amorphous TiO_2 and $TiO_{1.965}Cl_{0.035}$ models calculated by DFT. **e,** Schematics of a possible mechanism of pinhole formation in Cl-containing amorphous TiO_2 films during PEC water oxidation.

To reveal the protection performance of this homogeneous amorphous TiO_2 thin film, the complete n-Si/TiO_2/Ni photoanode was placed in a 1M KOH aqueous solution under 1 sun illumination for PEC water oxidation tests. Chronoamperometry test at a bias of 1.8 V versus reversible hydrogen electrode (RHE) revealed a quick photocurrent density (J_{ph}) decay (**Figure 1b**), where the original value dropped by 10% within just 30 hours. At the point of failure, a large number of interconnected pores appeared on the electrode surface, suggesting low stability of this TiO_2 coating. These pores were evolved from small pinholes as early as a few hours of operation. The large pores would isolate the Si photoabsorber from Ni catalyst layer, and facilitate the formation of insulating SiO_x that limits the hole transport from Si to Ni catalyst. As a result, the Si/TiO_2/Ni photoanode PEC performance was impaired. Considering the presence of an appreciable amount of precursor ligand residues (Cl from $TiCl_4$ precursor) in the film, the unreacted Cl ligands acted as the terminating point in the Ti-O-Ti network, and thus could introduce a more permeable amorphous lattice allowing fast reaction between OH^- and Ti-O. In addition, DFT calculation revealed that residual Cl ligands could also induce in-gap defect states at the middle of the band gap and shifted Fermi level from 2.71 eV (**Figure 1c**) to 4.14 eV (**Figure 1d**) closer to conduction band, which can enhance the hole conductivity of the amorphous TiO_2 film. This localized conductivity increase is able to induce local OH^- accumulation at the electrode surface, which facilitate the reaction between OH^- and TiO_2. Together, in the PEC system, Cl residues could enable a faster dissolution of TiO_2 and a rapid diffusion of OH^- to reach the vulnerable Si surface (**Figure 1e**).

Water-Treated Amorphous TiO_2 with Improved Stoichiometry and PEC Stability. It is intuitive to hypothesize that a higher stability may be achieved by reducing the residual Cl ligands in amorphous TiO_2 film. Meanwhile, no crystallization or phase transformation should be induced. To achieve this goal, a post-ALD water treatment procedure is developed to reduce the residual Cl ligands and maintain amorphous film homogeneity simultaneously. As schematically illustrated in **Figure 2a**, after the regular TiO_2 ALD cycles are completed, the sample was kept in the growth

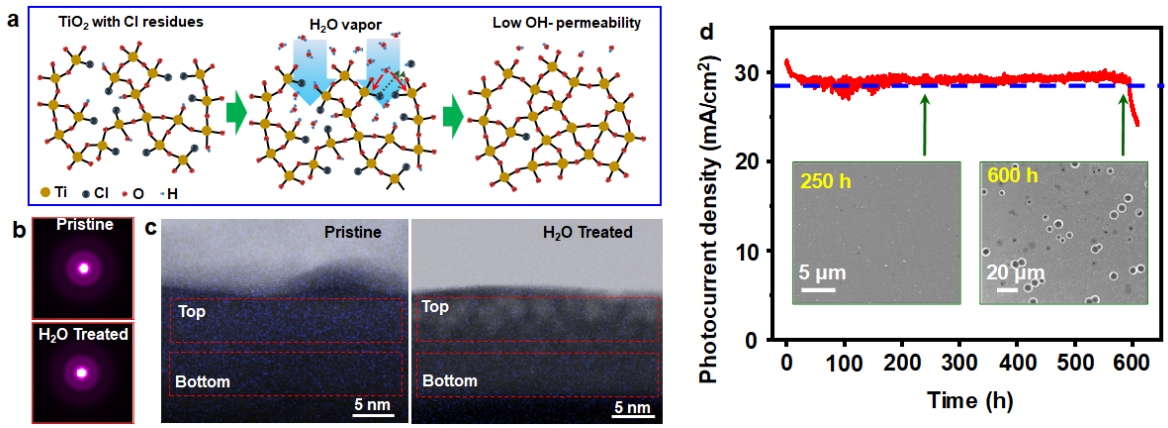

Figure 2. a, Schematics of water treatment showing the unreacted Cl ligands in amorphous TiO_2 (Left) being removed by reacting with H_2O molecules diffused through the film surface (center), and forming a more continuous, interconnected Ti-O-Ti network. **b,** 4D-STEM nano-diffractions and **c,** cross-sectional EDS Cl mapping of pristine and water-treated TiO_2 films. **d,** Chronoamperometry of the Si/TiO2/Ni electrode with post-ALD water-treated TiO_2 film. It shows ~600-hour stable photocurrent. Inset are SEM images of photoanode surface at two reaction time during PEC test showing the slow corrosion of electrode surface.

chamber subjecting to additional 2400 water pulses under the same temperature and vacuum. During this treatment, water molecules could diffuse into the amorphous TiO_2 matrix and react with the dangling Cl ligands, which raises the film's stoichiometry and improves the Ti-O-Ti network continuity. This post-ALD water treatment could well preserve the surface flatness and conformality of the as-deposited TiO_2 film. No additional nanoparticles were observed from the film surface. Four-dimensional scanning electron microscopy (4D-STEM) based characterizations were used to confirm the elemental and structural change from water treatment. Presence of two burry rings in the averaged nanodiffraction patterns revealed that no additional crystallization was induced by the water treatment as compared to the pristine TiO_2 film (**Figure 2b**). The change of Cl distribution was directly visualized using long-time energy dispersive spectroscopy (EDS) Cl mapping acquired from the cross-section of both TiO_2 film samples. Compared to the uniform distribution of Cl signal in the pristine TiO_2 film **(Figure 2c)**, Cl signal in the water-treated TiO_2 film was clearly decreased with a concentration gradient, where the Cl signal was nearly undetectable from the top ~5 nm region. These characterizations further confirmed that post-ALD water treatment was able to partially remove residual Cl ligands without introducing additional crystallization to the amorphous ALD TiO_2 films. The chronoamperometry test was conducted at an external bias of 1.8 V versus RHE. A stable J_{ph} at ~30 mA/cm^2 was recorded for up to ~600 hours (**Figure 2d**), about one order of magnitude longer than the pristine TiO_2-protected Si photoanodes.

This post-ALD water treatment is fundamentally different from other regular approaches to improve the stoichiometry of ALD films. Reducing the residual ligands (*i.e.* raising the ALD reaction completeness to improve the stoichiometry) and suppressing the crystallization are always coupled and anti-correlated in regular ALD processes. For example, extending the length of the ALD water pulse can improve the reaction completeness per cycle. However, the extended reaction time could also facilitate surface diffusion of as-deposited species that were loosely bonded to the surface. This may enable the rearrangement of surface atoms and form local nuclei on the surface,[5] which could serve as seeds for TiO_2 to grow into nanoparticles. In our post-ALD water

treatment, the ALD growth was completed. The completely coordinated Ti-O in the 3D amorphous TiO_2 matrix largely restricted their diffusion to form an ordered TiO_2 crystal lattice.

Future Plans

Following this work, we plan to further understand chemical and structural stability of amorphous ALD thin films in correlation to impurities and additional doping elements. Based on our discovery that foreign elements may tune the interatomic distance in amorphous film, we envision this phenomenon can manipulate the film's chemical stability and mechanical strength, which may bring the stability of amorphous thin film to new horizon. We will combine ALD synthesis and characterizations with advanced STEM techniques and atomic modeling to test this hypothesis to bring transformative science of synthesizing amorphous thin films with a high stability, with direct impacts to the next-generation energy harvesting devices.

References

[1] K. Sun, F. H. Saadi, M. F. Lichterman, W. G. Hale, H.-P. Wang, X. Zhou, N. T. Plymale, S. T. Omelchenko, J.-H. He, K. M. Papadantonakis, Stable solar-driven oxidation of water by semiconducting photoanodes protected by transparent catalytic nickel oxide films. *Proceedings of the National Academy of Sciences* 112, 3612-3617 (2015).

[2] Y. W. Chen, J. D. Prange, S. Dühnen, Y. Park, M. Gunji, C. E. D. Chidsey, P. C. McIntyre, Atomic layer-deposited tunnel oxide stabilizes silicon photoanodes for water oxidation. *Nature materials* 10, 539-544 (2011).

[3] S. M. George, Atomic layer deposition: an overview. *Chemical reviews* 110, 111-131 (2010).

[4] Y. Yu, C. Sun, X. Yin, J. Li, S. Cao, C. Zhang, P. M. Voyles, X. Wang, Metastable Intermediates in Amorphous Titanium Oxide: A Hidden Role Leading to Ultra-Stable Photoanode Protection. *Nano Lett.* 18, 5335-5342 (2018).

[5] J. Shi, Z. Li, A. Kvit, S. Krylyuk, A. V. Davydov, X. Wang, Electron Microscopy Observation of TiO2 Nanocrystal Evolution in High-Temperature Atomic Layer Deposition. *Nano Lett.* 13, 5727-5734 (2013).

Publications

1. Y. Dong, M. Abbasi, J. Meng, L. German, C. Corey, J. Li, Z. Zhang, D. Morgan, J. Hwang, X. Wang, *Substantial lifetime enhancement for Si-based photoanodes enabled by amorphous TiO_2 coating with improved stoichiometry*, Nature Communications, **14**, 1865 (2023)

2. M. Abbasi, Y. Dong, J. Meng, D. Morgan, X. Wang, J. Hwang, *In situ observation of medium range ordering and crystallization of amorphous TiO2 ultrathin films grown by atomic layer deposition*, APL Mater. **11**, 011102 (2023)

3. J. Meng, M. Abbasi, Y. Dong, C. Carlos, X. Wang, J. Hwang, D. Morgan, *Experimentally informed structure optimization of amorphous TiO2 films grown by atomic layer deposition*, Nanoscale, **15**, 718 (2023)

4. J. Sui, J. Li, L. Gu, C. Schmidt, Z. Zhang, Y. Shao, E. Gazit, P. Gilbert, X. Wang, *Orientation-controlled crystallization of γ-glycine films with enhanced piezoelectricity*, J. Mater. Chem. B, **10**, 6958-6964 (2022)

5. G. Yan, Y. Dong, T. Wu, S. Xing, X. Wang, *Mesoporous Ultrathin In2O3 Nanosheet Cocatalysts on a Silicon Nanowire Photoanode for Efficient Photoelectrochemical Water Splitting*, ACS Applied Materials & Interfaces, **13**, 52912-52920 (2021)

6. Y. Zhao, Y. Wang, Y. Dong, C. Carlos, J. Li, Z. Zhang, T. Li, Y. Shao, S. Yan, L. Gu, J. Wang, X. Wang, *Quasi-Two-Dimensional Earth-Abundant Bimetallic Electrocatalysts for Oxygen Evolution Reactions*, ACS Energy Lett. **6**, 3367-3375 (2021)

7. Y. Dong, J. Li, F. Yang, Y. Wang, Z. Zhang, J. Wang, Y. Long, X. Wang, *Bioresorbable Primary Battery Anodes Built on Core–Double-Shell Zinc Microparticle Networks*, ACS Applied Materials & Interfaces, **13**, 14275–14282 (2021)

8. M. Abbasi, J. Meng, Y. Dong, D. Morgan, X. Wang, J. Hwang, *4D-STEM Determination of Atomic Structure of Amorphous Materials for Renewable Energy Applications*. Microscopy and Microanalysis, **27**, 396-398 (2021).

Novel Chalcogenide Sodium Superionic Conductors: in situ Neutron Diffraction and ex situ Studies

Hui Wang and Badri Narayanan (Mechanical Engineering, University of Louisville, Kentucky)

Keywords: Na-ion conductors, Synthesis, Ion Conductivity, Doping, Interface

Research Scope: The major goal of this project is to understand the cation/anion doping effect on the structure and ion transport of novel sodium (Na) superionic conductors ($Na_{3-x}A_xSbS_{4-y}X_y$) by the combination of material synthesis, neutron technology and other characterization as well as theoretical simulation. The project's proposed technology involves the following objectives: (1) Synthesize new Na-ion conductors (Na_3SbS_4 with anion or cation doping) with high phase purity and determine their structural features; (2) Understand Na-ion conductive properties of new Na-ion conductors through integration of experiments and theory; (3) Investigate the interface stability of novel Na superionic conductors with electrode materials in solid-state Na batteries. Our team is working in collaboration with Oak Ridge National Laboratory (ORNL) and the neutron diffraction experiment is being conducted in Spallation Neutron Source (SNS, a DOE user facility).

Recent Progress. So far, we have made significant achievements on both synthesis/experimental characterizations and theoretical simulations. In terms of the experimental side, we have completed the following objectives: (1) investigate the in-situ synthesis for Na_3SbS_4 with anion or cation doping by advanced neutron diffraction; (2) study the interface stabilization of Na_3SbS_4 family conductors toward Na metal. The achievements in theory/simulation side are included in a separate abstract. Below, we mainly describe the key experimental results obtained from the synthesis and interface studies of Na_3SbS_4 family superionic conductors.

1. Monitoring structural evolution of pristine and doped Na_3SbS_4 conductors during synthesis by advanced Neutron diffraction experiments. Neutron diffraction has been proven to be efficient to track the phase transition of solid conductors with varying temperatures.[1] In this project, we employed *in situ* neutron diffraction to study the synthesis process of Na_3SbS_4 family conductors (pristine Na_3SbS_4 (NSS), anion-doped NSS, and cation-doped NSS) to understand their synthetic mechanism from the solid-state reactions.[2] This is the *first time* visualization of in situ synthesis studies of Na_3SbS_4 family conductors, revealing its phase formation temperature, molten state, and recrystallization, and phase transition process.

In this work, the anion doping is selected as Se^{2-} to replace S^{2-} ($Na_3SbS_{3.5}Se_{0.5}$, NSSE) The solid-state reactions involve the precursors of Na_2S, Sb_2S_3, and S for pristine Na_3SbS_4, and adding the stoichiometric ratio of Se for Se-doped NSS. *Figure 1a* shows the intensity contour plots with temperature, which clearly indicates the decrease in precursor peaks and appearance of new product peaks (Na_3SbS_4) after 300 °C. To better understand the reaction mechanism, the temperature dependence of peak intensity for Na_2S precursor and Na_3SbS_4 product is analyzed in *Figure 1b*. The Na_3SbS_4 peak is observed to jump quickly, suggesting a rapid reaction process to

the final product. The intensity contour plots of in-situ ND patterns for Na_3SbS_4 upon cooling process are shown in *Figure 1c*. There are clearly three regions observed: molten state, cubic structure after recrystallization, and tetragonal structure range. For 12.5% mol Se-doping, $Na_3SbS_{3.5}Se_{0.5}$ sample also shows a fast solid reaction with a sharp increase of the product peak between 290-305 °C (*Figure 1d*). Up on the cooling process, the characteristic peaks of $Na_3SbS_{3.5}Se_{0.5}$ shows the similar slight left-shift (*Figure 1e*). Nevertheless, when the temperature cools down to 150 °C, $Na_3SbS_{3.5}Se_{0.5}$ remains a cubic structure, in contrast to a tetragonal phase for pure Na_3SbS_4. The *cubic-to-tetragonal* phase transition temperature is observed to decrease to 110 °C for $Na_3SbS_{3.5}Se_{0.5}$ (vs. 165 °C for Na_3SbS_4). Moreover, the effects of Se-doping contents were also investigated by the synthesis of $Na_3SbS_{4-y}Se_y$ conductors.[3]

In addition, we also studied the cation-doing effect on the synthetic reaction of Ca-doped Na_3SbS_4 ($Na_{2.8}Ca_{0.2}SbS_4$) by introducing Ca^{2+} to partially replace Na^+ with the addition of CaS to the precursors of Na_2S, Sb_2S_3, and S. These precursors were sealed in a quartz tube under vacuum and heated from room temperature to 650 °C with the neutron diffraction continuously tracking the structural changes. *Figure 1f* displays the 3D intensity contour plot between the temperature range of 100-350 °C. It clearly shows that the precursor materials decrease while new phase emerges during the heating process. Meanwhile, the intermediate phases are also observed, which is different from the observation in Na_3SbS_4 and $Na_3SbS_{3.5}Se_{0.5}$. Further analysis is currently underway to gain a deeper understanding.

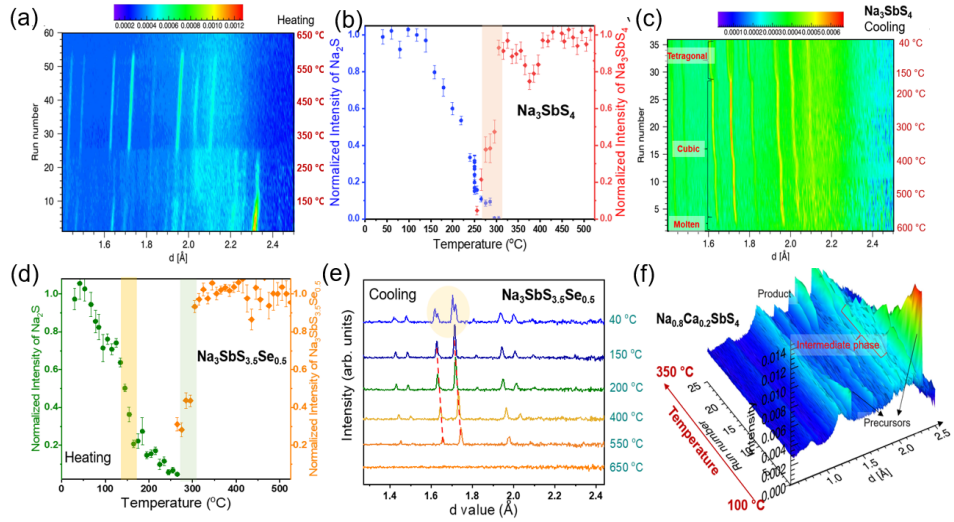

Figure 1. (a) Virtual plots of in situ neutron diffraction (ND) for the synthesis of Na_3SbS_4; (b) Variation trends of Na_2S reactant and product as function of temperature for Na_3SbS_4; (c) Virtual plots of in situ ND during the cooling process; (d) Variation trends of Na_2S reactant and product as function of temperature for $Na_3SbS_{3.5}Se_{0.5}$; (e) neutron diffraction patterns of $Na_3SbS_{3.5}Se_{0.5}$ at different temperature; (f) 3D intensity contour plots of Ca-doped $Na_{2.8}Ca_{0.2}SbS_4$ from in situ neutron diffraction.

2. Efficient interface stabilization of Na_3SbS_4 family conductors toward Na metal. We first studied the interface stability of Na_3SbS_4 SE towards Na metal by employing Na symmetric cells and X-ray photoelectron spectroscopy (XPS). The results suggested serious interfacial reactions due to the decomposition of NSS. To enhance the stability of the interface, we have investigated

various strategies for interface modification by introducing an artificial interlayer between Na metal and NSS SE (*Figure 2a*). The designed interlayer should effectively: (1) prevent detrimental side reactions resulting from the decomposition of NSS SE; (2) enable uniform Na deposition and thereby alleviating dendrite formation; and (3) facilitate intimate contact, reducing interfacial resistance and promoting the formation of a stable solid electrolyte interphase (SEI).

We have studied different strategies for artificial interlayer, such as the introduction of ionic liquid (IL), or the addition of a phase transition co-polymer.[4,5] For the ionic liquid (IL) as the interlayer, it has low concentration of 0.2 M and donated as (PYR/Na)TFSI, which contains PYR14TFSI blended with NaTFSI. The (PYR/Na)TFSI interlayer was introduced at both Na/SE and SE/FeS_2 interfaces, assisting to form thin and continuous SEI layers (*Figure 2b*).[4] The efficiency interlayer was also indicated by the close values of impedance for the Na|SE|FeS_2 battery before and after cycling in EIS measurements (*Figure 2c*). *Figure 2d* compared the XPS spectra of F1s, Sb 3d, S2p and N1s for Na/NSS interface with and without (PYR/Na)TFSI) interlayer. It is observed that the presence of NaF and the absence of Na_2S in the formed SEI. These results indicate that (PYR/Na)TFSI interlayer is efficient to prevent reductive reactions and enable the formation of a stable SEI composed of NaF. *In the second case*, we designed and demonstrated a phase-transition copolymer as the interlayer between Na anode and NSS sulfide SE. The interlayer is an amphiphilic triblock copolymer, which consists of poly(ethylene glycol)-block-poly(propylene glycol)-block-poly(ethylene glycol) (PEG-PPG-PEG) blended with sodium salt (NaTFSI) (denoted as PPP/NaTFSI). This co-polymer exhibits a phase transition temperature ranging between 30-50 °C, accompanied by a distinct visual observation and ionic conductivity (*Figure 2e and f*). The presence of PPP/NaTFSI interlayer also modifies the surface morphology

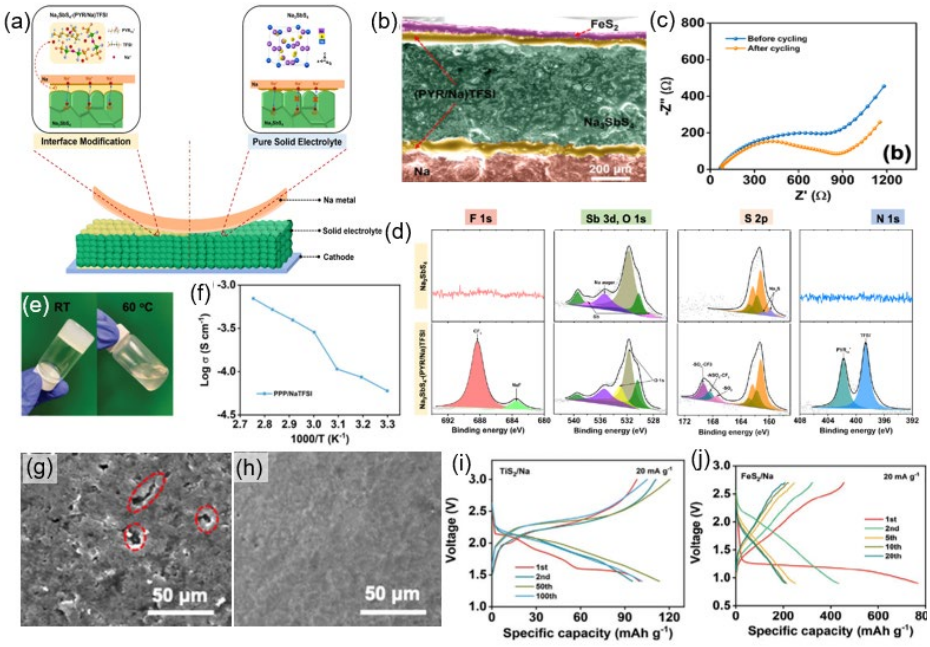

Figure 2. (a) Schematic diagram of Na/Na_3SbS_4 interface w/wo interlayer; (b) Cross-sectional SEM image and (c) EIS plots of Na|NSS|FeS_2 with interlayer after cycling; (d) XPS spectra of Na_3SbS_4 SE toward Na after cycling in Na||FeS_2 cell; (e) digital phot of phase transition co-polymer; (f) the variation of conductivity dependent on temperature; SEM images of (g) bare Na_3SbS_4 SE pellets and (h) with interlayer; charge/discharge curves of (i) Na||TiS_2 and (j) Na||FeS_2 cells, respectively.

of cold-pressed Na_3SbS_4 pellet (minor cracks in *Figure 2g*) to become fully smooth and uniform (*Figure 2h*). As a result, the discharge/charge voltage profiles of TiS_2|NSS/PPP/NaTFSI|Na battery show great specific capacity at a current density of 20 mAg^{-1} (*Figure 2i*), whereas pure Na_3SbS_4 pellet cannot work due to the huge interface resistance. Moreover, with such interlayer, FeS_2|NSS|Na cell can deliver a higher specific capacity of 200 mAh g^{-1} at 20 mA g^{-1} after 20 cycles when cycled at 50 °C (*Figure 2j*). In addition, the interface stability of doped NSS towards Na metal is currently being investigated, such as Se-doped NSS.

Future Plans. For this project, the future work involves the efforts on synthesis/experimental characterizations as well as the theoretical simulations. In terms of the experimental side, we will expand our work on (1) perform and analyze in-situ experiment (e.g., neutron) results on cation-doped Na_3SbS_4; (2) assemble the solid-state Na batteries using doped Na_3SbS_4 as SE without interlayer and understand the interfacial reactions. From the theoretical perspective, we will carry out ab initio molecular dynamics (AIMD) simulation to examine the interface stability between doped Na_3SbS_4 with Na metal.

References

1 Y. Chen, L. Yang, F. Ren and K. An. *Visualizing the Structural Evolution of LSM/xYSZ Composite Cathodes for SOFC by in-situ Neutron Diffraction*. Sci Rep-Uk **4**, 5179 (2014). https://doi.org:10.1038/srep05179

2 S. Halacoglu, S. Chertmanova, Y. Chen, Y. Li, M. Rajapakse, G. Sumanasekera, B. Narayanan and H. Wang. *Visualization of Solid-State Synthesis for Chalcogenide Na Superionic Conductors by in-situ Neutron Diffraction*. ChemSusChem **14**, 5161-5166 (2021). https://doi.org:https://doi.org/10.1002/cssc.202101839

3 S. Halacoglu, Y. Li, W. Arnold, V. Shreyas, X. Guo, J. B. Jasinski, B. Narayanan and H. Wang. *Solvent-free and low temperature synthesis of chalcogenide Na superionic conductors for solid-state batteries*. Chemical Engineering Journal **468**, 143624 (2023). https://doi.org:https://doi.org/10.1016/j.cej.2023.143624

4 Y. Li, S. Halacoglu, V. Shreyas, W. Arnold, X. Guo, Q. Dou, J. B. Jasinski, B. Narayanan and H. Wang. *Highly efficient interface stabilization for ambient-temperature quasi-solid-state sodium metal batteries*. Chemical Engineering Journal **434**, 134679 (2022). https://doi.org:https://doi.org/10.1016/j.cej.2022.134679

5 Y. Li, W. Arnold, S. Halacoglu, J. B. Jasinski, T. Druffel and H. Wang. *Phase-Transition Interlayer Enables High-Performance Solid-State Sodium Batteries with Sulfide Solid Electrolyte*. Advanced Functional Materials **31**, 2101636 (2021). https://doi.org:https://doi.org/10.1002/adfm.202101636

Publications

1. S. Halacoglu, S. Chertmanova, Y. Chen, Y. Li, M. Rajapakse, G. Sumanasekera, **B. Narayanan and H. Wang,** *Visualization of Solid-State Synthesis for Chalcogenide Na Superionic Conductors by in-situ Neutron Diffraction*, ChemSusChem, **14**, 5161-5166 (2021). doi:https://doi.org/10.1002/cssc.202101839
2. S. Halacoglu, Y. Li, W. Arnold, V. Shreyas, X. Guo, J. B. Jasinski, **B. Narayanan and H. Wang,** *Solvent-free and low temperature synthesis of chalcogenide Na superionic conductors for solid-state batteries*, Chemical Engineering Journal, **468**, 143624 (2023). doi:https://doi.org/10.1016/j.cej.2023.143624
3. Y. Li, S. Halacoglu, V. Shreyas, W. Arnold, X. Guo, Q. Dou, J. B. Jasinski, **B. Narayanan and H. Wang,** *Highly efficient interface stabilization for ambient-temperature quasi-solid-state sodium metal batteries,* Chemical Engineering Journal, **434**, 134679 (2022). doi:https://doi.org/10.1016/j.cej.2022.134679
4. Y. Li, W. Arnold, S. Halacoglu, J. B. Jasinski, T. Druffel and H. Wang, *Phase-Transition Interlayer Enables High-Performance Solid-State Sodium Batteries with Sulfide Solid Electrolyte*, Advanced Functional Materials, **31**, 2101636 (2021). doi:https://doi.org/10.1002/adfm.202101636

5. F. Guo, S. Jagadeesan, R. Pidathala, S.-W. Kim, X. Shan, N. Deskins, M. Abeykoon, G. Kwon, D. Olds, **B. Narayanan**†, X. Teng†. *Revitalizing Iron Redox by Anion-Insertion-Assisted Ferro- and Ferri-Hydroxides Conversion at Low Alkalinity*. Journal of American Chemical Society, **144**, 11938–11942 (2022) **DOI:** https://doi.org/10.1021/jacs.2c03113
6. X. Shan, R. Pidathala, S.-W. Kim, W. Xu, M. Abeykoon, G. Kwon, D. Olds, **B. Narayanan** and X. Teng. *Exemption of lattice collapse in Ni–MnO_2 birnessite regulated by the structural water mobility.* Journal of Materials Chemistry A 9, 23459 (2021) **DOI:** https://doi.org/10.1039/D1TA06716H

Mapping the synthetic routes for 2-dimensional materials

Boris I. Yakobson, Rice University, biy@rice.edu

Keywords: 2D materials, lateral epitaxy, 1D nucleation, gas phase reactions, growth-precursors

Research Scope

Recent decades were marked by the increasing interest in two-dimensional (2D) materials, driven by discoveries of their new properties, useful functionalities and hence potential applications. A family of 2D materials widened from graphene to transitional metal dichalcogenides (TMD), hBN, borophene, and many others. The strong dependence of the properties on the structural quality of all such materials calls for an in-depth understanding and control of the processes in their synthesis. The exfoliation of layered bulk materials into atomic 2D sheets, while intuitive, is not scalable. On the other hand, their synthesis through chemical vapor deposition (CVD) involves complex gas-solid chemistry, which works empirically, but the theoretical understanding of reactions and sentient design remains in infancy, motivating the goal of this project: to develop the state-of-the-art multiscale models of 2D-layers on substrates, the atomistic mechanisms of their nucleation (when the 2D island may or may not be preferred over the 3D cluster) and growth.

Recent Progress

While considering the synthesis process of any material, one is faced with the question of the *immediate growth precursor*, whose accretion to the growing crystal is the last step of perhaps many. The complexity of the synthesis setup, the use of various feedstocks in different states of matter (gas, liquid, solid), the catalysts, and other assisting substances make the determination of these fundamental building blocks extremely challenging, yet necessary for evaluating the growth rate, anisotropy, and product morphology. For MoS_2, as an *archetypal TMD-example*, we demonstrate how complex gas phase reactions lead to form the precursor and then how the chemistry of this process can be modified to accelerate the synthesis of the TMD [1,2]. Why the MoS_2? It is one of the most promising materials for optoelectronics: a semiconductor with a visible-range band gap, high mobility, and a plethora of extraordinary properties. While the main production recipe of chemical vapor deposition (CVD) is known, the actual chemical transformations during the synthesis remain largely unknown, hindering process optimization. Combining ab initio molecular dynamics (AIMD) and first-principles calculations allowed us to determine the complete scenario of MoS_2 monolayer growth at the atomic level. We find that solid MoO_3 precursor sublimates forming ringlike molecules Mo_3O_9, which then serve as gas-phase Mo-carrier, undergoing sulfurization in three main stages: ring opening, chain breaking (the rate-limiting step), and further sulfurization. The fully sulfurized MoS_6 molecule emerges as an immediate gas precursor to the crystal growth [1] as it reacts to join the MoS_2-layer edge, releasing a S_4 molecule.

When halide salts were discovered to promote CVD growth for a broad "library" of TMD, reported as collaborative work [i], it compelled us to look intently into underlying mechanisms [2]. The sulfurization of molybdenum *oxyhalides* MoO_2X_2 (X = F, Cl, Br, and I) ─ the form of Mo-feedstock dominating in salt-assisted synthesis, was found to display much lower activation barriers than that of molybdenum *oxide* in conventional "saltless" growth of MoS_2. We further found that the rate-limiting barriers depend linearly on the electronegativity of the halogen element, with oxyiodide having the lowest barrier, pointing to further process optimization of TMD syntheses.

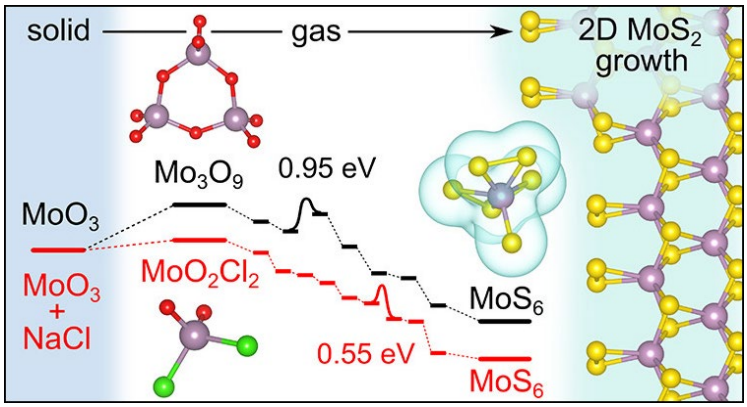

Figure 1. Schematic comparison of the gas phase reactions for salt-assisted and saltless growth of MoS_2 emphasizing the reduction of the critical barrier with the inclusion of salt [1,2].

Another synthesis in great demand, of hBN—*a wide band gap semiconductor*—is supplied with ammonia borane (AB) feedstock. Excessive hydrogen in H_3BNH_3 hinders the growth and must be removed on the way, prior to hBN formation. Our first-principles calculations combined with SG-AIMD simulations (the first-principle umbrella sampling) of the gas-phase pyrolytic dissociation of AB show that partially dehydrogenated molecules up to H_2BNH_2 encounter a very high barrier to being added to the hBN edge. Instead, we find the HBNH to be a realistic precursor to the hBN growth, with a moderate reaction barrier. This partial dehydrogenation of the AB occurs through complex gas-phase reactions involving BH_4^- and NH_4^+ ions, resulting in a somewhat slow gas-phase synthesis. In comparison, on catalytic Ni or boron surfaces—typical for the growth of hBN or BNNTs, respectively—the barriers to AB dehydrogenation are much reduced, yielding BNH and BN dimers as the primary precursors [ii].

Large, quality 2D monocrystals are highly sought after yet hard to achieve; unlike graphene, most TMD and h-BN lack symmetry, permitting the nucleation of mutually inverted pieces, merging into polycrystals replete with grain boundaries. On vicinal, miscut substrate surfaces, such growing pieces orient alike, enabling the growth of large 2D monocrystals. The compelling questions of how such a growth process can operate and through what key mechanisms the nuclei align are crucial in guiding the substrate selection for optimal synthesis of many materials. To this end, the basic crystallography and our atomistic theory revealed how the undulations of the ever-wandering steps do not, quite surprisingly, disturb the orientations of the attached 2D nuclei! Their directions remain robust owing to the *complementarity* between the meandering step and h-BN counterpart if their kinks have negligible misfit, $\delta k < 0.1$ Å. Further, the stronger chemical affinity of metal to the N atoms at the zigzag edge of h-BN singles out its particular orientation (without evidence of any epitaxy to the surface). Monocrystal integrity

requires unhindered growth spillover across the steps and the seamless healing of the residual fissures caused by the very same steps necessary for co-orientation. MD simulations show this happening for the steps not taller than the BN bond, s < 1.44 Å. These criteria "really work," pointing to [−1 1 2] steps on the Cu (110) surface and success in experiments, while other possibilities on Cu (111) have also been predicted [iii] followed by spectacular *wafer-size* realization by collaborators at TSMC, Taiwan [iv].

To exemplify the great potential of lateral 2D epitaxy, we extend the methodology into yet unmapped territory toward pioneering the *synthesis of "free" borophene* ─ a monolayer of boron atoms ─ on the surface of non-bonding insulating hBN. Currently, borophenes are all synthesized on and stay bound to metal substrates, hampering both characterization and use. Growth on an inert insulator would allow facile exfoliation, but the weak adhesion promotes no 2D nucleation. Naturally present 1D-defects, the step-edges on an h-BN miscut substrate, enable boron epitaxial assembly, reduce the nucleation dimensionality, eliminate the nucleation barrier reduced below 1.1 eV, to yield a $v_{1/9}$ phase [3]. Weak borophene adhesion to the insulator makes it readily accessible for comprehensive property tests or transfer into the device setting. Few labs now attempt its realization.

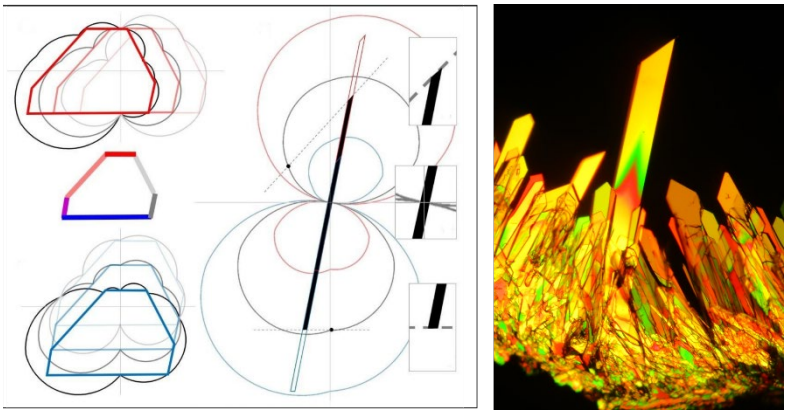

Figure 2. Left: black-gray curves are the edge energies versus direction, for various arbitrary closures, with Wulff shape expressly invariant (center). Middle: Wulff construction computed for expressly asymmetric (C1) salt [4]. Right: Druses of potassium dichromate K2Cr2O7 in cross-polarized light [Wikimedia Commons].

2D crystals' geometry is readily seen in microscopy, compared to multifaceted 3D forms. This revives a fundamental question of their *equilibrium shapes*: the Wulff construction relies on known or computed edge energies, while for many important materials, the very definition of edge energy is not possible. The lack of symmetry in SnS, SnSe, GeS, GeSe, etc. makes the surface or edge energies undefinable (gauge invariance corollary, J. Cahn, 1975) and leaves no foothold for the Wulff approach. This fundamental long-standing problem we have solved just recently [4]: by complementing rigorous DFT-computed total energy expressions with extra *closure equations* (containing arbitrary energy parameters), one solves an algebraic system, and obtains the true shape, invariant to the arbitrary choices made. This allows one, for the first time, a systematic way to predict the shapes of low or no-symmetry 2D (and 3D) crystals to match the observations of synthesized materials.

Future Plans

Near term, ongoing large-scale simulations, and data analysis to prove an important "order from disorder" trend, perhaps general for 2D materials synthesis. In exploring the nucleation and growth of hBN islands on metal substrates, e.g. Cu (111), we discovered a somewhat paradoxical tendency. While a perfect high-quality substrate permits nucleation of mutually inverted islands, eventually merging into polycrystalline low-quality hBN, the disordered at realistic growth temperature substrate surfaces contain a variety of defects, a sea of meandering steps caused by thermal entropic processes. Counterintuitively, this disorder ensures perfect monocrystalline growth of 2D materials by providing stronger lateral (layer edge-to-step of the substrate) epitaxy, as mentioned above [iii-v]. Moreover, the higher the energy of the surface defects (steps, kinks, corners), the more attractive they are to hBN nucleation. Completing this study should clear the path to an important paradigm change in edge-epitaxial growth of 2D material,

While mapping the synthetic routes for 2-dimensional materials, we reveal two universally present, distinct yet complementary aspects: one, the details of gas-phase reactions from the original feedstock-ingredients to the last immediate precursor-units that assemble into 2D-lattice. Second, the substrate features that facilitate nucleation of 2D-material are generally weakly bonded at the plane-to-plane interface so that epitaxy is dominated by stronger lateral edge-to-step interactions. Having these now successfully explored and even exploited in ground-breaking experiments in collaborators' labs, we will take this approach to a systematic level in order to explain and optimize synthesis in other important ways and for novel materials.

Example targets include control over the thickness, the number of layers of the grown material, affecting important properties. The number of layers is not well regulated, even for such cornerstone materials as graphene. Some others, like MoS_2, display self-limiting nature of growth, yielding strictly monolayer. With the recent rise of non-van der Waals 2D materials, whose corresponding bulk is not layered at all, the understanding thickness control is even more important. Furthermore, this would be beneficial for materials novel in the 2D family, such as perovskites, whose energy harvesting ability depends on the thickness. We will investigate the mechanism of material-substrate interaction, including surface and sub-surface diffusion, dissolution, and chemical reactions governing the layer deposition and thickness. We will expand work into understanding critical degradation challenges, an important example being the halide perovskite photoelectrodes for water splitting.

References

i. J. Zhou, J. Lin, X. Huang, Y. Zhou, Y. Chen, J. Xia, H. Wang, Y. Xie, H. Yu, J. Lei, D. Wu, F. Liu, Q. Fu, Q. Zeng, C.-H. Hsu, C. Yang, L. Lu, T. Yu, Z. Shen, H. Lin, B.I. Yakobson, Q. Liu, K. Suenaga, G. Liu, and Z. Liu, *A library of atomically-thin metal chalcogenides*, Nature **556**, 355–359 (2018)

ii. T. Cheng, K.V. Bets, B.I. Yakobson, *Ammonia borane CVD in h-BN and BNNTs synthesis: unraveling the reactions and intermediates by ab initio computations,* in preparation.

iii. K.V. Bets, N. Gupta, and B.I. Yakobson, *How the complementarity at vicinal steps enables growth of 2D monocrystals*, Nano Letters **19**, 2027-2031 (2019).

iv. T.A. Chen, C.P. Chuu, C.C. Tseng, C.K. Wen, H.S.P. Wong, S. Pan, R. Li, T.A. Chao, W.C. Chueh, Y. Zhang, Q. Fu, B.I. Yakobson, W.-H. Chang, L.-J. Li, *Wafer-scale single-crystal hexagonal boron nitride monolayers on Cu (111)*, Nature **579**, 219-223 (2020).

v. K.V. Bets and B.I. Yakobson, *Entropic origin of the hBN monocrystallinity on Cu (111) surface, in preparation*

Publications (10/16)

1. J. Lei, Y. Xie, and B.I. Yakobson, *Gas-phase "prehistory" and molecular precursors in monolayer metal dichalcogenides synthesis: The case of MoS_2*, ACS Nano **15**, 10525-10531 (2021).
2. J. Lei, Y. Xie, A. Kutana, K.V. Bets, and B.I. Yakobson, *Salt-assisted MoS2 growth: Molecular mechanisms from the first principles*, JACS **144**, 7497-7503 (2022).
3. Q. Ruan, L. Wang, K.V. Bets, and B.I. Yakobson, *Step-edge epitaxy for borophene growth on insulators*, ACS Nano **15**, 18347-18353 (2021).
4. L. Wang, S.N. Shirodkar, Z. Zhang, and B.I. Yakobson, *Defining shapes of two-dimensional crystals with undefinable edge energies*, Nat. Comput. Sci. **2**, 729-735 (2022).
5. L. Qiu, X. Zhang, X. Kong, I. Mitchell, T. Yan, S.Y. Kim, B.I. Yakobson, and F. Ding, *Theory of sigma bond resonance in flat boron materials*, Nat. Commun. **14**, 1804 (2023).
6. W. Chen, K.V. Bets, R. Salvatierra, G. Gao, C. Choi, X. Wang, J. Li, C. Kittrell, N. La, J. Chen, K. Wyss, L. Eddy, P. Scotland, B. Li, B. Deng, M. Tomson, Y. Han, B.I. Yakobson, J.M. Tour, *Battery metals recycling by flash Joule heating*, **ChemRxiv,** Sci. Adv. *submitted* (2023).
7. A. Kutana, T. Altalhi, Q. Ruan, J.J. Zhang, E.S. Penev, and B.I. Yakobson, *Stability and electronic properties of gallenene*, Nanoscale Adv. **4**, 1408-1413 (2022).
8. Y. Xu, P. Zhang, X. Xuan, M. Xue, Z. Zhang, W. Guo, and B.I. Yakobson, *Borophane Polymorphs*, J. Phys. Chem. Lett. **13**, 1107-1113 (2022).
9. E.S. Penev, Y. Liu, T. Altalhi, A. Kutana, and B.I. Yakobson, *Stable Low-Dimensional Boron Chalcogenides from Planar Structural Motifs*, J. Phys. Chem. A **125**, 6059-6063 (2021).
10. E.S. Penev, N. Marzari, and B.I. Yakobson, *Theoretical prediction of two-dimensional materials, behavior, and properties*, ACS Nano **15**, 5959-5976 (2021).

Descriptor-enabled high-entropy materials design and discovery

Liping Yu (PI) and Yingchao Yang (co-PI), University of Maine, Orono

Keywords: materials design and discovery, high entropy materials, layered 2D transition metal chalcogenides, solid state reaction synthesis, first principles calculations.

Research Scope

As the development of new binaries and ternaries approaches the limit of feasible combinations, high-entropy materials (HEMs), which consist of at least four principal elements, have emerged as a rapidly growing research field for functional materials design. [1] This project predicts, synthesizes, and characterizes a class of new layered 2D HEMs and explores their use as flexible electrodes in next-generation batteries and supercapacitors. The 2D HEMs of focus are layered transition metal chalcogenides M_nX_{2n}, where n = 4, 5, and 6 (representing the number of equiatomic constituent metals M), and X is S, Se, or Te, in either 1H or 1T structure. These materials, which have the capability to accommodate significant lattice strain, have the potential to yield a considerable improvement in electrode performance.

The project addresses four fundamental questions: (i) what combinations of elements can give rise to stable and synthesizable 2D-HEMs? (ii) what is the driving mechanism for the stability and synthesizability of crystalline single-phase 2D HEMs? (iii) what is the role of local chemical disorder and defects on the macroscopic electronic and mechanical properties? and (iv) what is the actuating charge storage mechanism of the selectively synthesized 2D HEMs for use as batteries and supercapacitor electrodes?

The research adopts an integrated theory-experiment approach involving high-throughput first-principles calculations, modeling, data mining, experimental synthesis, characterization, and device applications. Advanced computing resources and state-of-the-art experimental facilities at ORNL are used. Two postdoctoral scientist and two graduate students at UMaine are trained and co-advised by the research staff at ORNL, along with collaborative scientific interactions, to advance the field of 2D-HEMs.[2]

Recent Progress

The research has made substantial progress toward the rational computational design and experimental synthesis and characterization of predicted 2D-HEMs.

- *Developed a highly predictive Mixed Enthalpy-Entropy descriptor (MEED) for high-throughput first principles screening of synthesizable new HEMs over large chemical spaces.* As illustrated in Fig.1, the MEED comprises two distinctive parameters: (i) ΔH_r (the difference in formation energy per atom between the solid solution and the most stable

compound formed by its constituent elements), and (ii) $\langle|\Delta E_D|\rangle$ (the average of absolute differences in defect formation energy among all possible substitutional point defects in the respective constituent binaries in the same crystal structure of the HEM. The ΔH_r parameter describes the relative synthesizability of a solid solution with respect to its most stable competing compound, based on the enthalpy contribution. It aligns well with the common wisdom that compounds with more dissimilar bonding characters are harder to mix and form a single-phase solid solution. Meanwhile, the $\langle|\Delta E_D|\rangle$ parameter describes the entropy forming ability from the spread of defect formation energy spectrum. These two parameters, taken together, account for the material-specific actuating enthalpy-entropy competition that determines the stability and formation of solid solution phases. They can be easily and rapidly calculated fully from first principles without using large alloy superstructures and without considering numerous competing phases that are hard to determine and visualize.

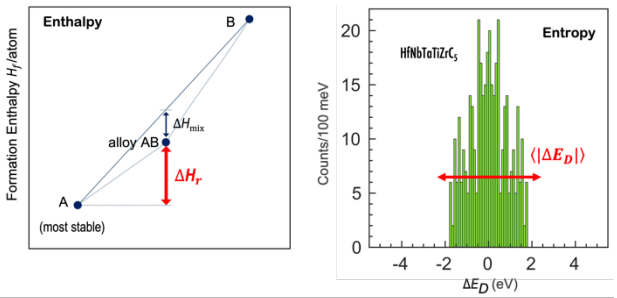

Fig.1 | The schematic diagram of MEED parameters. Left: the ΔH_r parameter defines the difference in formation energy per atom between the AB solid solution and its more stable competing phases A; Right: the $\langle|\Delta E_D|\rangle$ parameter measures the spread of defect formation energy spectra and hence also the entropy forming ability.

- *MEED benchmark*. The MEED was benchmarked on the rock-salt metal carbide systems. The metal elements are chosen from eight refractory metals (Hf, Nb, Mo, Ta, Ti, V, W, and Zr). As shown in Fig.2, the MEED not only successfully identifies all experimentally reported single-phase high-entropy metal carbides (marked as green circles), but also clearly separates these experimentally reported HEMs, in both ΔH_r and $\langle|\Delta E_D|\rangle$, from those experimentally known multiphase ones (marked by red circles). [3] The separation curve is not a fitting to experimental data; rather, it is a dimensionless physical quantity that unifies ΔH_r and $\langle|\Delta E_D|\rangle$ via normalization. The predictivity of MEED goes beyond existing semi-empirical descriptors that either assume an ideal configurational mixing or assume a universally unimportant

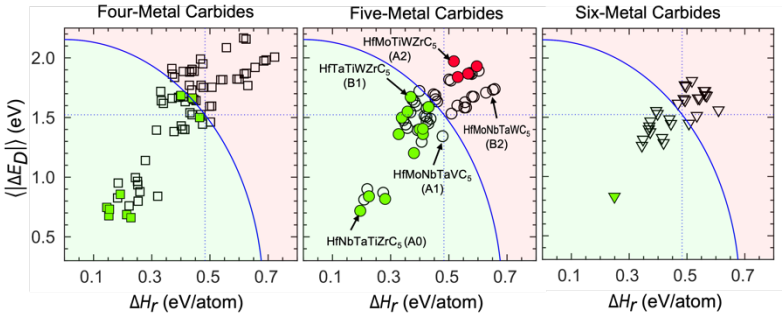

Fig.2 | The MEED benchmark over four-/five-/six-metal carbide systems. Green symbols represent experimentally synthesized single-phase high-entropy materials. Red symbols represent those experimentally reported multiple-phase compounds.

enthalpy of mixing over their competing phases. [4] The MEED can be also applied to unravel chemical and structural trends in synthesizability among different HEMs.

- *Discovery of new layered 2D HEMs by MEED.* The predictions were conducted using the same eight-element set of metals for carbides. MEED values were calculated for all 926 different high-entropy chalcogenides, including four-, five-, and six-metal sulfides/selenides/tellurides, in both 2H and 1T structures. Results shown in Fig.3 are the MEED values for 2H structures. Tens of them were predicted to be highly stable and easily synthesizable. Some interesting trends were also found. For instance, (i) the 2H-phase high-entropy metal chalcogenides are generally easier to synthesize than the 1T-phase high-entropy metal chalcogenides; (ii) the number of MEED-predicted top candidates decrease as the number of constituent metal elements increases; (iii) the scaling relationship between ΔH_r and $\langle|\Delta E_D|\rangle$ is rather scattered. For a same or similar ΔH_r, the $\langle|\Delta E_D|\rangle$ can still vary significantly from one compound to another, and vice versa. This variation suggests that the critical role of the enthalpy-entropy competition in controlling phase stability and formation.

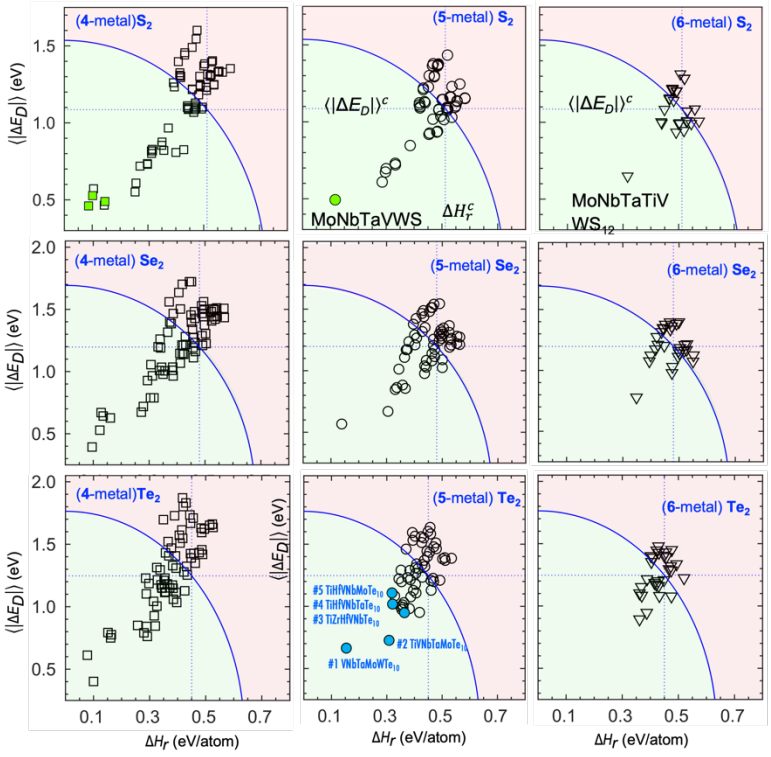

Fig.3 | MEED-predicted layered 2H-MX_2 HEMs. Green symbols represent those that were experimentally reported in the literature, whereas blue symbols represent those that were synthesized in this project by our experimental co-PI Yang's group.

- *Experimental synthesis and validation*. During the course of this research, one five-metal sulfide ($MoNbTaVWS_{10}$) and three four-metal sulfides ($MoNbTaVS_8$, $MoNbVWS_8$, and $MoNbTaWS_8$) were experimentally reported. [5] Remarkably, all these experimentally reported 2D transition metal sulfides (highlighted in green) were found to be the top candidates of the MEED prediction. The predicted 2H crystal structure and compositions also agree well with experiments. Using the solid-state reaction growth method, our experimental co-PI group attempted to synthesize the top five predicted high entropy 2D metal tellurides, namely, $VNbTaMoWTe_{10}$, $TiVNbTaMoTe_{10}$, $TiZrHfVNbTe_{10}$, $TiHfVNbTaTe_{10}$, and $TiHfVNbMoTe_{10}$. All of them were successfully synthesized. Fig.4

summarizes some SEM and, TEM results, which clearly demonstrate the layered 2D single crystalline structures and uniform element distributions.

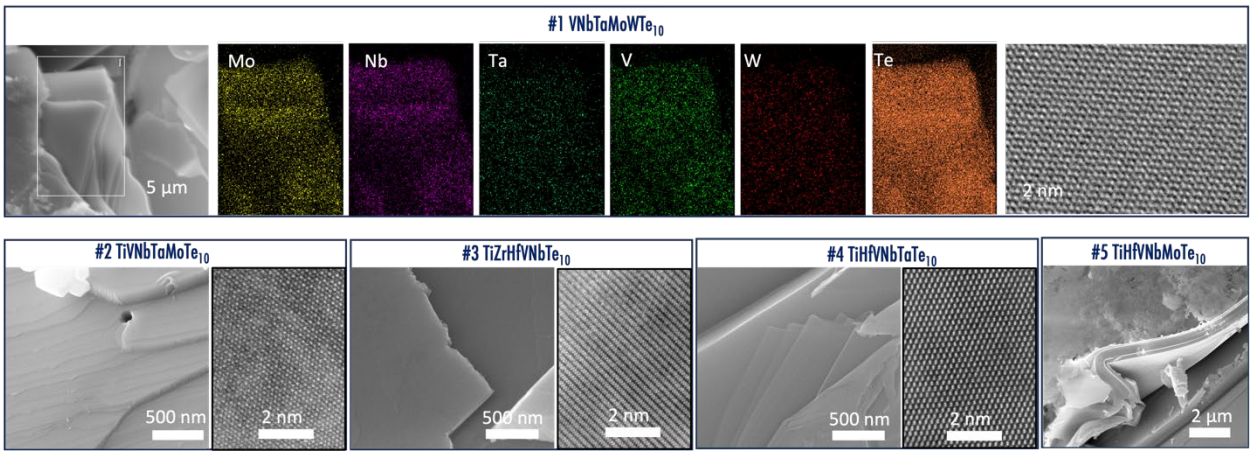

Fig.4 | Experimental validation for the top five layered 2D high-entropy metal tellurides predicted MEED. The SEM and TEM results demonstrate the successful synthesis of these high-entropy tellurides.

Future Plans

More top MEED-predicted 2D HEMs (sulfides, selenides, and tellurides) will be attempted for experimental synthesis using both solid state reaction and CVD methods. The growth conditions and controlling parameters will be further optimized for synthesizing these materials. For those experimentally synthesized 2D HEMs, state-of-the-art facilities, including SEM, STEM, EELS, AFM, and MicroRaman at CNMS at ORNL, will be applied to characterize and investigate their structural, electronic, mechanical, and defect properties, in conjunction with first principles methods. The charge-storage mechanism of these layered 2D HEMs will also be investigated and explored for Li/Na-ion batteries and supercapacitors.

References

1. E. P. George, D. Raabe, and R. Ritchie, , *High-Entropy alloys*, Nat. Rev. Mater. **5**, 4 (2019).

2. S. K. Nemani, M. Torkamanzadeh, B. C. Wyatt, V. Presser, and B. Anasori, Functional two-dimensional high-entropy materials, *Communications Materials* **4,** 16 (2023).

3. P. Sarker, T. Harrington, C. Toher, C. Oses, M. Samiee, J.-P. Maria, D. W. Brenner, K. S. Vecchio, and S. Curtarolo, *High-Entropy High-Hardness Metal Carbides Discovered by Entropy Descriptors*, Nat. Commun. **9**, 4980 (2018).

4. U. Mizutani, *Hume-Rothery Rules for Structurally Complex Alloy Phases* (CRC Press, 2016).

5. J. Cavin, A. Ahmadiparidari, L. Majidi, A. S. Thind, S. N. Misal, A. Prajapati, Z. Hemmat, S. Rastegar, A. Beukelman, M. R. Singh, K. A. Unocic, A. Salehi-Khojin, B. Mishra, *2D High-Entropy Transition Metal Dichalcogenides for Carbon Dioxide Electrocatalysis*, Adv. Mater. **33**, 2100347 (2021).

Publications

1. **D. Dey, L. Laing, and L. Yu,** ***Descriptor-Enabled Rational Design of High-Entropy Materials Over Vast Chemical Spaces*****, arXiv:**2301**.06554 (2023).**
2. **S. Maity, D. Dey, A. Ghosh, S. Masanta, B. K. De, H. S.Kunwar, B. Das, T. Kundu, M. Palit, S. Bera, K. Dolui, L. Yu, A. Taraphder, S. Datta, Proximitized spin-phonon coupling in topological insulator due to two-dimensional antiferromagnet, arXiv:**2212**.12772 (2023).**
3. **D. Dey, A. Ray, and L. Yu, Intrinsic Ferromagnetism and Restrictive Thermodynamic Stability in MA_2N_4 and Janus $VSiGeN_4$ monolayers, Phys. Rev. Materials** 6**, L061002 (2022).**
4. **B. St Laurent, D. Dey, L. Yu, and S. Hollen, Atomic-Scale Investigation of Oxidation at the Black Phosphorus Surface, ACS Applied Electronic Materials** 3**, 4066(2021).**
5. **J. Pan, Y. Zhang, J. Zhang, H. Banjade, J. Yu, L. Yu, S. Du, A. Ruzsinszky, Z. Hu, Q. Yan, Auxetic Two-Dimensional Transition Metal Selenides and Halides, npj Computational Materials** 6**, 154 (2020).**

The Surface Chemistry of the Atomic Layer Deposition of Thin Solid Films

Francisco Zaera

Department of Chemistry, University of California, Riverside, CA 92521

Email: zaera@ucr.edu

Keywords: ALD, Surfaces, Thin Films, Mechanisms.

Research Scope

The general objective of our project is to develop a molecular-level understanding of the thermal reactions associated with atomic layer deposition (ALD). ALD is one of the dominant technologies for the growth of nanometer-sized conformal films in many industrial applications. In microelectronics in particular, ALD can be used for the growth of diffusion, adhesion, and protection barriers and of metal interconnects, structures that are central to the buildup of diodes, transistors, and other elements within integrated circuits. More recently, the applications of ALD has been extended to areas related to energy production and use such as solar cells and photovoltaics, batteries, fuel cells, and catalysts and photocatalysts. All these processes require the deposition of isotropic films on complex topographies under mild conditions and with monolayer control. ALD is particularly suited to all those uses, but many questions concerning the underlying surface chemistry need to be answer to improve performance. Our mechanistic studies of ALD reactions are being pursued with the aid of surface-sensitive techniques such as X-ray photoelectron (XPS), low-energy ion scattering (LEIS), temperature programmed desorption (TPD), and infrared (IR) spectroscopies.

Recent Progress

Mechanistic studies of Cu, Ni, and Ru ALD.

The initial work in this project, which focused primarily on the chemistry of Cu amidinate precursors on metal surfaces, has been expanded to other ligands, substrates, and metals. A theory component has been added to our research as well. In collaboration with Prof. Noboru Takeuchi of UNAM (Mexican Autonomous National University), we have studied the surface chemistry of copper(I)−N,N′-dimethylacetamidinate on Ni(110) using DFT and contrasted it with similar calculations we previously carried out on Cu(110).[1] At low coverages, it was found that, in its most stable configuration, the molecular adsorption of copper(I)–N,N′-dimethylacetamidinate dimers occurs with the Cu atoms occupying surface hollow sites. The ligands reorient away from those metal centers, and the N atoms develop new direct bonds with surface Ni atoms. However, this configuration is not stable and decomposes by losing both ligands to the surface. In the final state, the two ligands bind via their N atoms to Ni atoms one lattice space away from the sites where the Cu atoms remain, with their molecular planes perpendicular to that of the surface. This is in contrast with what happens in the case of adsorption on Cu(110), where the Cu atoms from

the metalorganic complex still occupy hollow sites but where only one of the ligands breaks away and binds directly to the surface; the other remains on top of the two Cu ions. In terms of the energetics of adsorption and decomposition, the reactions on Ni(110) are much more exothermic than on Cu(110). Further analysis of the distribution of charge within the adsorbates shows a minor reduction of the Cu atoms of the dimer upon interaction with the surface; full reduction to metallic copper is complete only when both ligands fully migrate to their new Ni surface sites.

The molecular details of the ALD of metallic Cu on SiO_2 substrates using iminopyrrolidinate complexes were characterized under UHV conditions by TPD, in its temperature ramping and isothermal modes, and by XPS, with the aim of addressing two specific issues.[2] First, it was demonstrated that H_2 is quite inefficient as a reducing agent and cannot remove the organic ligands in the adsorbed species during the ALD cycles; insufficient ligand removal leads to the incorporation of impurities in the growing films. On the other hand, atomic hydrogen can accomplish both metal reducing and ligand removal functions and can be incorporated in ALD processes to deposit incremental amounts of Cu in sequential cycles. The second aspect addressed in that project is the fact that the deposited metallic Cu grows in the form of 3D NPs rather than as conformal 2D films. The TPD (Fig. 1) and XPS evidence collected in our studies points to a mechanism where individual Cu atoms, once cleaned from their organic ligands and reduced to their metallic state, become quite mobile and diffuse on the SiO_2 surface to form the 3D nanostructures. Similar Cu atom mobility and sintering were seen even in Cu physical vapor deposition processes carried out at room temperature and may therefore be an intrinsic feature of these ALDs regardless of the source of the metal atoms. This particular result points to the need to block metal atom mobility on silica surfaces, possibly via their silylation, to minimize metal sintering.

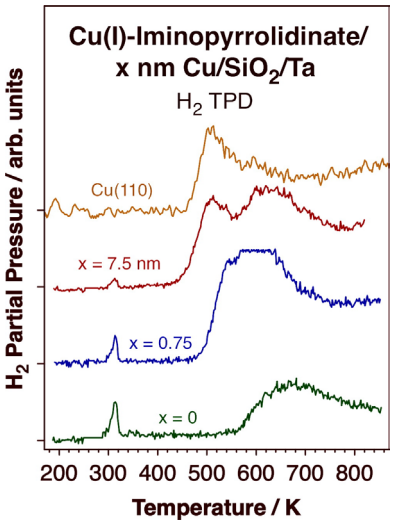

Fig. 1. H_2 TPD traces for Cu(I)-sBu-IP adsorbed at 450 K on SiO_2/Ta vs. Cu surface coverage. The two peaks seen for the nominally thick (7.5 nm) Cu film, due to desorption from Cu (~510 K) and SiO_2 (~630 K), indicate Cu 3D nanoparticle formation.

The mechanism of the thermal conversion of bis(2,2,6,6-tetramethyl-3,5-heptanedionato)-nickel(II) ($Ni(TMHD)_2$) and the protonated ligand (TMHD-H) adsorbed on TaO_x and SiO_2/TaO_x surfaces was also characterized by a combination of TPD and XPS experiments (Fig. 2).[3] A stepwise decomposition was observed with $Ni(TMHD)_2$ encompassing at least four different stages (Fig. 2): (1) a ligand loss, to release TMHD-H; (2) a surprising ligand fractioning via the scission of an inner C–C bond within the central β-diketonate moiety to produce an aldehyde

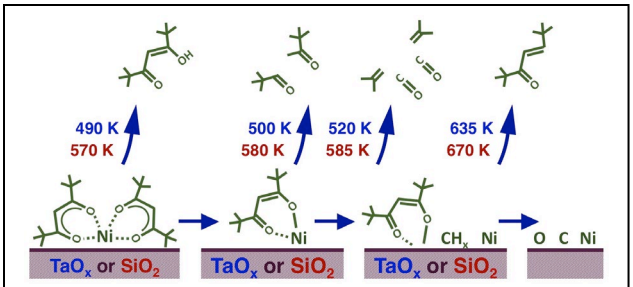

Fig. 2. Mechanism of the thermal decomposition of bis(2,2,6,6-tetramethyl-3,5-heptanedionato)-nickel(II).

(pivaldehyde) and a ketone (pinacolone); (3) further ligand splitting following a more extensive cracking to yield an olefin (from dehydrogenation of the terminal tert-butyl group), carbon monoxide, and adsorbed methylene groups; and finally, (4) the loss of one oxygen atom from the remaining ligands to produce the corresponding enone. As these conversions take place, the Ni ion is reduced, first to a partially oxidized intermediate, as the first ligand is removed, and then to its metallic state as the remaining organic fragments migrate to the surface. A similar sequence was seen on both surfaces, but with the transitions taking place at higher temperatures on SiO_2.

Finally, the evolution of the surface during the steps that comprise the ALD of Ru films on a Ni substrate using $Ru(tmhd)_3$ and molecular oxygen was characterized using a combination of XPS and Reflection Absorption Infrared Spectroscopy (RAIRS) spectroscopies.[4] The uptake of the Ru metalorganic precursor was determined to be activated, involving the average loss of two out of the three ligands (and the retention of the third, in molecular form, at the surface-vacuum interface), and self-limited, as required in ALD. The reaction of the resulting layer from that first half of the ALD cycle with O_2 proved to be more complex: in addition to the desired removal of the carbon-containing material, the Ni substrate becomes oxidized, and some Ru is etched away in the form of the volatile RuO_4 gas. By testing different combinations of exposures and temperatures it was determined that Ru film growth was possible, but tuning and optimizing the ALD or atomic layer etching (ALE) process conditions for maximum film growth or removal per cycle proved difficult. Replacing O_2 with H_2 was shown not to be viable either, as such an agent can reduce the nickel oxide formed after O_2 treatments (in fact, $Ru(tmhd)_3$ can do this as well) but not remove the carbonaceous material deposited on the surface by the Ru precursor. The use of N_2O showed much promise, being capable of removing most of the surface carbon without affecting the Ru film or the substrate (Fig. 3).

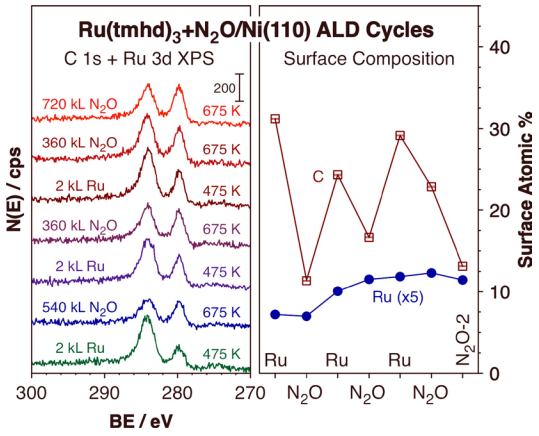

Fig. 3. Left: C 1s and Ru 3d XPS after each half-cycle of an 3 Ru ALD cycle process. Right: Ru and C surface atomic % estimated from the XPS data. Slow Ru growth was detected, without the buildup of carbon contamination or the oxidation of the surface.

ALD on mesoporous materials.

The ALD of ZrO_2 thin films over the mesopores of SBA-15 using tetrakis(dimethylamino)-zirconium(IV) (TDMAZ) as the precursor was also tested.[5] It was determined that, as the average size of the pores decreases (with increasing number of cycles), their size distribution remained narrow, indicating an homogeneous distribution of the ZrO_2 throughout the surfaces of the SBA-15 pores. This conclusion was confirmed by TEM and XPS. The deposition rate appears to slow down after 4 cycles, an observation that we explain by relating the kinetic diameter of TDMAZ with the pore diameter of SBA-15 after 4 deposition cycles: mass transport limitations may be affected by complex factors like electronic effects caused by exposed ZrO_2 surface and the multi-directionality of the adsorbed precursor molecules in the pore walls.

Future Plans

The funding for this proposal expires this year. In our renewal, we have proposed to partially redirect our attention to the preparation of the substrates to manipulate the ALD of metals. Our hypothesis is that the structure of the metals grown by ALD can be tuned via appropriate preconditioning of their surfaces. Specifically, we believe that the size and surface density of metal NPs ALD-grown on oxide surfaces may be controlled by adjusting the surface density of the ALD nucleation sites and/or by derivatizing those sites to change their surface chemistry. We speculate that a high density of nucleation sites may lead to the rapid coalescence of the developing metal NPs in the early stages of the ALD to create 2D films and that, conversely, a lower nucleation site density should allow for the NPs to grow in size before interacting with each other, especially if additional chemical barriers are added to the surface via silylation or other derivatization reactions. Our objective is to study the molecular chemistry that can afford such control, in particular the use of surface preconditioning as a way to define the characteristics of the metal NPs grown by ALD. We propose to test three approaches for this surface modification: (1) the addition of silanol groups using alkoxysilanes or similar precursors to increase the density of surface nucleation sites; (2) the silylation of the substrate to partially block its nucleation sites; and (3) the derivatization of the silanol sites with other molecular functionalities to modify the surface chemistry of the metal ALD.

References

1. Takeuchi, N.; Ventura-Macias, E.; Guerrero-Sánchez, J.; Zaera, F. *Density Functional Theory Study of the Adsorption and Dissociation of Copper(I) Acetamidinates on Ni(110): The Effect of the Substrate*. J. Phys. Chem. C, **124**, 15366-15376 (2020).
2. Yao, Y.; Chen, B.; Zaera, F. *On the Mechanism of the Atomic Layer Deposition of Cu Films on Silicon Oxide Surfaces: Activation Using Atomic Hydrogen and 3-Dimensional Growth*. Chem. Mater., **35**, 2155–2164 (2023).
3. Motin, M. A.; Zaera, F. *Thermal Chemistry of Nickel Diketonate Atomic Layer Deposition (ALD) Precursors on Tantalum and Silicon Oxide Surfaces*. J. Phys. Chem. C, **125**, 22006–22022 (2021).
4. Qin, X.; Zaera, F. *Atomic Layer Deposition of Ruthenium Films Using Ruthenium Diketonates and O_2, H_2, or N_2O: The Role of Ruthenium Etching*. J. Phys. Chem. C, **126**, 12527-12535 (2022).
5. Ke, W.; Liu, Y.; Wang, X.; Qin, X.; Chen, L.; Palomino, R. M.; Simonovis, J. P.; Lee, I.; Waluyo, I.; Rodriguez, J. A.et al. *Nucleation and Initial Stages of Growth During the Atomic Layer Deposition of Titanium Oxide on Mesoporous Silica*. Nano Lett., **20**, 6884-6890 (2020).

Publications

1. Md. Abdul Motin and Francisco Zaera, *Thermal Chemistry of Nickel Diketonate Complexes on Silicon and Tantalum Oxide Surfaces As It Relates to Atomic Layer Deposition (ALD) Applications*, J. Phys. Chem. C, **125**, 22006-22022 (2021). DOI: 10.1021/acs.jpcc.1c07071
2. Francisco Zaera, Francisco Zaera, *Molecular Approaches to Heterogeneous Catalysis*, Coord, Chem. Rev., **448**, 214179 (15 Pages) (2021). INVITED: Special Virtual Issue, "Molecular Approaches to Heterogeneous Catalysis". DOI: 10.1016/j.ccr.2021.214179
3. Xiangdong Qin, Francisco Zaera, *Atomic Layer Deposition of Ruthenium Films Using Ruthenium Diketonates and O_2, H_2, or N_2O: The Role of Ruthenium Etching*, J. Phys. Chem. C, **126(30)**, 12527-12535 (2022). DOI: 10.1021/acs.jpcc.2c04266
4. Francisco Zaera, *Designing Sites in Heterogeneous Catalysis: Are We Reaching Selectivities Competitive With Those of Homogeneous Catalysts?*, Chem. Rev., **122(9)**, 8594-8757 (2022). DOI: 10.1021/acs.chemrev.1c00905
5. Letícia F. Rasteiro, Md Abdul Motin, Luiz H. Vieira, Elisabete M. Assaf, Francisco Zaera, *Growth of ZrO_2 films on Mesoporous Silica Sieve via Atomic Layer Deposition (ALD)*, Thin Solid Films, **768**, 139716 (6 pages) (2023). DOI: 10.1016/j.tsf.2023.139716
6. Yunxi Yao, Bo Chen, and Francisco Zaera, *On the Mechanism of the Atomic Layer Deposition of Cu Films on Silicon Oxide Surfaces: Activation Using Atomic Hydrogen and 3D Growth*, Chem. Mater., **35(5)**, 2155-2164 (2023). DOI: 10.1021/acs.chemmater.2c03789

Seeing buried metal/oxide interfaces in action

Guangwen Zhou

Department of Mechanical Engineering, State University of New York, Binghamton, NY

Keywords: Interfacial Transformation; Dislocation; Stop-and-Go Kinetics; In-situ Transmission Electron Microscopy

Program Scope

Nearly all metals are reactive in their functioning environments and form spontaneously an oxide skin. This oxide skin governs the real-world interactions of the metals with their outer environment and plays a key role in a vast array of environmental and technological processes, including the protection of metallic components against corrosion for sustainable use, production of important chemicals in heterogeneous catalysis and fabrication of gate oxides for electronic devices. Much of our current knowledge of metal oxidation is based upon work at the mesoscale that is too coarse to reflect the underlying microscopic details. Acquiring the ability to manipulate the microscopic processes governing the surface oxidation via either controlling the reaction environment or modifying the materials will have huge technological implications. The work therefore encompasses an atomic-scale study of oxidation by exploiting the unique capabilities of imaging, diffraction and spectroscopy of complementary in-situ techniques to dynamically monitor the surface oxidation processes under practically relevant conditions of temperature and pressure. Each of the in-situ reactions is coordinated intimately by a number of theoretical modeling techniques ranging from the density-functional theory to first-principles thermodynamics and reactive molecular dynamics simulations by the incorporation of temperature and pressure effects, which allow for identifying how the interplay between thermodynamics driving force and kinetic obstacles determines the lively dynamics of surface oxidation. The sum of the experimental and theoretical efforts promises to establish the fundamental principles capable of controlling the chemical and physical interactions of metals and alloys with their functioning environments. The knowledge gained from this program will lead to smarter utilization of gas-surface reactions for a wide variety of energy technological applications such as corrosion, heterogeneous catalysis, thin film processing, and electronic device fabrication.

Recent Progress

Most engineering materials are based on multiphase microstructures produced either through the control of phase equilibria or by the fabrication of different materials as in thin-film processing. In both processes, the microstructure relaxes toward equilibrium by misfit dislocations across the heterophase interfaces[1-2]. Despite their ubiquitous presence, directly probing the dynamic action of misfit dislocations under real conditions has been unachievable owing to their buried nature. Using the $Cu_2O \rightarrow Cu$ transformation as an example, we demonstrate the unique role of misfit dislocations in modulating the oxide-to-metal interfacial transformations in an

intermittent manner, by which the lateral flow of interfacial ledges is pinned at the core of misfit dislocations until the dislocation climbs to the new oxide/metal interface location, thereby resulting in the stop-and-go kinetics of the interfacial reaction[3]. Together with atomistic calculations, we identify that the pinning effect is associated with the non-local transport of metal atoms to fill vacancies at the dislocation core. The work highlights the unique capabilities of in-situ electron microscopy in providing mechanistic insight into solid-solid interfacial transformations, and the results have substantial implications in utilizing structural defects at buried interfaces to modulate mass transport and transformation kinetics.

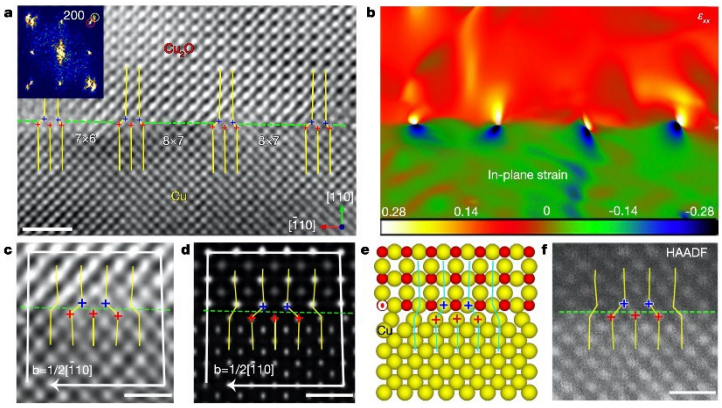

Fig. 1: **Formation of mismatch dislocations at the Cu_2O/Cu interface. a**, HRTEM image of a Cu_2O/Cu interface formed by oxidation of a Cu(110) facet at pO_2= 0.67 Pa and T =623 K. The core regions of four mismatch dislocations are marked with crosses. **b**, In-plane strain map (ε_{xx}) obtained by GPA of the HRTEM image in **a**. **c**, **d**, Experimental and simulated HRTEM micrographs showing the dislocation core structure, where the Burgers circuits are marked by white lines. **e**, DFT-relaxed Cu_2O(110)/Cu(110) interface structure used for HRTEM simulations in **d**. **f**, HAADF-STEM image of a typical mismatch dislocation. Scale bar, 1 nm (**a**), 0.5 nm (**c**, **d**, **f**).

Fig. 1a shows a high-resolution transmission electron microscopy (HRTEM) image of a Cu_2O(110)/Cu(110) interface formed from the in-situ oxidation of Cu. The Cu_2O/Cu interface location is marked by the green dashed line in Fig. 1a, showing four mismatch dislocations with both the 7×6 and 8×7 coincidence-site-lattice configurations in which 6 (or 7) Cu spacings in Cu_2O match 7 (or 8) Cu spacings in the Cu substrate. The large natural lattice misfit between Cu and Cu_2O makes the formation of a coherent interface energetically unfavorable, thereby resulting in an array of dislocations to release the misfit strain. This is confirmed from the geometrical phase analysis (GPA) of the HRTEM image, showing concentrated strains around the dislocation core. Fig. 1c is a zoom-in HRTEM image of a typical mismatch dislocation, showing a Burgers vector of $\mathbf{b} = \frac{1}{2}[\bar{1}10]$. This is further confirmed by HRTEM image simulations (Fig. 1d) using the density-functional theory (DFT) optimized Cu_2O(110)/Cu(110) interface structure (Fig. 1e) and by high-angle annular dark-field (HAADF) imaging (Fig. 1f).

The Cu_2O/Cu interfaces serve as a platform to visualize the dynamic action of mismatch dislocations by switching from O_2 to H_2 gas flow to induce the reduction of Cu_2O to Cu. Fig. 2a-d presents in-situ HRTEM images of the $Cu_2O \rightarrow$Cu transformation along the Cu_2O(110)/Cu(110) interface. As indicated by yellow dashed lines in Fig. 2a-d, the Cu_2O/Cu interface is initially flat and is observed to migrate toward the Cu_2O side as the Cu_2O is transformed to metallic Cu along the Cu_2O/Cu interface. The interface is measured to migrate by ~ 1.8 nm toward the Cu_2O side

within a time elapse of 102 s. As indicated by the blue and red arrows in Fig. 2b-c, the $Cu_2O \rightarrow Cu$ transformation occurs via the lateral flow of atomic ledges along the Cu_2O/Cu interface. The epitaxial Cu_2O/Cu interface is maintained through the ledge flow. However, the in-situ TEM observation shows a striking stop-and-go manner of the $Cu_2O \rightarrow Cu$ transformation, by which the lateral propagation of the Cu_2O/Cu interface ledges is regularly interrupted with short pauses that range from 2 s to 6 s, as shown in the distance-time plot (Fig. 2e) of the lateral propagation of ledges 1 and 2 marked in Fig. 2b-c. Meanwhile, the Cu_2O surface undergoes slight decay, as indicated by tracing the temporal evolution of the oxide surface in Fig. 2d.

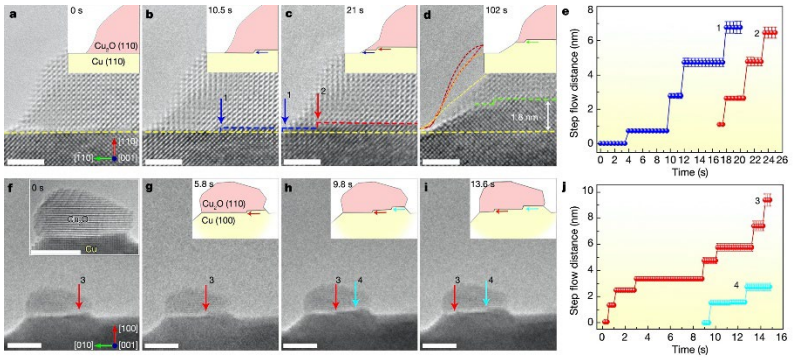

Fig. 2: **In-situ TEM visualization of the stop-and-go ledge flow of the $Cu_2O \rightarrow Cu$ interfacial transformations at 623 K and 5.3 Pa of H_2 gas.** **a-d**, Time-sequence HRTEM images showing the $Cu_2O \rightarrow Cu$ transformation along the $Cu_2O(110)/Cu(110)$ interface. Arrows 1 and 2 mark the Cu_2O/Cu interfacial ledges. **e**, Distance-time plot showing the lateral flow of ledges 1 and 2 in a stop-and-go manner. **f-i**, Time-sequence TEM images showing the $Cu_2O \rightarrow Cu$ transformation along the $Cu_2O(100)/Cu(100)$ interface. Arrows 3 and 4 mark the lateral flow of the Cu_2O/Cu interfacial ledges. **j**, Distance-time plot showing the stop-and-go flow of ledges 3 and 4. Scale bar, 2 nm (**a-d**), 5 nm (**f-i**).

The intermittent interfacial transformation is also observed along the (100) interface. Fig. 2f-i illustrates another example of the $Cu_2O \rightarrow Cu$ transformation, where the in-situ TEM observation is made at a relatively low magnification in order to visualize the entire interface of a small Cu_2O island on Cu(100). The inset HRTEM image in Fig. 2f confirms the (100)-type interface. The $Cu_2O \rightarrow Cu$ transformation occurs via lateral ledge flow along the interface, as indicated by the arrows in Fig. 2f-i. Similarly, the transformation shows the stop-and-go movement of ledges with short pauses, as illustrated in the distance-time plot (Fig. 2j) of the lateral propagation of ledges 3 and 4 marked in Fig. 2f-i.

Future Plans

We will continue in-situ electron microscopy, X-ray spectroscopy and scattering experiments with coordinated modeling to address a number of critical issues:

(i) **Atomic-scale dynamics of gas/oxide interfacial reactions**. Surface-induced breaking of translation symmetry of a crystalline oxide results in various types of coordinately unsaturated cations/anions and surface restructuring that dictate the surface reactivity for a wide range of interfacial phenomena and are crucial to many materials applications such as in catalysis, fuel reactions, and corrosion protection. Yet, identifying the stability, functionality and activity of the coordinated unsaturated sites of gas-oxide interfaces remains challenging owing to their dynamic

behaviors in reacting gas and temperature environments and issues with current characterization tools. We will overcome this challenge by employing environmental TEM to atomically monitor the gas/oxide interfacial reactions by introducing a reactive gas to the sample area while simultaneously probing atomic structural evolution in the outermost surface layer and sub-surface layers of the oxides. Our preliminary in-situ TEM observations show cyclic self-refresh between oxygen-rich and oxygen-deficient surface reconstructions of CuO in H_2 that are chemically active and inactive for H_2O formation, respectively. After a period of chemical inactivity, the oxygen-deficient surface re-oxidizes back to the oxygen-rich termination due to the outward diffusion of lattice oxygen from the subsurface, which thereby results in spatiotemporally separated redox reaction steps at the oxide surface. We will continue the study for potentially manipulating the surface reactivity of oxides by tuning this separation of the redox steps at oxide surfaces.

(ii) **Multi-interfacial migration and transformations**. Redox phase transformations are driven chemically and differ from the conventional theory of phase transformations in solids, where phase transformations are typically driven by physical parameters. The situation becomes even more complex for transition metal oxides, where the redox-induced interconversion of various metal oxidation states results in multiple phase boundaries that separate chemically and structurally distinct oxides and suboxides. How these phase transformations occur in tandem and how the resulting phase boundaries propagate synergistically are fundamentally intriguing and control many industry-relevant processes, including heterogeneous catalysis, electrochemical reactions, and environmental stability of oxide coatings. Our preliminary study showed the capability of in-situ TEM to determine the reaction pathway of CuO→ monoclinic Cu_4O_3 → Cu_2O and identify active interfacial sites at the atomic scale. We will continue the study with more systematic measurements along with DFT modeling of the experimental results.

(iii) **Tuning the chemical activity of oxide overlayers by peroxide species**. Excessively adsorbed oxygen is often present at oxide surfaces in an O_2 atmosphere to result in the oxidation of lattice O into peroxide species that are characterized by relatively short O-O bonding. Using CuO as an example, our recent AP-XPS work showed that peroxide species formed by excessively adsorbed O from gaseous O_2 act as a promotor to significantly enhance CuO reducibility in favor of H_2 oxidation but conversely as an inhibitor to suppress CuO reduction against CO oxidation[4]. This provides direct evidence of the distinct chemical properties between adsorbed O species from gaseous O_2 and lattice O in the catalytic oxidation reactions. We will employ a combination of ambient-pressure X-ray photoelectron spectroscopy and in-situ grazing incidence X-ray diffraction to study the broader applicability of such chemistry in tuning the chemical activity of surface oxide using peroxide species to modify the adsorption properties of coordinatively unsaturated sites. The work will provide mechanistic insights into the effect of gaseous O_2 on the reactivity of oxide catalysts and have practical implications for using adsorbed oxygen to tune the activity of redox sites for catalytic oxidation reactions.

References:

1. J. M. Howe, R. C. Pond, & J. P. Hirth, *The role of disconnections in phase transformations*, Prog. Mater. Sci. **54**, 792 (2009).
2. J. P. Hirth, & T. E. Mitchell, *The role of interface structure in oxidation reactions*, Acta Mater. **56**, 5701 (2008).
3. X. H. Sun, D. X. Wu, L. F. You, S. D. House, X. B. Chen, M. Li, D. N. Zakharov, J. C. Yang, G. W. Zhou, *Dislocation-induced stop-and-go kinetics of interfacial transformations*, Nature **607**, 708 (2022)
4. Y. G. Zhu, J. Y. Wang, S. B. Patel, C. R. Li, A. Head, J. A. Boscoboinik, G. W. Zhou, *Tuning the surface reactivity of oxides by peroxide species*, Proceeding of the National Academy of Sciences **120**, e2215189120 (2023)

Publications in the Last Two Years

1. Y. G. Zhu, J. Y. Wang, S. B. Patel, C. R. Li, A. Head, J. A. Boscoboinik, G. W. Zhou, *Tuning the surface reactivity of oxides by peroxide species*, Proceeding of the National Academy of Sciences **120**, e2215189120 (2023)
2. X. B. Chen, J. Y. Wang, Y. G. Zhu, Z. Xie, S. Ye, K. Kisslinger, S. Hwang, D. Zakharov, G. W. Zhou, *Atomistic Origins of Reversible Noncatalytic Gas-Solid Interfacial Reactions*, Journal of the American Chemical Society **145**, 3961 (2023)
3. X. H. Sun, D. X. Sun, L. F. Zou, S. D. House, X. B. Chen, M. Li, D. N. Zakharov, J. C. Yang, G. W. Zhou, *Misfit-dislocation induced stop-and-go kinetics of interfacial transformations*, Nature **607**, 708 (2022)
4. J. Y. Wang, C. R. Li, Y. G. Zhu, J. A. Boscoboinik, G. W. Zhou, *In-situ Monitoring of H_2-induced Nonstoichiometry in Cu_2O*, Journal of Physical Chemistry Letters **13**, 5597 (2022)
5. D. X. Wu, Y. G. Zhu, W. T. Shan, J. Y. Wang, Q. Liu, G. W. Zhou, "*Revealing an intermediate Cu-O/OH superstructure on Cu(110)*", Journal of Physical Chemistry Letters **13,** 2396 (2022)
6. Y. G. Zhu, D. X. Wu, C. R. Li, X. Tong, J. A. Boscoboinik, J. T. Sadowski, G. W. Zhou, "*Atomistic mechanisms of the initial oxidation of stepped $Cu_3Au(100)$*", Physical Review B **105,** 075422 (2022)
7. X. B. Chen, Z. Y. Liu, D. X. Wu, N. Cai, X. H. Sun, D. N. Zakharov, S. Hwang, D. Su, G. F. Wang, G. W. Zhou, *Passive oxide film growth observed on the atomic scale*, Advanced Materials Interfaces **9**, 2102487 (2022)
8. C. R. Li, Y. G. Zhu, D. X. Wu, J. A. Boscoboinik, G.W. Zhou, "*Effect of surface segregation on the oxidation resistance of Cu3Pt(100)*", Physical Review Materials **6,** 025801 (2022)
9. X. H. Sun, D. X. Wu, W. H. Zhu, X. B. Chen, R. Sharma, J. C. Yang, G. W. Zhou, "*Origin of the Autocatalytic Reduction of Monoclinic CuO in a Hydrogen Atmosphere*", Journal of Physical Chemistry Letters **12**, 9547 (2021)
10. X. Sun, D. Wu, W. Zhu, Y. Zhu, W.A. Saidi, J.A. Boscoboinik, J. C. Yang, R. Sharma, G. W. Zhou**,** *"Atomically visualizing cyclic self-refreshing of gas-oxide interfaces",* Nature Materials (revision and resubmission, 2023)

[1]. Ràfols-Ribé, J., Will, P. A., Hänisch, C., Gonzalez-Silveira, M., Lenk, S., Rodríguez-Viejo, J., and Reineke, S. High-performance organic light-emitting diodes comprising ultrastable glass layers. *Sci. Adv.*, 4, eaar8332 (2018).

[1]. Bangsund, J. S., Van Sambeek, J. R., Concannon, N. M., and Holmes, R. J. Sub-turn-on exciton quenching due to molecular orientation and polarization in organic light-emitting devices. *Sci. Adv.* 6, eabb2659 (2020).

[1]. Cheng, S., Lee, Y., Yu, J., Yu, L., and Ediger, M. D. Surface equilibration mechanism controls the stability of a model co-deposited glass mixture of organic semiconductors. *J. Phys. Chem. Lett.* 14, 4297-4303 (2023).

[1]. Ferron, T. J., Fiori, M. E., Ediger, M. D., DeLongchamp, D. M., and Sunday, D. F. Molecular Orientation of Birefringent Organic Glasses at Heterointerfaces. *JACS Au.* 2023 (submitted).

Publications supported by DOE BES

1. Cheng, S., Lee, Y., Yu, J., Yu, L., and Ediger, M. D. Surface equilibration mechanism controls the stability of a model co-deposited glass mixture of organic semiconductors. *J. Phys. Chem. Lett.* 14, 4297-4303 (2023).

2. Ferron, T. J., Thelen, J. L., Bagchi, K., Deng, C., Gann, E., de Pablo, J. J., Ediger, M. D., Sunday, D. F., and DeLongchamp, D. M. Characterization of the interfacial orientation and molecular conformation in a glass-forming organic semiconductor. *ACS Appl. Mater. Interfaces* 14, 2, 3455 (2022).

3. Fiori, M. E., Bagchi, K., Toney, M. F., and Ediger, M. D. Surface equilibration mechanism controls the molecular packing of glassy molecular semiconductors at organic interfaces. *Proc. Natl. Acad. Sci. U.S.A.* 118, e2111988118 (2021).

4. Bagchi, K., Fiori, M. E., Bishop, C., Toney, M. F., and Ediger, M. D. Stable Glasses of Organic Semiconductor Resist Crystallization. *J. Phys. Chem. B* 125, 461-466 (2021).

Author
Index

Participant

List

First Name	Last Name	Institution
Amin	Ahmadisharaf	Kansas State University
Lynden	Archer	Cornell University
Michael	Arnold	University of Wisconsin, Madison
Scott	Auerbach	University of Massachusetts, Amherst
Stacey	Bent	Stanford University
Mariana	Bertoni	Arizona State University
Ksenia	Bets	Rice University
Ivan	Bozovic	Brookhaven National Laboratory
Claudia	Cantoni	U.S. Department of Energy
Gerbrand	Ceder	Lawrence Berkeley National Laboratory
Julia	Chan	Baylor University
Lei	Cheng	Oak Ridge National Laboratory
Zhe	Cheng	Florida International University
Paulette	Clancy	Johns Hopkins University
Amy	Clarke	Colorado School of Mines
Jeffrey	Comer	Kansas State University

Ryan	Comes	Auburn University
Paul	Crowell	University of Minnesota
Joshua	Damron	Oak Ridge National Laboratory
James	De Yoreo	Pacific Northwest National Laboratory
Volkmar	Dierolf	Lehigh University
James	Dorman	U.S. Department of Energy
Yingge	Du	Pacific Northwest National Laboratory
Mark	Ediger	University of Wisconsin, Madison
Anter	El-Azab	Purdue University
James	Engstrom	Cornell University
Chang-Beom	Eom	University of Wisconsin, Madison
Wei	Fan	University of Massachusetts, Amherst
Andrei	Fedorov	Georgia Institute of Technology
Kristen	Fichthorn	Pennsylvania State University
Michael	Fitzsimmons	U.S. Department of Energy
Tim	Fitzsimmons	U.S. Department of Energy
Sergey	Frolov	University of Pittsburgh
Nicolas	Gaillard	University of Hawaii

Aura	Gimm	U.S. Department of Energy
Rachel	Goldman	University of Michigan
Matthias	Graf	U.S. Department of Energy
Sumner	Harris	Oak Ridge National Laboratory
Ryan	Hartman	New York University
Rigoberto	Hernandez	Johns Hopkins University
Jennifer	Hoffman	Harvard University
Jinwoo	Hwang	Ohio State University
Himanshu	Jain	Lehigh University
Bharat	Jalan	University of Minnesota
Rongying	Jin	University of South Carolina
David	Johnson	University of Oregon
Alain	Karma	Northeastern University
Tiffany	Kaspar	Pacific Northwest National Laboratory
Jason	Kawasaki	University of Wisconsin, Madison
Logan	Kearney	Oak Ridge National Laboratory
Carolyn	Koh	Colorado School of Mines
Maik	Lang	University of Tennessee

Benjamin	Legg	Pacific Northwest National Laboratory
Mo	Li	Georgia Institute of Technology
Dongsheng	Li	Pacific Northwest National Laboratory
Rebecca	Lindsey	University of Michigan, Ann Arbor
Xi	Ling	Boston University
Jun	Liu	Pacific Northwest National Laboratory/University of Washington
Bin	Liu	Kansas State University
Zhiqiang	Mao	Pennsylvania State University
Michael	Markowitz	U.S. Department of Energy
John	Marohn	Cornell University
Noa	Marom	Carnegie Mellon University
Alex	Martinson	Argonne National Laboratory
Claudia	Mewes	U.S. Department of Energy
Tim	Mewes	U.S. Department of Energy
Raul	Miranda	U.S. Department of Energy
Atieh	Moridi	Cornell University
Julia	Mundy	Harvard University
Badri	Narayanan	University of Louisville

Amit	Naskar	Oak Ridge National Laboratory
Eric	O'Quinn	University of Tennessee
Eugene	Olevsky	San Diego State University
Jeremy	Palmer	University of Houston
Chris	Palmstrom	University of California, Santa Barbara
Michelle	Personick	Wesleyan University
Vlad	Pribiag	University of Minnesota
Jeffrey	Rimer	University of Houston
Jennifer	Roizen	U.S. Department of Energy
Yavuz	Savsatli	Rice University
Linda	Schadler Feist	University of Vermont
Viviane	Schwartz	U.S. Department of Energy
Gurjyot	Sethi	Univeristy of Utah
Ashwin	Shahani	University of Michigan
Lior	Shani	University of Minnesota
William	Shelton	Louisiana State University
Elizabeth	Sooby	University of Texas, San Antonio
Wenhao	Sun	University of Michigan, Ann Arbor

Jianwei	Sun	Tulane University
Peter	Sushko	Pacific Northwest National Laboratory
Maria	Sushko	Pacific Northwest National Laboratory
Ming	Tang	Rice University
Jinhui	Tao	Pacific Northwest National Laboratory
Andre	Taylor	New York University
Michael	Tringides	Ames National Laboratory/Iowa State University
Lauren	Walters	Lawrence Berkeley National Laboratory
Qiang	Wang	Colorado State University
Xudong	Wang	University of Wisconsin, Madison
Haiyan	Wang	Purdue University
Le	Wang	Pacific Northwest National Laboratory
Hui	Wang	University of Louisville
Michael	Whittaker	Lawrence Berkeley National Laboratory
Lane	Wilson	U.S. Department of Energy
Kai	Xiao	Oak Ridge National Laboratory
Wenwu	Xu	San Diego State University
Boris	Yakobson	Rice University

Shuolong	Yang	University of Chicago
Judith	Yang	University of Pittsburgh
Liping	Yu	University of Maine
Francisco	Zaera	University of California
Yan	Zeng	Lawrence Berkeley National Laboratory
Xiaoqi	Zheng	University of Wisconsin, Madison
Guangwen	Zhou	Binghamton University